A STUDY OF THE HIGH TEMPERATURE SUPERCONDUCTOR $YBA_2CU_3O_{7-\delta}$ AND ITS COBALT-DOPED DERIVATIVE

Wendy J. Webster

A Thesis Submitted for the Degree of PhD
at the
University of St Andrews

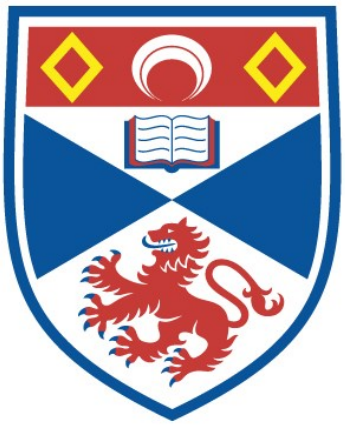

1994

A Study of the High Temperature Superconductor, $YBa_2Cu_3O_{7-\delta}$ & Its Cobalt-Doped Derivative.

A thesis presented

by

Wendy J. Webster BSc.(Hons)

to

The University of St Andrews

in Application for the Degree of

Doctor of Philosophy.

May 1993

ProQuest LLC.
789 East Eisenhower Parkway
P.O. Box 1346
Ann Arbor, MI 48106 – 1346

TL
B424

Abstract

Static nuclear magnetic resonance (NMR) techniques have been used to study the magnetic hyperfine interactions of ^{63}Cu and ^{89}Y nuclei in the superconducting (T=1.5K) and normal (T=160-300K) states of the pure and cobalt doped Y-Ba-Cu-O layered cuprate systems. Sample quality and physical characteristics are well supported by magnetic susceptibility, Hall effect and X-ray diffraction measurements.

We report ^{63}Cu NMR spin echo experiments, performed at 1.5K and 141MHz, on a uniaxially aligned sample of undoped $YBa_2Cu_3O_7$. By working at such low temperatures T, we provide clear confirmation that the spin components of the ^{63}Cu Knight shift, at both crystallographic sites and in all directions, vanish as $T\rightarrow 0$, leaving the orbital shift as the residual shift. This is indicative of singlet spin pairing in the superconducting state. The size and anisotropy of the $^{63}Cu(1,2)$ orbital shifts are consistent with a localised moment model in which there is a single hole of $d_{x^2-y^2}$ ($d_{y^2-z^2}$) symmetry in the d-shell shell of the Cu(2) (Cu(1)) ion. By working at high fields, where the demagnetisation corrections are much smaller, we are able to conclude that the disparity in the $K^c_{orb}(1,2)$ results from previous studies can be traced directly to discrepancies in the demagnetisation corrections, while inconsistencies in the $K^{a,b}_{orb}(1,2)$ components result from difficulties in analysing the restricted powder pattern.

The effects of the atomic substitution of Co into the $YBa_2(Cu_{1-x}M_x)_3O_{6.9}$ ($0\leq x\leq 0.04$) system have been investigated via an integrated ^{89}Y and ^{63}Cu NMR study on aligned powders. Combined susceptibility, X-ray and NMR measurements indicate that the Co ion substitutes preferentially at the Cu(1) site and bears a magnetic moment of around $3.7\mu_B$, consistent with a Co^{3+} localised moment of intermediate spin state (s=1). Theoretical modelling of the dipolar fields induced by such a moment suggest that the ^{89}Y and $^{63}Cu(2)$ NMR shifts and linewidths cannot be explained by a dipolar mechanism alone. The T_c of the system is found to plateau at ~92K for x%<2.8, but then falls rapidly. This change in T_c is found to coincide with a macroscopic orthorhombic (O) to tetragonal (T) structural transition at x=2.8%. The presence of a true $O\rightarrow T$ transition is also supported by changes in the ^{89}Y chemical shift. Falling hole concentration with increasing x indicates that T_c is not determined by the planes hole concentration alone. Correlations between the ^{89}Y Knight shift and T_c, and between ^{89}Y magnetic shifts for Co doped and oxygen depleted samples with the same T_c, suggest that decreases in T_c result from a reduction of the DOS at the Fermi level and that the mechanism responsible for T-dependent behaviour in both systems may be the same and directly related to T_c.

The complete devastation observed in the low temperature c//B $^{63}Cu(2)$ spectra for x%>0.5 is consistent with strong inhomogeneity in the Van Vleck component of the planes susceptibility. Finally, correlations between the ^{89}Y and $^{63}Cu(2)$ Knight shifts provide strong evidence in favour of a single quantum spin fluid.

Declaration

I, Wendy J. Webster, hereby certify that this thesis has been composed by myself, that it is a record of my own work and that it has not been accepted in partial or complete fulfilment of any other degree or professional qualification.

I was admitted to the Faculty of Science of the University of St Andrews under Ordinance General no.12 during October 1988, and as a candidate for the degree of Doctor of Philosophy during October 1989.

In submitting this thesis to the University of St Andrews, I understand that I am giving permission for it to be made available for use in accordance with the regulations of the university library for the time being enforced, subject to any copyright vested in the work not being affected thereby. I also understand that the title and abstract will be published, and that a copy of the work may be made and supplied to any bona fide library or research worker.

W. J. Webster

Certificate

I hereby certify that Wendy J. Webster has spent nine terms undertaking research work in the J. F. Allen Physical Sciences Laboratory of St Salvator's College, at the University of St Andrews, under my direction. She has fulfilled the conditions of Ordinance No. 16 (St Andrews) and she is qualified to submit the following thesis in application for the degree of Doctor of Philosophy.

Dr D.P.Tunstall
Research Supervisor

This thesis is dedicated to

my family and friends,

for their continuous support and encouragement.

For Jennifer & Sandy,

who had faith when

no-one else knew that it was needed.

'Happiness makes living easier,

but unhappiness offers us the chance to grow beyond ourselves'

Margaret Baker.
'Love Unveiled', Norwich, 1981

Acknowledgements

I would like to thank my supervisor, Dr. David Tunstall, for his guidance and encouragement during my time at the University of St Andrews. I would also like to extend my thanks to the staff and research students of the Department of Physics & Astronomy for the excellent facillities made available to me and for the constant support and good humour, which made this research so enjoyable. I am particularly indebted to Dr. Philip Mason for the many helpful discussions on all things cryogenic, and for his advice and assistance with the computer programming. Thanks are due also to Dr. Myriam Solanki-Moser for her extensive calculations of the exact Hamiltonian and for the many patient explanations and fruitful discussions. Two of my fellow research students, Guangping Dai and Heather Booth, provided invaluable assistance with the experimental work towards the end of the project, for which, I am very grateful. The use of the Bruker MSL-500 spectrometer was made considerably easier by Dr. Sam Arumagum, who freely imparted his expert knowledge of this machine on numerous occassions.

I would like to acknowledge the technical assistance of the support services within the department, without whom much less might have been achieved. In particular, I would like to thank the cryogenics staff, Reg Gavine and Andy Barman for supplying copious amounts of liquid helium and nitrogen and also Bob Mitchell for servicing the high field magnets. In addition, thanks go to Jim Clarke of the engineering workshop who constructed many of the NMR probes, to Fritz Akerboom who produced much of the specialist glassware and to the electronics workshop as a whole, who provided the electronic wizardry.

High temperature superconductivity is, by its very nature, an interdisciplinary subject. It is for this reason that not only other departments within this university were involved in this study, but also various departments in other institutions. I would particularly like to thank Dr. John Irvine and Prof. Anthony West at the University of Aberdeen for supplying the pure $YBa_2Cu_3O_{7-\delta}$ 'Aberdeen' sample and Pam Freeman of the Interdiscplinary Research Centre (IRC) in Superconductivity at the University of Cambridge for synthesizing all of the Co doped Y-Ba-Cu-O samples. I am grateful to Prof. Peter Edwards (now of the University of Birmingham, but formally of the IRC, Cambridge) for forging our initial link with the IRC and to Dr. John Cooper (IRC) who performed the early characterisation experiments on the Co-doped samples. Further characterisation of samples was carried out with the cooperation of the Department of Geology and the Gatty Marine Laboratory at St. Andrews. With this in mind, I wish to extend my appreciation to Angus Calder and Donald Herd (Geology) for their assistance with the X-ray diffraction measurements and scanning electron microscopy, respectively.

Many thanks also go to Irvine Davidson (Gatty) for his guidance in SEM and microprobe analysis and for trusting me with his high resolution microscope.

I am indebted to the Science and Engineering Research Council (SERC) for their financial support and to both SERC and the University of St Andrews for providing me with the funds to attend the M^2S-HTSC-III International Superconductivity conference held in Kanazawa, Japan during my final year.

Finally, I would like to thank my family and friends for always being there and providing so much support. Special thanks go to my long suffering flatmates, Sandy, Jennifer and Paula who, for many months now, have listened to me talk of nothing but thesis! I cannot thank you enough for giving me so much of your time, understanding and encouragement.

The text in this thesis has been word processed on an Apple Macintosh™ computer using Microsoft WORD 4.0™, Times 12 font. Unless otherwise stated, all graphical plots contained in this work were created with the use of Abelbeck KaleidaGraph™ V.2.1.3 software. This graphics package was also used to perform some of the data analysis. The diagrams were patiently constructed using Silicon Beach SuperPaint™ v2.0a software.

Contents

Summary

Chapter 1 presents a summary of the historical development of superconductivity, from its discovery in conventional metals and alloys to its rediscovery at much higher temperatures in the new copper oxide ceramics. The fundamental magnetic and electronic properties common to all hole-doped layered cuprates are then detailed along with a brief introduction to the current theoretical models. Finally, the basic concepts which make nuclear magnetic resonance such a useful tool with which to study superconductivity are presented.

Chapter 2 focusses on the physical and chemical characteristics of the pure and doped Y-Ba-Cu-O systems, with particular reference to the cobalt-doped material, while chapter 3 reviews the necessary NMR background theory. In addition, the final sections of chapter 3 present an overview of the Knight shift information recently obtained from ^{89}Y and ^{63}Cu NMR studies on the $YBa_2Cu_3O_{7-\delta}$ material.

All aspects of the experimental work are described in chapter 4. As well as including a detailed investigation of powder alignment (via X-ray diffraction and scanning electron microscopy analytical methods), chapter 4 also introduces the pulsed NMR techniques and spectrometers used during this work.

The following two chapters contain the results of our experimental studies on uniaxially aligned powders. Firstly, chapter 5 presents the findings of the low temperature (T=1.5K) ^{63}Cu NMR investigation on the pure Y-Ba-Cu-O (Aberdeen) system. The orbital components of the Knight shift are calculated directly from the experimental results via exact diagonalisation of the Hamiltonian, while the spin components are deduced by comparison with existing normal state studies. The detailed sample characterisations (involving T_c, crystallographic, magnetic susceptibility and Hall effect measurements), which were performed on a series of Co-doped Y-Ba-Cu-O samples, are then presented in chapter 6 - along with a variable temperature study of the normal state ^{89}Y magnetic shift as a function of Co concentration. Chapter 6 also reports the room and low temperature ^{63}Cu NMR results taken on the Co-doped system at high fields.

With the help of some computer modelling, the size and effects of the dipolar fields introduced into the Y-Ba-Cu-O system via the chemical substitution of cobalt are addressed in the penultimate chapter.

Finally, chapter 8 presents the conclusions distilled from this research and provides suggestions for further work.

Chapter 1

Introduction

1.1 Historical Perspective

1.1.1 Conventional Superconductivity

The phenomenon of superconductivity is surely one of the most unusual and spectacular in solid state physics today. The remarkable combination of electric and magnetic properties, which appear when certain materials are cooled to low temperatures (~4K), was discovered in 1911 by Heike Kamerlingh Onnes[1] (University of Leiden), soon after he first liquified helium[2]. Onnes found that, at some sharply defined 'critical' (or 'transition') temperature T_c, the resistivity of a number of pure metals fell abruptly from a finite value to zero. The 'normal' state resistivity ($T>T_c$) appeared to be characteristic of a normal metal ($\rho(T)=\rho_0+BT^5$), but in the temperature region extending below T_c, the metal entered a resistanceless 'superconducting' state, which was later found to be an intrinsic property of the metal and independent of sample purity.

By 1914, Onnes had observed[3] that superconductivity could be destroyed by applying an external magnetic field equal to or greater than some 'critical field', $H_c(T)$. Furthermore, the superconductivity of a wire carrying a current could be quenched[4] when the current reached a critical value, J_c. As Silsbee[5] later pointed out, for sufficiently thick samples (where surface effects can be ignored), the critical current is merely that current value which creates a field equal to $H_c(T)$ at the surface of the superconductor.

In these early years, it became evident that superconductivity occured within a surface passing through T_c, $H_c(T)$, and J_c - and that outside the surface a sample reverted back to its 'normal' state electrical resistivity.

For over twenty years after the discovery of superconductivity, the phenomenon was thought to be essentially the manifestation of zero resistance. However, in 1933, W. Meissner and R. Ochsenfeld discovered that a sample which was cooled in a magnetic

---

1 H. K. Onnes, *Leiden Comm.* **119b, 120b, 122b, 124c** (1911)

2 H. K. Onnes, *Proc. Acad. Sci. Amst.* **11** 168 (1908)

3 H. K. Onnes, *Leiden Comm.* **139f** (1913)

4 H. K. Onnes, *Leiden Comm.* **133d** & **suppl. no. 34** (1913)

5 F. B. Silsbee, *J. Wash. Acad. Sci.* **6** 597 (1916)

field of less than $H_c(T)$, spontaneously expelled the field as soon as the specimen became superconducting[6]. Independent of whether the external field was applied above or below the transition, the superconductor behaved as a perfect diamagnet. Induced surface screening currents, just sufficient to create an opposing internal field of the correct value, invoke a resultant field of zero in the sample and so, unlike perfect conductors, a material in the superconducting state *never* allows magnetic flux to exist inside its interior.

As a consequence of the 'Meissner-Ochsenfeld effect', currents can only flow on the surface of a superconductor and cannot pass through the body of it. Maxwell's equation, curl $\mathbf{B}=\mu_0 \mathbf{J}$, dictates that if $\mathbf{B}=0$ inside the superconductor, then $\mathbf{J}=0$ also†. It is, however, physically impossible to have current confined entirely to a surface, as this implies no thickness. In practice, the currents flow in a thin surface layer, which has a thickness of the order of 10^{-5}cm, known as the 'penetration depth' (λ). Consequently, the applied magnetic field does not abruptly drop to zero at the surface of the superconductor, but diminishes gradually within the penetration depth, where the screening currents are flowing.

Superconductors are grouped into two categories according to the way in which the transition from the superconducting state to the normal state proceeds when an applied field exceeds $H_c(T)$. 'Type I' or 'soft' materials exhibit perfect diamagnetism below $H_c(T)$, but as the applied field approaches $H_c(T)$, the entire specimen enters the normal state practically instantaneously (figure 1.1(a)). In 'type II' or 'hard' materials, the transition to a completely normal state happens gradually. The penetration of flux is characterised by a lower critical field $H_{c1}(T)$, below which flux is completely expelled, and an upper critical field*, $H_{c2}(T)$, above which the flux penetrates perfectly (figure 1.1(a)). Between $H_{c1}(T)$ and $H_{c2}(T)$, there is a partial penetration of flux, with the microscopic structure of the sample having filamentary normal and superconducting regions. This state is known as the 'mixed', 'intermediate' or 'vortex' state and has been studied in detail by A. A. Abrikosov[7]. Figure 1.1(b) shows the corresponding B-field curves for both type I and type II superconducuctors.

Generally, type I behaviour is typical of almost all elements, whereas type II behaviour is characteristic of most alloys (and also elements Tc, V and Nb). The H_c for type I is typically 0.01 Tesla, and the H_{c2} in the type II superconductors can be as high as 22 Tesla (where 1 Tesla (T) = 10^4 Gauss (G)). Commercial solenoids wound from type II superconductors produce steady high fields in the region of 10T or more.

---

6 W. Meissner & R. Ochsenfeld, *Naturwissenschaften* **21** 787 (1933)

† This rule applies to transport currents as well as diamagnetic screening currents.

* where $H_{c2}(T)>H_{c1}(T)$

7 A. A. Abrikosov, *Sov. Phys. JETP* **5** 1174 (1957)

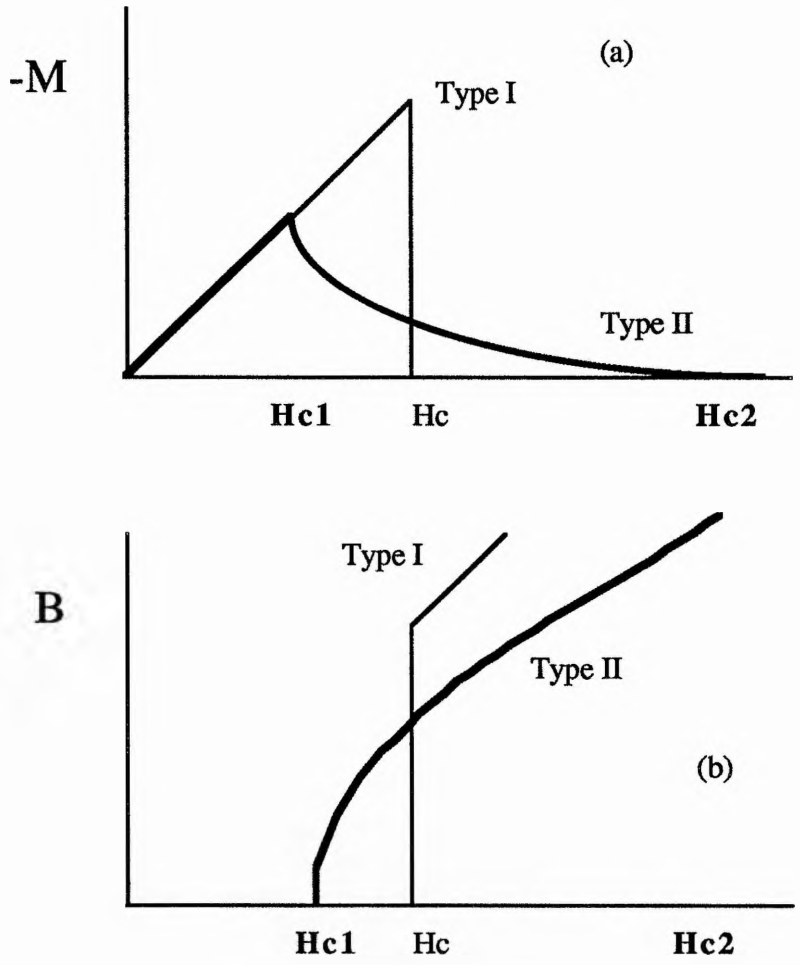

Figure 1.1

(a) The Magnetisation and (b) the B-field Curves for Type I and Type II Superconductors

The transition from the normal to superconducting state is a virtually perfect 'second-order' transition*. No latent heat transformation is associated with the phase transition and there is an anomalous discontinuity in the electronic component of the specific heat. Figure 1.2 shows the low temperature specific heat of normal (C_n) and superconducting (C_s) gallium. The behaviour can be described by equations (1.1) and (1.2),

$$C_n = C_n^{el} + C_n^{lat} = \gamma T + A\left(\frac{T}{\theta_D}\right)^3 \qquad (1.1)$$

$$C_s = C_s^{el} + C_s^{lat} = a\exp\left(\frac{-\Delta}{k_B T}\right) + A\left(\frac{T}{\theta_D}\right)^3 \qquad (1.2)$$

---

* Note that in the presence of a magnetic field, the normal to superconducting phase transition is *first order*, i.e. there is latent heat involved.

where a and Δ are constants, γ and k_B are the Sommerfield and Boltzmann constants respectively, θ_D is the Debye temperature and A is a numerical constant with the same value for all metals. The cubic term is the Debye term, arising from the lattice vibrations, and the linear term represents the electronic excitations, i.e the temperature dependence of the energy for a Fermi electron gas.

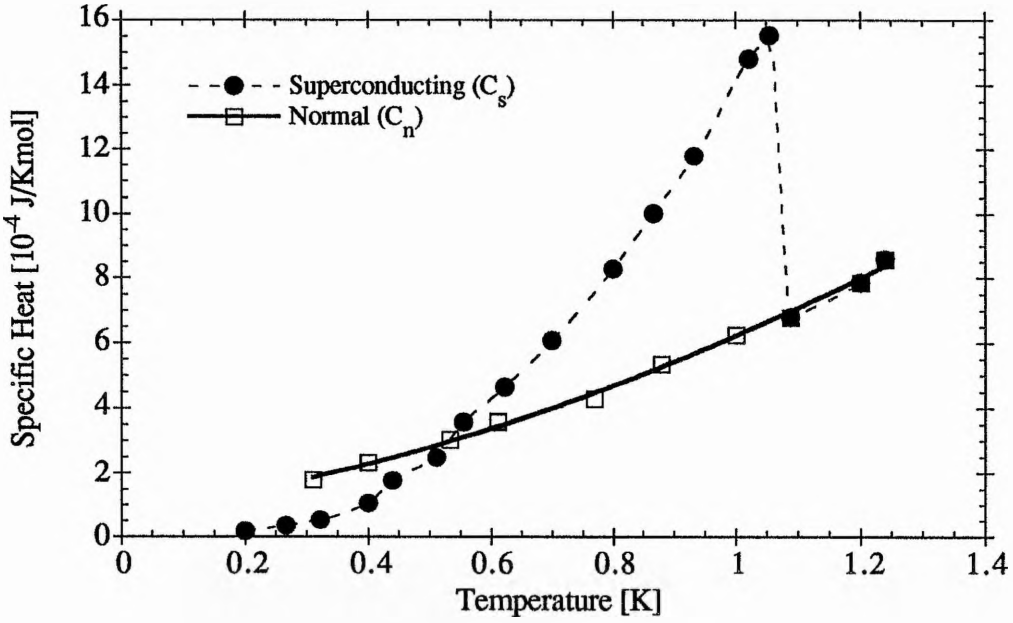

Figure 1.2

Temperature dependence of the specific heat of normal and superconducting gallium[8].

An analysis of the normal and superconducting behaviour indicates that the contribution from the phonons is unchanged† and that the electronic term is much more strongly temperature-dependent in the superconducting state (see Eq 1.2). Such an exponential variation is indicative of the existence of a finite gap in the energy spectrum of the electrons, separating (by Δ) the ground state from the lowest excited state. Indeed, both theory and experiment support this idea and indicate that the energy gap is of the order of $k_B T_c$.[9,10] In some cases, 'gapless' superconductivity can occur if there is a very low

---

8 Data taken from N. E. Phillips, *Phys. Rev.* **134** 385 (1964): the normal phase below T_c is produced by applying a 0.02 Tesla magnetic field, which destroys the superconductivity, but is assumed to have a negligible effect on the specific heat.

† generally assumed because there are no changes in lattice parameters and only very small differences in the elastic properties.

9 A comprehensive review of early experiments which distinctly indicate the presence of an energy gap is given by D. H. Douglass, Jnr and L. M. Falicov, *Progress in Low Temp Phys.* Vol IV: ed, C. J. Gorter, New York, Interscience (1964).

density of states over a certain energy range, as opposed to a total absence of energy states.

Since the discovery of superconductivity, there has been a quest to find new materials with even higher transition temperatures. An initial scanning of the pure metals led to the discovery of a total of 26 superconducting metals with transition temperatures ranging from 0.01K in tungsten to 9.3K in niobium. Further work on alloys and compounds produced more superconductors by the thousand[11]. Up until 1986, the highest confirmed T_c of any superconductor was 23.3K, observed by L.R. Testardi et al[12] in spluttered films of Nb_3Ge. Many attempts to raise the T_c still further, failed[13].

1.1.2 Established Theory

The macroscopic and microscopic characteristics of conventional superconductors have been the subject of numerous phenomenological theories*. Many of the properties can be explained if it is supposed that, below the transition temperature, the conduction electrons separate into two groups, with some behaving as super-electrons (superfluid) able to pass through the superconductor without collisions, and the remainder (normal fluid) acting as normal conduction electrons would in a metal.

One of the first detailed treatments of the superconducting state was by Gorter and Casimir[14], who formulated a 'two fluid model' based on thermodynamic arguments. By assuming that the superconducting phase transition was completely analogous to any other phase transition, they concluded that at temperatures below T_c, the entropy of the superconducting phase was lower than that of the normal phase, and so of a higher order than it. Their arguments also provided a satisfactory explanation for the parabolic temperature dependence of the critical field, proposed by Tuyn[15] several years earlier.

Gorter and Casimir's work was swiftly followed by a phenomenological theory of the macroscopic electromagnetic behaviour of a superconductor, developed by Fritz and

---

10 I. Giaver, *Phys. Rev. Lett.* **5** 147 (1960)

11 B. W. Roberts, *Superconductive Materials And Some of Their Properties,* NBS Technical Note **408** (1966)

12 L. R. Testardi, J. H. Wernick & W. A. Royer, *Solid State Comm.* **15** 1 (1974)

13 A review of the state of superconductivity at this time and on the possibility of high temperature superconductivity is given in, B. T. Matthias, *Physics Today,* p 23 August 1971

* A phenomenological theory is one where an arbitrary postulate is made in order to fit the facts.

14 C. J. Gorter & H. B. G. Casimir, *Physica* **1** 306 (1934)

15 W. Tuyn, *Leiden Comm.* **191b** (1928)

Hans London[16]. The London analysis is based on a 'two-fluid' concept, which hinges on the crucial assumption that, at $T<T_c$, only a fraction $n_s(T)/n$ (where $n_s(T)$ is the superfluid density) of the conduction electrons (n) are capable of participating in a supercurrent. Such a theory predicts that below T_c, no electric field exists within a superconductor, unless the supercurrent is changing with time. The solutions to the London equations imply that a magnetic field vanishes in the bulk of a superconductor, decaying from the surface within a characteristic length known as the 'London penetration depth' (λ_L). In postulating their equations, the London brothers added the important restriction that $\mathbf{B}=0$ inside the superconductor, regardless of its history[17]. This is the fundamental property of the Meissner-Ochsenfeld effect.

Up until the early 1950's, the successful and complementary two-fluid 'local' models† of Gorter & Casimir and the Londons provided useful tools in the semi-quantitative analysis of a number of problems involving superconductors*. However in 1953, after much experimentation, A. B. Pippard[18] concluded that the London equations should be replaced by a non-local theory.

From experiments done on dilute alloys of indium and tin, Pippard found that the penetration depth began to increase substantially when impurities were introduced which lowered the normal electronic mean free path ℓ, below a certain distance. Pippard postulated that the effect only became apparent when ℓ fell below a distance ξ_P, now known as the 'Pippard coherence length'. He suggested that the superconducting state was one of long range order which extended over this distance ξ_P ($\sim 10^{-4}$ cm)[19].

In 1950, V. L. Ginzburg and L. D. Landau[20] used a alternative phenomenological approach to describe the superconducting to normal phase transition in zero field. Their work later moved away from the purely classical workings of London to predict the effect of a magnetic field in terms of a complex order parameter ϕ, using quantum mechanics. Central to the Ginzburg-Landau theory is the fundamental length $\xi_{GL}(T)$, which is defined

---

16 F. London & H. London, *Proc. Royal Soc.* (London) **A149 71** (1935): *Physica* **2** 341 (1935): F. London, *Superfluids*, vol 1: Wiley, New York (1954).

17 See A. C. Rose-Innes & E. H. Roderick, *Introduction to Superconductivity*, chapter 3, Pergamon Press, 1st edn. (1969)

† i.e. they relate the current density at a point **r** to the electromagnetic potential at the *same* point

* Except in situations when size and surface effects are important.

18 A. B. Pippard, *Proc. Royal Soc.* **A203** 210 (1950): *Proc. Royal Soc.* **A216** 547 (1953)

19 See 'Superconductivity' by M. Tinkham in *Low Temperature Physics*, ed. by C. DeWitt, B. Dreyfus & P. G. de Gennes, Gordon & Breach Publishers, New York (1962).

20 V. L. Ginzburg & L.D. Landau, *Sov. Phys. J.E.T.P.* **20** 1064 (1950)

as the coherence length for variations of the magnitude of ϕ. The Ginzburg-Landau parameter κ, is also defined by the theory,

$$\kappa = \frac{\lambda}{\xi} \tag{1.3}$$

where $\kappa < 1/\sqrt{2}$ for type I superconductors and $\kappa > 1/\sqrt{2}$ for type II materials. Within the structure of the Ginzburg-Landau theory, κ is taken to be independent of temperature, implying that lengths $\lambda(T)$ and $\xi(T)$ have very similar temperature dependences.

The present form of the Ginzburg-Landau theory is now referred to as GLAG theory. Abrikosov[21] (1957) extended the theory in some detail to explain the magnetic behaviour of type II superconductors and Gor'kov[22] (1959) reformulated the equations starting from the microscopic theory. Gor'kov's development has meant that GLAG theory can now be extended to a wider temperature range than the original theory allowed[23].

Theories so far had described superconductivity from a purely macroscopic view point, but in 1950, Herbert Fröhlich[24] initiated a theory which was microscopic in nature. He proposed that electron-phonon interactions were crucial to superconductivity, and suggested that, for an isotope of a given element, T_c should be proportional to the Debye temperature, θ_D. Elsewhere, this notion was being verified experimentally by two independent groups led by Maxwell[25] and Reynolds[26]. They deduced that,

$$T_c M^a = \text{constant} \tag{1.4}$$

where M is the isotopic mass and a is an experimentally determined constant found to be approximately 1/2, in most cases[27]. The result in (1.4) is now a fundamental property of superconductivity, known as the 'isotope effect'. It demonstrates that the atomic lattice plays an important role in determining the behaviour of the conduction electrons in a superconductor.

---

21 See ref. 7 and also, D. R. Tilley & J. Tilley, *Superfluidity and Superconductivity*, p312, 3rd edn., Adam Hilger Publishers (1990).

22 L. P. Gor'kov, *Sov. Phys. J.E.T.P* **9** 1364 (1959)

23 A detailed examination can be found in P. G. de Gennes, *Superconductivity of Metals and Alloys*, chapter 6 and 7, W. A. Benjamin Inc, New York (1966)

24 H. Fröhlich, *Phys. Rev.* **79** 845 (1950)

25 E. Maxwell, *Phys. Rev.* **78** 477 (1950)

26 C. A. Reynolds, B. Serin, W. H. Wright & L. B. Nesbitt, *Phys. Rev.* **78** 487 (1950)

27 For numerical values of a, see E. A. Lynton, *Superconductivity*, pp 93, Chapman & Hall (1969).

It was not until 1956, when a study by Leon Cooper[28] suggested that an electron-phonon-electron interaction in the superconducting state could produce a net attractive force between two electrons, that the microscopic theory of superconductivity really began to take shape. Cooper proposed that under an apparent attractive force, the electrons would couple forming a stable bound state, known as a Cooper pair.

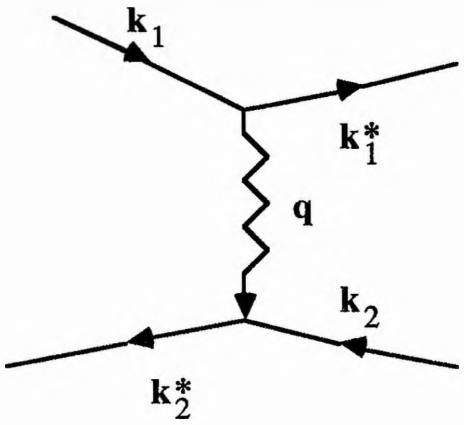

Figure 1.3

Phonon exchange between electrons. The initial and final wave vectors for the first and second electron are represented by $\mathbf{k}_1$ and $\mathbf{k}_1^*$, and $\mathbf{k}_2$ and $\mathbf{k}_2^*$, respectively, and the virtual phonon wave vector is denoted by $\mathbf{q}$.

Such a pairing interaction (represented by a Feynman diagram in figure 1.3) would undoubtedly be extremely weak for 2 electrons in isolation; however, Cooper showed that in the presence of a Fermi sphere of additional electrons, a pair of electrons acting via an attractive potential (-V) and confined to states within an energy $\hbar\omega$ just above the Fermi surface, could form a bound state† - *no matter how weak* the attractive interaction was.

By 1957, Leon Cooper in partnership with John Bardeen and J. Robert Schrieffer, had produced a classic set of papers[29] which now form the basis of our current understanding of the microscopic quantum theory of conventional superconductivity. The

---

28 L. N. Cooper, *Phys. Rev.* **104** 1189 (1956)

† where $\hbar\omega$ is of the order of the average phonon energy of the metal and where the sea of electrons within the Fermi surface is not influenced by the potential V.

29 J. Bardeen, L. N. Cooper & J. R. Schrieffer, *Phys. Rev.* **106** 162 (1957): *Phys. Rev.* **108** 1175 (1957)

BCS theory, as it known, is quite complex and involves advanced quantum mechanical treatments, which will not be detailed here.[19,30]

Extending Cooper's two electron model, the BCS theory proposed that there was a highly correlated ground state at absolute zero and zero current, where the electron states near to the Fermi surface were fully occupied with pairs of electrons of opposite spin and wave vector $(+\mathbf{k}_1\uparrow,-\mathbf{k}_1\downarrow)^*$. A pair had zero momentum, implying that the state was not current carrying. Above absolute zero, some electrons would be excited across the energy gap, thus breaking the Cooper pair. At T_c, the thermal energy would be sufficient to break up all pairs and the superconducting state would cease to exist.

Many of the theoretical predictions of BCS have been confirmed by experiment. Most importantly, the BCS theory predicts that at absolute zero, the energy gap is,

$$\Delta(0) \approx 3.5\, k_B T_c \qquad (1.5)$$

This fundamental result is independent of the phenomenological parameters, and appears to hold for a large number of superconductors to within about 10%[31]. The observation of a fundamental flux quantum, Φ_0, equal to exactly $h/2e$, strongly supports the idea that quantisation is connected with the pairing of electrons.[32,33]

The BCS microscopic theory has become one of the most successful theories in solid state physics; so complete was it, in its description and prediction of experimentally observable properties, that it somewhat quenched most research in the field except for continuing research into applications. Many theoreticians have reformulated the theory, often writing it in a simpler form: the most notable attempts are those of Bogoliubov[34], Valatin[35], Nambu[36] and Eliashberg[37].

---

30 A review of the developments in superconductivity up to 1961 is given by J. Bardeen & J. R. Schrieffer, *Progress in Low Temperature Physics*, Volume 3: ed. C.J. Gorter, North-Holland (1961); the article has recently been reprinted as a separate booklet by North-Holland (1991)

* This implies that at temperatures between T_c and 0 K, the superconducting material always has *some* unpaired electrons (known as *quasiparticles* or simply *normal* electrons).

31 See R. Mersevey & B. B. Schwartz, *Superconductivity*, ed. R D. Parkes, Dekker, New York (1969) for a summary of the experimental data.

32 B. S. Deaver, Jr. & W. M. Fairbank, *Phys. Rev. Lett.* 7 43 (1961)

33 R. Doll & M. Näbauer, *Phys. Rev. Lett.* 7 51 (1961)

34 N. N. Bogoliubov, *Nuovo Cimento* 7 6 794 (1958): N. N. Bogoliubov, V. V. Tolmache & D. V Shirkov, *A New Method in the Theory of Superconductivity*, Consultants Bureau, New York (1959)

35 J. Valatin, *Nuovo Cimento* 7 843 (1958)

36 Y. Nambu, *Phys. Rev.* **117** 648 (1960)

37 G. M. Eliashberg, *Sov. Phys. J.E.T.P* **11** 696 (1960)

1.2 High Temperature Superconductivity

1.2.1 Introduction

A dramatic revival of superconductivity came in 1986, when George Bednorz and Alex Müller[38] (Zürich) observed that La_2CuO_4 doped with hole-donating barium ($La_{1.85}Ba_{0.15}Cu0_4$) began its superconducting transition at 35K. Initial scepticism, created by the BCS prediction that superconductivity could not exist above 25K, was soon quashed when the findings were confirmed by independent researchers.[39,40] The discovery was hailed as the birth of 'High Temperature (HiT_c) Superconductivity' and signalled the start of a highly intensive effort, devoted to the understanding and production of these new materials.

A major breakthrough came in January 1987, with the discovery of $YBa_2Cu_3O_{7-\delta}$ (abbreviated to YBCO or 123), a HiT_c superconductor with a T_c of around 93K. The compound, synthesized by Paul Chu and M.K.Wu at the University of Houston[41], was the first material capable of superconductivity above liquid nitrogen temperatures (77K).

By 1988, the focus of attention was on two new families of compounds with still higher transition temperatures. First came the announcement by Hiroshi Maeda[42] (Japan) of superconductivity at 120K in a Bi-Sr-Ca-Cu-O material. A similar report promptly followed from the laboratory of Hermann and Sheng[43], indicating that a Tl-Ba-Ca-Cu-O compound had a transition temperature of 140K†.

The highest confirmed transition temperature attained to date was found by varying the stoichiometry of the constituent elements in the Tl material. The thallium phase, $Tl_2Ba_2Ca_2Cu_3O_{10}$, has a T_c of 125K[43,44] and is often referred to as the 2223 phase - as for brevity these cuprate compounds are known by their constituent ratios.

---

38 J. G. Bednorz & K. A. Müller, *Z. Phys. B* **64** 189 (1986): *Revs. Mod. Phys.* **60** 585 (1988)

39 S. Ushida, H. Takagi, K. Kitazawa & S. Tanaka, *Jpn. J. Appl. Phys.* **26** L1 (1987)

40 C. W. Chu, P. H. Hor, R. L. Meng, L. Gao, Z. J. Huang & Y. Q. Wang, *Phys. Rev. Lett.* **58** 405 (1987)

41 M. K. Wu, J. R. Ashburn, C. J. Torng, P. H. Hor, R. L. Meng, L. Gao, Z. J. Thiang, Y. Q. Wang & C. W. Chu, *Phys. Rev. Lett.* **58** 908 (1987)

42 H. Maeda, Y. Tanaka, M. Fukitomi & T. Asano, *Jpn. J. Appl. Phys. Lett.* **27** L209 (1988)

43 A. M. Hermann, Z. Z. Sheng, D. C. Vier, S. Shultz & S. B. Oseroff, *Phys. Rev. B* **37** 9742 (1988): Z. Z. Sheng & A. M. Hermann, *Nature* **332** 55 (1988): *Nature* **332** 138 (1988)

† This T_c turned out to be false, but the material was nevertheless a HiT_c superconductor.

44 R. M. Hazen, L. W. Finger, R. J. Angel, C. T. Prewitt, N. L. Ross, C. G. Hadidiacos, P. J. Heaney, D. R. Veblen, Z. Z. Sheng, A. El. Ali & A. M. Hermann, *Phys. Rev. Lett.* **60** 1657 (1988)

In 1989, Tokura et al[45] replaced the Nd^{3+} ions in Nd_2CuO_4 with electron donating Ce^{4+} ions, to produce a HiT_c superconductor with a T_c in the 20-30K range. The discovery of $Nd_{2-x}Ce_xCuO_4$ was an interesting development of the Cu-O containing (cuprate) system as it implied the existence of both hole-doped or p-type (the Y, Tl and Bi based materials) and electron-doped or n-type (Ce and Nd based compounds) superconductors.

The discovery of superconductivity in the Ba-K-Bi-O system[46,47] has created much interest, in recent years. Amongst this group of compounds, which also includes the Pb-substituted system, $Ba_{0.6}K_{0.4}BiO_3$ has the highest T_c at 30K, at the present time. Curiously, unlike the other HiT_c oxides discovered, the cubic bismuthates contain no copper. A number of experimental works[48,49] indicate that conventional phonon-mediated interactions may be responsible for bismuthate superconductivity and it is currently believed that the compounds fit into the BCS theoretical framework.[48,50]

Until recently, superconductors based on large organic molecules, such as $(BEDT\text{-}TTF)_2Cu[NCS]_2$, have achieved only mediocre transition temperatures of around 11K. However, the separation of a new stable allotrope of carbon, C_{60}, from 'soot' by Kroto and Smalley et al[51] in 1985, opened up a new field of research based on the 'bucky-ball' or C_{60}-based Buckminsterfullerine*.

Two recent reports found unambiguous evidence that both thin films and polycrystalline powders of C_{60} doped with potassium[52] (K_3C_{60}) and rubidium[53] (Rb_3C_{60}) become superconducting at around 18K and 30K, respectively. The compound

---

45 Y. Tokura, H. Takagi & S. Ushida, *Nature* **337** 345 (1989)

46 L. F. Mattheiss, E. M. Gyorgy & D. W. Johnson, *Phys. Rev. B* **37** 3735 (1988)

47 R. J. Cava, B. Batlogg, J. J. Krajewski, R. Farrow, L. W. Rupp, Jr., A. E. White, K. Short, W. F. Peck & T. Kometani, *Nature* **332** 814 (1988)

48 M. F. Hundley, J. D. Thompson & G. H. Kwei, *Solid State Comm.* **70** 1155 (1989)

49 Z. Sclesinger, R. T. Collins, J. A. Calise, D. G. Hinks, A. W. Mitchell, Y. Zheng, B. Dabrowski, N. E. Bickers & D. J. Scalapino, *Phys. Rev. B* **40** 6862 (1989)

50 See J. C. Phillips, *Physics of High Temperature Superconductors*, p120, 1st edn., Academic Press (1989) for information on the electronic structure and other details.

51 H. W. Kroto, J. R. Heath, S. C. O'Brien, R. F. Cure & R. E. Smalley, *Nature* **318** 162 (1985)

* After the dome-like geodesic structures designed by the architect, Richard Buckminster-Fuller.

52 R. C. Haddon, A. F. Hebard, M. J. Rosseinsky, D. W. Murphy, S. J. Duclos, K. B. Lyons, B. Miller, J. M. Rosamilia, R. M. Fleming, A. R. Kortan, S. H. Glarum, A. V. Makhija, A. J. Muller, R. H. Eick, S. M. Zahurak, R. Tycko, G. Dabbagh & F. A. Thiel, *Nature* **350** 320 (1991)

53 K. Holczer, O. Klein, S. M. Huang, R. B. Kaner, K. J. Fu, R. L. Whetten & F. Diederich, *Science* **252** 1154 (1991)

which now holds the record for the highest reproducible T_c in an organic superconductor is Cs_2RbC_{60}, which is found to have a transition temperature of 33K[54]. Reports of superconductivity at 42.5K in $Rb_{2.7}Tl_{2.2}C_{60}$ remain unconfirmed.

1.2.2 Fundamental Properties of the Layered Cuprates

Progress in the field of HiT_c superconductivity has advanced significantly since 1986. As a consequence of improvements in the synthesis and characterisation of materials, researchers now have high quality samples on which to apply a wide variety of experimental techniques. Studies on the Cu-O containing materials, known as the cuprates, have proved fruitful and have enabled scientists to establish an overall picture of the behaviour of these materials.

A common feature of the cuprate structure is the CuO_2 plane. Each Cu atom within the two-dimensional plane is strongly bonded, in a nearly square planar configuration, to four oxygen atoms - with a Cu-O-Cu bond angle of nearly 180°. The sheets of CuO_2 have a constant oxygen concentration and can occur singly or in groups. Individual planes within a group are separated by metal atoms and as a general rule T_c increases with the number of planes (N) in close proximity. A prime example of this feature is shown[55] in the thallium materials, where compounds containing one, two or three closely spaced CuO_2 planes separated by Ca atoms, have T_c's of 80, 105 and 125K respectively†. Groups of CuO_2 planes are bridged by a given number of X-O layers, where X = a metal such as Ba, Pb, La, Cu or Tl.

It is thought that the superconductivity in the layered cuprates arises from the strongly correlated motion of holes (in p-type) or electrons (in n-type) in the CuO_2 plane, with the intercalated (X-O) layers controlling the necessary carriers or coupling mechanism and providing extra structural stability. In such a 'charge transfer' system, the CuO_2 layers become known as the 'conduction layers' and the intercalated layers are the 'charge reservoirs'. The number of carriers in the conduction layer is determined by the charge transfer between the conduction layer and the reservoir, and this in turn is controlled by the overall crystal structure, the available oxidation states of the atoms and competition between oxidation (or reduction) of the metal atoms in the reservoir.

---

54 K. Tanigaki, T. W. Ebbesen, S. Saito, J. Mizuki, J. S. Tsai, Y. Kubo & S. Kuroshima, *Nature* **352** 222 (1991)

55 See R.M. Hazen, 'Crystal Structures of High Temperature Superconductors' in *Physical Properties of High Temperature Superconductors*, chapter 3, Vol. II : ed. D. M. Ginsberg, World Scientific (1990).

† The T_c has been shown to decrease when n = 4, implying that there is some limit to the number of consecutive close-spaced planes.

Each superconducting cuprate family is derived from an insulating antiferromagnetic (AF) phase in which there is no charge transfer to the planes (see section 1.2.3). Sufficient doping of the parent system via chemical substitution or varying O-stoichiometry, causes the AF to be suppressed and the system undergoes a transition from the insulating state to a metallic state, which has a superconducting ground state. Over doping causes a further transition to a normal metal state.

The unit cell of a layered cuprate tends to have **a** and **b** axes (in the plane parallel to the CuO_2 sheets) of approximately equal length and a **c**-axis which is generally 3 or 4 times longer. Such a crystallographic make-up suggests that these materials should be extremely anisotropic and this is indeed the case. The unusual normal state electronic properties are highly anisotropic, with the resistivity showing a metallic-like behaviour *in* the planes (i.e. increasing with temperature and of the form, $\rho_{ab}(T)=\rho_0 + \alpha T$, where α is equivalent to $d\rho/dT$) and a semiconductor-like behaviour perpendicular to the planes (with ρ_c decreasing with increasing temperature). The resistivity in the c-direction is generally several orders of magnitude greater than that in the ab direction*. The $\rho_{ab}(T)$ curves for different optimised cuprate samples† are very similar in that they vary almost linearly with temperature and they are of approximately the same magnitude[56]. This provides further evidence that the planes of CuO_2 are the electronically active species, as they are the only common connection in otherwise very different structures.

From various macroscopic measurements taken in the superconducting state, it has become clear that cuprate superconductivity involves the pairing of electrons, with pairs having a singlet spin state and zero total momentum[57]. Direct measurements of the magnetic flux quantum (ϕ_0) imply that the value of ϕ_0 is approximately $h/2e$ - the same as that found in the classic superconductors[58].

A consequence of electron pairing, as predicted by BCS theory, is the isotope effect. At the present time, measurements of the isotope effect in high temperature superconductors have proved inconclusive: initial experiments on YBCO, in which up to 20% of the O^{16} was diffusively replaced by O^{18}, showed that there was no shift in the T_c

---

* For a summary of the standard results in YBCO($\delta\approx7$), see Appendix A.1

† Such as $Bi_2Sr_{2.2}Ca_{0.8}Cu_2O_8$, $Bi_{2.1}Sr_{1.9}CuO_6$, and $YBa_2Cu_3O_{7-\delta}$.

56 See 'Selected Experiments On High T_c Cuprates' by B. Batlogg in *High Temperature Superconductivity*, proceedings from the Los Alamos Symposium, eds. K. Bedell, D. Coffey, D. Meltzer, D. Pines & J. R. Schrieffer, Addison-Wesley (1989)

57 A. Furusaki & M. Tsukada, *Solid State Comm.* **78** 299 (1991)

58 See 'Flux Quantisation, Superconducting Mixed States, the Josephson Effect and SQUID Devices' (and references therein) by C. Gough in *High Temperature Superconductivity*, Proceedings of the 39th Scottish Summer School in Physics, eds. D. P. Tunstall & W. Barford, IOP Publishing (1991)

and that a, the exponent of the isotopic mass, was equal to zero[59,60] (within an error of ±0.02). Subsequent experiments concluded[61,62] that there was a small isotope effect in $La_{2-x}Sr_xCuO_{4-y}$ - but, significantly smaller than that predicted by BCS theory, indicating that phonon coupling was playing a significant, but not necessarily dominant role. Further work[63] on YBCO produced a detectable depression in T_c of around 0.4K, when up to 90% of the oxygen was replaced by O^{18}. The interpretation of the isotope results remains controversial, but the general consensus of opinion is that in the La compound, a phonon-coupling mechanism may be supplemented by an electronic mechanism, whereas in the YBCO material the electronic mechanism completely dominates.

Reports of the superconducting energy gap, Δ, are also inconclusive and too numerous to mention in this brief section: the reader is referred to an article by Tinkham and Lobb[64] and the references therein. Suffice to say that common values for the ratio $2\Delta/k_BT_c$ seem to range from 5 to 8 - slightly larger than the weak-coupling BCS limit of 3.5. Values of 3-4 have also been reported and, as yet, are not excluded as a possibility. The energy gap appears to be larger within the Cu-O planes than in the direction perpendicular to them.

In these new materials, the Ginzburg-Landau coherence length, $\xi_{GL}(T)$, (and presumably, the Pippard coherence length,* ξ_P) is extremely small and anisotropic,

---

59 B. Batlogg, R. J. Cava, A. Jayaraman, R. B. van Dover, G. A. Korouklis, S. Sunshine, D. W. Murphy, L. W. Rupp, H. S. Chen, A. White, K. T. Short, A. M. Mujsce & E. A. Rietman, *Phys. Rev. Lett.* **58** 2333 (1987)

60 L. C. Bourne, M. F. Commie, A. Zettl, H. C. zur Loye, S. W. Keller, K. L. Leary, A. M. Stacy, K. J. Chang, M. L. Cohen & D. E. Morris, *Phys. Rev. Lett.* **58** 2337 (1987)

61 B. Batlogg, G. Kourouklis, W. Weber, R. J. Cava, A. Jayaraman, A. E. White, K. T. Short, L. W. Rupp & E. A. Rietman, *Phys. Rev. Lett* **59** 912 (1987)

62 T. A. Faltens, W. K. Ham, S. W. Keller, K. J. Leary, J. N. Michaels, A. M. Stacy, H. C. zur Loye, D. E. Morris, T. W. Barbee III, L. C. Bourne, M. L. Cohen, S. Hoen & Z. Zettl, *Phys. Rev. Lett* **59** 915 (1987)

63 K. J. Leary, H. C. zur Loye, S. W. Keller, T. A. Faltens, W. K. Ham, J. N. Michaels & A. M. Stacy, *Phys. Rev. Lett.* **59** 1236 (1987): H. C. zur Loye, K. J. Leary, S. W. Keller, W. K. Ham, T. A. Faltens, J. N. Michaels & A. M. Stacy, *Science* **238** 1558 (1987).

64 M. Tinkam & C. J. Lobb, 'Physical Properties of the New Superconductors' in *Solid State Physics*, Vol. 42 : eds. H. Ehrenreich & D. Turnbull, Academic Press (1989)

* ξ_{GL} is the range of propogation of a disturbance in the *magnitude* of the superconducting order parameter Ψ (i.e. the density of Cooper pairs), whereas ξ_P is the range of propogation of a variation in the *phase* of Ψ and therefore the supercurrent. ξ_p can only be determined by indirect methods and experimental data is not available at this point.

typically, ranging from 0.5 to 30Å in the low temperature limit† (depending on the sample and crystallographic direction). The penetration depth seems to be very long (of the order of thousands of Ångstroms compared with around 400Å for niobium) and again anisotropic. These extreme characteristic lengths put the cuprate superconductors in the 'extreme type II' category (i.e. $\lambda/\xi \gg 1$) and in the 'clean' limit ($\xi(T=0) \ll \ell$, the electronic mean free path*) near T_c. A number of properties stem from such characteristic lengths: for example, the low temperature values of the upper critical field H_{c2} are large (up to 230 T at 11K for a single crystal of YBCO with the field direction parallel to the ab plane[65]) and there is a weak pinning of the fluxoids (around T_c) associated with the short coherence length, which leads to a reduced J_c (around 10^{4-6} Acm^{-2}, at present).

1.2.3 Electronic Structure & Magnetism of the Hole-doped CuO_2 Planes

The identification of the crystal structures of cuprate superconductors sparked an extensive investigation into the relationship between superconductivity and the magnetic, crystal and electronic structures of the systems. Although rapid progress is still being made and it would be premature to draw any firm conclusions at present, there are a number of points which consistently emerge as common features of all the hole-doped cuprate superconductors**.

Fairly conclusive evidence indicates that cuprate superconductors contain a set of quasi-two-dimensional CuO_2 planes capable of sustaining a critical density of itinerant carriers within a given concentration range. The CuO_2 planes of the parent or undoped compounds (i.e. the La_2CuO_4 or $YBa_2Cu_3O_6$ phase) adopt an insulating, AF state, which stems from a Mott-Hubbard[66] or 'charge transfer' type insulating lattice. In such a lattice, it is energetically impossible for doubly occupied states to form at low temperature because of strong Coulomb repulsion. Thus the lowest energy electronic excitations are spin excitations only. In the parent cuprates, the energy scale of the spin flip (magnetic) excitations, determined by the Heisenberg coupling constant ($J \approx 0.1$eV), is clearly smaller than the charge (particle-hole) excitation energies of ~2eV. It is this separation between

---

† It is not uncommon for a *conventional* superconductor to have a value ranging from a few hundred to several thousand Angstroms.

* Typically 100-200Å

65 A. Umezawa, G. W. Crabtree, J. Z. Liu, T. J. Moran, S. K. Malik, L.H. Nunez, W. L. Kwok & C. H. Sowers, *Phys. Rev. B* **38** 2843 (1988)

** All examples will be given with reference to the YBCO system.

66 N. F. Mott, *Metal-Insulator Transitions*, chapter 4: Taylor & Francis Publishers (1974)

charge and spin excitations which puts the CuO_2 planes into the class of Mott-Hubbard insulators.

In the undoped sheets, the oxidation state of oxygen is O^{2-} ($2p^6$), whilst that of copper is Cu^{2+} ($3d^9$). The Cu valence electrons have a ground state configuration of $(d_{xy})^2$ $(d_{xz})^2$ $(d_{yz})^2$ $(d_{z2})^2$ $(d_{x2-y2})^1$ - thus there is an unpaired d_{x2-y2} orbital in the sheet pointing at the plane oxygens. The holes on the Cu do not move freely but are localised on the Cu site by the strong onsite Coulomb interaction and the material is an insulator, which is AF due to the 'superexchange' interaction between the Cu 3d and O 2p orbital electron states.

The size of the ordered moment observed in the antiferromagnetically ordered phase is $\approx 0.6\mu_B$ per Cu. This is close to the ionic value and implies that a local desciption of Cu as Cu^{2+} moments is applicable.

There are few examples where a Mott insulator can be doped to produce a metal. However, in the case of the cuprates, doping the parent AF insulator with holes produces a metallic state (a doped-Mott insulator) which is a superconductor at a temperature of around 90K and above. For example: the addition of oxygen to the undoped, tetragonal $YBa_2Cu_3O_6$ insulator introduces electron holes into the CuO_2 planes† because of electron transfer away from the planes. These holes are largely on the oxygen site and therefore acquire a spin. When at a small concentration, the holes are localised by their donors and quantitatively the properties of the material do not change very much. At a hole concentration of 0.15 per CuO_2 plane, the holes delocalise, due to 'magnetic frustration', causing the long range AF order to give way to a 'frozen spin' phase which persists up to a hole concentration of 0.175. Beyond this hole concentration superconductivity appears, a structural transition occurs, and the T_c increases to a maximum. Over doping causes the T_c to fall again as the material enters into a normal metallic state.

Band structure calculations[67] have shown rather conclusively that the relevant states are holes in the Cu $3d_{x2-y2}$ orbitals and the O $2p_{\sigma x}$ and O $2p_{\sigma y}$ orbitals. At the Fermi level there is a band which is formed from a strong admixture of the Cu $3d_{x2-y2}$ and O 2p orbitals. Bonding between the orbitals has a strongly covalent character, which arises because the 3d and 2p levels are very close in energy. A number of experimental reports have revealed that the highest occupied electronic states are the ones near the Fermi energy, E_F. The states have been found to exhibit 3d and 2p character with a predominance of 2p. As a result, the holes introduced into the CuO_2 sheets via doping are not located only at the Cu sites or only at the O sites, but have a mixed character. The hole

† In terms of δ, the hole concentration increases with decreasing δ.

67 Reviewed by W. Pickett, *Rev. Mod. Phys.* **61** 433 (1989)

essentially resides in a region where the O and Cu wavefunctions are strongly overlapped and hybridised and can also be mostly on the Cu or mostly on the O.

Figure 1.4 shows the atomic configuration in the CuO_2 plane. The relevant hopping integrals (t) and interactions V between holes on neighbouing Cu and O sites are labelled for reference. The quantity t will be discussed further in section 1.2.4.

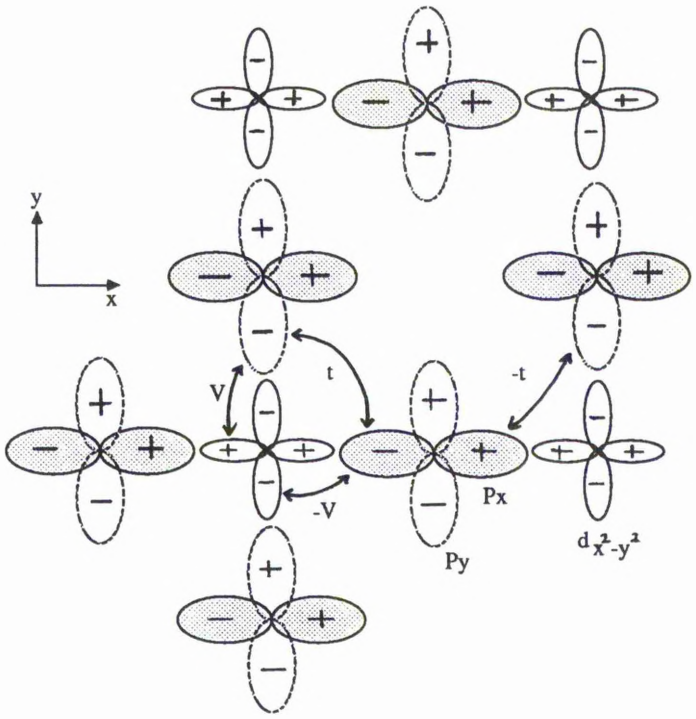

Figure 1.4

Atomic Orbital Configuration in the CuO_2 layer. The hopping integral t and the interaction V are indicated.

1.2.4 Current Theoretical Models of the Cuprates

As a detailed analysis of the theoretical aspects of the oxide superconductors is out of the scope of this text, the salient points and theories will merely be mentioned and the reader referred to extended texts, where necessary.

A plethora of ideas that could explain the behaviour of HiT_c superconductors has been put forward since their discovery. The evolution of more reliable experimental data in recent years has, however, put a severe constraint on the possible explanations of such behaviour. Any theory must not only explain the novel superconducting properties of the

cuprate system, but also the unusual normal state properties[56], such as the linear temperature dependence of the resistivity, the flat Raman scattering background and the unusual nuclear magnetic resonance relaxation behaviour.

The current debate about the normal state concerns the origin of the metallic character of the oxides. All known metals have, up to now, been described as 'Fermi liquids'. The Landau theory of Fermi liquids[68] uses a system of non-interacting fermions (Fermi gas) with the electron-electron interactions added, to describe the effect of interelectron electrostatic interactions. The nature of the low energy excited states (known as quasi particles) of the interacting electron system, are found to be qualitatively similar to that of free electron system. The quasi particles are in a one-to-one correspondence with the single particle excitations of the free electron gas and have the same spin and charge as an electron. Thus, a conventional Fermi liquid picture forecasts that there is a Fermi surface in **k**-space that encloses a known volume, to which the low energy excitations are confined. There is a discontinuity in the momentum distribution n(**k**) across the Fermi surface and the quasi particles have an infinite lifetime at the Fermi surface. The electronic properties of the system can be predicted on the basis of the Fermi surface.

All theories proposed to explain the behaviour of HiT_c cuprates fall into two broad categories. Bearing in mind that it has definately been established that Cooper pairs exist in the superconducting state and that there is undeniable evidence[69] that a Fermi surface exists, there are those theorists who assume that the cuprates are Fermi liquids in the normal state and that one of the many pairing mechanisms available is responsible for superconductivity. On the other hand, there are those which assert that the cuprates are not Fermi liquids and propose some new 'exotic' theory to explain the normal and superconducting properties. These two categories further subdivide to give a large number of distinct theories. Some theories modify the conventional Fermi liquid behaviour, such as the 'marginal'[70] and 'nested'[71] Fermi liquid theories.

Modelling HiT_c superconductors as strongly correlated quasi-two dimensional electron systems seems to be the most common starting point for theorists. Anderson[72] pointed out early on that a suitable theoretical framework for describing a correlated system, where magnetism and superconductivity are in close proximity, is the Hubbard

---

68 L. Landau, *Sov. Phys. JETP* **3** 920 (1957): *Sov. Phys. JETP* **5** 10 (1957).

69 W. E. Pickett, H. Krakauer, R. E. Cohen & D. J. Singh, *Science* **255** 46 (1992)

70 C. M. Varma, P. B. Littlewood, S. Schmitt-Rink, E. Abrahams & A. E. Ruckenstein, *Phys. Rev. Lett.* **63** 1996 (1989)

71 J. Ruvalds & A. Virosztek, *Phys. Rev. B* **43** 5498 (1991)

72 P. W. Anderson, *Science* **235** 1196 (1987)

model[73]. Basically, each of N atom sites on a two dimensional square lattice† is occupied by one electron*. The spin direction is taken to change from neighbour to neighbour, so there is an AF ground state. If a further electron with a given spin is introduced into the system, it can be accommodated at one of the N/2 atoms which already has an electron with oppposite spin. Due to the Pauli exlusion principle, there is an onsite Coulomb repulsion U for electrons of the same spin occupying the same site. The other parameters which contribute to the Hubbard Hamiltonian are the nearest neighbour hopping integral t, which gives imformation of the probability of an electron hopping from one localised site to another, and z, the number of nearest neighbour sites. Some theorists work in the weak coupling limit where U«zt and others go the opposite way to the strong coupling limit, where U»zt. Examples of models which start from the weak coupling limit are the 'spin bag' approach of Schrieffer[74] and the 'heavy fermion' model of Pines[75]. Such theories are Fermi liquid based and are built on the idea that spin-wave excitations mediate the pairing and take on the role of the phonons in conventional superconductivity.

The 'two band' ideas of Emery[76] originate from a strong coupling limit. One of the most well known strong coupling theories is the t-J model, where t represents the hopping integral and J is the Heisenberg exchange interaction ($J=t^2/U$)[77]. The model, which is based on a simplified Hubbard Hamiltonian, assumes that there is only one spatial state per unit cell in the undoped cuprates and that each site is singly occupied by one hole. Since U for doubly occupied states is assumed to be large, the only relevant degree of freedom at low energies is the spin, which is coupled to its neighbours by J. Doping produces doubly occupied sites, which have no spin due to the formation of a 'Zhang-Rice singlet'[78] (a hole on the oxygen site forms a tightly bound singlet with a

---

73 J. Hubbard, *Proc. Royal Soc. A* **276** 238 (1963): *Proc. Royal Soc. A* **277** 237 (1963)

† Analytic solutions to the Hubbard Hamiltonian in one dimension have been known for some time, but the solutions to the 2D system are a relatively new problem for theorists. See 'Strong Correlation & High Temperature Superconductivity' by V. J. Emery in the text referenced in ref. 77.

* or holes (the model works for both carriers)

74 J. R. Schrieffer, X. G. Wen & S. C. Zhang, *Phys. Rev. Lett.* **60** 944 (1988): A. Kampf & J. R. Schrieffer, *Phys. Rev. B* **41** 6399 (1990)

75 P. Monthoux, A. V. Balatsky & D. Pines, *Phys. Rev. Lett.* **67** 3448 (1991)

76 V. J. Emery, *Phys. Rev. Lett.* **58** 2794 (1987): V. J. Emery & G. Reiter, *Phys. Rev. B* **38** 4547 (1988)

77 See 'Introduction to the Theory of Strongly Correlated Electrons' by T. M. Rice in *High Temperature Superconductivity,* Proceedings of the 39th Scottish Summer School in Physics, eds. D. P. Tunstall & W. Barford, IOP Publishing (1991)

78 F. C. Zhang & T. M. Rice, *Phys. Rev. B* **37** 3759 (1988)

local copper spin, thereby removing the spin from participation in low energy phenomenon) but carry the charge of the doped hole. Singlets can hop to neighbouring sites provided the site is not already doubly occupied.

A number of alternative theories exist which are not based on Fermi liquid theory and are therefore deemed as exotic. In his resonating valence band model (RVB), Anderson[72] postulates a new state of matter. The spin and charge associated with the electron holes in the CuO_2 planes are assumed to dissociate into two quasi particles known as a holon (with unit charge and no spin) and a spinon (with no charge and 1/2 integral spin). Other exotic theories involve anyons[79] (a charged quasi particle in a 2D system with statistics intermediate between those of fermions and bosons) and bipolarons[80] (in which charge carriers bind into pairs to form bosonic, rather than fermionic, excitations).

The theories proposed are many and varied. Some theorists believe that a fuller picture will be revealed when more specific and satisfactory solutions to the general 2D Hubbard Hamiltonian are found.

1.3 Nuclear Magnetic Resonance

1.3.1 Introduction

Nuclear Magnetic Resonance (NMR) spectroscopy has been used extensively in this work to probe the microscopic nature of the YBCO system.

Since the pioneering work of Purcell[81], Bloch[82] and Gorter[83] in the 1940's, the field of NMR has grown extensively, both in terms of advanced theory and complex instrumentation[84]. It is not the intention here to discuss the principles of the subject in any detail, but merely to provide a general basis on which the more extensive concepts given in chapter 3 may rest. For a comprehensive theoretical overview, the reader is referred to

---

79 F. Wilczek, *Scientific American* **264** 24 (1991)

80 See 'The Spin Polaron Model & the Comparison with Liquid Helium' by N. F. Mott in *High Temperature Superconductivity,* Proceedings of the 39th Scottish Summer School in Physics, eds. D. P. Tunstall & W. Barford, IOP Publishing (1991)

81 E. M. Purcell, H. C. Torrey & R. V. Pound, *Phys. Rev.* **69** 37 (1946)

82 F. Bloch, W. W. Hansen & M. Packard, *Phys. Rev.* **69** 127 (1946)

83 C. J. Gorter & L. J. F. Broer, *Physica* **9** 591 (1942)

84 An exposé of experimental techniques and apparatus can be found in E. Fukushima & S. B. W. Roeder, *Experimental Pulse NMR - A Nuts & Bolts Approach,* Addison-Wesley (1981).

more extended texts[85].

1.3.2 Basic Concepts

The phenomenon of NMR is based upon the spin of a nucleus and its classical characteristic frequency of gyroscopic precession in an applied magnetic field. All nuclei with an odd mass number possess spin and an intrinsic spin angular momentum denoted by $\mathbf{I}\hbar$ (where **I** is 'nuclear spin'). The ratio of the angular momentum and its associated magnetic moment $\boldsymbol{\mu}$ is known as the gyromagnetic ratio, γ (i.e. $\boldsymbol{\mu}=\gamma\mathbf{I}\hbar$, where **I** and $\boldsymbol{\mu}$ are parallel and γ is itself an intrinsic property of a particular nuclear species). In the presence of an applied magnetic field of strength **B**, the energy of interaction between the field and an isolated magnetic moment $\boldsymbol{\mu}$ is given by the Zeeman splitting term ($\mathcal{H}_Z$), which is described by the simple Hamiltonian, $\mathcal{H}_Z = -\boldsymbol{\mu}.\mathbf{B}$. Defining the z-direction to be along the field $\mathbf{B_0}$, such that $\mathbf{B}=\mathbf{B_0}\mathbf{z}$, leads to

$$\mathcal{H}_Z = -\mu_Z B_0 = -\gamma\hbar B_0 I_Z \qquad (1.6)$$

Quantum theory dictates that the allowable nuclear spin states are quantised, restricting I_Z to a set of discrete values m_I and defining the (2I+1) allowed energies as

$$\mathcal{H}_Z = -m_I \gamma \hbar B_0 \qquad (m_I = I, I\text{-}1.....\text{-}I) \qquad (1.7)$$

These energies form a set of equally spaced Zeeman energy levels where the separation between adjacent levels is $\gamma\hbar B_0$. In order to detect such levels, transitions are induced between two nuclear spin states, via the application of an oscillating magnetic field, $\mathbf{B_1}$, perpendicular to the static field $\mathbf{B_0}$. Absorption of energy occurs when the frequency of the oscillating field statisfies the resonance condition, derived from the Bohr frequency requirement. That is, when

$$\hbar\omega_0 = \gamma\hbar B_0$$

or

$$\omega_0 = \gamma B_0 \qquad (1.8)$$

Equation (1.8) defines the Larmor frequency, ω_0 and specifies that either frequency or B-field can be varied in order to achieve resonance. The range of frequencies of

---

85 For example: C. P. Slichter, *Principles of Magnetic Resonance*, Springer-Verlag (1990); E. R. Andrew, *Nuclear Magnetic Resonance*, Cambridge University Press (1955); J. Winter, *Magnetic Resonance in Metals*, Clarendon Press (1971); A. Abragam, *Principles of Nuclear Magnetism*, Oxford University Press (1989).

electromagnetic radiation required to excite transitions between energy levels falls in the radiofrequency (rf) band of the spectrum. The energy contribution that the rf $\mathbf{B_1}$ field makes to the total energy associated with the nucleus (due to the interaction $-\boldsymbol{\mu}.\mathbf{B_1}$) can, for future reference, be labelled $\mathcal{H}_1$.

In a macroscopic assembly of identical nuclei in a magnetic field, the population of spins in any one energy state is governed classically by Boltzmann statistics. For simplicity, consider a sample containing spin 1/2 nuclei: each individual nucleus has two possible energy levels corresponding to $m_I=\pm 1/2$. For nuclear spins in equilibrium at a spin temperature T_s, the Boltzmann distribution is such that the population of the lower level ($m_I=+1/2$) is greater than that of the upper level ($m_I=-1/2$). Thermal equilibrium is maintained by weak spin-spin interactions and the constant T_s is equal to the temperature of the surroundings, commonly referred to as the lattice temperature, T_L. The pulse application of an alternating $\mathbf{B_1}$ field and the subsequent absorption of quanta of energy corresponds to some of the excess spins 'flipping' from a lower energy state to higher adjacent one (following the selection rule, $\Delta m_I=\pm 1$). The system is perturbed and the value of T_s is raised above that of T_L (which is assumed to stay constant due to negligible interaction between the spin system and the lattice). In order to regain equilibrium the spin system must lose 'heat' to the lattice (until $T_s=T_L$) and the population ratio must approach its equilibrium value. The perturbed spins flip back to their equilibrium state giving up energy equal to the difference in energy between adjacent levels†. The population difference is found to approach equilibrium exponentially in a characteristic time, T_1, known as the 'spin-lattice relaxation time'.

In order to describe the concept of relaxation, Bloch[86] (1946) studied an ensemble of nuclei in a magnetic field from a purely classical and macroscopic viewpoint. The total magnetic moment or magnetisation $\mathbf{M}$ of a macroscopic sample is the resultant of the individual magnetic moments $\boldsymbol{\mu}_i$. At thermal equilibrium, the precessional phases of $\boldsymbol{\mu}_i$ are random and so $\mathbf{M}$ takes on a static value $\mathbf{M_0}$ along the z direction (i.e.along $\mathbf{B_0}$). The pulse application of an oscillating $\mathbf{B_1}$ field rotates $\mathbf{M_0}$ away from $\mathbf{B_0}$ in such a way that $\mathbf{M_0}$ starts to precess at an angle θ about $\mathbf{B_0}$. The components of $\mathbf{M_0}$ along the x and z directions are given by $M_x=M_0\sin\theta$ and $M_z=M_0\cos\theta$, respectively. In order to regain its original configuration, the perturbed spin system must relax back to thermal equilibrium with its surroundings (the lattice) and the individual spins must achieve thermal equilibrium with neighbouring spins. Two time constants can be identified for these relaxation processes. The steady reduction of the transverse magnetisation, M_x (referred to as 'free induction decay' (FID)) is due to the interactions amongst the individual spins

---

† This is the energy detected by a tuned receiver coil in an NMR experiment.

86 F. Bloch, *Phys. Rev.* **70** 460 (1946)

and occurs over a time scale known as the 'spin-spin' or 'transverse' relaxation time, T_2. The T_2 relaxation process takes place without any change in the total magnetic moment along $\mathbf{B_0}$. Instead, the exchange of energy between the spins and the lattice determines the remagnetisation of $\mathbf{M_0}$ along $\mathbf{B_0}$ and this is characterised by the 'spin-lattice' or longitudinal relaxation time, T_1.

Experimentally, T_1 is found to vary from milliseconds to days depending on the sample, while T_2 is generally of the order of submilliseconds. T_1 is very temperature dependent and in the solid state, $T_1 \gg T_2$.

One of the simplest pulse experiments rotates $\mathbf{M_0}$ through an angle of 90° using a suitable excitation known as a 90° pulse. When θ=90°, the transverse magnetisation $\mathbf{M_x}$ (with amplitude equal to M_0) rotates at a frequency of ω_0 about **B**, inducing an oscillatory magnetic flux in the receiver coil of the NMR experiment. The exponential FID obtained as a result of the T_2 relaxation process is Fourier transformed and the real part produces an absorption lineshape. In different systems, the spectral lineshape is broadened and shifted by varying amounts depending on the contributions made by a number of spin-spin and spin-lattice interactions. Here, only the interactions relevant to the solid state and metallic systems are of any concern. Much of the work introduced in the proceeding paragraphs is extended in chapter 3.

In the solid state, the dominant nuclear-nuclear interaction is the nuclear magnetic dipole interaction. For a system of nuclear spins in a magnetic field $\mathbf{B_0}$, each spin is subject to the static field $\mathbf{B_0}$ and also to a varying local field produced by its neighbours. The variation of local fields throughout the sample leads to a broadening of the resonance line. In addition to a magnetic moment, nuclei with I>3/2, also possess an electric quadrupole moment caused by a non-spherical distribution of nuclear charge. Quadrupole interactions between the quadrupole moment and the electric field gradient (EFG), are found to produce a series of symmetrically displaced lines (quadrupole splitting) around ω_0, known as satellites, and these can broaden the lineshape if they are not resolved. In metals, an indirect nuclear spin-spin interaction via the conduction electrons can broaden the resonance linewidth if it occurs between unlike nuclei. Where the interaction is between like-nuclei, the linewidth is reduced. Such interactions are generally labelled 'exchange interactions'. Field inhomogeneity is also known to contribute to line-broadening.

In metallic systems, such as the normal state of a BCS superconductor, the shift of a resonance line is known as the 'magnetic shift (ΔK)', since it shifts the line by an amount proportional to the magnetic field. In an applied field $\mathbf{B_0}$, and in the absence of nuclear electric quadrupole effects, the shifted NMR frequency ω, is given by

$$\omega = \omega_0 (1+ \Delta K) = \gamma B_0 (1+ \Delta K) \qquad (1.9)$$

where ω_0 is the Larmor frequency.

The magnetic shift (ΔK) is the sum of two terms - the Knight shift (K) and the chemical shift (σ). The chemical shift stems from the effects of non-conduction electrons shielding the nucleus from the applied magnetic field. The interaction of the nuclear spins with the diamagnetism of the closed electron shells is evidently orbital in nature and generally represents only a small shift in the spectral line.

The most significant metallic shift is known as the Knight shift, after its discoverer Walter Knight[87,88]. It accounts for the magnetic hyperfine interactions between the electrons and the nuclei, and has both orbital (K_{orb}) and spin (K_s) contributions. The K_{orb} term* derives from the orbital Van Vleck paramagnetism, which arises when the application of a magnetic field causes an admixture of electron ground states and higher electron states. The spin contribution K_s reflects the change in the magnetic field seen at the nucleus due to the interaction of nuclear spins with the spin paramagnetism of the conduction electrons. Such contributions mean that the Knight shift is the most reliable measure of the electronic susceptibility of a system in the superconducting state, particularly the spin susceptibility.

Since the dominant mechanism† of spin-lattice relaxation in a normal metal is due to the scattering of the conduction electrons, a relationship exists between the Knight shift (K) and the spin-lattice relaxation time (T_1), such that

$$\frac{1}{T_1 T} \alpha K^2 \qquad (1.10)$$

where T = temperature in K. This relationship is known as the Korringa relation after its discoverer[89].

Experimentally, metallic shifts in resonant frequency (or magnetic field) are converted to parts per million (ppm) or percentage shift relative to a reference sample, in which the same nuclei are in an environment where the shifts are small in comparison to the Larmor frequency. Such reference nuclei are often referred to as 'bare' nuclei (as oppossed to 'metallic' nuclei). In addition to shifting the line, anisotropic Knight shifts in polycrystalline samples of non-cubic metals are found to have a broadening effect on the NMR lineshape.

---

87 W. D. Knight, *Phys. Rev.* **76** 1259 (1949)

88 C. H. Townes, C. Herring & W. D. Knight, *Phys. Rev.* **77** 852 (1950)

* The K_{orb} term is also known as the Van Vleck shift, K_{VV}.

† Note that other mechanisms, such as the orbital shift and quadrupolar relaxation, will also contribute to the spin lattice relaxation.

89 J. Korringa, *Physica* **16** 601 (1950)

1.3.3 Application to Superconductivity

Historically, the knowledge gained from NMR experiments has made a vital contribution to the understanding of superconductivity. The technique provides a particularly sensitive probe of the microscopic properties of these materials, since the onset of superconductivity significantly modifies the environment to which the nuclear spins are coupled. In addition, the spin dependent nuclear coupling energies are small in comparison to the electron and phonon energies, so the nuclei act as an almost invisible probe of many solid state phenomena.

However, the manifestation of the Meissner effect below T_c effectively restricts the NMR experiment to being no more than a surface probe technique - since the magnetic field only penetrates over a distance of the order of the penetration depth λ_L. Although such restrictions are significantly reduced in samples where the dimensions are comparable to or smaller than λ_L (such as thin films, wires or grains), an incomplete Meissner effect and only partial penetration of flux induces field inhomogeneities and diamagnetic shifts, which need to be taken into account. Early experiments on colloidal mercury by Knight[90] gave almost the same results as similar experiments performed on bulk samples.

Over the years, a number of static (shift and lineshape) and dynamic (relaxation) NMR experiments have been used to probe different features of the microscopic nature of BCS superconductors[91]:

(i) Information on the geometry of the vortex array in type II superconductors can be obtained from the measurement of the NMR lineshape and width. Here, the mixed state produces a distribution of inhomogeneous fields within the superconductor, which results in a broadening of the lineshape.

(ii) Within the flux lines of the vortex state, superconductivity is destroyed and the relaxation rate is effectively that of a normal metal. Thermal fluctuations of the magnetic flux lines, yield additional relaxation mechanisms which can be probed using NMR.

(iii) The condensation of conduction electrons into Cooper pairs below T_c, prevents them from contributing to the relaxation mechanisms and puts limitations on the scattering of the remaining excited state electrons. Schrieffer[92] developed a

---

90 W. D. Knight, G. M. Androes & R. H. Hammond, *Phys. Rev.* **104** 852 (1956)

91 A review of NMR in the superconducting state of BCS materials is given by D. E. Maclaughlin in *Solid State Physics*, Vol 31, ed. H. Ehrenreich, F. Seitz & D. Turnbull, Academic Press (1976).

92 J. R. Shrieffer, *Theory of Superconductivity*, Benjamin, New York (1964)

'coherence factor' to describe the development of pairing and its effect on scattering rates. In 1957, Hebel and Slichter[93] derived the spin-lattice relaxation rate in the superconducting state using the BCS framework. By including contributions from the orbital and core polarisation (see chapter 3), they were able to predict that just below T_c there would be an increase in the spin-lattice relaxation rate ($1/T_1$). Since the peak in $1/T_1$ was due to an increase in the density of states at the Fermi level and also to the coherence factor, it became known as the 'coherence peak'. It was first demonstrated experimentally by Hebel and Slichter in Al and later seen by Redfield and Anderson[94]. Experimental support for the BCS pairing theory was now available.

(iv) The creation of an energy gap (Δ) in the superconducting state, causes the number of excitations at *low temperatures* ($T<0.5T_c$) to be proportional to $\exp(-2\Delta/k_BT)$. The NMR relaxation rate $(1/T_1)^{\dagger}$ is also found to fall off exponentially and in proportion to this quantity, reflecting the fact that electrons must be excited across the energy gap in order to contribute to nuclear relaxation (Masuda & Redfield[95] (1962)). Gapless superconductivity can also be monitored by the effect that it has on the T_1 vs T slope.

(v) Yosida's BCS-based theoretical calculation[96] of the electronic spin susceptibility as a function of temperature (below T_c), predicted that the pairing of electrons in the BCS ground state (T=0) should manifest itself as a zero Knight shift*. However, initial experiments by Reif[97] in 1956, showed that when the Knight shift of Hg was extrapolated to T=0, it was in fact nonvanishing. This blatant contradiction of the singlet spin pairing theory was not due to the failure of BCS, but to the incomplete understanding of the mechanisms contributing to the Knight shift. The discrepancy was soon reconciled by the idea that the Knight shift has an orbital contribution, which is particularly strong in transition metals. Such a contribution is not affected by the pairing of electrons, nor by the actions of the spins. The Knight shifts of

---

93 L. C. Hebel & C. P. Slichter, *Phys. Rev.* **113** 1504 (1957)

94 A. G. Redfield & A. G. Anderson, *Phys. Rev.* **116** 583 (1959)

† Note that in the superconducting state, T_1 ceases to obey the Korringa relation in (1.9).

95 Y. Masuda & A. G. Redfield, *Phys. Rev.* **125** 159 (1962)

96 K. Yosida, *Phys. Rev.* **110** 769 (1958)

* Since, at the time, the electron spin susceptibility was considered to be the only contribution to the Knight shift and this was found to be zero at T=0.

97 F. Reif, *Phys. Rev.* **102** 1417 (1956): *Phys. Rev.* **106** 208 (1957)

mercury and tin, were found to have a large contribution due to the strong spin-orbital coupling induced in the conduction electron gas by the boundary in small particles. Subsequent experiments[98] on ^{27}Al finally produced data which was a good fit to the Yosida function, since spin-orbit coupling is small in Al.

NMR has proved to be a valuable tool with which to study superconductivity - not only did it verify aspects of the BCS theory, but also supported the extended theories of the more exotic superconductors, such as superfluid ^{3}He and heavy fermion systems.

The beauty of NMR lies in its ability to probe the static and dynamic electronic structure of different sites in a material. It is for this reason that the technique occupies a unique position in the study of HiT$_c$ superconductivity, along with the complementary methods of muon spin resonance (μsr) and Mössbauer effects. The new ceramic superconductors contain an abundance of nuclei which are available for study using NMR, such as ^{89}Y, ^{63}Cu, ^{65}Cu, ^{139}La, ^{205}Tl and, if it is isotopically enriched, ^{17}O. In many of the compounds, there are at least two nuclei in a single structure which can be probed, and in some cases there are three (e.g YBCO) or four (e.g the Tl-Pb-Y-Ca-Cu-Sr-O system).

Due to the large number of (i) sites and (ii) static and dynamic NMR techniques available, the experimental results (particularly on YBCO) are many and varied, and to list them here would be a fruitless task. Instead, the reader is referred to a review paper by Pennington and Slichter[99] in which the NMR results on YBCO are discussed, often with reference to the other cuprate systems. A recent article by Alloul,[100] which highlights the fundamental magnetic properties of the cuprates, is also relevant reading. Of course, many NMR results on YBCO will also be given, in context, throughout the rest of this document.

One aspect of NMR which will only be mentioned subsequently in passing is the nuclear relaxation rate. The normal state spin-lattice relaxation rate ($1/T_1$) is found to be Korringa-like ($(T_1T)^{-1}$=constant) for the ^{89}Y and ^{17}O nuclei in the fully oxygenated $YBa_2Cu_3O_7$ compound. This is in contrast to the $(T_1T)^{-1}$ for the ^{63}Cu nucleus which clearly does not obey any form of the Korringa law, since it has a distinct, much

---

98 H. L. Fine, M. Lipsicas & M. Strongin, *Phys. Lett.* **29A** 366 (1969)

99 C. P. Pennington & C. P. Slichter, 'Nuclear Resonance Studies In $YBa_2Cu_3O_{7-\delta}$', in *Physical Properties of High Temperature Superconductors*, chapter 5, Vol. II : ed. D. M. Ginsberg, World Scientific (1990).

100 H. Alloul, 'Magnetic Properties of the Cuprates', in *High Temperature Superconductivity*, Proceedings of the 39th Scottish Summer School in Physics, eds. D. P. Tunstall & W. Barford, IOP Publishing (1991).

enhanced temperature-dependence compared to ^{89}Y. Similarly, the $(T_1T)^{-1}$ for ^{63}Cu and ^{89}Y have very different temperature dependences in the oxygen depleted YBCO system.

Below T_c, the most striking confirmation of the BCS pairing theory - the Hebel-Slichter coherence peak - is distinctly absent in the relaxation rate profiles of all three nuclei. Instead, $1/T_1$ is found to decrease rapidly below T_c, and at low temperatures the exponential decay set out by BCS theory, is replaced by some sort of power law temperature-dependence[99]. A number of theories have tried to explain the anomolous features of the relaxation rate, but as yet there is no general consensus[101,102].

---

101 A. J. Millis, H. Monien & D. Pines, *Phys. Rev. B* **42** 167 (1990): H. Monien, P. Monthoux & D. Pines, *Phys. Rev. B* **43** 275 (1991): H. Monien, D. Pines & M. Takigawa, *Phys. Rev. B* **43** 258 (1991).

102 C. M. Varma, P. B. Littlewood & S. Schmitt-Rink, *Phys. Rev. Lett.* **63** 1996 (1989): P. C. Hammel, M. Takigawa, R. H. Heffner, Z. Fisk & K. C. Ott, *Phys. Rev. Lett.* **63** 1992 (1989)

Chapter 2

The Y-Ba-Cu-O System & Its Doped Derivatives

2.1 The Pure Y-Ba-Cu-O System

2.1.1 Introduction

The Y-Ba-Cu-O system is the most studied and probably best understood of all the high temperature superconductors, to date. Research activity has concentrated primarily on the YBCO system for a number of reasons: virtually single phase materials can be easily prepared using standard solid state synthesis techniques; the system is most amenable to crystal growth, and to the preparation of both thin and thick films on a number of substrates; oxygen stoichiometry can be controlled more accurately in YBCO than in any of the other layered cuprates; the normal and superconducting state properties can be studied extensively using chemical substitution at the Y, Ba and Cu sites; there is a general absence of intergrowth effects (except for twinning) and the anisotropy of the YBCO crystal is less than in the other high temperature superconductors; finally, its high transition temperature means that relatively inexpensive nitrogen systems can be used to cool it to its superconducting state.

The $YBa_2Cu_3O_{7-\delta}$ system is known to crystallise into two different structures depending on the oxygen content, controlled by δ. A non-superconducting tetragonal phase forms when $0.5<\delta\leq1.0$ and a superconducting orthorhombic phase exists when $0\leq\delta<0.5$. Preliminary structural details of the YBCO system were initially elucidated using single crystal X-ray and electron diffraction.[1,2,3] Such studies were hindered by the presence of twinning and anion disorder in the system and failed to predict the precise positions of the oxygens anions. It was not until the first powder neutron diffraction

---

1 R. M. Hazen, L. W. Finger, R. J. Angel, C. T. Prewitt, N. L. Ross, H. K. Mao, C. G. Hadidiacos, P. H. Hor, R. L. Meng & C. W. Chu, *Phys. Rev. B* **35** 7238 (1987)

2 L. LePage, W. R. McKinnon, J. M. Tarascon, L. H. Greene, G. W. Hull & D. A. Hwang, *Phys. Rev. B* **35** 7245 (1987).

3 T. Siegrist, S. Sunshine, D. W. Murphy, R. J. Cava & S. M. Zahurak, *Phys. Rev. B* **35** 7137 (1987)

studies[4,5,6] (with Rietveld refinements) that the oxygen positions were determined with any certainty.

Figures 2.1(a) and (b) show the currently accepted structures of the orthorhombic (O) (δ=0) and tetragonal (T) (δ=1) phases of YBCO. The notation used to label the Cu and O sites is now a fairly standard, but by no means universal one, first devised by Jorgenson et al[7,8] (Note the crystallographic axis convention also).

2.1.2 Structure of the Superconducting Orthorhombic Phase

The superconducting orthorhombic structure (figure 2.1(a)) is usually described in terms of CuO_2 planes, consisting of Cu(2) sites neighboured by O(2) and O(3), and Cu-O chains containing the Cu(1) and O(1) atoms along the b axis. O(4) is known as the 'bridging' or 'apical' oxygen and sits between the planes and the chains. There are two crystallographically distinct Cu atoms (one Cu(1) and two Cu(2)) and four different kinds of oxygen sites in the structure.

The orthorhombic Pmmm* crystal structure can be viewed as a defect perovskite lattice[9], consisting of three perovskite cubes stacked with Ba-Y-Ba ordering along the z-axis. The ideal 'triple' perovskite unit cell is expected to have 9 possible O atoms and so in comparison, the $YBa_2Cu_3O_7$ unit cell is 'oxygen deficient'. A similar conclusion is reached if one uses formal balancing of charges on the cations: the number of oxygens needed per unit cell are 8, 6.5 and 5, if the charges on all of the copper cations are assumed to be +3, +2 and +1 respectively.

Oxygen deficiencies are located in the Y layers, where O atoms are completely missing, and in the basal copper plane, where for $YBa_2Cu_3O_7$, the O(5) positions are vacant (see Figure 2.1(b) for comparison) at room temperature.

---

4 J. J. Capponi, C. Chaillout, A. W. Hewat, P. Lejay, M. Marezio, N. Nguyen, B. Raveau, J. L. Soubeyroux, J. L. Tholence & R. Tournier, *Europhys. Lett.* **3** 1301 (1987)

5 M. A. Beno, L. Soderholm, D. W. Cappone II, D. G. Hinks, J. D. Jorgenson, I. K. Schuller, C. U. Segre, K. Zhang & J. D. Grace, *Appl. Phys. Lett.* **51** 57 (1987)

6 F. Beech, S. Miraglia, A. Santoro & R. S. Roth, *Phys. Rev. B* **35** 8778 (1987)

7 J. D. Jorgenson, M. A. Beno, D. G. Hinks, L. Soderholm, K. J. Volin, R. L. Hitterman, J. D. Grace, I. V. Schuller, C. U. Segre, K. Zhang & M. S. Kleefisch, *Phys. Rev. B* **36** 3608 (1987)

8 J. D. Jorgenson, B. W. Veal, W. K. Kwok, G. W. Crabtree, A. Umezawa, L. J. Nowicki & A. P. Paulikas, *Phys. Rev. B* **36** 5731 (1987)

* Pmmm is the space group - equivalent to D_{2h}^1 and No. 47 in the International Tables.

9 of which $CaTiO_3$ is a prototype, see R. M. Hazen, *Scientific American*, p52, June 1988.

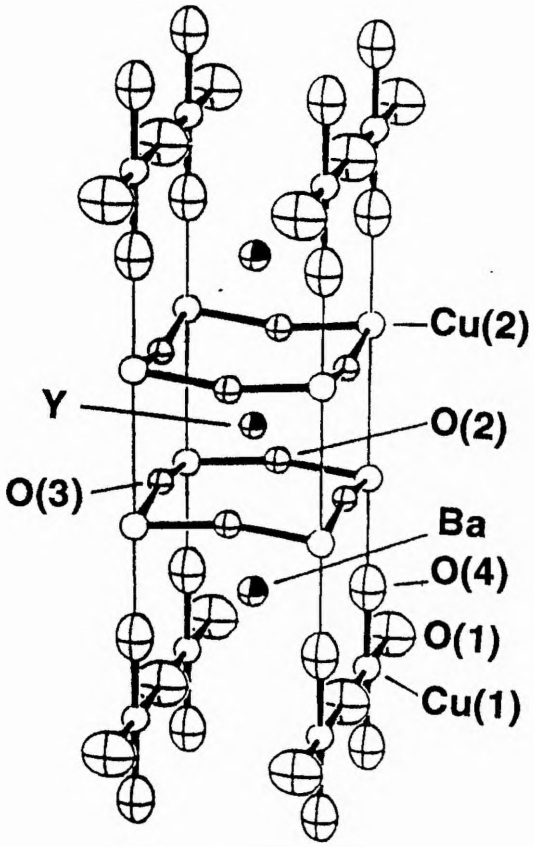

Figure 2.1(a)

Figure 2.1(a)

Structure of the Superconducting Orthorhombic $YBa_2Cu_3O_7$ phase. The ellipsoids schematically represent the probability density for each site.

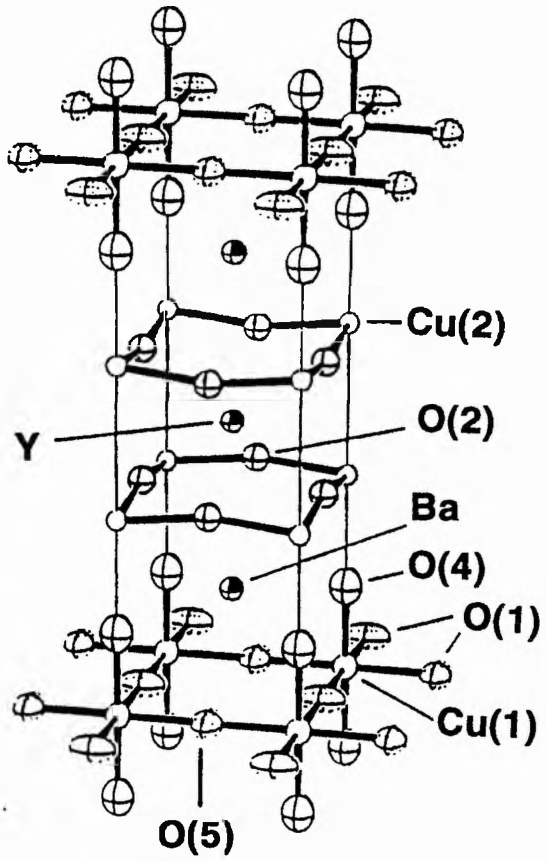

Figure 2.1(b)

Figure 2.1(b)

Structure of the Non-superconducting Tetragonal $YBa_2Cu_3O_{7-\delta}$ phase. For $\delta=1$ the oxygen atoms denoted by dashed ellipsoids are missing. In this situation CuO_4 dumbells are formed which are oriented along the c-axis. The O(5) sites are labelled here for clarity.

A mixed Cu valency exists as a result of the oxygen deficiency. Since the Cu(2) is found to be in the 2+ state, charge balance suggests that the four Cu(1) sites must contain Cu^{3+} ions†, giving an average Cu valency of +2.33. The Cu(1) atoms have a 4-fold square planar oxygen coordination, while the Cu(2) atoms are 5-fold coordinated with respect to oxygen. The Cu(2) atoms sit at the apex of a pyramid with two O(2) and two O(3) forming a square plane in the ab plane. The Y^{3+} ion is 8-fold coordinated by a distorted cube of O(2) and O(3) ions and the Ba^{2+} has a 10-fold oxygen coordination when the O(1) site is fully occupied.

Appendix A.3 gives selected bond lengths and angles for an orthorhombic near $YBa_2Cu_3O_7$ structure. It is worth noting that the longest Cu-O distance is the Cu(2)-O(4) bond, suggesting that the copper in the planes is only weakly linked to those in the chains via the apical oxygen. The Cu(1)-O(1) bond length is the shortest within the structure and is probably a consequence of the Cu^{3+} ion's preference for the chain site.

2.1.3 The Orthorhombic to Tetragonal Transition

The crystal structure and electrical properties of $YBa_2Cu_3O_{7-\delta}$ are strongly dependent on the value of δ. In situ X-ray and neutron diffraction experiments[7] have shown that a continuous, second order[10] orthorhombic to tetragonal transition occurs with increasing δ. A sample of δ=0 is found to evolve oxygen as a continuous function of temperature, when heated in a controlled atmosphere. With a slow loss of oxygen, the orthorhombic distortion* of the sample gradually decreases, until at some point, sufficient oxygen (δ>0.5) has been lost for the structure to become tetragonal. At high temperatures, under equilibrium conditions, experimental evidence[11] suggests that the orthorhombic to tetragonal transition always occurs at δ=0.5 ($O_{6.5}$), irrespective of the conditons used to 'boil off' the oxygen. The critical factor in controlling the transition is the oxygen composition of the sample.

The transition is fully reversible and the superconducting orthorhombic phase can be generated by slow cooling the tetragonal phase back through the transition, in an oxygen-rich atmosphere. The tetragonal phase can be preserved at room temperature by heating the sample at elevated temperatures (about 900°C) and then quenching rapidly into

---

† The nominal chemical formula is generally written as $YBa_2Cu(2)_2^{2+}Cu(1)_1^{3+}O_7$.

10 P. P. Frietas & T. S. Plaskett, *Phys. Rev. B* **36** 5723 (1987)

* where orthorhombic distortion = (b - a)/(b + a)

11 P. Strobel, J. J. Capponi, C Chaillot, M. Marezio & J. J. Tholence, *Nature* **327** 306 (1987)

liquid nitrogen[8] or mercury[12] (for example). In all cases the tetragonal phase is still found to be non-superconducting.

Samples of intermediate oxygen content (i.e. $\delta \neq 0$ or 1) can be prepared by quenching the parent tetragonal (O_6) phase from high temperatures under controlled conditions. Such samples exhibit a smooth variation of T_c as a function oxygen content, with the samples becoming insulators at $\delta=0.5$. An alternative method of preparation is to remove oxygen from the orthorhombic (near O_7) phase at considerably lower temperatures (approximately 500°C)[13]. The variation of T_c with oxygen content in samples prepared by this method is significantly different from that found in the samples quenched from the tetragonal phase. Figure 2.2 shows T_c as a function of δ for samples synthesized at lower temperatures.

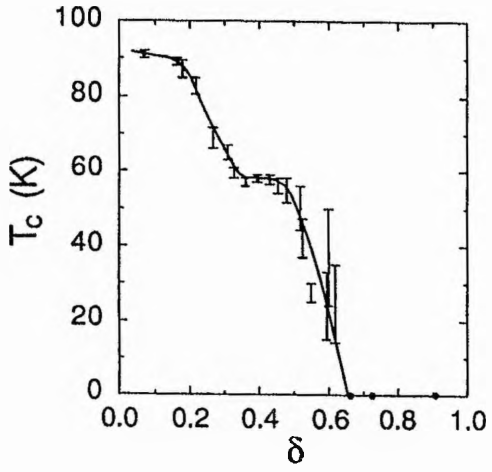

Figure 2.2

T_c of oxygen deficient samples of $YBa_2Cu_3O_{7-\delta}$ produced by quenching into liquid nitrogen from various oxygen partial pressures at 520°C. The δ values are determined by weight loss measurements referenced to a starting composition of $YBa_2Cu_3O_{6.93}$.
(After Jorgenson et al[13])

It is evident that a 'two plateau' phenomenon exists in such a function. In the range $0<\delta<0.2$, commonly referred to as the '90K plateau', T_c decreases by a small amount. It then falls rapidly down to a '~60K plateau' which exists in the range $0.35<\delta<0.45$. For

---

12 C. Namgung, J. T. S. Irvine, J. H. Binks & A. R. West, *Supercond. Sci. Technol.* **1** 169 (1988)

13 J. D. Jorgenson, B. W. Veal, A. P. Paulikas, L. J. Nowicki, G. W. Crabtree, H. Claus & W. K. Kwok, *Phys. Rev. B* **41** 1863 (1990)

$\delta>0.5$, T_c again drops rapidly, with samples finally becoming non-superconducting at an oxygen content of 6.35 ($\delta\approx0.65$)*, where the orthorhombic structure collapses into tetragonal symmetry.

Figure 2.1(b) shows the crystal structure of the parent tetragonal O_6 phase (space group P4/mmm)†. This insulating AF phase is stable at high temperatures and is found to be non-superconducting at all temperatures. Lower oxygen content results in a decrease in the average valence of Cu, which falls to +1.67 at $\delta=1$. This leads to an effective increase in the a and c parameters and a decrease in the b parameter - until at the orthorhombic to tetragonal transition the a and b parameters become equal. There is also a discontinuous jump in the c parameter and the cell volume at the transition (see Appendix A.2). At O_6 the square pyramidal coordination of the Cu(2) atom remains intact, but the square planar cordination of the Cu(1) degenerates to a simple 2-fold linear coordination. In the limit $\delta=1$, Cu(1) is in a Cu^+ or $3d^{10}$ state.

Appendix A.4 shows the standard bond lengths and angles for the near O_6 material. The long Cu(2)-O(4) bond length observed in the orthorhombic structure becomes longer in the reduced material and the Cu(1)-O(4) bond becomes shorter. This indicates a further decrease in the coupling between the Cu(1) chains and Cu(2) planes.

2.1.4 Oxygen Ordering

The orthorhombic to tetragonal transition is an order-disorder transformation. At $\delta=0$, the oxygens in the 1-dimensional chains of the orthorhombic structure are ordered and there is evidence that, at room temperature, the O(1) site is fully occupied while the O(5) site is vacant. This phase is known as the 'ortho I' phase. As δ is increased there is a continuous disordering of the oxygen atoms into the normally vacant O(5) site. The increasing vacancies at the O(1) site and the increasing occupancy of the O(5) site completely disrupt the 1D chains of the orthorhombic structure. At the transition, the O(1) and O(5) sites become tetragonally equivalent, giving rise to a disordered 2-dimensional Cu-O network in the basal plane. As δ approaches one (i.e. O_6), there is insufficient ordering to establish a preferred chain direction** and so the oxygens randomly occupy the O(5) and O(1) sites, leaving the average structure tetragonal.

---

* A significant number of studies now treat $O_{6.35}$ as the critical oxygen content for the orthorhombic to tetragonal transition.

† This space group corresponds to D_{4h}^1 or No. 123 in the international tables.

** And hence there are no chains in the O_6 structure.

A number of reports using XANES[14] and electron diffraction[15,16] on the near $O_{6.5}$ material suggest that there are two types of coordination present at the Cu(1) site - namely the 4-fold square planar coordination (as in the orthorhombic O_7 structure) and the 2-fold linear coordination found in the tetragonal O_6 structure. The results are consistent with an ordered $O_{6.5}$ superstructure in which oxygen is removed from the O(1) position in alternate Cu(1)-O(1) chains. Strings of oxygen vacancies are created along the b-axis in the basal plane and the unit cell is doubled along the a-axis ('ortho II' phase). Similar studies have also revealed the existence of a vacancy-ordered superstructure for other specific values of δ (i.e. δ=0.25) and it is now generally believed that such a superstructure is responsible for the '60K plateau' observed in the T_c results.

Recent calculations by Poulson et al[17] based on the ortho I and ortho II phases, strongly suggest that orthorhombic symmetry (at least on a local scale*) is a necessary condition for superconductivity in the YBCO system.

2.1.5 Variation of Copper Valency & Hole Concentration

It is evident that the $Cu(2)^{2+}$ state and its associated magnetic moment are preserved from the AF state through to the metallic/superconducting state. The valency of the Cu(1) ion, on the other hand, is found to increase linearly with increasing oxygen content[18] and to have a direct effect on the charge transfer from the planes. In the insulating O_6 material (δ=1), all of the Cu(1) sites are in a Cu^+ state and do not possess a magnetic moment. As the oxygen concentration increases in the chains, the $Cu(1)^+$ ions are gradually converted to $Cu(1)^{2+}$ ions and charge imbalance results in greater charge transfer from the planes. At δ=0.5, the ordering of oxygen in the ortho II phase results in up to half of the Cu(1) ions retaining a linear coordination. These ions remain in the Cu^+ state leaving up to 0.5 holes per formula unit to be distributed between the other copper atoms. Such holes are stabilised in the CuO_2 planes by the internal c-axis electric field and the T_c of the system rises.

---

14 K. V. R. Rao & K. B. Garg, *Bull. Mater. Sci.*, **14** 853 (1991)

15 C. Chaillout, M. A. Alario-Franco, J. J. Capponi, J. Chenavas, J. L. Hodeau & M. Marezio, *Phys. Rev. B* **36** 7118 (1987)

16 C. H. Chen, D. J. Werder, L.F. Schneemeyer, P. K. Gallagher & J. V. Waszczak, *Phys. Rev. B* **38** 2888 (1988)

17 H. F. Poulson, N. H. Anderson, J. V. Anderson, H. Bohr & O.G. Mouritsen, *Nature* **349** 594 1991.

* which are maybe too small to be probed experimentally, or which have not previously been examined.

18 R. J. Cava, A. W. Hewat, E. A. Hewat, B. Batlogg, M. Marezio, K. M. Rabe, J. J. Krajewski, W. F. Peck Jr. & L. W. Rupp, *Physica C* **165** 419 (1990)

Further addition of oxygen in the range $0.5>\delta>0.25$ converts the remaining $Cu(1)^{+}$ ions to $Cu(1)^{2+}$. In this interval, no holes are created in the planes and the '60K plateau', indicated by the T_c variation, results. At $\delta=0.25$, another oxygen-ordered superstructure forms in which the partially occupied chains contain $Cu(1)^{2+}$ ions with the b-axis oxygen sites alternately occupied and vacant. The localised spins on the $Cu(1)^{2+}$ ($3d^9$) ions can order AF via the Cu^{2+}-O^{2-}-Cu^{2+} superexchange interaction, just as with the $Cu(2)^{2+}$ ions.

As δ decreases below 0.25 and approaches zero, the $Cu(1)^{2+}$ ions are converted to $Cu(1)^{3+}$ ions, causing additional holes to form in the CuO_2 layers and the T_c to rise to a maximum at $\delta=0.09$. By $\delta=0$, the *nominal* valence on the chain copper is 3+. Initially, no direct experimental evidence existed to support the presence of an exotic Cu^{3+} ion in YBCO[19], but more recent XPS studies[20] indicate that the ion is clearly present. Theoretically, Emery[21] postulates that the Cu configurations in pure YBCO can be represented by $(Cu_{1-2y})^{+}(Cu_{2+2y})^{2+}$ for the tetragonal phase and $(Cu_{1-y})^{+}(Cu_{2+y})^{2+}$ in the orthorhombic phase (where $y = 1-\delta$). The absence of a Cu^{3+} ion is evident.

The variation in hole concentration as a function of δ has been investigated experimentally using chemical titration methods and Hall effect techniques. In such studies, the Hall coefficient, R_H (= 1/nec, where n is the carrier concentration, e is the carrier charge and c is the speed of light) is often converted to a Hall number per unit cell, n_H (where $n_H = V_{cell}/e.R_H$ and V_{cell} is the volume of the unit cell) for easy comparison between systems.

Figure 2.3 shows the room temperature variation of n_H with δ for a ceramic sample of $YBa_2Cu_3O_{7-\delta}$. Generally, the plot can be broken down into three distinct regions[22]: for $0<\delta<0.1$, n_H decreases sharply with δ, due to the decrease in conductivity in the chains; in the range $0.1<\delta<0.68$, n_H appears to vary exponentially as the R_H becomes more and more associated with the CuO_2 planes alone[23]; finally as δ exceeds 0.68, the sample becomes non superconducting and n_H again falls rapidly.

In all of the ceramic cuprates, R_H is found to be positive (hole-like) and to follow anomalous normal state behaviour, by increasing monotonically with decreasing

---

19 H. Zhang, S. Q. Feng, Q. R. Feng & X. Zhu, *Mod. Phys. Lett.* **5** 511 (1991)

20 W. R. Flavell & R. G. Egdell, *Phys. Rev. B* **39** 231 (1989)

21 See 'Strong Correlations & High Temperature Superconductivity' by V. J. Emery in *High Temperature Superconductivity,* Proceedings of the 39th Scottish Summer School in Physics, eds. D. P. Tunstall & W. Barford, IOP Publishing (1991)

22 J. R. Cooper, S. D. Obertelli, A. Carrington & J. W. Loram, *Phys. Rev. B* **44** 12086 (1991)

23 Y. Tokura, J. B. Torrance, T. C. Huang & A. I. Nazzal, *Phys. Rev. B* **38** 7156 (1988)

temperature[24]. There is generally good agreement between total carrier concentrations obtained from iodometric titrations and those deduced from Hall effect measurements- except where the latter is strongly temperature dependent and cannot identified with n. Data obtained from both methods seems to indicate that there is no linear correlation between hole concentration and T_c[25].

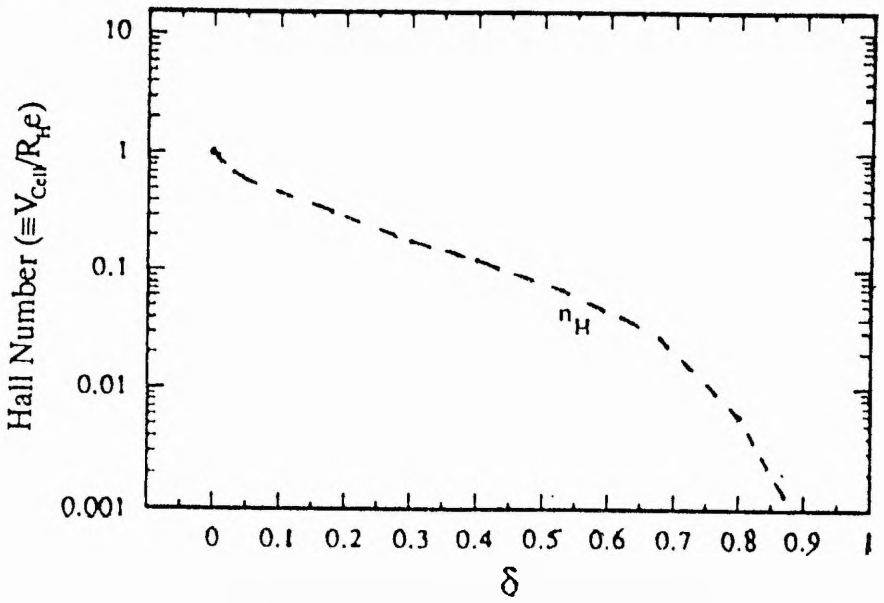

Figure 2.3

Semi-logarithmic plot of the variation of the Hall number, n_H with δ in the $YBa_2Cu_3O_{7-\delta}$ system at room temperature.

(Adapted from Cooper et al[22])

2.1.6 Magnetic Structure

From the standard YBCO phase diagram with respect to oxygen, shown in figure 2.4, it is evident that the $YBa_2Cu_3O_{7-\delta}$ system exhibits either superconductivity or long range antiferromagnetic order depending on the oxygen composition.

At the lower oxygen extreme, the parent $YBa_2Cu_3O_6$ (δ=1) compound has localised magnetic moments on the $Cu(2)^{2+}$ sites associated with the Cu 3d holes and the $Cu(1)^+$ site has no magnetic moment. The local spins on the Cu(2) sites couple antiferromagnetically within the planes and the high exchange coupling between spins

---

[24] See 'The Hall Effect & Its Relation to Other Transport Phenomena in the Normal State of the High Temperature Superconductors' by N. P. Ong, *Physical Properties of High Temperature Superconductors*, Vol II: ed D. M. Ginsberg, World Scientific Publishers (1989).

[25] B. Batlogg in *High Temperature Superconductivity*, Los Alamos Symposium, eds. K. Bedell, D. Coffey, D. Meltzer, D. Pines & J. R. Scrieffer, Addison-Wesley (1989)

(J~1500K) generally categorises the compound as a 2D spin 1/2 Heisenberg AF. A three-dimensional (3D) AF ordered state (known as AF1) results from weak interactions (presumably dipolar due to the absence of a bridging O) between planes ($J_\perp/J \sim 10^{-5}$) and yields a Néel temperature of around 420K. The magnetic structure, elucidated by neutron diffraction techniques,[26,27] is formed from two simple sublattices in which the unit cell is doubled in the ab plane with respect to the crystallographic unit cell. The Cu(2) spins lie in the plane perpendicular to the c-axis pointing in the [100] direction and are found to have a saturated magnetic moment, μ of $(0.64\pm0.05)\mu_B$ at zero temperature (cf. expected moment for Cu^{2+} in the $3d_{x2-y2}$ state in octahedral symmetry is $\mu \approx 1.05\mu_B$).

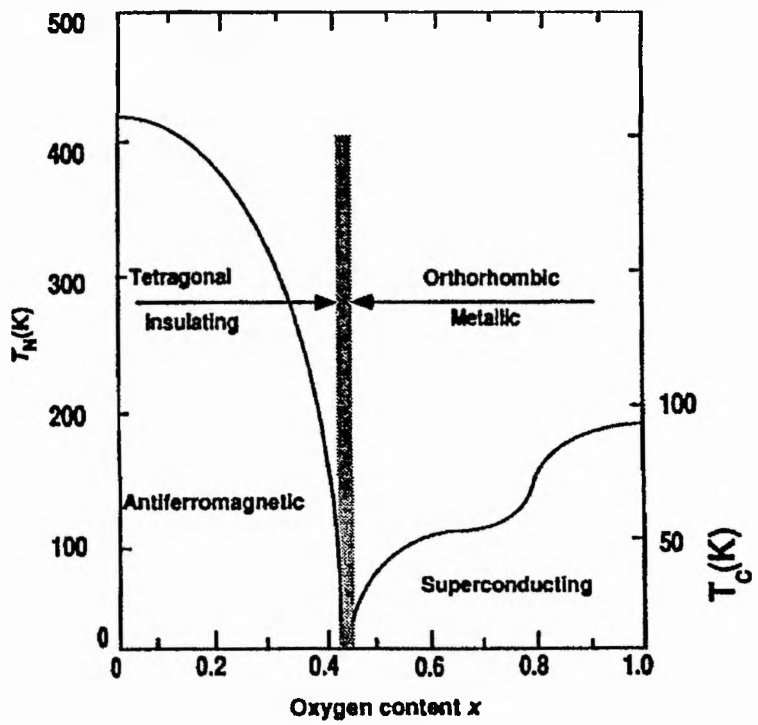

Figure 2.4

Schematic temperature-O concentration phase diagram for $YBCO_{6+x}$ (where $\delta=1-x$) showing the superconducting regime, the insulating-metallic boundaries, the magnetic-non magnetic boundaries and the structural transitions. Shaded region indicates a 'miscibility gap' where metallic or semiconductor behaviour is not well defined (Pickett et al[28]).

---

26 J. M. Tranquada, A. H. Moudden, A. I. Goldman, P. Zolliker, D. E. Cox, G. Shirane, S. K. Sinha, D. Vaknin, D. C. Johnson, M. S. Alvarez, A. J. Jacobson, J. T. Lewandowski & J. M. Newsam, *Phys. Rev. B* **38** 2477 (1988)

27 H. Yasuoka, T. Shimizu, Y. Ueda & K. Kosuge, *J. Phys. Soc. Jpn.* **57** 2659 (1988)

28 W. E. Pickett, H. Krakauer, R. E Cohen & D. J. Singh, *Science* **255** 46 (1992)

The introduction of oxygen into the O(1)/O(5) sites of the parent (O_6) compound converts $Cu(1)^{+}$ into $Cu(1)^{2+}$ as the O^{2-} ion draws an electron from each of its neighbouring Cu ions. The Néel temperature T_N, has been shown[29] to decrease by less than 0.5% for $\delta \sim 0.9$ and the physical parameters which relate to the magnetic properties, such as the AF correlation length (ξ) and $J_\perp$, appear to change little for $1 \geq \delta \geq 0.9$. In addition, the magnetic order is not altered until δ becomes less than 0.8, strongly suggesting that for $1 \geq \delta > 0.8$, the holes created at the Cu(1) site by the introduction of oxygen are mainly localised at that site[30].

The magnetic moments which begin to appear at the Cu(1) site with decreasing δ can couple AF and eventually produce a second type of AF ordered phase which is decoupled from the static AF order of the Cu(2) sites. However, at very low oxygen concentrations, any two neighbouring Cu(1) sites bridged by an oxygen atom are coupled into a spin singlet via the strong superexchange AF coupling through the oxygen orbitals. The resulting singlet may also become decoupled from the AF lattice.

At an oxygen concentration corresponding to $\delta=0.9$, the Néel temperature for the CuO chains is $T_{N2}=80\pm10$K compared with $T_{N1}=410\pm20$K for the CuO_2 planes. As δ decreases below 0.8, both T_{N1} and T_{N2} decrease rapidly as the interplanar coupling is frustrated by the appearance of a magnetic moment at the chain site and the long range ordering is destroyed with the onset of hole doping†. It has been suggested that the 3d hole of the $Cu(1)^{2+}$ is orthogonal to the 3d holes in the CuO_2 planes and so the plane-chain-plane coupling can be expected to be ferromagnetic[31]. The 3D AF ordering of Cu spins occurs throughout the tetragonal region of the phase diagram, finally giving way to an disordered spin glass phase at around $\delta \approx 0.6$ ($T_N=0$) and then to superconductivity beyond this. As yet, AF order and superconductivity have not been found to coexist at the same composition. Beyond $\delta<0.9$ and for its whole range of existence, the magnetic behaviour of the $Cu(1)^{2+}$ ion is determined by the short range ordering of the oxygens.

It has been implied in a number of theories that AF ordering corresponds to a strong limit of the correlation of electrons in the Cu-O orbits within the CuO_2 plane and that superconductivity appears midway between the strong and weak correlation limit. Further experimental evidence is needed to confirm whether or not magnetic interactions are essential for the stabilisation of the superconducting electronic ground state.

---

29 H. Alloul, T. Ohno & P. Mendels, *Jnl. Less Comm. Metals* **164-165** 1022 (1990)

30 P. Mendels, H. Alloul, J. F. Marucco, J. Arabski & G. Collin, *Physica C* **171** 429 (1990)

† For $\delta>0.65$, neutron diffraction experiments do not indicate any significant magnetic moments on the oxygen ions.

31 J. M. Tranquada, *J. Appl. Phys.* **64** 6071 (1988)

2.1.7 Twinning & Defect Structures

In general, the oxide superconductors can support a wide variety of structural defects[32]. Due to the existence of the two closely related tetragonal and orthorhombic structures, twinning is by far the most common structural defect in the 123 material. Twinning is an internal planar defect. A crystal is twinned when one portion of the lattice is a 'mirror image' of the neighbouring portion - the 'mirror' being the 'twin plane boundary'. In the 123 material, transformation twins form during the cooling from the tetragonal to orthorhombic phase (during synthesis) and so only the orthorhombic phase is found to be heavily twinned†. The 2-fold symmetry of the basal plane of the bulk orthorhombic structure is broken when oxygen ordering in the basal plane causes an elongation of the b-axis and a contraction of the a-axis[33]. A mirror plane is generated along the [110] crystal plane and dense arrays of parallel twins with spacings of 20 to 100nm are observed over an entire sample of YBCO(δ=0). A number of models have been proposed for the YBCO twin boundary structure[34], some of which are reviewed in ref. 32. It should be noted that untwinned crystals of YBCO can be produced by applying hydrostatic pressure to the 123 crystal during cooling through the tetragonal to orthorhombic phase transition.

Two new phases of YBCO are formed if stacking faults are periodically introduced into the 123 structure. The so-called 124 or $YBa_2Cu_4O_8$ structure is produced when extra Cu-O layers are inserted between the Ba-O layers in *every* 123 unit cell, giving rise to double Cu-O layers. By introducing extra Cu-O layers in *every other* 123 unit cell, it has also been possible to produce crystals in which single and double Cu-O layers alternate regularly. This structure corresponds to an ideal composition of $Y_2Ba_4Cu_7O_{14}$ or $123^{1/2}$. Both the 124 and $123^{1/2}$ compounds are orthorhombic with the 124 material having a T_c of 81K and the ytterbium derivative of $123^{1/2}$ having a T_c of 86K.

In a recent article[35] Jorgenson developes the relationship between defects, defect ordering and superconductivity in YBCO. He concludes that defects formed in the charge reservoir layer can function as a doping mechanism which creates carriers and gives rise

---

32 Details of such defects can be found in R. Beyers & T. M. Shaw, 'The Structure of $Y_1Ba_2Cu_3O_{7-\delta}$ and its Derivatives' in *Solid State Physics*, Vol. 42 : eds. H. Ehrenreich & D. Turnbull, Academic Press (1989).

† Twins are absent from the tetragonal structure and are thought to be impossible by symmetry: see Brokman, ref. 33.

33 A. Brokman, *Solid State Comm.* **64** 257 (1987)

34 E. A. Hewat, M. Dupuy, A. Bourret, J. J. Capponi & M. Marezio, *Solid State Comm.* **64** 517 (1987)

35 J. Jorgenson, *Physics Today*, p34 June 1991

to superconducting behaviour in a material that may normally be an insulator. Defects associated with the conduction plane can destroy superconductivity, whilst defect ordering can enhance or suppress the charge transfer depending on the remaining structure.

2.2 The Substituted Y-Ba-Cu-O System

2.2.1 Introduction

Chemical substitution has been employed extensively in the YBCO system to determine essential information, such as the oxidation states of Cu, the relative importance of the Cu(1)-O chains and Cu(2)-O planes, the effect of magnetic impurities and the distortion of the crystal lattice. Some degree of substitution (either partially or totally) has been achieved on each site in the YBCO structure, to date. What has emerged so far from the analysis is that properties which play a significant role in controlling the T_c in conventional superconductivity - such as cell volume, crystal structure distortion, oxidation states and, to some extent, the pair breaking effect of magnetic impurites, become less important, secondary parameters in high temperature superconductors. The T_c of YBCO seems to be determined primarily by its electronic structure.

The application of pressure is known to have a positive effect on the T_c of YBCO. Chemical pressure can be induced by selectively replacing a large size ion with a smaller one. The ionic radius, charge and valence of the substituted ion with respect to the replaced ion is of major consequence.

As it is generally accepted that superconductivity occurs in the CuO_2 planes and that T_c is proportional to the concentration of mobile holes in the planes, there are 3 important catagories of substitution: (i) those which have little or no effect on the planes; (ii) those which indirectly effect the planes via the charge transfer mechanism and (iii) those which directly effect the planes due to precise substitution for the Cu(2) ion in the planes.

The following sections discuss the general effects of common substitutions in the YBCO system. Some of the more important substitutions are detailed in Appendix A, while the less common ones are discussed in a schematic survey by Felner[36].

---

[36] I. Felner, *Thermochimica Acta* **174** 41 (1991)

Standard substitutions within the YBCO system are represented by the following general formula, which defines the subscript convention for x, y, and z:

$$Y_{1-z}RE_z(Ba_{1-y}A_y)_2(Cu_{1-x}M_x)_3O_{7-\delta} \qquad (2.1)$$

where RE = almost any trivalent Rare Earth element (e.g. La, Nd, Sm, Eu, Gd, Dy, Ho, Er, Tm, Yb, Pr or Lu) (see Appendix A.5)

A = generally an alkaline-earth element or other divalent ion (e.g Ca, Sr, Cd, Pb or Sn) (see Appendix A.6)

M = commonly a transition metal (e.g. Co, Fe, Zn, Ni) or non-transition metal (e.g. Al, Au, Ga, Ag) (see Appendix A.7)

x, y, z $\leq$ 1, generally and $0 \leq \delta \leq 1$.

2.2.2 Rare-Earth Substitution For Y

Most of the RE elements readily form the orthorhombic 123 structure, when partially or fully substituted for Y.[36,37] The notable exceptions are Ce and Tb, which are unable to form the orthorhombic structure due to the ease with which they form Ce^{4+} and Tb^{4+} ions. The 123 material seems reluctant to tolerate non-trivalent ions at the Y site. It is anticipated that the 123 structure will also form for PmBCO, but as yet the system has not been sythesized due its rapid radioactive decay.

The total substitution of RE elements for Y does not significantly change the superconducting transition temperature of the material, despite the considerable electronic magnetic moment that the majority of the RE's possess†. The same orthorhombic crystal structure is obtained for all 12 of the RE-substituted compounds (listed under the general formula) and T_c's of around 90K are achieved for all, except $PrBa_2Cu_3O_{7-\delta}$, which is not superconducting down to 4K (see Appendix A.5.2). The substitution of Y for Pr leads to a superconducting to AF transition with increasing z (T_{N2}=325K for $PrBa_2Cu_3O_7$) - even though the materials are oxygen rich[38]. A similar phase diagram to that observed in the pure YBCO system as a function of oxygen, is found in the $Y_{1-z}Pr_zBa_2Cu_3O_{7-\delta}$ system as a function of z.

---

37 See 'Rare Earth & Other Substitutions in High Temperature Superconductors' by J. T. Market, Y. Dalichaouch & M. B. Maple, *Physical Properties of High Temperature Superconductors*, Vol I: ed D. M. Ginsberg, World Scientific Publishers (1989) and references therein.

† due to their partially filled 4f electron shells

38 I. Felner, U. Yaron, I. Nowik, E. R. Bauminger, Y. Wolfus, E. R. Yacoby, G. Hilscher & N. Pillmayer, *Phys. Rev. B* **40** 6739 (1988)

Long range magnetic ordering has been reported in Gd, Dy, Er and Ho.[39,40] The Gd system has proved particularly interesting. Mössbauer experiments have provided evidence for the absence of conduction electrons at the Gd site in the $GdBa_2Cu_3O_{7-\delta}$ lattice indicating that there is no exchange coupling of the Gd ion with the conduction electrons[40]. This could explain why the superconductivity coexists with long range antiferromagnetic order and why RE substitution has little effect on T_c. In the $Y_{1-z}Gd_zBa_2Cu_3O_{7-\delta}$ system, the Néel temperature of Gd appears to be proportional to the Gd concentration for $z>0.2$.

Whilst partial substitution by other, smaller trivalent ions, divalent and monovalent ions is limited by the radius and valence of the donor ion, some success has been achieved in substituting such ions as Al, Ga, Tl, Ca & Na into the YBCO structure at the Y site[36].

2.2.3 Isovalent & Non-Isovalent Ion Substitution for Cu

The chemical substitution of various transition and non-transition metal ions for Cu in the 123 compound has proved fruitful. Not only are there two distinct copper sites available for substitution, but also a considerable combination of trivalent, divalent, magnetic and non-magnetic ions which are readily soluble in the YBCO structure at the Cu site.

Whilst some atoms are able to substitute preferentially for the Cu ions in either the planes or the chains, others replace the Cu randomly on both crystallographic sites. In many cases, partial substitution for Cu induces an orthorhombic to tetragonal structural transition. The substituted tetragonal phase is somewhat different to that which occurs as a result of the variation of δ in $YBa_2Cu_3O_{7-\delta}$. The non-superconducting tetragonal (I) phase which appears in the pure YBCO system at $\delta \geq 0.65$ has a c-axis which is greater than $3a_{tetragonal}$, but is comparable to $3b_{orthorhombic}$. The stretching of the c-axis during the orthorhombic to tetragonal transition is the result of oxygen vacancies appearing in the basal plane. In contrast, the substituted tetragonal (II) phase is a direct consequence of the impurites doped onto the Cu site. This phase usually has an oxygen content greater than 7 and a c/a ratio of 3, the same as for the orthorhombic cell. In short, the tetragonal (II) phase has an orthorhombic local symmetry, with accidentally equal a and b axes.

Most of the work on Cu substitution has concentrated on the elemental series from Mn to Ga, but a number of studies have also used other metalloids such as Ag, Au and

---

39 B. W. Lee, J. M. Ferreira, Y. Dalichaouch, M. S. Torikachvili, K. N. Yang & M. B Maple, *Phys. Rev. B* **37** 2368 (1988)

40 E. E. Alp, L. Soderholm, G. K. Shenoy, D. G. Hinks, D. W. Copone II, K. Zhang & B. D. Dunlap, *Phys. Rev. B* **36** 8910 (1987)

Al. In contrast to rare earth substitution on the Y site, each element doped on the Cu site is known to suppress T_c continuously as a function of dopant content, x. The variation of T_c with x% for a number of common dopants is given in figure 2.5.

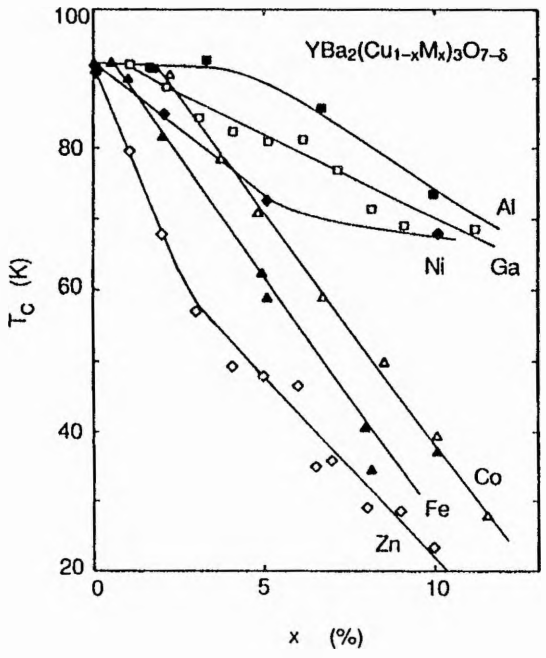

Figure 2.5

T_c vs dopant concentration x for $YBa_2(Cu_{1-x}M_x)_3O_{7-\delta}$.
M = Al (solid squares), Ga (open squares), Ni (solid diamonds), Co (open triangles), Fe (solid trangles) and Zn (open diamonds).
(Source : Markert et al[37] and references therein)

Unexpectedly, non-magnetic Zn impurites have a more drastic effect on the superconducting properties than any magnetic impurity. Ni appears to have the least overall effect, with T_c decreasing rapidly at low concentrations but being much less dramatic at high Ni content.

The substitutions appear to fall naturally into two categories. The divalent ions, Zn and Ni, are able to substitute onto the 5 coordinate Cu(2) site. Such substitutions do not cause disorder in the chains and so the orthorhombicity and oxygen content of the doped structures are left intact. In the case of Zn, the 3d level is completely full and so the substitution of Zn for Cu(2) eliminates 3d holes, causing a decrease in the density of states at the Fermi level and a rapid decrease in T_c. Doping at the Cu(2) site seems most effective in reducing T_c, irrespective of whether the dopant is magnetic or not.

The trivalent dopant ions of Fe, Co, Ga and Al have a higher oxidation state and can be expected to occupy the site with the higher oxygen coordination. Since the Cu(2)-Cu(2) spacing prevents the trivalent ions' preferred octahedral coordination from forming at the Cu(2) site, the trivalent dopants substitute almost exclusively on the Cu(1) site. In order to increase their oxygen coordination, the trivalent ions draw excess oxygen into the structure, which progressively leads to a disordering of the oxygens in the basal copper plane. Such disorder is presumed to be the cause of the orthorhombic to tetragonal (II) transition. However, electron diffraction studies[41] of Fe doped YBCO suggest that the tetragonal phase is *not* a result of the general disordering of the Cu(1)-O chains, but is a manifestation of a microdomain structure, consisting of small, ordered, orthorhombic domains - the size of which decrease or become finer with increasing x. Similar behaviour could be expected for Co, Ga and Al doping, if the same mechanism for the structural transition applies (see chapter 6). Clustering of iron along the [110] planes of the crystal has also been observed and there are some reports[42] of AF ordering of Fe doped Cu(2) sites beyond x=20%.

An important point to note is that the orthorhombic to tetragonal (II) transition does not influence the variation in T_c. In many cases, the substituted tetragonal (II) material remains superconducting up to high values of x.

Magnetic susceptibility data suggests that Mn, Fe, Co and Ni all retain some magnetic moment in YBCO, but that the moment is reduced from the free ion value because of the crystalline electric fields surrounding the atoms[43].

Substitution studies in YBCO seem to reinforce that the existence of two crystallographically independent Cu sites is vital to superconductivity. The role of oxygen in determining structural symmetry and controlling the coordination number and oxidation state of the Cu(1) site has been established. It appears that site selectivity is governed by the valence state of the dopant ion and that neither the variation of T_c nor the crystallographic transition are a result of magnetic effects.

2.2.4 Other Substitutions

Since both the Y and Ba atoms represent equivalent sites in the original perovskite structure, some research has focussed on the substitution of Ba and its similarity to Y replacement. The isovalent alkaline-earth ions, Sr^{2+}, Ca^{2+} and Mg^{2+}, have a similar

---

41 P. Bordet, J. L. Hodeau, P. Strobel, M. Marezio & A. Santoro, *Solid State Comm.* **66** 435 (1988)

42 M. Matsumura, H. Yamagata, Y. Oda & N. Kawaji, *J. Phys. Soc. Jpn.* **59** 424 (1990)

43 Y. Xu, R. L. Sabatini, A. R. Moodenbaugh, Y. Zhu, S. G. Shyu, M. Suenaga, K. W. Dennis & R. W. McCallum, *Physica C* **169** 205 (1990)

chemistry to Ba, and are known to substitute at the Ba site with varying solubilities. Other divalent ions seem reluctant to replace Ba, whilst some monovalent and trivalent ions show a preference for the Y site over the Ba site. Appendix A.6 shows the effects of various dopants which replace Ba. The dopants appear to have individualistic effects on the superconductivity of the system and there seem no obvious trends†.

Substitution for oxygen by such ions as F^-, Cl^- and S^{2-} is possible, but has proved complex via solid state sythesis methods. The solid fluorine starting compounds are difficult to decompose and to incorporate in the YBCO structure. Alternative methods of preparation have produced conflicting data. The superconducting properties of YBCO and its substituted systems are strongly dependent on oxygen concentration and one would expect that substitution at the O site would produce appreciable changes. However, there are reports that $YBa_2Cu_3O_6S$ is a single phase orthorhombic material with a T_c of ~92K*. Fluorine doping also has little effect on T_c up to a critical concentration, after which it undergoes an orthorhombic to tetragonal transition. Fluorine is structurally incorporated into the vacant O(5) sites.

Co-doping or double-doping of two independent sites in YBCO has been investigated in detail. For example, a study[44] of the co-substitution of Ca^{2+} for Y^{3+} and Al^{3+} for Cu(1) shows that co-doping has a counterbalance effect on T_c causing it to be suppressed much more slowly than with either of the dopants individually. Al controls the structural transition and the marginal decrease in oxygen concentration is attributed to the opposite effect of addition and reduction of the oxygen content by the substitution of Al^{3+} and Ca^{2+}, respectively. Other co-doped systems with different M^{3+} ions give similar results.

Materials enriched in Ba^{135}, Ba^{136}, Cu^{63} or Cu^{65} show no isotope shift associated with the cation lattice. The substitution of O^{16} by O^{18} in YBCO has already been discussed in section 1.2.2.

---

† Though, it is important to remember that the properties of *any* substituted system are highly dependent upon the synthesis conditions.

* The phase is unstable and generates a mixed phase material after a few days.

44 Y. Zhao, H. K. Liu & S. X. Dou, *Physica C* **179** 207 (1991)

2.3 The Cobalt-Doped System

2.3.1 Introduction

Much of the experimental work for this thesis has been performed on the cobalt-doped YBCO system. The following sections aim to summarize the essential features of the system, highlighting the basic changes which occur with the addition of cobalt and the similarities which become apparent when compared to the pure system.

Cobalt is naturally a ferromagnetic material with an electronic configuration of [Ar] $3d^7\ 4s^2$. The two 4s electrons are readily removed to form the Co^{2+} (cobaltous) ion, which is the most common state. Although, in principle, the removal of the odd 3d electron should lead to the formation of the cobaltic 3+ ion, in practice this does not happen. The Co^{3+} ion is found to exist only in complex ions or crystal lattices, where additional electron orbitals are filled.

Cobalt has been a fairly common dopant in a number of systems for many decades and its properties have been well catalogued[45]. Its doping in insulators often ends up as non-magnetic, particularly if it enters the system in the +3 state[46]. Cobalt doping in noble metals is characterised by a Kondo system with very high T_K[47].

Cobalt is readily soluble in the YBCO structure, producing a single phase material, up to a doping level of $x\%\approx30$[48]. It is now well-established that the T_c of $YBa_2(Cu_{1-x}Co_x)_3O_{7-\delta}$ remains fairly constant and equal to around 90K at low Co concentrations and then decreases continuously to less than 4.2K at $x\%>13$[49,50] (figure 2.5). The sudden rapid decrease in T_c ($dT_c/dx\approx6$K/atomic%) coincides with an observed structural transition from orthorhombic to tetragonal† symmetry, bought about by an increase in oxygen content and a disordering of the oxygens in the basal plane.

For further reference, appendix A.8 presents various structural and state parameters which characterise the Co-doped system.

---

45 See for example, A. Narath, *Phys. Rev. B* **13** 3724 (1976)

46 A. Abragam & B. Bleaney, *Electronic Paramagnetic Resonance of Transition Ions*, Oxford University Press (1970)

47 R. Tournier & A. Blandin, *Phys. Rev. Lett.* **24** 397 (1970)

48 S. Terada, N. Kobayashi, H. Iwasaki, A. Tokiwa, M. Kikuchi, Y. Syono & Y. Muto, *Physica B* **165** 1545 (1990)

49 I. Felner, E. R. Bauminger, D. Hechel, U. H. Yaron & I Nowik, *Physica A* **168** 229 (1990)

50 Y. Oda, H. Toyoda, N. Kawaji, I. Nakada & K. Asayama, *Jpn. Jnl. Appl. Phys.* **27** L1702 (1988)

† In the Co-doped system, any reference to the tetragonal (II) phase will be abbreviated by 'tetragonal phase' and reference to the chain site implies the Cu(1) site. (The tetragonal phase has no chain site).

2.3.2 Crystal Structure

Neutron diffraction,[51,52] Mössbauer studies,[53] Raman spectroscopy[54] and X-ray techniques[55] all provide strong evidence to suggest that Co substitutes preferentially at the Cu(1) chain site in the YBCO structure (at least for concentrations of x%<27[56,†]). Furthermore, such studies[48-56] demonstate that there is a simultaneous uptake of extra oxygen into the system, in an amount consistent with Co^{3+} replacing Cu^{2+}. Comparative investigations[56] of the well-defined trivalent Al substituted system provide additional evidence to support the idea that cobalt enters the Cu(1) site in the higher +3 valence state.

In order to achieve charge balance and the preferred octahedral coordination, the Co^{3+} ions gradually draw one extra oxygen into the O(1) site for every two Co atoms substituted in the Cu(1) plane[51]. As with decreasing oxygen concentration in the pure system, addition of cobalt and oxygen into the basal plane leads to a gradual disordering of the O(1) oxygens into the normally vacant O(5) sites. The structure remains orthorhombic up to a critical cobalt concentration, x_c, but then undergoes an orthorhombic to tetragonal transition over a narrow range of composition, indicated by a sharp anomally in the c lattice parameter (see appendix A.8). At the transition, there is equal probability that the O(1) and O(5) sites will be occupied. The transition generally occurs at around x%=3, but is found to vary according to sample history. One study[57] found that at x%=2.5, the resulting compound was a two-phase mixture of tetragonal and orthorhombic phases, but that by x%=3 the structure had become purely tetragonal.

Figure 2.6(b) shows a schematic drawing of the tetragonal Co-doped YBCO structure - illustrating the octahedral coordination of the Co^{3+} ion at the Cu(1) site. For comparison, figure 2.6(a) presents the structure of $YBa_2Cu_3O_{7-\delta}$ before the addition of Co - illustrating the original square planar Cu(1) coordination.

The disordering of the chains which drives the orthorhombic to tetragonal transition is thought to be primarily due to the octahedral preference of the Co^{3+} ion, rather than the

---

51 P. F. Miceli, J. M. Tarascon, L. H. Greene, P. Barboux, F. J. Rotella & J. D. Jorgenson, *Phys. Rev. B* **37** 5932 (1988)

52 P. Zolliker, D. E. Cox, J. M. Tranquada & G. Shirane, *Phys. Rev. B* **38** 6575 (1988)

53 A. Nath, Z. Homonnay, S. D. Tyagi, Y. Wei, G-W. Jang & C. C. Chan, *Physica C* **171** 406 (1990)

54 M. Kakihana, L. Börjesson, S. Erikson, P. Svetlindh & P. Norling, *Phys. Rev. B* **40** 6787 (1989)

55 F. Bridges, J. B. Boyce, T. Claeson, T. H. Geballe & J. M. Tarascon, *Phys. Rev. B* **39** 11603 (1989)

56 J. M Tarascon, P. Barboux, P. F. Miceli, L. H. Greene, G. W. Hull, M. Eibschutz & S. A. Sunshine, *Phys. Rev. B* **37** 7458 (1988)

† Beyond this concentration 10-20% of the Co impurites substitute at the Cu(2) sites.

57 J. F. Bringley, T. Chen, B. A. Averill, K. M. Wong & S. J. Poon, *Phys. Rev. B* **38** 2432 (1988)

filling of the O(5) oxygen sites†. Although the transformation to tetragonal symmetry is found to coincide directly with a dramatic drop in T_c, the superconductivity of the Co-doped system is not inhibited by the transition. The material is still found to be superconducting well into the tetragonal region of the phase diagram.

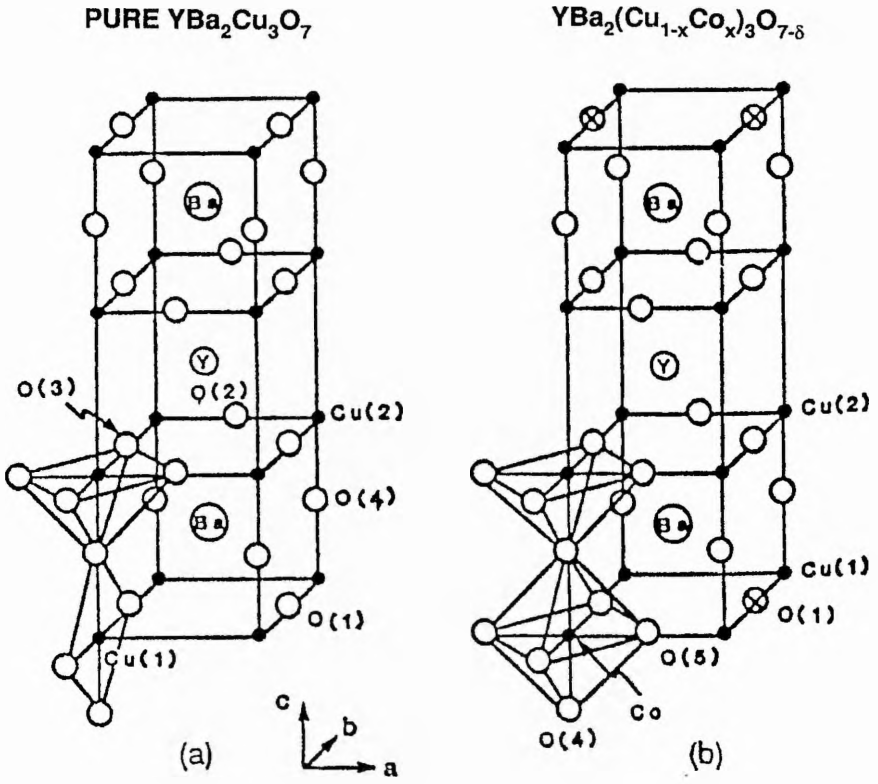

Figure 2.6

Schematic drawings of the structures of (a) the orthorhombic system before Co doping and (b) the resultant tetragonal structure upon Co doping at the Cu(1) site (open circles represent full occupancy of oxygen & crossed circles represent disordered oxygens). Again the notation established by Jorgenson is used. (After Bringley et al[57])

The structural changes which occur as a result of Co doping are found to parallel similar changes which take place in the undoped material as oxygen is removed. Indeed, it is interesting to note that the cell volume increase generated by adding one Co per formula unit ($3Å^3$) is identical to that induced by the removal of one oxygen atom from the pure material. The most evident changes of local structure which occur with the addition of Co or removal of oxygen are the shift of O(4) away from Cu(2) and the shift of Ba towards the CuO_2 plane (See appendix A.8). These changes are accompanied by a

† Presumed because of the low value of x_c.

net increase in the Cu(1)/Co(1)-Cu(2) distance compared to the Cu(1)-Cu(2) distance in the pure material, suggesting that the chains are further decoupled from the planes in the Co system[58]. The variation of T_c with selected Cu-O bond lengths gives an identical correlation for the Co doped and oxygen deficient systems[59] (see appendix A.8). In particular, the T_c systematically decreases with the Cu(1)-O(4) bond length and finally reaches zero only when the distance becomes smaller than 1.82Å. Both Co doping and oxygen removal electrically isolate the chains from the planes. The induced changes in electron distribution around the CuO_2 plane seem to be similar in both cases.

Several researchers[52,55] have found evidence to suggest that the Co(1) sites are distorted along the [110] direction, creating short and long Co-O bond lengths in the Cu(1)-O(1)/O(5) plane. Microprobe techniques such as TEM[60,61] and electron and X-ray diffraction[62] show that at low Co concentrations the microstructure features [110]-type orthorhombic twin domains. The typical domain size decreases with increasing Co content and for x%>2.25 appears to favour a 'tweed' morphology, such as that observed in partially reduced undoped material. The tetragonal phase is suspected to be a pseudotetragonal structure consisting of differently oriented orthorhombic domains[63].

2.3.3 Hall Effect & Oxygen Concentration

As shown in figure 2.7, the oxygen content of $YBa_2(Cu_{1-x}Co_x)_3O_{7\pm\delta}$ increases almost linearly with cobalt concentration,[56,64] rising above the stoichiometric O_7 value for x%>20. Unexpectedly, as the oxygen content increases, the Hall number n_H, falls rapidly with an approximately exponential dependence[65] upon x% (figure 2.8). A steep

---

58 L. C. Sengupta, B. Roughani, J. Aubel, S. Sundaram & W. C. H. Joiner, *Physica C* **165** 125 (1990)

59 P. F. Miceli, J. M. Tarascon, L. H. Greene, P. Barboux, J. D. Jorgenson, J. J. Rhyne & D. A. Neumann, *Mat. Res. Soc. Symp. Proc.* **156** 119 (1989)

60 H. Renevier, J. L. Hodeau, T. Fournier, P. Strobel, M. Marezio, J. C. Martinez & J. J. Prejean, *Jnl. Less Comm. Metals*, **164 & 165** 907 (1990)

61 W. W. Schmahl, A. Putnis, E. Salje, P. Freeman, A. Graeme-Barber, R. Jones, K. K. Singh, J. Blunt, P. P. Edwards, J. Loram & K. Mirza, *Philos. Mag. Lett.* **60** 241 (1989)

62 H. Renevier, J. L. Hodeau, P. Bordet, J. J. Capponi, M. Marezio, F. Baudelet, H. Tolentino, G. Tourillon, E. Dartige, A. Fontaine, J. C. Martinez & J. J. Prejean, *Physica C* **162-164** 51 (1989)

63 E. Salomons & D. de Fontaine, *Phys. Rev. B* **42** 10152 (1990)

64 Y. K. Tao, J. S. Swinnea, A. Manthiram, J. S. Kim, J. B. Goodenough & H. Stienfink, *J. Mater. Res.* **3** 248 (1988)

65 J. Clayhold, S. Hagen, Z. Z. Wang, N. P. Ong, J. M. Tarascon & P. Barboux, *Phys. Rev. B* **39** 777 (1989)

temperature dependence of n_H is observed in lightly doped samples (~0.66%), but this diminishes rapidly as x% increases. At a doping level of 10%, n_H is virtually independent of temperature[66] and can be strictly identified with the carrier density, n.

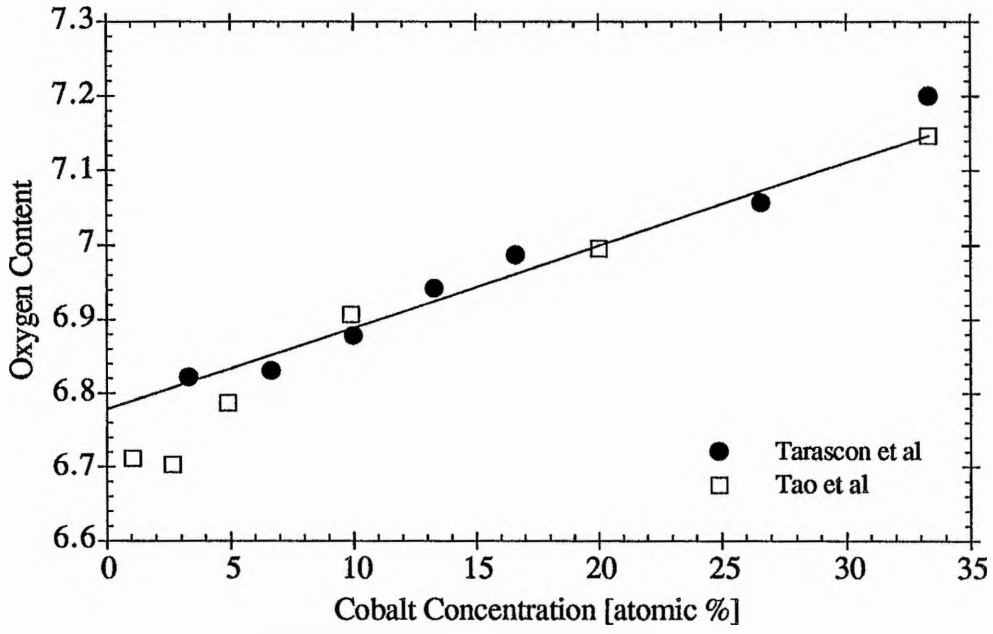

Figure 2.7

Total oxygen content of $YBa_2(Cu_{1-x}Co_x)_3O_{7\pm\delta}$ as a function of x% cobalt. (Adapted from data collected via thermogravimetric analysis (TGA) & iodometric titration methods by Tarascon et al[56] & Tao et al[64])

The exponential concentration dependence of n_H, depicted in figure 2.8, is found to be similar to the O-dependence of n_H in $YBa_2Cu_3O_{7-\delta}$ (figure 2.4). This may somehow indicate a link between the mechanisms operating in each system.

The variation in Hall number suggests a fall in the total number of holes in the system as x% rises. This may be explained if we surmise that part of the extra electrons donated by the Co^{3+} ion is compensated by the increasing oxygen content, but remaining electrons reduce the hole density in the planes. Simple valence balancing suggests that each Co^{3+} ion decreases the hole concentration in the planes by 1 hole/unit cell. However, if every additional oxygen is bound by two Co ions, as implied by various researchers,[51,56] then the increase in oxygen content compensates for the extra electrons donated by the 3+ ion completely and some other mechanism must be responsible for the fall in the number of holes. A possible scenario is that the displacement of the O(4) oxygen away from the CuO_2 planes (with increasing x%) may have some bearing on the

---

66 J. Clayhold, N. P. Ong, Z. Z. Wang, J. M. Tarascon & P. Barboux, *Phys. Rev. B* **39** 7324 (1989)

relative chemical potential of the holes in the planes and chains. The relative potential could change in such a way as to induce electron transfer back to the planes, causing a rapid drop in the hole concentration. Indeed, the overlap integral between the Cu(2) $3d_{z^2}$ and O(4) p_z states decreases exponentially with the Cu(2)-O(4) separation, implying that the electron transfer should increase in an exponential fashion.

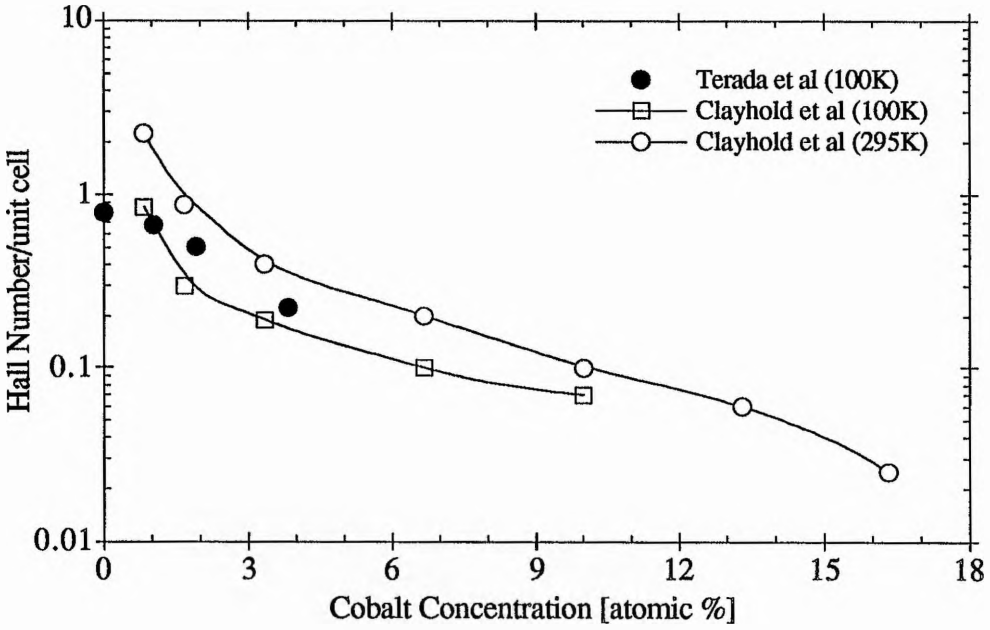

Figure 2.8

The Hall number n_H at 100K & 295K plotted against Co concentration (atomic %) in $YBa_2(Cu_{1-x}Co_x)_3O_7$.
The lines are drawn as a guide to the eye.
(Replotted from data obtained by Terada et al[48] & Clayhold et al[65])

As in the pure system, investigations[48,67] indicate that no correlation exists between T_c and hole concentration. T_c does not seem to be determined by hole concentration alone.

2.3.4 Magnetic Structure

The addition of a magnetic Co ion to the pure YBCO system introduces another variable into an already complex phase diagram. At the present time, the magnetic order of the system has not received much attention and the conflicting data which already

---

[67] N. Kawaji, K. Muranaka, Y. Oda & K. Asayama, *Physica B* **165 & 166** 1543 (1990)

exists is not sufficient to compose the 3D phase diagram needed to elucidate the magnetic properties as a function of oxygen and cobalt. Research has generally been restricted to a few groups, who have performed experiments on a limited number of Co-doped samples with known x and δ values.

Two neutron scattering studies executed by Miceli et al[68,69] show that at low Co concentrations (6.66%) for nominally oxygen deficient samples (δ=0.55)*, two AF transitions occur with the variation of temperature. The AF1 phase associated with the magnetic ordering of the Cu(2) sites is found to have a T_{N1} of 415K, while the AF2 phase allied to the Cu(1) ordering (in addition to the plane site ordering) has a T_{N2} of 211K. Interplane AF coupling in the AF1 state produces a magnetic cell with a c-axis equal to that of the crystallographic cell. However, as soon as magnetic ordering occurs at both plane and chain sites (AF2), the c-axis interval of the magnetic cell becomes doubled ($c_{mag}=2c_{crystal}$). The spins are found to point in the in-plane direction, perpendicular to the c-axis, with a magnetic moment of $(0.044\pm0.005)\mu_B$ for the chain sites and $(0.44\pm0.04)\mu_B$ for the plane sites.

An oxygen dependence study of the above sample suggests that the two transition temperatures associated with the AF1 and AF2 states increase with decreasing oxygen concentration - as shown in the phase diagram (with respect to oxygen) in figure 2.9†. At an oxygen content equivalent to δ=0.63 (δ_0), T_{N1} and T_{N2} become equal implying that for $\delta\geq\delta_0$, the planes and chains order simultaneously at a single transition temperature. Below this characteristic Néel temperature there is only one phase present, namely AF2. As the oxygen content becomes greater than 6.82, long range magnetic ordering disappears and the compound becomes superconducting, finally reaching a maximum T_c of 60K at δ=0. Qualitatively, the behaviour of T_{N1} is similar to that observed in $YBa_2Cu_3O_{7-\delta}$ as a function of δ, but the addition of Co appears to push the AF to superconducting transition to a higher oxygen content.

Similar neutron scattering experiments were also performed on oxygen rich samples (δ=0.09) whose the Co composition was well outside the range required for

---

68 P. F. Miceli, J. M. Tarascon, L. H. Greene, P. Barboux, M. Giroud, D. A. Neumann, J. J. Rhyne, L. F. Schneemeyer & J. V. Waszczak, *Phys. Rev. B* **38** 9209 (1988)

69 P. F. Miceli, J. M. Tarascon, P. Barboux, L. H. Greene, B. G. Bagley, G. W. Hull, M. Giroud, J. J. Rhyne & D. A. Neumann, *Phys. Rev. B* **39** 12375 (1989)

* Such a sample is tetragonal and non-superconducting.

† Note that it is more advantageous to study the AF2 phase as a function of oxygen content in the Co-doped system because a Co-concentration of 6.66% naturally produces a tetragonal symmetry over the entire range of oxygen content. The added complications of an orthorhombic to tetragonal transition and oxygen superlattices are thus eliminated.

superconductivity (x%=26.66). Here, the AF ordered moments located on both Cu sites were judged to be equivalent ($[0.68\pm0.06]\mu_B$) and were found to order at a single transition temperature of 435K. The progressive increase in T_{N2} with the addition of cobalt, from 80K (0%Co) to 211K (6.66%Co) to 435K (26.66%Co), indicates that the presence of Co encourages magnetic ordering on the Cu(1) site. The AF exchange interaction within the Cu(1) plane and indeed between the Cu(1) and Cu(2) planes may well be enhanced by the Co substitution. Co ions do not appear to contribute to the long-range magnetic order of the system.

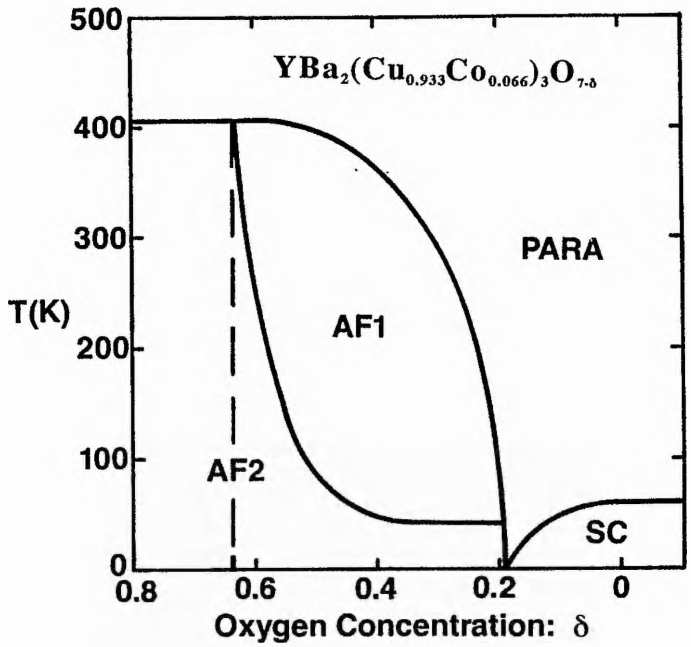

Figure 2.9

The schematic phase diagram of $YBa_2(Cu_{0.933}Co_{0.066})_3O_{7-\delta}$. The oxygen dependence of the Néel temperatures, T_{N1} & T_{N2} (associated with the AF1 & AF2 phases described in the text) are shown along with the variation of T_c. The dashed line at $\delta_0=0.63$ corresponds to the composition at which T_{N1} first becomes equal to T_{N2}. (adapted from ref. 69)

More recent Mössbauer studies performed by Hechel et al[70] on samples with similar compositions give very contradictory results when compared to the Miceli work. In fully oxygenated samples, researchers find that as the Co concentration approaches 13%, there is a superconducting to AF transition in which only the Cu(2) sites order AF. When samples are oxygen deficient ($\delta=1$), the Cu(2) sites alone are AF ordered for all values of x (T_{N1}=420K). Hechels results clearly show the existence of only one magnetic

[70] D. Hechel, I. Nowik, E. R. Bauminger & I. Felner, *Phys, Rev. B* **42** 2166 (1990)

transition temperature at 400K (corresponding to the ordering of the plane sites) for oxygen deficient compounds with x%=6.66. For samples with a higher Co concentration of 26.66%, and δ=1, the group observe two transition temperatures, T_{N1} at 435K (plane) and T_{N2} at 220K (chain), indicating the presence of two uncoupled magnetic sublattices. Two lower Néel temperatures were also found for similar fully oxygenated samples. These results are in complete opposition to those found by Miceli et al, and strongly indicate that the nature and origin of the magnetic ordering in Co-doped YBCO is not well understood.

Chapter 3

Background Theory & Its Application to Superconductivity

3.1 Introduction

In different systems, the NMR spectral lineshape is broadened and shifted by varying amounts depending on the contributions made by a number of spin-spin and spin-lattice interactions. This work is concerned with solid state metallic systems and essentially concentrates on the small hyperfine interactions between the nuclear magnetic and electric moments and the magnetic and electric fields generated by the environmental electrons. In order to put these hyperfine interactions into some context, the initial sections of this chapter describe the fundamental nuclear-nuclear and nuclear-electron magnetic and electric interactions which make NMR such a useful probe of the solid state. Since one cannot hope to cover such a vast topic as nuclear magnetism in a brief overview, reference is also made to more extended texts such as those of Abragam[1], Slichter[2], Winter[3], Rushworth & Tunstall[4] and Andrew[5].

The general description of hyperfine interactions introduced in earlier sections is later extended to the metallic system and then finally applied to HiT$_c$ superconductivity.

3.2 The Nuclear Spin Hamiltonian

3.2.1 Introduction

The total energy associated with a nucleus of non-zero spin ($I \neq 0$) can be expressed in Hamiltonian form as

$$\mathcal{H}_{tot} = \mathcal{H}_Z + \mathcal{H}_1 + \mathcal{H}_D + \mathcal{H}_Q + \mathcal{H}_{en} + \ldots \qquad (3.1)$$

---

1 A. Abragam, *Principles of Nuclear Magnetism*, Oxford University Press (1989)

2 C. P. Slichter, *Principles of Magnetic Resonance*, Springer-Verlag (1990)

3 J. Winter, *Magnetic Resonance in Metals*, Clarendon Press (1971)

4 F. A. Rushworth & D. P. Tunstall, *Nuclear Magnetic Resonance*, Gordon & Breach (1973)

5 E. R. Andrew, *Nuclear Magnetic Resonance*, Cambridge University Press (1955)

where $\mathcal{H}_Z$ is the Zeeman interaction energy,
$\mathcal{H}_1$ is the rf field/radiation interaction energy
$\mathcal{H}_D$ is the magnetic dipole-dipole interaction energy,
$\mathcal{H}_Q$ is the electric quadrupole interaction energy,
and $\mathcal{H}_{en}$ is the hyperfine interaction energy.

Here, the $\mathcal{H}_z$ and $\mathcal{H}_1$ terms are externally imposed Hamiltonians, whereas the remaining Hamiltonians are 'internal' to the microscopic system under investigation. By monitoring the effect that some of these 'internal' interactions (i.e. $\mathcal{H}_Q$ and $\mathcal{H}_{hf}$) have on the Zeeman energy levels, one has a useful probe of the local electronic environment.

In order to elucidate on the contributions made by the individual interactions, each term in equation (3.1) will be introduced in greater detail in the following sections.

3.2.2 The Zeeman & Rf Field Interactions

In chapter 1, it was shown that the Zeeman Hamiltonian operator describing the Zeeman energy due to the interaction $-\boldsymbol{\mu}_z.\mathbf{B}_0$, is given by

$$\mathcal{H}_Z = -\gamma\hbar\, B_0 I_Z \tag{3.2}$$

Although many systems can be adequately described by considering a single nucleus, when dealing with the solid state, all N spins have to be taken into account. If each individual spin has a total angular momentum of $\hbar$I, then the full Zeeman Hamiltonian which describes the interaction of N spins with an external field, applied along the z-axis, is given by

$$\mathcal{H}_Z = -\gamma\hbar\, B_0 \sum_{i=1}^{N} I_z^i \tag{3.3}$$

where i is an index which labels the N nuclear spins.

$\mathcal{H}_1$ represents the energy due to the interaction $-\boldsymbol{\mu}.\mathbf{B}_1$. Generally, $B_1 \ll B_0$ and so $\mathcal{H}_1$ can be treated as a small perturbation† of the Zeeman energy in the absence of other interactions. The Hamitonian, $\mathcal{H}_1$ can be represented as a function of the raising and lowering operators

$$I^+ = I_x + i\, I_y \tag{3.4a}$$

$$I^- = I_x - i\, I_y \tag{3.4b}$$

† Thus standard quantum mechanical perturbation theory can be applied to calculate the effects of B_1.

by

$$\mathcal{H}_1 = \frac{-\gamma\hbar B_1}{2}\,(I^+e^{-i\omega t} + I^-e^{i\omega t}) \qquad (3.5)$$

where for nuclei with positive γ, I^+ is characteristic of radiative transitions, since it increases m by 1 and I^- is characteristic of absorptive transitions, since it decreases the m value by 1.

3.2.3 The Magnetic Dipole-Dipole Interaction

In solids, the dominant nuclear-nuclear interaction is the nuclear magnetic dipole interaction. Consider a system of nuclear spins in an applied magnetic field $\mathbf{B_0}$: each spin is subject not only to the static $\mathbf{B_0}$ field, but also to the local magnetic field produced by all its neighbours. Since this local field varies from nucleus to nucleus, the absorption frequency varies throughout the sample, resulting in a broadening of the spectral line.

The classical expression for the interaction energy E between two magnetic dipoles of moment $\boldsymbol{\mu_1}$ and $\boldsymbol{\mu_2}$, separated by a distance $\mathbf{r_{12}}$ is

$$E_{12} = \frac{\mu_0}{4\pi}\left(\frac{\boldsymbol{\mu_1}\cdot\boldsymbol{\mu_2}}{r_{12}^3}\right) - \frac{3\,(\boldsymbol{\mu_1}\cdot\mathbf{r_{12}})(\boldsymbol{\mu_2}\cdot\mathbf{r_{12}})}{r_{12}^5} \qquad (3.6)$$

Extending this to a system of N spins produces the dipolar Hamiltonian, which is written generally as,

$$\mathcal{H}_D = \frac{\mu_0}{4\pi}\sum_{j<k}^{N}\left(\frac{\boldsymbol{\mu_j}\cdot\boldsymbol{\mu_k}}{r_{jk}^3}\right) - \frac{3\,(\boldsymbol{\mu_j}\cdot\mathbf{r_{jk}})(\boldsymbol{\mu_k}\cdot\mathbf{r_{jk}})}{r_{jk}^5} \qquad (3.7)$$

By transforming the Hamiltonian into the spherical coordinate system and rewriting it in terms of nuclear spin ($\boldsymbol{\mu}=\gamma\hbar\mathbf{I}$) and the raising and lower operators (3.4), it can be shown that equation (3.7) can be expressed as a function of the sum of six dipolar contributions, A-F. Term A represents the classical interaction between two dipoles, whilst term B - the 'flip-flop' term - induces mutual spin flips between dipoles. The terms C and D flip one spin only and the E and F terms flip both spins in the same direction. The effect of terms C to F is to produce absorption lines at frequencies 0 and $2\omega_0$. These lines are so weak, however, that they are taken to be negligible and the dipolar Hamiltonian is essentially truncated to contain only the A and B terms. Since the remaining A and B terms commute with the Zeeman Hamiltonian and therefore cannot exchange energy with it, the truncated dipolar and Zeeman Hamiltonians are effectively decoupled and the dipolar terms can again be treated as a perturbation of the Zeeman energy.

3.2.4 The Electric Quadrupole Interaction

Nuclei with I>1/2 possess an electric quadrupole moment, which acts as a measure of the non-sphericity of the electric charge distribution* within a nucleus. The electric quadrupole moment interacts with electrostatic potentials of lower than cubic symmetry to produce a perturbation of the nuclear energy levels. The (2I+1) Zeeman substates each correspond to a different orientation relative to B_0, so if the electric interaction also depends on orientation, then the individual substates may be perturbed differently by the electric interaction.

Classically, the interaction energy E of a nuclear charge density distribution $\rho(r)$ with an external electric potential V(r) is given by

$$E = \int \rho(r)\, V(r)\, d\tau \tag{3.8}$$

where the integral is taken over volume elements within the nucleus.
Expanding V(r) in a Taylor's series about the origin (r=0) gives,[2,4,6]

$$E = \int \rho(r) d\tau \left[V(0) + \sum_{\alpha} V_{\alpha}(0)\, \alpha + \frac{1}{2!} \sum_{\alpha,\beta} V_{\alpha\beta}(0)\, \alpha\beta + ... \right] \tag{3.9}$$

where $\alpha, \beta = x, y, z$ (the cartesian components of r) and where V_α and $V_{\alpha\beta}$ are defined by

$$V_{\alpha} = \left(\frac{\partial V(r)}{\partial \alpha} \right)_{r=0} \tag{3.10}$$

and

$$V_{\alpha\beta} = \left(\frac{\partial^2 V(r)}{\partial \alpha \partial \beta} \right)_{r=0} \tag{3.11}$$

In the expression for the interaction energy (3.9), the first term represents the electrostatic energy of the nucleus taken as a point charge. Since this term is independent of nuclear size, shape and orientation, it is of no interest here. The second term represents the interaction of the electric dipole moment of the nucleus. This term vanishes since the nuclear centre of mass and the centre of charge coincide†. The third term is known as the

---

* Effectively, the electric charge can be drawn out into a cigar shape or flattened to a plate from.

6 M. H. Cohen & F. Reif, *Solid State Physics* **5** 321 (1957)

† Since the nucleus has a well defined parity.

quadrupole term as it involves the interaction of the nuclear quadrupole moment with the electric field gradient (EFG) at the nucleus. The quadrupole term is orientation dependent and is the largest correction to the point charge interaction. The next non-zero term involves a hexadecapole[7], but this and any higher terms which follow are usually negligible, so only the quadrupole term is considered.

The quadrupole term involves nine components, but a 'principal axis coordinate system (PACS)' may always be chosen for the electric field gradient ($V_{\alpha\beta}$), such that $V_{\alpha\beta} = 0$ for $\alpha \neq \beta$ - leaving only V_{xx}, V_{yy} and V_{zz} as the non-zero components*. Since V must satisfy Laplace's equation,

$$\nabla^2 V = 0 \tag{3.12}$$

which, evaluated at the origin, gives

$$\sum_{\alpha} V_{\alpha\alpha} = V_{xx} + V_{yy} + V_{zz} = \frac{\partial^2 V}{\partial x^2} + \frac{\partial^2 V}{\partial y^2} + \frac{\partial^2 V}{\partial z^2} = 0 \tag{3.13}$$

the field gradients can be described by two parameters,

$$eq = V_{zz} = \frac{\partial^2 V}{\partial z^2} \tag{3.14}$$

and

$$\eta = \frac{V_{xx} - V_{yy}}{V_{zz}} \tag{3.15}$$

where e is the electronic charge, q is the 'field gradient' and η (where $0 \leq \eta \leq 1$) is known as the 'asymmetry parameter', since it measures the departure of the field gradient from cylindrical symmetry. V_{zz} is referred to as the 'electric field gradient (EFG)'.

Note that for axial symmetry of field gradient, $V_{xx} = V_{yy}$ and so $\eta = 0$. For nuclei in a cubic environment, $V_{xx} = V_{yy} = V_{zz}$ and hence the quadrupole interaction vanishes. Since there is also no orientation dependence of the charge distribution for nuclei with spin 0 or 1/2, quadrupole effects are only observed for nuclei with $I > 1/2$ in non-cubic environments.

After a rather complex transformation[7], the simplified quadrupole Hamiltonian can be written, in the PACS, as

---

* where generally, one defines the principal axes so that the z-axis lies along the direction of the maximum field gradient and the x axis lies along the minimum, i.e. $|V_{zz}| \geq |V_{yy}| \geq |V_{xx}|$.

7 See ref 2, chapter 10.

$$\mathcal{H}_Q = \frac{e^2qQ}{4I(2I-1)}\left[3I_z^2 - I^2 + \frac{1}{2}\eta\,(I_+^2 + I_-^2)\right] \qquad (3.16)$$

where Q is the 'nuclear electric quadrupole moment', defined classically as,

$$Q = \frac{1}{e}\int \rho(r)\,(3z^2 - r^2)\,d\tau \qquad (3.17)$$

If $\mathcal{H}_Q$ is small compared to the Zeeman Hamiltonian, then first order perturbation theory is sufficient to calculate the effect of the quadrupole interaction on a nuclear energy level. Such perturbation calculations yield the expression

$$E_m^1 = \frac{e^2qQ}{8I(2I-1)}(3m^2 - I(I+1))\,(3\cos^2\theta - 1) \qquad (3.18)$$

for the energy change of each substate m, where θ is the angle between B_0 and the principle z-axis. Thus, one finds that $m=\pm 1/2$ levels are both shifted by the same amount and so the central resonance line remains at ω_0, unshifted by the quadrupole interaction. The remaining energy levels are no longer equally spaced and this results in a series of (2I-1) satellite lines symmetrically positioned about the central line. When the satellite lines remain unresolved, they produce a broadening of the resonance line, but if such lines are far from the central line, the quadrupole effect manifests itself through a reduction in intensity of the central line.

If $\mathcal{H}_Q$ is of the same order as the Zeeman Hamiltonian (i.e. $e^2qQ \sim \gamma\hbar B_0$) then second order perturbation must be considered. This produces

$$E_m^2 = -h\left(\frac{\upsilon_Q^2}{12\upsilon_L}\right)m\left(\frac{3\mu^2}{2}(1-\mu^2)(8m^2-4a+1) + \frac{3(1-\mu^2)^2\,(-2m^2+2a-1)}{8}\right) \qquad (3.19)$$

where the standard 'abbreviation' terms used are

$$\upsilon_Q = \frac{3e^2qQ}{2I(2I-1)h} \qquad (3.20)$$

$$a = I(I+1) \qquad (3.21a)$$

$$\mu = \cos\theta \qquad (3.21b)$$

and

$$\upsilon_L = \frac{\gamma B_0}{2\pi} \qquad (3.21c)$$

and where υ_Q is the expression for the pure quadrupole frequency ($\pm 3/2 \leftrightarrow \pm 1/2$ transition) and υ_L is the Larmor frequency. In this case, the central line may also be shifted and second order quadrupole broadening may be obtained. Note that an additional term, known as the quadrupole coupling constant C_q, is also generally defined and is given as

$$C_q = \frac{e^2qQ}{h} \tag{3.22}$$

Finally, it should be noted that external charges can distort the core electrons and so the actual field gradient V_{zz} seen by the nucleus differs from that calculated in the absence of distortion V_{zz}^0, so that

$$V_{zz} = V_{zz}^0 (1+\gamma) \tag{3.23}$$

where γ is the Sternheimer anti-shielding factor[8].

3.2.5 The Nuclear-Electron Magnetic Hyperfine Interaction

The Hamiltonian describing the interaction between a nuclear moment μ_I and an electron with orbital moment μ_L and spin moment μ_S may be written

$$H_{en} = -\frac{\mu_0}{4\pi}\left[\frac{2\mu_I.\mu_L}{r^3} - \left(\frac{\mu_S.\mu_I}{r^3} - \frac{3(\mu_I.r)(\mu_S.r)}{r^5}\right) + \frac{8\pi}{3}\mu_I.\mu_S\,\delta(r)\right] \tag{3.24}$$

The first term represents the nuclear coupling to the magnetic field produced at the nucleus by the electron orbital momentum. In diamagnetic materials, where the nucleus is surrounded by filled electron shells with zero orbital and spin angular momentum, this term vanishes. In paramagnetic materials, the unbalanced spin is often quenched by the crystalline electric field and so the term becomes negligible.

The second term, in round brackets, is the classical dipolar interaction between the electron spin and the nuclear spin. In diamagnetic materials, this term vanishes, whereas in paramagnetic substances, rapid electron spin-flips due to exchange coupling causes the nucleus to see a time averaged dipolar field which is much less than that produced by a static spin moment. Hence, this coupling in paramagnetic materials is also small. The dipolar term has two important properties: (i) it vanishes if the nucleus is in a site of cubic symmetry and (ii) the dipolar approximation is only valid for a distance r greater than the nuclear radius. In order to compensate for (ii), a third term, called the 'Fermi contact

---

8 R. M. Sternheimer, *Phys. Rev.* **84** 244 (1951)

interaction', is included in (3.24). This term replaces the spin dipolar term when r becomes small and it contains a delta function to ensure that only those electrons with finite probability density at the nucleus (i.e. s-electrons) can contribute.

The contact term can also contribute indirectly through an important interaction known as 'core polarisation'. In transition metals, the d valence electrons outside the filled atomic core, can distort the core orbitals via an exchange interaction (see below). The distorted core s-states then interact with the nucleus via the direct contact process, producing an additional hyperfine field. Note that in the absence of outer electrons, the core s-electrons are exactly paired and no hyperfine field is present. Thus, where outer electrons are present, the total hyperfine field is obtained by summing over all pairs of core s-electrons whose exact spin-pairing is altered by the exchange.

Although it has already been stated that, in diamagnetic materials, the first order coupling between the electron spins and the nuclei vanishes, there is a second order coupling which must be considered. Such a coupling originates from the fact that the presence of a nuclear moment on a lattice site has the effect of making that site more favourable to an electron of parallel moment. Due to the presence of electron bonds, a neighbouring electron will tend to have an anti-parallel spin and so its associated nucleus will also have a preferred anti-parallel spin. If either nucleus reorients its spin moment, the neighbouring nucleus will also reverse its spin, in order to maintain an anti-parallel spin configuration. Thus, an effective indirect nuclear-nuclear exchange coupling results. The 'exchange interaction' for a system of spins can be respresented by the effective exchange Hamiltonian,

$$\mathcal{H}_{\text{eff}} = \sum_{i,j} A_{ij}(r_{ij})\ \mathbf{I}_i.\mathbf{I}_j \qquad (3.25)$$

where r_{ij} is the distance between the two nuclei.

In solids, the primary effect of the exchange interaction is to alter the resonance linewidth[9]. Where the indirect coupling is between 'like' nuclei, the linewidth is reduced, but where it is between 'unlike' nuclei the linewidth is broadened.

3.3 Magnetic Hyperfine Shifts in Metallic Systems

Since the NMR of the normal state of BCS superconductors can be adequately described by the NMR of a metallic system, it is appropriate here to elucidate on the effects of hyperfine interactions in a classical metal.

---

9 M. A. Ruderman & C. Kittel, *Phys. Rev.* **96** 99 (1953)

3.3.1 The Magnetic & Chemical Shifts

In a metallic system, the conduction electrons interact with the nuclei via the interactions described in section 3.2.5. The result of these interactions manifests itself as an extra (local) field at the nucleus and corresponds to a shift in the NMR resonance line. The ratio of this particular resonance field shift to the applied field is known as the Knight shift† (K). Since the Knight shift is of great importance in the study of superconductivity, it will be discussed in more detail in the following section.

It is well known[1,2] that in any non-metallic solid, there exists a shift which is orbital in origin, called the chemical shift (σ). The chemical shift results from the nuclear spin interaction with the diamagnetism of closed shell electron orbits. Essentially, the electrons in filled orbitals are induced to circulate around the nucleus about the direction of the applied field $\mathbf{B_0}$, inducing an associated magnetic moment, $\boldsymbol{\mu}_{\mathbf{ind}}$. The induced magnetic field produced by $\boldsymbol{\mu}_{\mathbf{ind}}$ opposses the primary $\mathbf{B_0}$ field* (cf. Lenz's law) and so the electrons effectively 'shield' the nucleus from the full influence of $\mathbf{B_0}$. Since this shielding effect depends on the distribution of electrons around the nucleus, the chemical shift naturally has different values in different chemical compounds. In a solid, the chemical shift depends upon the direction of field. The chemical shift Hamiltonian is given as

$$\mathcal{H}_\sigma = \gamma\hbar\, \mathbf{I}.\boldsymbol{\sigma}.\mathbf{B_0} \qquad (3.26)$$

where $\boldsymbol{\sigma}$ is the chemical shift tensor. The frequency shift is of the order σ_{zz}, where σ_{zz} is the component of σ along B_0.

The chemical shift also contributes to the resonance shift in metallic systems, due to the existence of inner shell electrons. The 'total magnetic shift' (ΔK) of a (metallic) resonance line, taken with respect to an unshifted resonance line††, is therefore given by

$$\Delta K = \frac{\Delta B}{B_0} = \sigma + K \qquad (3.27)$$

where ΔB is the total 'extra' field seen at the nucleus.

---

† Note that an older convention regarded the total shift in metals as the Knight shift. In this instance, the Knight shift contributes to the total shift, which is called the 'magnetic' shift.

* implying a negative susceptibility (χ_{dia}), i.e. diamagnetism.

†† defined as the resonance frequency (or field) of a nucleus in a closed shell diamagnetic salt reference compound, for which K=0 and for which σ is defined to be zero.

3.3.2 The Knight Shift

In normal state metals, the conduction electron susceptibility can be divided into three contributions,

$$\chi_{cond} = \chi_s + \chi_{orb} + \chi_d \tag{3.28}$$

where χ_s is the s-type Pauli spin susceptibility, χ_{orb} is the Van Vleck orbital susceptibility (also labelled χ_{vv} in some instances) and χ_d represents the Pauli spin susceptibility of non s-type electrons (i.e. the d-type electrons will be of importance in transition metals). Each term of the susceptibility contributes to the Knight shift,
i.e

$$K = K_s + K_{orb} + K_d = a\chi_s + b\chi_{orb} + c\chi_d \tag{3.29}$$

For s-electrons, χ_{orb} and χ_d are effectively zero and so the NMR shift is dominated by K_s via the Fermi contact interaction. Given the third term in equation (3.24), the Fermi contact interaction can be represented by

$$\mathcal{H}_{en}^{con} = \frac{\mu_0}{4\pi}\left[\frac{8\pi}{3}\gamma_e\gamma_n\hbar^2\,\mathbf{I.S}\;\delta(r)\right] \tag{3.30}$$

where γ_e and γ_n are the electron and nuclear gyromagnetic ratios, and **S** and **I** are the electron and nuclear spin, respectively. Such an interaction generates a scalar 'contact' Knight shift contribution K_s, which is given as

$$K_s = \frac{\mu_0}{4\pi}\left[\frac{8\pi}{3}\langle|u_k(0)|^2\rangle_{E_F}\right]\chi_s = H_{hf}^s\frac{\chi_s}{\mu_B} \tag{3.31}$$

where $\langle|u_k(0)|^2\rangle_{E_F}$ denotes the s-electron density at the nucleus averaged over the Fermi surface and where H_{hf}^s is defined as the s-hyperfine field per Bohr magneton (μ_B). Generally, K_s is positive (paramagnetic), temperature independent* and directly proportional to applied field. χ_s is in units of susceptibility per atom.

For non s electrons, the Knight shift typically has substantial spin and orbital contributions. The spin contribution originates from the core polarisation effect of non-s itinerant electrons. Core polarisation constitutes the only means whereby nuclei can respond strongly to d-band susceptibility, since non-s wave functions vanish at the nucleus and so the direct contact interaction also vanishes. In transition metals, the core

---

* since the polarisation of s-type electrons which produces χ_s is independent of temperature.

polarisation term may be dominant and may lead to a Knight shift contribution K_d which is represented by

$$K_d = H_{hf}^d \frac{\chi_d}{\mu_B} \tag{3.32}$$

where H_{hf}^d is the corresponding hyperfine field, determined by the electronic structure of the material. The Knight shift due to the core polarisation can be either positive or negative, but invariably the constant c in equation (3.29) turns out to be negative, producing a core polarisation field which is opposed to the applied field. The K_d term is usually smaller than that due to s contact.

As indicated in section 3.2.5, the spin dipolar term gives no contribution to the Knight shift in metals of cubic symmetry. Note that in non-cubic metals or where electrons are of non-s type, the presence of a non-zero dipolar term leads to an anisotropy in the Knight shift and resonance line broadening.

The orbital term[10] in equation (3.24) does not contribute to the Knight shift in first order, since in metals the conduction electrons are not localised and have no orbital angular momentum†. However, non-s electrons can produce a second order orbital contribution to Knight shift via an orbital hyperfine interaction given by

$$\mathcal{H}_{en}^{orb} = \frac{\gamma_e \gamma_n \hbar^2 \mathbf{L}.\mathbf{I}}{r^3} \tag{3.33}$$

where **L** is the electron orbital angular momentum.

The associated contribution to the Knight shift is directly related to χ_{orb} (which is usually much less than χ_s) and is given by

$$K_{orb} = 2\chi_{orb} \left\langle \frac{1}{r^3} \right\rangle = H_{hf}^{orb} \frac{\chi_{orb}}{\mu_B} \tag{3.34}$$

where $\langle 1/r^3 \rangle$ is the averaged value over the conduction electron wavefunction and where H_{hf}^{orb} is the corresponding hyperfine field. K_{orb} is generally known as the Van Vleck (orbital) shift, and is sometimes represented by the symbol K_{vv}.

The Van Vleck orbital paramagnetism χ_{orb} results from the interaction of the applied field $\mathbf{B_0}$ and the orbital momentum, which can distort occupied states by mixing in unoccupied states from above Fermi level (provided the conduction band has some

---

[10] A. M. Clogston, A. C. Gossard, V. Jaccarino & Y. Yafet, *Phys. Rev. Lett.* **9** 262 (1962)

† The orbital angular momentum is said to be 'quenched'.

non-s character)*. These distorted states then act via the first order term to produce a non-zero orbital shift which is paramagnetic in sign. The size of the orbital paramagnetism and of the shift is independent of the spin state of the conduction electrons, and of the density of states at the Fermi surface, and so is expected to be independent of temperature. The shift does however depend on the symmetry of the filled orbital electron states and is therefore anisotropic. Generally, the Van Vleck term is only important for non-degenerate partially filled orbital electronic states, over which the average of $1/r^3$ has to be taken.

A final point which should be mentioned whilst on the subject of Knight shifts, involves the Korringa relation. Korringa showed that for the s-Fermi contact interaction, a simple relation links K_s and T_1, the spin-lattice relaxation time,

$$T_1 T K_s^2 = \left(\frac{h}{4\pi k_B}\right)\frac{\gamma_e^2}{\gamma_n^2} S_K \qquad (3.35)$$

where T = temperature in K, k_B is the Boltmann constant and the factor S_K is included to take account of the effects of the electron-electron interactions (i.e dimensionality of the electron dynamics, which is equal to one for a 3D free electron gas)[11]. A similar relation can be found to hold for the core polarisation interaction[12]. Since K_{orb} is derived from a second order effect, a Korringa type relation does not hold for the orbital interaction.

3.4 NMR Shifts in BCS Superconductors

Early Yosida theory[13] predicts that the 'Knight shift' of a BCS superconductor falls to zero at T=0, since all the BCS ground state pairs contribute nothing to the electron spin susceptibility. As indicated in chapter 1, Yosida behaviour has only been confirmed for simple elemental superconductors, such as aluminium[14], where low atomic weight yields weak spin-orbit coupling and leaves the contact term as the lone contribution to the Knight shift.

In many BCS superconductors, the Knight shift is non-zero at T=0, due to considerable contributions from spin-orbit coupling and Van Vleck orbital

---

* The mixing produces states with slightly 'unquenched' orbital angular momentum.

11 See D. Pines, *Solid State Physics*, Vol. 1, ed. H. Ehrenreich, F. Seitz & D. Turnbull, Academic Press (1955)

12 Y. Yafet & V. Jaccarino, *Phys. Rev.* **133** A1630 (1964)

13 K. Yosida, *Phys. Rev.* **110** 769 (1958)

14 H. L. Fine, M. Lipsicas & M. Strongin, *Phys. Lett.* **29A** 366 (1969)

paramagnetism. Since the orbital shift is independent of the spin state of conduction electrons, it will not be affected by spin pairing in the superconducting state and, along with the chemical shift, will contribute to the observed magnetic shift at T=0.

In superconductors where d-band electrons participate in the formation of Cooper pairs, the core polarisation contribution to the Knight shift vanishes in the superconducting state. In narrow d-band materials (i.e V_3X compounds), where the bandwidth is comparable to k_BT, the d-band susceptibility and the core polaristion contribution to the Knight shift are found to be temperature dependent.

For further details of NMR in the superconducting state of BCS materials, the reader is referred to a review article by D. E. MacLaughlin (1976)[15].

3.5 NMR in HiT$_C$ Superconductors

NMR has been used extensively to study the hyperfine interactions of ^{89}Y, ^{63}Cu, ^{65}Cu, ^{139}La, ^{205}Tl and, if it is isotopically enriched, ^{17}O nuclei in the HiT$_c$ cuprates. However, in the interests of brevity, the following discussion will be restricted to the more relevant ^{89}Y and ^{63}Cu nuclei of the YBCO system.

3.5.1 NMR Samples

Anisotropy is a key feature of all HiT$_c$ cuprates. However, working with anisotropic powders in NMR has its disadvantages. Once in the magnetic field, the crystallite axes in the powder take on random orientations with respect to the applied field. The large distribution of orientation angles gives rise to a resonance with a broad frequency spread, which is often difficult to interpret.

In order to elucidate the anisotropic properties of the cuprates, many researchers have found it advantageous to work with single crystals. However, uni-phase single crystals have proved difficult to grow and resulting crystals have invariably been very small (~1mg). With a technique such as NMR, small samples lead to weak signals and extensive signal averaging is required to enhance the signal and obtain a reliable response.

In 1987, Farrell et al[16] produced pseudo-single crystal specimens by exploiting the magnetic anisotropy of the cuprates. If a crystal possessing an anisotropic (normal state) magnetic susceptibility is placed in a strong magnetic field, it will tend to rotate to an

---

15 D. E. MacLaughlin, *Solid State Physics*, Vol 31, ed. H. Ehrenreich, F. Seitz & D. Turnbull, Academic Press (1976)

16 D. E. Farrell, B. S. Chandrasekhar, M. R. DeGuire, M. M. Fang, V. G. Kogan, J. R. Clem & D. K. Finnemore, *Phys. Rev. B* **36** 4025 (1987)

angle which minimises its energy in the field. This corresponds to a state where the axis of maximum susceptibility is parallel to the applied magnetic field. The normal state magnetic anisotropy* of $YBa_2Cu_3O_7$ is positive[17] and equal to $1x10^{-4}cm^3$/mole, and so Farrell was able to demonstrate that single crystal grains of $YBa_2Cu_3O_{7-\delta}$, suspended in an epoxy, crystallographically aligned at room temperature with their c-axes pointing along the direction of the magnetic field. Once the epoxy is set, the crystallites remain uniaxially aligned in the non-magnetic matrix.

In an NMR experiment, the aligned specimen may be oriented with the 'powder' c-axis at any angle to the magnetic field. In the case where the c-axis lies along the applied field (c//B), the oriented powder is expected to be equivalent to a single crystal. However, in practice, the c-axis alignment is often found to be a few degrees out, and so invariably single crystal NMR results in narrower lines. When the c-axis is oriented perpendicular to the applied field (c⊥B), the aligned powder produces a 'restricted' powder pattern, since the field is random in the a-b plane. Here, single crystals hold the advantage over oriented powders as they can be aligned with any principal axis along the direction of the applied field.

A number of research groups[18,19,20] have noted that below T_c, the superconducting grains of $YBa_2Cu_3O_{7-\delta}$ orient with the a-b plane parallel to the field, since $\chi_\perp > \chi_{//}$†. Two studies[18,21] also conclude that at low temperatures, pure YBCO crystallites align c⊥B, with the b-axis predominantly lying along the direction of the field.

3.5.2 ^{89}Y NMR in YBCO

The ^{89}Y NMR magnetic shift ($^{89}\Delta K$) has been measured for a range of $YBa_2Cu_3O_{7-\delta}$ samples, both as a function of δ and temperature[22]. A general working definition of the ^{89}Y magnetic shift, with respect to an $^{89}YCl_3$ reference sample, has appeared as

$$^{89}\Delta K(\delta) = {}^{89}\sigma(\delta) + {}^{89}K_s(\delta) \qquad (3.36)$$

---

* which is probably due to anisotropy in the Van Vleck paramagnetic susceptibility of the Cu-O layers.

17 K. Fukuda, S. Shamota, M. Sato & K. Oda, *Solid State Comm.* **65** 1323 (1988).

18 S. Solin, N. Garcia, S. Vieira & M. Hortal, *Phys. Rev. Lett.* **60** 744 (1988)

19 J. M. Tranquada, A. I. Goldman, A. R. Moodenbaugh, G. Shirane, S. K. Sinha, A. J. Jacobson & J. T. Lewandowski, *Phys. Rev. B* **37** 519 (1988)

20 W. C. Lee & D. C. Johnson, *Phys. Rev. B* **41** 1904 (1990)

† where $\chi_{//}$ and $\chi_\perp$ are the susceptibilities parallel and perpendicular to the c-axis, respectively.

21 M. Solanki-Moser, D. P. Tunstall & W. J. Webster, *Supercond. Sci. Technol.* **3** 464 (1990)

22 H. Alloul, T. Ohno & P. Mendels, *Phys. Rev. Lett.* **63** 1700 (1989)

where $^{89}\sigma$ is the chemical shift contribution due to filled electronic shells and includes the Van Vleck term K_{orb} (i.e. $^{89}\sigma$ represents the total orbital shift, $^{89}\sigma \equiv \sigma + K_{orb}$) and $^{89}K_s(\delta)$ is the Knight shift contribution† due to the spin susceptibility of the CuO_2 planes (i.e $^{89}K_s$ represents the total spin shift, $^{89}K_s(\delta) \equiv K_s + K_d$).

The structural parameters of the CuO_2 layer in YBCO are almost independent of temperature and O content, and so the chemical shift $^{89}\sigma$ is also expected to be temperature independent . $^{89}\sigma$ can be obtained experimentally from the extrapolation to T=0 of a plot of $(T_1T)^{-1/2}$ vs. $^{89}\Delta K$, since $^{89}K_s(T)$ is zero from the Korringa relation. It is now generally accepted that the chemical shift of orthorhombic $YBa_2Cu_3O_7$ is approximately equal to +200ppm[23].

For δ=0 samples, the ^{89}Y magnetic shift is found[22] to have a Pauli-like temperature independence, at least above T_c, indicating that K_s is temperature independent. As δ increases, large reductions of $|^{89}\Delta K|$ appear at low temperatures. This can only be associated with a reduction in the total spin susceptibility χ_s and suggests that the magnetic properties of YBCO cannot be linked to the non-interacting electron band. In addition, $^{89}\Delta K$ scales well with the macroscopic susceptibility χ_m for all oxygen concentrations[24], implying that (i) a single T-dependent susceptibility describes the magnetic properties of the system and that (ii) the Y site probes this dominant T dependent contribution to χ_m.

The macroscopic susceptibility χ_m of the system thus has temperature dependent and temperature independent contributions, which can be represented by

$$\chi_m = \chi_0(\delta) + \chi_1(\delta, T) \qquad (3.37)$$

where

$$^{89}\Delta K = \beta(\delta) + {}^{89}\alpha\chi_1(\delta, T) = {}^{89}\sigma(\delta) + {}^{89}K_s(\delta, T) \qquad (3.38)$$

and $^{89}\alpha$ is the hyperfine coupling. Both the division of χ_m and the value of $^{89}\sigma$ cannot be accurately known, and so it is not directly possible to say whether $^{89}K_s$ and $^{89}\alpha\chi_1$ are equivalent.

The origins of the hyperfine field can be analysed by considering the position of the ^{89}Y ion in the YBCO structure. Since eight Cu ions and eight O ions surround the Y, it seems plausible to suggest that the ^{89}Y nuclear spin should couple to the electronic spin

---

† Note that in the field of HiT_C, the term 'Knight shift' is frequently reserved to describe the electron spin contribution to the total shift and is thus labelled K_s.

23 R. Dupree, Z. P. Han, D. McK. Paul, T. G. N. Babu & C. Greaves, *Physica C* **179** 311 (1991)

24 H. Alloul, T. Ohno & P. Mendels, *Jnl. Less Comm. Metals*, **164-165** 1022 (1990)

susceptibilities of Cu and O (χ_s(Cu) and χ_s(O)) via two independent hyperfine couplings, $^{89}\alpha$(Cu) and $^{89}\alpha$(O). If this is the case, $^{89}K_s$ can quite generally be written[24] as

$$^{89}K_s = 8\,^{89}\alpha(Cu)\,\chi_s(Cu) + 8\,^{89}\alpha(O)\,\chi_s(O) \qquad (3.39)$$

It has been deduced from experiment that the direct hyperfine coupling $^{89}\alpha$(Cu) of the ^{89}Y to the Cu susceptibility is dominant[25]. However, others suggest[24] that the Y and Cu atomic orbitals (AO) are far enough apart to render $^{89}\alpha$(Cu) negligible. Since by symmetry, there is no direct overlap of the Cu $3d_{x2-y2}$ orbital with the Y 5s atomic orbital, the only possible contribution to $^{89}\alpha$(Cu) is via a small Cu $3d_{x2-y2}$–Y 4d hybridisation.

In contrast, a direct overlap exists between the Y 5s and O $2p_\pi$ orbitals, since these O orbitals point towards the Y nuclei[26]. This yields a large positive contribution to the hyperfine field $^{89}\alpha$(O). On the other hand, the O $2p_\sigma$ atomic orbitals have no direct overlap with the Y 5s orbitals, by symmetry, and so only produce a large negative contribution to $^{89}\alpha$(O) via an exchange polarisation of the inner filled O $2p_\pi$ orbitals†.

The experimental data[22] indicates that the hyperfine coupling $^{89}\alpha$ of the ^{89}Y nuclei with the susceptibility of the CuO_2 planes is negative, and approximately independent of δ, to within experimental accuracy. This strongly suggests that the Y nuclear spins are coupled to the oxygen orbitals and it favours the theory of Cu 3d-O $2p_\sigma$ bonding of the hole orbitals.

3.5.3 ^{63}Cu NMR in YBCO

The accuracy of early Cu NMR experiments on random powders was restricted by large quadrupole interactions, which broaden the central transition line. Recent NMR studies on single crystals and aligned powders have, however, yielded more precise data on the anisotropic shifts at both Cu sites in YBCO.

A general ionic model, based on the well-established concepts described in previous sections, is often used to give a semi-quantitative analysis of the normal state magnetic and hyperfine behaviour of YBCO. It is useful here to define the basic model and some of the terms associated with it.

---

25 P. Butaud, M. Horvatic, Y. Berthier, P. Segransan, Y. Kitaoka & C. Berthier, *Physica C* **166** 301 (1990)

26 F. J. Adrian, *Phys. Rev. Lett* **61** 2148 (1988): *Phys. Rev. Lett.* **63** 691 (1989)

† which is induced by the hole spin density on the O $2p_\sigma$ orbitals.

In general, a paramagnetic metal is characterised by a spin susceptibility*,

$$\chi_s(\mathbf{q}, \omega) = \chi_s'(\mathbf{q}, \omega) + i\chi_s''(\mathbf{q}, \omega) \qquad (3.40)$$

where each component is a function of the wave vector **q** and the frequency ω. The term $\chi_s'(0,0)$ is called the 'static uniform susceptibility' and is essentially probed through a study of the Knight shift. The disspative or dynamic term, $\chi_s''(\mathbf{q},\omega)$ is explored via nuclear relaxation studies.

For $T>T_c$, the measured macroscopic susceptibility χ_m along a given crystal axis α (=a, b, c) is the sum of the spin term $\chi_s'(0,0)$, the Van Vleck orbital term χ_{orb} and the core diamagnetic term χ_{dia}, i.e.

$$\chi_{m,\alpha} = \chi'_{s,\alpha}(0,0) + \chi_{orb,\alpha} + \chi_{dia,\alpha} \qquad (3.41)$$

Earlier work on d-band metals by Clogston et al[27], suggests that NMR shift data may be used to further decompose the susceptibility into its component parts. In the YBCO system, $\chi_{orb,\upsilon}$ and $\chi'_{s,\upsilon}(0,0)$ can be broken down into contributions that reside primarily on the Cu(1) and Cu(2) sites, giving,

$$\chi_{orb,\alpha} = {}^{63}\chi^{\alpha}_{orb}(1) + 2\,{}^{63}\chi^{\alpha}_{orb}(2) \qquad (3.42)$$

and

$$\chi'_{s,\upsilon}(0,0) = {}^{63}\chi^{\alpha}_{s}(1) + 2\,{}^{63}\chi^{\alpha}_{s}(2) \qquad (3.43)$$

where 1 and 2 signify Cu(1) and Cu(2), respectively. Note that the orbital susceptibility of the system arises almost exclusively from the Cu 3d electrons, and that the spin susceptibility is expected to reside on the Cu sites, but has some O 2p character due to hybridisation.

Generalising (3.29), we can expect the Cu Knight shift K for each site (1 or 2) and in each direction α, to have a spin contribution and an orbital contribution, i.e

$${}^{63}K^{\alpha}(1,2) = {}^{63}K^{\alpha}_{s}(1,2) + {}^{63}K^{\alpha}_{orb}(1,2) \qquad (3.44)$$

where each term is related to its respective susceptibility (given in (3.42) and (3.43)) via

---

* Note that for 3d metals, spin-orbit coupling mixes a small amount of orbital character into $\chi_s(q,\omega)$.

27 A. M. Clogston, V. Jaccarino & Y. Yafet, *Phys. Rev. A* **134** 650 (1964)

hyperfine coupling constants[28] A^{α} (where using the notation of (3.39) $^{63}\alpha = A/\gamma_e\gamma_n\hbar^2$),

$$K^{\alpha}_{orb}(1,2) = \frac{1}{\gamma_e\gamma_n\hbar^2}\left[A_{orb}\,\chi^{\alpha}_{orb}(1,2)\right] \qquad (3.45)$$

$$K^{\alpha}_{s}(1,2) = \frac{1}{\gamma_e\gamma_n\hbar^2}\left[A_c(1,2) + A_{cp}(1,2) + A^{\alpha}_{dip}(1,2) + A^{\alpha}_{so}(1,2)\right]\chi^{\alpha}_{s}(1,2) \qquad (3.46)$$

and where orbital (A_{orb}), contact (A_c), core polarisation (A_{ac}), dipolar (A_{dip}) and spin-orbit (A_{so}) contributions have been included*.

For a K-χ analysis, it is necessary to experimentally determine the anisotropic components of the macroscopic susceptibility, $\chi_{m,c}$ and $\chi_{m,ab}$. Accurate NMR shift data must also be obtained from NMR experiments on single crystals or aligned powder samples, which are fixed at various orientations (c//B, b//B and a//B) with respect to the B-field. Due to demagnetisation currents which arise in the 'mixed' state below T_c, the magnetic field inside a type II superconductor is not equal to the applied field. Therefore, an essential step in obtaining accurate measurements of K is the determination of the demagnetisation correction. This will be discussed in greater detail in chapter 5.

In order to separately estimate the K_{orb} and K_s terms, the total shift obtained by experiment in the superconducting state is extrapolated to T=0. Since the K_s term is assumed[29] to reduce to zero at T=0, at both sites and in all directions, the temperature-independent K_{orb} component can be deduced from the residual shift. A theoretical estimate is generally used to derive A_{orb}, allowing $\chi^{\alpha}_{orb}(1,2)$ to be found from equation (3.45). Such an estimate leads to

$$A_{orb} = \frac{\gamma_e\gamma_n\hbar^2}{\langle r^3\rangle} \qquad (3.47)$$

where $\langle r^{-3}\rangle$ is invariably taken to be 6.3 atomic units (a.u) from EPR data[30] obtained on compounds containing Cu^{2+}.

Once the χ_{orb} components have been deduced and an estimate[31] has been made for χ_{dia}, these terms can be subtracted from the component macroscopic susceptibilities to

---

28 F. Mila & T. M. Rice, *Physica C* **157** 561 (1989)

* Note that the superscript '63' has been omitted for clarity.

29 M. Takigawa, P. C. Hammel, R. H. Heffner & Z. Fisk, *Phys. Rev. B* **39** 7371 (1989)

30 A. Abragam & B. Bleaney, *Electron Paramagnetic Resonance of Transition Ions*, Clarendon Press (1970)

31 A. Junod, A. Bezinge & J. Muller, *Physica C* **152** 50 (1988) (χ_{dia} = -1.75x10^{-4} emu/mol f.u.)

leave the component spin susceptibilities (see equation (3.41)). The spin contribution to the Knight shift can then be analysed.

Note that the spin susceptibility is found to be approximately isotropic, while the orbital susceptibility has a large anisotropy[28,29].

The local symmetry around the Cu(1) site indicates that the ground state involves the mixing of two 3d wave functions, Cu $3d_{x2-y2}$ and Cu $3d_{3z2-r2}$. For the Cu(2) site, the ground state is a nearly pure $3d_{x2-y2}$ orbital with excited states d_{xy} and d_{yz},d_{zx} at crystal field splitting energies of Δ_0 and Δ_1, respectively (where $\Delta_0=E(d_{xy})-E(d_{x2-y2})$ and $\Delta_1=E(d_{xz,dyz})-E(d_{x2-y2})$). The excited states account for the orbital susceptibility and also give rise, through the spin-orbit Hamiltonian term $\lambda\mathbf{L}.\mathbf{S}$ (where $\mathbf{L}$ is the angular momentum, $\mathbf{S}$ is the spin and λ is the coupling strength), to an electronic g-shift and modified spin hyperfine constants.

Since a detailed analysis of the spin contributions for the two Cu sites can be found elsewhere[28], only the much quoted expression for the hyperfine Hamiltonian for the Cu(2) nuclear spin $\mathbf{I}_i$ will be given here,

$$H_{hf}(2) = \sum_i \sum_\alpha A^\alpha I_i^\alpha S_i^\alpha + \mathbf{B}\mathbf{I}_i \cdot \sum_{j(nn)} \sigma_j \qquad (3.48)$$

where the second term is an isotropic contribution which describes the transferred hyperfine field from nearest neighbour Cu(2) spins σ_j (S=1/2). This extra term is added because a purely on-site hyperfine interaction is not sufficient to explain the observed anisotropy of the nuclear spin-lattice relaxation time of the Cu(2) nuclei. The T_1 measurements reveal that the c-axis hyperfine fluctuations are predominant. This conflicts with the shift data which indicates that $K_s^c(2) \ll K_s^{ab}(2)$.

The resulting spin Knight shift is given by[28,32]

$$K_s^\alpha(2) = \frac{1}{\gamma_e\gamma_n\hbar^2}\left[A^\alpha\chi_s + B\chi_\sigma\right] \qquad (3.49)$$

where χ_σ is the susceptibility associated with the spin σ.

---

32 H. Monien, D. Pines & C. P. Slichter, *Phys. Rev. B* **41** 11,120 (1990)

3.6 Second Order Quadrupole Plus Anisotropic Knight Shift Pattern

A useful method of collecting NMR data is via spin echo experiments. Such techniques will be discussed in greater detail in chapter 4. With an external field of several Tesla, NMR spin echo experiments yield complex spectra which are mainly determined by Zeeman energy and, in cases where the nucleus has I>1/2, by the quadrupole interaction with the electric field gradient at the nucleus. In metallic systems, Knight shifts (K) occur as corrections only, but can provide valuable information on the electron spin susceptibility and magnetic properties of the conduction electrons.

It is possible to determine the properties of the electric field gradient tensor and the Knight shift tensor at particular sites in a crystalline solid, by fitting data acquired from a combination of zero-field nuclear quadrupole resonance (NQR) and NMR experiments, to known expressions for the quadrupole and Knight shifts. In parts of this study, we are specifically concerned with the Knight shift tensor at the ^{63}Cu(2) site in pure YBCO, and so the following expressions for the quadrupole interaction and the Knight shift will be derived (using known characteristics) with this site in mind.

For a spin 3/2 nucleus, all the $\pm 1/2 \leftrightarrow \pm 3/2$ transitions are known to be degenerate[1] and lead to a single NQR line at some quadrupole frequency, υ_{NQR}. The nuclear quadrupole frequency of this signal is related to the pure quadrupole frequency υ_Q and to the principal components of the EFG tensor present at the Cu site, via the expression[6]

$$\upsilon_{NQR} = \upsilon_Q \sqrt{1 + \tfrac{1}{3}\eta^2} \equiv \frac{eQV_{zz}}{2h}\sqrt{1 + \tfrac{1}{3}\eta^2} \qquad (3.50)$$

where the equivalence has been derived using equations (3.14) and (3.20) and by utilising the fact that I=3/2 for Cu. The NQR frequency of ^{63}Cu(2) is now well established from experiment and is detailed in chapter 5.

In order to determine V_{zz} and η separately, one must complement the NQR data by measuring the Cu NMR spectrum. The high magnetic field of the NMR experiment splits the four 2I+1 levels, and this results in a central transition ($-1/2 \leftrightarrow +1/2$) near the Larmor frequency υ_L and two satellite transitions at $\upsilon_L \pm \upsilon_{NQR}(\theta, \phi)$. The υ_{NQR} now has a strong dependence on the Euler angles (θ, ϕ) - the polar angles of B_0 with respect to the principal

axis system of the EFG*. Since the satellite transitions are significantly broadened by the angular dependence of υ_{NQR}, they are difficult to identify and will be not be considered here.

Experimentally, it is found that the ^{63}Cu(2) central transition is broadened by second order quadrupole interactions and that the EFG has axial symmetry about the c-axis. From the extended theory of quadrupole effects, it can be shown that for an axially symmetric field gradient ($\eta \approx 0$), the second order electric quadrupole shift υ_{EQ} for the central transition has an orientation dependence described by[6]

$$\upsilon_{EQ} = \frac{\upsilon_{NQR}^2}{16\upsilon_L}\left[(a - \tfrac{3}{4})\,(9\mu^2 - 1)\,(1 - \mu^2)\right] \qquad (3.51)$$

where a, μ and υ_L are defined by equation (3.21) and θ is the angle between z and B_0. For I=3/2, (3.37) reduces to

$$\upsilon_{EQ} = \frac{6\upsilon_{NQR}^2}{32\upsilon_L}\left[(9\cos^2\theta - 1)\,(1 - \cos^2\theta)\right] \qquad (3.52)$$

where the θ dependence has been shown explicitly.

In addition, the Knight shift of ^{63}Cu(2) is also found to have axial symmetry about the c-axis and is strongly anisotropic. The component of K parallel to the field B_0 generally has an orientation dependence on the Euler angles (θ, ϕ)†. However, when the nucleus is in an environment of axial symmetry, K depends on θ but not on the azimuthal angle ϕ. The orientational Knight shift $K(\theta)$ can be shown to be of the form[33]

$$K(\theta) = K_{iso} + K_{ax}(3\cos^2\theta - 1) \qquad (3.53)$$

where K_{iso} is the isotropic shift (applicable to solids in the absence of quadrupole or axial effects) and K_{ax} is the axial shift. The isotropic shift can be calculated from the centroid of the resonance, and the axial shift from the difference in frequency $\upsilon_{//}$ and $\upsilon_{\perp}$, when the c axis is parallel and perpendicular to the B_0 field, respectively. Subsequently, K_{iso} and K_{ax} can be defined by

---

* Note that since the z-axis of the EFG has been observed to lie parallel to the crystallographic c-axis for the Cu(2) site in YBCO, the labels of the two axes are frequently interchanged in the following discussion.

† where the principal axis system of the Knight shift and EFG tensors are expected to coincide.

33 G. C. Carter, L. H. Bennett & D. J. Kahan, *Progress in Materials Science*, Vol 20, Pergamon Press (1977)

$$K_{iso} = \frac{1}{3}(K_{//} + 2K_{\perp}) \tag{3.54}$$

and

$$K_{ax} = \frac{1}{3}(K_{//} - K_{\perp}) \tag{3.55}$$

where essentially $K_{//}$ is the Knight shift along the c-axis at the Cu(2) site and $K_{\perp}$ is the Knight shift in the direction of the a-b plane of the crystal - providing the principal axes of the axial shift tensor, the EFG tensor and the crystallographic system all coincide.

The final equation describing the observed frequencies for the second order quadrupole plus anisotropic Knight shift pattern of the central transition (m=±1/2) of the Cu(2) resonance in YBCO is given as

$$\upsilon(m \leftrightarrow m\text{-}1) = \upsilon_L + \frac{6\upsilon_{NQR}^2}{32\upsilon_L}(9\cos^2\theta - 1)(1 - \cos^2\theta) - \left[\frac{1}{3}(K_{//} + 2K_{\perp}) + \frac{1}{3}(K_{//} - K_{\perp})(3\cos^2\theta - 1) \times \frac{\upsilon_L}{100}\right] \tag{3.56}$$

where the fact that the Knight shift components are represented as percentages of υ_L has been accounted for.

If the c-axis of an aligned YBCO sample is rotated in the plane parallel to B_0 (such that θ is the angle between c and the applied field), a plot of observed resonance frequency vs. θ would produce a sample rotation pattern[6]. Such a pattern could be fitted to equation (3.42) and the unknown values of $K_{//}$ and $K_{\perp}$ obtained.

Chapter 4

Experimental Methods & Techniques

4.1 Introduction

Broadly speaking, this chapter is split into two: the first half contains the sample characterisation and the alignment methods, and the second half details the subsequent analysis of the powder and magnetically aligned samples using NMR techniques.

Initially, scanning electron microscopy (SEM) and X-ray diffraction (XRD) techniques were used on two undoped YBCO samples (labelled JM21* and the Aberdeen sample†) to gain an insight into the morphology and structure of unaligned powder specimens. The powders were then magnetically aligned in an epoxy resin and X-rayed again to check the validity of the alignment procedure. The alignment of the Aberdeen sample was subsequently examined using an NMR rotation pattern, obtained by orienting the crystallographic c-axis at different angles to the $\mathbf{B_0}$-field and acquiring a ^{63}Cu NMR spin echo spectrum (at 1.5K and 141MHz) at each angle. The results of the analysis of the pure YBCO system can be found in chapter 5.

Two batches of cobalt doped YBCO samples were prepared by Pam Freeman at the Interdisciplinary Research Centre (IRC), University of Cambridge. The first batch contained 4 samples with 0%, 1.5%, 2.8% and 4% Co doping and the second contained a further 6 samples with 0%, 0.05%, 0.15%, 0.3%, 0.5% and 1.0% Co doping. After initial characterisation at the IRC, the powder samples were aligned in epoxy resin (via improved alignment procedures), X-rayed and studied at different temperatures using ^{89}Y and ^{63}Cu NMR spectroscopy (performed on a Bruker MSL-500 spectrometer). The results of the analysis of the Co-doped samples can be found in chapter 6.

All samples were prepared by standard solid state reaction methods. The JM21 and Aberdeen samples were synthesized from a mixture containing stoichiometric amounts of Y_2O_3, $BaCO_3$ and CuO. The mixture was fired twice in air at around 900°C for 12 hours in an alumina crucible, with intermediate regrinding and repelletising. The final annealing process was carried out in flowing oxygen at 930°C over a period of 12 hours, and the

---

* courtesy of The Johnson Matthey Company.

† courtesy of John Irvine and Anthony West, Department of Chemistry, University of Aberdeen.

resulting compound was allowed to cool in oxygen at a rate of 50°C/hour. The slightly different method of preparation used for the Co doped samples, involved the inclusion of regulated amounts of Co_3O_4 in the starting mixture. The final annealing process also had multiple cooling stages to allow for a more controlled uptake of oxygen into the system. The full method of preparation is detailed elsewhere[1].

Since reaction with water depletes the superconducting properties of the YBCO ceramic (by decreasing the volume fraction of the superconducting phase), all pellet samples obtained were kept under constant vacuum, and were ground into fine powders using an agate pestle and mortar (to avoid contamination), only when needed.

4.2 Powder Analysis

4.2.1 Scanning Electron Microscopy

The preliminary analysis of the powdered JM21 sample using microscopic techniques was part of an on-going process used to establish satisfactory preparation procedures prior to powder alignment. An initial investigation of the JM21 powder using a Jena 125X light microscope and a JEOL JCX A733 (backscatter) SEM revealed that the sample contained a broad range of different sized crystallites - ranging from <1μm for fragments of crystals to ~200μm for large clusters of crystals. Since the crystallites within a cluster appeared to be attracted to each other by minute amounts of water vapour, the sample was subjected to small bursts of 'beam heating' within the SEM to alleviate the problem. At magnifications higher than x1500, the beam heating of this microscope was sufficient to vapourise some of the crystallites, and so an alternative method of observation was sort.

After several days of 'drying out' in an evacuated dessicator containing silica gel, the sample was transferred to an argon glove box†, where it was reground thoroughly using a dehydrated agate pestle and mortar. A small amount of sample was then dusted onto a copper stud and coated with a 10nm layer of gold (in an evacuated splutter), ready for mounting in a more sophisticated JEOL JSM 35CF scanning electron microscope.

The imaging method[2] of the SEM allows high resolution representations of the sample to be observed, even at very high magnifications. Essentially, the SEM utilises a

---

1 W. W. Schmahl, A. Putnis, E. Salje, P. Freeman, A. Graeme-Barber, R. Jones, K. K. Singh, J. Blunt, P. P. Edwards, J. Loram & K. Mirza, *Philos. Mag. Lett.* **60** 241 (1989)

† In which the amounts of water vapour and oxygen in the atmosphere were controlled to within 1ppm.

2 See *Scanning Electron Microscopy & X-ray Microanalysis* by J. I. Goldstein, Plenum, New York (1981)

very fine probing beam of electrons which sweeps over the sample and at any instant excites the material, so that it emits a variety of radiations. The signal, which is proportional to the amount of radiation leaving an individual point on the sample at any moment, is then used to modulate the brightness of the beam of a cathode ray tube (CRT) as it sits on the corresponding point of the image. As the probing beam scans across the surface of the specimen exciting individual points in rapid succession, an exact image is built up on the CRT display due to the one-to-one correspondence between the single position of the electron beam and the single position of the cathode ray beam, at any instant in time. The human eye is able to register this point by point sequence as a complete image, since the points follow one another very rapidly. In this case, the image was also recorded in its entirety by allowing the point by point sequence to build up on a photographic film.

There were certain advantages to using the JEOL JSM 35CF SEM: firstly, the beam heating was insufficient to affect the sample, even at magnifications as high as x15,000, and secondly, the SEM sample stage had the ability to tilt and rotate the sample as well as manoeuvre it in the transverse plane, giving the controller the advantage of being able to view the sample or individual crystallites from all angles.

Since the SEM micrographs gave clear evidence that the JM21 sample now contained a large proportion of single crystals (approximately 10μm across the major axis) and relatively few clusters (mostly less than 100μm across), the powder analysis progressed onto X-ray diffraction.

4.2.2 X-Ray Diffraction (XRD)

Typically, interatomic distances in a solid are of the order of a few Ångstroms, and so hard X-rays, with characteristic wavelengths in the range 1-10Å, are used as an electromagnetic probe of the microscopic structure of solids. In 1913, the pioneering work of Bragg[3] showed that X-rays are diffracted by crystals in a manner which is dependent on the wavelength of the rays (λ) and the space lattice of the crystal.

The crystal can be regarded as a set of parallel planes of ions, spaced a distance d apart. In effect, the planes behave as lightly silvered mirrors, specularly† reflecting only a small fraction of the incident X-ray radiation. Sharp peaks are observed in the intensity of scattered radiation when X-rays, reflected by ions in successive parallel planes, constructively interfere. Since the path difference between successive reflected rays is $2dSin\theta$, where θ is the angle of incidence of the X-ray measured from the reflection

---

3 W. L. Bragg, *Proc. Cambridge Phil. Soc.* **17** 43 (1913)

† In specular reflection the angle of incidence equals the angle of reflection.

plane, it is clear from simple X-ray theory that the Bragg condition must apply for constructive interference to occur. The Bragg condition, which is derived elsewhere[4], is given by

$$n\lambda = 2d\text{Sin}\,\theta \qquad (4.1)$$

where n is an interger known as the order of the corresponding reflection.

It is usual to specify a particular plane in a lattice by its 'Miller indices'. The Miller indices are a set of three integers (hkl) which determine the position and orientation of a crystal plane in relation to three mutually perpendicular crystallographic vector axes, **a**, **b** and **c**. Any individual plane intercepts these axes at lattice points A, B and C such that the vectors **OA**, **OB** and **OC** (referenced to some common origin, O) lie in the direction of **a**, **b** and **c**, respectively. The distances |OA|, |OB| and |OC| are found in terms of the respective lattice constants |a|, |b| and |c|, such that n_a, n_b and n_c are the multiplying factors (i.e |OA| = n_a |a|, etc). The reciprocals of n_a, n_b and n_c are then taken and reduced to the three smallest integers h, k and l which still preserve the same ratio. The final result is enclosed in parentheses (hkl) and is known as the set of Miller indices for that particular plane.

It can be shown[4] that for a given crystallographic system, the interplanar spacing d_{hkl}, of a specified plane (hkl) can be represented in terms of the crystal lattice parameters a, b and c. In the case of the orthorhombic (where a≠b≠c) and tetragonal (where a=b≠c) structures, the relationships are given as,

$$d_{hkl}\,(\text{orthorhombic}) = \frac{1}{\left[\left(\frac{h}{a}\right)^2 + \left(\frac{k}{b}\right)^2 + \left(\frac{l}{c}\right)^2\right]^{\frac{1}{2}}} \qquad (4.2)$$

$$d_{hkl}\,(\text{tetragonal}) = \frac{a}{\left[h^2 + k^2 + \left(\frac{a}{c}\right)^2 l^2\right]^{\frac{1}{2}}} \qquad (4.3)$$

A standard X-ray powder method[4] was used to determine the crystallographic nature of all of the samples used in this experimental analysis: small amounts of each powder sample were carefully mounted onto individual plates using acetone, and then loaded into a fully automated Philips PW1049 X-ray diffractometer. X-rays produced from a copper

---

4 M. F. C. Ladd & R. A. Palmer, *Structure Determination by X-Ray Crystallography*, Plenum (1979).

target* (Cu K_α wavelength, λ_{Cu} = 1.54050Å) were fired through a 1° divergence slit and irradiated the sample on one side. With this experimental arrangement, diffracted rays leave the specimen along the generators of cones concentric with the original beam. The generators make an angle of 2θ with the direction of the incoming beam and backscatter radiation can be detected at angles of 2θ between 5° and 90°. The number of X-ray counts per second at each angle is recorded systematically so that a spectrum of X-ray intensity vs. diffraction angle (2θ) is obtained. All X-ray spectra incorporated in this work were accumulated at room temperature.

In order to identify the peaks, experimental values of 2θ were compared with computer generated tables of 'theoretical' 2θ values. The d_{hkl} parameters were first calculated by inputting standard values of the lattice constants a, b and c into equation (4.2) and successively incrementing the integers h, k and l. The conversion of d_{hkl} to 2θ was then performed using equation (4.1). The computer program which generates the tables of theoretical 2θ values is given in appendix C.1.

4.3 Alignment Procedure

4.3.1 Introduction

When using NMR techniques to study YBCO, it is desirable to work with accurately aligned powder samples (see chapter 3, section 3.5.1), which are well characterised. The basic method developed by Farrell et al[5] for 'freezing' small amounts of uniaxially aligned crystals in a non-magnetic matrix of epoxy resin at room temperature, has been used extensively in this study to align all samples prior to analysis by NMR. In place of the weakly diamagnetic Duro TM-51 resin employed in the original study, Stycast 1266, a transparent, non-magnetic, high impact epoxy resin, capable of withstanding temperatures as low as 1.5K, was used. In all cases, the resin part A and the volatile catalyst part B of the epoxy were measured out by weight†, and part A was vacuum pumped for 30 minutes to eliminate dissolved air and water. The composite was subsequently vacuum pumped for a few minutes to expel any air trapped during the mixing process.

---

* Note that the copper target was subsequently replaced by a cobalt target (Co K_α wavelength, λ_{Co} = 1.7902Å), and the system was computerised so that the peak information could be obtained with greater accuaracy.

5 D. E. Farrell, B. S. Chandrasekhar, M. R. DeGuire, M. M. Fang, V. G. Kogan, J. R. Clem & D. K. Finnemore, *Phys. Rev. B* **36** 4025 (1987)

† see appendix D.4 for manufactures instructions & commercial specifications.

Recent microstructural studies by De Guire et al[6] and Low et al[7] on thermoset powder-epoxy composites have concluded that an epoxy resin coating is an effective barrier against the aqueous decompostion of YBCO. These results, added to our own experience, allow us presume that an epoxy set YBCO sample can withstand exposure to air for much longer periods of time than the powder sample, giving us more freedom to manipulate the samples without the need of an inert atmosphere or sealed tubes.

Since one of the aims of this project was to establish an effective alignment procedure, it seems appropriate here to detail not only the final technique employed (section 4.3.6), but also the development stages (sections 4.3.2 to 4.3.5) which culminated in the use of this technique.

4.3.2 Initial Technique

In preparation, the JM21 and Aberdeen samples were thoroughly ground in an argon atmosphere until the mean grain size was approximately 10μm. The resulting powder was then weighed in order to produce a stycast to powder ratio of 5 to 1 by volume. On removal from the glove box, the sample was rapidly and assiduously mixed by hand with freshly prepared stycast in a cylindical glass tube. Thereafter, the glass tube was sealed and placed in a 9T magnetic field, in such a way that the longitudinal axis of the cylinder was perpendicular to the direction of the field. The powder-epoxy composite was allowed to cure over a period of 15 hours at a constant temperature of 300K, maintained by a heater coil. After the setting procedure was complete, the proposed c-axis, which lay parallel to the end face of the cylinder in the direction of the field, was marked on one end of the sample using a scoring implement. To determine the degree of alignment, the two samples were subsequently analysed using X-ray and microscopy techniques.

4.3.3 X-ray & Microscopic Analysis of Aligned Powders

Whilst maintaining the alignment, a 1mm thick disc was sliced from the end of the cylinder using a clean diamond rotary saw. The discs from each sample were mounted onto individual plates, and loaded into the diffractometer in such a way that the c-axis alignment was in the plane perpendicular to the plane of the X-ray beam (see figure 4.1(a)). With this configuration, all orientations of the c-axis within the disc plane are equivalent (thus figure 4.1(a) would produce the same X-ray spectrum as figure 4.1(b)).

---

6 M. R. De Guire, I. Manas-Zloczower, M. Tabib-Azar, D. E. Farrell, C. J. Kim, W. H. Lu, H. Ng & F. Rayal, *Jnl. Mater. Sci.* **25** 2881 (1990)

7 I. M. Low & F. W. Lim, *Jnl. Mater. Sci. Lett.* **10** 1119 (1991)

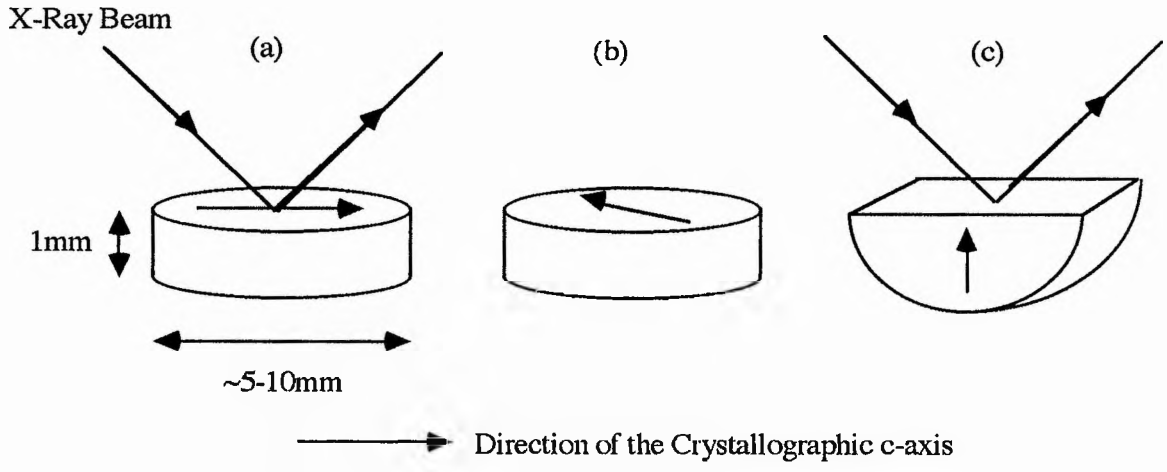

Figure 4.1

A schematic drawing of the various orientations of an aligned epoxy set YBCO disc, with respect to an incident X-ray beam. Note that the X-ray spectra obtained from orientations (a) and (b) would be identical.

During this and subsequent procedures, the diffractometer setup remained the same as that established in section 4.2.2, and in each case, the spectrum of X-ray intensity vs. diffraction angle (2θ) was analysed in a similar fashion to the powder spectrum. For comparative purposes, the discs were later (after the microscopic analysis) cut along their diameter, and each half disc was mounted in the diffractometer with its c-axis plane parallel to the X-ray beam plane (see figure 4.1(c)).

For samples oriented as in figure 4.1(a), all the (hkl) reflections with non-zero l values should be absent from the final spectrum. Samples oriented in the fashion of figure 4.1(c) should produce a spectrum in which all l=0 reflections have disappeared.

In order to obtain some visual representation of the dispersion and alignment of the crystallites in the resin, the aligned disc samples were also analysed using the JEOL JCX A733 electron microscope. To prevent the discs from rotating in the microscope, they were mounted together in a circular die using another epoxy resin, known commercially as Epicure. After polishing, the epoxy block was mounted in the SEM such that the marked c-axis of each disc lay vertically on the viewing screen. This provided a convenient reference axis.

4.3.4 Failure of Initial Technique

The initial studies on the JM21 and Aberdeen samples indicated that there was a discrepancy of approximately 30° between the true c-axis alignment and the marked c-axis. Further studies on the Aberdeen sample using NMR techniques (see section 4.7 and

chapter 5) later confirmed this fact. Several sources of error were envisaged. Firstly, the microscopy scans suggested that the single crystallites, which were virtually free in the ground powder, had a tendency to cluster in the epoxy resin. These clusters appeared to be concentrated around the edges of the discs, leaving the central area fairly sparcely populated. Such a high density of crystallites in the outer regions of the disc lead us to believe that individual crystallites were prevented from aligning c parallel to B by the intervention of neighbouring crystallites. Some of the crystallites were effectively oriented in random directions, but the overall effect was that clusters of crystallites were seen at an angle of 30° to the expected c-axis.

In addition, the cross section of the disc was peppered with a number of small air bubbles, which again caused the powder to be irregularly dispersed.

It was also thought that the method of transfering the mark of the expected c-axis from the glass tube to the aligned sample was inadequate. Such a crucial stage in the sample preparation should be dealt with in a more methodical and failsafe manner. To this end, it was proposed that two methods of engraving the sample be employed - one at each end of the cylinder. Upon removal from the field, the c-axis was marked onto the glass sample tubes (which were held rigid in a brass former and were unable to rotate) in indelible ink. Using a fine diamond circular glass saw positioned along the ink line, the glass was carefully etched away until the cutting edge made an incision in the set epoxy. A similar ink line was drawn on the opposite face of the glass tube. A 0.8mm hole was then drilled through the glass and into the sample, at either end of the line. The glass was subsequently broken away, leaving the sample with two definite alignment marks.

4.3.5 Pilot Studies of Fine Powder Dispersion in Epoxy Resin

In order to determine the most ideal preparative conditions needed to obtain thorough dispersion of YBCO powder in epoxy resin, a pilot study was performed using aluminium powder of similar grain size. In this study, there were three variables: the type of epoxy resin (Stycast or Epicure), the dispersion method (chemical, ultrasonic or physical agitation) and the aluminium packing fraction in the resin (either 0.1 or 0.2)*.

It was expected that the crystallites would have less of a tendency to clump when in Epicure since it was slightly less viscous than stycast, and that a packing fraction of 0.1 would aid the dispersion of the powder†. In order to disperse the powder, three distinct methods were used: (i) a few drops of a chemical flocculant, known as Olaic acid, was mixed into the powder-epoxy composite; (ii) after a preliminary mix by hand, the powder

---

* By volume

† Although in the long run it may weaken the NMR signal.

was dispersed using a Mullard MEL Ultrasonic gun and (iii) the composite was physically agitated for 15 minutes, by hand, using a plastic stirrer. In all cases, the sample tubes were sealed with a rubber bung and the air was removed from the tube using a fine wire inserted between the bung and the glass. The composites were then left to cure at room temperature for a period of 15 hours. Once set, the specimens were removed from their glass tubes. A 1mm disc was sliced from the end of the cylinder and mounted in the JEOL JCX A733 microscope, as before. Even at a low magnification, it was possible to view the dispersion of the powder over the entire disc.

The results were fairly straightforward and conclusive.

(i) In each sample containing the chemical flocculant, large crators or holes had appeared in the set sample - almost as if the acid had burnt through or reacted with the epoxy. The powder dispersion was very poor.

(ii) In the cases where dispersion had been by ultrasonic gun and the packing fraction was 0.2, the powder was fairly well spread, but crystallites tended to clump (randomly) in regions of the disc. With a packing fraction of 0.1, the powder was very evenly distributed across the disc and few air bubbles were present. However, in the Epicure the crystallites appeared to be larger than in the stycast and it was difficult to determine whether these crystallites were small clusters or large single crystals. In Stycast, the distribution was good and on the whole the crystal grains were small. Crystal clusters were not evident, in this case.

(iii) Powder samples dispersed using physical agitation were characterised by a large number of small air bubbles. Overall, the powder distribution was fairly good, with a small amount of clustering occuring in each sample - but to a lesser extent in the specimens where the packing fraction was 0.1. The distribution and grain size of these samples was similar to that found in the Epicure/ultrasonic gun samples.

Evidently, the best way of ensuring a thorough distribution of small, unclustered crystallites is by using a powder dispersed in Stycast by an ultrasonic gun, at a packing fraction of 0.1.

4.3.6 Final Technique

The experience gained from the above investigations on the JM21, Aberdeen and Al powder samples allows us to formulate a fairly simple, but reliable sample preparation, alignment and characterisation procedure. In summary:

(i) Sample pellets are ground into fine powders (mean particle size of 10μm) in an argon atmosphere using an agate pestle and mortar. A 10μm micro sieve may be used, if necessary.

(ii) A small amount of each powder is analysed using the X-ray powder diffraction (XRD) method described in section 4.2.2.

(iii) The powders are weighed out accurately to ensure an epoxy to powder ratio of 10 to 1. (In order to calculate the mass of powder which will result in this ratio, the volume of the sample tube and bung, and density of the sample must be known).

(iv) Freshly prepared and pumped stycast is added to the sample tube containing the measured powder, and the composite is mixed, initially by hand, using a stirrer. The powder is then efficiently dispersed in the epoxy resin using an ultrasonic gun - applied for a period of 2 minutes.

(v) The sample tube is then sealed at one end using a rubber bung. Air expulsion is achieved by slowly removing the fine wire which was inserted between the tube wall and the bung.

(vi) Each sample tube is mounted into a brass former which is able to rigidly hold up to nine specimens. An extension probe, heater coil and thermocouple are attached to the former and the extire assembly is inserted into the room temperature bore of a specially designed cryostat.

(vii) The composites are allowed to cure for 15 hours in an 8 Tesla field at a temperature of approximately 320K.

(viii) Upon removal from the field, the c-axis was marked on the samples using the method developed in section 4.3.4. A disc was cut off the end of the cylindrical sample and X-rayed in the fashion of section 4.3.3, using the orientation depicted in figure 4.1(a).

The two batches of Co-doped YBCO samples were aligned using the above method. In all cases, a comparison of the powder and aligned XRD spectra showed that the alignment was accurate to within a few degrees.

For each Co% used, three different sizes of aligned samples were produced. To enable the 6mm diameter sample, used in the 141MHz low temperature spectrometer, to be mounted in a rotation probe (section 4.7.2), the specimen was first glued onto a stycast post. A 10mm sample was required in order to obtain the Y NMR spectra, while a 5mm specimen was needed to record the room temperature Cu NMR data (section 4.8.2).

4.4 IRC Characterisation of Co-doped Powders

Powder specimens taken from the first batch of Co-doped samples (containing 0, 1, 2.8 and 4 %Co†) have been studied extensively at the IRC, Cambridge, using a variety

† a 7% Co sample was also prepared and the IRC results presented here may include this sample.

of techniques. The wide range of experimental work performed on these samples includes a microstructural characterisation[1], a high resolution specific heat analysis[8], critical current[9] and electrical resistivity[10] measurements, microwave[10] characteristics and magnetic susceptibility studies[11]. In addition, critical temperature (T_c) data was deduced from resistivity, specific heat and a.c. inductance measurements. Hall effect data obtained for these samples, subsequently proved to be unreliable (see chapter 6).

While the T_c data is of general interest to this study, it is the magnetic susceptibility data which will prove particularly useful in the analysis of the NMR results in later chapters. The magnetic susceptibility data was taken using a commercial Quantum Design SQUID magnetometer from just below T_c to 330K in fields of 5T (50,000 gauss). The appropriate corrections were made for the presence of the quartz sample tubes in the final analysis.

The initial characterisation of the second batch of Co-doped samples was limited to an XRD analysis and a.c. susceptibility measurements (see appendix B).

4.5 Pulsed NMR Spectroscopy

The first NMR experiments performed by the Bloch and Purcell teams (1946) were based on a continuous wave (cw) NMR method. In such experiments, the sample is placed in a constant $\mathbf{B_0}$ field and then continuously irradiated with a slowly varying radiofrequency, so as to scan the resonance of interest. The NMR spectrum obtained is simply a plot of the absorption of energy vs. frequency and is known as the spectrum in the 'frequency domain'. Provided the scan is performed sufficiently slowly, the absorption signal obtained at each frequency corresponds to the 'steady state', in which the tendency of the rf field to equalise the population of the Zeeman levels is balanced by the inclination of the thermal motions to restore the Boltzmann distribution. In early cw experiments, the absorption lineshape was found to be dominated by the inhomogeneities in the static field $\mathbf{B_0}$ (which cause a spread in the Larmor frequencies over the entire sample) and so the natural linewidth ($\sim 1/T_2$) was different from the observed linewidth. This problem has largely been overcome by the development of more sophisticated magnets with highly homogeneous fields.

---

8 J. W. Loram, K. A. Mirza, P. A. Freeman & J. J. Tallon, *Supercond. Sci. Technol.* **4** S184 (1990)

9 F. J. Blunt, A. M. Campbell, P. P. Edwards, J. E. Evetts, P. A. Freeman, J. Johnson, J. W. Loram, K. A. Mirza, A. Putnis, E. Salje & W. W. Schmall, *Physica C* **162-164** 1605 (1989)

10 A. Porch, J. R. Cooper, H. M. Cheah, J. S. Edmends & J. R. Waldram, *Physica B* **165-166** 1199 (1990)

11 J. R. Cooper, *Supercond. Sci. Technol.* **4** S181 (1990)

The introduction of 'pulse' NMR methods by Torrey[12] (1949) and Hahn[13] (1950), allowed transient nuclear induction signals to be observed at resonance (both during the pulse (Torrey) and after the pulse (Hahn)) and so enabled accurate measurements of relaxation phenomenon to be made directly. The particularly useful pulse method devised by Hahn provides the basis of all the NMR experiments performed in this work, and will now be described with reference to the schematic diagram of a modern pulse NMR spectrometer, shown in figure 4.2.

In any pulse experiment, the oscillating rf field is modulated into pulses by turning the rf irradiation on and off for given periods of time. In order to produce an rf pulse, a continuous rf signal from a stable frequency generator is gated on and off with a switch. The switch is simultanously linked to a variable pulse generator which produces pulses of the required length. These low power pulses are then fed through an amplifier which boosts them up to the required rf power level (typically 100-1000 watts).

The rf voltages produced are applied to the NMR probe which is effectively an LC circuit tuned to the Larmor frequency. The sample to be investigated sits in a coil (oriented in the x-y plane, at right angles to the $\mathbf{B_0}$ field) which forms the inductance of the circuit. Active (or passive) circuit components are incorporated at positions A and C in figure 4.2 to achieve matching between the amplifiers and the coil*.

The sinusoidal rf current in the transmitter coil generates a linearly polarized magnetic field (equal to $2B_1\cos\omega t$ and of the order of mT) in the x-direction, which can be resolved into two counter rotating vectors each of magnitude B_1. Within the sample, the rotating field induces a rotating magnetisation **M** in the x-y plane which is monitored by the spectrometer. At this point it is useful to introduce a coordinate transformation which is commonly used in NMR to help visualise the motion of the magnetisation under the influence of the $\mathbf{B_1}$ field. In this transformation, the laboratory Cartesian axes are designated x, y and z while a rotating frame has axes labelled x', y' and z'. The rotating frame is spinning with respect to the laboratory frame at an angular frequency of $-\omega$ about the z-axis.

In the absence of a $\mathbf{B_1}$ field, the magnetisation which precesses at ω_0 in the laboratory frame now precesses at a reduced frequency of $(\omega_0-\omega)$ in the rotating frame. This is equivalent to precessional motion in an apparent field along the z'-axis of $(\omega_0-\omega)/\gamma$ or $\mathbf{B_0}(1-\omega/\omega_0)$. The $\mathbf{B_1}$ field is now applied. Since one of its resolved component vectors will be spinning in the same sense as the Larmor precession and at the same frequency†

---

12 H. C. Torrey, *Phys. Rev.* **76** 1059 (1949)

13 E. L. Hahn, *Phys. Rev.* **80** 580 (1950)

* The output of the amplifier is terminated to 50Ω and the probe is matched to 50Ω by A and C.

† The other component can be neglected since it has little interaction with the magnetisation.

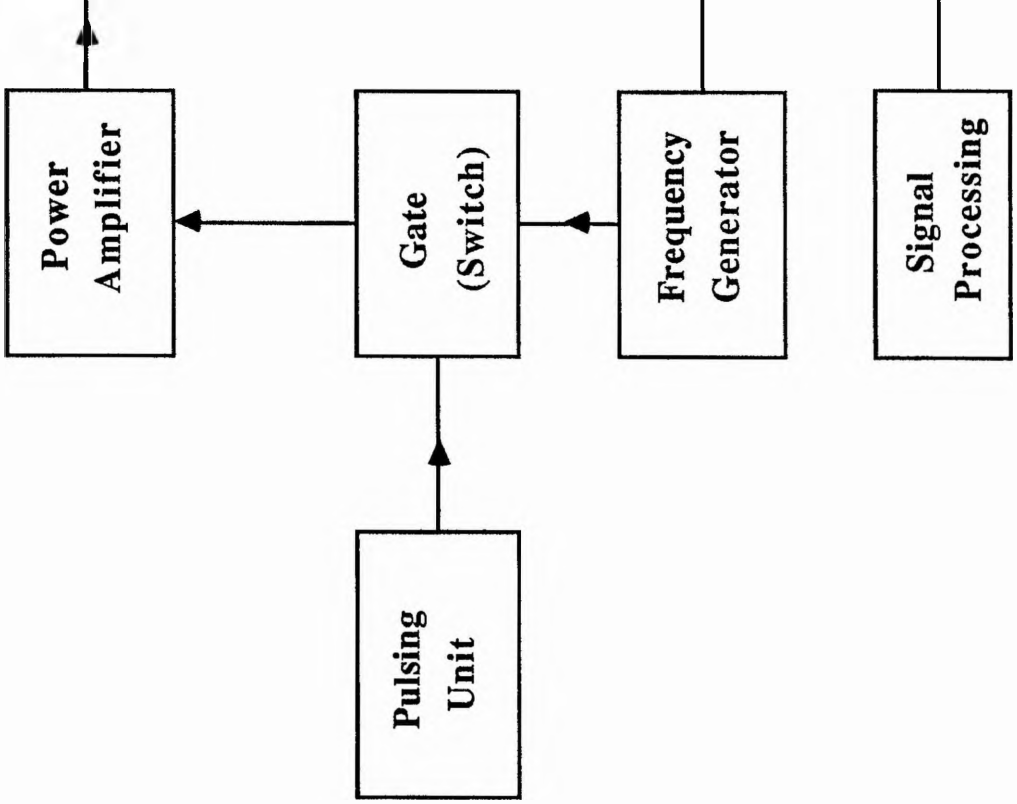

Figure 4.2

A Schematic Diagram of a Modern Pulse Spectrometer. A, B & C are described in the text.

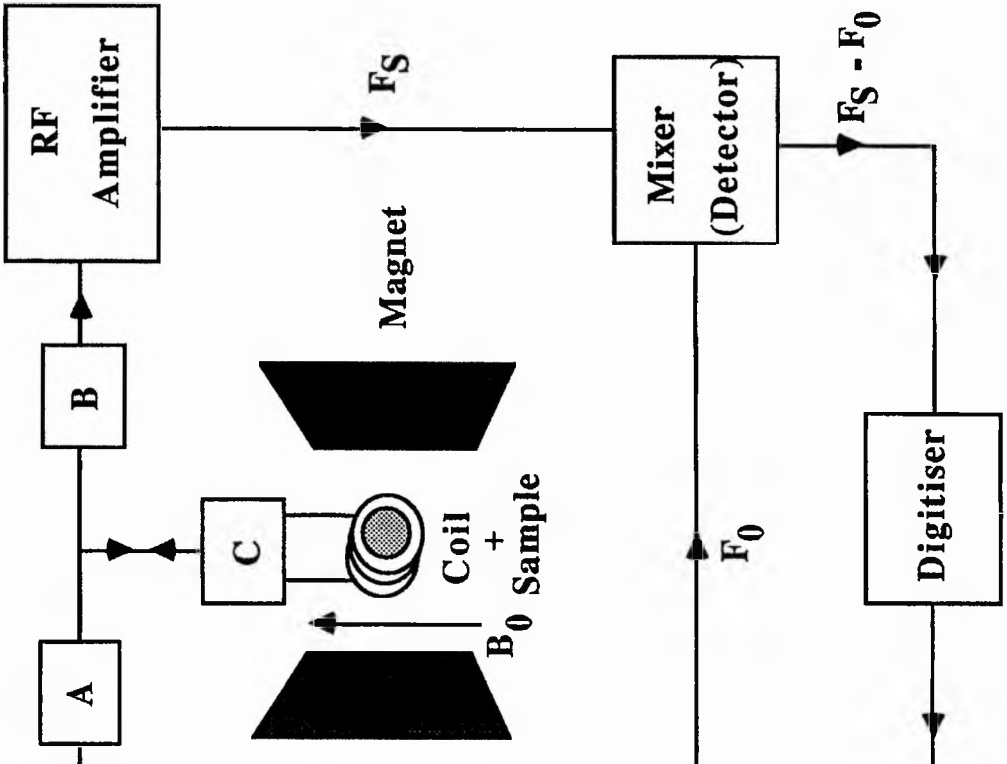
RF
Amplifier
B
A
C
Coil
+
Sample
B_0
Magnet
F_S
Mixer
(Detector)
$F_S - F_0$
F_0
Digitiser

as the rotating axes, B_1 will appear stationary in the x' direction of the rotating frame. The vector sum of $(\omega_0-\omega)/\gamma$ and B_1 allows us to define an effective field $\mathbf{B_{eff}}$ about which the magnetisation **M'** now precesses (at a frequency of $-\gamma\mathbf{B_{eff}}$) in the rotating frame (figure 4.3(a)). When the applied radiofrequency is changed so that $\omega=\omega_0$, $\mathbf{B_{eff}}$ becomes equivalent to $\mathbf{B_1}$ and points in the x'-direction. The magnetisation vector **M'** now traces out a flat disc in the y'-z' plane with a frequency of $-\gamma\mathbf{B_1}$ (figure 4.3(b)).

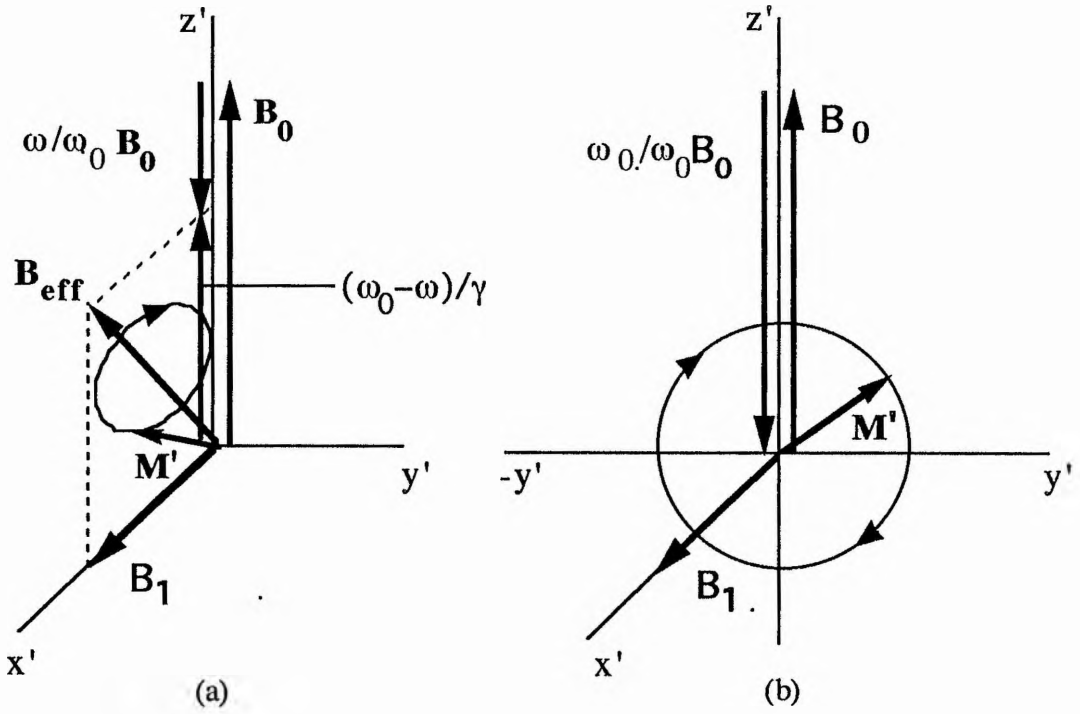

Figure 4.3

(a) $\omega<|\gamma\mathbf{B_0}|$: **M'** precesses around a $\mathbf{B_{eff}}$ field in the rotating frame.

(b) $\omega=\omega_0$ and so $\mathbf{B_{eff}}=\mathbf{B_1}$: **M'** traces out a disc in the y'-z' plane of the rotating frame. $\mathbf{B_1}$ has been exaggerated for clarity in both cases.

It can now be seen that, in the rotating frame, the application of a $\mathbf{B_1}$ field oscillating at the resonance frequency ω_0, tips the magnetisation vector **M'** away from its equilibrium direction parallel to $\mathbf{B_0}$. The angle through which **M'** rotates in the y'-z' plane is dependent on the duration and intensity of the pulse. At the end of a pulse of duration t_w, the magnetisation vector **M'** will have been tipped through an angle θ given by

$$\theta = \gamma B_1 t_w \qquad (4.4)$$

Typically, t_w is adjusted so that the angle θ is 90° ($\pi/2$) or 180° (π).

Consider a 90° pulse: assuming that the amplitude B_1 is sufficiently large and the duration of the pulse t_w is short (i.e. much less than T_2 and typically 1 to 50μS), relaxation effects during the 'on' period of the pulse will be negligible and the vector **M'** will be turned into the x'-y' plane. Immediately after the pulse the magnetisation lies stationary in the y' direction of the rotating frame. At the same instant in the laboratory frame, **M** is precessing in the plane perpendicular to the static field at the Larmor frequency. In a perfectly homogeneous $\mathbf{B_0}$ field, the behaviour of **M** is governed by the relaxation processes and so the component in the plane perpendicular to $\mathbf{B_0}$ (i.e M_y) precesses at ω_0 with an exponentially decaying amplitude. This decaying magnetisation induces a voltage (at ω_0) in a receiver coil whose axis lies in the x-y plane. A plot of signal intensity as a function of time, of course, produces a free induction decay (FID).

In practice, the field inhomogeneity of $\mathbf{B_0}$ is substantial and so effectively the decay is more rapid. Field inhomogeneity results in a spread of different Larmor frequencies over the entire volume of the sample. Each region of the sample therefore has its own component magnetisation, known as a spin isochromat, which precesses at its own characteristic Larmor frequency. Some portions of the sample experience a slightly larger field and so the resulting spin isochromat precesses faster than those stemming from a slightly lower field. Consequently, the individual spin isochromats get out phase with one another, and this is seen in the rotating frame as a dephasing of the total magnetisation. The effect of the application of a 90° pulse to a sample in an inhomongenous $\mathbf{B_0}$ field is shown in figure 4.4. The view is from the rotating frame.

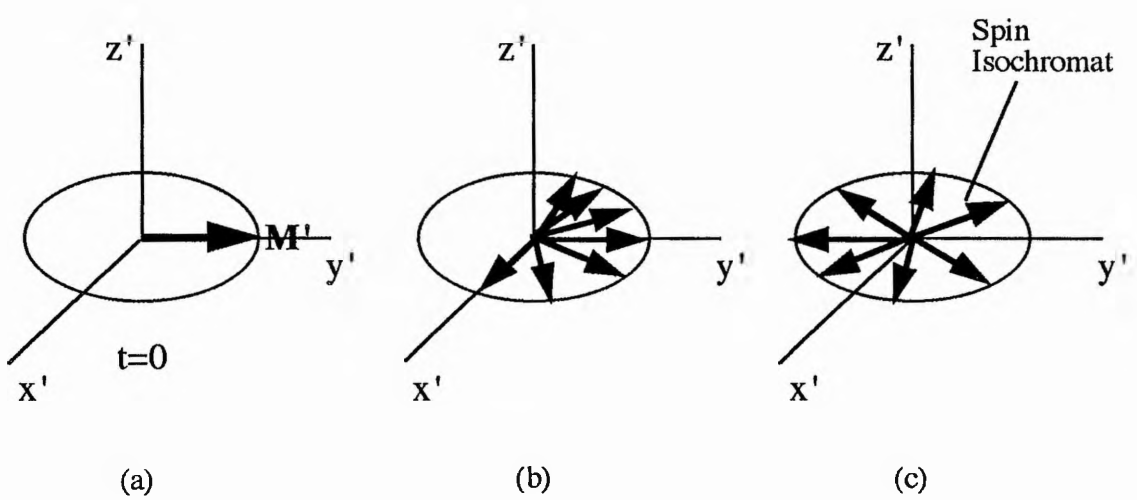

Figure 4.4

(a) The total magnetisation M' is along the y' axis immediately after a 90° pulse. (b) Shortly afterwards some of the individual spin isochromats start getting ahead and some get behind. (c) M' is completely dephased and the net magnetisation along y' is zero.

The net magnetisation along the y' axis evidently decays to zero as the spin isochromats fan out in the x'-y' plane and so the signal induced in the receiver coil also decays to zero. This decaying signal gives a free induction decay. Two mechanisms therefore contribute to the total free induction decay observed; the relaxation processes and the field inhomogeneity. The time constant which describes the characteristic decay of magnetisation in the x-y plane is labelled T_2^*, where $1/T_2^* = 1/T_2 + \gamma\Delta B_0$ such that ΔB_0 is the field inhomogeneity and T_2 is the time constant for the decay of one spin isochromat in the absence of ΔB_0.

In many modern pulse spectrometers, the receiver and transmitter coils are typically the same coil and so the electronic circuitry at C (figure 4.2) acts to prevent any interactions between the transmitter and receiver sections of the spectrometer. During the 'on' period of the pulse, the sensitive receiver is protected from the large voltage of the transmitter pulse by diodes in the circuit at C. However, the isolation is never perfect and so in practice some of the transmitter pulse leaks through into the receiver. Consequently, for a short period of time after the pulse, the initial part of the FID is corrupted by pulse leakage. In addition, it is found that the start of the FID is tainted by the decay of the rf pulse (ringdown) and by mechanical oscillations generated in the probe by the application of the pulse. The total time in which the FID is corrupted by these effects is known as the 'deadtime' of the probe. To minimize such effects, the signal is sent to the receiver only after a time period equivalent to the deadtime has elapsed. Generally, the receiver recovers within a few microseconds after the pulse.

The voltage induced in the receiver coil is of the order of a few microvolts and so after being fed through a coupling 'matchbox' at B (with same function as 'matchbox' at A), it is amplified using a tuned rf preamplifier. Once the rf signals are large enough, they are sent to a detector (or mixer) which removes the rf carrier signal, so that only the signal envelope remains. The detected signal is then amplified further and fed through a number of filters before being digitised and recorded.

The essential function of the receiver is to detect and amplify the signal without introducing further noise and distortion. In reality though additional noise is generated from each stage of the spectrometer and from external sources, hence the need for initial filter stages in the receiver section.

In a pulse NMR experiment, the irradiation frequency υ_0 (or carrier frequency) is chosen to be close to the resonant frequency of the nucleus to be examined. So far we have half assumed that the initial pulse produces a monochromatic radiofrequency sinewave. However, Fourier analysis shows that the applied rectangular pulse will contain a distribution of frequencies centred on υ_0. The conversion from the time domain to the frequency domain is performed using a mathematical operation known as a Fourier

transform (FT). Figure 4.5 shows the frequency domain (F(υ)) equivalent of a rectangular pulse of duration t_w and frequency υ_0 in the time domain (f(t)).

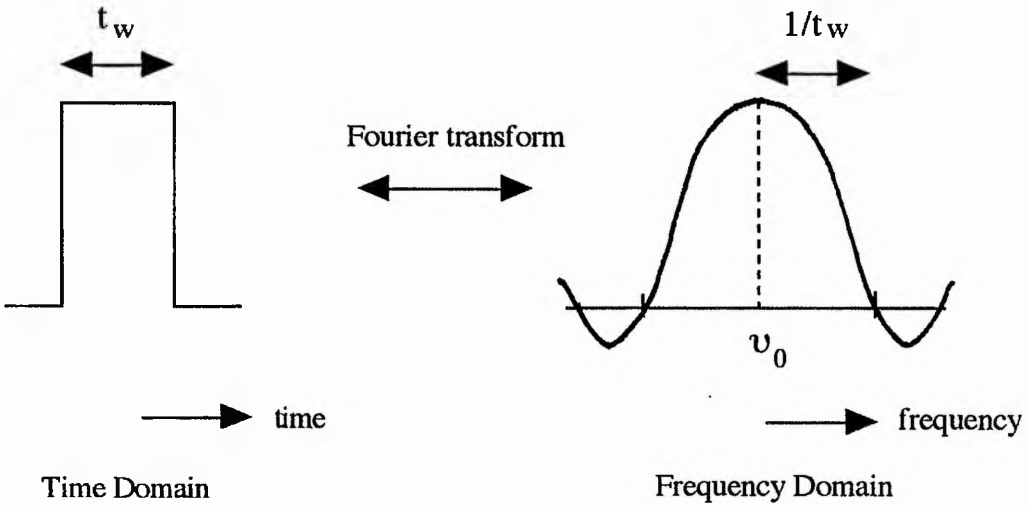

Figure 4.5

An rf pulse of duration t_w and frequency υ_0 depicted in the time and frequency domains.

It can shown that the resulting function in the frequency domain is of the form,

$$F(\upsilon) = \frac{\sin \pi(\upsilon-\upsilon_0)t_w}{\pi(\upsilon-\upsilon_0)} \qquad (4.5)$$

Evidently, when we apply the rf pulse, we are irradiating the sample with a range of different frequencies at one instant. The resulting FID (or interferogram) is therefore a superposition of sinewaves whose frequencies, amplitudes and phases correspond to the lines which make up the NMR spectrum in the frequency domain. That is to say, the Fourier transform of a free induction decay obtained in the time domain of a pulse NMR experiment corresponds to the frequency domain spectrum obtained from a cw experiment. This fact was first proved by Lowe and Norberg[14] in 1957 and was later pioneered experimentally by Clark[15] in 1964 and then by Ernst and Anderson[16] in 1966.

The advantages of using pulse NMR as opposed to cw NMR now become apparent. The same information can be obtained from a pulse experiment in only a

---

14 I. J. Lowe & R. E. Norberg, *Phys. Rev.* **107** 46 (1957)

15 W. G. Clark, *Rev. Sci. Instr.* **35** 316 (1964)

16 R. R. Ernst & W. A. Anderson, *Rev. Sci. Instr.* **37** 93 (1966)

fraction of the time taken to perform a cw experiment. In addition, the signal to noise ratio (S/N) can be vastly improved in a pulse experiment by summing the FID's from successive pulses. Here the repetition time for applying pulses must be greater than T_1 so that the magnetisation has time to recover back to its equilibrium position along $\mathbf{B_0}$. An optimum repetition time must be found in order to maximise the S/N ratio. The improvement in the S/N ratio obtained from accumulating n FID scans is the product of $\sqrt{n}$ and the S/N ratio for one spectrum.

4.6 Spin Echo Techniques

Due to the nature of the Fourier transform, broad lines in the frequency domain have short FID's in the time domain. If an FID is sufficiently short, then all the relevant information may be lost in the deadtime of the probe. In such cases, a technique known as 'spin echoes' is used.

In 1950, Hahn[13] made the remarkable discovery that if two rf pulses separated by a time τ were applied to a spin system, then a third spontaneous 'pulse' appeared at time 2τ. He called this spontaneous pulse a 'spin echo'. The phenomenon of spin echoes can readily be explained in classical terms within the rotating frame, using figures 4.6(a)-(d).

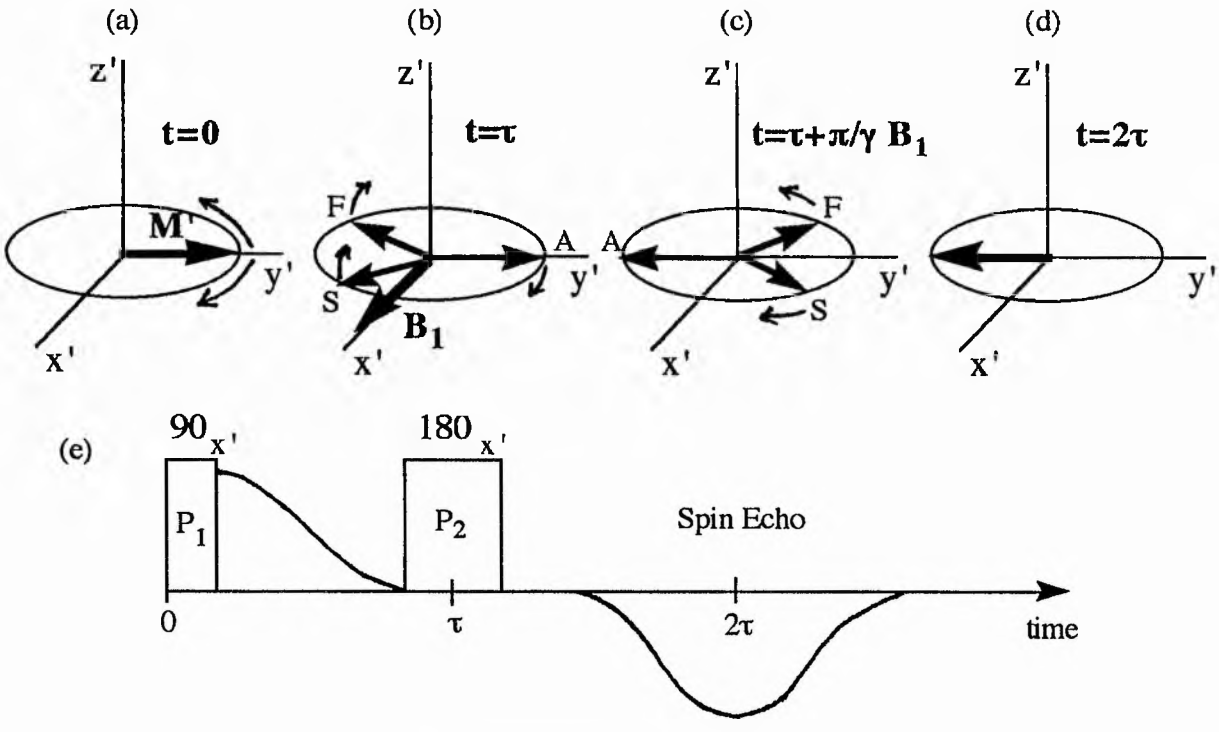

Figure 4.6

(a)-(d) The formation of a spin echo in the rotating frame (e) the 90°-τ-180° pulse sequence.

Suppose that a 90° pulse (P_1) is applied in the x' direction, at time t=0, to a sample sitting in an inhomogeneous $\mathbf{B_0}$ field. Immediately after the pulse the magnetisation lies in the y' direction (figure 4.6(a)). Shortly afterwards the spin isochromats will have dephased in the x'-y' plane, with some isochromats precessing faster (F) and some slower (S) than the average spin isochromat (A). The signal therefore decays. At a time τ ($<T_2$) a second 180° pulse (P_2) is applied along the x' axis (figure 4.6(b)). This has the effect of rotating any spin isochromats left in the x'-y' plane† through an angle of 180° about x' (figure 4.6(c)). As a result all the spin isochromats that were ahead of the average are now behind it by the same amount. Similarly, the spin isochromats which were behind the average are now ahead by an equivalent angle. Each spin isochromat continues to move in the same direction as before and so now the spin isochromats begin to pick up the phase differences at the same rate as they had lost them before the 180° pulse was applied. Hence, after a time 2τ, the net magnetisation will be refocussed along the -y' axis, and will produce an inverted spin echo signal (figure 4.6(d)). Effectively, the spin echo, which consists of two FID's back-to-back, is only produced for an instant, since at $t>2\tau$ the spin isochromats begin to fan out again.

Although a $90°_{x'}$-τ-$180°_{x'}$ pulse sequence was used here as an example, other combinations of 90° and 180° pulses can be applied in any ±x' or ±y' direction so as to produce a net magnetisation along chosen ±x' or ±y' axes. Evidently, the spin echo technique described above is an ingenious way of removing the effects of $\mathbf{B_0}$ field inhomogeneity. However, if the field inhomogeneity is sufficiently large, its effects may still obscure the natural T_2 in a relaxation experiment. To this end, multipulse sequences such as the famous 'Carr-Purcell[17] (CP) spin echo train' can be used. In a conventional two pulse spin echo experiment, a sequence of measurements are made, each at different τ. A plot of the echo amplitude vs 2τ produces T_2. However, CP found that by first applying a 90° pulse along x' and then applying n successive 180° pulses at 3τ, 5τ, 7τ etc. also along the x' direction, they could aquire the whole spin echo sequence in one shot. The relaxation measurements are easily deduced since the amplitude of the successive spin echoes, which form at 2τ, 4τ, 6τ, 8τ etc., decays exponentially with T_2. Meiboom-Gill[18] later modified the CP technique by adding a phase alteration to allow for the fact that the pulse rotations may deviate slightly from 180°. After a large number of pulses in the CP train, the phase errors accummulate leading to short T_2's. The entire

---

† Note that any magnetisation along the z' direction would be inverted to the -z' direction and would not effect the magnetisation in the x'-y' plane.

17 H. Y. Carr & E. M. Purcell, *Phys. Rev.* **94** 630 (1954)

18 S. Meiboom & D. Gill, *Rev. Sci. Instr.* **29** 688 (1958)

modified sequence is now known as the 'Carr-Purcell-Meiboom-Gill' or 'CPMG' pulse sequence.

Since relaxation times are not measured in this work, only simple pulse sequences, such as 90°-τ-90° and 90°-τ-180°, are necessary. In the rotating frame, a $90°_{x'}$-τ-$90°_{x'}$ pulse sequence produces the famous 'eight-ball echo' pattern, detailed by Hahn in his original 1950 paper[13]. At a time interval of τ after the second 90° pulse, the different isochromatic moments lie in a figure of eight curve superimposed on a sphere and produce a resultant along the y' axis. This resultant gives rise to an echo signal at t=2τ, which has the same sign as the FID (i.e it is not inverted).

The following sections detail the two NMR pulse spectrometers used and the experimental procedures applied in order to obtain NMR data on the YBCO system.

4.7 The Low Temperature 141MHz Spectrometer

4.7.1 Spectrometer Design

The configuration of this home-built spectrometer is the same as that represented in figure 4.2, with a coil system based on the single coil series resonant circuit of Clark and McNeil[19] (1973). A block diagram of the spectrometer and its commercial specifications can be found in figure D.1 of appendix D. It should be noted that two pulse amplifiers are incorporated in series and that the voltage supply to the final tube stage of the driving amplifier (AR) is cut off during the 'receive' time by a blanking pulse† fed from the pulse generator. To prevent rf leakage, many of the coaxial cables which link the main units of the spectrometer are screened.

The master frequency of the spectrometer is constantly tuned to 141MHz, so that field swept experiments can be performed. Since this spectrometer is only used to study spin echo signals of copper nuclei (γ=11.285 (bare nucleus) or 11.311 (metal)), a magnetic field of at least 12.35T is required.

The cryomagnet system consists of an Oxford Instruments three coil 12.7T superconducting magnet housed in a standard liquid helium/liquid nitrogen cryostat. The helium chamber of the cryostat is connected to a closed helium recovery system which feeds helium boil off gas (6l/hr) into a return line. When the cryogen vessels are partially full, cryopumping in the vacuum chambers helps to provide an effective vacuum which insulates the He and N jackets further. The field homogeneity of the 12.7T magnet is

---

19 W. G. Clark & J. A. McNeil, *Rev. Sci. Instr.* **44** 844 (1973)

† Note that the blanking pulse is long enough, so that the spin echo signal has long gone before the blanking pulse appears.

quoted as 1 in 10^5, which is adequate for the spin echo experiments performed here. In order to obtain values of magnetic field during each experiment, a copper magneto-resistance probe (magprobe) was used. This consists of a non-inductively wound coil of fine Cu wire, which is placed at centre field and linked to an external simple measuring circuit (see appendix D, figure D.2). Since the voltage across the coil (measured for a constant input current of 51.04 mA) varies with field, it provides a sensitive probe of the magnetic field. Periodically, throughout the experiment, the voltage readings are calibrated against a Cu metal (γ=11.311) reference sample (see section 4.7.2), thus providing a suitable field vs. magprobe voltage calibration curve with which to evaluate the corresponding field values of other voltage readings. The resulting errors incurred using this method of calibration range from 0.001T to 0.01T. During the experiments on ^{63}Cu in the YBCO system, the field calibration was such that 1μV$\approx$3 Gauss.

4.7.2 Low Temperature Probe & Sample Rotation Mechanism

Figure 4.7 shows a schematic diagram of the home-made low temperature sample probe used in conjunction with the 141MHz spectrometer. The probe consists of two separate components: the sample probe and the probe sleeve. Effectively, the delicate sample probe is housed within the probe sleeve, and the top plates of the two are vacuum sealed together (using bolts and strategically placed O-rings) to provide a self-contained sample chamber which is capable of holding liquid helium.

The sample probe is essentially a long stainless steel tube with a Teflon (PTFE) sample holder at one end and a steel top plate at the other. The top plate incorporates (i) a gas exit port, which links the probe to a helium return line via a valve and a vacuum pump (ii) a stoppered helium inlet port, which enables the probe to be filled with liquid helium via a transfer tube (iii) a sealed port containing a DIN pin socket, used to connect a helium level probe (situated close to the sample) to a volt meter outside the probe and (iv) an O-ring sealed exit port through which the specimen channel cables are linked to the rest of the spectrometer. Inserted down the middle of the stainless steel support tube is a half steel-half 'bakelite' gear rod†, which is fastened to a Teflon cog system at the lower (bakelite) end. The upper (steel) end of the gear rod and the outer sheath of the support tube protrude a few inches above the top plate, so that the gear rod can be freely rotated from outside of the sealed probe. The cog mechanism consists of two wheels. One wheel, fixed in the horizontal plane, is rotated by the gear rod. This in turn rotates a second orthogonal wheel which is attached (via a stycast post) to an aligned epoxy sample. Both wheels have an equal number of teeth so that the rotation at the top and

† used because it is non-copper containing, non-magnetic and has useful thermal properties.

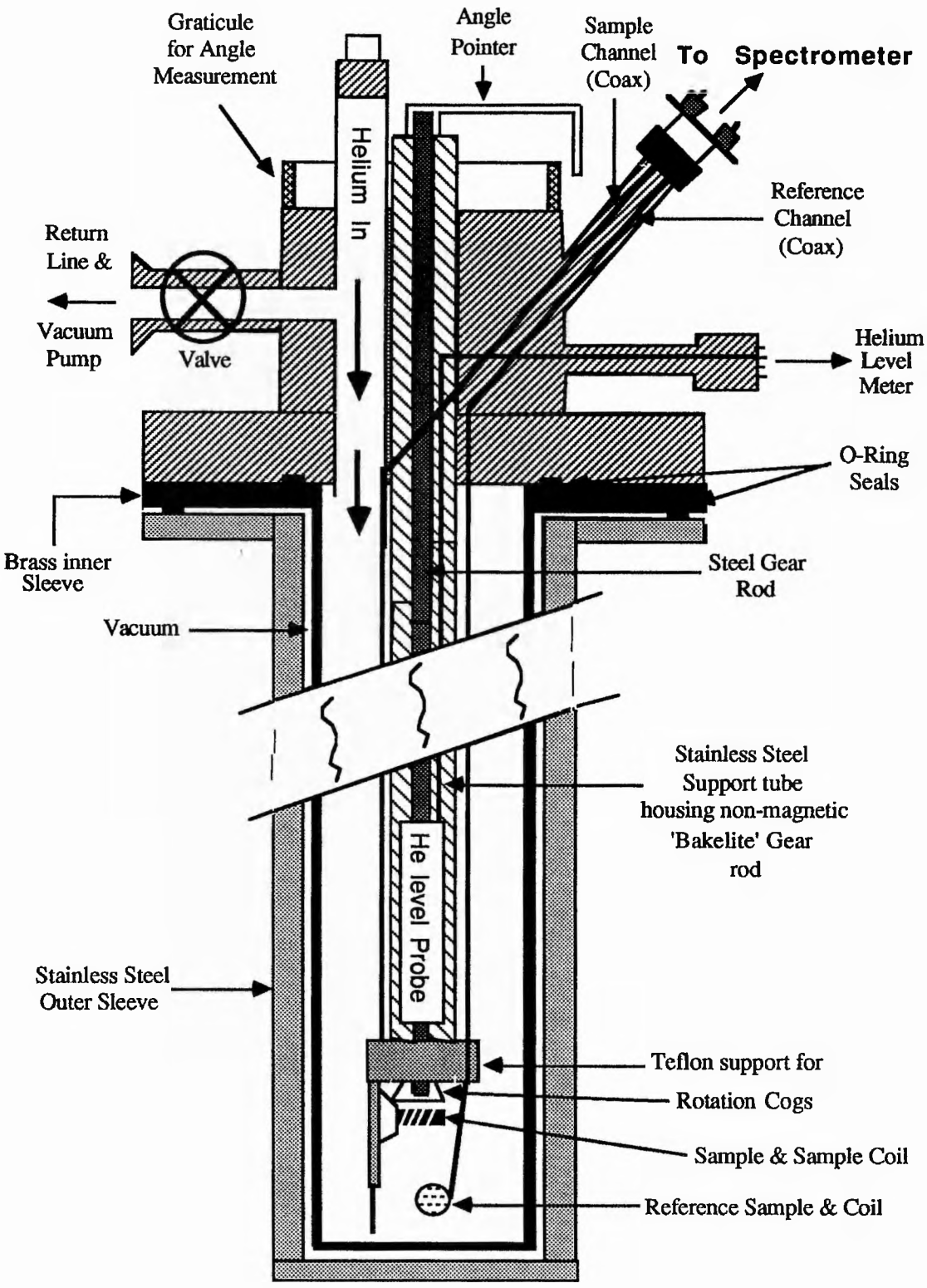

Figure 4.7

A schematic diagram of the low temperature probe used with the 141MHz spectrometer.

bottom of the gear rod is linear. A fine pointer and angle graticule fastened to the top end of the rod provide accurate angle measurement.

The aligned YBCO sample sits in a coil, made from four turns of annealed (99.99% pure) 1mm diameter silver wire. The coil is oriented in the x-y plane, orthogonal to the $\mathbf{B_0}$-field, as required by theory. Either end of the sample coil is soldered to the inner and outer sheaths of a coaxial cable. To enable the area around the sample to be copper free, a silver coaxial cable has been specially designed for this probe (see figure D.3 in appendix D for the construction details). The silver coax extends a distance of approximately 15 cm from the sample coil and is then replaced by a Farnell semi rigid 3.58mm diameter copper coax (50Ω matched and with a capacitance of 96 pFm^{-1}), which is strapped along the length of the support tube until it protrudes out of the required exit port. A 50Ω BNC socket connects the copper coax to the sample matchbox and the rest of the spectrometer (figure D.1). This coil and coax system constitutes the sample channel.

The field calibration, described earlier, requires that there be a reference sample situated near to the YBCO sample. To this end, a reference channel similar to the sample channel is incorporated on the probe. The channel consists of a reference coil, of three turns of silver wire, oriented orthogonally to both the sample coil and $\mathbf{B_0}$-field, but still in the x-y plane. The coil is attached directly to a Farnell copper coax, which extends to the exit port as before. A reference matchbox, separate from the sample matchbox, is used to couple the reference channel to the spectrometer. Due to the difference in coil positions in the applied field, a field correction of 6 Gauss must be added to the sample channel field values.

The reference sample itself is an epoxy set mixture of a number solids containing useful nuclei, such as ^{31}P (T_2~50μs), ^{71}Ga (T_2~100μs), ^{65}Cu (T_2~40μs) and most importantly ^{63}Cu (T_2~40μs). The samples in both channels are covered in Teflon tape, so that the particulary large fluorine signals obtained from the PTFE could be used to tune the spectrometer. Similarly large signals from the protons in the stycast were also used to tune the matchbox, tuner and preamplifier sections of the spectrometer to 141MHz.

Finally, the probe sleeve consists of an inner brass sleeve and an outer stainless steel sleeve bolted together across an O-ring. Extra connecting tubes and a valve straddle the two sleeves enabling the space between them to be evacuated to a pressure of approximately 10^{-5} Torr (at room temperature). Once the complete probe is inserted into the helium chamber of the magnet cryostat, the vacuum between the inner walls improves sufficiently well (by cryopumping) so as to allow the liquid helium in the probe cavity to pump down to 4.5 Torr. This corresponds to a temperature of 1.505K. A concluding note should be made here: the Farnell coax cable was chosen in particular for its comparatively low Cu heat conductivity. A number of other commercial cables which were experimented with, were found to input too much heat into the probe from the

spectrometer and surroundings. As a result, the helium filled probe cavity could not be pumped down to the required pressure and the set temperature of 1.5K could not be achieved.

4.7.3 Experimental Procedure

For both the pure and Co-doped YBCO samples, central transition* ($m_I=\pm 1/2$) ^{63}Cu(1)/(2) NMR spectra were obtained at 1.5K by scanning the magnetic field (at a fixed frequency) and measuring the spin echo amplitude. A 90°-τ-90° pulse sequence with a pulse width of 7μs and a separation time of 70μs was found to produce a sizeable spin echo with the same sign as the FID. Between 16 and 128 successive echo signals were acquired and averaged (depending on sample and spectrometer setup) in order to improve the signal to noise. In many cases, a S/N ratio of 10:1 was obtained. In this system, the repetition time for applying consecutive pulse sequences is dependent upon the T_1 of the Cu site under investigation. Recent NQR relaxation measurements[20] on the near 0_7 material at helium temperatures suggest that the spin-lattice relaxation time for the Cu(1) site is sample dependent and that overall $T_1(^{63}Cu(1))$ is shorter than $T_1(^{63}Cu(2))$ (i.e. 5 ms for Cu(1) compared to 3 secs for Cu(2), for one particular sample). A suitable repetition rate for Cu(2) in all the samples investigated was 0.391Hz (or 1 pulse every 2.56 secs). The optimum repetition rate for Cu(1) turned out to be sample dependent and varied from 0.781Hz (1 pulse every 1.28 secs) to 3.125Hz (1 pulse every 0.32 secs).

It should be noted that studies by Walstedt et al[21] also indicate that the Cu(2) spin lattice relaxation rate is highly anisotropic in the temperature range $100K \leq T \leq 300K$ and that T_1^{-1} is approximately 3.5 times greater when the quantisation axis is in the a-b plane as opposed to along the c axis. In this investigation, there was no evident to suggest that at 1.5K a faster repetition time enhanced the θ=90° Cu(2) signal (either in the Co-doped or pure YBCO samples) and so, in the interest of consistency, the same repetition rate was used to obtain all Cu(2) signals.

For each oriented Co-doped sample, a ^{63}Cu(1)/(2) spectrum was collected at θ=0° (c//B) and at θ=90° (c⊥B), where θ is the angle between the c-axis alignment and the

---

* Note that at 141MHz the central transition line of ^{65}Cu and the low field satellites of ^{63}Cu and ^{65}Cu are expected to be at much lower field positions (see D. P. Tunstall & M. E. Solanki-Moser, *Mod. Phys. Lett. B* **2** 723 (1988)) and are therefore separated from the central ^{63}Cu line.

20 See R. E. Walstedt & W. W. Warren, Jr. in *Mechanisms of High Temperature Superconductivity*, ed. H. Kamimura & A. Oshiyama, p137, Vol 11, Springer-Verlag, Berlin (1989).

21 R. E. Walstedt, W. W. Warren, Jr., R. F. Bell, G. F. Brennert, G. P. Espinosa, R. J. Cava, L. F. Schneemeyer & J. V. Waszczak, *Phys. Rev. B* **38** 9299 (1988)

applied field. In the resulting spectra, the difference between the observed field position of the relevant peak and the calculated field position of the 'bare' copper nucleus determines the Knight shift. Additional spectra were obtained for the Aberdeen sample in which the marked c-axis was oriented at various angles between -70° and +75°, either side of the applied field direction. In order to identify and define the c-axis orientation of this sample, a rotation pattern was constructed by plotting the field positions of the Cu(2) peaks against the corresponding angle. A 'best fit' MINITAB statistical regression analysis (see appendix C.2 for the procedure and computer program) of the rotation pattern produced numerical values for the υ_Q, $K_{//}$, $K_\perp$ and η fit parameters and also allowed the angle of c-axis misalignment to be estimated. In this instance, the angular form used for the fitting procedure was the known second order quadrupole plus anisotropic Knight shift pattern[22] (described in chapter 3).

The experimental resonance fields obtained from the complete Aberdeen θ=0° and θ=90° spectra were subsequently corrected for demagnetisation effects. Thereafter, the Knight shift tensor was numerically determined using the exact Hamiltonian for the Zeeman and quadrupole energy (see appendix C.4).

4.8 The Bruker MSL-500 Variable Temperature Spectrometer*

4.8.1 Spectrometer Design

The Bruker MSL-500 spectrometer† is a commercially built machine, capable of performing pulse NMR spectroscopy over a continuous frequency range of 17 to 215 MHz (low frequency transmitter) and at a proton frequency of 500MHz (proton frequency transmitter). A constant magnetic field of 11.74T is supplied by an Oxford Instruments 89mm diameter bore superconducting cryomagnet, housed in an elevated liquid helium-liquid nitrogen cryostat. Since field inhomogeneity is not a complication with the broad NMR lines observed in this work, the room temperature shim coils in the magnet bore were constantly maintained at the setting used for high resolution liquid work.

The overall operation of the spectrometer is controlled by an Aspect 3000 computer, running standard Bruker DISMSL software. The DISMSL program allows

---

22 G. C. Carter, L. H. Bennett & D. J. Kahan, *Metallic Shifts in NMR*, part 1, Progress in Materials Science 20 (1977)

* A comprehensive manual is produced for every section of the Bruker spectrometer. These documents should be consulted for further details of the spectrometer, magnet and software.

† Hereafter, referred to as the 'MSL spectrometer'.

data acquisition and data manipulation to be performed simultaneously in three independent channels (or windows). An onboard system process controller (SPC) manages the transmitters and receivers and can be programmed (using a highly structured Bruker specific programming language) to perform any form of complex pulse routine.

The setup of the spectrometer hardware is much the same as that depicted in figure 4.2. Continuous frequencies generated by a frequency synthesizer (1Hz resolution) are gated, via an rf interface, by the pulses produced by the SPC. At this point the pulses, which have amplitudes of the order of hundreds of millivolts, are fed through a low power (~100W) broadband amplifier and then through a high power (~1000W maximum) transmitter with variable output power. Finally the pulses are fed, via a simple tuning circuit, into an rf coil surrounding the sample. The sample, coil and tuning circuits are all housed in an NMR probe which is inserted into the bore of the magnet from the underside.

Subsequently, the voltage induced in the coil is amplified by a 50dB preamplifier. The preamplifier can be tuned to the required frequency by inserting plug-in units which also act as rf filters. Each plug-in unit covers a certain frequency range in the interval 17 - 215 MHz. The signal is then passed to a broadband receiver, whose gain and phase are controlled by the SPC. For our purposes, the receiver uses 'quadrature phase sensitive detection' (quad PSD), an explanation of which is given in a later section on pulse programs (section 4.8.3). Once detected, the resultant audio signals are further amplified, and then passed through low pass filters, which cut out 'white noise' signals produced by the detection system. The data is acquired (and signal averaged) by the computer in the time domain and the resulting FID is then digitised, into a format suitable for storage, by a multiplexed analogue to digital converter. The digitisation is performed by sampling the FID at discrete points which are separated by a fixed time interval, known as the dwell time (DW). The reciprocal of the dwell time, 1/DW, is called the sampling rate (or sampling frequency). If the sampling frequency is greater than 125kHz, the computer automatically selects a 9 bit digitiser for the conversion, but if it is less than this value a 12-bit digitiser is chosen. A small range, high resolution 16-bit digitiser is also available, but this is much slower and its use must be programmed into the computer. The digitised signals are stored in data memory blocks, ready for manipulation at a later time.

4.8.2 Variable Temperature NMR Probes

Since individual Bruker multi-nuclear solenoid probeheads are built to tune in a given frequency range*, two different solenoid probeheads are required to study ^{89}Y (γ=2.087, υ_0=24.506MHz) and ^{63}Cu (γ(bare)=11.285, υ_0(bare)=132.486MHz). The

* within the low frequency interval that the spectrometer covers

probeheads are based on a similar design, with each having a solenoid coil (set in epoxy for electrical insulation) and a simple tuning circuit fixed around a PTFE former†. The size of the coil on the ^{63}Cu probe is such that a 5mm diameter by 40mm long epoxy set YBCO sample is required. A 10mm diameter by 25mm long epoxy sample is accommodated by the ^{89}Y probehead coil.

Once attached to a low temperature probe stem, the sample probehead is covered by double-walled glass dewar. Machined slots at the opposite end of the stem allow a heater coil to be inserted into the body of the probe. A glass coupling system enables the probe to be connected to an insulated, double-walled stainless steel flexitube, which is linked to a heater network at the far end. Once inserted into a dewar of liquid nitrogen, the heater network produces nitrogen gas of approximately the required temperature and feeds it through the flexitube, into the probe and over the sample. This direct nitrogen evaporation system is managed by a Bruker Variable Temperature Controller, which samples the feedback voltages from two copper-constantan thermocouples, one placed in the probe near to the sample and the other positioned in the nitrogen dewar. The controller simultaneously judges the heat input required by the nitrogen evaporation heater and the probe heater, and balances these inputs until the set temperature is achieved and maintained. The base temperature obtained using this system is 160K. An error of ±0.5 degrees in the required temperature range of 160K to 300K is quoted by Bruker. In this work, the probes were not used at temperatures above 300K. Even when the probe heater was not required for temperature control (i.e. at room temperature), it was still inserted into the probe, to enable the external conditions to be duplicated throughout all experiments.

With the spectrometer and probe setup described above, only rather long deadtimes of between 30 and 50μs could be achieved. This could not be improved upon and remains a feature of the spectrometer hardware.

4.8.3 Pulse Programs

Before describing the specific pulse programs employed in this project, it is appropriate to define some of the terms and experimental methods used in modern pulse FT spectroscopy.

As shown in section 4.5, the application of an rf pulse at a frequency of υ_0 irradiates the sample with a range of frequencies centred on the carrier frequency, υ_0. The envelope of the power distribution in the frequency domain corresponds to a (sin x)/x (or

† Note that since the coil in the Bruker-supplied copper frequency range probehead was made from copper, a replica probehead had to be made which contained a silver coil.

sinc) function and the separation of the discrete frequency components is inversely proportional to the pulse repetition rate or aquisition time (AQ). The irradiation frequency bandwidth itself is proportional to $1/t_w$ (see figure 4.5). The pulse width t_w must therefore be sufficiently small so that the irradiation bandwidth is large compared to the spectral width (SW) chosen. If this criterion is met then the frequency bandwidth will be sufficient to irradiate the whole frequency spectrum of the nucleus under investigation, and the power distribution will be constant across the range of interest. In high resolution work, spectral widths are typically $\leq 10^4$ Hz, and so pulse widths of around 200μs are required to observe the NMR line.

During this investigation, resulting FID's have been detected by 'Quadrature Phase Sensitive Detection' (quad PSD). The use of quad PSD can be explained by first looking at single PSD. In the rotating frame, the components of the magnetisation in the plane perpendicular to the applied field are often labelled u and v, where u is the 'in-phase' component in the direction of B_1 (say along x') and v is the 'out-of-phase' component, which in our example, would be along y'. A single phase sensitive detector fed with the carrier frequency measures only one component of the magnetisation at any one time - i.e it determines the magnitude of the frequency difference between the sample signal and the carrier frequency. It is therefore unable to establish the sense of the rotation of the magnetisation - i.e. whether the sample signal is precessing slower or faster than the carrier frequency. When using a single PSD, to avoid a single spectral line being detected at two different frequencies symmetrically located about υ_0 (i.e. the positive frequencies being reflected or 'folded' onto the negative frequencies), the transmitter frequency must be deliberately set at one extreme end of the spectral region. This method of detection has a distinct disadvantage: although the signals are gathered from a bandwidth of Δf on one side of the transmitter frequency, the noise components are still accepted over the whole bandwidth spanning $\pm\Delta f$ with respect to the transmitter frequency, and so the noise power of the spectrum is immediately doubled.

When using a quad PSD system, the sample signal is fed to two identical PSD's whose reference signals are phase shifted by 90°. With this setup, both the in-phase and out-of-phase components can be measured simultaneously and so the quad PSD can distinguish signal frequencies which are higher and lower than the irradiation frequency. This has the advantage that the transmitter frequency can be set to the centre of the spectral region, and thus a pulse of given width can encompass twice the spectrum width. The signal to noise is subsequently improved by a factor of $2^{1/2}$ over that obtained using a single PSD.

With quadrature phase sensitive detection, two measurements are taken every time the FID is sampled and the signal is represented as a complex number, $S_1 + iS_2$. The real and imaginary parts are stored in separate data memory blocks and then quadrature

Fourier transformation converts them into real and imaginary frequency spectra. According to Nyquist's sampling theorem, the digitising (or sampling) frequency (F=1/DW) is directly related to the measured frequency range (spectral width, SW) via the equation, F=2SW. Thus, if a signal is sampled at a frequency F, the highest measured frequency will be F/2. Applied to the digitisation of the FID, Nyquist's theorem means that the sampling rate should be high enough to give at least two data points per cycle of the highest frequency component.

Many modern pulse programs include an extensive 'phase cycling' sequence[23], which improves the performance of quadrature detection schemes by eliminating any mismatch between the two PSD's. Essentially, phase cycling involves repeatedly changing the phase of the rf pulses applied to the system. A simple phase cycle may consist of four stages in which the applied pulses are consecutively phase shifted by 0° (+X), 90° (Y), 180° (-X) and 270° (-Y). The receiver reference phase is changed correspondingly and the appropriate addition or subtraction of the signals along +X, +Y, -X or -Y proves particularly useful at reducing baseline artifacts and ringdown effects.

In this work, ^{89}Y NMR data (on both the pure and Co-doped YBCO samples) was obtained using a standard Bruker program called QUADCYCL. This single-pulse program applies a 90°-τ-(acquire) pulse sequence to the sample in conjunction with an 8-step phase cycle. The ^{63}Cu NMR data was gathered using a standard Hahn two pulse spin echo sequence of the form 90°-τ-180°-τ'-(acquire). In order to reduce baseline distortions, due to the ringing of the probe, a 16-step phase cycling sequence, devised by Kunwar et al[24], was employed. The listings of both pulse programs can be found in appendix C.3.

4.8.4 Data Aquisition & Manipulation

Successive ^{89}Y FID signals were acquired and averaged (at a spectrometer frequency (SF) of 24.506 MHz) after a typical pulse sequence consisting of a 90° pulse of 20μs (D1) and a ringdown delay of 50μs (D3). The recycle delay after each scan (D0) was typically 20s and the acquisition time (AQ) was of the order of few milliseconds. After approximately 3000 FID scans had been collected and averaged in the time domain, the first few points of the digitised FID (which had been corrupted due to the probe deadtime, etc.) were excluded and the rest of the FID was Fourier transformed to produce a frequency domain spectrum. No attempt was made to smooth the FID by line-broadening techniques prior to FT. First and second order phase corrections were then

---

[23] R. Freeman, *A Handbook of Nuclear Magnetic Resonance*, Longman (1988)

[24] A. C. Kunwar, G. L. Turner & E. Oldfield, *Jnl. Mag. Res.* **69** 124 (1986)

carried out on the frequency domain spectrum, in a rather subjective manner, by eye. During the phase correction procedure an attempt was made to mix the two signals obtained from the quad PSD, in order to produce a 'pure' absorption spectrum. Baseline corrections were subsequently applied, via the computer, where necessary.

All ^{89}Y frequency spectra were referenced to the frequency line produced by a 1M aqueous solution of YCl_3 at room temperature.

Frequency spectra were obtained for each pure and Co-doped YBCO sample at various temperatures in the range 160-300K-with the crystallographic c-axis first oriented c//B and then c⊥B. In addition, room temperature spectra were collected for the pure YBCO sample at various orientations of the c-axis with respect to the applied field.

In order to produce a ^{63}Cu spin-echo, a Hahn pulse sequence consisting of a 90° pulse of width 5μs (D1) followed by a tau delay (D6) of 40μs, then a 180° pulse of width 10μs (D2) followed by a deadtime delay (D3) of 38μs, was applied to the sample, at a given frequency. The timings of the spectrometer were set so that only the second half of the echo, from the maximum amplitude onwards, was displayed on the monitor. The visible portion of the echo in the time domain was then Fourier transformed to produce the corresponding frequency domain signal. Phase and baseline corrections were applied, as required, and the signal intensity at zero ppm was noted. In addition, the signal was integrated and the area recorded. A ^{63}Cu frequency spectrum was constructed for each sample by performing a point by point frequency sweep through the spectral region of interest and acquiring a spin echo signal at each frequency. The spectrometer frequency was incremented by either 10kHz or 100kHz depending on the region of interest and the preamplifier was retuned at each new frequency. A plot of signal intensity (or area) vs spectrometer frequency produced the required frequency spectrum.

This procedure was repeated (at room temperature) for all samples at both the c//B and c⊥B orientations.

Chapter 5

Results of the Pure Y-Ba-Cu-O System

This chapter brings together the SEM analysis of the undoped, powdered JM21 $YBa_2Cu_3O_{7-\delta}$ specimen, with the SEM and X-ray characterisation of the powder and aligned Aberdeen sample. The low temperature ^{63}Cu NMR investigation of the uniaxially oriented Aberdeen $YBa_2Cu_3O_{7-\delta}$ powder is also detailed in the latter part of this chapter.

5.1 Scanning Electron Microscope Analysis

Some of the objectives of the present study are to examine the morphology of YBCO powder and to develop satisfactory preparatory procedures for the powder, prior to magnetic alignment. The primary aims of the preparatory techniques used in this work are (i) to obtain an homogenous powder sample, which is made up of relatively small ($\leq 10\mu m$) crystallites, platelets or single crystals, (ii) to avoid unnecessary clumping of the crystallites, both prior to, and during, magnetic alignment. It seems logical to assume that a powder sample which is made up of minute, free-moving (that is, unrestricted) crystallites will tend to align more completely and uniformly when dispersed in an epoxy resin and subjected to a strong magnetic field, than would an inhomogeneous, close-packed (i.e. clumped or clustered) powder, under the same conditions. This is possibly because small particles rotate in the epoxy with less resistance under the torque applied by the magnetic field during the cure.

Plates 1 to 8 show a selection of micrographs, which were taken on the powdered and aligned Aberdeen and JM21 samples, at various stages during the investigation. Two different scanning electron microscopes were used to collect the images, namely the JEOL JCX A733 (low resolution, 15kV acceleration voltage) and the JEOL JSM 35CF (high resolution, 10kV acceleration voltage). Since some of the results of the SEM analysis have already been detailed in the methodology of chapter 4, each plate will be discussed only briefly, in order (see overpage):

PLATE 1

Sample: JM21 powder
Microscope used: JEOL JCX A733
Magnification: +1500
Sample Coating: 20nm layer of carbon

This secondary electron image (SEI) micrograph was taken on a small amount of the JM21 sample which had been hand ground in air for a short period of time. It shows a large variation of crystal size ranging from fragments of crystals (<1μm) to what appear to be large clusters of crystallites, approximately 100-200μm across the major axis. Such a sample would be difficult to align, since the crystallites are not free to orient themselves parallel to the magnetic field. Instead, what would probably happen is that the net magnetisation of each particular cluster would align parallel to field, leaving the individual crystallites, which have come together in a random fashion to make up cluster, only partially oriented.

PLATE 2

Sample: JM21 powder
Microscope used: JEOL JSM 35CF
Magnification: +2,000
Sample Coating: 10nm layer of gold

This plate was acquired at a fairly low magnification so that a general, overall view of the powder could be obtained. The dehydrated JM21 powder sample shown in this micrograph had been thoroughly crushed in an argon atmosphere for a period of about one hour, prior to examination. Although there are many crystal fragments (≤1μm), the majority of the sample seems to be made up of single crystals, varying in size from approximately 5μm to 10μm. A scan across the entire specimen window indicated that only about 5% of the sample consisted of 'clustered' crystallites. The size of these clusters ranged from 20 to 50μm across the major axis and so were considerably smaller than those seen in the previous micrograph. There is now clear evidence that with this method of preparation, the sample contains a large proportion of single crystals. It is thus anticipated that a substantial percentage of crystallites in this specimen will fully align under the influence of a magnetic field.

Plates 3, 4, 5 and 6 which follow were acquired at the same time as plate 2 and are different views (at higher magnifications) of the same sample.

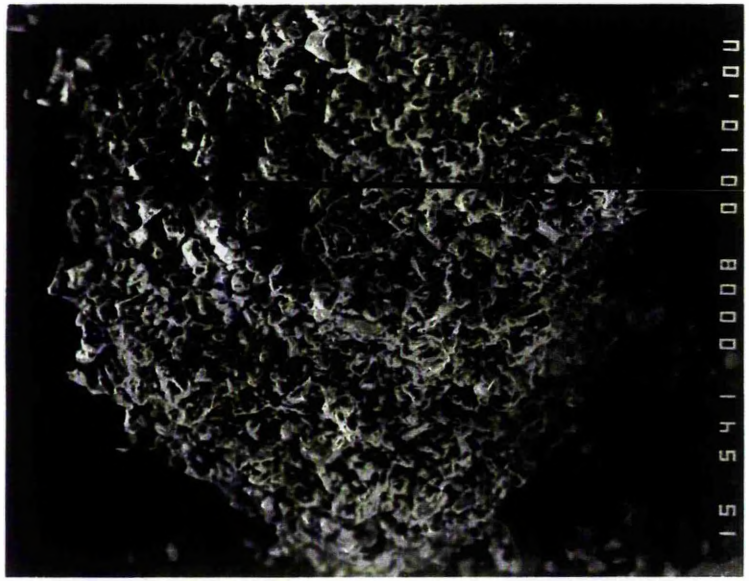

Plate 1

Plate 2

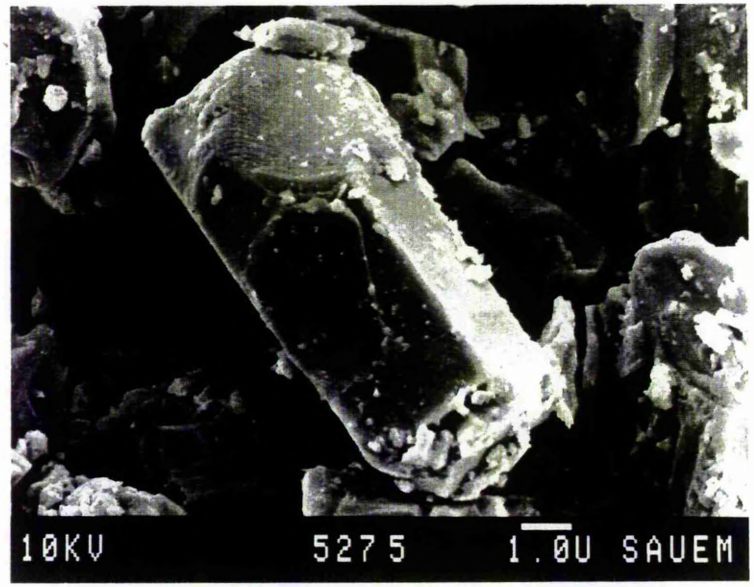

Plate 3

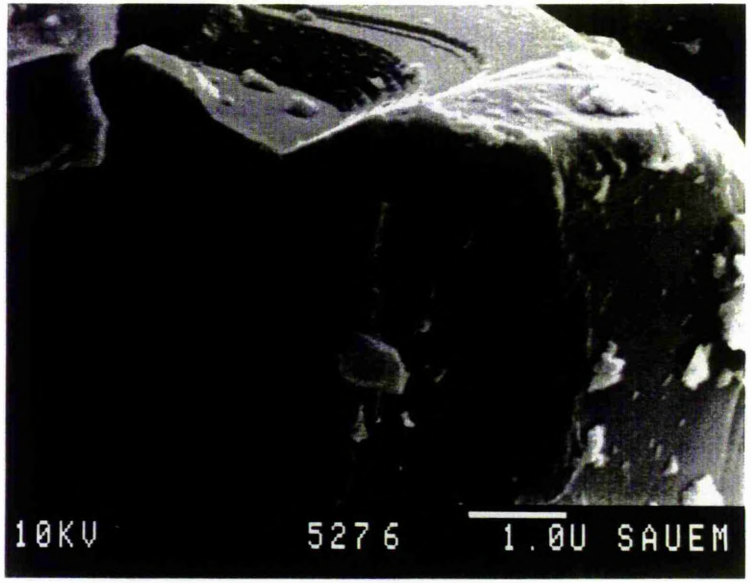

Plate 4

PLATE 3
Sample: JM21 powder
Microscope used: JEOL JSM 35CF
Magnification: +7,800
Sample Coating: 10nm layer of gold

The single crystal image presented in plate 3 is typical of those found throughout the crushed JM21 sample. The dimensions of this particular crystal (2.5μm x 2.85μm x 7.9μm) are in a similar ratio (a:b:c=1.00:1.14:3.16) to the dimensions of the $YBCO_7$ unit cell, indicating that this crystal is indeed an orthorhombic single crystal. Note that although there are many fragments adhering to the crystal, the smooth faces of the crystal are clearly visible.

PLATE 4
Sample: JM21 powder
Microscope used: JEOL JSM 35CF
Magnification: +15,000
Sample Coating: 10nm layer of gold

This micrograph presents an image of a highly magnified single orthorhombic crystal which has had the corner 'chipped' off. Crystal planes, which in this case are separated by approximately 0.2μm or 2000Å, are clearly visible at the top left hand corner of the crystal.

PLATE 5
Sample: JM21 powder
Microscope used: JEOL JSM 35CF
Magnification: +13,000
Sample Coating: 10nm layer of gold

The crystal displayed in plate 5 is interesting because it has very definite, smooth faces and appears to show some dislocation or secondary growth from the parent crystal. Planar defects, such as twinning along the [110] plane and stacking faults on the [001] plane, are common in the YBCO structure[1], but are generally only observed in high

1 Details of such defects can be found in R. Beyers & T. M. Shaw, 'The Structure of $Y_1Ba_2Cu_3O_{7-\delta}$ and its Derivatives' in *Solid State Physics*, Vol. 42 : eds. H. Ehrenreich & D. Turnbull, Academic Press (1989).

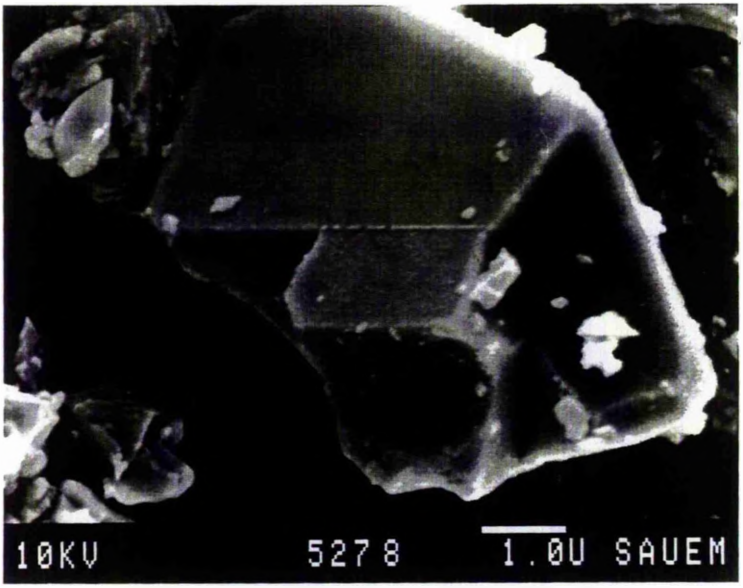

Plate 5

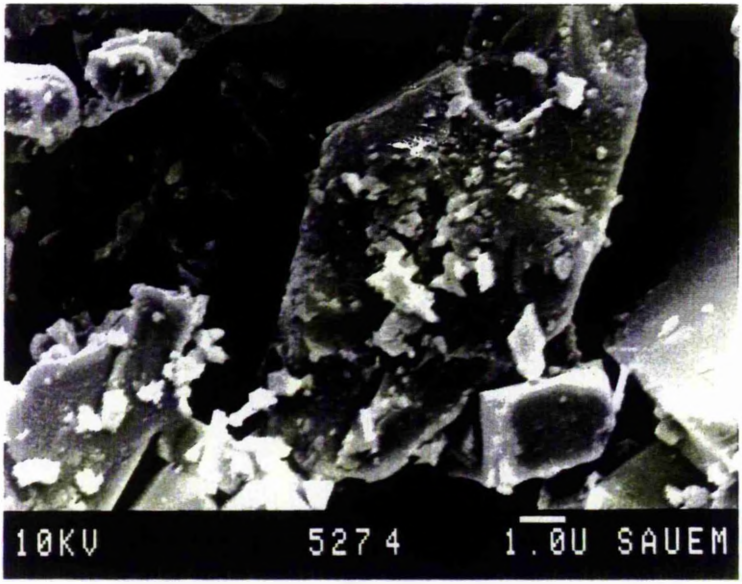

Plate 6

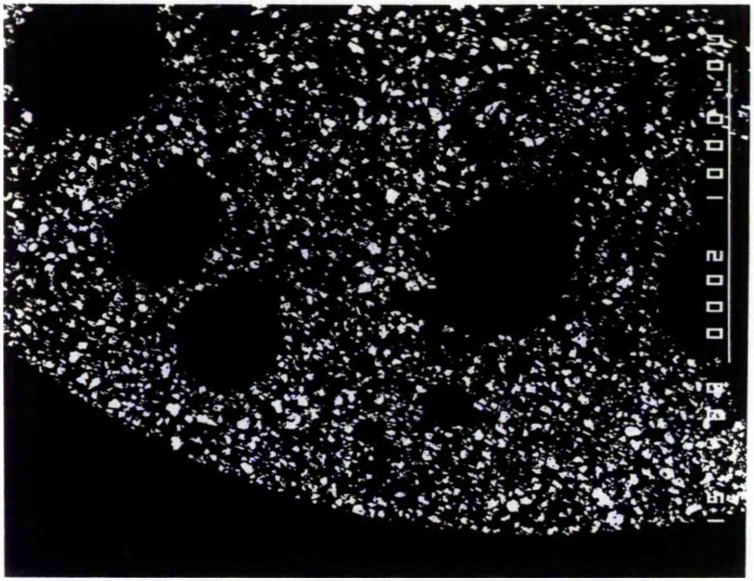

Plate 7

c ←

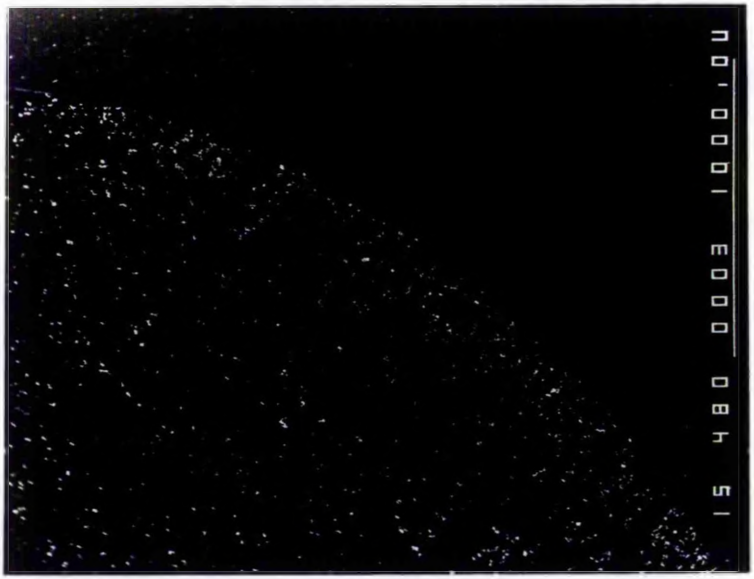

Plate 8

resolution, high magnification microstructural studies[2], where the field of view is of the order of nanometers.

PLATE 6

Sample: JM21 powder
Microscope used: JEOL JSM 35CF
Magnification: +7,800
Sample Coating: 10nm layer of gold

The crystal in the centre of the frame in plate 2 has been magnified considerably in this plate. The image is that of a parent crystal with a secondary crystal growth along a common boundary.

PLATE 7

Sample: Aberdeen powder aligned in Stycast epoxy resin
Microscope used: JEOL JCX A733
Magnification: +480
Sample Coating: 20nm layer of carbon

Plate 7 shows a compositional backscatter image of the aligned, epoxy-set Aberdeen sample. To provide a convenient reference axis, the sample disc was oriented so that the marked c-axis lay parallel to the vertical axis of the viewing screen. This oriented sample was produced by thoroughly mixing the crystallites into the stycast by hand, and then allowing the composite to cure in a 9T magnetic field for about 15 hours (T=295K). Note that no method of dispersion was employed, apart from physical agitation with a stirrer.

Even though the grains seemed fairly evenly distributed throughout the epoxy resin, it was noted that there was a slight tendency for the crystallites to be concentrated towards the edges of the disc. Over the small section of the sample presented in plate 7, the density of crystallites appears to be reasonably uniform, with an epoxy to powder ratio of about 3:1 (instead of the 5:1 ratio originally calculated). Parts of the disc are also peppered with air bubbles (visible as large black circular anomalies in the micrograph) which vary in diameter from 100μm to 900μm. No crystallites appear in the immediate vicinity of the air bubbles, adding to the non-uniform distribution of the powder in some regions of the disc.

At magnifications approaching x1500 (not shown) it was possible to see the orientation of the crystallites. Surprisingly, the single crystals appeared to be oriented at

---

2 For example, see J. Y. Henry, P. Burlet, A. Bourret, G. Roult, P. Bacher, M. J. G. M. Jurgens & J. Rossat-Mignod, *Solid State Comm.* **64** 1037 (1987)

about 30 to 40 degrees to the vertical, while the majority of crystallite clusters (which now occupied close to 30% of the sample and appeared particularly in the highly concentrated outer regions of the disc) took on, what seemed like, random orientations.

PLATE 8
Sample: JM21 powder aligned in Stycast epoxy resin
Microscope used: JEOL JCX A733
Magnification: +480
Sample Coating: 20nm layer of carbon

The JM21 sample presented in this secondary electron image was uniaxially aligned using the same methods as those described for the Aberdeen sample in plate 7. The crystallites, which appear to be smaller (5-10μm) in this sample than in the Aberdeen sample, are highly concentrated around the edges of the disc, with the centre of the disc being populated by only a few crystal grains. It is estimated that approximately 75% of the crystallites are congregated around the outskirts of the disc. The slightly lower packing fraction of 0.1 used in the alignment is evident from this micrograph, but such a packing fraction makes little difference to the crystallite alignment - which (when viewed at higher magnifications) still appears to be out by 30 to 40 degrees to the vertical. Note that an overall scan of the disc showed no evidence of the air bubbles, which were so prevalent in the Aberdeen sample. The relatively few crystallites clusters which appear in this sample are less than 25μm across the major axis.

5.2 X-ray Analysis of Powder & Aligned Samples

Since the JM21 sample was eliminated from further investigation, due to the anomalously weak ^{63}Cu NMR signal obtained from the aligned specimen at low temperatures, the rest of this chapter will concentrate on the X-ray and NMR results acquired from the Aberdeen sample, alone.

Before being set in epoxy, the Aberdeen sample was analysed using standard X-ray powder diffractometry. The resulting XRPD spectrum, which could be indexed according to the orthorhombic space group expected for pure $YBa_2Cu_3O_{7-\delta}$ ($\delta \leq 0.65$), is presented in figure 5.1(a). The splitting of the [013] and [110/103] peaks (see inset) and the [213] and [116/123] peaks are particularly indicative of the orthorhombic structure. As anticipated from an earlier analysis performed by the Aberdeen group[3], the spectrum shows no evidence of impurity phases and the sample is single phase.

---

3 J. T. S. Irvine & A. R. West, *private communication.*

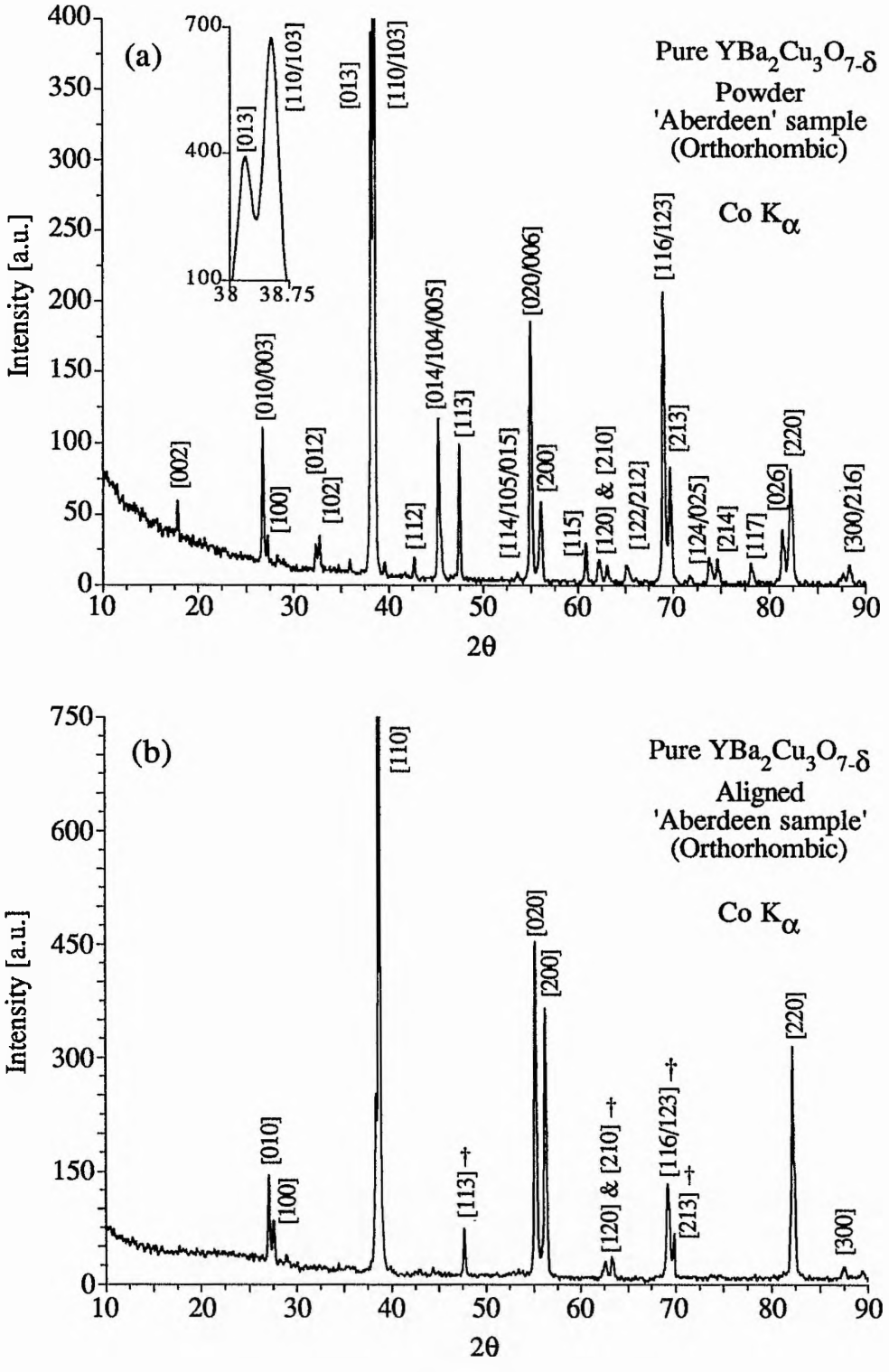

Figure 5.1

X-ray Spectra of the (a) free powder and (b) aligned (with the c-axis in the plane perpendicular to the incident X-rays) pure YBCO Aberdeen sample. The inset in (a) shows the characteristic splitting of the [013] and [110/103] peaks. Note that (i) the [110] peaks have been truncated to half of their full intensity and (ii) the peaks indicative of unaligned powder are labelled with †.

At room temperature, the lattice parameters deduced from the [hkl] reflections of the X-ray (free) powder spectrum are,

$$a=3.817 \pm 0.002 \text{ Å}$$

$$b=3.881 \pm 0.002 \text{ Å}$$

and $$c=11.671 \pm 0.006 \text{ Å}$$

which produce a unit cell volume of

$$V=172.892 \text{ Å}^3$$

and a degree of orthorhombicity of

$$\frac{(b-a)}{a} = 1.677 \times 10^{-2}.$$

The Aberdeen sample was oxygenated during growth under the conditions required for full oxygen uptake. As no independent analysis (such as thermogravimetric analysis (TGA)) was performed on the sample, we must to rely on the lattice constants derived from the XRPD results to determine the actual oxygen concentration.

An extensive review of the YBCO crystal structure has been made by Hazen[4] (1990). In particular, the review includes tables of refined lattice parameters obtained, via various techniques, on undoped samples of YBCO with a wide range of oxygen concentrations. Our results compare favourably with those deduced from a room temperature neutron powder diffraction (NPD) study[5] performed on a fully oxygenated $YBa_2Cu_3O_7$ sample. The refined lattice parameters interpreted from this investigation are a=3.8172Å, b=3.8822Å and c=11.6707Å, which lead to a cell volume of 172.9496Å^3 and a degree of orthorhombicity of 1.703×10^{-2}. Similar room temperature results can also be found in other studies made on the O_7 material[6,7]. Since slight variations in oxygen content lead to considerable changes in the lattice parameters[5] (particularly the c-lattice constant (see appendix A.2)) and a substantial decrease in the orthorhombicity, we can say with some certainty that the Aberdeen sample has lattice constants which are appropriate to an oxygen concentration of 7 atoms per unit formula. This diagnosis is further supported by the parallel study conducted on this sample by the Aberdeen group[3].

---

4 R. M. Hazen in *Properties of High Temperature Superconductors*, Vol. II, ed. D. M. Ginsberg, World Scientific, Singapore (1990)

5 D. E. Cox, A. R. Moodenbaugh, J. J. Hurst & R. H. Jones, *J. Phys. Chem. Solids* **49** 47 (1988)

6 F. Beech, S. Miraglia, A. Santoro & R. S. Roth, *Phys. Rev. B* **35** 8778 (1987)

7 G. Calestini & C. Rizzoli, *Nature* **328** 606 (1987)

After the setting procedure, the alignment of the c-axes was checked with the same X-ray diffractometry technique employed by Farrell et al[8]. Sample slices were cut from the aligned cylindrical specimen in such a way that the c-axis was in the plane of the slice. X-ray scattering from this plane was then monitored. The alignment information distilled from the resulting XRPD pattern (figure 5.1(b)) is presented in table 5.1.

Sample	No. of l=0 Peaks	Average Peak Enhancement	Stray l≠0 peaks	Net Stray Peak Height	Degree of alignment
Aberdeen	7	3.00	[113]	4	82%
			[120]	1	
			[210]	2	
			[116/123]	8	
			[213]	3	

Table 5.1

Summary of the information obtained from the X-ray spectrum of the epoxy set uniaxially aligned Aberdeen sample. The net stray peak height is measured as a percentage of the [110] peak height.

The estimated degree of c-axis alignment which appears in the last column of the table is based on the average enhancement of the l=0 peaks (weighted slightly towards the dominant [110], [020] and [200] reflections) and the number and intensity of the much diminished stray peaks. The X-ray characterisation of the epoxy sample is consistent with just over 80% of the crystallites oriented c//B and so the alignment of Aberdeen sample looks considerably better than anticipated from the SEM analysis. A preliminary glance at the results of both the X-ray and SEM analyses suggests that a substantial portion of the crystallites may be well be aligned c//B, but that the c-axis marking on the sample may be wrongly placed. Such a scenario would not be detected by the X-ray methods used here, since all orientations of the c-axis within the plane of the disc are equivalent (see figure 4.1), as evidenced by theory and experiment. The c-axis alignment in the Aberdeen sample is further examined during the low temperature NMR experiments, discussed next.

---

[8] D. E. Farrell, B. S. Chandrasekhar, M. R. DeGuire, M. M. Fang, V. G. Kogan, J. R. Clem & D. K. Finnemore, *Phys. Rev. B* **36** 4025 (1987)

5.3 Low Temperature ^{63}Cu NMR

5.3.1 Introduction

Both isotopes of copper have a nuclear spin of 3/2 (with an abundance ratio of N_{63}:N_{65}=69%:31%) and each has a large, but slightly different, quadrupole moment Q (^{63}Q=−0.15 and ^{65}Q=−0.16 e x $10^{-24}cm^2$, giving $^{65}Q/^{63}Q$=1.081)[9] and gyromagnetic ratio γ ($^{63}\gamma/2\pi$=11.285 and $^{65}\gamma/2\pi$=12.089 MHz/T).

Crystal structure studies[10] have shown that the crystalline a, b and c axes of YBCO are the principal axes of both the electric field gradient and the Knight shift. The EFG at the Cu(2) site has been found to be axially symmetric (η~0) about the c-axis[11], while at the Cu(1) site the EFG is highly asymmetric (η~1)[12,13]. These circumstances may arise because the EFG tensors have two major contributions, a dominant one (~65MHz) from the open Cu d-shell and a partially cancelling contribution from the surrounding lattice. The site symmetry is orthorhombic for both the Cu(1) and Cu(2) sites and above T_c, the Knight shift tensor is found to be axially symmetric for both sites.

In the near O_7 (δ=0) material, the two inequivalent Cu sites give rise to two ^{63}Cu NQR lines at 22.05 MHz (Cu(1)) and 31.5 MHz (Cu(2)) and to two ^{65}Cu NQR lines at frequencies of 20.5 MHz (Cu(1)) and 29.0 MHz (Cu(2))[14,15]. The assignment of the two ^{63}Cu NQR lines to their respective crystallographic sites was the subject of much debate early on in the proceedings, but strong evidence, provided by independent experiments[11,12,13,16,17], has helped to clarify the site assignment to that given above. The two ^{63}Cu-^{65}Cu doublets have been observed at the same frequency positions in both

---

9 As determined by the Cu^{2+} ESR experiments of B. Bleaney, K. D. Bowers & M. H. L. Pryce, *Proc. Royal Soc.* **A228** 147 (1955). Note that the theoretical calculations of Sternheimer produce a Q ratio of -0.211, see R. M. Sternheimer, *Phys. Rev* **164** 10 (1967).

10 J. E. Greedan, A. H. O'Reilly & C. V. Stager, *Phys. Rev. B* **35** 8770 (1987)

11 R. E Walstedt, W. W. Warren Jnr., R. Tycko, R. F. Bell, G. F. Brennert, R. J. Cava, L. Schneemeyer & J. Waszczak, *Phys. Rev. B* **38** 9303 (1988)

12 C. H. Pennington, D. J. Durand, D. B. Zax, C. P. Slichter, J. P. Rice & D. M. Ginsberg, *Phys. Rev. B* **37** 7944 (1988)

13 T. Shimizu, H. Yasuoka, T. Imai, T. Tsuda, T. Takabatake, Y. Nakazawa & M. Ishikawa, *J. Phys. Soc. Jpn.* **57** 2494 (1988)

14 H. Lutgemeier & M. W. Pieper, *Solid State Comm.* **64** 2647 (1987)

15 M. Mali, D. Brinkmann, L. Pauli, J. Roos & H. Zimmermann, *Phys. Lett. A* **124** 112 (1987)

16 P. C. Hammel, M. Takigawa, R. H. Heffner & Z. Fisk, *Phys. Rev. B* **38** 2832 (1988)

17 Y. Kohori, H. Shibai, Y. Oda, T. Kohara, Y. Kitaoka & K. Asayama, *J. Phys. Soc. Jpn.* **57** 744 (1988)

the superconducting state (T=1.3K[18] and 4.2K[19]) and in the normal state (T=300K)[20], suggesting that the EFG within the penetration depth agrees with the value in the bulk.

In the antiferromagnetic material (δ=1), only the Cu(1) sites contribute to the NQR spectrum, producing lines at ~28MHz (^{65}Cu(1)) and ~30MHz (^{63}Cu(1))[21,22]. Note that the υ_{NQR} of 30MHz for ^{63}Cu(1) is shifted greatly from the value of 22.05MHz observed for the same ^{63}Cu(1) site in the O_7 material. Due to the similarity of the quadrupole couplings experienced by Cu(2) in the O_7 material and Cu(1) in the O_6 material, the site assignment of the NQR lines for intermediate oxygen concentrations ($0<\delta<1$) is fairly difficult. The Cu(2) sites in the O_6 compound carry a magnetic moment and so lead to an antiferromagnetic zero-field NMR spectrum (AF or ZFNMR) at 90MHz (corresponding to a strong hyperfine field of 7.665T for the Zeeman splitting residing on the Cu(2) sites)[23]. The AFNMR spectrum, which has six lines (three ^{63}Cu and three ^{65}Cu), has an electric quadrupole splitting (22.87MHz) which proves that the hyperfine field is perpendicular to the symmetry axis of the EFG[24].

Some of the ^{63}Cu NQR/NMR parameters of $YBa_2Cu_3O_{7-\delta}$ which will be used during the course of this investiagation are summarised in table 5.2, overpage.

The natural characteristics of the Cu nucleus make it an attractive nucleus for study using NMR and NQR. If we add to this the essential facts that CuO_2 planes are a common feature of all the HiT_c superconductors discovered so far and that in nearly all theories of HiT_c, the Cu atoms play an integral role, we can see the importance of studying the Cu nucleus via microscopic techniques.

In the remainder of this section, the low temperature (T=1.5K) ^{63}Cu NMR results obtained at high fields of 13T on the uniaxially aligned Aberdeen sample will be presented. As well reporting some features of the magnetic alignment process, the work will also make a contribution to the study of low temperature Knight shifts and demagnetisation corrections.

---

18 H. Yasuoka, T. Shimizu, T. Imai, S. Sasaki, Y. Ueda & K. Kosuge, *Hyperfine Int.* **49** 167 (1989)

19 H. Lutgemeier, *Physica C* **153-155** 95 (1988)

20 A. J. Vega, W. E. Farneth, E. M. McCarron & R. K. Bordia, *Phys. Rev B* **39** 2322 (1989)

21 P. Butaud, M. Horvatic, Y. Berthier, P. Segransan, C. Berthier, P. Lejay & J. Y. Henry, *Physica C* **153-155** 741 (1988)

22 J. M. Tranquanda, D. E. Cox, W. Kunnmann, H. Moudden, G. Shirane, M. Suenaga, P. Zolliker, D. Vakuin, S. K. Sinha, M. S. Alvarez, A. J. Jacobson & D. C. Johnson, *Phys. Rev Lett* **60** 156 (1988)

23 H. Yasuoka, T. Shimizu & Y. Ueda & K. Kosuge, *J. Phys. Soc. Jpn.* **57** 2659 (1988)

24 Y. Yamada, K. Ishida, Y. Kitaoka, K. Asayama, H. Takagi, H. Iwabuchi & S. Uchida, *J. Phys. Soc. Jpn.* **57** 2663 (1988)

Site ↓	Oxygen Content → / Temperature [K] →	6.00 / 1.3	6.00 / 300	6.91 / 1.3	7.00 / 300
^{63}Cu(1)	υ_{NQR} [MHz]	30.11(2)	29.9	22.00	22.05
	η	0	0	0.95	1
	B_{hf} [T]*	<0.01	<0.02	<0.02	<0.02
^{63}Cu(2)	υ_{NQR} [MHz]	22.87(5)†		31.54	31.5
	η	0		0.01	0
	B_{hf} [T]*	7.665(5)†		<0.01	<0.02
Ref.		18,23	20	18,23	20

Table 5.2

^{63}Cu NQR/NMR parameters of $YBa_2Cu_3O_{7-\delta}$ in the normal & superconducting states, where υ_{NQR} is the NQR frequency, η is the asymmetry parameter and B_{hf} is the internal hyperfine field. * = estimated from the NQR linewidth & † = calculated from the AFNMR spectrum.

5.3.2 Orientation Dependence of the Cu(2) Peak

In order to define and identify the true c-axis orientation of the epoxy set Aberdeen sample, a ^{63}Cu(2) rotation pattern was constructed. Field-swept ^{63}Cu NMR spin echo spectra were acquired (at υ_L=141MHz and T=1.5K) for a number of orientations θ (where $-70° \leq \theta \leq +75°$)† of the marked c-axis with respect to the applied B-field. At most orientations, the Cu(2) and Cu(1) peaks were not resolved, but since the Cu(2) peak was the bigger resonance whenever they were resolved, we can surmise that the peak corresponding to the overall echo intensity maximum was that of Cu(2). The resulting Cu(2) peak field values, obtained from each spectrum, were plotted as a function of θ. Comparison with a theoretical curve, calculated using the measured parameters of Takigawa et al[25,26] (i.e. υ_{NQR}=31.5MHz, $K_{//}$=1.15%, $K_{\perp}$=0.19% and η=0 acquired on a similar $YBCO_7$ sample), immediately confirmed that the c-axis orientation of the Aberdeen sample was misaligned by approximately +30° to the vertical – as suspected from the SEM analysis.

By subtracting 30° from the experimental θ values, one obtains an approximate set of values for the true c-axis orientation, θ' (where $-100° \leq \theta' \leq +45°$) which, along with

† The positive angle is defined in the clockwise direction.

25 M. Takigawa, P. C. Hammel, R. H. Heffner & Z. Fisk, *Phys. Rev B* **39** 7371 (1989)

26 M. Takigawa, P. C. Hammel, R. H. Heffner, Z. Fisk, J. L. Smith & R. B. Schwarz, *Phys. Rev B* **39** 300 (1989)

the peak field coordinates, can be refined using a MINITAB 'best fit' regression analysis (detailed in appendix C.2). The angular form used in the MINITAB fitting procedure was the known second-order quadrupole plus anisotropic Knight shift pattern described in section 3.6 of chapter 3. Note that during the analysis, no attempt was made to take account of the diamagnetic correction factors.

The best fit to the experimental data was obtained with $\theta'=\theta'+1°$, indicating that the overall misorientation of the c-axis in the Aberdeen sample is +29°. The orientation-corrected rotation pattern is shown in figure 5.2, along with the theoretical prediction.

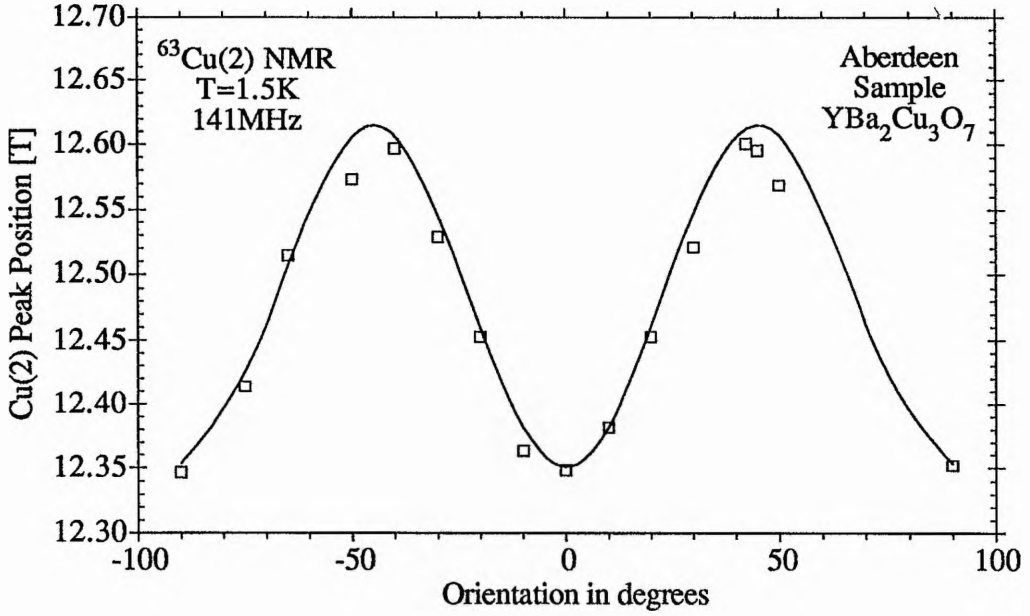

Figure 5.2

Cu(2) rotation pattern for the uniaxially aligned Aberdeen sample, taken at a temperature of 1.5K & a frequency of 141MHz. The open squares represent the orientation-corrected experimental data and the full line is a theoretical prediction using the measured parameters of Takigawa et al[25,26] (see text).

Our ability to fit the experimental rotation pattern with best-fit parameters of

$$\upsilon_{NQR}=31.5 \text{ MHz}$$
$$K_{//}=1.24\%$$
$$K_{\perp}= 0.32\%$$

and

$$\eta=0$$

which are appropriate to the axially symmetric Cu(2) site, completely vindicates our assumption that the maximum echo intensity corresponds to the Cu(2) peak for all orientations. The fit is rather satisfactory, especially when account is taken of the diamagnetism; if this had been allowed for, the main effect would be that the experimental

values close to 0° would be moved down by ~0.01T (100Gauss). Note the coincidence at this frequency (141MHz) whereby at 0° the large Knight shift leads to a resonance at about 12.35T and at 90° the large quadrupole shift leads to peak position at approximately the same field. Note also that, at this frequency, the unshifted 'bare', zero quadrupole interaction, ^{63}Cu nuclear resonance is around 12.5T. (12.4945T). Due to the function of the curve shown in figure 5.2 (see equation (3.56)), the maximum peak field always occurs at $\mu^2=\cos^2\theta=5/9$, i.e at orientation angle of $\theta=\pm 41.81°$.

The identification of the true orientation of the c-axis in this aligned sample is a prerequisite for the more complete evaluation of the Knight shift tensors, which will be presented in the next section.

5.3.3 Parallel & Perpendicular Orientations

Figures 5.3 (a) and (b) show the low temperature ^{63}Cu spin echo spectra of the Aberdeen sample, now correctly oriented with the applied field parallel and perpendicular to the crystallographic c-axis, respectively. Once again the spectra were collected at a temperature of 1.5K and at a spectrometer frequency of 141MHz.

In the case of the parallel orientation, two peaks are observed in the ^{63}Cu spectrum. We find from calculation that the low field/high intensity peak results from Cu(2) and the slightly higher field peak derives from Cu(1). The c⊥B spectrum, on the other hand, has three intensity maxima which can be identified as the Cu(1) a//B (low field), the Cu(2) (mid-field) and the Cu(1) b//B (high field) peaks.

To start the analysis, we first correct the experimental fields of resonance by the demagnetisation values proposed by Takigawa et al[25,26], i.e by subtracting 14.1mT and 3.6mT for c//B and c⊥B, respectively. For comparison, we also analyse the data using the slightly different internal field corrections (i.e. -6.2mT for c//B and -2.5mT for c⊥B) deduced by Barrett et al[27,†]. Thereafter, the Knight shift tensor is determined numerically, via calculation of the predominant features originating from the Zeeman and quadrupole contributions alone (see appendix C.4). In order to yield a high accuracy, the resonance frequencies (and hence fields) are obtained from numerical diagonalisation of the exact Hamiltonian, instead of using perturbation expressions[28]. The deviations of the calculated field positions from the diamagnetically corrected, experimentally measured ones then provide an estimate of the corresponding Knight shift components.

---

27 S. E. Barrett, D. J. Durand, C. H. Pennington, C. P. Slichter, T. A. Friedmann, J. P. Rice & D. M. Ginsberg, *Phys. Rev. B* **41** 6283 (1990)

† At present, these groups are the only known researchers to have deduced the demagnetisation factor.

28 M. Solanki-Moser, *private communication.*

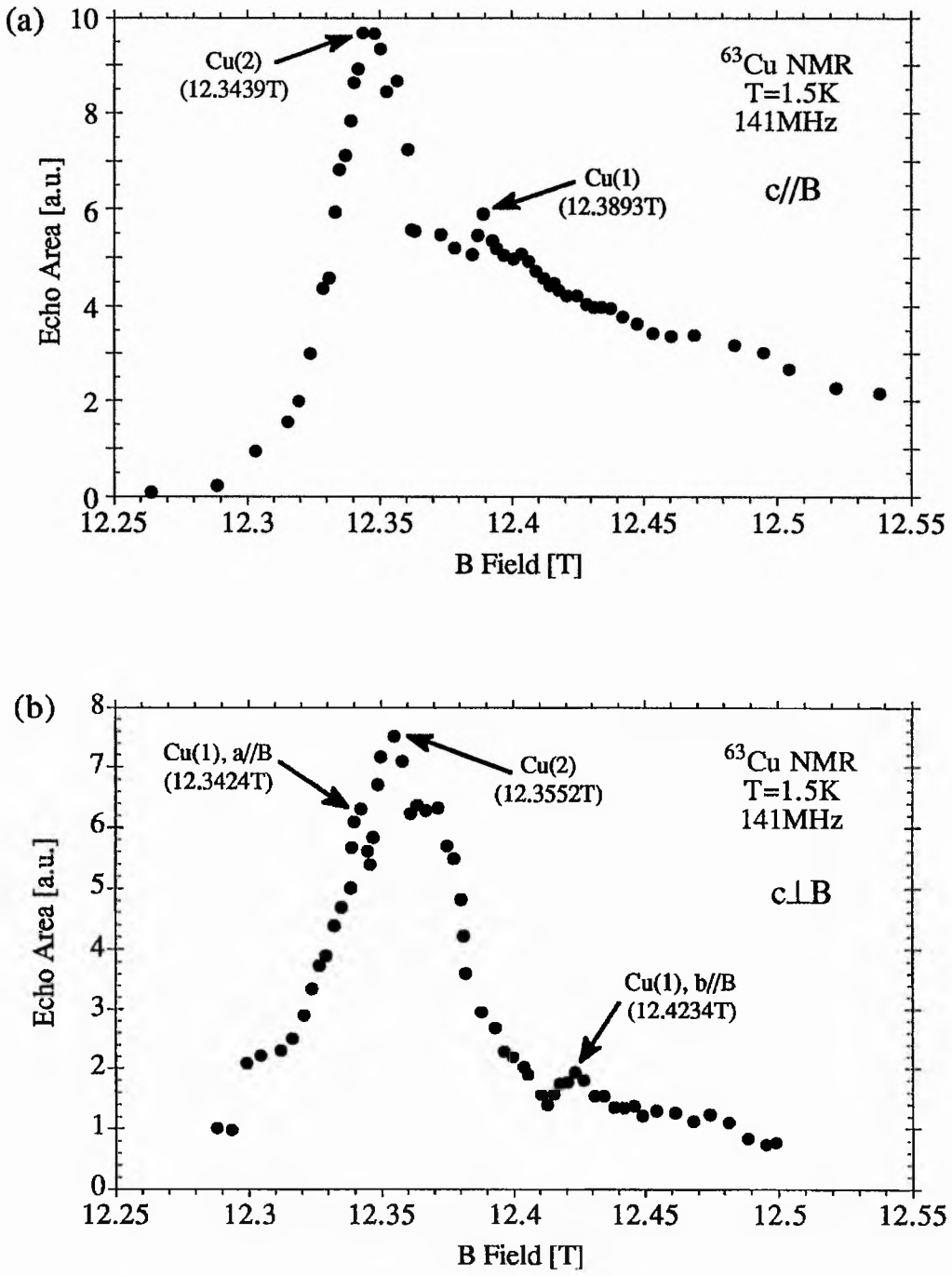

Figure 5.3

The central transition (m=1/2 ↔ −1/2) ^{63}Cu spin echo intensity as a function of applied magnetic field for the uniaxially aligned Aberdeen sample, oriented with (a) the c-axis parallel to the B-field and (b) the c-axis perpendicular to the applied B-field. These spin echo spectra were collected at a frequency of 141MHz and a temperature of 1.5K. The precise experimental peak positions are labelled. Note that at this frequency the unshifted 'bare', zero quadrupole interaction, ^{63}Cu nuclear resonance is at 12.4945T.

Note that the two orientations c//B and c⊥B are sufficient to evaluate the complete Knight shift tensor, since, for the axially symmetric Cu(2) site, c//B corresponds to θ=0° and c⊥B to θ=90° (where θ is the angle between the main principal axis of the EFG tensor (i.e. c for Cu(2)) and the applied B-field). Therefore K^c and $K_\perp=K^a=K^b$ result.

For Cu(1), a single crystal-like situation exists only for c//B, with θ=90° (b is the main principal axis) and ϕ=0 (where ϕ is the angle between B_{xy}, the projection of the field onto the plane perpendicular to the main principal axis, and x=c (see appendix C.4)), giving K^c. c⊥B produces a (2D) powder pattern (ϕ=90°, θ=random) with intensity maxima for θ=0°, 45° and 90°, i.e for B parallel to b, for B at 45° to a and b and for B parallel to a. This gives K^a and K^b.

At a temperature of T=1.5K, the Knight shift determined from our results is almost purely orbital in origin. Based on Barrett et al's assumption that their shift data at 4.2K is sufficiently close to T=0 for $^{63}K_s$ to equal zero, we can equate our experimentally determined shift exclusively with the orbital contribution to the Knight shift, $^{63}K_{orb}$. With this in mind, we now compare (see table 5.3) the explicitly derived, diamagnetically corrected $^{63}K_{orb}$ terms obtained from the Takigawa and Barrett analyses with our two sets of corrected values for the total Knight shift at 1.5K.

$^{63}K^{\alpha}_{orb}$ (1,2)	This work with the Takigawa Correction (%)	Takigawa et al (%)	This work with the Barrett Correction (%)	Barrett et al (%)
K^a_{orb} (1)	1.12 ± 0.03	1.18 ± 0.02	1.11 ± 0.03	1.08 ± 0.04
K^b_{orb} (1)	0.45 ± 0.06	0.43 ± 0.02	0.44 ± 0.06	0.27 ± 0.04
K^c_{orb} (1)	0.34 ± 0.02	0.31 ± 0.08	0.28 ± 0.01	0.25 ± 0.01
K^a_{orb} (2)	0.21 ± 0.02	0.24 ± 0.02	0.20 ± 0.02	0.28 ± 0.02
K^b_{orb} (2)	0.21 ± 0.02	0.24 ± 0.02	0.20 ± 0.02	0.28 ± 0.02
K^c_{orb} (2)	1.33 ± 0.02	1.35 ± 0.08	1.27 ± 0.01	1.28 ± 0.01
$K_{orb,iso}$ (1)	0.64	0.64	0.61	0.54
$K_{orb,ax}$ (1)	-	-	-	-
$K_{orb,iso}$ (2)	0.58 (0.62)	0.61	0.56 (0.62)	0.61
$K_{orb,ax}$ (2)	0.37 (0.31)	0.37	0.36 (0.31)	0.34

Table 5.3

The orbital $^{63}K^{\alpha}_{orb}$(1,2) (where α=a,b,c), isotropic $K_{orb,iso}$ & axial $K_{orb,ax}$ Knight shift for the chain (1) and plane (2) sites in $YBa_2Cu_3O_7$. The results obtained from the present study at 1.5K have been appropriately corrected using the demagnetisation factors proposed by the Takigawa[25] & Barrett[27] groups.

In addition, the isotropic and axial shifts, calculated from the $K^{a,b,c}$ components using equations (3.54) and (3.55) (i.e $K_{iso}=[K^a+K^b+K^c]/3$ and $K_{ax}=[K^c-K^{a,b}]/3$), are also given in table 5.3. The equivalent shifts obtained from the rotation pattern calculations are included in brackets for Cu(2).

The results obtained with the Takigawa internal field correction appear to compare favourably with the orbital Knight shift values of Takigawa et al, indicating that the assumptions made by these researchers in order to derive the demagnetisation corrections may well be valid. Some of the results acquired using the Barrett demagnetisation factors are in close agreement with the Barrett orbital Knight shift values, but others still resemble the Takigawa results.

5.4 Discussion

It is evident from the preliminary SEM characterisation of the powdered JM21 sample that, provided samples are thoroughly ground in an inert atmosphere, one can keep crystallite clusters to a minimum and effectively obtain a high proportion (~95%) of single crystallites in the powder. There is, however, an inherent problem with mixing the finely ground powder into the stycast resin by hand. It seems that dispersion of the powder using physical agitation is not sufficient to provide a uniform distribution of crystallites throughout the resin and only results in the formation of clusters* in the more densely populated sites of the sample - such as the outer perimeter. In highly populated areas of the specimen, the motion of crystallites during alignment is impeded by neighbouring crystallites/clusters and so the re-orientation of the crystallographic c-axes is not as complete as one would expect from a free flowing powder.

As a result of the pilot dispersion studies on aluminium powder (see section 4.3.5), a method of alignment was devised which incorporated the use of an ultrasonic drill to thoroughly disperse the powder in the epoxy resin. This alignment technique (see section 4.3.6) proved much more successful (as witnessed by X-ray analysis) and was used to align all of the Co-doped YBCO samples discussed in chapter 6.

The evidence supplied by the electron microscope for the anomalous +30° misalignment of the c-axis was later reinforced by the ^{63}Cu NMR orientation analysis. Both of these analytical techniques use the orientation line marked on the sample as a reference, and both are very sensitive to the orientation of the c-axis within the plane of the disc. Notably, the one method of alignment determination (i.e X-ray analysis) which did not rely upon the orientation of the c-axis in the plane of the disc (see figure 4.1), produced results indicative of fairly good c-axis alignment (~82%). This provides

* At least 30% of the powder forms clusters when in the epoxy resin.

substantial evidence to suggest that the crystallites were well aligned but that the c-axis fixed on the sample was marked wrongly. We can look to the NMR spin echo spectra for further support of this theory: if a substantial fraction of the sample was not aligned c parallel to B, then the individual spectra obtained at θ=0° and 90° (correctly oriented) would be considerably broadened by the spread in orientation of the crystals. In the free powder spectrum for this sample, the pattern is so broadened by random orientation that the ^{63}Cu peaks can bearly be distinguished. Thus, the very fact that (i) the ^{63}Cu NMR spectra are significantly narrower for the aligned sample relative to the powder sample and that (ii) the complex structure of the ^{63}Cu peaks is not obscurred by broadening, gives some credibility to the argument that the Aberdeen sample has substantial alignment.

Another line of thought which was initially pursued was the possibility of the epoxy exerting some sort of stress or hydrostatic pressure on the crystallites. This would have the effect of 'sqeezing' the crystallites out of their true c-axis alignment, especially at low temperatures. An estimate of the hydrostatic pressure exerted at low temperatures by Stycast 1266, was made made by studying the effect that the epoxy had on the superconducting phase transition of lead[29]. The stress exerted by the epoxy was found to be negligible and so the hydrostatic pressure theory could not explain the misalignment of the c-axis. Comparisons of the X-ray spectra for this sample, showed no evidence of broadening in the epoxy-set sample relative to the powder sample. This was taken as further evidence that the stress exerted by the epoxy was negligible.

Thus, a wrongly marked c-axis fixed to a fairly well-aligned sample seems to be the most plausible scenario for the apparent misalignment of the c-axis. As a result of these findings, various methods were devised to ensure accurate marking of the sample, during the alignment procedure (see section 4.3.4).

It has been established by various research groups[30,31] that thermosetting epoxy has no deleterious effect on the superconducting transition of the ceramic that it encases. Thus, the NMR results obtained on the epoxy set sample should be fairly representative of those acquired on specimens aligned using other, more mechanical, methods[32,33]. If we add to this the fact that thermal expansion of $YBa_2Cu_3O_{7-\delta}$ across the temperature

---

29 R. C. Hawker-Cole, *private communication.*

30 M. R. De Guire, I. Manas-Zloczower, M. Tabib-Azar, D. E. Farrell, C. J. Kim, W. H. Lu, H. Ng & F. Rayal, *Jnl. Mater. Sci.* **25** 2881 (1990)

31 I. M. Low & F. W. Lim, *Jnl. Mater. Sci. Lett.* **10** 1119 (1991)

32 A. F. Hepp, J. R. Gaier, G. A. Landis & S. G. Bailey, *Adv. Ceramic Mater.* (in press)

33 A. Lusnikov, L. L. Miller, R. W. McCallum, S. Mitra, W. C. Lee & D. C. Johnson, *Jnl. Appl. Phys.* **65** 3136 (1989)

range 4 to 300K is negligible[34], we can confidently expect to be able to thermally cycle the epoxy set YBCO samples between 1.5K and room temperature, without any deterioration in the quality of the sample or the NMR results. We now turn to a discussion of the NMR data at 1.5K.

In this work, we report measurements of the ^{63}Cu Knight shift in the superconducting state of what we now know to be fully oxygenated $YBa_2Cu_3O_7$ (T=93K). At such low temperatures as 1.5K and at applied fields (B_0) of around 12.4T, where $B_{c1} \ll B_0 \ll B_{c2}$, the sample grains are in the 'mixed' state (i.e. their form is a vortex or fluxoid lattice) and the presence of demagnetising screening currents creates a magnetic field inside the grains (B_{int}) which differs from the applied field. In order to obtain the shift of the resonance line, one must know the precise magnetic field inside the sample grain. Thus, when using NMR in the superconducting state, the determination of the demagnetisation (or diamagnetic) correction becomes of great importance. In the absence of facilities with which to make our own estimate of the demagnetisation correction, we have no alternative but to use the methods of the Takigawa and Barrett groups to determine the internal field correction for our applied field value.

From combined measurements of the resonant frequency and macroscopic magnetisation M as a function of applied field at 7K, the Los Alamos group, led by Takigawa and Hammel[25,26], are able to determine a relationship between the internal magnetic field correction and M at this specific temperature (i.e. field correction=$-4\pi dM|\beta$, where $\beta_{//}=0.7$ and $\beta_{\perp}=0.65$). At each new temperature, they measure the value of M by experiment and then use the deduced relationship to calculate the corresponding internal field correction. The magnetisation is measured up to 5T experimentally, while values of M at higher fields are determined by extrapolation using $M=a+bInB_0$, where a and b are constants*. For the conditions of applied field used in our experiments, we deduce from Takigawa's workings a negative internal field correction of -14.1mT for the c//B results and -3.6mT for the c⊥B results. Takigawa et al[25] note in their discussion of the demagnetisation correction that uncertainties arise in their extrapolation of M at higher fields. They also believe that a small upturn in the temperature variation of the diamagnetically corrected c//B Knight shift below 15K, is spurious. Unfortunately for us, these are the very extremes (high field, low temperature) at which our data is taken.

Recently, the experiments of Takigawa et al have been repeated by Barrett et al[27]. In an effort to obtain definitive measurements, Barrett et al determine the internal field

---

34 E. Salomons, H. Hemmes, J. J. Scholtz, N. Koeman, R. Brouwer, A. Driessen, D. E. De Groot & R. Griessen, *Physica B* **145B** 253 (1987)

* The values of a and b at ~12.4T are found to be -52.66 and +7.61, and -14.74 and +2.13 for the c//B and c⊥B orientations, respectively.

correction directly by monitoring the resonance frequency of the ^{89}Y nucleus. Such a measurement gives high precision and is fairly reliable because the ^{89}Y Knight shift is known to be an order of magnitude smaller than the ^{63}Cu shifts.[35,36,37] Due to the long spin lattice (T_1) relaxation time of ^{89}Y at low temperatures†, and since the ^{89}Y gyromagnetic ratio is so low ($^{89}\gamma/2\pi$=2.086MHz/T), Barrett et al employ two particular NMR techniques to observe the ^{89}Y nucleus in the superconducting state of $YBCO_7$. To collect the data, a Carr-Purcell-Meiboom-Gill sequence is used[38] in conjunction with a $\pi/2$-π spin echo sequence. The Y line is recorded point by point, using a small B_1 field to excite one region of the line without perturbing other regions and the spectra is frequency swept at constant field to avoid any possible hysteresis.

At any temperature, the ^{89}Y resonance frequency $^{89}\upsilon$ will be given by

$$^{89}\upsilon = (1 + {}^{89}\Delta K(T)) \frac{^{89}\gamma}{2\pi} B_{int} \qquad (5.1)$$

where $^{89}\Delta K(T)$ is the ^{89}Y magnetic shift with respect to YCl_3 and B_{int} is the required internal field. In their calculations, Barrett et al quote an error of ±0.006% for $^{89}\upsilon$ and ±0.005% for $^{89}\Delta K$. They find that at T=4.2K, B_{int} is 0.05% lower than B_0 when c//B, and 0.02% lower when c⊥B. At fields of around 12.4T, this leads to negative internal field corrections of -6.2mT for c//B and -2.5mT for c⊥B.

Both Takigawa et al and Barrett et al determine the total Knight shift $^{63}K^{\alpha}(1,2)$ over a wide range of temperature and find that, on the whole, it falls considerably as the temperature drops below T_c* (though they do observe substantially different temperature dependences). In the normal state, where $^{63}K^{\alpha}(1,2)$ appears to be virtually temperature independent for both sites and for all α, a close look at the <u>total</u> Knight shift tensor shows that the component values obtained by Barrett et al are in good agreement with the findings of Takigawa et el. In addition, the results coincide with those deduced from the single crystal studies of Pennington et al[39] and Kheinmaa et al[40]. However, an oriented

---

35 J. T. Markert, T. W. Noh, S. E. Russek & R. M. Cotts, *Solid State Comm.* **63** 847 (1987)

36 H. Alloul, T. Ohno & P. Mendels, *Phys. Rev. Lett.* **63** 1700 (1989)

37 G. Balakrishnan, R. Dupree, I. Farnan, D. McK Paul & M. E. Smith, *Physica C* **21** L847 (1988)

† At 4K, the T_1 of ^{89}Y is 8 minutes. Note also that in the superconducting state, the Y lines are too broad relative to the B_1 field to be measured by the FT of the spin echo signal.

38 See C. P. Slichter, *Principles of Magnetic Resonance*, Springer-Verlag (1990)

* Note, however, that Barrett et al find $^{63}K^{c}(2)$ to be approximately constant over the entire temperature range 4.2–120K, while Takigawa et al witness a slight upturn in their $^{63}K^{c}(2)$ results below ~50K.

39 C. H. Pennington, D. J. Durand, C. P. Slichter, J. P. Rice, E. D. Bukowski & D. M. Ginsberg, *Phys. Rev. B* **39** 2902 (1989)

powder analysis by Brinkmann[41,42], in which the errors are known to be large, produces Knight shift components which deviate considerably from the Barrett/Takigawa/ Pennington/Kheinmaa values.

In their analyses of the normal state Knight shifts, the Takigawa and Barrett groups decompose the total Knight shift into its spin ($^{63}K_s(T)$) and orbital ($^{63}K_{orb}$) contributions (see equation (3.44)) by assuming that the spin component vanishes at T=0 - as in typical BCS superconductors. The temperature variation of $^{63}K^{\alpha}$ below T_c is then associated with the change in $^{63}K_s$ (and hence the electron spin susceptibility, χ_s) and the residual Knight shift at very low temperatures is the orbital shift alone. Such an assumption is only appropriate if the pairing in the superconducting state is singlet and if the effect of the spin-orbit scattering is negligible. After initially surmising that a simple BCS picture holds for Cu (where the spin-orbit coupling is fairly weak), both research groups investigate the consequences for the orbital component and conclude, with some conviction, that they are wholly justified in making the assumption that $K_s(T=0)=0$. Other independent groups are in agreement[42,43]. After the decomposition of the Knight shift, we note that there is some discrepency between the orbital and spin components obtained by the Takigawa and Barrett groups.

Since this work has been performed at 1.5K, we can assume that the spin contribution to the measured Knight shift is approximately zero. Hence, our results are a direct measure of the temperature-independent orbital shift and no uncertainties are incurred in extrapolating the total shift to absolute zero. In addition, our data is acquired at high field (~12.4T), where demagnetisation effects, although still imperfectly known, are considerably smaller than those experienced during the Takigawa and Barrett experiments. With this knowledge at hand, we now discuss the orbital shift results for each Cu site in turn, starting with Cu(1).

It can be seen from table 5.3 that the use of the Takigawa demagnetisation factors produces results for the Cu(1) orbital Knight shift which are almost coincident with the corresponding Takigawa results. The values for the Cu(1) K^{a}_{orb} components appear to deviate most, but in retrospect this can expected since, in both studies, the a//B peak

---

[40] I. A. Kheinmaa, A. V. Vainrub, Ya. O. Past, V. A. Miidel, A. V. Miller, I. F. Shchegolev, G. A. Emel'chenko & V. A. Tatarchenko, *J.E.T.P. Lett.* **48** 186 (1988)

[41] D. Brinkmann, Z. *Naturforsch.* **45a** 393 (1990)

[42] D. Brinkmann in *Progress in High Temperature Superconductivity*, Vol. 21, p230, World Scientific (1990)

[43] R. E. Walstedt, W. W. Warren Jr., R. F. Bell, R. J. Cava, G. P. Espinosa, L. F. Schneemeyer & J. V. Waszczak, *Phys. Rev. B* **41** 9574 (1990)

position* was the most difficult to locate in the 'restricted' powder pattern produced for c⊥B. In view of this fact, the errors quoted by Takigawa et al for the $K^{a,b}(1)$ orbital shift components seem optimistically small, especially when account is taken of the demagnetisation correction. Both the Takigawa $K_{orb}(1)$ results themselves and the orbital shift components deduced from this study using the Takigawa corrections, show considerable anisotropy.

The use of the Barrett internal field corrections with our NMR data produces a slightly different set of orbital shift results for Cu(1). Interestingly, at our high field, the internal field correction deduced for c⊥B from the Barrett paper (-2.5mT) is quite similar to that obtained from the Takigawa paper (-3.6mT). This suggests that any K^{α}_{orb} component established from our data using the c⊥B Barrett correction will compare favourably with the corresponding orbital component obtained using the Takigawa c⊥B demagnetisation factor. This is indeed borne out by the experimental results (see table 5.3), which indicate that the component values for $K^{a}_{orb}(1)$ and $K^{b}_{orb}(1)$ are virtually independent of the demagnetisation correction used, within experimental error. Note that the $K^{a}_{orb}(1)$ values we obtain using both corrections are much closer to the Barrett result than to the Takigawa result. This evidently suggests that either our raw experimental data scales with that of Barrett, but differs from the Takigawa data, or that Takigawa's demagnetisation correction becomes erroneous at the lower fields that he uses. Either way the $K^{b}_{orb}(1)$ data, which is still in agreement with the Takigawa findings, conflicts with these ideas.

In the case of the c//B orientation, the Barrett correction at fields of ~12.4T (i.e. -6.2mT) is less than half that derived by Takigawa (-14.1mT). Such a relatively large change in the demagnetisation factor produces a K^{c}_{orb} value which deviates considerably from the Takigawa-corrected result. Instead, the Barrett-corrected K^{c}_{orb} component compares rather well with the Barrett data.

The Cu(1) Knight shift (K_s plus K_{orb}) components in the normal state are large and positive, and show considerable anisotropy (i.e $K^{a}(1)=1.38\%$, $K^{b}(1)=0.55\%$ and $K^{c}(1)=0.60\%$)[39]. In the earlier works of Pennington et al[39] and Adrian[44] it was shown that the normal state Cu(1) electric field gradient tensors can be modelled using a simple point-ion picture. In this model, there is crystal-field splitting of the electronic energy levels (which accounts for the orbital susceptibility) and the chain site copper is approximated to a Cu^{2+} ion with a single hole sitting in the y^2-z^2 orbital of the d-shell (ground state). Each Cu(1) possesses an electron spin one-half and is therefore near to the permanent electron spin magnetic moment limit.

---

* and indeed the b//B peak position.

44 F. Adrian, *Phys. Rev. B* **38** 2426 (1988)

In an ionic permanent moment model, the orbital contribution to the Knight shift (see equation (3.34)) is given by[38]

$$K^{\alpha}_{orb} = 4\mu_B^2 \left\langle \frac{1}{r^3} \right\rangle \sum_n \frac{|\langle 0|L_\alpha|n\rangle|^2}{E_n - E_0} = 2 \left\langle \frac{1}{r^3} \right\rangle \chi^{\alpha}_{orb} \qquad (5.2)$$

where χ^{α}_{orb} is the orbital contribution to the magnetic susceptibility, $\langle 1/r^3 \rangle$ is the average conduction wavefunction, μ_B is the Bohr magneton and where the conventional crystallographic axes, α=a,b,c, are taken to be the principal axes of the orbital shift. $\langle 0|$ and $|n\rangle$ are the ground and excited states of the system, respectively.

The first equality in equation (5.2) can be evaluated for Cu(1): to a first approximation, the crystal field for the Cu(1) site can be viewed as being axially symmetric, with an axis of four-fold symmetry pointing in the a-direction. Note that the normal state Knight shift and spin lattice relaxation tensors for this site are also found to have near axial symmetry about the a axis (where the x,y,z axes are taken as being parallel to the crystallographic a,b,c axes) and so some experimental data exists to support this assumption. Defining the energy of the $3d_{y^2-z^2}$ state as zero, one finds that a hole in the $3d_{y^2-z^2}$ orbital produces orbital shift components given by

$$K^{xx}_{orb} = \frac{16\mu_B^2}{E_{yz}} \left\langle \frac{1}{r^3} \right\rangle \qquad (5.3a)$$

and

$$K^{yy}_{orb} = K^{zz}_{orb} = \frac{4\mu_B^2}{E_{xz}} \left\langle \frac{1}{r^3} \right\rangle \quad \text{for axial symmetry} \qquad (5.3b)$$

where it is assumed that E_{xz}=E_{xy}. From equations (5.3) (a) and (b), one obtains

$$\frac{K^{xx}_{orb}}{K^{yy}_{orb}} = \frac{K^{xx}_{orb}}{K^{zz}_{orb}} = \frac{4E_{xz}}{E_{yz}} \qquad (5.4)$$

Theoretical estimates of the crystal field splittings by McMahan et al[45] suggest that E_{xz} and E_{yz} should be approximately equal, with E_{xz} being slightly larger, if anything. For a hole in the $3d_{y^2-z^2}$ orbital, the orbital shift anisotropy for Cu(1) is therefore estimated as being slightly greater than 4 to 1.

---

[45] A. K. McMahan, R. M. Martin & S. Satpathy, *Phys. Rev. B* **38** 6650 (1988)

While Barrett et al obtain

$$\frac{K^{a}_{orb}(1)}{K^{b}_{orb}(1)} \approx \frac{K^{a}_{orb}(1)}{K^{c}_{orb}(1)} \approx 4.15 \qquad (5.5a)$$

for the Cu(1) site, the Takigawa results lead to

$$\frac{K^{a}_{orb}(1)}{K^{b}_{orb}(1)} \approx 2.74 \quad \text{and} \quad \frac{K^{a}_{orb}(1)}{K^{c}_{orb}(1)} \approx 3.81 \qquad (5.5b)$$

With the Takigawa correction, our results produce

$$\frac{K^{a}_{orb}(1)}{K^{b}_{orb}(1)} \approx 2.49 \quad \text{and} \quad \frac{K^{a}_{orb}(1)}{K^{c}_{orb}(1)} \approx 3.29 \qquad (5.5c)$$

And similarly with the Barrett correction,

$$\frac{K^{a}_{orb}(1)}{K^{b}_{orb}(1)} \approx 2.52 \quad \text{and} \quad \frac{K^{a}_{orb}(1)}{K^{c}_{orb}(1)} \approx 3.96 \qquad (5.5d)$$

Overall, the Barrett et al results (5.5a) seem to confirm an ionic model in which a single hole occupies the Cu(1) $3d_{y2-z2}$ orbital. Therefore, these results strongly support the idea that the K_s is zero at zero temperature. The Takigawa data and Barrett-corrected results, however, only provide near confirmation for the K^{a}_{orb}:K^{c}_{orb} ratio. The ratios for K^{a}_{orb}:K^{b}_{orb} derived from Takigawa and both sets of corrected results are much smaller than anticipated from an ionic model in which only the hyperfine interactions associated with the on-site Cu-3d spin are included.

A glance at table 5.3, indicates that the Cu(2) K^{α}_{orb} results show trends which are similar to the Cu(1) results, in terms of the demagnetisation corrections. Within experimental error, the Takigawa-corrected $K^{\alpha}_{orb}(2)$ data is in good agreement with the absolute Cu(2) orbital shifts of Takigawa, while the similarity of the Barrett and Takigawa c⊥B demagnetisation factors (at 12.4T) places the Barrett-corrected data for the $K^{a,b}_{orb}(2)$ components in almost perfect alignment with the corresponding Takigawa-corrected components. The somewhat smaller c//B internal field correction of Barrett et al means that the Barrett-corrected K^{c}_{orb} shift is identical to that obtained from the Barrett study, within error. Note that the Barrett results for the Cu(2) site are of similar magnitude to those acquired for the chain site.

As with the Cu(1) site, the normal state electric field gradient tensor for Cu(2) can be fitted to the ionic Cu^{2+} model[39,44]. In the case of the Cu(2) site, the d-shell hole is

expected to be in the x^2-y^2 orbital and the crystal field splitting (and the normal state Knight shift tensor) is axially symmetric around the c-axis[46]. Evaluating the first equality in equation (5.2) and defining the energy of the $3d_{x2-y2}$ state as zero, one finds that a single hole in the $3d_{x2-y2}$ orbital produces orbital shift components given by

$$K_{orb}^{zz} = \frac{16\mu_B^2}{E_{xy}} \left\langle \frac{1}{r^3} \right\rangle \tag{5.6a}$$

and

$$K_{orb}^{xx} = K_{orb}^{yy} = \frac{4\mu_B^2}{E_{yz}} \left\langle \frac{1}{r^3} \right\rangle \quad \text{for axial symmetry} \tag{5.6b}$$

McMahan et al[45] give the energies of a hole in various d-states as E_{xy}=2.0eV and E_{xz}=E_{yz}=2.2eV. The theoretical orbital shift anisotropy for a hole in the $3d_{x2-y2}$ orbital of $Cu(2)^{2+}$ is then

$$\frac{K_{orb}^{zz}}{K_{orb}^{xx}} = \frac{K_{orb}^{zz}}{K_{orb}^{yy}} = \frac{4E_{yz}}{E_{xy}} = 4.4 \tag{5.7}$$

From experiment, for Cu(2), Barrett et al deduce

$$\frac{K_{orb}^{c}(2)}{K_{orb}^{a}(2)} = \frac{K_{orb}^{c}(2)}{K_{orb}^{b}(2)} = 4.57 \tag{5.8a}$$

while the Takigawa results give

$$\frac{K_{orb}^{c}(2)}{K_{orb}^{a}(2)} = \frac{K_{orb}^{c}(2)}{K_{orb}^{b}(2)} = 5.63 \tag{5.8b}$$

With the Takigawa and Barrett corrections, our results produce

$$\frac{K_{orb}^{c}(2)}{K_{orb}^{a}(2)} = \frac{K_{orb}^{c}(2)}{K_{orb}^{b}(2)} = 6.33 \tag{5.8c}$$

---

46 Note that R. E. Walstedt, W. W. Warren Jr., R. F. Bell, G. F. Brennert, G. P. Espinosa, R. J. Cava, L. F. Schneemeyer & J. V. Waszczak, *Phys. Rev. B* **38** 9299 (1988), have shown that the description in terms of weakly interacting electrons moving in a hybridized $Cu3d_{x2-y2}$-$O2p_{\sigma}$ band, as predicted by band theory, fails.

and

$$\frac{K^{c}_{orb}(2)}{K^{a}_{orb}(2)} = \frac{K^{c}_{orb}(2)}{K^{b}_{orb}(2)} = 6.35 \qquad (5.8d)$$

respectively.

The orbital Knight shift values of Barrett et al appear to confirm that a Cu^{2+} ionic permanent picture holds for both Cu(1) and Cu(2). The assumption that a single hole occupies the d-shell orbital at both Cu sites is validated and there is strong evidence to suggest that K_s vanishes at zero temperature. The results from this and the Takigawa study are less convincing, since the ratios of $K^{c}_{orb}(2)$: $K^{a,b}_{orb}(2)$ are much higher than expected and the ratios of $K^{a}_{orb}(1)$: $K^{b}_{orb}(1)$ are considerably lower.

Before commenting further on the orbital Knight shifts, it is useful to obtain the corresponding normal state spin components. Since the normal state $K^{\alpha}(1,2)$ tensor is now fairly well defined[25,27,39,40], we can deduce K^{α}_{s} from our results by subtracting the corrected orbital shifts from the corresponding normal state Knight shifts of Pennington et al[39].

$^{63}K^{\alpha}_{s}$ (1,2)	This work with the Takigawa Correction (%)	Takigawa et al (%)	This work with the Barrett Correction (%)	Barrett et al (%)
K^{a}_{s} (1)	0.26 ± 0.03	0.16 ± 0.02	0.27 ± 0.03	0.25 ± 0.04
K^{b}_{s} (1)	0.10 ± 0.03	0.18 ± 0.02	0.11 ± 0.03	0.29 ± 0.04
K^{c}_{s} (1)	0.26 ± 0.02	0.29 ± 0.08	0.32 ± 0.01	0.33 ± 0.01
K^{a}_{s} (2)	0.38 ± 0.02	0.37 ± 0.02	0.39 ± 0.02	0.30 ± 0.02
K^{b}_{s} (2)	0.38 ± 0.02	0.37 ± 0.02	0.39 ± 0.02	0.30 ± 0.02
K^{c}_{s} (2)	-0.06 ± 0.02	-0.08 ± 0.08	0.00 ± 0.01	-0.01 ± 0.01
$K_{s,iso}$ (1)	0.21	0.21	0.23	0.29
$K_{s,ax}$ (1)	-	-	-	-
$K_{s,iso}$ (2)	0.23	0.22	0.26	0.20
$K_{s,ax}$ (2)	-0.15	-0.15	-0.13	-0.10

Table 5.4

The normal state spin $^{63}K^{\alpha}_{s}$ (1,2) (where α=a,b,c), isotropic $K_{s,iso}$ & axial $K_{s,ax}$ Knight shifts for the chain (1) and plane (2) sites in $YBa_2Cu_3O_7$. The spin shift results obtained from the present study were deduced by subtraction of the Takigawa and Barrett-corrected orbital shifts (see table 5.3) from the corresponding normal state Knight shifts of Pennington et al[39].

The prominent features of table 5.4 can be summarised: for Cu(1), the spin shift of Barrett et al is found to be close to isotropic, with a mean value of 0.29% averaged over all field orientations. In contrast, the Takigawa results are only approximately equal for the Cu(1) shifts in which B_0 is perpendicular to the crystallographic c-axis. From our results, only the $K^a_s(1)$ and $K^c_s(1)$ components are similar for each set of corrections. The $K^c_s(1)$ shift values are consistent over all the studies, while the $K^a_s(1)$ results compare well for all, except the Takigawa case. Note that the $K^b_s(1)$ components are dissimilar in each case. On the Cu(2) site, the spin shift is found to be extremely anisotropic, with Barrett et al finding the $K^{a,b}_s(2)$ values comparable in magnitude to $K^{\alpha}_s(1)$. Within error, the Takigawa $K^{a,b}_s(2)$ shifts are in good agreement with the corresponding components obtained from both of our corrected sets of data, but all are considerably removed from the values acquired by Barrett. In all studies, the $K^c_s(2)$ shift is essentially zero, indicating that the normal state Knight shift along the c-axis of Cu(2) is dominated by the orbital contribution.

The questions which now logically follow are: 'Which complete set of Knight shift results seem most plausible? Do the orbital and spin Knight shift components deduced from these studies fit with the relaxation data and can the broader picture still be explained using the ionic permanent moment model?' These questions will be approached tentatively and briefly.

The ionic model described earlier uses the simplest Hamiltonian coupling the nuclear spin of the $Cu^{2+}(1,2)$ with the on-site electronic spin. From this model, normal state Knight shifts can be explained and reasonable values can be obtained[39,44] for the hyperfine couplings A^{α} and spin susceptibility χ_s. However, there are a number of NMR results which clearly appear as anomalies in such a model. For example, the Knight shift tensor for the Cu(1) site is difficult to understand, since its anisotropy conflicts with the apparent isotropy of the Cu(1) spin lattice relaxation time. In an attempt to explain this, Pennington et al[39] have suggested that the Cu(1) spin lattice relaxation may result from a transferred hyperfine coupling of the Cu(1) nuclear spin to the spin of the hole on the bridge (O(4)) and/or chain (O(1)) oxygens. Through the mixing of the Cu 4s orbitals with the oxygen hole orbitals, such a mechanism would produce isotropic coupling. Provided the oxygen holes are in a conduction band, this predicts an isotropic spin shift, in addition to an isotropic spin lattice relaxation rate which is proportional to temperature.

Additional anomalies include the normal state shift data presented here, which indicate that both the Cu(1) and Cu(2) atoms have substantial isotropic and positive components to their spin shifts (which decrease as T falls below T_c). This result is surprising since the hyperfine field from unfilled d-shells is expected to produce an isotropic core polarisation contribution which is negative. In fact, from the simple ionic model of Pennington, one expects that the ratio of $K^c_s(2)/K^{a,b}_s(2)$ should be equal to

-2.8. This is clearly not the case in either our corrected results or the Takigawa and Barrett experiments, where the ratios range from 0.15 to 0.33. Takigawa et al speculate that the positive shift is again the result of a transferred hyperfine coupling to the oxygens.

In light of these anomalies to the ionic model, independent studies by Mila and Rice (MR)[47], Monien, Pines and Slichter (MPS)[48] and Monien and Pines (MP)[49] have analysed the results of Takigawa et al. In addition, MPS and MP also consider the Barrett data along with Walstedt and Warren[50] (WW) and Bulut and Scalapino[51] (BS).

Firstly, MR use a single component model in which the Cu d-spins are strongly hybridized with the oxygen holes and in which the Cu atoms act like permanent magnetic moments with fluctuating orientations. They exploit the fact that $K_s(T=0)$ is assumed to be zero and build a phenomenological analysis to explain the unusual combination of anisotropies of Knight shift and relaxation rates obtained (for Cu(1) and Cu(2)) by Takigawa and Pennington, respectively. In addition to the on-site hyperfine fields due to the spin-dipolar, core polarisation and spin-orbit interactions, MR introduce a second term to their spin Hamiltonian (see equation (3.48)) which they assign as the transferred hyperfine field from neighbouring Cu^{2+} spins*. They argue that his term could be the source of the isotropic hyperfine field and from its size, show that it must be acting on the Cu-nuclei through the Cu-4s wavefunctions (since the Cu-s orbitals have a huge isotropic contact interaction)[52]. On the plane sites, the transferred hyperfine field is found to dominate, but on the chain sites there can be a substantial contact on-site term due to the large deviation from tetragonal symmetry at these sites. Using this extended ionic model, MR are able to find a consistent explanation for the Takigawa Knight shifts, but the precise quantitative results they obtain are subject to a number of approximations which they make during the the analysis. A final point to note about the MR analysis is that due to the local symmetry around the Cu(1) site, they assume that the wave functions involve the mixing of $3d_{x^2-y^2}$ and $3d_{3z^2-r^2}$ components, and not a purely $3d_{y^2-z^2}$ component.

---

47 F. Mila & T. M. Rice, *Physica C* **157** 561 (1989)

48 H. Monien, D. Pines & C. P. Slichter, *Phys. Rev. B* **41** 11,120 (1990)

49 H. Monien & D. Pines, *Phys. Rev. B* **41** 6297 (1990)

50 R. E. Walstedt & W. W. Warren, *Science* **248** 1082 (1990)

51 N. Bulut & D. Scalapino, preprint submitted to *Phys. Rev. B.*

* They assume that the orientations of neighbouring Cu d-spins are uncorrelated.

52 Note here that the band structure calculations of P. Monthoux, *Phys. Rev. B* **41** 11,128 (1990) show that band theory is adequate to describe Cu(1), but fails with Cu(2). The calculations also suggest that the Cu(1) Knight shift and relaxation times could be explained by the presence of some 4s character at the Fermi level.

They then further assume that in this case the $d_{x^2-y^2}$ wavefunction is dominant, and procede with the analysis in the same way as with Cu(2).

The more recent study of MP has attempted to reconcile the rapid drop in $1/T_1$ which occurs for Cu(2) at T_c (i.e. the absence of the Hebel-Slichter peak)[53] with a similar decrease in the Cu(2) spin Knight shift. The MP model uses an extended ionic permanent moment picture in which the $Cu(2)^{2+}$ spins are strongly hybridized with the planar oxygen holes in such a way that the quasiparticles in the resulting Fermi liquid behave very much like local moments in the neighbourhood of a Cu nucleus, while maintaining an essentially itinerant character elsewhere†. MP thus propose that the positive isotropic shift arises from an interaction between the Cu nucleus and a hole on the oxygen, instead of a coupling of the Cu nucleus and the electron spin of a neighbouring Cu - as in the MR study. In their model, MP assume that since the local moments at adjacent copper sites couple antiferromagnetically, the quasiparticles of the hybridized hole-Cu^{2+} Fermi liquid will also interact antiferromagnetically. By treating the Cu^{2+} spins in the superconducting state as an antiferromagnetically coupled Fermi liquid, they find that it is possible to provide a consistent account of the temperature dependences of both the Cu(2) spin-lattice relaxation rate and the Knight shift measurements of Takigawa and Barrett. In addition, MP consider whether the spin components of the Cu(2) Knight shifts obtained by Takigawa and Barrett can be fitted using the assumptions of the usual BCS isotropic s-wave state, or whether the anisotropic s and d wave states are required. Good fits are found for the Barrett data using the isotropic s-wave, anisotropic s-wave, d-wave and d-wave with an admixture of high l terms framework, while the Takigawa data works best with the d-wave and anisotropic d-wave assumptions.

The collected works of Monien, Pines and Slichter (MPS) and Barrett et al approach the analysis of the spin-lattice relaxation anisotropy and Knight shift from a slightly different angle. Using the knowledge accrued from previous models, MPS conclude that it may be necessary to consider either or both the transferred hyperfine structure and the coupling to the oxygen, depending on the circumstances. Firstly, for Cu(1) in the normal state, they realise that both the spin-lattice relaxation rate ($W^{1a}(1)=1.1$, $W^{1b}(1)=0.9$ and $W^{1c}(1)=0.8$ $msec^{-1}$, as defined* and measured by Pennington) and the spin component of the Knight shift (as measured by Barrett et al)

---

53 W. W. Warren Jr., R. E. Walstedt, G. F. Grennert, G. P. Espinosa & J. P. Remeika, *Phys. Rev. Lett.* **59** 1860 (1987) : R. E. Walstedt, W. W. Warren Jr., R. F. Bell, G. F. Brennert, G. P. Espinosa, J. P. Remeika, R. J. Cava & R. A. Reitman, *Phys. Rev. B* **36** 5727 (1987)

† Note that they assume that this is the case both above and below T_c.

* e.g., $W^{1c} = \frac{3}{2} \gamma_n^2 [\overline{(h^a)^2} + \overline{(h^b)^2}] \tau_0$, where τ_0 is the correlation time of the exponential correlation function and $\overline{(h^\alpha)^2}$ is the mean square value of the magnetic field $h^\alpha(t)$. See ref 38 & 39.

are, to a good approximation, isotropic. In addition, they find that the size of T_1 and the spin shift are related by the Korringa relation (equation 3.35) for nuclei relaxed by electrons in a conduction band (or Fermi liquid). The S_K factor (see section 3.3.2) is found to be 0.36, which is suggestive of some antiferromagnetic interaction between conduction electrons†. This is all very well until the anisotropy of the orbital shift is considered. As we have seen in this discussion, the anisotropic orbital shifts deduced by Barrett indicate that Cu(1) has a local moment and a valence of Cu^{2+}. Surprisingly, though, neither the Cu(1) spin Knight shift, nor $1/T_1$ show any of the anisotropy expected from an interaction with a local moment. Thus, it seems that the Cu(1) 3d-spin does not contribute to the either the spin lattice relaxation or the spin shift. Barrett et al tentatively suggest that the spin correlation time of the Cu(1) moment is very short ($\ll 10^{-15}$s), so that the spin is rapidly scattered, and that the moment has a very small spin susceptibility. Meanwhile, the band theory calculations of Monthoux[52] indicate that the direct hyperfine coupling of the Cu(1) nuclei to the on-site Cu spins are substantially smaller than the corresponding coupling on the Cu(2) sites. It appears therefore that the spin shift and the T_1 for the chain site must originate from a transferred hyperfine coupling to the conduction band of the O(1), and possibly O(4), oxygen ($2p_\sigma$) holes via an admixture of the Cu-4s states. If this is the case, then the temperature dependence of $K_s(1)$ arises solely from the temperature dependence of the hole susceptibility χ_h.

In contrast to Cu(1), the Cu(2) spin lattice relaxation tensors are anisotropic ($W^{1a}(2)=4.7$, $W^{1b}(2)=4.7$ and $W^{1c}(2)=1.05$ msec^{-1})[39]. Using a model for uncorrelated d-spins similar to Mila and Rice, MPS find that the Cu(2) spin lattice relaxation data can be explained by a mechanism which includes the direct hyperfine coupling of the Cu(2) nucleus to the rapidly fluctuating on-site d-shell moment and an isotropic transferred hyperfine coupling to the neighbouring Cu d-spins. To account for the equally anisotropic spin component of the Cu(2) Knight shift (from Barrett et al), MPS require not only the direct on-site (anisotropic) hyperfine coupling and the isotropic transferred hyperfine coupling to nearest neighbour spins, but also a second transferred hyperfine coupling to the oxygen holes (as originally suggested by Takigawa et al). The so-called d-spin contribution ($K_{d\text{-}s}$) and isotropic hole contribution (K_h) to the spin Knight shift are proportional to the susceptibilities, $\chi_{d\text{-}s}$ and χ_h, so that K^α_s is given by

$$K^\alpha_s = \frac{(A^\alpha+4B)\chi^\alpha_{d\text{-}s} + B_h\chi_h}{\gamma_c\gamma_n\hbar^2} \qquad (5.9)$$

† $S_K=1.0$ for non-interacting conduction electrons or holes. Essentially, $S_K=0.36$ is in the weak coupling limit.

where $\chi^{\alpha}_{d\text{-}s}$ represents the spin susceptibility of the Cu^{2+} local moments and χ_h is the susceptibility assigned to the distinct oxygen hole contribution which originates on the chains and is coupled to the Cu(2) (4s) via the O(4) oxygens. Note that due to symmetry the planar holes do not couple to the Cu(2) s-states.

In the case of c//B, $K^c_{d\text{-}s}$ and K^c_h are of opposite sign and Barrett et al deduce that the two contributions cancel perfectly, leaving the normal state K^c_s equal to zero. Since K_s can never increase below T_c, we must assume that K^c_s remains at zero in the superconducting state. This would then explain the temperature independence of K^c_s. MPS find that it is conceivable that the second 'hole' term in equation (5.9) may vanish. In this situation, either $\chi^c_{d\text{-}s}$ must equal zero or $A^c \cong -4B$, for $K^c_s=0$. Since $\chi^c_{d\text{-}s}$ is not zero in the normal state, it seems unlikely that it is zero over all temperatures and so one must conclude that the latter statement is true. However, there are two domains: that of the uncorrelated spin and that of the antiferromagnetically-correlated spin. MPS find good agreement with the experimental data if the d-spins are strongly A.F. correlated.

After a detailed study, MPS conclude that the Cu(2) T_1 anistropy and Knight shift may be understood in either of two regimes. Firstly, if the oxygen holes play no part (i.e. $A^{\alpha} \cong -4B$) and a single band theory (in which there is a large transferred hyperfine interaction ($4B=32.0T$)[48]) is applicable, then there must be strong antiferromagnetic correlations at the nearest neighbour Cu sites. Secondly, if the orientations of the d-spins of neighbouring Cu(2)'s are not correlated, then the shift must have two components, one from the $Cu(2)^{2+}$ spin excitations and one from oxygen holes.

It is important to note that, although MPS could fit the Takigawa data for the Cu(2) Knight shifts using their model, they were unable to find a satisfactory explanation for the Cu(1) data.

Finally, WW take the Barrett shift data and analyse it using the single component model of Mila and Rice. The results they obtain for the hyperfine couplings and component susceptibilities differ in only minor ways to those deduced by MR with the use of the Takigawa data.

With these models in mind, we can now summarise the general findings of this NMR study, starting with the demagnetisation corrections. The fact that our Takigawa-corrected orbital shifts are very similar to the corresponding Takigawa results, first of all suggests that the extrapolation of the Takigawa magnetisation data M to higher fields incurrs negligible error. Secondly, it indicates that the spurious upturn in the c//B Takigawa components is due to some intrinsic function of the c//B demagnetisation correction. We deduce this because our $K^c_{orb}(1,2)$ values are particularly dependent on the demagnetisation correction used.

It is quite clear that, at our high fields, the size of the c⊥B internal field correction, as deduced from the individual studies of Barrett and Takigawa, is not an issue. Both of these studies indicate similar c⊥B demagnetisation factors which, when used in conjunction with the experimental data, produce a range of rather inconsistent values for the orbital shift components $K^{a,b}_{orb}(1,2)$. Clearly, the important factor which dominates at this orientation is the large uncertainty incurred in deducing peak positions from the c⊥B restricted powder pattern. The fundamental problems underlying the derivation of the peak positions from the restricted powder pattern have been recognised by Walstedt et al[54]. In a recent study, Walstedt et al refuse to use experimental data to determine $K^{a,b}_{s}(1)$ claiming that it is too inaccurate. Instead they deduce these shifts from the anisotropy in the susceptibility data.

A glance at both the orbital and spin shifts in tables 5.3 and 5.4 shows that the $K^{b}(1)$ components are by far the most inaccurate results obtained from this study. The most consistent component derived from the c⊥B spectrum is evidently $K^{a}(1)$. For Cu(1), it is highly likely that the invariably large value obtained for the $K^{b}_{orb}(1)$ component is the cause of the low $K^{a}_{orb}(1)/K^{b}_{orb}(1)$ ratio obtained in equation (5.5) (c) and (d). If the $K^{b}_{orb}(1)$ value were the same as the $K^{c}_{orb}(1)$ result, as anticipated from the symmetry of the EFG and relaxation data, the corresponding ratios would confirm an ionic Cu^{2+} model. A similar case can be made for the Cu(2) site, where the $K^{a}_{orb}(2)= K^{b}_{orb}(2)$ is consistently smaller.

For data obtained from the c//B spectra the reverse appears to be true. The fact that our Takigawa-corrected components ($K^{c}_{orb}(1,2)$) correspond with the Takigawa results, while the Barrett-corrected components coincide with the Barrett data, indicates that the raw experimental information, acquired from each study, scales very well. This is because the pseudo single crystal-like situation which occurs for c//B is expected to result in a well-defined spectrum. Instead, in this case, the disparity in results between Takigawa and Barrett can be traced to the large difference in the demagnetisation corrections obtained for the c//B orientation.

Most importantly, a comparison of our very low temperature results with the magnitude of the extrapolated Takigawa and Barrett $K^{\alpha}_{orb}(1,2)$ shifts confirms that the K^{α}_{s} components do vanish at zero, for both sites and in all directions, leaving the orbital shift as the residual shift. This is indicative of singlet spin pairing.

Taking into account all the NMR data available, it would seem that that the Knight shift results of this work and the results of both Takigawa et al and Barrett et al can best be explained using an extended ionic permanent moment model of one form or another.

---

54 R. E. Walstedt, R. F. Bell, L. F. Shneemeyer, J. V. Waszczak & G. P. Espinosa, *Phys. Rev. B* **45** 8074 (1992)

Qualitatively, we can say that our Takigawa-corrected data for Cu(2) can be explained using the single component model of Mila and Rice*. Because the results are so similar, we anticipate that the hyperfine couplings and susceptibility components will be virtually identical to those calculated by MR. We will not repeat the data here. Although our Cu(1) orbital shifts are consistent with the MR model, it is unlikely that this is the case for the corresponding spin shifts, as the $K^b_s(1)$ value seems so inaccurate. A similar situation is apparent for the Barrett corrected data. From the findings of Monien, Pines and Slichter, we can expect that the Takigawa-corrected and Barrett-corrected results for Cu(2) can be explained by the MPS model. This is evidently not the case for Cu(1), since the MPS model relies on the isotropy of the Cu(1) spin shift and requires that the orbital shift be axially symmetric about the a-axis. Neither of these conditions are satisfied by our Cu(1) data.

A final point which should be made concerns the application of the demagnetisation and the orbital shift data in a wider sphere. In recent studies on the 60K material, both Takigawa et al[55] and Walstedt et al[56] use the orbital shift components, obtained by Barrett et al on the $YBCO_7$ (T=93K) material, to calculate the corresponding spin Knight shift components from their total shift data. Two conclusions can be drawn from these studies: firstly, they show that the orbital shift components, along with the corresponding demagnetisation corrections, are expected to be the same for all superconducting compositions of $YBCO_{7-\delta}$ ($0 \leq \delta \leq 0.65$). Secondly, they show, along with a number of other studies, that researchers (including Takigawa et al) accept that the Barrett et al derivation of the normal state Knight shifts is the correct one.

---

* This model has been updated somewhat by Walstedt et al, ref. 54. Using more accurate normal state Knight shift data and the low temperature orbital shifts of Barrett et al[27], they are able to remove the restriction that the Cu(1) and Cu(2) site spin susceptibilities are equal and isotropic.

55 M. Takigawa, A. P. Reyes, P. C. Hammel, J. D. Thompson, R. H. Heffner, Z. Fisk & K. C. Ott, *Phys. Rev. B* **43** 247 (1991)

56 R. E. Walstedt, W. W. Warren Jr., R. F. Bell, R. J. Cava, G. P. Espinosa, L. F. Shneemeyer & J. V. Waszczak, *Phys. Rev. B* **41** 9574 (1990)

Chapter 6

Results of the Co-Doped Y-Ba-Cu-O System

6.1 Sample Characterisation

Detailed investigations[1,2,3,4,5,6] on four out of the ten Co-doped YBCO powder samples were performed at the IRC in Cambridge, prior to magnetic alignment. The T_c's of the remaining six samples were also measured, but further analysis of these specimens by the IRC was suspended, due to uncertainties in sample purity. Some of the raw data obtained from the characterisation of the second batch of samples has been included in appendix B for reference.

6.1.1 T_c Measurements & Structural Analysis

Figure 6.1 shows the variation of the superconducting transition temperature T_c of $YBa_2(Cu_{1-x}Co_x)_3O_{7-\delta}$ as a function of cobalt concentration in atomic %. The T_c's for the four higher concentration samples have been determined inductively, resistively[4] (at the midpoint of the resistive transition curve) and via specific heat methods[2], while those for the lower atomic % samples were determined from inductance measurements alone (labelled 'a.c. susceptibility' in figure 6.1).

In the region x%<3, the T_c is either (i) almost insensitive to Co substitution (as established by a.c. susceptibility measurements) or (ii) shows a small increase, up to an x value of between 1% and 3%, depending on the method used to obtain the critical temperature. For x%>3, T_c decreases rapidly for all methods of determination, with an

---

1 W. W. Schmahl, A. Putnis, E. Salje, P. A. Freeman, A. Graeme-Barber, R. Jones, K. K. Singh, J. Blunt, P. P. Edwards, J. Loram & K. Mirza, *Philos. Mag. Lett.* **60** 241 (1989)

2 J. W. Loram, K. A. Mirza, P. A. Freeman & J. J. Tallon, *Supercond. Sci Technol.* **4** S184 (1990)

3 F. J. Blunt, A. M. Campbell, P. P. Edwards, J. E. Evetts, P. A. Freeman, J. Johnson, J. W. Loram, K. A. Mirza, A. Putnis, E. Salje & W. W. Schmahl, *Physica C* **162-164** 1605 (1989)

4 A. Porch, J. R. Cooper, H. M. Cheah, J. S. Edmends & J. R. Waldram, *Physica B* **165-166** 1199 (1990)

5 J. R. Cooper, *Supercond. Sci. Technol.* **4** S181 (1990)

6 H. S. Obhi & E. K. L. Salje, *Physica C* **171** 547 (1990)

approximately linear dependence on x of $dT_c(\rho)/dx = -6.9 \times 10^2$ K/Co ion per Cu site, where $T_c(\rho)$ is the transition temperature established from the restivity data. This value compares well with that of -6.0×10^2 K/Co ion per Cu site, obtained by Aoki et al[7] and -7×10^2 K/Co ion per Cu site deduced by Langen et al[8].

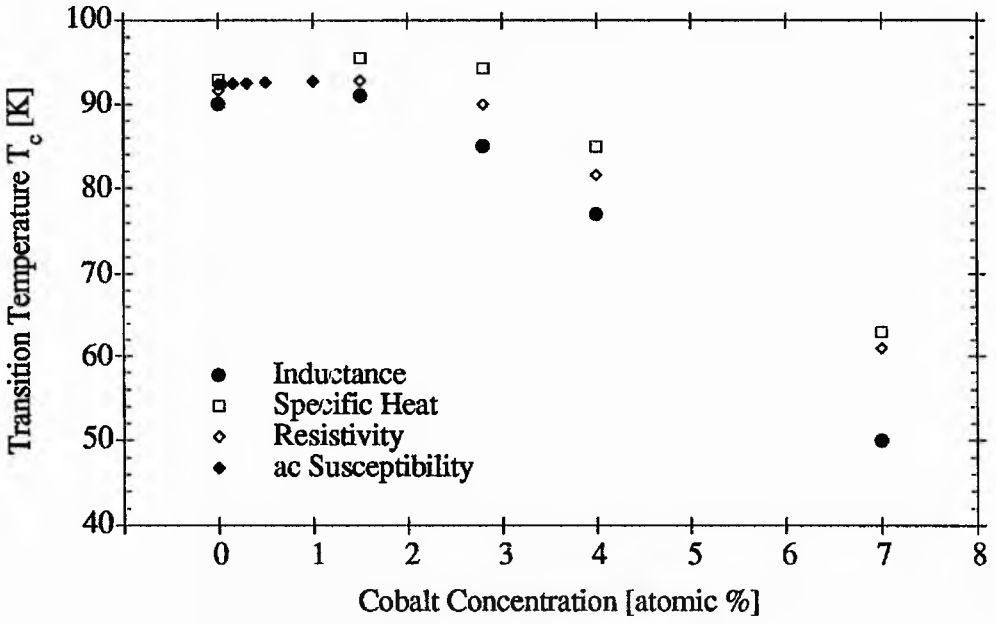

Figure 6.1

The variation of T_c with cobalt concentration. The resistivity data is taken at the midpoint of the transition. Note that for the lower Co concentrations only one method has been used to obtain the T_c data. (Data courtesy of J. R. Cooper & P. A. Freeman, IRC, Cambridge)

A study of the Co concentration dependence of the macroscopic lattice parameters reveals that, in this system, the macroscopic orthorhombic to tetragonal transition occurs at $x_c\% \approx 2.8$ (see figure 6.2)[1]. It appears therefore that the characteristic change in T_c observed at x%~3 coincides with the macroscopic orthorhombic to tetragonal structural transition at $x_c\% \approx 2.8$. Similar T_c behaviour has been observed in a number of studies[7,8,9,10] and in each case the dramatic drop in T_c has been linked to the structural

---

7 R. Aoki, S. Takahashi, H. Murakami, T. Nakamura, T. Nakamura, Y. Takagi & R. Liang, *Physica C* **156** 405 (1988)

8 J. Langen, M. Veit, M. Galffy, H. D. Jostarndt, A. Erle, S. Blumenröer, H. Schmidt & E. Zirngiebl, *Solid State Comm.* **65** 973 (1988)

9 J. M. Tarascon, P. Barboux, P. F. Miceli, L. H. Greene, G. W. Hull, M. Eibschutz & S. A. Sunshine, *Phys. Rev. B* **37** 7458 (1988)

transformation, bought about by the disordering of the O(1) oxygens into the O(5) site as the Co tries to achieve its preferred octahedral coordination.

Doping with non-magnetic Ga and Al also results in a rapid decrease in T_c at concentrations beyond x_c, but the suppression is less pronounced than with the magnetic Co ion (see figure 2.5). It is therefore tempting to suggest that small magnetic pair-breaking effects may contribute to the excess degradation of T_c observed in the Co doped material. The reduction of T_c cannot, however, be explained by magnetic pair-breaking alone, since Fe and Co doping have similar effects on both the resistivity and T_c data, and yet the magnetic moment of the Fe ion is considerably larger (~5μ_B) than the moment of the Co ion (~3.7μ_B).

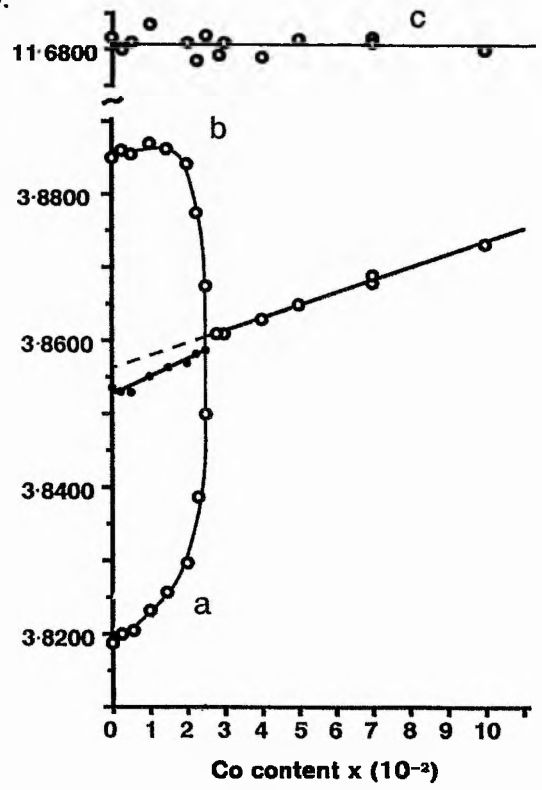

Figure 6.2

Variation of the macroscopic lattice parameters of $YBa_2(Cu_{1-x}Co_x)_3O_{7-\delta}$ as a function of Co content x - as determined by X-ray powder diffraction[1] at 295K.

Figure 6.2 shows the variation of the lattice parameters of $YBa_2(Cu_{1-x}Co_x)_3O_{7-\delta}$ as a function of x. Despite the fact that increasing Co-concentration in the region $x>x_c$ produces a definite linear increase in the lattice parameter a, no significant change is detected in the c lattice parameter over the entire concentration range studied. These

[10] J. F. Bringley, T. M. Chen, B. A. Averill. K. M. Wong & S. J. Poon, *Phys. Rev. B* **38** 2432 (1988)

results imply that with increasing x, the oxygen content of the system varies only slightly from the value of 6.9 (δ=0.1) determined for the x=0 sample. In fact, at x%=2.8 the oxygen content is still found[11] to be at 6.9. By a Co concentration level of x%=10, the oxygen content of the system has decreased to 6.8.

It should be noted that additional information gained from transmission electron micrographs of these samples suggests that an orthorhombic microdomain structure extends well into the macroscopically 'tetragonal' region of the phase diagram[1].

6.1.2 Normal State Magnetic Susceptibility

In order to investigate the magnetic character of the Co substituted YBCO system, normal state magnetic susceptibility measurements were taken on sintered powder samples using a Quantum Design SQUID magnetometer, from just below T_c to 330K in fields of 5T. The resulting Curie plots for the higher Co concentration samples are shown in figure 6.3.

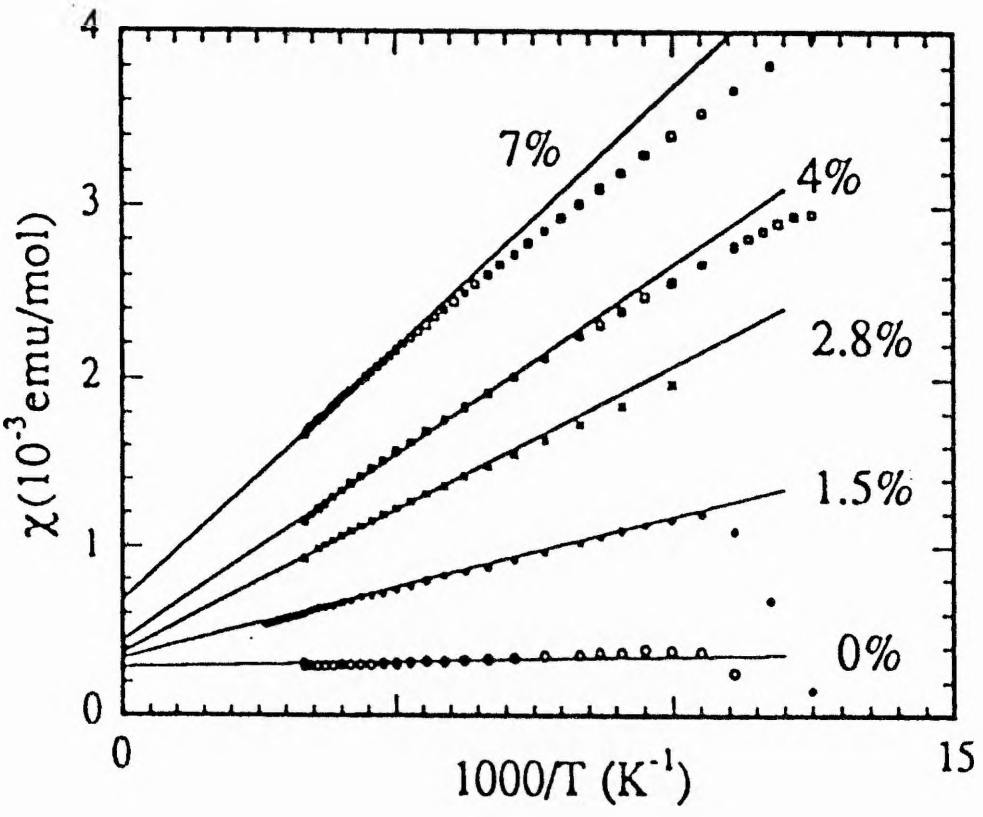

Figure 6.3

Curie plots showing the temperature dependence of the magnetic susceptibility χ(T) of five Co doped YBCO samples, with dopant levels ranging from 0 to 7 atomic %[5,11].

---

[11] A. Carrington, A. P. Mackenzie, C. T. Lin & J. R. Cooper (unpublished).

For the pure YBCO sample with x=0, the macroscopic susceptibility $\chi(T)$ remains almost temperature independent over the range studied. This is in good agreement with reports from other research groups and indicates that the oxygen stoichiometry of the sample is near O_7 - since only full stoichiometric samples with $\delta=0$ show an absolute temperature independent susceptibility.[7,12,13,14,15] The insensitivity of a positive magnetic susceptibility to temperature is typical of metallic systems, where the conduction electrons are considered essentially to be free and non-localised. The magnetic susceptibility data therefore seems to suggest that localised models cannot be used for the 3d electrons of the Cu ion in $YBa_2Cu_3O_7$.

With the addition of Co, all samples show a paramagnetic susceptibility dependence which characteristically decreases with increasing temperature. The $\chi(T)$ data of figure 6.3 can be fitted to the Curie law expression

$$\chi(x,T) = \chi_0(x) + \frac{C(x)}{T} \qquad (6.1)$$

where $\chi_0(x)$ is the temperature independent susceptibility (i.e. the contributions from the weak Pauli spin paramagnetism of the metallic conduction-band electrons and the atomic diamagnetism†) and C(x) is the Curie constant. Note that a reasonable fit to (6.1) is obtained only down to temperatures of 10 to 20% higher than the zero-field value of T_c. Data below the point where the beginning of the transition to the superconducting state leads to a deviation from the Curie law, was not taken into account. The values of C and χ_0 obtained from the $\chi(T)$ data are illustrated as a function of Co concentration (atomic %) in figure 6.4.

The temperature independent susceptibility χ_0 can be seen to increase substantially with Co concentration. By a concentration level of 4%, the increase in χ_0 is almost equal to the total measured susceptibility of the pure YBCO sample. At this stage, the origin of the extra χ_0 introduced by doping is unclear, though it has been speculated that it may be distributed between the planes and the chains. For confirmation of this supposition, we

---

12 Y. C. Yang, Y. B. Zha, W. C. Yuan, J. Lan, Z. X. Lui, G. Z. Li & Y. X. Sun, *Journal de Physique*, supplement 12, **49** C8-2201 (1988)

13 S. W. Cheong, S. E. Brown, Z. Fisk, R. S. Kwok, J. D. Thompson, E. Zirngiebl, G. Gruner, D. E. Peterson, G. L. Wells, R. B. Schwarz & J. R. Cooper, *Phys. Rev. B* **36** 3913 (1987)

14 T. R. McGuire, T. R. Dinger, P. J. P. Freitas, W. J. Gallagher, T. S. Plaskett, R. L. Sandstrom & T. M. Shaw, *Phys. Rev. B* **36** 4032 (1987)

15 H. Theuss & H. Kronmüller, *Physica C* **178** 37 (1991)

† The total orbital diamagnetism of the composing ions is generally estimated at -0.19×10^{-3} emu/unit cell.

turn later to the microscopic probe of NMR. It should be noted, however, that similar results have been obtained by Yamada et al[16]. These results are also plotted in figure 6.4, for comparison.

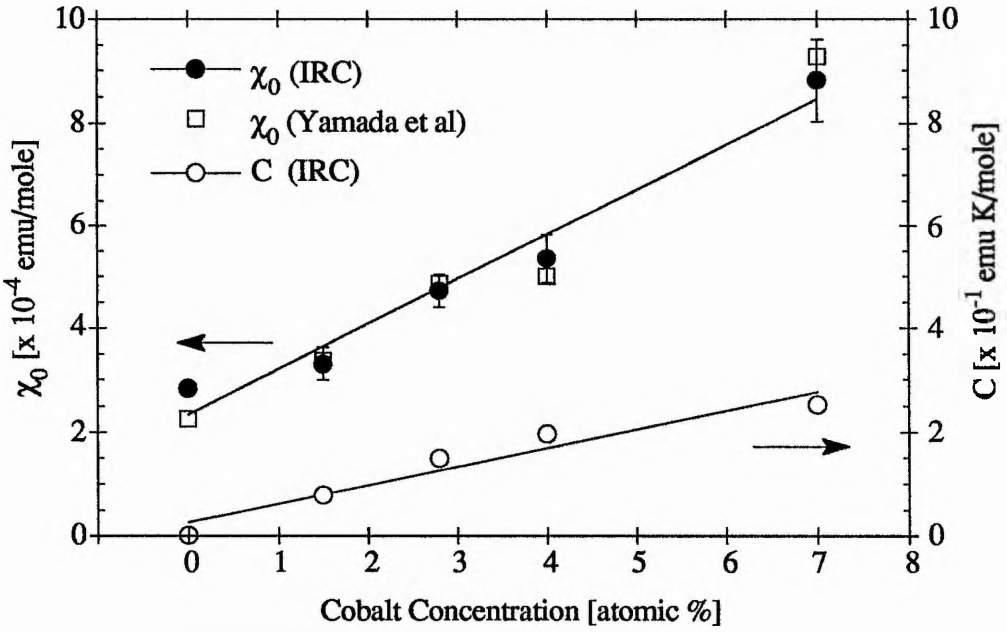

Figure 6.4

Cobalt concentration dependence of the temperature independent paramagnetic susceptibility term χ_0 (with an IRC quoted error of ± 3%) and the Curie constant C. Lines are a guide to the eye only.
(IRC data evaluated from figure 6.3. Other data adapted from Yamada et al[16]).

The Curie constant is a measure of the effective magnetic moment on each ion site. Here, it is found to increase linearly with cobalt concentration, at least up to x%=4, suggesting that the temperature dependent Curie paramagnetism comes from the substituted Co ions and from any effects induced on the host lattice as a result of the substitution. If the density of magnetic atoms/ions (N) responsible for the Curie paramagnetism in the crystal is known, then the effective magnetic moment (in units of the Bohr magneton, μ_B) per Co ion P_{eff} can be evaluated from the relation

$$C = \frac{N P_{eff}^2 \mu_B^2}{3 k_B} \qquad (6.2)$$

16 Y. Yamada, Y. Oda, N. Kawaji, H. Yamagata & K. Asayama, *J. Phys. Soc. Jpn.* **58** 3053 (1989)

where k_B is the Boltzmann constant. The values of P_{eff} computed from the C vs. Co% data are presented in figure 6.5. Again the results of Yamada et al[16] are included for comparison.

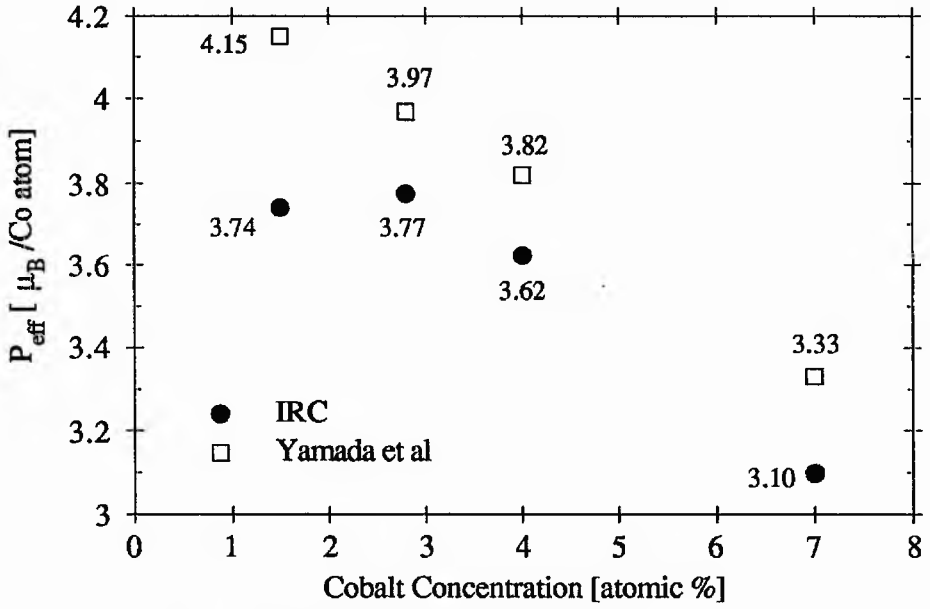

Figure 6.5

Dependence of the effective magnetic moment per Co ion (in units of μ_B)* P_{eff} on the Co concentration of $YBa_2(Cu_{1-x}Co_x)_3O_{7-\delta}$.
(Error is ± 0.20 μ_B per Co atom)

Although the absolute values of P_{eff} do not coincide with those of Yamada, quantitatively the fall in P_{eff} with increasing Co concentration compares well in the region x%≥2.8†. The P_{eff} calculated for the 1.5% sample seems to be anomalous, since other researchers[7] obtain a value similar to that of Yamada. Magnetic susceptibility has proven notoriously difficult to measure with any accuracy in these materials, as even minute amounts of spurious phases can produce anomalous Curie contributions, especially at low temperatures[17]. In fact, it has been shown that the two most common impurity phases, $BaCuO_2$ and Y_2BaCuO_5, produce strong Curie-Weiss behaviour[18].

Note that while the T_c is unaffected or enhanced in the region 0≤x%≤3, a substituted Co ion induces a magnetic moment of around 3.7 ± 0.2 Bohr magnetons.

---

* Also known as the effective Bohr magneton number.

† i.e $dP_{eff}/dx=-16.1\mu_B/Co^2$ for the IRC data and $-15.2\mu_B/Co^2$ for the Yamada data

17 W. C. Lee & D. C. Johnson, *Phys. Rev. B* **41** 1904 (1990)

18 A. J. Twin, J. S. Abell & I. R. Harris, *Jnl. Less Comm. Metals* **164 & 165** 1136 (1990)

Generally, the magnetic moment in Bohr magnetons is defined as

$$P_{eff} = g\sqrt{J(J+1)} \tag{6.3}$$

where, for a free atom, the g factor is given by the Landé g equation,

$$g = 1 + \frac{J(J+1) + S(S+1) - L(L+1)}{2J(J+1)} \tag{6.4}$$

However, in transition metal ions such as Cu and Co, the ground state is found to be very different from that of a free ion. Since the 3d electron shell responsible for producing the magnetic moment in a transition metal ion is the outermost shell, there is a strong interaction between the 3d shell and the inhomogeneous crystal (electric) field produced by neighbouring ions in the crystal. As a result, the orbital angular momentum of the electrons in the 3d shell is 'quenched' and the net value of L falls to zero. Therefore, in the case of the Cu and Co ion, J=S and equations (6.3) and (6.4) reduce to

$$P_{eff} = 2\sqrt{S(S+1)} \tag{6.5}$$

Table 6.1 presents the calculated effective magnetic moments for various isolated Cu and Co ions. Comparisons with the experimental value are given, where available.

Ion	Configuration	Basic Level	P_{eff} (calc) $=g\sqrt{J(J+1)}$	P_{eff} (calc) $=2\sqrt{S(S+1)}$	Measured moment (salt)
Co^{+}	$3d^8$	$^3F_4$	5.59	2.83	-
Co^{2+}	$3d^7$	$^4F_{9/2}$	6.63	3.87	4.8
Co^{3+}	$3d^6$	$^5D_4$	6.71	4.89	-
Cu^{2+}	$3d^9$	$^2D_{5/2}$	3.55	1.73	1.9
Cu^{3+}	$3d^8$	$^3F_4$	5.59	2.83	-

Table 6.1

Effective magnetic moments for isolated Cobalt & Copper ions in units of Bohr magnetons. The basic level notation is $^{2S+1}X_J$, where X = S, P, D, F etc. corresponds to L = 0, 1, 2, 3 etc.

Evidently, the magnetic moments P_{eff} obtained from our results (figure 6.5) are more consistent with the spin only value expected for Co^{2+} ($3.87\mu_B$) than for Co^{3+} ($4.89\mu_B$). This is in direct opposition to other measurements, such as specific heat[2], which indicate the existence of a Co^{3+} ion. Can these P_{eff} results be explained on the basis that a Co^{3+} ion is present ?

Cobalt is usually stabilised in the high spin Co^{3+} state (S=2, $P_{eff}=4.89\mu_B$) by octahedrally coordinating with six oxygen ligands. However, when substituted into the Cu(1) site of the orthorhombic YBCO structure, the Co ion is forced to occupy a four ligand coordination in square-planar symmetry. Generally, this symmetry corresponds to the Co^{3+} low spin state, where S=1 and $P_{eff}=2.8\mu_B$. As x increases, the substituted Co ion tends to the stable octahedral Co^{3+} state by introducing extra oxygen into the ligand sites. After the orthorhombic to tetragonal transition, the Co ion at the Cu(1) site is octahedrally coordinated with six oxygen ligands.

At lower concentrations, the P_{eff} values estimated from experiment (~$3.7\mu_B$) are almost exactly between the two values expected for high spin ($4.89\mu_B$) and low spin ($2.8\mu_B$) Co^{3+}. As the Co concentration increases, the P_{eff} tends towards the Co^{3+} low spin value. A similar trend is observed in both the Yamada and Aoki results, although the absolute values of P_{eff} are slightly larger (the values of Yamada are just within the error of our values, for most concentrations). This possibly indicates that the low P_{eff} values obtained for our samples are a result of weak Curie contributions due to a lower Co ion concentration than that calculated during synthesis. The trend in all these results appears to contradict the fact that the Co(1) site is octahedrally coordinated in the tetragonal structure, and therefore should have P_{eff} value which reflects the high spin Co^{3+} state. Thus, if we still insist that the Co ion is in the 3+ state, then we must look towards an additional mechanism, such as magnetic superexchange and spin ordering, or an intermediate spin state to explain the P_{eff} results.

6.1.3 Hall Effect Measurements

The Hall effect measurements taken on the higher concentration samples have been included here for completeness. However, the results may be unreliable due to some sample contamination which may have occured during the specific heat experiments†. Resistivity data, taken after the Hall effect measurements, revealed that the 4% and possibly the 1.5% samples had been contaminated by oil, used to suspend the samples during the specific heat experiments. The 2.8% and 7% samples did not appear to be contaminated by the process.

† Note that all the data presented in the previous sections was taken on the uncontaminated samples, before the specific heat experiments were performed.

Figure 6.6 shows the Hall number, n_H (defined as $V_{cell}/R_H e$) as a function of temperature T.

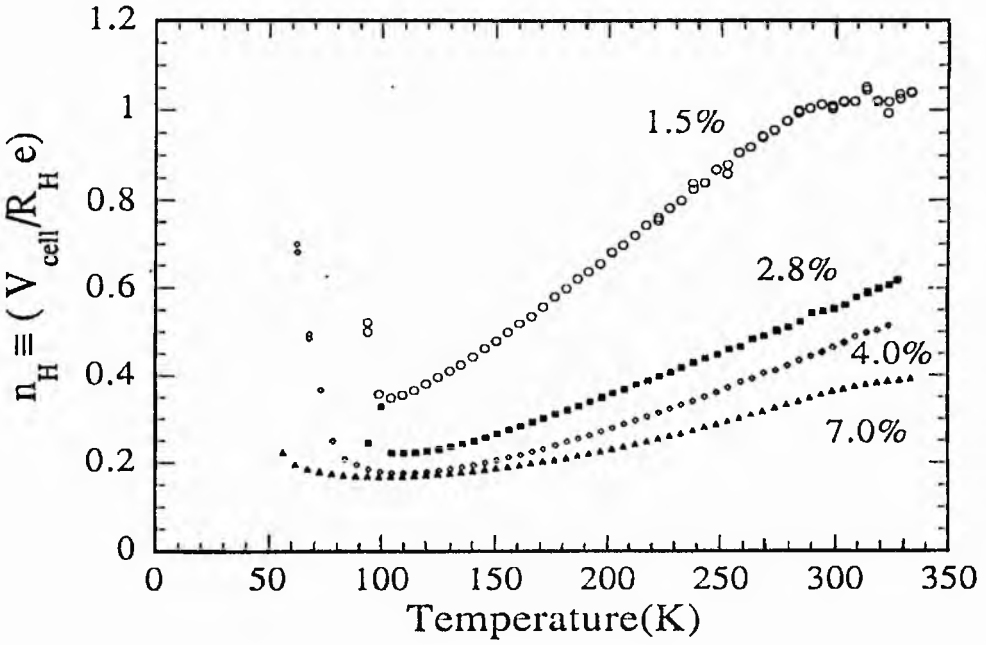

Figure 6.6

Variation of Hall number n_H per unit cell with temperature in $YBa_2(Cu_{1-x}Co_x)_3O_{7-\delta}$, where x=0.015, 0.028, 0.04 & 0.07 (Data courtesy of J. R. Cooper & A. Carrington).

In the range $100 \leq T \leq 300K$, the Hall number for the 1.5% sample has a strong, almost linear T dependence. The absolute data values and the average slope, $dn_H/dT=3.25 \times 10^{-3}$ $n_H V/K$, are found to compare well with those obtained by Clayhold et al[19] for a 1.66% Co doped sample (where $dn_H/dT=3.7 \times 10^{-3}$ $n_H V_{cell}/K$). As the superconductivity is suppressed by increasing Co concentration, the average slope decreases, until at 7% the value of dn_H/dT is equal to 1.0×10^{-3} $n_H V_{cell}/K$. Here, for a similar sample with 6.66% Co doping, Clayhold et al obtain an average slope of 0.4×10^{-3} $n_H V_{cell}/K$ from absolute n_H values which are about half the magnitude of our measurements.

Due to its strong temperature dependence in the lower concentration samples, n_H cannot be strictly identified with the carrier concentration, n. This renders a quantitative analysis of the Hall data, in terms of effective carrier concentrations, rather meaningless. However, a qualitative interpretation of the results suggests that there is a fall in the total number of itinerant holes in the system as the Co concentration rises. Since the

---

[19] J. Clayhold, N. P. Ong, Z. Z. Wang, J. M. Tarascon & P. Barboux, *Phys Rev B* **39** 7324 (1989)

temperature dependence of the Hall number falls with the suppression of superconductivity (the T_c decreases from ~90K to ~50K over the concentration range studied), the strong temperature dependence may arise from anomalous Hall currents associated with the carriers responsible for superconductivity.

6.1.4 X-Ray Analysis of Powder & Aligned Samples

An additional X-ray powder diffraction analysis was used to characterise all of the powder samples, prior to magnetic alignment. The [hkl] peaks were identified by comparing the experimental values of 2θ with computer generated tables of 'theoretical' 2θ values (see appendix C.1), calculated using equations (4.1) and (4.2). All spectra could be indexed according to the orthorhombic/tetragonal space group expected for YBCO and its cobalt-doped derivative.

Figure 6.7(a) shows the X-ray powder spectrum for the 0.3% Co doped sample. This spectrum is typical of all of the powder samples studied and shows no evidence of any impurity phases[20]. Even the spectrum for the 0.5% sample (see figure 6.7(d)), which is thought to be contaminated by glass[21] and which exhibits anomalous features (at around 60K) in the a.c. susceptibility curve (see appendix B), shows no impurity peaks.

As the structure changes with increasing Co concentration, slight variations are observed in the [013], [116/123] and [213] reflections. In the 0% spectrum (see figure 5.1), the [013] and [110/103] peaks are distinct and do not overlap. This is indicative of an orthorhombic structure in which 3a≠c. With increasing x, the [013] and [110/103] peaks begin to merge, until at 1.5% Co there is complete overlap – signifying that the orthorhombic structure now has a c-axis equivalent to 3a. The orthorhombic to tetragonal transition is accompanied by an overlap of the [116/123] and [213] peaks. As Co content rises, the peak intensity of the [116/123] peak becomes weaker, while the peak intensity of the [213] peak gets stronger. This produces an intensity inversion between the two peaks at Co concentrations near to the orthorhombic to tetragonal transition. The two reflections eventually merge into single peak in the tetragonal phase, as can be seen in the X-ray powder spectrum of the tetragonal 4% Co doped sample, which is included as figure 6.7(c).

---

[20] Note that the XRD patterns for all known impurity phases in YBCO have have been calculated and systematically catalogued by A. M. T. Bell, see *Supercond. Sci. Technol.* **3** 55 (1990)

[21] P. A. Freeman, *private communication.*

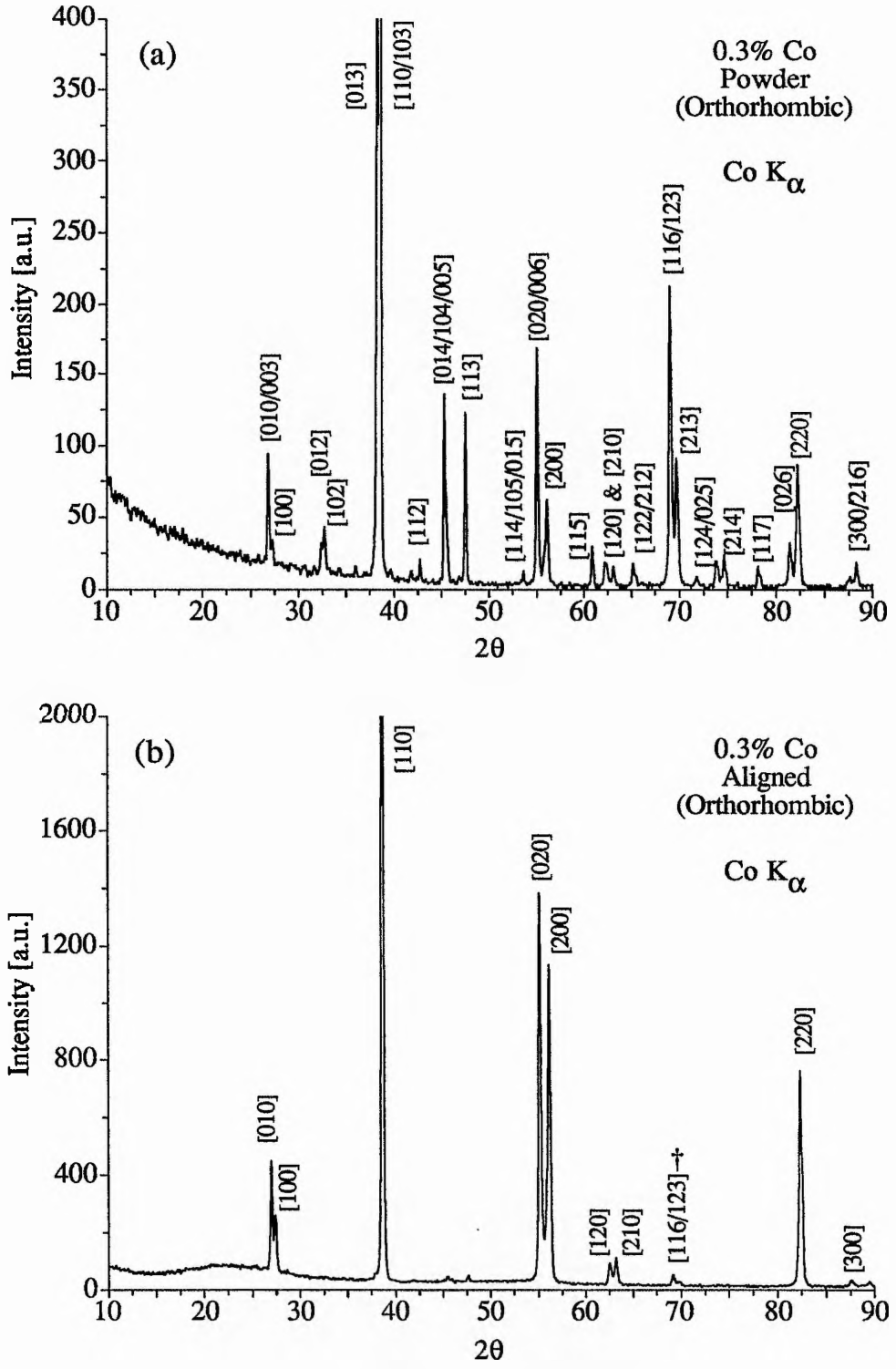

Figures 6.7 (a) & (b)

X-ray Spectra of the (a) 0.3% Co doped YBCO powder and (b) aligned 0.3% Co doped sample, with c-axis in the plane perpendicular to the incident X-rays. Note that (i) the [110] peaks have been truncated to half of their full intensity and (ii) the peaks indicative of unaligned powder are labelled with †.

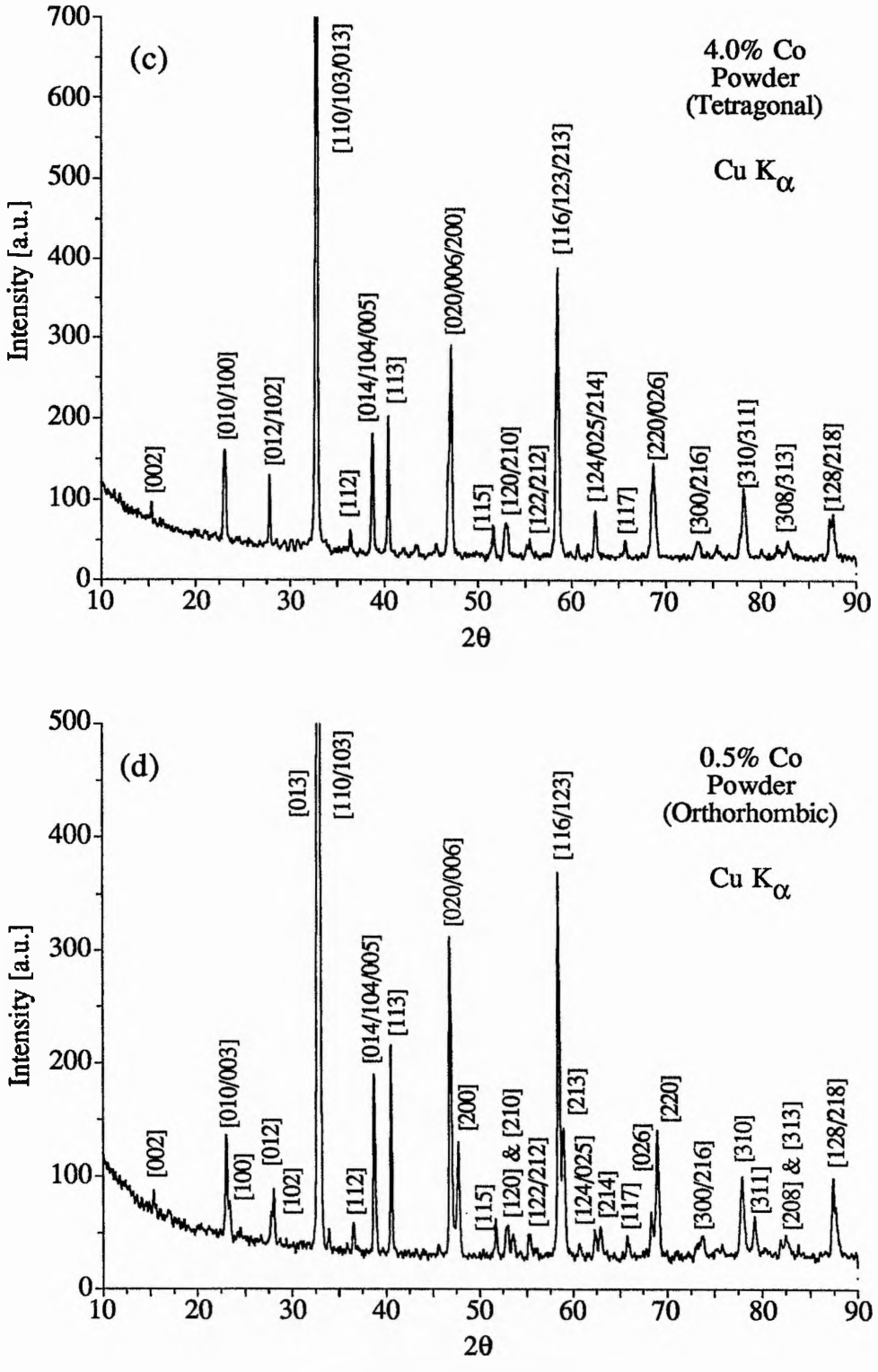

Figures 6.7 (c) & (d)

X-ray Spectra of the (c) 4% Co doped YBCO powder and (d) 0.5% Co doped YBCO powder samples. The [110] peaks have again been truncated to half of their full intensity.

In order to deduce the crystal lattice parameter a from the powder X-ray results, the sin θ values for the [h00] reflections were plotted against h (or equivalently n = 1, 2, 3 etc. in equation (4.1)). From this graph, the gradient (λ/2d) gives the d-spacing, which, in this case, is equivalent to the lattice constant a. Similar sinθ vs. k and sinθ vs. l plots allow the values of the b and c lattice parameters to be calculated from the [0k0] and [00l] reflections, respectively. On occasions, there were too few reflections to produce a reliable result and so other [hkl] reflections were included in the determination of the lattice parameter. Figure 6.8 presents the cobalt concentration dependence of the lattice parameters a, b and c, as determined from the X-ray analysis performed in St. Andrews.

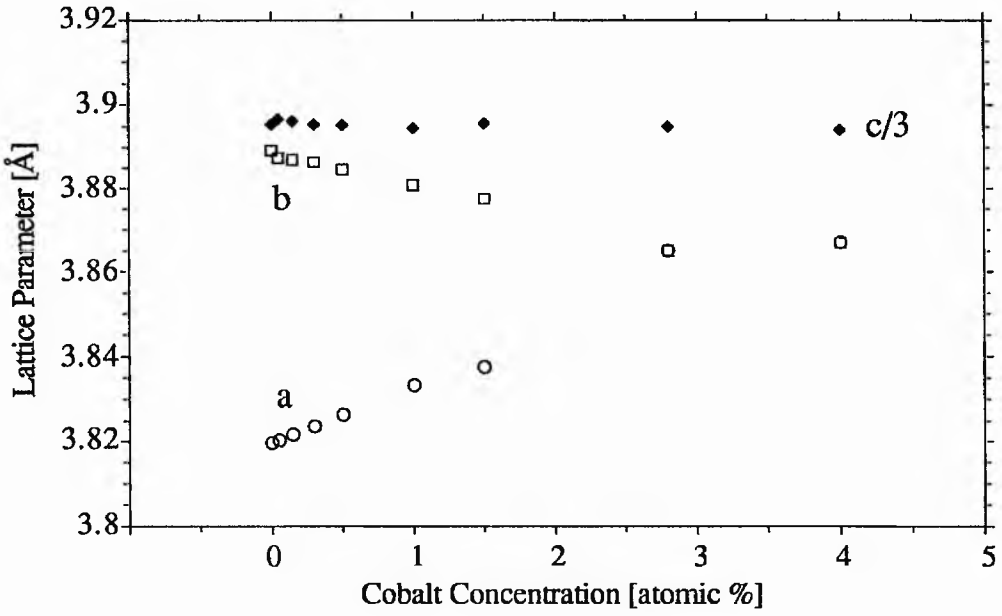

Figure 6.8

Variation of macroscopic lattice parameters of $YBa_2(Cu_{1-x}Co_x)_3O_{7-\delta}$ as a function of Co concentration, as deduced from X-ray powder diffraction experiments performed at room temperature.

The results of the analysis are very similar to those obtained by the IRC in figure 6.2†. The c lattice parameter fluctuates around the 11.68 Å (c/3=3.893 Å) level and is not appreciably affected by the increase in Co concentration. The a and b lattice parameters increase and decrease respectively with increased doping, until at 2.8% the two parameters are equal (~3.865Å). Evidently, this suggests that the orthorhombic to

† Note that in order to obtain the lattice parameters at the lower Co concentrations (figure 6.2), the IRC used a completely different batch of samples to those used here. Although X-ray spectra were taken (see appendix B), no detailed structural analysis was performed by the IRC on the lower concentration samples used in this work.

tetragonal transition occurs at x%≤2.8. There are signs that the a lattice constant is beginning to increase as the dopant level rises beyond 2.8%.

In order to determine the degree of c-axis alignment in the epoxy set (10mm) samples, an X-ray analysis was performed on a small specimen disc, placed in the plane perpendicular to the incident X-rays. Figure 6.7(b) shows the X-ray spectrum of the aligned 0.3% sample. A comparison with figure 6.7(a) reveals that all the [hk0] reflections present in the powder spectrum are still present in the aligned sample spectrum, and are in fact enhanced, as would be expected. All the peaks with l≠0 are absent, except for a small stray peak (labelled †), which appears at 2θ=69.059° and can be indexed as [116/123]. Such a peak is indicative of some unaligned powder.

Similar spectra were obtained for the other samples studied. With the exception of the 0.5% sample, the alignment of the second batch of samples (0% to 1% Co) was considerably better than that of the first batch (1.5% to 4% Co). A more quantitative evaluation of the degree of alignment can be estimated using the parameters in table 6.2.

Co Content (%)	No. of l=0 Peaks	Average Peak Enhancement	Stray l≠0 peaks	Net Stray Peak Height	Degree of alignment
0	7	4.50	–	–	95%
0.05	6	11.0	–	–	96%
0.15	7	3.10	[116/123]	2	93%
0.30	8	8.80	[116/123]	0.5	97%
0.50	5	3.65	[005/014/104] [116/123] [213]	2 4 2	83%
1.00	7	12.0	–	–	98%
1.50	5	3.50	[102] [005/014/104] [113] [116/123]	8 15 12 27	77%
2.80	4	3.80	[102] [005/014/104] [113] [201] [116/123]	5 7 9 9 32	75%
4.00	5	3.50	[005/014/104] [111] [116/123]	3 7 4	82%

Table 6.2

Summary of information obtained from the X-ray spectra of the epoxy set uniaxially aligned Co-doped YBCO samples. The net stray peak height is measured as a percentage of the [110] peak height.

The information in columns 2 to 5 was deduced directly from the X-ray spectra. Note that in cases where peaks appeared with l≠0, the [116/123] peak was always present. In the 1.5% and 2.8% samples, the l≠0 stray peaks were sizeable, but more often such peaks were only just visible above the noise of the spectrum.

An attempt to *calculate* the degree of alignment using the peak intensity methods suggested by Lusnikov et al[22], only led to inconsistent answers. Such results cast a doubt on the validity of Lusnikov's assumptions. Instead, an *estimate* of the degree of c-axis alignment was made, based on the enhancement of the l=0 peaks and the number and intensity of stray (l≠0) peaks which appeared in each spectrum (see table 6.2).

Generally, a powder alignment is considered a reasonable success if at least 75-80% of the powder is aligned. As Co concentration increases beyond 1%, the degree of alignment appears to decrease. This may be due to the effects of the added dopant or may be a result of the alignment techniques used on the first batch of powders. Since the 0.5% sample was aligned at the same time as the other well-aligned low Co% samples, the relatively poor alignment of the 0.5% sample may indicate an impurity phase.

6.2 ^{89}Y NMR Results

6.2.1 Introduction

The ^{89}Y isotope is 100% abundant. Since it is a spin 1/2 nucleus, it has no electric quadrupole moment and its resonance displays no shift and broadening from electric field gradient effects†. In some NMR experiments, the small gyromagnetic ratio ($^{89}\gamma$=2.086) of the ^{89}Y nucleus has been known to limit sensitivity and signal-to-noise ratios.

In the $YBa_2Cu_3O_{7-\delta}$ structure, the ^{89}Y nucleus is nested between adjacent CuO_2 planes and is thought to be of lesser importance to superconductivity, since its replacement by almost any other rare earth element is not detrimental to superconductivity. Nevertheless, Y NMR makes a vital contribution to our understanding of YBCO, as it provides indirect information about the CuO_2 planes.

^{89}Y NMR experiments have been performed on all nine Co-doped samples in the temperature range 160-300K (normal state), at both c//B and c⊥B orientations. In addition, the orientation dependence of the room temperature ^{89}Y magnetic shift ($^{89}\Delta$K) was obtained for the pure YBCO (x=0) sample. These results will be presented in the following sections and then discussed in conjunction with the Cu results in section 6.4.

---

22 A. Lusnikov, L. L. Miller, R. W. Callum, S. Mitra, W. C. Lee & D. C. Johnson, *Jnl. Appl. Phys.* **65** 3136 (1989)

† Therefore, any information which may have been gained about the EFG is lost.

6.2.2 Orientation Dependence of the x=0 Sample at 295K

Initial ^{89}Y NMR experiments performed on the pure YBCO (x%=0) sample at 295K, indicate that the frequency spectrum for the c parallel to B (c//B) orientation has two peaks, one at -94ppm (peak 1) and one at -149ppm (peak 2), relative to a 1M aqueous solution of YCl_3. Peak 2 (where $^{89}K_s$=-349ppm, since $^{89}\sigma$=+200ppm) coincides with the single peak obtained by other researchers[23,24] for near O_7 uniaxially aligned YBCO samples oriented c//B, while peak 1 remains anomalous, at present. In order to determine the origin of the double peak, a study was made of the orientation dependence of the room temperature ^{89}Y magnetic shift.

Figure 6.9 shows the ^{89}Y NMR spectra for the pure $YBa_2Cu_3O_{7-\delta}$ sample oriented with its c-axis at 0°, 30°, 45°, 60° and 90° relative to the B-field. A further spectrum taken at c135°B has been omitted from figure 6.9 for clarity, but will be included in future discussions. The signal-to-noise ratios of these spectra are typical of those obtained from the MSL-500 spectrometer used to acquire all of the ^{89}Y NMR data. The magnetic shifts $^{89}\Delta K$ and the linewidths $^{89}\Delta\upsilon_{1/2}$, which were deduced from fitting a Lorentzian function to the frequency spectra in figure 6.9, are presented in figures 6.10 and 6.11.

The line splitting observed for c//B is also clearly seen at the 30° orientation. As the angle θ between the c-axis and the B-field increases to 45°, the two peaks begin to merge and so the less intense peak 1 appears as a broad shoulder on the larger peak 2. The peaks can still be deconvoluted into two Gaussians or Lorentzians at θ=45°. Figure 6.10 indicates that the magnetic shift of peak 1 stays approximately constant at around -94ppm (with the limits of experimental error) over the θ range 0° to 60°, and then 'dips' slightly to -87ppm (i.e. K_s=-287ppm) for c⊥B. Over the same range, the magnetic shift of peak 2 decreases almost linearly, until at θ=60°, both peaks have merged into a single line at -94 ppm. The linewidths* (figure 6.11) of both peaks are the same at each orientation, except for c//B and c45°B, where they differ by values which are well within the error. For $0°\leq\theta\leq60°$, $\Delta\upsilon_{1/2}$ remains fairly constant (within the error) at approximately 1.2±0.25kHz†. The minimum linewidth, which is only slightly narrower at 1.0kHz, appears for the single resonance line at C⊥B. The absolute values of $^{89}\Delta\upsilon_{1/2}$(c//B, peak 2) and $^{89}\Delta\upsilon_{1/2}$(c⊥B) obtained here at room temperature are in good agreement with the constant value of 1.1kHz found at both orientations for $T>T_c$ by Carretta et al[23,25].

---

23 P. Carretta & M. Corti, *Phys. Rev. Lett.* **68** 1236 (1992)

24 S. E. Barrett, D. J. Durand, C. H. Pennington, C. P. Slichter, T. A. Friedmann, J. P. Rice & D. M. Ginsberg, *Phys. Rev. B* **41** 6283 (1990)

* Taken at the 'full width at half intensity (FWHM)' point of the spectral line .

† where 1kHz ≡ ~41ppm ≡ ~0.48mT

25 P. Carretta, *Phys. Rev. B* **45** 5760 (1992)

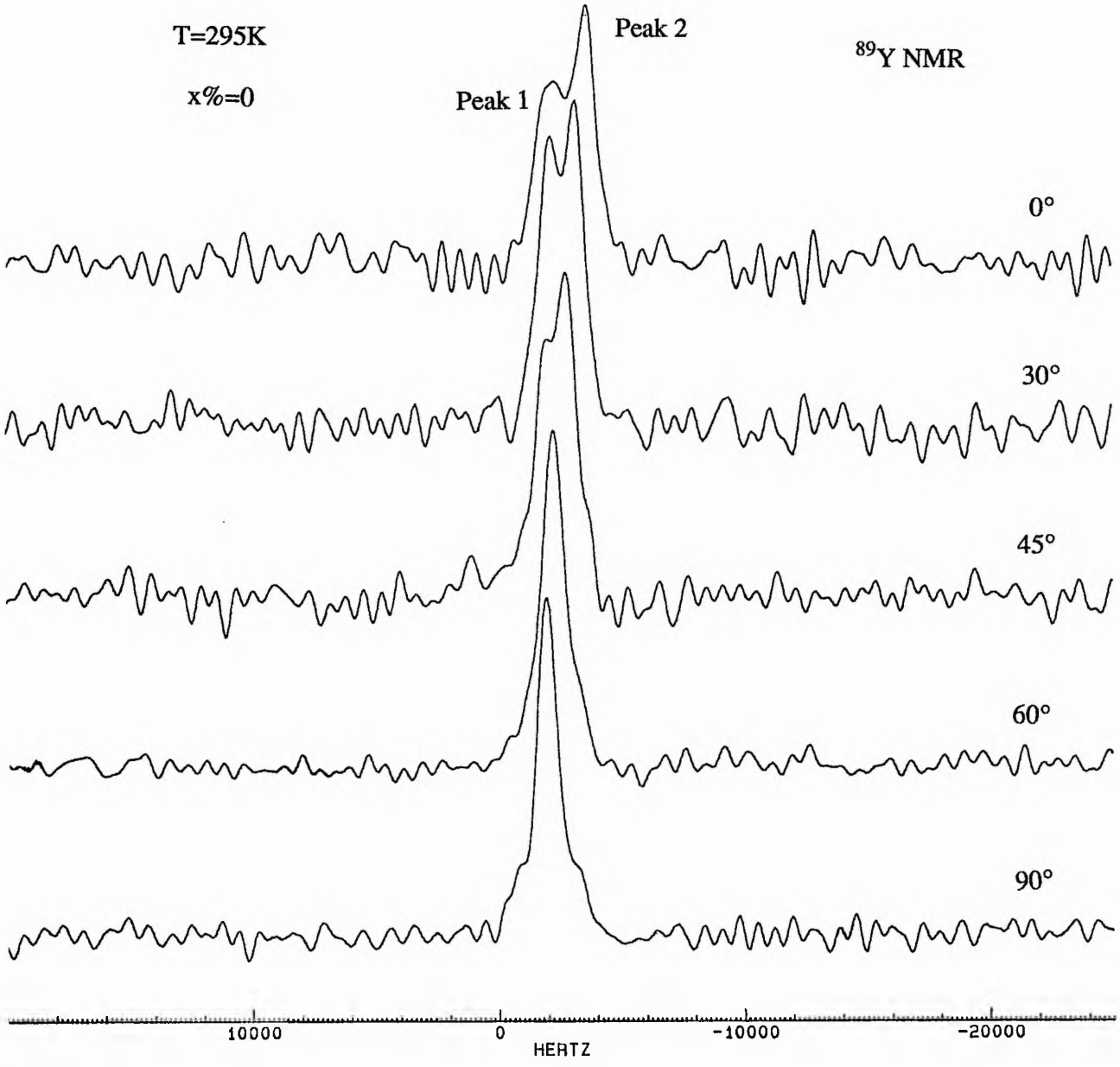

Figure 6.9

Room temperature ^{89}Y NMR (frequency) spectra of a uniaxially aligned pure $YBa_2Cu_3O_{7-\delta}$ (x%=0) sample oriented with the c-axis at different angles relative to the B-field. Note that these spectra are not drawn relative to the YCl_3 line, which appears at +83ppm (υ_0=24.506MHz, B=11.74T).

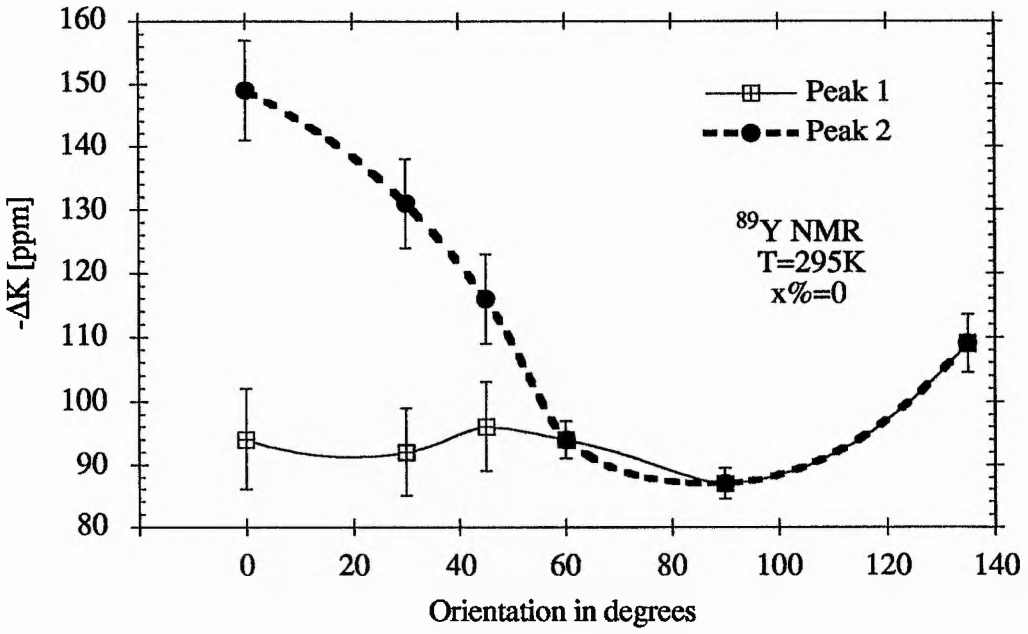

Figure 6.10

Variation of the room temperature ^{89}Y magnetic shift (ΔK) of uniaxially aligned $YBa_2Cu_3O_{7-\delta}$ (x%=0) with orientation. All shifts are relative to the YCl_3 line.

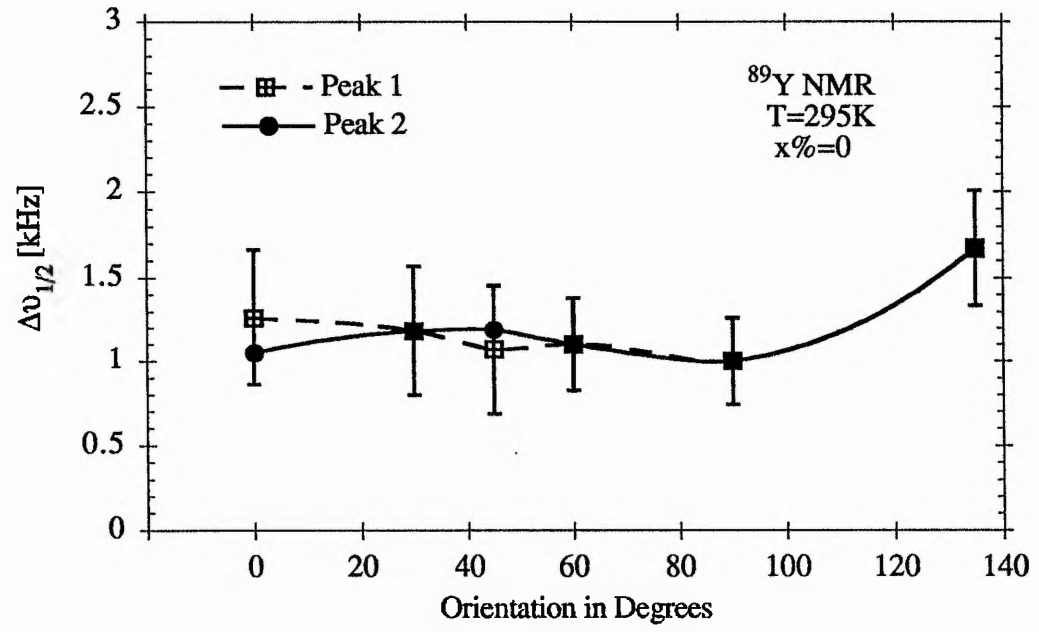

Figure 6.11

The linewidths $\Delta\upsilon_{1/2}$ (full width at half intensity) corresponding to the ^{89}Y NMR spectra & shifts given in figures 6.9 & 6.10

Finally, the single resonance line at the θ=135° orientation is shifted to -109ppm and has a linewidth of 1.67kHz. If this sample were truly unaxially aligned, the spectrum obtained at this orientation would be equivalent to that acquired at θ=45°.

Two other research groups have reported line splitting of the ^{89}Y NMR peak in YBCO. Kramer et al[26] (1987) observe a double peak resonance for a powder sample of $YBa_2Cu_3O_7$ at 100K (4.7T, 9.798MHz)). Their room temperature measurements, however, produce a single peak with a resonance linewidth of 2kHz. They attribute the line splitting to a modulated charge density at the Y site, which is possibly associated with the development of a charge density wave (CDW) or spin density wave (SDW). They also point out that a doubling of the unit cell or an incommensurate modulation (as commonly observed in the Bi-Sr-Ca-Cu-O system[27]) would both give rise to a split spectrum.

A more recent paper by Brom & Alloul[28] (1991) also reports a second ^{89}Y resonance line at a temperature of ~100K, but this time in an aligned $YBa_2Cu_3O_7$ sample, oriented c//B. The additional line occurs at a frequency about 2kHz higher than the established O_7 peak and is present at temperatures down to 70K, where the two lines merge as a result of increasing linewidth in the superconducting state. Just above T_c, the intensities of the two lines are of the same order of magnitude. Brom & Alloul suggest that small differences in oxygen content, which generally lead to a broadening of the spectrum below 150K, manifest themselves as a second resonance line at temperatures of 100K and below. As T drops below 70K, the line splitting decreases due to a fall in the Knight shift.

The ^{89}Y NMR results taken on the present sample in the temperature range 180-295K, at the c//B orientation, are presented in figure 6.12. Our ^{89}Y results show evidence of line splitting over the entire T range studied. It is therefore difficult to compare the present results with those of Kramer et al and Brom & Alloul, since our observations of line splitting are so different and occur over a much wider temperature range. In order to check the presence of line splitting in other samples, the ^{89}Y NMR experiments were repeated on a different pure YBCO specimen, which had comparable sample charateristics and had been aligned using the same techniques. Similar results were obtained, which suggests that the double peak may possibly be a result of the alignment methods used or some intrinsic characteristic of our NMR set-up. However, all possible sources of

---

26 G. J. Kramer, H. B. Brom, J. van den Berg, P. H. Kes & D. J. W. IJdo, *Solid State Comm.* **64** 705 (1987)

27 Y. LePage, W. R. McKinnon, J. M. Tarascon & P. Barboux, *Phys. Rev. B* **40** 6810 (1989)

28 H. B. Brom & H. Alloul, *Physica C* **177** 297 (1991)

additional signal, such as the sample holder, stycast 1266 resin, thermocouple, etc. were eliminated from the investigation.

A similar double peak ^{89}Y spectrum is also obtained at 295K for a partially (50%) aligned $(Tl_{0.5}Pb_{0.5})Sr_2(Ca_{0.5}Y_{0.5})Cu_2O_7$ sample, oriented with the majority c-axis parallel to the applied field[29]. A study of the orientational properties of such a sample reveals that the anomalous peak (peak 1) has no orientation dependence and that the expected peak (peak 2) again moves towards the anomalous peak with increasing θ. By θ=45°, the two peaks are just distinguishable and by θ=90°, only a single narrrow peak remains, just as with the YBCO sample.

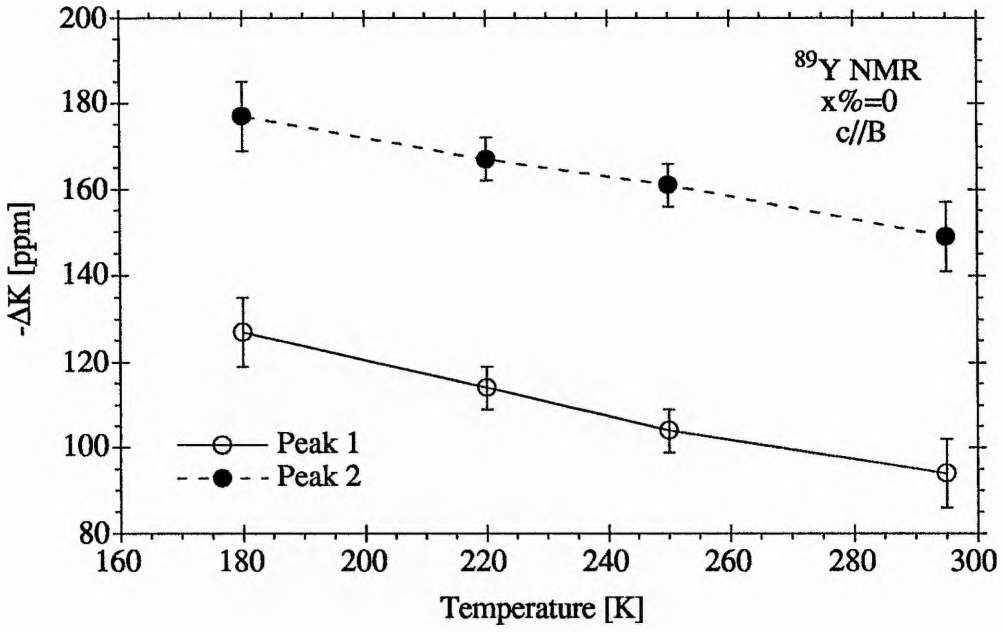

Figure 6.12

Temperature variation of the magnetic shifts of the two peaks observed in the ^{89}Y spectra of the x%=0 sample, oriented c//B.

Since peak 1 in the ^{89}Y spectrum of the present sample is invariant to rotation, it may be possible to identify it with the random powder element of the sample. The peak obtained from an ^{89}Y NMR scan of the tightly packed random powder form of this 0% sample occurs at -76ppm. This is in good agreement with the values obtained by other researchers[30], but evidently, peak 1 and the random powder peak do not coincide (since it

---

29 G. Dai, D. P. Tunstall, W. J. Webster, H. F. Booth, S. Arumagum, R. S. Liu & P. P. Edwards, to be published in the proceedings of the Beijing International Conference on High T_c Superconductivity '92, May 25-29th 1992, World Scientific Publications (1993).

30 H. Alloul, T. Ohno & P. Mendels, *Phys. Rev. B* **63** 1700 (1989)

is probable that even in a tightly packed random powder, some alignment occurs). The resonance lineshape for a truly random powder was first calculated by Bloembergen and Rowland[31] (1953) and represents contributions from all crystal orientations combined. Since it is statistically probable that the major contribution will come from the crystallites oriented at 90° to the applied field, the position of the intensity maximum for a random powder coincides with that obtained from the resonance of a single crystal with its major axis oriented perpendicular to the field. In the present case, it is interesting to note that the position of the unexplained peak 1 (-94ppm), coincides almost exactly with the room temperature ^{89}Y peak position obtained by other researchers* for uniaxially aligned samples oriented c⊥B (-95ppm)[23,24].

A random powder theory is further supported by the data given in figure 6.12. Decreasing temperature produces a diamagnetic shift in both peaks. The magnetic shifts of the two peaks appear (within the error) to have approximately the same linear temperature dependence (i.e 0.287ppm/K for peak 1 and 0.243ppm/K for peak 2), with the net difference between the peak positions remaining at about 54ppm, over the entire temperature range. The fact that the magnetic shifts have the same temperature dependence must surely rule out the possibility that the second peak is due an impurity phase. Such a phase would produce shifts with a distinct temperature dependence, even if the secondary phase varied only in its oxygen content[30]. In any case, it is highly likely that an impurity peak would have an orientation dependence and that such a phase would have shown up on the X-ray analysis.

Although a random powder theory seems the most plausible argument for the existence of the second peak (given the experimental data), a number of doubts still remain. For example, in many of the ^{89}Y spectra, peak 1 has an intensity which is only slightly less than that of peak 2. This would imply that a relatively large proportion of the powder was unaligned. However, according to the X-ray analysis of this sample only 5% of the powder remain unaligned. In addition, attention should be drawn to the fact that the theoretical lineshape also has a low field tail, which is not observed in our ^{89}Y spectra.

6.2.3 Concentration Dependence of the Magnetic Shift at 295K

Figure 6.13 shows the concentration dependence of the room temperature magnetic shifts for c//B and c⊥B. All magnetic shifts were accurately obtained using an MSL Lotentzian fitting program and are shown relative to a 1 molar aqueous solution of YCl_3. The errors have been calculated from observations of the S/N ratio for each spectrum.

---

31 N. Bloembergen & T. J. Rowland, *Acta Metallurgica* **1** 731 (1953)

* Our results for c⊥B (-87±3ppm) are slightly smaller and are not within the error.

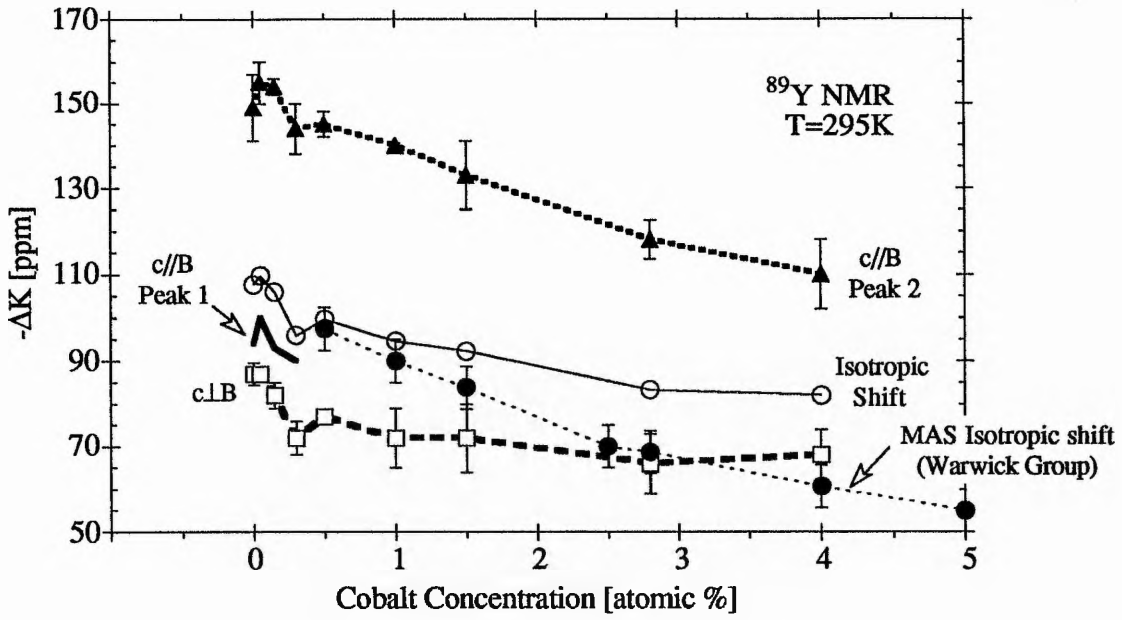

Figure 6.13

Cobalt concentration dependence of the room temperature ^{89}Y magnetic shift of $YBa_2(Cu_{1-x}Co_x)_3O_{7-\delta}$. The isotropic shifts were calculated from ΔK values at the c//B & c⊥B orientations. For comparison, the MAS isotropic shift results of the Warwick group[32,33] have been included.

Note that peak 1 is present up to x%= 0.3.

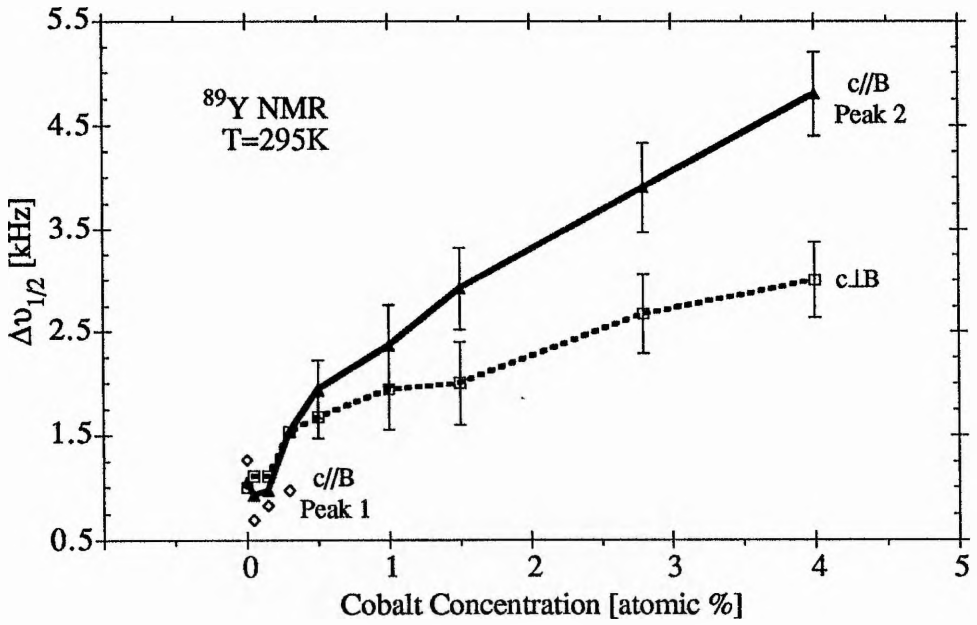

Figure 6.14

Linewidths of the ^{89}Y NMR peaks, whose magnetic shifts are depicted in figure 6.13. At low concentrations, the error bars have been omitted for clarity and should be approximately ±0.29kHz for the c//B orientation and ±0.23kHz for the c⊥B orientation.

The total isotropic shifts† ΔK_{iso}, also shown in figure 6.13, have been calculated for our aligned (static) samples using equation (3.54),

$$\Delta K_{iso} = \frac{1}{3}(\Delta K_{//} + 2\Delta K_{\perp}) \qquad (6.6)$$

where $\Delta K_{//}$ and $\Delta K_{\perp}$ are the magnetic shifts obtained when the sample is aligned c//B and c⊥B, respectively. The total isotropic shifts acquired this way are directly equivalent to the isotropic shifts obtained from an NMR Magic Angle Spinning (MAS) experiment performed on a powder sample. Such an MAS experiment on the Co-doped system has recently been undertaken by the Dupree group[32,33] at Warwick University. Their results are shown for comparison in figure 6.13. The MAS isotropic shifts for x%≥2.5 were linearly interpreted from the study of Dupree et al[32], while the MAS shifts for the 0.5%, 1.0% and 1.5% samples were adapted from the work of Gencten[33]. The corresponding linewidths deduced from our c//B and c⊥B ^{89}Y NMR spectra are given in figure 6.14.

At low Co concentrations (x%≤0.3), similar trends are observed for the c//B and c⊥B orientations, both in the magnetic shift* and in the linewidth. With the addition of small amounts of Co (i.e 0.05%), the magnetic shifts $\Delta K_{//}$ and $\Delta K_{\perp}$ become *slightly* more diamagnetic. However, as the Co concentration is increased further, $\Delta K_{//}$ and $\Delta K_{\perp}$ become more paramagnetic (i.e. more positive), both 'rising' abruptly at x%=0.3 (this point seems genuine since the same magnetic shift value was obtained repeatedly). For x%≥0.5, $\Delta K_{//}$ shifts paramagnetically, increasing almost linearly with the addition of Co, while $\Delta K_{\perp}$ remains approximately constant (within experimental error) at -68ppm. Note that line splitting exists for the c//B orientation up to x%=0.3 and that peak 1 seems to follow the same trend as peak 2.

In the concentration interval 0≤x%≤0.15, the corresponding linewidths $\Delta\upsilon_{1/2}$(c//B) and $\Delta\upsilon_{1/2}$(c⊥B) remain approximately constant, within experimental error. Beyond x%=0.3 (where $\Delta\upsilon_{1/2}$=1.53kHz for both orientations), these linewidths increase almost linearly with the addition of Co - with $\Delta\upsilon_{1/2}$(c//B) rising more steeply (0.855kHz/Co%) than the c⊥B linewidth (0.397kHz/Co%). There seems little evidence of an anomaly in linewidth at x%=0.3. It is difficult to compare any of our static linewidth results with those deduced from the Dupree study since the MAS technique used by Dupree would average out certain contributions, such as the dipolar fields from the Co moment, and would thus narrow the ^{89}Y NMR line considerably. However, it is interesting to note that

---

† as opposed to the isotropic Knight shift K_{iso}

32 R. Dupree, A. Gencten & D. McK. Paul, *Physica C* **193** 81 (1992)

33 A. Gencten, PhD. Thesis, University of Warwick (1992) (unpublished)

* In all of the discussions that follow, the term 'c//B magnetic shift ($\Delta K_{//}$)' will refer to the shift obtained from peak 2, unless otherwise stated.

Alloul et al[34] have performed ^{89}Y NMR experiments on Co-doped random powder samples in the same concentration range and obtain similar static linewidth data to ours.

As $\Delta K_{//}$ and $\Delta K_{\perp}$ follow the same trend at low Co concentrations, so does ΔK_{iso}. However, since the isotropic shift is weighted towards $\Delta K_{\perp}$ by equation (6.6), the absolute values of ΔK_{iso} are closer to $\Delta K_{\perp}$ than to $\Delta K_{//}$. This weighting also means that ΔK_{iso} rises less rapidly than $\Delta K_{//}$, as the Co content increases above x%=0.5.

The isotropic shift deduced from our absolute c//B and c⊥B shift results for the near O_7 pure YBCO sample (-107±10ppm) is similar to that obtained for stoichiometric $YBa_2Cu_3O_7$ by the Warwick group[32,35,36] (-103±5ppm) and by other researchers[23,24,30] (-113±10ppm). In addition, the shift value for the 0.5% sample coincides with the Warwick result and ΔK_{iso} for the 1.0% sample is also well within the error. For x%≥1.0, it is evident that our results present a slight departure from those of the Warwick group. It can however be said that both sets of results breakdown into two regimes: in the concentration range 0≤x%≤2.5 (regime 1), the Warwick data has a linear concentration dependence which intersects the x%=0 line at the expected value of -103ppm. If we omit the rogue x%=0.3 point from our data, our results (0≤x%≤2.8) show a somewhat less steep but nevertheless linear concentration dependence which also extrapolates to our undoped ΔK_{iso} value of -107ppm. In the second regime (x%≥2.5), the results of both groups indicate that ΔK_{iso} varies linearly with concentration, but at a different rate to respective results in regime 1. Interestingly, although the absolute values and trends obtained by both groups in regime 2 are very distinct, both lines extrapolate to approximately the same shift value at x%=0 (-90±5ppm for the Warwick group and -87±5ppm for the present work). It is expected that the difference (+13-20ppm) between these extrapolated values and the absolute values obtained directly from an undoped $YBCO_7$ sample can be attributed to the change in chemical shift which occurs as the structure transforms from an orthorhombic to tetragonal (II) structure at around x%=2.5.

6.2.4 Temperature Dependence of the Magnetic Shift

Figures 6.15 to 6.18, which follow, show the temperature variation of the ^{89}Y magnetic shifts and corresponding linewidths for various uniaxially aligned Co-doped YBCO samples (0≤x%≤4) oriented with c parallel and c perpendicular to the applied B-field. These quantities have again been deduced from the ^{89}Y frequency spectra using a Lorentzian fitting program. The magnetic shifts are all referenced to the YCl_3 line.

---

[34] H. Alloul, P. Mendels, H. Casalta, J. F. Marucco & J. Arabski, *Phys. Rev. Lett.* **67** 3140 (1991)

[35] G. Balakrishnan, R. Dupree, I. Farnan, D. McK. Paul & M. E. Smith, *J. Phys. C* **21** L847 (1988)

[36] Z. P. Han, R. Dupree, D. McK. Paul, A. P. Howes & L. W. J. Caves, *Physica C* **181** 355 (1991)

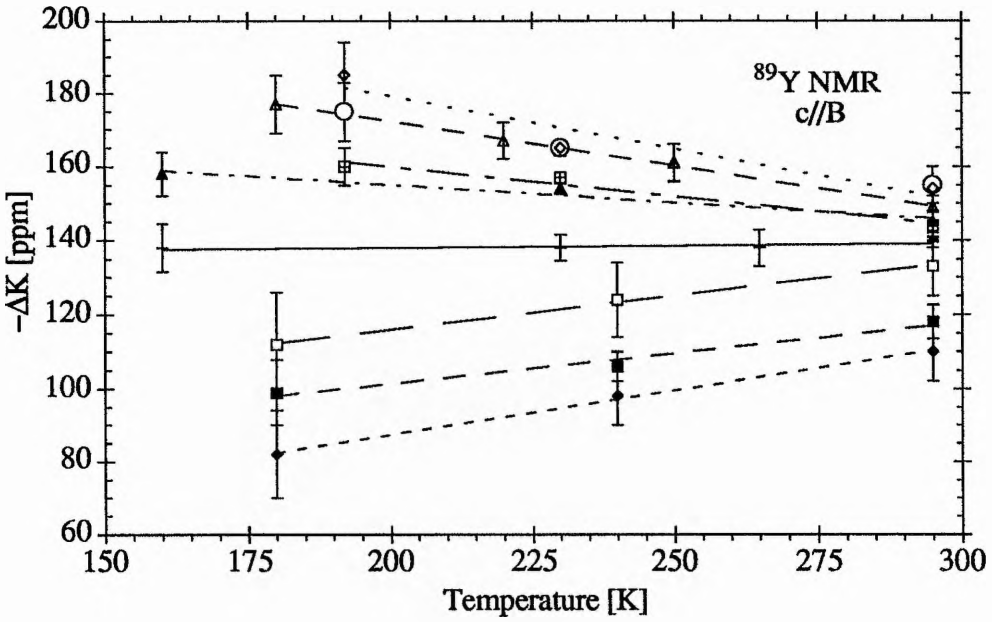

Figure 6.15

Temperature variation of the ^{89}Y magnetic shift for various samples of $YBa_2(Cu_{1-x}Co_x)_3O_{7-\delta}$, oriented with the c-axis parallel to the applied B-field.

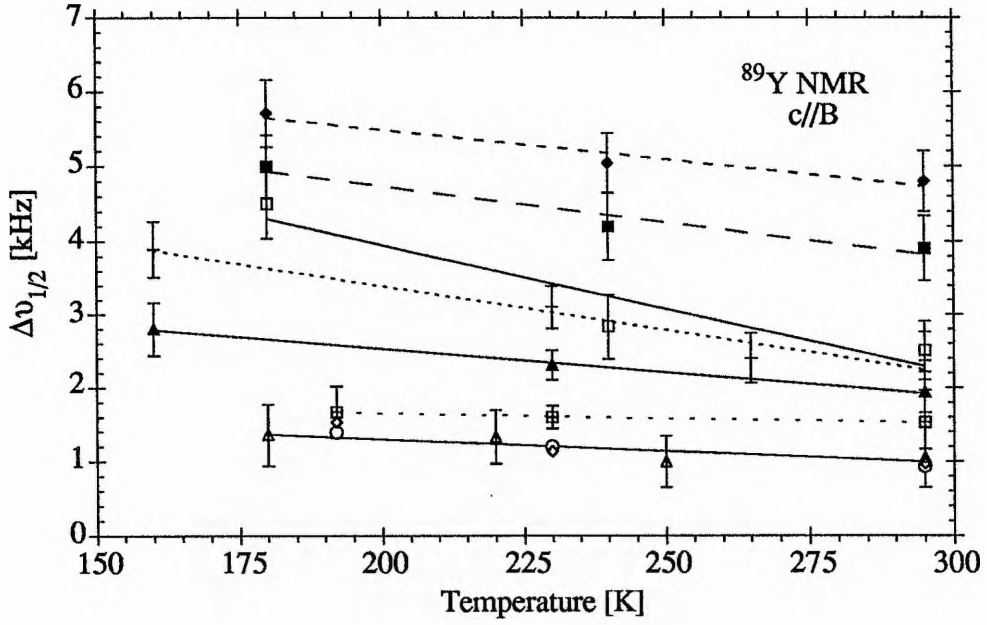

Figure 6.16

Linewidths corresponding to the magnetic shift data given in figure 6.15. The key to symbols which follows applies to all of the ^{89}Y NMR plots: open triangle=0%, open circle=0.05%, open diamond =0.15%, hatched square=0.3%, closed triangle=0.5%, plus sign=1.0%, open square=1.5%, closed square=2.8% and closed diamond=4.0% Co.

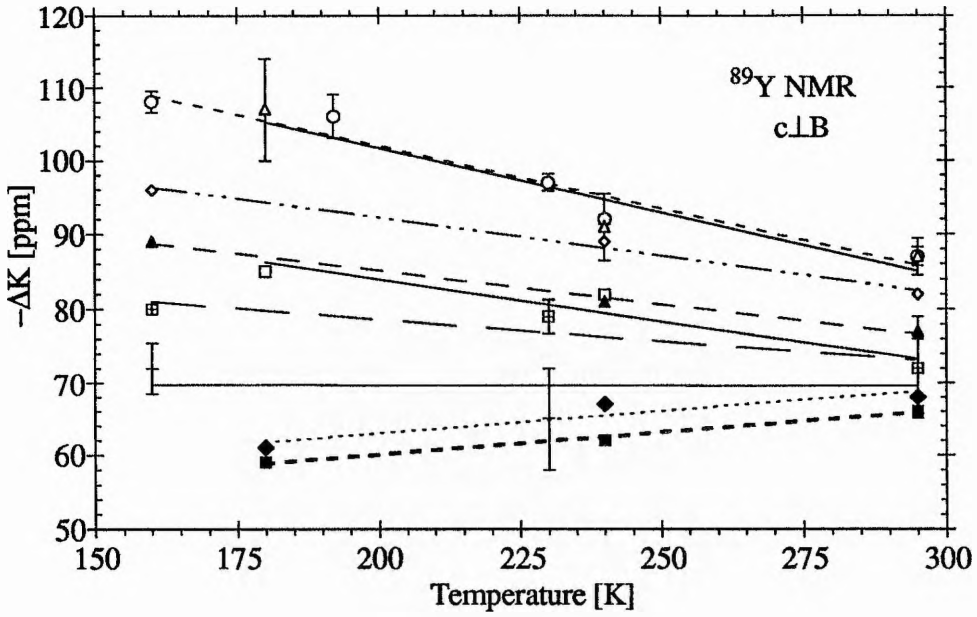

Figure 6.17

Temperature variation of the ^{89}Y magnetic shift for various samples of $YBa_2(Cu_{1-x}Co_x)_3O_{7-\delta}$, oriented with the c-axis perpendicular to the applied B-field. Some error bars have been omitted for clarity & should be of the order of ±2ppm for low Co% and ±7ppm for high Co% (a few ppm larger at lower T).

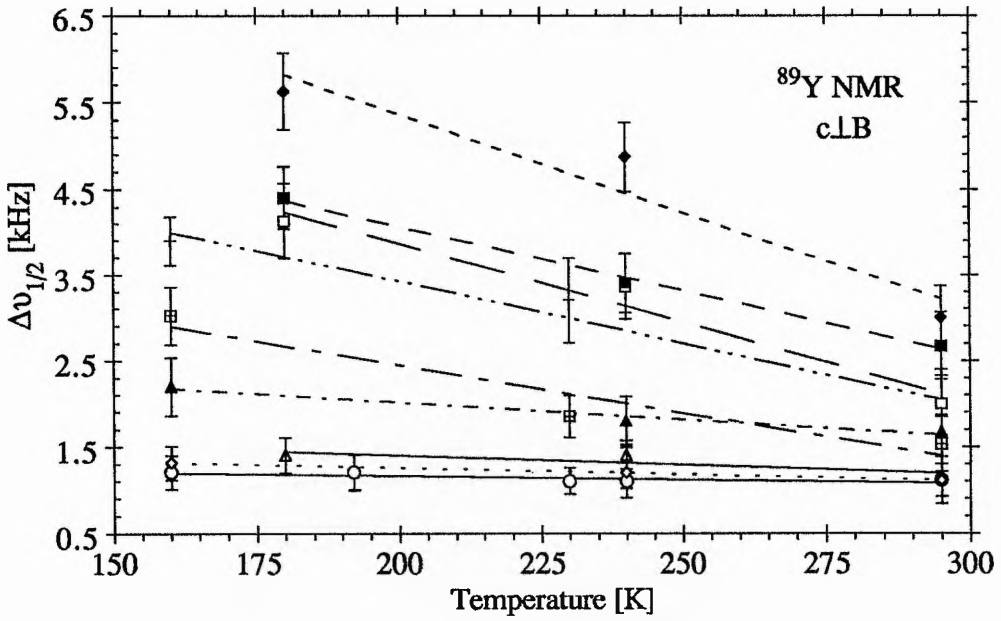

Figure 6.18

Linewidths corresponding to the ^{89}Y magnetic shift data given in figure 6.17. The key to symbols is: open triangle=0%, open circle=0.05%, open diamond =0.15%, hatched square=0.3%, closed triangle=0.5%, plus sign=1.0%, open square=1.5%, closed square=2.8% and closed diamond=4.0% Co.

In the temperature range studied, the magnetic shift and linewidth appear to vary linearly† with temperature (within experimental error) for each concentration and at both orientations. An overall view of the results shows that $|\Delta K|$ is greater for the c//B orientation than for the c⊥B orientation, with $\Delta K_{//}$ also having rather more marked temperature dependencies than $\Delta K_{\perp}$. The linewidths are, however, of similar magnitude in both cases. Evidently, a comparison of figures 6.15 and 6.17 shows that there is considerable anisotropy in shift between c parallel and c perpendicular to B.

For $x\% \leq 0.5$, the magnetic shifts at both orientations become less paramagnetic as the temperature falls. In both cases, the temperature dependence (and magnitude) of the magnetic shift for the 0% sample is identical to that of the 0.05% sample ($d(\Delta K_{//})/dT$= 0.241ppm/K and $d(\Delta K_{\perp})/dT$=0.170ppm/K), implying that such minute amounts of Co have little effect on the variation of ΔK with temperature. With c parallel to B, the addition of 0.15% Co produces a temperature variation in $\Delta K_{//}$ ($d(\Delta K_{//})/dT$=0.287ppm/K) which is very similar to that observed in the 0% sample. However, with the same specimen in the c perpendicular orientation, the temperature variation of $\Delta K_{\perp}$ has already begun to depart from the trends set by lower percentage samples. As the Co concentration is increased further, both $\Delta K_{//}$ and $\Delta K_{\perp}$ become less dependent on temperature, with $d(\Delta K_{//})/dT$ decreasing sequentially with increasing Co content and $d(\Delta K_{\perp})/dT$ decreasing progressively for all Co concentrations, except the 0.3% sample (which appears to be less dependent on temperature than the 0.5% sample). At 1.0% Co, the shift is virtually temperature independent at both orientations with a $d(\Delta K_{//})/dT$=−0.011ppm/K and a $d(\Delta K_{\perp})/dT$=−0.012ppm/K.

For samples with a Co concentration in the range $1.5 \leq x\% \leq 4.0$, $\Delta K_{//}$ is again modified by temperature, but this time with the shift becoming more positive (more paramagnetic) at low temperatures. Note that $d(\Delta K_{//})/dT$ is very similar for the 1.5% and 2.8% samples (-0.17ppm/K), but is slightly larger (-0.24ppm/K) for the 4.0% sample. With the uniaxially aligned sample oriented c perpendicular to B, the trends in ΔK for $x\% > 1$ are slightly different to those highlighted in figure 6.15. To begin with, $\Delta K_{\perp}$ for the 1.5% sample becomes more negative (i.e more diamagnetic, $d(\Delta K_{\perp})/dT$= 0.112ppm/K) with decreasing temperature, in total contrast to the shifts for the 2.8% and 4% samples which become more positive as T falls. Within the limits of experimental error, the shifts for the 2.8% and 4% specimens have the same temperature dependence ($d(\Delta K_{\perp})/dT$=−0.061ppm/K), with the absolute values of $\Delta K_{\perp}$ being slightly greater for the 4% sample.

---

† The lines of best fit were found by applying standard line fitting (least squares) techniques to the available data. All lines are drawn as a guide to the eye only.

For the low percentage samples ($0 \leq x\% \leq 0.15\%$), the linewidths corresponding to the c//B and c⊥B ^{89}Y resonances appear to be approximately independent of temperature (within the limits of experimental error), with $\Delta\upsilon_{1/2}$(c//B) and $\Delta\upsilon_{1/2}$(c⊥B) remaining at values of 1.19±0.33kHz and 1.16±0.20kHz, respectively. Increasing the Co concentration to 0.3% produces a slightly broader, but nevertheless, temperature independent linewidth for the ^{89}Y c//B peak. On the other hand, the same Co concentration induces considerable broadening in the c⊥B peak at low temperatures. Furthermore, at the lowest temperature (160K), the 0.3% ^{89}Y resonance is almost 1kHz broader than the 0.5% resonance at this orientation. If we overlook the anomalous temperature dependence of the 0.3% c⊥B linewidth, we can see that both $\Delta\upsilon_{1/2}$(c//B) and $\Delta\upsilon_{1/2}$(c⊥B) follow similar trends for $x\% \geq 0.5$: for each individual concentration, $\Delta\upsilon_{1/2}$ increases as the temperature decreases. In addition, $\Delta\upsilon_{1/2}$ and $d(\Delta\upsilon_{1/2})/dT$ get progressively larger with increasing Co concentration. At 160K, the linewidths of the c//B and c⊥B ^{89}Y peaks for the 4% sample are 5.71±0.45kHz and 5.63±0.44kHz. Thus, the linewidths and errors at this temperature and concentration are considerable. It is interesting to note that the magnetic shifts which were 'out of sequence' in figures 6.15 and 6.17 (particularly the 0.3% results) were deduced from NMR lines which are significantly broadened at low temperatures. It is often difficult to evaluate the peak position of a broad resonance with any accuracy.

In order to put the results obtained for the temperature variation of the ^{89}Y magnetic shift into some context, the total isotropic shifts were calculated† and compared to those acquired at similar temperatures (150-295K) and concentrations (i.e. x%=0, 0.5, 1.0, 2.5 and 5 in $YBa_2(Cu_{1-x}Co_x)_3O_7$) by the Warwick group, using MAS[32,33,35]. The results of the calculations and the comparison are presented in figure 6.19. The errors accumulated in the addition of $\Delta K_{//}$ and $\Delta K_{\perp}$ mean that the uncertainies in ΔK_{iso} are around ±10ppm for the lower percentage samples and ±17ppm for higher ones (i.e. $x\% \geq 1\%$).

Discussing the present results first: the quasi-identical isotropic shifts for the 0% 0.05% and 0.15% samples are displaced to less paramagnetic values as temperature decreases, with a common $d(\Delta K_{iso})/dT$ value of 0.180ppm/K. As the Co concentration rises, ΔK_{iso} rapidly becomes less dependent on T, until at a Co content of 1.5%, the shift appears to be completely invariant to temperature. At the same time, the absolute values of ΔK_{iso} decrease with the addition of Co, up to this point. The isotropic shifts for both the 2.8% and 4.0% samples have similar, but weak temperature dependences, with ΔK_{iso} moving to slightly more paramagnetic values ($d(\Delta K_{iso})/dT \sim -0.095$ppm/K) with falling temperature.

† using true and interpolated values of $\Delta K_{//}$ and $\Delta K_{\perp}$ in equation (6.6).

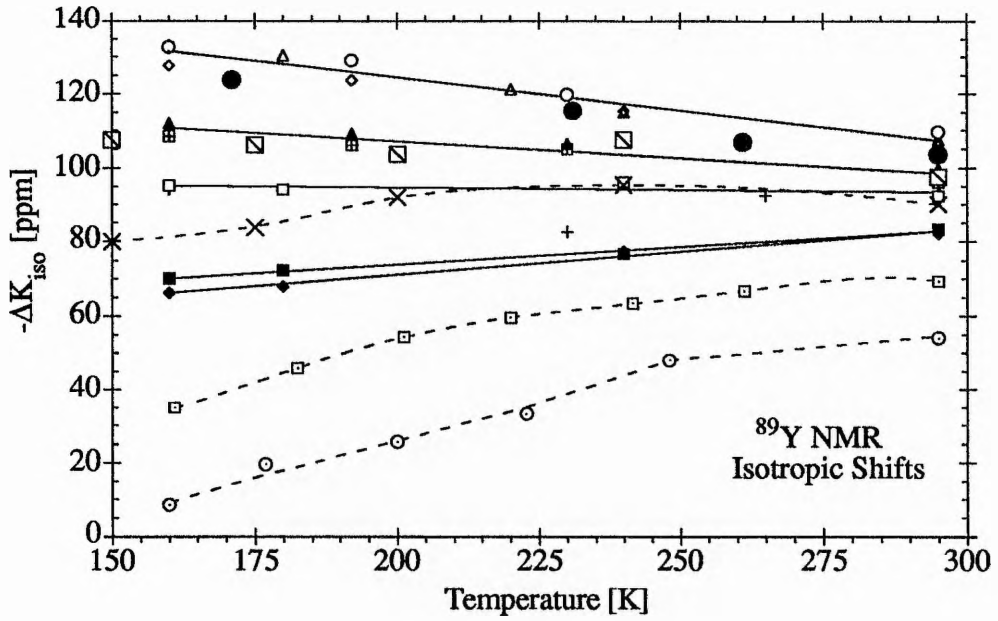

Figure 6.19

The temperature variation of the ^{89}Y isotropic shifts, calculated for various Co concentrations. Key: open triangle=0%, open circle=0.05%, open diamond =0.15%, hatched square=0.3%, closed triangle=0.5%, plus sign=1.0%, open square=1.5%, closed square=2.8% and closed diamond=4.0% Co. The results from the Warwick MAS study[32,33,35] are represented by large filled circle=0%, open square with diagonal=0.5%, cross=1.0%, open dotted square=2.5% and open dotted circle=5.0%. Lines are drawn as a guide to the eye only.

It is clear from our results, that for each individual Co concentration, the isotropic shift is only weakly dependent on temperature and that, even at low temperatures, the shift varies only moderately with Co content (at 160K, the paramagnetic variation of shift in going from 0% to 4% is 67ppm).

At the time of writing, the only results available for quantitative comparison with our ^{89}Y NMR results are those of Warwick group. As can be seen from figure 6.19, the temperature dependence and magnitude of their dynamic isotropic shift values[33,35] for pure $YBa_2Cu_3O_7$ and x%=0.5 are in fairly good agreement with those calculated from our static parallel and perpendicular shifts for equivalent samples. The temperature dependencies of the 1.0% samples in both studies are also coincident down to T=200K, but below this temperature the Warwick results rapidly become T dependent. Contrary to our data on the 2.8% and 4% specimens, they also obtain a considerable temperature dependence in ΔK_{iso} for both the 2.5% and 5% samples[32]. As mentioned previously, in our static aligned samples, Co doping at 4% causes a significant increase in linewidth at low temperatures (see figures 6.16 and 6.18). Such large linewidths could mask any small changes in shift which may occur as a result of Co doping. The linewidths obtained by the Warwick group are considerably narrower than those acquired from our static

NMR experiments (i.e. 1.75kHz for the 2.5% sample at 160K). Narrow linewidths can be expected from an MAS technique, since spinning the sample averages out dipolar contributions to $\Delta\upsilon_{1/2}$, including any dipolar field induced by the Co moments. Thus, it is also possible that in our static experiments, the temperature and orientation dependent dipolar fields created by Co doping may obscure any shift changes which might occur. The dipolar fields induced by Co doping will be discussed further in chapter 7.

6.3 ^{63}Cu NMR Results

6.3.1 Introduction

To complement some of the ^{89}Y NMR results, frequency-swept ^{63}Cu NMR spin echo spectra were acquired at room temperature on all nine Co-doped samples, oriented with their crystallographic c-axes parallel to the applied B-field. Similar experiments were also performed on selected samples oriented c⊥B.

One of the first room temperature ^{63}Cu NMR spin echo spectra collected for the pure YBCO (x=0) system was acquired using a tightly packed random powder sample. The spectrum obtained from such a sample is depicted in figure 6.20.

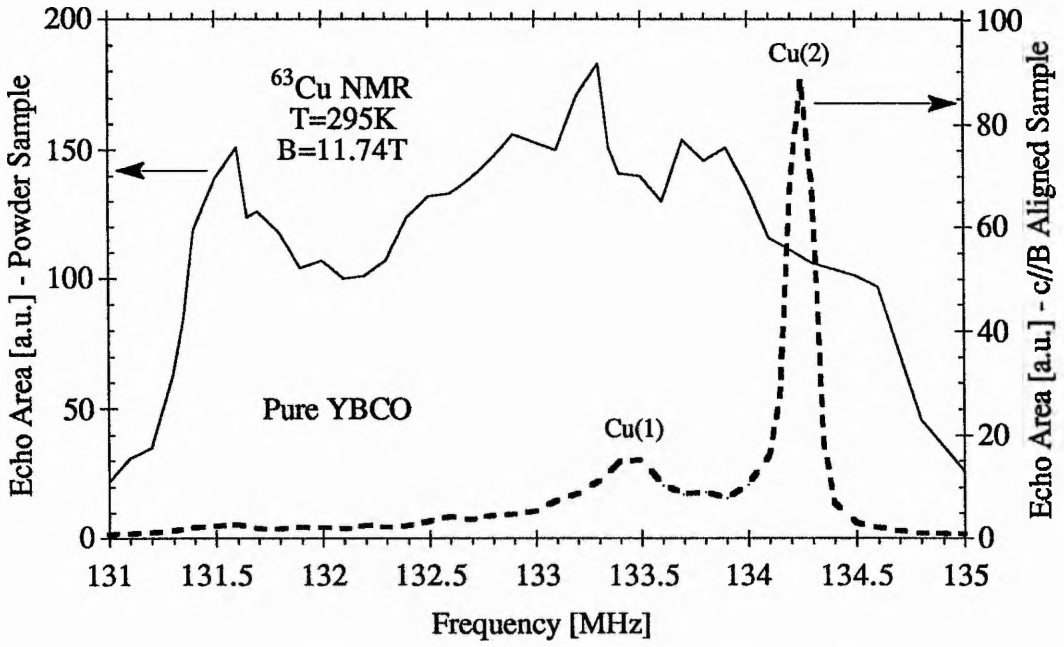

Figure 6.20

The room temperature ^{63}Cu NMR random powder pattern for a pure (x=0) YBCO sample (solid line), acquired at an applied field of 11.74T. The spectrum obtained from the same sample, aligned and with its c-axis parallel to the B-field, is included for comparison (dashed line). Note the difference in y-axis scales.

To facilitate comparison, the room temperature ^{63}Cu NMR spectrum of the same sample uniaxially aligned with c//B is included. Evidently, as one might expect from the large distribution of orientation angles which arise in the random powder, the powder pattern is very broad ($\Delta\upsilon_{1/2}$ is of the order of 4000kHz) and irregular, and the Cu peaks corresponding to the inequivalent plane and chain sites in YBCO cannot be identified. On the other hand, the Cu(1) and Cu(2) peaks in the aligned powder spectrum, are easily recognised, well-defined and very much narrower ($\Delta\upsilon_{1/2}$=378kHz and 156kHz for Cu(1) and Cu(2), respectively) in comparison. The greater intensity apparent for the powder spectrum can be attributed to the somewhat larger quantity of sample used. The integrated area under a spin echo curve is a measure of the number of nuclei which contribute to the NMR line. In this case, the ratio of the integrated area under the two curves in figure 6.20 suggests the number of Cu nuclei which contribute to the entire random powder spectrum is 14 times greater than that which contributes to the aligned powder spectrum.

Although very little quantitative information can be the gleaned from the static random powder pattern, it has been included here to emphasize the importance of using high quality, uniaxially-aligned samples in the NMR study of anisotropic HiT_c superconductors.

In order to investigate the low temperature response of Cu nuclei in the Co-doped YBCO system, we also report (section 6.3.3) field-swept ^{63}Cu spin echo spectra taken at T=1.5K, for both the c//B and c⊥B orientations, using the 141MHz spectrometer.

6.3.2 Concentration Dependence at 295K

Figure 6.21(a) shows a series of room temperature c//B ^{63}Cu NMR spin echo spectra, obtained (at B=11.74T) over the entire range of Co-concentration, $0 \leq x\% < 4$. Figure 6.21(b) presents a similar picture for the c⊥B orientation, but uses a much reduced sample set. All the information distilled from these raw ^{63}Cu spectra are reflected in figures 6.22 and 6.23, which show the peak positions and the full linewidth at half maximum ($\Delta\upsilon_{1/2}$), respectively, for both orientations. Since the computer-controlled spectrometer set-up was adjusted to create the same conditions for each experiment, there is a direct correlation between the peak heights and linewidths for each (1g) sample.

A glance at figure 6.21(a) gives the general impression that, as well as becoming less intense and broader, the c//B Cu(2) peak shifts down in frequency as the cobalt concentration increases. On closer examination (figure 6.22), the c//B Cu(2) peak frequency seems to be characterised by a step-like function: up to a concentration of 0.3%, it is found to stay approximately constant (within experimental error) at an average level of 134.265MHz. As the concentration increases to x%=0.5, the peak frequency value drops slightly to 134.235MHz, but remains constant at this value to a dopant level

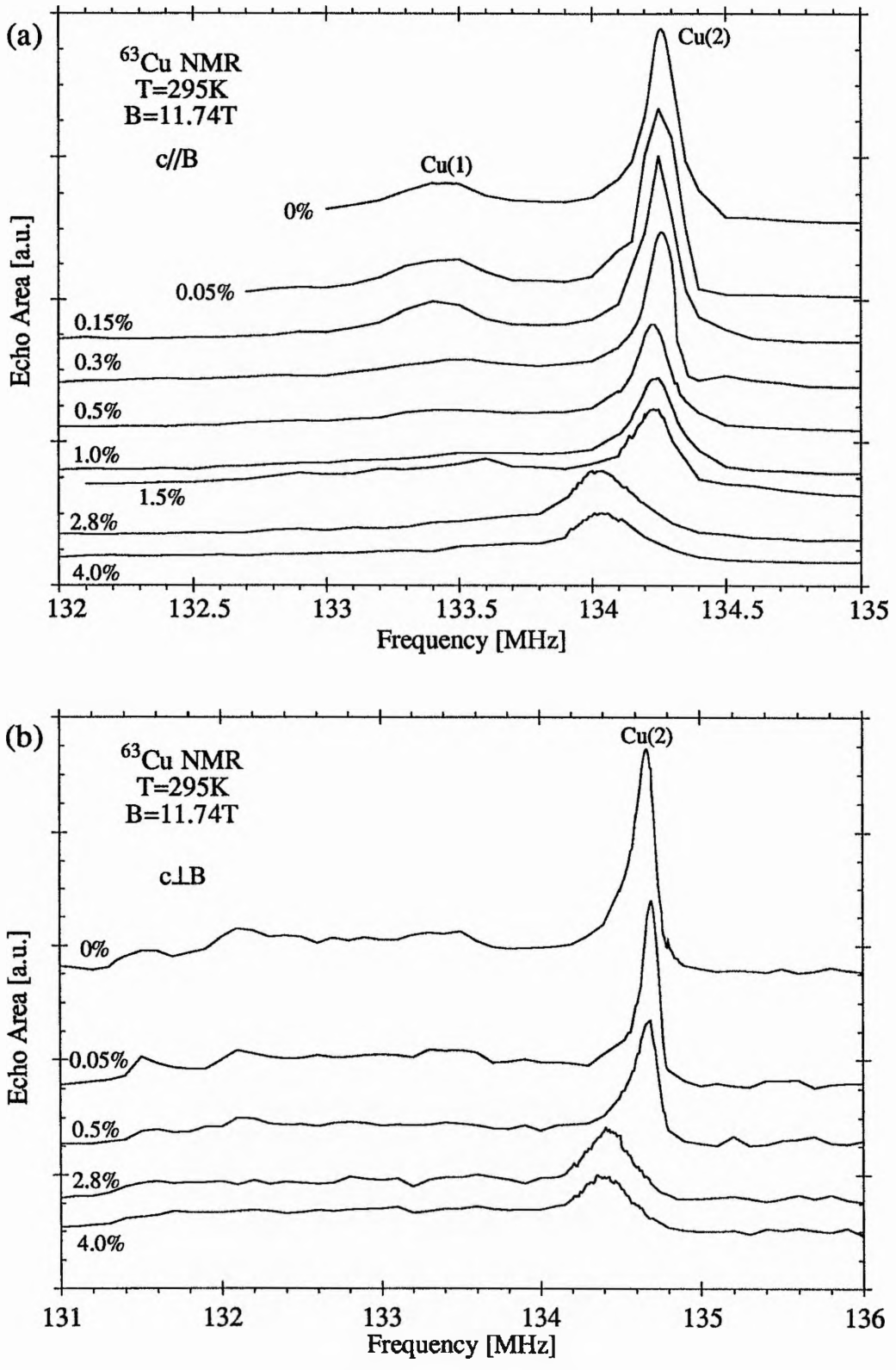

Figures 6.21 (a) & (b)

Room temperature ^{63}Cu NMR spectra acquired at B=11.74T on a set of $YBa_2(Cu_{1-x}Co_x)_3O_{7-\delta}$ ($0 \leq x\% \leq 4$) samples aligned (a) c//B and (b) c⊥B. Each curve has been displaced for ease of visibility.

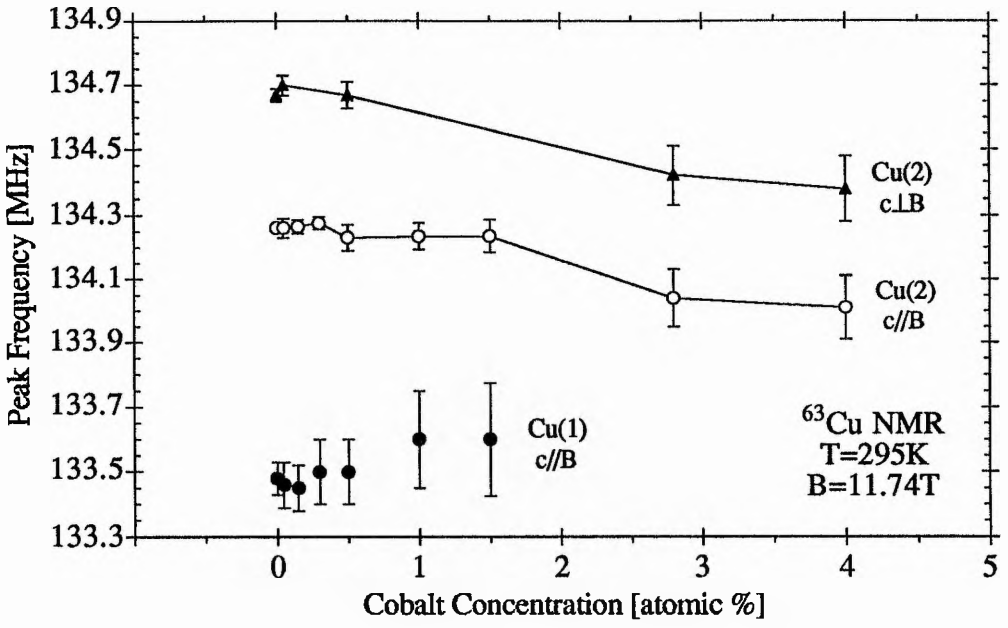

Figure 6.22

The Cu(1) and Cu(2) peak frequency positions deduced from the room temperature ^{63}Cu NMR spectra (figure 6.21), plotted as a function of Co concentration.

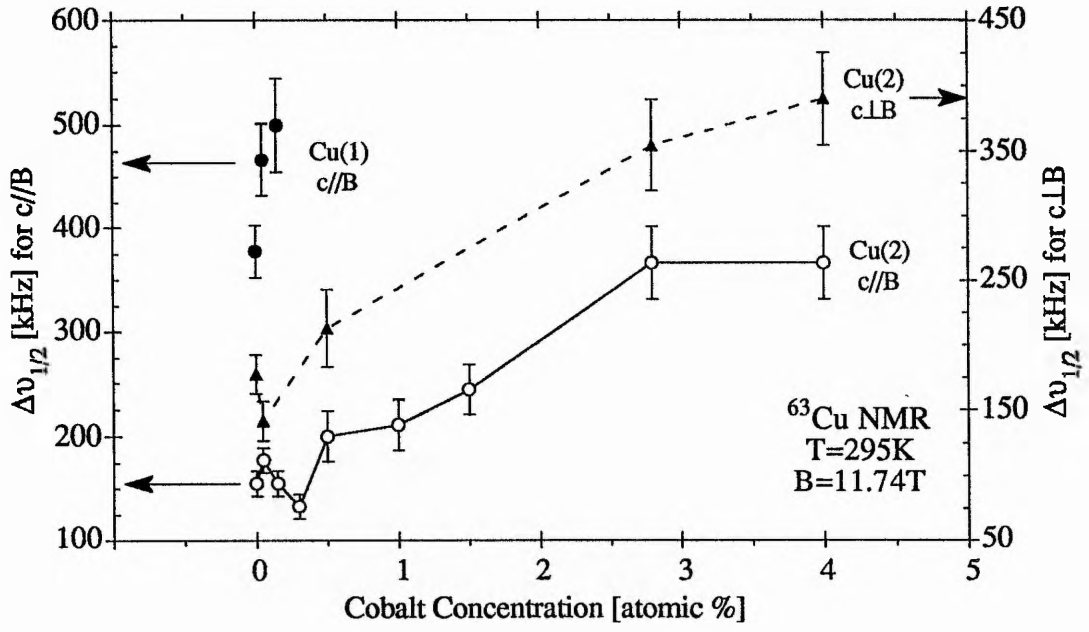

Figure 6.23

The corresponding linewidths of the ^{63}Cu NMR lines depicted in figure 6.21, plotted as a function of Co concentration. Note the difference in y-axis scale for the parallel and perpendicular orientations.

of 1.5%. Somewhere between 1.5% and 2.8% Co, the structure undergoes an orthorhombic to tetragonal transition. This structural transition is accompanied by a considerable drop in frequency to 134.04MHz, a frequency position which falls only slightly as the concentration rises to 4.0%. Although the mid-range Co concentrations (x%=1.0~1.5) have not been examined for the c⊥B orientation, there is some evidence in figure 6.22 to suggest that the c⊥B Cu(2) peak frequency may follow a similar step-like decrease with increasing Co content. Note, however, that at θ=90° there is a considerable quadrupole contribution which leads to a peak position that is, on average, 0.4 MHz greater than that seen for the c//B orientation. Note also that at this B-field (11.74T), the unshifted 'bare', zero quadrupole interaction, ^{63}Cu nuclear resonance occurs at 132.49MHz.

Clearly, there is a steady broadening in the planes Cu resonance for both orientations as the amount of Co increases. Although a double y-axis plot has been used for ease of visibility in figure 6.23, in actual fact the linewidths for any given sample in the c⊥B orientation are almost coincident (within error) with the corresponding linewidths for the c//B orientation. Evidently, as the Cu(2) peaks get broader, it becomes increasing difficult to pin point the exact peak position and to identify the spectral baseline. Thus, the errors involved in the linewidth and peak position plots are significantly larger for the 2.8% and 4% samples.

We now turn to the results for the Cu(1) peak. It is clear from figures 6.21(a) and (b) that, at both the parallel and perpendicular orientations, the Cu(2) peak is dominant. The chains Cu resonance is visible only as a broad hump in the c parallel to B spectrum. The various kinks and waves that appear in the c⊥B pattern, cannot be distinguished from the baseline roll and so cannot be identified as Cu(1) peaks with any certainty. Considering the c//B spectrum alone then, we find that as we increase the Co concentration from 0% to 0.15%, the Cu(1) peak gets rapidly broader, but its centroid does not shift in frequency, within experimental error. On the expanded scale of figure 6.21(a), the peak then disappears for x%=0.5 and beyond. However, if each spectrum is plotted separately, the, by now extremely broad Cu(1) peak, can still be distinguished at concentrations as high as 1.5% Co. Since it becomes increasingly difficult to identify the centroid of the peak at higher concentrations, the peak frequencies for the 0.5% to 1.5% sample are plotted with ever increasing error bars in figure 6.22. The uncertainty in the Cu(1) peak linewidth for samples with x≥0.3 is considered too great for the results to even be plotted in figure 6.23. However, for reference, the Cu(1) $\Delta\upsilon_{1/2}$ for the 1.5% specimen is tentatively estimated at around 1300 kHz. There is no evidence of a Cu(1) peak in either the 2.8% or 4% Co spectra.

6.3.3 Low Temperature ^{63}Cu NMR Results

Figures 6.24 (a) and (b) present the low temperature ^{63}Cu NMR results taken on the on the $YBa_2(Cu_{1-x}Co_x)_3O_{7-\delta}$ system at T=1.5K and υ_L=141MHz. Since no attempt was made to simulate the same conditions for each experiment (as it quite difficult to do so with the low temperature spectrometer), all the spectra have been scaled so that the maxima of the Cu(2) peaks occur at the same echo area value. The peaks have then displaced for ease of visibility.

At both orientations, the dominant peak again originates from the Cu(2) nuclei. For the 0% sample, the centroid of the Cu(2) peak lies at the expected field position of 12.344T for the θ=0° and at 12.356T for θ=90°. With the appropriate Barrett[37] demagnetisation corrections, these values produce Cu(2) Knight shift components of $K^c(2)$=1.27±0.01% and $K^{a,b}(2)$=0.20±0.02%, as in the Aberdeen sample.

The chains Cu peak with b//B is evident only for the pure YBCO (x%=0) sample, where it occurs at a field position of around 12.387T for c//B and 12.425T for c⊥B. With the use of the Barrett[37] demagnetisation factors these values again produce Knight shift components similar to those found in the Aberdeen sample (i.e. $K^c(1)$=0.28±0.01% and $K^b(1)$=0.44±0.06%)†. The Cu(1) a//B peak is absent from all the c⊥B spectra, but this is probably due to lack of resolution.

For θ=90° (figure 6.24(b)), there is a small broadening effect with Co doping. While the Cu(1) peak gets rapidly washed out by the addition of 1.5% Co, the centroid of the Cu(2) peak remains at the same field position as that found in the 0% sample and is apparently unaffected by increasing Co concentration (except for the slight broadening) right up to 4%.

It is clear from figure 6.24(a) that the situation is very different for the c parallel B orientation. Firstly, we note that by a Co concentration of 0.05%, the Cu(1) peak has become washed out. The Cu(2) peak, whilst getting slightly broader, remains at the same field position up to a Co content of x%=0.15. As we increase the amount of Co in the system to 0.3% and 0.5%, the Cu(2) peaks start to broaden out and shift up field. Finally, and most surprisingly, as x% rises beyond 0.5, there is an almost total destruction of the c//B NMR spectra. Although, it is difficult to judge exactly where the peak lies for the 1.0% sample, whatever is left of the 1.5% to 4% spectra at these low temperatures is shifted to the high field side, i.e. the shift on the planes is very much reduced.

---

[37] See S. E. Barrett, D. J. Durand, C. H. Pennington, C. P. Slichter, T. A. Friedmann, J. P. Rice & D. M. Ginsberg, *Phys. Rev.* B **41** 6283 (1990) and also chapter 5 of this work.

† Note that we still obtain an orbital Knight shift value of 0.44% for the $K^b(1)$ component, a value which is somewhat removed from that of 0.27% deduced by Barrett (see section 5.3.3).

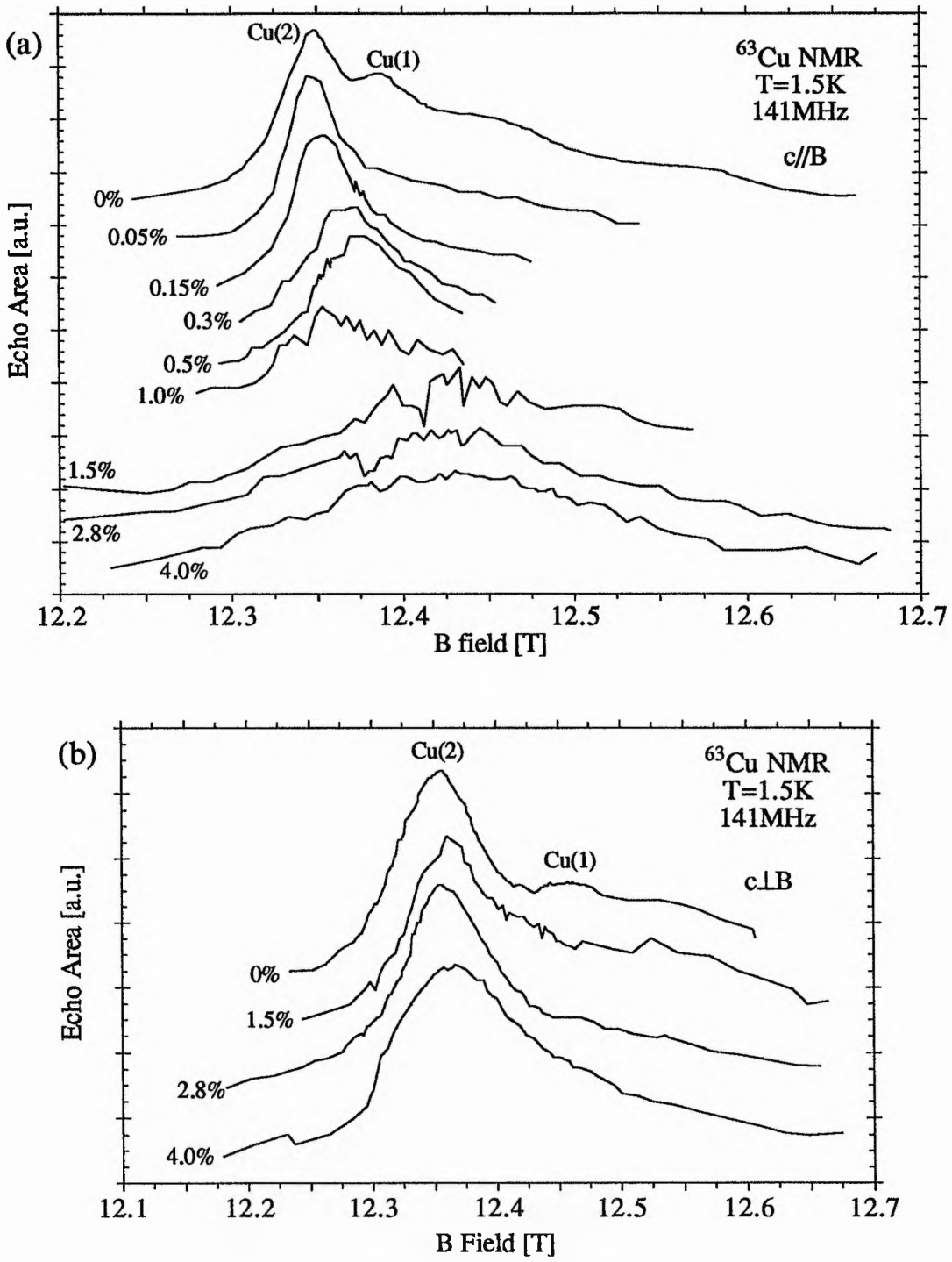

Figure 6.24

Low temperature ^{63}Cu NMR spin echo spectra of $YBa_2(Cu_{1-x}Co_x)_3O_{7-\delta}$ ($0 \leq x\% \leq 4$) - acquired at a frequency of 141MHz and at a temperature of 1.5K - with the crystallographic c-axis aligned (a) parallel to the applied B-field and (b) perpendicular to the applied B-field. Note that each curve has been displaced in the y direction for ease of visibility.

6.4 Discussion

6.4.1 Introduction

In this study, we have used two probes to characterise the magnetic behaviour of the Co-doped YBCO system: (i) magnetic susceptibility and (ii) NMR at the ^{89}Y and ^{63}Cu sites. In addition, various methods have been employed to determine the T_c variation as a function of Co concentration and X-ray powder diffraction techniques have been used to define the crystallographic structure and corresponding lattice parameters. In the discussion which follows, we try and address whether the observed microscopic NMR data is compatible with the macroscopic data, and indeed whether there is any correlation between the magnetic data and the trends in transition temperature and structure.

In order to avoid too much confusion, each of the issues raised in this section will be examined under separate subheadings. It should however be kept in mind that many of the issues are related.

6.4.2 Sample Quality

Since the properties of the Y-Ba-Cu-O system are extremely sample dependent, it is as well to try and define the sample system studied, as far as possible. Here we will briefly summarize the basic characteristics of our aligned system, as deduced from the sample characterisation and NMR experiments.

Firstly, we note the sample purity: the X-ray analyses performed at the IRC and in the present study show no evidence of impurity phases being present in any of the nine Co-doped YBCO samples studied. However, the inability to obtain sensible specific heat measurements on the lower percentage (0% to 1.0%) samples led the IRC to believe that there was some problem with the purity of these samples. Fortunately, nuclear magnetic resonance is also a sensitive indication of sample purity. An overall view of the NMR results provides little evidence to support the presence of impurity phases: the raw ^{89}Y NMR frequency spectra obtained for all samples showed no distinct impurity peaks*. In addition, the general trends in the ^{89}Y magnetic shift as a function of Co content and temperature could be related to the properties of the system and were compatible with the work of other groups. The ^{63}Cu NMR spectra also showed no signs of impurity peaks, within the frequency window investigated. Note that the devastated ^{63}Cu spectra obtained at low temperatures were particularly evident for the higher Co concentration samples,

---

* As discussed in section 6.2.2, we consider the origins of the anomalous peak 1 to be something other than sample impurity.

which were well-characterised and known to be impurity-free. In addition, the magnetic susceptibility data provides non-structural corroborative evidence for good phase purity. With all this supporting evidence in mind, we can state that to the best of our knowledge the samples used in this study were free from impurity†. We confidently believe that the NMR results reported here refer to the pure phases at each Co concentration.

The X-ray diffraction investigation strongly suggests that each sample in the Co-doped series has an oxygen content of around 6.9 (δ=0.1). While the almost temperature independent magnetic susceptibility of the pure YBCO sample (see figure 6.3) reinforces the fact that the oxygen content is fairly near to O_7, the lack of variation in the structural c-lattice parameter with Co-concentration (figures 6.2 & 6.8) indicates that the oxygen content does not change significantly with increasing x. Although little work has been done on the oxygen content of Co-doped YBCO at low concentrations, it seems evident from the previous studies (see section 2.3.3) that the uptake of extra oxygen into the system is only prevalent at Co-concentrations greater than around 3%. Below this concentration level, the total oxygen content is approximately constant*, since the Co^{3+} ion achieves its preferred octahedral coordination via the internal redistribution of oxygen between the O(1) and O(5) sites. Our results provide qualitative agreement with this idea, though we observe no detectable rise in oxygen content at x%=4.

The final point on sample quality is made with reference to the alignment properties of two particular samples - the 0.3% and 0.5% samples used in the ^{89}Y NMR investigation. According to the analysis of the aligned-sample X-ray data presented in table 6.2, the 0.3% Co sample is well-aligned with a quantitative degree of alignment of 98% and with an XRPD pattern (figure 6.7(a)) which shows no evidence of an impurity phase. Despite this fact, the room temperature ^{89}Y magnetic shifts for both the c//B and c⊥B orientations are uncharacteristically high and seem out of sequence with the results for the surrounding concentrations. This is also true for the variation of magnetic shift with temperature. The slightly anomalous data obtained for this sample could be geniune, in which case something peculiar is happening at 0.3% Co which doesn't appear to be prevalent at any other concentration and is not evident from the structure. However, since the trend in the room temperature ΔK is similar at both orientations, the more likely explanation is that the c-axis marked on the sample did not reflect the true c-axis of the crystallites, leaving the sample constantly misaligned with respect to the B_0-field††. Due

---

† Or that any impurity was present in such minute amounts that it was undetectable by the methods used here and therefore could not be expected to interfere with the results.

* The only proviso to this statement is that all the samples must be prepared by the exact same method.

†† Note that according to figure 6.10, the room temperature shift becomes more positive as the c-axis orientation deviates from θ=0 and so shift for the 0.3% moves in the right direction.

to this unforeseen error, the data for the 0.3% sample will be omitted from any further analysis.

The 0.5% sample seems less well aligned than the other low percentage samples which were uniaxially aligned at the same time (see table 6.2). This lower degree of alignment (83%) was thought to be indicative of some contamination, since it had been earlier suggested that this sample was contaminated by a small amount of glass. Such impurites did not however show up during the X-ray analysis of the powder and evidently had no affect on the NMR results. Alternatively, the lower alignment factor may simply have been due to insufficient powder dispersion or some other artifact of the alignment procedure. In real terms, the alignment of the 0.5% sample is good and the sample produced very reasonable NMR results which were comparable with those of the Warwick group.

6.4.3 Evidence for Chain Site Substitution

Independent studies based on neutron diffraction, Raman and Mössbauer spectroscopy and X-ray diffraction techniques (see chapter 2) have all provided strong evidence to suggest that a Co^{3+} ion substitutes preferentially at the Cu(1) site in the Y-Ba-Cu-O system. In this study, the fairly rapid broadening and eventual disappearance of the Cu(1) peak, observed with the addition of cobalt in both the superconducting and normal state ^{63}Cu NMR spectra (figures 6.21 & 6.24), provides further qualitative evidence of chain site substitution in this system. Clearly, as the sphere of influence of the cobalt grows on the chain site, the Cu(1) peak gets rapidly washed out. The diminishing height and broadening of the Cu(2) peaks in the room temperature ^{63}Cu spectra are much less severe and are therefore more characteristic of indirect effects (such as the influence of the dipolar fields from the Co) which occur as a result of substitution on the chain sites.

A more quantitative analysis of the effects that Co substitution has on the room temperature ^{63}Cu NMR lines is given in the following sections.

6.4.4 Analysis of the Intregrated Area Under the Room Temperature ^{63}Cu NMR Spin Echo Curves

It has already been mentioned elsewhere in this chapter that the integrated area under a spin echo curve provides a measure of the number of specific nuclei which contribute to the NMR line. In this study, the integrated area under the ^{63}Cu spin echo peaks could serve as a useful indication of the effect that Co has on the number of ^{63}Cu nuclei which contribute to the resonance.

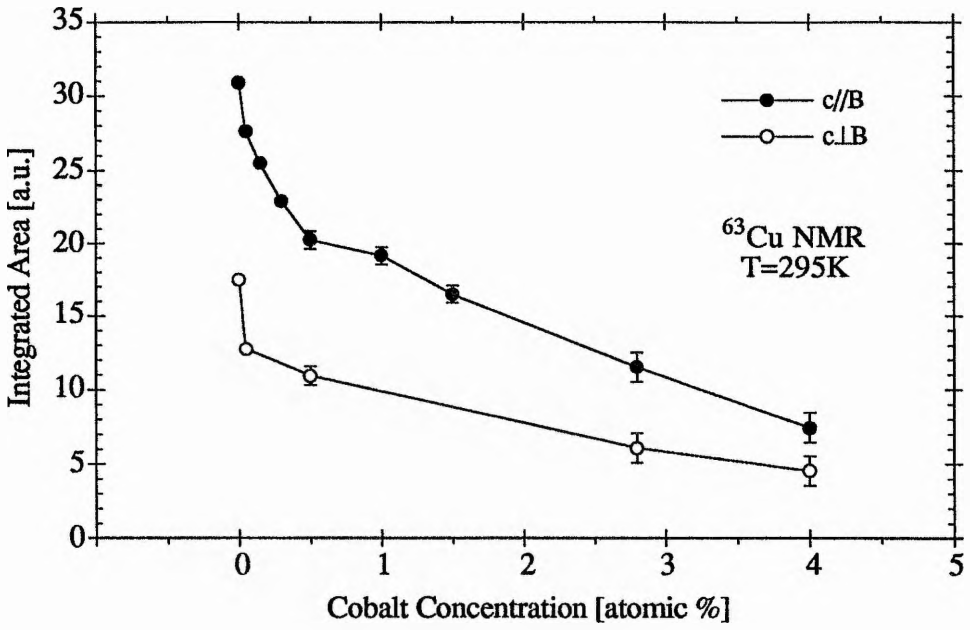

Figure 6.25

A plot of the integrated area under the room temperature ^{63}Cu NMR curves shown in figure 6.21 (normalised to 1g of sample) vs. Co concentration.

Figure 6.25 shows the integrated area under the previously presented c//B and c⊥B room temperature ^{63}Cu NMR spectra (figures 6.21(a) and (b)), plotted as a function of Co concentration. In each case, the baseline at the high frequency end of the spectrum was extended across the whole frequency range and was taken to represent the zero signal limit. The area under each curve was then integrated between the frequency limits of 133 MHz and 135 MHz†, using a statistical graphics program. Since the spectrometer setup was considered to be the same during each experiment, and since the integrated area at each Co concentration was normalised to represent a 1g powder sample, we confidently predict a direct correlation across the whole concentration range.

As the Co content rises from 0 to 0.5%, the total number of ^{63}Cu(1) and ^{63}Cu(2) nuclei at both orientations falls rapidly. Beyond x%=0.5, however, the decrease is much more shallow and almost linear. Two important points can be made about the data; firstly, considering the relatively small amounts of cobalt which are being added to system, the number of ^{63}Cu nuclei which contribute to the NMR line seems to fall rather dramatically with Co concentration. In qualitative terms, this observation is reminiscent of the phenomenon of 'wipe-out' which is seen in the NMR of a number of dilute* alloy

† This frequency region intentionally encompasses the area under both the Cu(1) and Cu(2) peaks.

* 'dilute' in this context means that the distance between impurities is large enough to consider them as practically isolated in the pure matrix.

systems[38,39], such as copper-manganese[40,41,42,43]. In this particular system, which is paramagnetic at T=300K, the transition metal impurity (Mn) acquires a localised magnetic moment when alloyed with the non-magnetic Cu host.

In early experiments (1953), Bloembergen and Rowland[40] found that the NMR signal in metallic copper decreased rapidly when small amounts of Mn impurity were introduced. Such an observation was explained in terms of second order quadrupolar perturbations[41-43]. For a pure host metal with I>1/2, the symmetry around the nuclear spin is assumed to be cubic and so the electric field gradients (EFG) at each lattice site vanish. However, the introduction of solute atoms gives rise to substantial field gradients (through the distribution of charge density) which interact with the near-neighbour Cu nuclear quadrupole moments. This interaction perturbs the energy levels of the nuclear dipoles in the magnetic field and shifts their transition energies appreciably. At low impurity concentrations (<1%), the electric field gradients are usually found to be so important that only the -1/2↔+1/2 transition contributes to the observed ^{63}Cu resonance and the satellite lines disappear. At higher concentrations, near-neighbour Cu nuclei which are located within a critical distance R_c of the impurity are submitted to such a strong field gradient that the ±1/2 transition becomes severely broadened. Such nuclei do not contribute to the resonance and are effectively 'wiped out'. Consequently, the intensity of the central line varies proportionately with $(1-c)^n$, the probability of finding a nucleus at a distance $R>R_c$ from the impurity, where c is the impurity concentration and n is the number of lattice sites within R_c (also known as the 'wipe out number'). It must be noted that in the Cu-Mn system, the magnetic shift may, in addition, be sufficiently large to render the resonance unobservable and these spins will also contribute to n*. This is particularly true at low temperatures where the magnetic effects become overwhelmingly dominant.

Previous studies on the Cu-Co dilute alloy system seem to indicate that isolated Co impurities in Cu are non-magnetic, whilst isolated pairs of neighbouring Co atoms are very nearly magnetic and groups of three Co atoms or more bear magnetic moments[44,45].

---

38 J. Winter, *Magnetic Resonance In Metals* (chapters 7 & 8), Clarendon Press (1971)

39 H. Alloul in *Nuclear Magnetic Resonance in Solids*, ed. Lievan Van Gerven, Plenum Press (1977)

40 N. Bloembergen & T. J. Rowland, *Acta. Met.* **1** 731 (1953)

41 T. J. Rowland, *Phys. Rev.* **119** 900 (1960)

42 W. Kohn & H. Vosko, *Phys. Rev.* **119** 912 (1960)

43 O. J. Lumpkin, *Phys. Rev.* **164** 324 (1967)

* The magnetic contribution may be witnessed by performing the experiment at different B_0-fields.

44 R. Tournier & A. Blandin, *Phys. Rev. Lett.* **24** 397 (1970)

45 R. J. Holliday & W. Weyhmann, *Phys. Rev. Lett.* **25** 243 (1970)

The magnetic properties of this alloy have also been interpreted in terms of a Kondo system with a very high T_K of about 1000K[46,47]. As far as we are aware wipe-out effects do not occur in the Cu-Co alloy. In view of the complexity of the Co-doped YBCO system, it is not possible to give a description of the diminishing contribution of Cu nuclei to the NMR line in terms of quadrupole wipe-out effects. We can only state that the observations made in both systems are qualitatively similar, and that the initial rapid drop in the number of Cu nuclei seen for Co contents of $x\% \leq 0.5$ (see figure 6.25) may be the result of wipe-out effects caused by single, isolated Co moments. Beyond this Co concentration, wipe-out effects may diminish due to Co-Co interactions.

The second point to stress about the data in figure 6.25 concerns the relation between the numbers of ^{63}Cu nuclei seen at each orientation. If twice the c⊥B integrated area is plotted on the same axes as the c//B curve shown in figure 6.25, we find that both curves are coincident and that the integrated areas follow exactly the same trend, within experimental error, at both orientations. This implies that at each Co concentration, the total number of ^{63}Cu nuclei that we see for c//B is always approximately twice that seen at c⊥B.

The fact that there is a considerable difference between the total number of Cu nuclei seen at c//B and c⊥B can be explained by first recalling the normal state components of conductivity along the a, b and c axes. From the values initimated in appendix A.1, we find that in the Y-Ba-Cu-O system, the conductivity in the c-direction (σ_c=0.188 $(m\Omega cm)^{-1}$) is always very much smaller than that in the a-b direction (σ_{ab}=9.091 $(m\Omega cm)^{-1}$). Now consider an YBCO crystal sitting in a standard NMR spectrometer with its c-axis parallel to the B_0-field. With the crystal in this configuration, the rf-field is applied in the direction parallel to the ab plane. Since the conductivity in this direction is high, the rf penetration around the planes will be good and so the NMR signal will be strong. In contrast, when the crystal is oriented c⊥B, the rf-field is applied parallel to the c-axis and so the rf-penetration is small and the NMR signal comparatively weak*. As the number of ^{63}Cu nuclei seen at c//B and c⊥B remains at a ratio of 2:1 over the entire Co concentration range, we can tentatively assume the ratio of σ_{ab}: σ_c also remains constant. We might also predict that the rf penetration depth in the direction parallel to the ab plane is approximately twice that in the direction perpendicular to the plane.

---

46 M. D. Daybell & W. A. Steyert, *Rev. Mod. Phys.* **40** 380 (1968)

47 S. Wada & K. Asayama, *J. Phys. Soc. Jpn.* **30** 1337 (1971)

* Note that in this model, we must assume that the rf penetration around the chain sites is independent of orientation.

6.4.5 Orbital & Spin Components of the ^{63}Cu Knight Shift

In this section, we use the available room and low temperature ^{63}Cu NMR data to evaluate the spin and orbital components of the Cu(2) Knight shift (at T=295K) as a function of Co concentration. Note that the disappearance of the Cu(1) peak in many of the superconducting and normal state ^{63}Cu NMR spectra prevents the evaluation of the Cu(1) Knight shift tensor.

As in chapter 5, the Knight shift components at T=1.5K and υ_L=141MHz were calculated by exact diagonalisation of the Hamiltonian. Since demagnetisation corrections have not been measured for the Co-doped system (nor indeed any other system apart from the $YBCO_7$ system), we must assume that, for a given B_0 field and field orientation, the Barrett demagnetisation corrections (obtained for the $YBa_2Cu_3O_7$ compound) are independent of cobalt doping and can be applied over the entire dopant range. Although it is quite possible that the superconducting fraction varies significantly with Co concentration, we note, in support of our assumption, that the Barrett demagnetisation corrections have already been convincing applied to all superconducting compositions ($0\leq\delta\leq0.35$) of the pure YBCO system in recent Knight shift studies (see section 5.4).

We must also further assume that the Knight shift at T=1.5K is purely orbital in origin (as suggested by the work on the Aberdeen sample) and subtract K_{orb} from the total ^{63}Cu shift at room temperature in order to deduce the spin component, K_s. We note, however, that this assumption is only valid if the Co magnetic moments do not persist in the superconducting state, as suggested by the absence of a low temperature Curie tail in the low Co% a.c. susceptibility measurements (see appendix B and also chapter 7). Where magnetic moments do exist in the superconducting state, the dipolar field from the moment would also contribute to the Knight shift at low temperature and the precise value of the orbital shift alone would be uncertain.

Although the ^{63}Cu NMR spectra at c//B and 1.5K were devastated for Co contents greater than 0.5%, we have attempted to fit a smooth curve (using statistical graphics software) to the available data in order to estimate the orbital component of the Knight shift for these samples. We do, however, accept that a large error is incurred in doing so. The resulting Knight shift components for the Cu(2) site are presented in table 6.3 (overpage).

Evidently, the a and b components of the orbital Knight shift are independent of Co doping and remain at the value set by the near O_7 YBCO sample. Since the total Cu Knight shift at room temperature changes little over the Co concentration range $0\leq x\%\leq0.5$, the corresponding $K^{a,b}$ spin shift components are constant at 0.30%, a value which is in exact correspondence with the Barrett result for $YBa_2Cu_3O_7$. Once the Co-doping has forced the structure to go tetragonal, the $K^{a,b}$ spin shift drops dramatically, falling to almost zero by x%=4.0.

Co %	$K^{c}_{orb}(2)$	$K^{c}_{s}(2)$	$K^{a,b}_{orb}(2)$	$K^{a,b}_{s}(2)$
0	1.27 ± 0.01	-0.03 ± 0.02	0.20 ± 0.02	0.30 ± 0.02
0.05	1.27 ± 0.01	-0.03 ± 0.02	0.20*	0.32 ± 0.02
0.15	1.27 ± 0.01	-0.03 ± 0.02	0.20*	-
0.3	1.09 ± 0.05	0.16 ± 0.05	0.20*	-
0.5	1.04 ± 0.05	0.18 ± 0.05	0.20*	0.30 ± 0.02
1.0	1.17 ± 0.15†	0.05 ± 0.15	0.20*	-
1.5	0.53 ± 0.12†	0.69 ± 0.12	0.20 ± 0.02	-
2.8	0.53 ± 0.12†	0.55 ± 0.12	0.20 ± 0.02	0.11 ± 0.04
4.0	0.53 ± 0.08†	0.53 ± 0.08	0.20 ± 0.02	0.08 ± 0.04

Table 6.3

The Cu(2) orbital & spin Knight shift components for the $YBa_2(Cu_{1-x}Co_x)_3O_{7-\delta}$ system at T=295K (where $0 \leq x\% \leq 4.0$). * = Expected result deduced from the general trend and † = orbital shift calculated from smooth curve fitted data.

Up to 0.15% Co, the component of the orbital shift along the c-axis is unaffected by the inclusion of Co ions at the chain site and its value of 1.27±0.01% again compares favourably with the corresponding Barrett result (1.28±0.01%) for the pure (δ=0) system. Further, subtraction of this orbital shift from the total c component of the ^{63}Cu Knight shift (1.24%) produces a shift contribution which is approximately zero, as in the $YBCO_7$ compound. Taken overall these Knight shift results suggest that 1 cobalt ion in every 222 (i.e 0.15% Co) Cu(1) ions is insufficient to produce any change in electronic structure at the Cu(2) sites and that the Monien, Pines and Slichter (MPS)[48] $Cu(2)^{2+}$ ionic model is still applicable (see section 5.4) up a Co concentration of 0.15%.

Beyond x%=0.15, the c component of the Knight shift becomes dependent on Co content, falling to around 85% of its previous value for the 0.3% and 0.5% samples and then to approximately 41% of this value for x%≥1.5%. The data for the 1.0% sample seems particularly unsatisfactory and will not be considered here. The relatively small decrease in the total c component Knight shift for 0.3% and 0.5% Co, coupled with the much larger decrease in K^{c}_{orb}, results in a considerable rise in the spin component, K^{c}_{s}.

---

[48] H. Monien, D. Pines & C. P. Slichter, *Phys. Rev. B* **41** 11,120 (1990)

This is further exemplified for the 1.5%, 2.8% and 4% samples, where the ratio of the spin to orbital components is approximately one.

In pure YBCO, there is little difference in the ^{63}Cu(2) peak positions for c//B and c⊥B at low temperature, since, at 141MHz, the large orbital shift for the c parallel orientation is balanced by a large quadrupole shift for the c perpendicular orientation, in such a way that the fields at resonance more or less coincide (see chapter 5)[49]. Here, for c⊥B, we only see minor changes in the spectra upon Co-doping, which naturally leads to the conclusion that doping at the chain site produces little change in the quadrupole interaction on the planes. For the c//B orientation, the situation is somewhat different; since the spin susceptibility is frozen out at 1.5K, it is plausible that the c//B data is consistent with considerable inhomogeniety in the planes, but only if that inhomogeneity affects the ^{63}Cu NMR through the orbital Knight shift.

Before entering into a discussion on the orbital components of the Knight shift, we will briefly examine the role of the changing spin components. In chapter 5, we noted that both the MPS[48] and Mila & Rice[50] (MR) analyses of the ^{63}Cu NMR data proposed a mechanism which included the direct anisotropic hyperfine coupling of the Cu(2) nucleus to the rapidly fluctuating on-site d-shell moment and an isotropic transferred hyperfine coupling to the neighbouring Cu spins. In addition, MPS require a second isotropic transferred hyperfine coupling to the oxygen holes. The d-spin ($K_{d\text{-}s}$) and isotropic hole contributions (K_h) to the spin Knight shift are proportional to the susceptibilities $\chi_{d\text{-}s}$ and χ_h, so that K^{α}_s is given by

$$K^{\alpha}_s = \frac{(A^{\alpha}+4B_1)\chi^{\alpha}_{d\text{-}s} + B_h\chi_h}{\gamma_e\gamma_n\hbar^2} \qquad (6.7)$$

where A^{α} is the hyperfine coupling of the nucleus to the on-site electron spin, B_1 is the transferred hyperfine coupling between a nucleus on one Cu site and the electron spin on an adjacent Cu site, $\chi^{\alpha}_{d\text{-}s}$ represents the spin susceptibility of the Cu^{2+} local moments and χ_h is the susceptibility assigned to the distinct hole contribution which originates on the chains and is coupled to the Cu(2) (4s) via the O(4) oxygens. At this stage, one might naturally wonder whether there is also a coupling to the holes on the oxygen of the Cu(2) plane. Simple symmetry arguments appear to rule out a coupling of such holes to the Cu(2) s states - at least for holes near the top of the O band. Another possibility of a contribution from the planar holes arises from the necessity that the planar O hole functions be orthogonalized to the Cu(2) x^2-y^2 hole state. This effectively mixes some Cu(2) x^2-y^2 function into the O band. Such effects can, however, be neglected since

---

[49] M. Solanki-Moser, D. P. Tunstall & W. J. Webster, *Supercond. Sci. Technol.***3** 464 (1990)

[50] F. Mila & T. M. Rice, *Physica C* **157** 561 (1989)

effects involving Cu 4s states dominate when they are present. Having made a case for the existence of the transferred hyperfine coupling B_h in equation (6.7), MPS then proceed to argue that this second isotropic 'hole' term vanishes. If this is the case, we must consider that either $\chi^c_{d\text{-}s}$ is equal to zero or that $A^c \cong -4B_1$ for $K^c_s=0$ (see table 6.3). It is now generally accepted that $\chi^c_{d\text{-}s}$ is non-zero and that, in fact, the hyperfine contributions A^c and $4B_1$ are equal and of opposite sign and so cancel perfectly.

From table 6.3, we observe that beyond x%=0.3, the spin component of the Knight shift in the c-direction ($K^c_s(2)$) increases with Co concentration from its value of zero at 0% and is positive. Since the spin Knight shift is proportional to the hyperfine coupling constants and the spin susceptibility, we must intimate that either the positive B_1 term in equation (6.7) gets progressively larger with increasing x and that the isotropic transferred hyperfine field between nearest neighbour Cu(2) spins dominates over the negative on-site term, or that the spin susceptibility $\chi^c_{d\text{-}s}$ is increasing with the addition of Co. Although the limitations of our susceptibility data do not permit a quantitaitve analysis of the spin component in the c-direction, we may qualitatively suggest that a changing spin susceptibility seems the most plausible reason for an increase in spin Knight shift. As the spin part of the conduction electron susceptibility is dependent upon the density of states at the Fermi level, an increase in the spin susceptibility implies an increase in the density of states. However, an alternative explanation can be gleaned from the definition of the $\chi_{d\text{-}s}$. The spin susceptibility of the Cu atom is defined by the relation,

$$\langle \mu^\alpha_s \rangle = \chi^s_{d\text{-}s} H_0 \qquad (6.8)$$

between the time averaged electron-spin magnetic moment $\langle \mu^\alpha_s \rangle$ induced on the Cu atom and the applied field H_0 acting along the α principal axis. Thus, it may be proposed that an increase in the spin susceptibility could result from an increase in the time averaged electron spin magnetic moment associated with Cu(2). Such a change in the Cu(2) magnetic moment upon Co-doping has already been suggested[51] and could arise via a coupling to the chain site through the O(4) bridging oxygens.

The opposite effect seems to be occuring for the a-b components of the spin Knight shift. For the pure sample, $K^{a,b}_s(2)$ is 0.30%. At a dopant level of 4%, the a-b component is approximately zero. Evidently, the Knight shift becomes increasingly dominated by the orbital shift in the a-b plane with the addition of Co, until at 4% Co the Cu(2) 3d spin does not appear to contribute to the Knight shift at all in this orientation.

An interesting feature of the low temperature ^{63}Cu(2) Knight shift data is the variation in the c-component of the orbital shift with increasing dopant, coupled with the complete insensitivity of the a-b orbital shift. In an attempt to account for this, we must

---

[51] E. Pollert, D. Sedmidubsky K. Knizek, Z. Jirak, P. Vasek & I. Janecek, *Physica C* **197** 371 (1992)

consider the crystal field splitting relevant to the Cu(2) site. In transition metals, the 3d shell responsible for paramagnetism is the outermost shell. The 3d shell experiences an intense inhomogeneous electric field produced by neighbouring ions. This inhomogeneous field is called the crystal field. The interaction of the paramagnetic ions with the crystal field splits the 2L+1 sublevels belonging to a given L, which are degenerate in the free ion. This splitting diminishes the contribution of the orbital motion to the magnetic moment.

In order to put the crystal field splitting into some context, it is useful here to introduce some of the basic ideas and terminology used in the ligand field theory of transition metal complexes. The metal orbitals which form σ bonds are $3d_{x^2-y^2}$, $3d_{z^2}$, 4s, $4p_x$, $4p_y$ and $4p_z$. We are interested in the 3d orbitals primarily here. In octahedral complexes, the $3d_{x^2-y^2}$ and $3d_{z^2}$ orbitals are equivalent and the corresponding molecular orbitals, $\psi(\sigma^b_{x^2-y^2})$ and $\psi(\sigma^b_{z^2})$ are degenerate. The bonding molecular orbital for this degenerate pair is labelled e_g. The three remaining valence orbitals, $3d_{xz}$, $3d_{yz}$ and $3d_{xy}$ are properly situated for π bonding. The three resulting d_π orbitals are again equivalent and are given the symbol t_{2g}. The two orbital sets e_g (mainly $3d_{z^2}$ and $3d_{x^2-y^2}$) and t_{2g} (mainly $3d_{xz}$, $3d_{yz}$ and $3d_{xy}$) may be further split by the presence of the crystal field, producing excited states.

In the YBCO system, the ground state of the planar Cu is a nearly pure $d_{x^2-y^2}$ orbital with excited states d_{xy} and d_{yz}, d_{xz} at energies Δ_0 and Δ_1 (see figure 6.26), where Δ_0 and Δ_1 are the crystal field splittings given by

$$\Delta_0 = E(d_{xy}) - E(d_{x^2-y^2}) \qquad (6.9a)$$

and

$$\Delta_1 = E(d_{xz}, d_{yz}) - E(d_{x^2-y^2}) \qquad (6.9b)$$

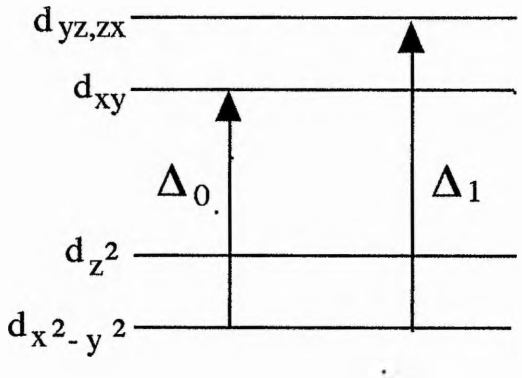

Figure 6.26

The crystal field energies for the Cu(2) sites in hole notation, where xyz = abc.

The excited states account for the orbital susceptibility. Following the analysis of Mila and Rice[50], the general formula for the orbital susceptibility (including covalency reduction effects) is

$$\chi^{\alpha}_{orb} = 0.81 \times 2\mu_B^2 \sum_n \frac{|< n|L^{\alpha}|3d_{x2-y2}>|}{E_n - E_0} \qquad (6.10)$$

where $|3d_{x2-y2}>$ is the ground state and $|n>$ is the excited state. This gives

$$\chi^{x,y}_{orb} = 0.81 \times 2\mu_B^2 \frac{1}{\Delta_1} \qquad (6.11a)$$

and

$$\chi^{z}_{orb} = 0.81 \times 2\mu_B^2 \frac{4}{\Delta_0} \qquad (6.11b)$$

Since

$$K^{\alpha}_{orb}(2) = A_{orb}(2)\, \chi^{\alpha}_{orb}(2) \qquad (6.12)$$

where the orbital hyperfine coupling, A_{orb}, is evaluated from the theoretical estimate,

$$A_{orb} = 2\, \gamma_e \gamma_n \hbar <r^{-3}> \qquad (6.13)$$

using[52] $<r^{-3}>$=6.3 a.u. for Cu^{2+}, we can calculate the crystal field splittings, Δ_0 and Δ_1 and deduce the orbital susceptibility for the pure and Co-doped systems using our orbital Knight shift values.

We consider the orbital susceptibility first: from our values of K^{α}_{orb}, we find that, for the 0% sample,

$$\chi^{c}_{orb}(2, x\%=0) = 10.56 \times 10^{-5} \text{ emu/mol} \qquad (6.14a)$$

and

$$\chi^{a,b}_{orb}(2, x\%=0) = 1.42 \times 10^{-5} \text{ emu/mol} \qquad (6.14b)$$

These values compare favourably with those obtained in previous analyses on the O_7 system by Mila & Rice[50] ($\chi^{c}_{orb}(2)$=9.6, $\chi^{a,b}_{orb}(2)$=1.7 x 10^{-5} emu/mol) and also by

---

[52] A. Abragam & B. Bleaney, *Electronic Paramagnetic Resonance of Transition Ions*, Oxford University Press (1970).

Walstedt & Warren[53] ($\chi^{c}_{orb}(2)=10.64$, $\chi^{a,b}_{orb}(2)=2.33 \times 10^{-5}$ emu/mol). With the addition of 4% Co, the c-component of the orbital susceptibility decreases while the a,b component remains constant, so that

$$\chi^{c}_{orb}(2, x\%=4) = 3.98 \times 10^{-5} \text{ emu/mol} \qquad (6.15a)$$

and

$$\chi^{a,b}_{orb}(2, x\%=4) = 1.42 \times 10^{-5} \text{ emu/mol} \qquad (6.15b)$$

These orbital susceptibilities are consistent with crystal field splittings of

$$\Delta_0 = 1.98 \text{ and } \Delta_1 = 3.59 \text{ eV} \qquad \text{for 0\% Co} \qquad (6.16a)$$

and

$$\Delta_0 = 5.27 \text{ and } \Delta_1 = 3.59 \text{ eV} \qquad \text{for 4\% Co} \qquad (6.16b)$$

Again, the values of $\Delta_{0,1}$ obtained here for the 0% sample vary in only minor ways to those deduced by Mila & Rice and Walstedt & Warren and they are in general agreement with the theoretical estimates from band calculations[54,55]. While the constant Δ_1 value for both samples indicates that the energy level of the d_{xz}, d_{yz} orbitals does not change relative to the $d_{x^2-y^2}$ orbital, the marked increase in the Δ_0 value for the 4% sample shows that the energy difference between the d_{xy} and $d_{x^2-y^2}$ orbitals increases with Co concentration. Since the spin orbit hyperfine coupling constant $A_{so}(\alpha)$ is a function of the crystal field splitting, such that

$$A^2_{so}(a,b) = \gamma_e\gamma_n\hbar^2 \langle r^{-3}\rangle \left[-\frac{11\lambda}{7\Delta_1}\right] \qquad (6.17a)$$

and

$$A^2_{so}(c) = \gamma_e\gamma_n\hbar^2 \langle r^{-3}\rangle \left[-\frac{6\lambda}{7\Delta_1} - \frac{8\lambda}{\Delta_0}\right] \qquad (6.17b)$$

where λ is the spin orbit coupling constant, we must surmise that the addition of 4% Co brings about a reduction in $A^2_{so}(c)$ by a factor of 2.5, but leaves the a,b component of the spin-orbit coupling unchanged.

An alternative explanation for the change in the Δ_0 crystal field splitting may also be proposed; provided that the energy levels of the d_{yx}, d_{zx} orbitals shift by the same amount as the ground state energy level, the observed increase in the Δ_0 value with the addition of

---

53 R. E. Walstedt & W. W. Warren, *Science* **248** 1082 (1990)

54 J. Yu, S. Massida, A. J. Freeman & D. D. Koeling, *Phys. Lett A* **122** 203 (1987)

55 A. K. McMahon, R. M. Martin, S. Satpathy, *Phys. Rev. B* **38** 6650 (1988)

Co is consistent with an unknown admixture of the $3d_{z2}$ orbital into the Cu(2) $3d_{x2-y2}$ ground state. The filling of the d_{z2} states on the Cu is generally bought about by a change in crystal field splitting due to the Coulomb interaction between the d-electrons and the p-holes. Such an admixture can also be expected to be produced by distortion (or inhomogeneity) around the Cu(2) sites. Yet another source of d_{z2} admixture may be band formation. There exists an overlap in the CuO_2 plane not only between the $3d_{x2-y2}$ and the p_σ orbitals of the oxygen, but also between the d_{z2} orbitals of the Cu and the same oxygen orbitals. Thus, p-d hybridisation will mix up all three kinds of orbitals, leading to the formation of hybrid bands with some admixture of d_{z2} orbitals. The likelihood of any of the above possibilities occuring may be increased by Co-doping.

Mixing of the $3d_{z2}$ and $3d_{x2-y2}$ wavefunctions is also expected to occur in the ground state of the Cu(1) site and has also been suggested as an explanation[56] for the polarised L-III X-ray absorption and EELS measurements taken on the Cu(2) site in the pure YBCO system with decreasing oxygen[57,58]. It should however be noted that the $K^c(2)$ NMR results[59,60] for the $YBa_2Cu_3O_{6.64}$ sample are virtually indistinguishable from that of the 90K phase, which has lead to the suggestion that the orbital shift $K^c_{orb}(2)$ is invariant to O-concentration in the pure system. This strongly indicates that very different mechanisms are operating with oxygen doping and Co-doping.

Finally, it is interesting to note that Zn doping at the Cu(2) site does not seem to produce any change in the c-orbital component of the Knight shift. The residual a-b component at 4.2K, $K^{a,b}_{orb}$, does, however, appear to increase with Zn concentration[61].

---

56 D. Khomskii & E. I. Neimark, *Physica C* **173** 342 (1991)

57 A. Bianconi, M. De Santis, A. Di Cicco, A. M. Flank, P. Lagarde, H. Katayama-Yoshida, A. Kotani & A. Macelli, *Phys. Rev. B* **38** 7196 (1988)

58 A. Nucker, H. Romberg, X. X. Xi, J. Fink, B. Gegenheimer & Z. X. Zhao, *Phys. Rev. B* **39** 6619 (1989)

59 M. Takigawa, A. P. Reyes, P. C. Hammel, J. D. Thompson, R. H. Heffner, Z. Fisk & K. C. Ott, *Phys. Rev. B* **43** 247 (1991)

60 R. E. Walstedt. W. W. Warren Jr., R. F. Bell, R. J. Cava, G. P. Espinosa, L. F. Schneemeyer & J. V. Waszczak, *Phys. Rev. B.* **41** 9574 (1990)

61 K. Ishida, Y. Kitaoka, T. Yoshitomi, N. Ogata, T. Kamino & K. Asayama, *Physica C* **179** 29 (1991)

6.4.6 Evidence for a Macroscopic Orthorhombic to Tetragonal Structural Transition

As discussed in chapter 2, structural studies involving X-ray[62,63,64] and neutron diffraction[62,65] techniques indicate that the substitution of trivalent ions such as Fe, Ga, Al and Co into the YBCO system leads to an orthorhombic to tetragonal (II) structural transition, which is presumed to be caused by a disordering of the oxygens in the basal Cu plane. Recent electron microscopy studies[66,67,68,69] have, however, re-examined the impurity-induced tetragonal phase in more detail (particularly in the Fe-doped material) and claim that it is a pseudotetragonal phase consisting of randomly oriented orthorhombic twin domains. When seen from X-ray and neutron diffraction experiments, the random orientation of such micro-domains would produce an *average* tetragonal phase with apparently equal a and b lattice parameters. In addition to experimental studies, several attempts have been made to theoretically model the effects that impurities at the Cu(1) site have on the local structure of the twin domains and on the oxygen vacancy ordering in the basal Cu plane[70,71,72,73,74]. Such studies indicate that short Cu-O chains are still present in the pseudotetragonal phase.

---

62 J. M. Tarascon, P. Barboux, P. F. Miceli, L. H. Greene, G. W. Hull, M. Eibschutz & S. A. Sunshine, *Phys. Rev. B* **37** 7458 (1988)

63 G. Xiao, M. Z. Cieplak, A. Gavrin, F. H. Streitz, A. Bakhshai & C. L. Chien, *Rev. Solid State Sci.* **1** (2) 323 (1987)

64 Y. Maeno, T. Tomita, M. Kyogoku, S. Awaji, Y. Aoki, K. Hoshino, A. Minami & T. Fujita, *Nature* **238** 512 (1987)

65 G. Xiao, M. Z. Cieplak, D. Musser, A. Gavrin, F. H. Streitz, C. L. Chien, J. J. Rhyne & J. A. Gotaas, *Nature* **332** 238 (1988)

66 Y. Xu, M. Suenaga, J. Tafto, R. L. Sabatini, A. R. Moodenbaugh & P. Zolliker, *Phys. Rev. B* **39** 6667 (1989)

67 G. Roth, G. Heger, B. Renker, J. Pannetier, V. Caignaert, M. Hervieu & B. Raveau, *Z. Phys. B* **72** 43 (1988)

68 Z. Hiroi, M. Takano, Y, Takeda, R. Kanno & Y. Bando, *Jpn. J. Appl. Phys.* **27** L580 (1988)

69 P. Bordet, J. L. Hodeau, P. Strobel, M. Marezio & A. Santoro, *Solid State Comm.* **66** 435 (1988)

70 I. S. Lyubutin, *Physica C* **182** 315 (1991)

71 E. Salomons & D. de Fontaine, *Phys. Rev. B* **42** 10,152 (1990)

72 G. Baumgärtel, P. J. Jensen & K. H. Bennemann, *Phys. Rev. B* **42** 288 (1990)

73 E. Takayama-Muromachi, *Physica C* **172** 199 (1990)

74 G. Baumgärtel & K. H. Bennemann, *Phys. Rev. B* **40** 6711 (1989)

In this study, the X-ray diffraction analysis (see section 6.1.4) suggests that, by a cobalt concentration of 2.8%, the macroscopic structure of the Co-doped system has switched from being orthorhombic to tetragonal. Such a structural transition appears to coincide with a rapid drop in T_c (section 6.1.4), a change in the linear concentration dependence of the room temperature ^{89}Y isotropic magnetic shift (section 6.2.3) and a considerable reduction in the total room temperature $^{63}Cu(2)$ a, b and c Knight shift components (sections 6.3.2 & 6.4.5). On a microscopic scale, TEM investigations on the present Co-doped samples suggest that an orthorhombic micro-domain structure exists well into the macroscopically 'tetragonal' region of the phase diagram[1,†]. With such confusion about the nature of the impurity-induced 'tetragonal' phase, it seems appropriate here to include any structural information which can be gleaned from the NMR study of the system.

The ^{89}Y NMR chemical shift has recently been shown to be an indirect probe of changes in crystallographic structure[33]. Evidently, similar nuclei experience different local fields if they are in different molecular or crystallographic surroundings and this is picked up, in part, as a change in chemical shift. In the YBCO system, the ^{89}Y chemical shift is expected to be sensitive to structure only to a distance of approximately 5Å from the Y site. Thus, if a true macroscopic orthorhombic to tetragonal structural transition exists in the present system, we should see a change in the ^{89}Y chemical shift with increasing Co content.

The ^{89}Y chemical shift, $^{89}\sigma$, in normal state $YBa_2Cu_3O_7$ was the subject of some debate early on in the proceedings. The initial work of Alloul et al[75] tentatively suggested that the $^{89}\sigma$ for $YBCO_7$ was equal to +22ppm relative to YCl_3. This value was soon ruled out as being too small by the high resolution NMR data of the Balakrishnan group[35], who proposed that the chemical shift for the normal state O_7 compound was around +200ppm relative to YCl_3 - thus leaving the Knight shift of the order of -300ppm. Subsequently, a number researchers have independently confirmed or utilised the fact that $^{89}\sigma$~+200ppm: the diamagnetic field corrections for the ^{63}Cu NMR results of Barrett et al[37] were established using an ^{89}Y Knight shift value of -300±50ppm. Both Takigawa et al[59] and Walstedt et al[60] independently combined their ^{63}Cu shift data on the $YBCO_{6.63}$ sample with the ^{89}Y shift data of Alloul et al[30] to obtain ^{89}Y chemical shift values of +200ppm and +175ppm, respectively. The work of Alloul et al[76] and Imai[77] also later produced chemical shift values of the order of +200±20ppm and +190ppm, respectively.

---

† Though, the size of these domains is observed to dramatically decrease with increasing Co content.

75 H. Alloul, P. Mendels, G. Collin & P. Monod, *Phys. Rev. Lett.* **61** 746 (1988)

76 H. Alloul, T. Ohno & P. Mendels, *J. Less Common Metals* **164-165** 1022 (1990)

77 T. Imai, *J. Phys. Soc. Jpn.* **59** 2508 (1990)

Taking a more fundamental approach, Dupree and Smith[78] investigated the ^{89}Y chemical shifts in a wide variety of yttrium oxides and concluded that the $^{89}\sigma$ value for YO_8 units typically ranged from +150 to +250ppm. In this study, we will take the chemical shift of normal state $YBa_2Cu_3O_{7-\delta}$ to be +200ppm relative to YCl_3.

As noted in section 6.2.3, the linear concentration dependence of the ^{89}Y isotropic magnetic shift has different slopes depending on the Co concentration range (see figure 6.13). For $0 \leq x\% \leq 2.8$, the shift data linearly extrapolates to a 0% value of -107ppm, whereas for $x\% \geq 2.8$, the extrapolated 0% value is -87ppm. The +20ppm difference in these values can be attributed to the change in chemical shift as the structure changes from orthorhombic to tetragonal with increasing Co concentration. Quantitatively, the *change* in chemical shift $\delta(^{89}\sigma(x))$ can be found by adapting equation (3.36), so that

$$\delta(^{89}\sigma(x)) = \delta(^{89}\Delta K(x)) - \delta(^{89}K_s(x)) \qquad (6.18)$$

where $\delta(^{89}\Delta K(x))$ is the change in ^{89}Y magnetic shift and $\delta(^{89}K_s(x))$ is the change in Knight shift as a function of Co concentration. By assuming that[33]

$$\delta(^{89}K_s(x)) = \frac{d(^{89}\Delta K)}{dx}\, x = 1.0833x \qquad (6.19)$$

where $d(^{89}\Delta K)/dx$ is the gradient of the high percentage line in figure 6.13 and by realising that $\delta(^{89}\Delta K(x)) = {}^{89}\Delta K(0) - {}^{89}\Delta K(x)$, it is possible to find the increase in chemical shift at each Co concentration. The absolute values of the normal state ^{89}Y chemical shift (i.e $\delta(^{89}\sigma(x))+200$ ppm) obtained by this method are presented as a function of x% in figure 6.27 (overpage).

Up to 2.8% Co, the ^{89}Y chemical shift changes in a similar fashion to the variation of the crystallographic a and b lattice parameters (see section 6.1.4 and appendix A.8). For concentrations equal to or greater than 2.8%, where the a and b lattice parameters are expected to vary only slightly with Co concentration, no change in chemical shift is detected and $^{89}\sigma$ remains static at a value of +220±5ppm. The fact that the ^{89}Y chemical shift initially varies with increasing Co content is a clear indication of a rapidly changing local environment around the Y site. The fact that these changes mimic those seen in the crystallographic lattice parameters, and have the same transitional concentration (x_c), must surely provide strong evidence to support the existence of a true macroscopic orthorhombic to tetragonal transition.

---

78 R. Dupree & M. E. Smith, *Chem. Phys. Lett.* **148** 41 (1988)

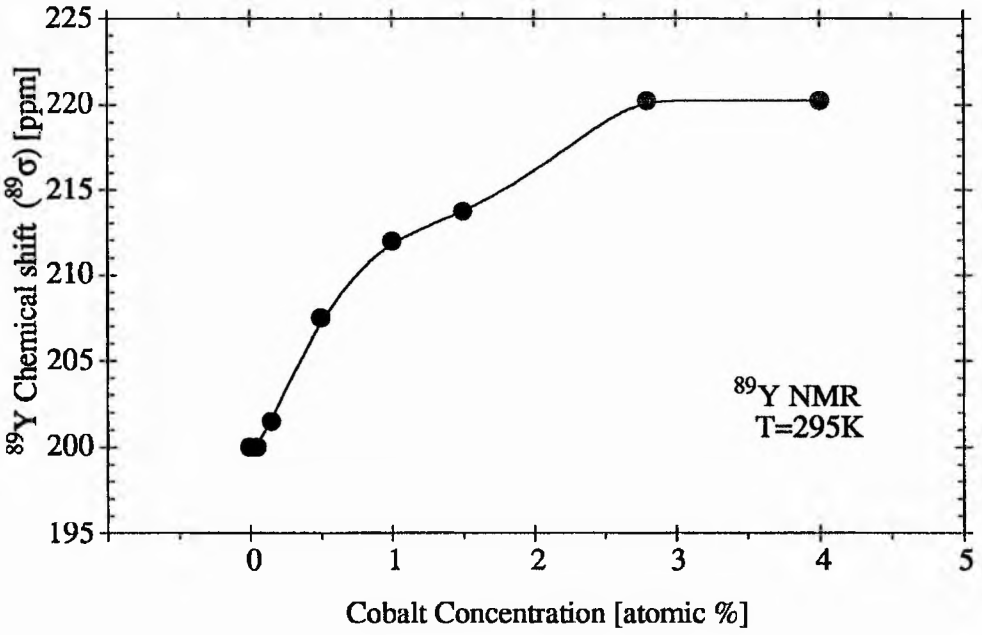

Figure 6.27

Variation of the normal state ^{89}Y Chemical shift ($^{89}\sigma$) with Cobalt Concentration. An error of ±5ppm applies.

Note that similar trends in the chemical shift are obtained in the room temperature ^{89}Y NMR study of Gencten[33], though the absolute values are generally slightly smaller than ours and outside the error by a few ppm. The difference between the room temperature ^{89}Y isotropic shift values found in this study and those found in the Gencten study (see figure 6.13) can probably be attributed to differing oxygen contents. Although the Gencten investigation implies that an O_7 system is used, the oxygen content is not strictly measured and there are a number of points to suggest that the Co doped samples studied definitely have an oxygen content less than 7.0, and probably less than 6.9. At 200K, Gencten also observes changes in chemical shift, but ones which are different to those at 295K. This surely implies a temperature dependent normal state chemical shift, which is unlikely, since the lattice parameters have a negligible temperature dependence[79].

Extending the general idea, Dupree et al[32] and Gencten[33] also find that ^{89}Y chemical shift changes occur for other chain site substitutions, such as Fe, Al and Ga.

---

[79] E. Salomons, H. Hemmes, J. J. Scholtz, N. Koeman, R. Brouwer, A. Driessen, D. E. De Groot & R. Griessen, *Physica B* **145B** 253 (1987)

6.4.7 Relation Between T_c & ^{89}Y Magnetic Shift

Figure 6.28 shows the correlation between the room temperature ^{89}Y magnetic shift and the average T_c (as measured via the various methods discussed in section 6.1) - with Co concentration as the implicit parameter.

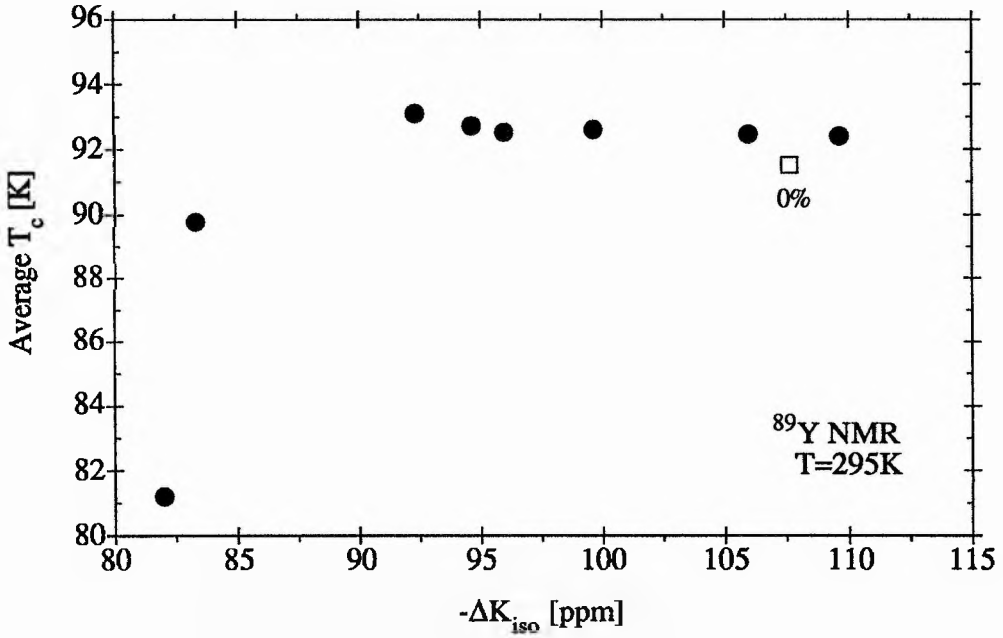

Figure 6.28

Variation of average T_c with the room temperature isotropic ^{89}Y magnetic shift. Co concentration is the implicit parameter. The 0% Co point has been included for reference.

At very low Co concentrations (x%=0.05), the T_c of the studied system (figure 6.1) coincidently rises as the room temperature ^{89}Y magnetic shifts (figure 6.13) become momentarily more diamagnetic. The ^{89}Y shifts then rapidly become more paramagnetic, while the T_c effectively remains constant up to about 1.5% Co. Beyond the orthorhombic to tetragonal transition (x%>1.5%), the ^{89}Y shift falls with T_c. A number of studies[32,33] obtain similar trends and find that beyond the orthorhombic to tetragonal transition, the T_c varies linearly with the ^{89}Y magnetic shift. In this study, we have insufficient samples in the relevant concentration range to draw this conclusion.

While the rapid change in the ^{89}Y magnetic shift for x%≤1.5 can probably be attributed to the changing chemical shift contribution ($^{89}\sigma$) with increasing Co concentration, the reason for the constant T_c in this concentration range still remains uncertain. We know that the oxygen content for all the samples studied is $O_{6.9}$. In the

pure system, the optimum oxygen concentration for the highest T_c (93.5K)[80,81] is $O_{6.95}$. This means that, in terms of δ, our system is slightly underdoped. When substituted into the chain site, the Co^{3+} ion donates extra electrons to the system. Since there is no uptake of extra oxygen to compensate for these additional electrons, it is anticipated that the extra electrons go to reducing the hole density in the planes. This is verified by a decrease in the Hall number at 295K with increasing Co concentration, as indicated by figure 6.6 (and section 2.3.3). As an initial point, we can therefore conclude that no correlation exists between T_c and the hole concentration in the planes, at least for x%≤1.5. This provides further evidence to suggest that T_c is not determined by hole concentration alone.

By substituting both the chemical (calculated in section 6.4.6) and isotropic magnetic shifts into equation (3.36), one is able to obtain a value for the ^{89}Y Knight shift $^{89}K_s(x)$ at each Co concentration. The variation of $^{89}K_s(x)$ with x is shown in figure 6.29 (see overpage).

Within experimental error, the Knight shift appears to remain approximately constant at around -307±0.5ppm for Co concentrations up to 1.5%. In a simple model, this would imply that the density of states at the Fermi level $N(E_F)$ is unchanged by the addition of Co ions up to this point. Since the T_c is also found to be constant in this concentration range (against a background of rapidly changing planar hole concentration), it seems plausible to suppose that the T_c may be dominated by the density of states at the Fermi level.

For x%≥2.8, the chemical shift has stabilised at +220ppm, and so any change in the ^{89}Y NMR shift now originates exclusively from the Knight shift contribution. Although the change in the Knight shift is small for x%≥2.8, its actual value is distinct from the constant Knight shift seen for x%<2.8. Since the Knight shift is related to the density of states at the Fermi surface and since there is a direct correlation between the ^{89}Y shift and T_c, it is probable, if we talk in terms of a Fermi liquid picture, that the decrease in T_c in this concentration range is due to a reduction of $N(E_F)$†. Qualitatively, the Co concentration dependence of the ^{89}Y magnetic shift is very similar to that observed in the pure system with decreasing oxygen content[30,35] and also in the interstitially-doped

---

80 J. D. Jorgenson, B. W. Veal, A. P. Paulikas, L. J. Nowicki, G. W. Crabtree, H. Claus & W. K. Kwok, *Phys. Rev. B* **41** 1863 (1990)

81 H. Alloul, A. Mahajan, H. Casalta & O. Klein, *Phys. Rev. Lett.* **70** 1171 (1993)

† Note that if we do not assume that a Fermi liquid picture applies, then the $N(E_F)$ is taken to be constant and we must talk in terms of a change in the 'spin fluid' susceptibility.

hydrogen system with increasing H concentration[82]. In both systems, the drop in T_c is found to be a reflection of the reduction of the density of states at the Fermi level. In addition, the Knight shift and the T_1 relaxation time are found to be related through the Korringa relation[32,33] (K^2T_1T=constant) for Co concentrations equal to or greater than 2.8%, further suggesting that the dominant cause for the change in shift and T_c is a reduction in the $N(E_F)$.

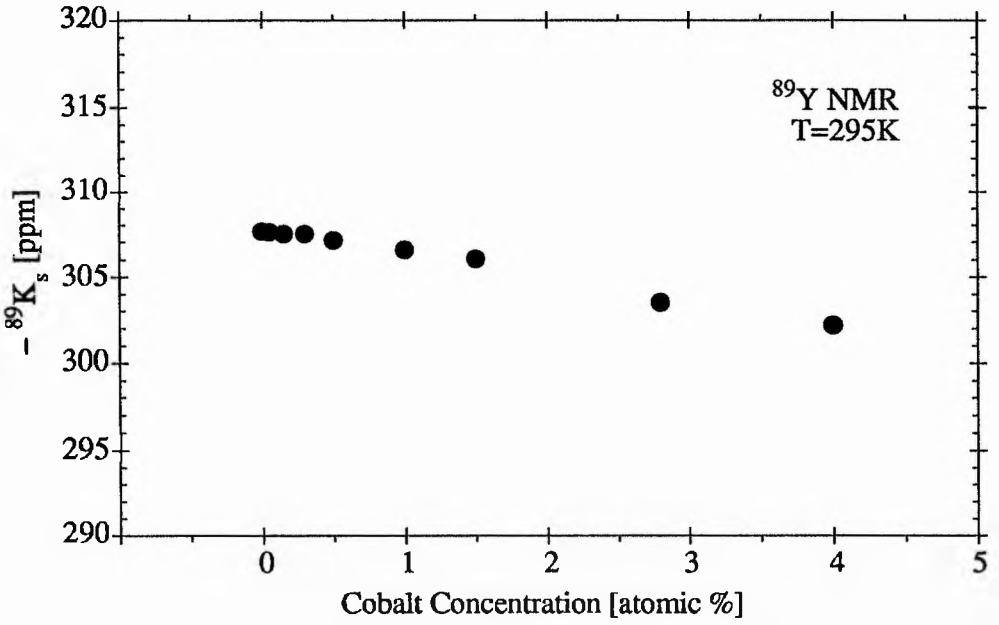

Figure 6.29

The variation of room temperature ^{89}Y Knight shift with Co concentration.

The rapid decrease in T_c for x%>1.5 can generally be associated with the loss of orthorhombicity of the system[8,9,10], though some researchers have also attributed it to the paramagnetic pair-breaking effects induced by magnetic moments[7]. From a study of the magnetic properties of O_2 annealed Co-doped YBCO, Yamada et al[16] conclude that decreases in T_c should be attributed to the properties of the oxygen ions in the system and not to magnetic effects. It is interesting to note that while the T_c is insensitive to Co concentration up to x%=1.5, the substituted Co ion induces a magnetic moment of about $3.7\mu_B$ onto a site which previously accommodated a P_{eff} of ~1.73 for the $Cu(1)^{2+}$ ion. This is a considerable magnetic moment which would be expected to have some effect on the YBCO system via the creation of dipolar fields around the Cu(1) site. It does however appear to have little effect on either T_c or the ^{89}Y Knight shift, further indicating that

82 S. D. Goren, C. Korn, V. Volterra, H. Riesemeier, E. Rossler, M. Schaefer, H. M. Vieth & K. Luders, *Phys. Rev. B* **42** 7949 (1990)

magnetic effects do not dominate. The dipolar fields created by the inclusion of Co magnetic moments at Cu(1) will be discussed further in chapter 7.

Further comparisons can be made between the Co doped system and the oxygen depleted 123 system. In particular, we note that the trends observed in the temperature dependence of ^{89}Y magnetic shift with increasing dopant concentration (figure 6.13) are qualitatively similar to those observed in the oxygen depleted pure YBCO system[30,35]. In fact, if the ^{89}Y shifts for the 2.8% Co doped YBCO (T_c=89K) sample are plotted (with temperature as the implicit variable) against the ^{89}Y shifts for $YBa_2Cu_3O_{6.92}$ - an oxygen deficient sample with the same T_c - a linear correlation is obtained (with $d\Delta K_{iso}(6.92)/d\Delta K_{iso}(2.8\%)\sim1$). A similar relation is also found to hold for the ^{89}Y shifts of the 4% Co doped sample and the oxygen deficient $YBa_2Cu_3O_{6.80}$ sample, which both have a T_c of around 80K† ($d\Delta K_{iso}(6.8)/d\Delta K_{iso}(4.0\%)\sim2$). These correlations are shown graphically in figure 6.30.

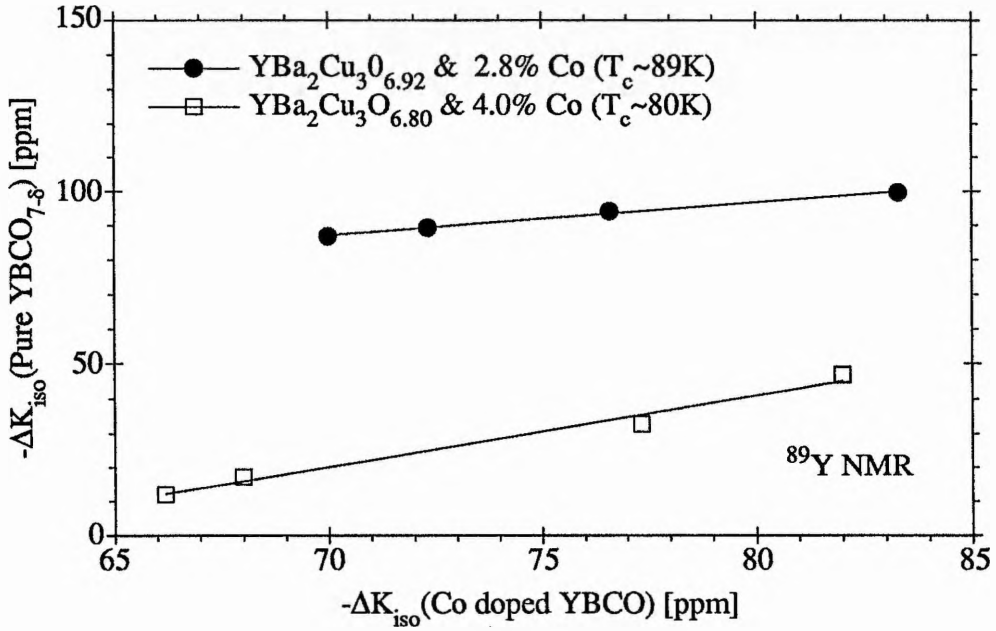

Figure 6.30

The ^{89}Y isotropic magnetic shifts of $YBa_2Cu_3O_{6.92}$ vs. $YBa_2(Cu_{1-x}Co_x)_3O_{6.9}$ with x%=2.8 (T_c~89K) and $YBa_2Cu_3O_{6.80}$ vs. $YBa_2(Cu_{1-x}Co_x)_3O_{6.9}$ with x%=4.0 (T_c~80K).
Note that temperature is the implicit variable.

† The ^{89}Y isotropic shift values for the $YBa_2Cu_3O_{6.92}$ and $YBa_2Cu_3O_{6.80}$ samples were calculated from refs. 23 and 35, respectively.

It has been suggested[30,35] that the temperature dependence of the ^{89}Y shifts in the oxygen depleted system might also be due to changes in the $N(E_F)$. The fact that a correlation exists between the temperature dependence of the ^{89}Y shifts in both oxygen depleted and Co doped systems with the same T_c, strongly suggests that the mechanism responsible for the temperature dependent behaviour in both systems may be the same and may be directly related to T_c.

Similar correlations have been obtained in the Co doped and oxygen depleted systems studied by Dupree et al[32] and Gencten[33]. It is also interesting to note that the ^{89}Y shifts in the $YBa_2Cu_4O_8$ system have the same temperature dependence as those in the oxygen depleted $YBa_2Cu_3O_{7-\delta}$ (δ=0.2) system with the same T_c[83].

6.4.8 Magnetic Effects of Cobalt Doping

HiT_c cuprates are closely related to magnetic insulators. Since modest doping of such insulators produces high temperature superconductivity, much theoretical interest has focussed on models involving a small number of itinerant charge carriers moving in a background of ordered or fluctuating magnetic moments (i.e spin polaron[84], spin bag[85] and spinon[86] theories). The essential interplay between the magnetic properties of the Cu 3d spins and the charge transport mediated by the O 2p holes is, however, still undefined. The nature of the charge and spin degrees of freedom in pure, normal state YBCO is usually discussed in terms of two broad pictures, which aim to describe the CuO_2 planes: the 'one component' picture and the 'two component' picture. In a two component model, one supposes that the electron spins on the Cu(2) d orbitals (which may be in the permanent moment limit (as in $YBCO_6$) but which may also have some important itinerant character) and planar O 2p holes are essentially two independent, decoupled systems. In the one component model, the two subsystems are expected to be coupled or hybridised into a single correlated spin system. In principle, a combination of NMR, NQR and macroscopic susceptibility experiments, which probe the local magnetic properties at different sites in the structure and the overall magnetism of the system, should provide crucial information on the relevant component model. At present, the Knight shift and

---

83 R. Dupree, Z. P. Han, D. McK. Paul, T. G. N. Babu & C. Greaves, *Physica C* **179** 311 (1991)

84 N. F. Mott, *Adv. in Phys.* **39** 55 (1990)

85 A. Kampf & J. R. Schrieffer, *Phys. Rev. B* **41** 6399 (1990)

86 P. W. Anderson, *Science* **235** 1196 (1987)

relaxation data at the Cu and Y sites in YBCO provide strong evidence in favour of a single quantum spin fluid[30,87,88].

In this work, we are presently interested in the appearance of extra magnetic susceptibility which is introduced into the YBCO system by Co doping. In particular, we want to ascertain where the extra susceptibility resides, whether it can be interpreted in a localised or delocalised picture and if this extra magnetism has a direct effect on the superconductivity in the planes.

The magnetic susceptibility data presented in section 6.1.2 seems relatively unambiguous. The cobalt ion appears to behave like a local moment with an induced temperature dependent Curie susceptibility suggestive of a P_{eff} of around 3.7μ_B. The Curie susceptibility is found to increase with Co concentration indicating a decreasing effective magnetic moment. In addition to the Curie moment associated with each Co, there is a temperature independent term which also increases with Co concentration. The extra susceptibility can be interpreted in several ways, of which two seem the most probable: (i) all such extra susceptibility is itinerant in nature and is associated with the planes and (ii) the temperature dependent term is associated with the chains and is due to local moments, whereas the temperature independent term is either distributed between the planes and the chains or else resides on the planes alone. Our listing of these particular options as a basis for discussion is founded on a number of factors. Oxygen vacancy effects have largely been interpreted through a model of type (i) and since many similarities exist between Co doping and oxygen depletion, model (i) must be an option. Co doping in other systems often ends up as non-magnetic, particularly if it enters in the 3+ state[52], whereas Co-doping in noble metals is characterised as a Kondo system[44] with a very high T_K. This previous experience of Co-doping gives us the freedom to suppose that any local moment-like terms that appear in the susceptibility of YBCO on doping do not necessarily have to be interpreted as local moments sitting on the chain sites.

In deciding between the relevant possibilities of the magnetic state, we rely heavily on the powder data of Alloul et al[30] and their investigation of oxygen stoichiometry effects on ^{89}Y isotropic shifts. In fact, we take this study as a model of the effect on shifts of a variation in hole concentration with no magnetic moment induced. A comparison of the T variation of the ^{89}Y shifts obtained in this study (figure 6.13) with those obtained by Alloul, immediately establishes that there are strong similarities, with the shifts generally becoming more positive with increasing x or δ. We can go further and seek to make this comparison more quantitative by first comparing the relative efficiency of the reduction of oxygen concentration and the increase in Co concentration in reducing

---

87 F. Mila & T.M. Rice, *Phys. Rev. B* **40** 11,382 (1989)

88 See M. Mehring, *Appl. Magn. Reson.* **3** 383 (1992) and references therein.

the hole concentration on the planes. From Hall effect studies, it is found[89] that the Hall number falls by an order of magnitude for a Co concentration of about 3% or for an O vacancy concentration of 1.5% (δ=0.1). The Alloul data indicates that a 2% oxygen vacancy concentration causes a 16ppm change in the ^{89}Y isotropic shift at T=295K and a 60ppm change at 160K. Our low temperature $^{89}\Delta K_{iso}$ data is very comparable, i.e. the change in the ^{89}Y shift caused by 2.8% or 4% Co-doping at 180K is also ~60ppm and this density of Co-doping from the Hall effect is the equivalent of 1.5% oxygen vacancies. The change in the room temperature shifts are also found to be comparable.

Although Co doping and oxygen depletion seem to produce proportionately similar effects in terms of hole concentration and ^{89}Y NMR shifts, when we compare the effects of the two doping mechanisms on the magnetic susceptibility, a marked difference emerges. The data of Parkin et al[90] on oxygen deficiency effects show that as oxygen is withdrawn from the YBCO lattice, the macroscopic magnetic susceptibility drops and becomes temperature dependent, with lower temperature producing lower χ_m. In contrast, our data shows an increase in macroscopic susceptibility as Co concentration increases and as temperature decreases. To make any sense of this magnetic data, we first return to the findings of the Alloul study[30]. In this study, the ^{89}Y nuclei are found to be a direct probe of the susceptibility of the CuO_2 planes. In particular, the ^{89}Y nuclear spin is found to be directly coupled to the planar oxygen orbitals and a shift of $^{89}\Delta K_{iso}$ to more positive values is an interpreted as a drop in planes magnetisation. Since our ^{89}Y results exhibit shifts which are very similar to those produced by oxygen stoichiometry effects, a plausible scenario for the increase in the magnetic susceptibility of our system is that all the measured susceptibility changes occur on the chains, apart from a relatively small drop in χ on the planes as x increases.

Further, we must note here that the ^{89}Y linewidths depicted in figures 6.16 and 6.18 show a marked contrast with the ^{89}Y powder data of Alloul et al. It is necessary to suppose under these circumstances that although the effect of O and Co concentration changes may be similar when discussing average ^{89}Y shifts, there must be substantial inhomogeniety induced on the planes susceptibility by Co that is not produced by oxygen vacancies. Such inhomogeneity on the planes is also suggested by the ^{63}Cu NMR.

Finally, in this section, we consider whether the Curie terms which appear in the susceptibility on doping, can realistically be interpreted as local moments sitting on the Cu(1) site. Firstly, we note that the Curie constant C, which reflects the effective magnetic moment on an ion site, increases proportionately with Co concentration. This

---

[89] N. Ong, *Physical Properties of High Temperature Superconductors*, Vol. II, ed. D. M. Ginsberg, World Scientific (1990)

[90] See Alloul et al, ref. 30.

strongly implies that the temperature dependent paramagnetism comes from the substituted Co ions and any induced effects on the host matrix as a result of the substitution. In addition, the paramagnetic moment is found to be independent of oxygen concentration, indicating that the induced moment is not associated with oxygen disorder[62]. From our brief analysis of the susceptibility terms in section 6.1.2, we found that the Curie contribution reflected an effective magnetic moment of around $3.7\mu_B$ per Co ion ($\equiv g\sqrt{S(S+1)}\mu_B$). The size of this paramagnetic moment is substantial, corresponding to a spin contribution of 2 to 3 electrons (assuming g=2). It is, however, less than the 4 unpaired electrons expected from the trivalent Co ion[91]. We have already established that a P_{eff} value of $3.7\mu_B$ is inbetween the two values of $4.9\mu_B$ (s=2) and $2.8\mu_B$ (s=0), which correspond to the Co^{3+} (d^6) high spin and low spin states, respectively. We may, however, consider an intermediate Co^{3+} spin state with s=1. In fact, similar magnetic moments per Co ion have been obtained for Co^{3+} in an intermediate electronic spin configuration in other oxides where the octahedral environment is distorted due to the presence of oxygen vacancies (such as the perovskite $Sr_2Co_2O_5$ phase)[92,93]. The intermediate spin state is generally metastable and transforms to a high spin state at elevated temperatures. It is, however, difficult to verify the intermediate state in YBCO using high temperatures, since the results are complicated by the loss of oxygen which occurs at temperatures above 400°C.

Having established from the magnetic data that there is a possibility that the Curie terms arise from a local Co^{3+} moment with an intermediate spin state, we now turn to the NMR data for support of this idea. At first sight, one would expect that the existence of randomly occuring Co moments at the Cu(1) sites would create large dipolar or RKKY local fields at the Y sites. Nuclear spins in the immediate vicinity of the local moments would be greatly shifted with respect to the NMR of a pure sample, while the superposition of the resonances for distant nuclei would yield a much broadened NMR line, which is temperature dependent. Of all the observable NMR nuclei in the YBCO system, the ^{89}Y NMR signal produces the narrowest line. ^{89}Y NMR is therefore the most sensitive probe of the existence of localised moments available to us.

Reflecting on the oxygen deficient studies of Alloul et al[30] once more, we find that, down to 100K, there is no evidence to suggest that the local moments, which appear on the Cu(1) sites at lower oxygen concentrations, cause any detectable line broadening in

---

91 P. F. Miceli, J. M. Tarascon, L. H. Greene, P. Barboux, F. J. Rotella & J. D. Jorgenson, *Phys. Rev. B* **37** 5932 (1988).

92 J. C. Grenier, S. Ghodbane, G. Demazeau, M. Pouchard & P. Hagenmuller, *Mater. Res. Bull.* **14** 831 (1979)

93 G. Thornton, B. C. Tofield & A. W. Hewat, *J. Solid State Chem.* **61** 301 (1986)

the ^{89}Y NMR of the pure system. We take this to imply that any inhomogeniety effects or disorder in the oxygen distribution which might occur in the doped system, have no effect on the linewidth and that subsequently any line-broadening observed may be associated exclusively with Co dopant. It can seen from figures 6.16 and 6.18 that, for a given Co concentration, the ^{89}Y linewidth *is* found to be temperature dependent, with the line becoming progressively broader with decreasing temperature and increasing Co concentration. Thus, it seems clear that the linewidth is due to some paramagnetic broadening and must be attributed to local moments which develop upon doping. This can be further confirmed by comparison with ^{89}Y NMR linewidth data obtained on Ga substituted samples[34]. The non-magnetic Ga ion is known to substitute on the Cu(1) site. It is found that the ^{89}Y NMR linewidth observed for $YBa_2(Cu_{1-x}Ga_x)_3O_{7-\delta}$ (with x up to 0.1) has no Curie contribution and, if anything, the linewidth gets slightly narrower as the temperature is lowered. A direct comparison of these Ga results with the Co data presented here allows us to conclude that the extra linewidth observed in the Co doped system is due to the Co local magnetic moment. In fact, in a recent paper, Alloul et al[34] obtain a direct Curie-type scaling between the line broadening and the local moment χ in the Co doped system†. Further work now needs to be done to help clarify whether the Co moments are entirely localised at the Cu(1) sites or result from disorder-induced carrier localisation.

In conclusion, Co-doping seems to produce an increase in χ_0 as well as giving rise to local moments on the chain sites. In a band picture, this corresponds to an increase in the density of states. In contrast, in a model in which there are magnetic moments on the planar Cu atoms, χ_0 is proportional to 1/J, where J is the antiferromagnetic exchange energy between neighbouring spins.

6.4.9 Correlation of the ^{63}Cu & ^{89}Y Knight Shifts

The one-component antiferromagnetic Fermi liquid theory proposed by Millis, Monien and Pines[94] (MMP) and Monien, Pines and Takigawa[95] (MPT) to explain the NMR results in the pure system, predicts that ^{89}Y and $^{63}Cu_{\perp}(2)$ shifts should have the same temperature dependence. In fact, in the $O_{6.64}$ system, Takigawa et al[59] has shown that the temperature dependence of the Knight shift can be plotted as a universal curve for ^{63}Cu, ^{89}Y and $^{17}O(2,3)$ Knight shifts, thus demonstating that all the hyperfine

† The limited temperature interval over which our results are taken do not permit us to obtain this relation from the present data.

94 A. J. Millis, H. Monien & D. Pines, *Phys. Rev. B* **42** 167 (1990)

95 H. Monien, D. Pines & M. Takigawa, *Phys. Rev. B* **43** 258 (1991)

interactions of these nuclei are caused by the same type of electrons in a single spin fluid. The same direct correlation has also been obtained between the $^{63}Cu_{\perp}(2)$ and ^{89}Y shifts in the $YBa_2Cu_4O_8$ system[83]. While the lack of experimental results on the temperature variation of the ^{63}Cu shifts, prevents us from performing a similar analysis in the present Co-doped system, we *are* able to ascertain whether there is a direct correlation between the room temperature shift results for the $^{63}Cu(2)$ and ^{89}Y nuclei as a function of Co concentration.

Figure 6.31 shows a plot of the total ($K_s(2)+ K_{orb}(2)$) room temperature $^{63}Cu(2)$ Knight shift against the room temperature ^{89}Y Knight shift, with Co concentration as the implicit variable.

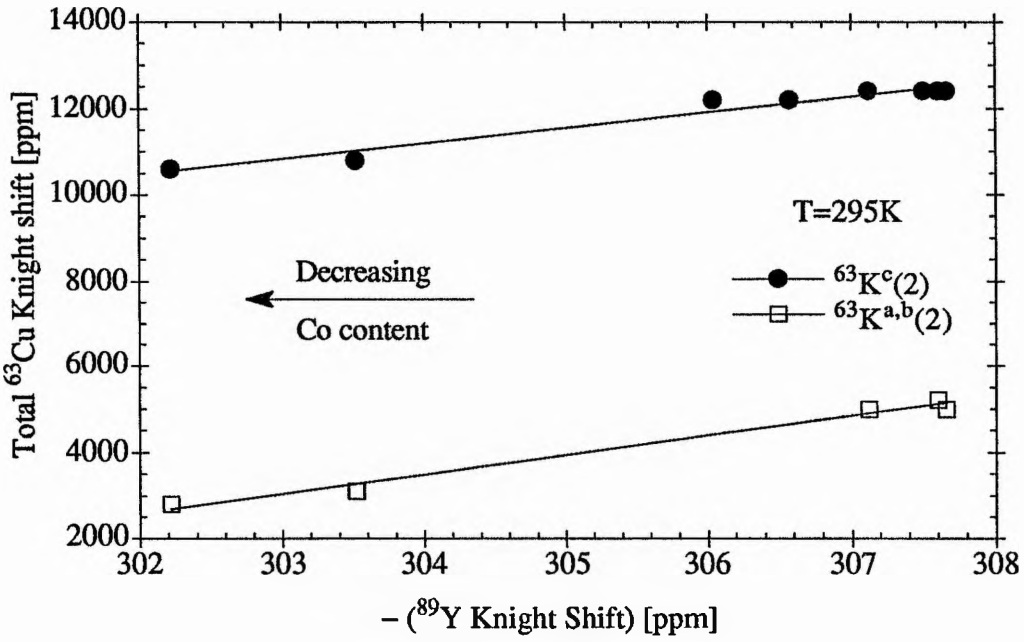

Figure 6.31

Correlation of the room temperature ^{63}Cu Knight shift with the room temperature ^{89}Y Knight shift, with Co concentration as the implicit variable.

Clearly, there is an approximately linear relation between both the c-components (gradient=-361) and the a,b, components (gradient=-451) of the ^{63}Cu Knight shift and the ^{89}Y Knight shift. It appears therefore that even with the addition of Co to the YBCO system, we still maintain some kind of direct correlation between the ^{63}Cu and ^{89}Y nuclei. We can only suppose that this implies that a single spin fluid, one component model still applies in the Co-doped system, at least at room temperature. To our knowledge, such a correlation has not been attempted in the pure system as a function of oxygen concentration.

Chapter 7

Computer Modelling of the Dipolar Fields in Co-Doped Y-Ba-Cu-O

7.1 Introduction

In this brief chapter, we address whether the dipolar fields associated with the Co moments on the Cu(1) site will induce systematic shifts on the ^{89}Y and $^{63}Cu(2)$ sites. In order to get some idea of the distribution of such dipolar fields, we have independently modelled the resultant dipolar effects that three isolated Co moments have on an extended lattice of Y and Cu(2) ions. Due to the very nature of the YBCO lattice and the randomness with which the Co ion enters the system, the full calculation is complex. However, with the use of a number of approximations, the calculation has been necessarily simplified.

While the basic outline and physics of the dipolar field model will be expounded in the following sections of this chapter, the dynamics of the computer model and the QuickBasic program itself will be presented in Appendix C.5. There are essentially three components to the dipolar field model (section 7.2): the calculation of the dipolar fields at one layer of Y or Cu from a single Co moment, using classical formulation; the expansion of this basic calculation to include three Co moments and an extended lattice of Y and Cu atoms; some statistical analysis to represent the distribution of Co moments in the YBCO lattice.

Note that a cobalt content of 1.5% was taken as a typical mid-range concentration and the whole calculation was performed for this sample only.

7.2 The Dipolar Field Model

7.2.1 The Classical Dipolar Field

The classical expression for the dipolar field $\mathbf{B}_{dip}$ at a distance $\mathbf{r}$ from a magnetic dipole of moment $\boldsymbol{\mu}$ is[1,2]

---

1 A. Abragam, *Principles of Nuclear Magnetism*, Oxford University Press (1989)

2 D. H. Martin, *Magnetism in Solids*, London Iliffe (1967)

$$B_{dip} = \mu_0 \left[\frac{-\mu}{r^3} + \frac{3(\mu.r)r}{r^5} \right] \tag{7.1}$$

where μ_0 is the permeability of a vacuum, and where

$$\mu = g\,\mu_B\,J \equiv P_{eff} \tag{7.2}$$

Here μ_B is the Bohr magneton, J (=L+S) is the total angular momentum quantum number and the g-factor is given by the Landé equation (see equation (6.4)). Note that μ is equivalent to P_{eff}, the effective magnetic moment in units of μ_B, in this case.

By combining equations (7.1) and (7.2) and taking the z-component of $\mathbf{B}_{dip}$, one obtains an expression for the dipolar field from a fully saturated Co moment oriented parallel to the c-axis as

$$[B_{dip}]_z = \frac{\mu_0 P_{eff}}{r^3} \left[1 - 3\cos^2\theta\right] \tag{7.3}$$

where the fact that $\mu.r=\mu r\cos\theta$ has been utilised and where θ is the angle between the z-axis (or equivalently the c-axis) and r.

Generally, the above expression is applicable at low temperatures and high fields (above 5T), since full magnetic saturation is only achieved under these conditions[3,†]. In order to account for the specific applied magnetic field (B_0) and upper temperature limit (T) of 295K used in our experiments, we must rely on the quantum theory of paramagnetism and the Curie law[3,4]. The general formulation of the Curie law (the derivation of which can be found in any solid state physics text) is

$$\chi(T) = \frac{M}{B_0} \equiv \frac{NJ(J+1)g^2\mu_B{}^2}{3k_BT} = \frac{NP_{eff}{}^2\mu_B{}^2}{3k_BT} = \frac{C}{T} \tag{7.4}$$

where M is the resultant magnetisation of the N atoms per unit volume responsible for the Curie paramagnetism in the crystal and C is the Curie constant. As we have already discussed in chapter 6, the strong interaction between the outer 3d shell of Co and the inhomogeneous crystal field produced by neighbouring ions in the crystal causes the orbital angular momentum (L) of the electrons in the 3d shell to be quenched. The net value of L falls to zero and so J=S (where S is the spin angular momentum quantum number) in equations (7.2) and (7.4) and in the Landé g-equation.

---

3 C. Kittel, *Introduction to Solid State Physics*, Wiley (1976)

† As T→ 0 for a fixed field, each ion becomes completely aligned by the field, with $|J_z|$ having its maximum value J. Thus P_{eff} is at its fully saturated value (see equation (6.3)).

4 N. W. Ashcroft & N. D. Mermin, *Solid State Physics*, HRW Publishers (1981)

The z-component of the dipolar field $[B_{dip}(T)]_z$ at a temperature T (where T>10K) can be found via re-arrangement of equation (7.4), to produce

$$[B_{dip}(T)]_z = \frac{\sqrt{J(J+1)}\, g\mu_B}{3k_BT} B_0 \times [B_{dip}]_z = \frac{P_{eff}\mu_B}{3k_BT} B_0 \times [B_{dip}]_z \qquad (7.5)$$

where $[B_{dip}]_z$ is given by equation (7.3). Using the second equality and a value of $P_{eff}=3.74\mu_B$/Co ion which is appropriate for the x%=1.5 sample, we find that, at an applied field of 11.75T for Y and 12.49T for Cu, the dipolar field at T=295K is

$$[B_{dip}(T)]_z \cong \frac{[B_{dip}]_z}{30} \qquad (7.6)$$

Equations (7.3) and (7.6) are the fundamental formulae upon which the calculation of the room and low temperature dipolar fields at Y and Cu sites from Co moment impurities are based. The following section provides a description of how the basic dipolar field calculation is extended to include the many Y and Cu lattice points and the several Co impurities which would be incorporated in the 'real' YBCO system.

7.2.2 Extension to the YBCO Lattice

The individual expanded calculations for the dipolar fields at the Y and Cu lattice points are very similar and differ only in the geometrical calculation of r and the number of lattice points incorporated in the computation. For simplicity, we have chosen to detail the calculation for yttrium sites only here.

The initial step in the model is to place a single Co moment at a Cu(1) site and to calculate (using equation (7.3)) the dipolar fields experienced by a two dimensional grid of Y atoms which sit at a perpendicular distance of (c/2) Å away from the Co moment (i.e. this is the first layer of Y atoms immediately above or below the Co(1) site, see figure 7.1). In order to perform this calculation, we need to find the Y-Co(1) distance r in equation (7.3). From simple trigonometric considerations, we see that the distance r_{xyz} from the Co(1) ion to any Y ion in (z+1) grid layers can be found in terms of the a, b and c lattice constants, such that

$$r_{xyz}^2 = a^2(x+\tfrac{1}{2})^2 + b^2(y+\tfrac{1}{2})^2 + c^2(z+\tfrac{1}{2})^2 \qquad (7.7)$$

where x, y and z are equal to 0, 1, 2, 3, etc and count the number of lattice constants a, b and c in the x, y and z directions, respectively. Note that the eight nearest Y neighbours to

the Co(1) ion would be indexed as x=0, y=0 and z=0, and that the first layer immediately above or below the Co ion is labelled z=0.

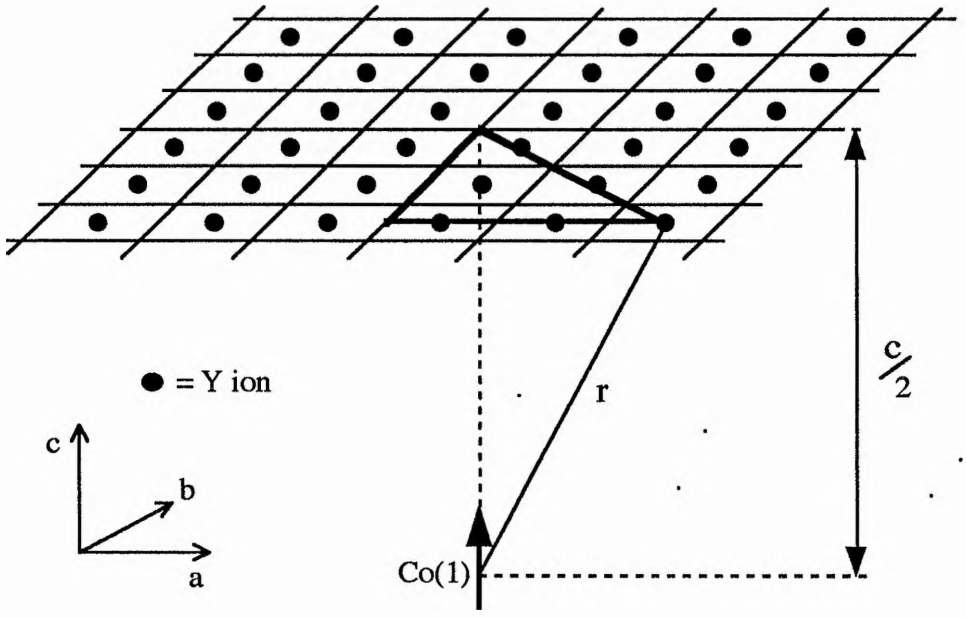

Figure 7.1

Diagramatic representation of the first layer of Y ions in relation to the Co moment at the Cu(1) site (not drawn to scale).

In order to get a general idea of the fall-off in magnitude of dipolar field with distance from the Co moment, the dipolar fields were initally calculated for a grid of (99 x 99) Y ions, such that the single Co ion sits at a perpendicular distance c/2 below the point (50,50). Evidently, the dipolar function will be symmetrical about the (50,50) point in both the x and y directions, but it is essential to keep the single Co moment at the centre of the grid in this way, since it allows maximum flexibility when adding additional Co moments and when extending the lattice in the x, y and z directions, at some later stage.

Having obtained the dipolar field values from a single Co moment at every position in a (99 x 99) grid of Y ions, it is now easy to see that a second isolated Co moment added to the system would produce an identical grid set of dipolar fields. Similarly with a third Co moment and so on. If the additional cobalt ions were added to the system in the same x-y plane as the first Co, as the influence of one Co moment overlaps with that of a second (and third), we are effectively moving one grid across another and adding together respective fields at chosen Y sites to obtain resultant dipolar field effects (see figure 7.2). This principle is the essential idea on which the bulk of the calculation of resultant dipolar fields at a range of Y sites is based.

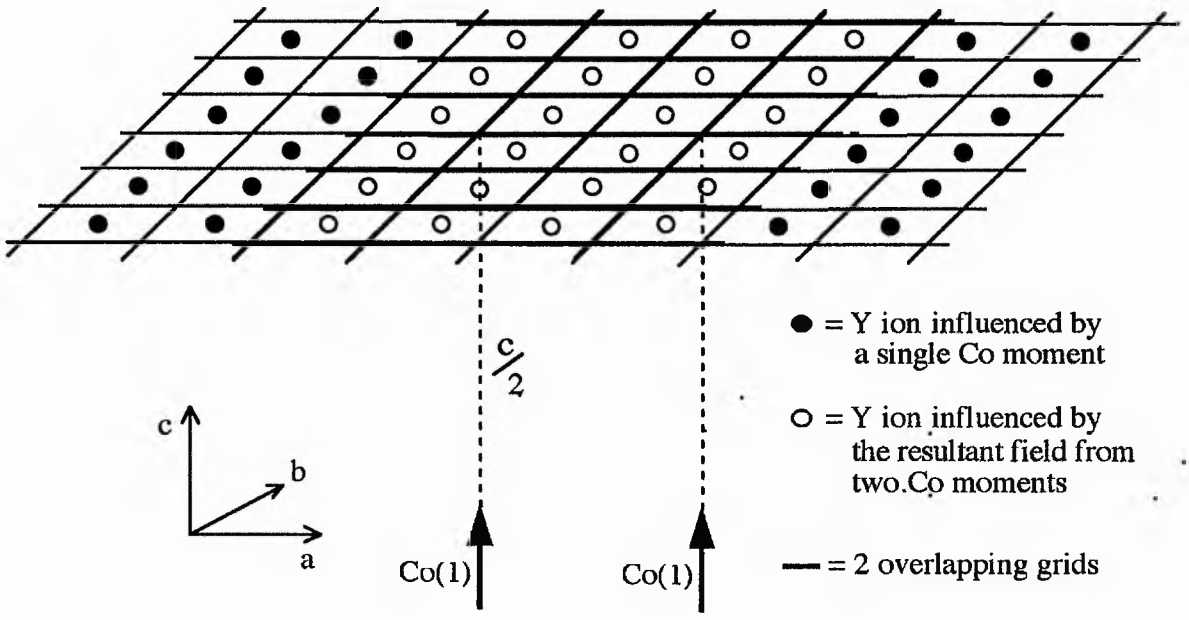

Figure 7.2

Schematic representation of the overlapping grid model used to calculate the resultant dipolar fields at Y sites from two or more Co(1) moments.

The basic methodology of the calculation of the resultant dipolar fields at the first layer of Y sites from three Co moments can now be summarised by the following points:

(i) Fix the first Co at a perpendicular distance of c/2 Å below the grid point (50, 50) and calculate the dipolar fields at each Y lattice point in the (99 x 99) grid, using equations (7.3) and (7.7) and using the fact that z=0 for the first layer. The integers x and y are successively incremented to move from Y site to Y site.

(ii) Having calculated the dipolar fields at each Y site from a single Co moment, focus on one chosen Y lattice point (k, l) and add a second Co moment at some point (m, n) in the same x-y plane as the fixed one. As m and n are successively incremented, the second Co moment moves around on a two dimension surface (which is defined only by the fact that it is a perpendicular distance of c/2 Å below the first layer of Y sites) and so the grid which is defined for the second moment moves across the static grid calculated for the first fixed moment. To obtain the resultant dipolar field at a given Y site (k, l) for a given configuration of Co moments, the dipolar fields from the fixed first Co and second Co, which is at some position (m, n), are added together†.

† Note that the sign of the individual dipolar field components will be accounted for by equation (7.3).

(iii) The same principle is used to extend the calculation to include a third Co moment at some position (s, t). Effectively, for a given Y site (k, l), the field from the fixed Co moment is added to the field from the second Co moment, which is now fixed at some position (m, n), while the third Co moment moves about the previously defined two dimensional surface with the incrementation of s and t. Once we have successively cycled through all the values of s and t and the fields from the third Co have been added to those of the temporarily fixed second Co and the static first Co moment, the second Co can be moved slightly and the whole process of incrementing s and t for the third Co can begin again. Thus, each resultant field from the three Co moments at any given Y site is defined by a unique set of parameters (k, l), (m, n) and (s, t). The vast numbers of resultant fields calculated this way are stored as an array by the computer (see appendix C.5.1).

So far, we have extended the calculation in the x-y plane and have only computed the dipolar fields for the Y sites in the first layer. It is now easy to see that, by adding an additional incrementration of z in equation (7.7), the calculation can be expanded in the c-direction to include successive layers of Y sites in the vertical z-plane.

At this stage in the computation, it is clear that we also need to (a) set some realistic limits on the calculation and (b) introduce some statistical factor which will account for the probability of finding 3 Co moments in any given configuration. Since the latter point is fairly crucial to the accuracy of the model, it will be discussed separately in the following section (7.2.3). It is also evident that the calculation has only dealt with the c//B orientation, so far, and we really need to account for the c⊥B orientation as well. This can easily be done by substituting $(\theta + 90)°$ for θ throughout the calculation.

A concentration of 1.5% Co suggests that, on average, 1 Co ion occurs in every 22 Cu(1) atoms. It therefore seems appropriate that the limits of the calculation should be set to approximately half the Co-Co distance (i.e the equivalent of 11a units in all directions). Note that 11a units in the c-direction encompasses 4 layers of Y ions and 8 layers of Cu(2) ions. We next have to ask the question: 'Are these limits realistic in terms of the magnitude of dipolar field ?' Well, from our initial calculations, 11a units takes the dipolar fields from a single Co down to the following values:

a max of +6.6 Gauss for Y ions, with the crystal orientation at c//B,

a max of -13.6 Gauss for Y ions, with the crystal orientation at c⊥B,

a max of +6.6 Gauss for Cu ions, with the crystal orientation at c//B

and a max of -12.2 Gauss for Cu ions, with the crystal orientation at c⊥B

In the Y NMR experiment, the c//B and c⊥B linewidths for the 1.5% sample at 160K are both around 4.5 kHz. Such a linewidth is equivalent to approximately 22 Gauss. Both linewidths are expected to be much broader at the lower temperatures at which this calculation is performed and so cut off points of around 6 Gauss and 13 Gauss for c//B and c⊥B, respectively, are much narrower than the experimental linewidths and therefore do not seem unreasonable. The $\Delta\upsilon_{1/2}$ value for low temperature ^{63}Cu(2) NMR line is of the order of hundreds of Gauss and so again the cut off points for the Cu calculation seem to be fairly acceptable.

Having calculated the resultant dipolar field effects that different configurations of three Co (note that the limitations on the movement of the Co ions will be discussed in section 7.2.3) have on an (11a x 11a x 11a) unit block of Y ions and having placed all available combinations of these fields in various arrays, it is now possible to try and deduce a spectrum from these answers. The spectrum we are looking for to compare with the experimental NMR spectra is a plot of the number of Y (or Cu) nuclei experiencing a given dipolar field vs. dipolar field in T. To achieve this, we effectively choose cut-off fields for the calculated resultant dipolar fields in the arrays. These limits, which we call the range, are larger than the cut-off fields used previously and are typically either ±0.001T (10 Gauss) or ±0.01T (100 Gauss). The dipolar field range -0.01T to +0.01T (for example) is then divided into a fixed number of 10,000 intervals or bins. The idea now is that the computer scans through the dipolar field arrays previously calculated and places each point in the array in the correct field interval. The number of Y ions experiencing a given dipolar field can be found by keeping a running tally of the number of points in each field interval. This principle is similar to the way in which a multi-channel analyser (MCA) works.

The final step in the model is to simply plot the number of points counted in each field interval (i.e. the number of Y ions experiencing a given dipolar field) against the field interval (dipolar field) itself.

7.2.3 Distribution of Co Moments

The calculation so far has not taken account of the fact that, due to the random positioning of the impurity Co atoms in the host lattice, some configurations of the three Co moments may be more probable than others. Somehow we have to account for this by modelling the distribution of the Co moments in the YBCO lattice.

The concept of statistically modelling particles which randomly occupy the sites of a lattice is well known, and has been discussed extensively in various cluster and

percolation problems which have appeared in the literature[5,6,7,8,9,10,11,12]. In particular, the ideas have been applied to study magnetic-nonmagnetic dilute alloy systems[13], magnetic impurities in metals[14] and the metal to non-metal transition in semiconductors[15].

The full statistical formulation of the random impurity is due to Markoff[16,17,18]. Although they have been used extensively in the study of NMR lineshapes due to magnetic impurities in metals[14], are the starting point of Anderson's treatment of dilute dipolar broadening[1,19], as well as Cohen and Reif's discussion of the quadrupolar broadening due to random crystalline imperfections[20], Markovian statistics are, by their very nature, extremely complex and are well outside the scope of this study. Instead, in this work, we will employ the simpler statistical formulation used by Alexander & Holcomb to study donor concentrations in semiconductors[15].

Following the work of Alexander & Holcomb, we can expect a roughly Poisson distribution of Co ions throughout the YBCO lattice. The probability distribution P(r) of a Poisson random variable is given by the equation

$$P(r) = \frac{\mu^r e^{-\mu}}{r!} \tag{7.8}$$

where the number of events, r equals 0, 1, 2..., where e is the exponential base, 2.71828

---

5 S. R. Broadbent & J. M. Hammersley, *Proc. Cambridge Phil. Soc.* **53** 629 (1957)

6 J. M. Hammersley, *Proc. Cambridge Phil. Soc.* **53** 642 (1957)

7 C. Domb, *Nature* **184** 509 (1959)

8 C. Domb & M. F. Sykes, *Phys. Rev.* **122** 77 (1961)

9 M. E. Fisher & J. W. Essam, *J. Math. Phys.* **2** 609 (1961)

10 M. E. Fisher, *J. Math. Phys.* **2** 620 (1961)

11 J. Hoshen & R. Kopelman, *Phys. Rev. B* **14** 3438 (1976)

12 See 'Simulation in Condensed Matter Physics 4' by D. W. Heermann in *Computational Physics*, Proceedings of the 32nd Scottish Univerisites Summer School in Physics, p29, Eds. R. D. Kenway & G. S Pawley, SUSSP Publishing (1987).

13 R. J. Elliott, B. R. Heap, D. J. Morgan & G. S. Rushbrooke, *Phys. Rev. Lett.* **5** 366 (1960)

14 R. E. Walstedt & L. R. Walker, *Phys. Rev. B* **9** 4857 (1974)

15 M. N. Alexander & D. F. Holcomb, *Rev. Mod. Phys.* **40** 815 (1968)

16 A. A. Markoff, *Wahrscheinlichkeitsrechnung*, Leipzig (1912): Quoted extensively in ref. 17.

17 S. Chandrasekhar, *Rev. Mod. Phys.* **15** 1 (1943): Also reprinted in ref. 18.

18 N. Wax (ed.), *Selected Papers on Noise & Stochastic Processes*, Dover, N. Y. (1954)

19 P. W. Anderson, *Phys. Rev.* **82** 342 (1951)

20 M. H. Cohen & F. Reif in *Solid State Physics*, Vol. 5, eds. F. Seitz & D. Turnbull, Academic Press (1957).

and where the mean, μ ($\mu>0$) is the average number of occurances and is given by

$$\mu = n\,p \tag{7.9}$$

In the general formulation,[21,22,23] n is the number of trials and p is the probability of one event happening. The Poisson distribution is a special case of the binomial distribution when p is very small (that is, the probability of the event happening is very small), but n is large enough ($n>20$) so that np is not insignifcant ($np<5$). Note that the probabilities P(r) are non-negative and sum to one, and thus form a discrete probability distribution.

Applying the Poisson distribution statistics to the case at hand, we find that the problem looks something like this: Suppose that we choose a macroscopic sample of Cu(1) atoms, n, within which r Co ions can be found. The number of Co ions per unit volume in the crystal structure is distributed with a Poisson distribution and the average density is μ ions per cm^3. For the 1.5% sample, the probability of finding a single Co (p) is (1.5 x 3)/100 or equally 1/22 = 0.045, since on average we expect 1 Co ion in every 22 Cu(1) ions. From these parameters, we can calculate the mean and hence the probability P(r) of finding r=0, 1, 2, 3 etc Co moments within given number of Cu(1) ions, provided we choose a suitable sampling number, n.

After some calculation and careful consideration, it is found that, for the 1.5% sample, the Poisson distribution figures are most reasonable for a sample size of n=64 Cu(1) ions (i.e. an (8a x 8a) unit surface in the x-y plane, in our model). In this case, the mean of the distribution is 2.88. Figure 7.3 (overpage) shows the Poisson distribution for μ=2.88.

In order to incorporate these probabilities into the dipolar field model, we simply multiply P(r) by the appropriate field contribution to the resultant dipolar field. That is, Pr(0) is multiplied by the dipolar field contribution with zero Co ions present (4.97 Gauss), Pr(1) is multipied by the sum of the dipolar field contributions with zero and one Co ions present and so on. The resultant dipolar field for a given set of (k, l) (m, n) and (s, t) values is then given by the summation of all the individual probability-accounted dipolar field contributions. It is these final resultant dipolar fields which are stored as arrays and then binned to give the theoretical spectrum.

In summary, the resultant dipolar fields from 3 Co ions, which were allowed to move on an (8a x 8a) surface in the x-y plane, were calculated for both Y and Cu ions in an extended YBCO structure. The distribution of Co ions within the lattice was

---

21 C. Chatfield, *Statistics For Technology*, Harmondsworth Penguin (1970)

22 M. R. Spiegel, *Schaum's Outline of Theory & Problems of Statistics*, Schaum Publishing (1961)

23 J. Topping, *Errors of Observation & Their Treatment*, IOP Publishing (1955)

represented by a Poisson distribution and the Y and Cu nuclei were chosen so that an (11a x 11a x 11a) block was defined within the lattice. This allowed the resultant dipolar fields to be calculated for up to 4 layers of Y ions and 8 layers of Cu(2) ions in the z-direction.

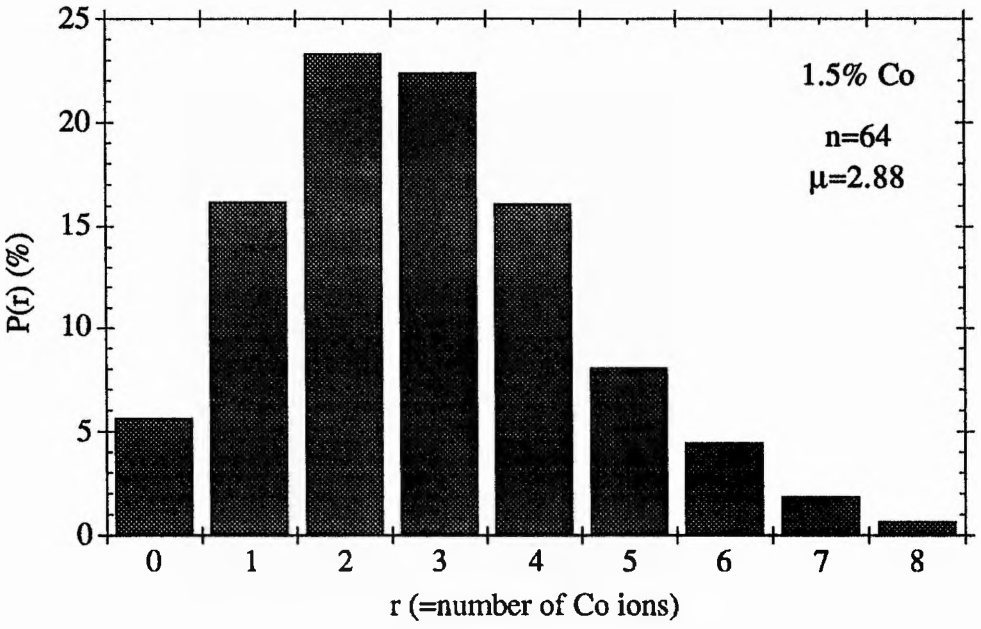

Figure 7.3

The Poisson distribution for a mean (μ) of 2.88.
This effectively represents the probability distribution of finding r Co ions in a sampling number of n=64 Cu(1) ions.

Note that although a fourth Co ion could have been added to the system it was calculated that the computer program would have taken 14 days of CPU time to produce one spectrum, without much improvement upon the 3 Co ion spectrum. The inclusion of a fourth Co ion was therefore omitted from the final model and program.

7.3 Results & Conclusions

In order to get some idea of the effects that a single Co moment (with a P_{eff} of $3.74\mu_B$/Co which is appropriate for the 1.5% sample) has on the first layer of Y and Cu ions in the YBCO lattice, the low temperature dipolar fields ($[B_{dip}]_z$) for the z=0 layer have been plotted as a function of the (k,l) coordinates, for both the Y and Cu site positions and at both the c//B and c⊥B orientations, in figures 7.4 to 7.7.

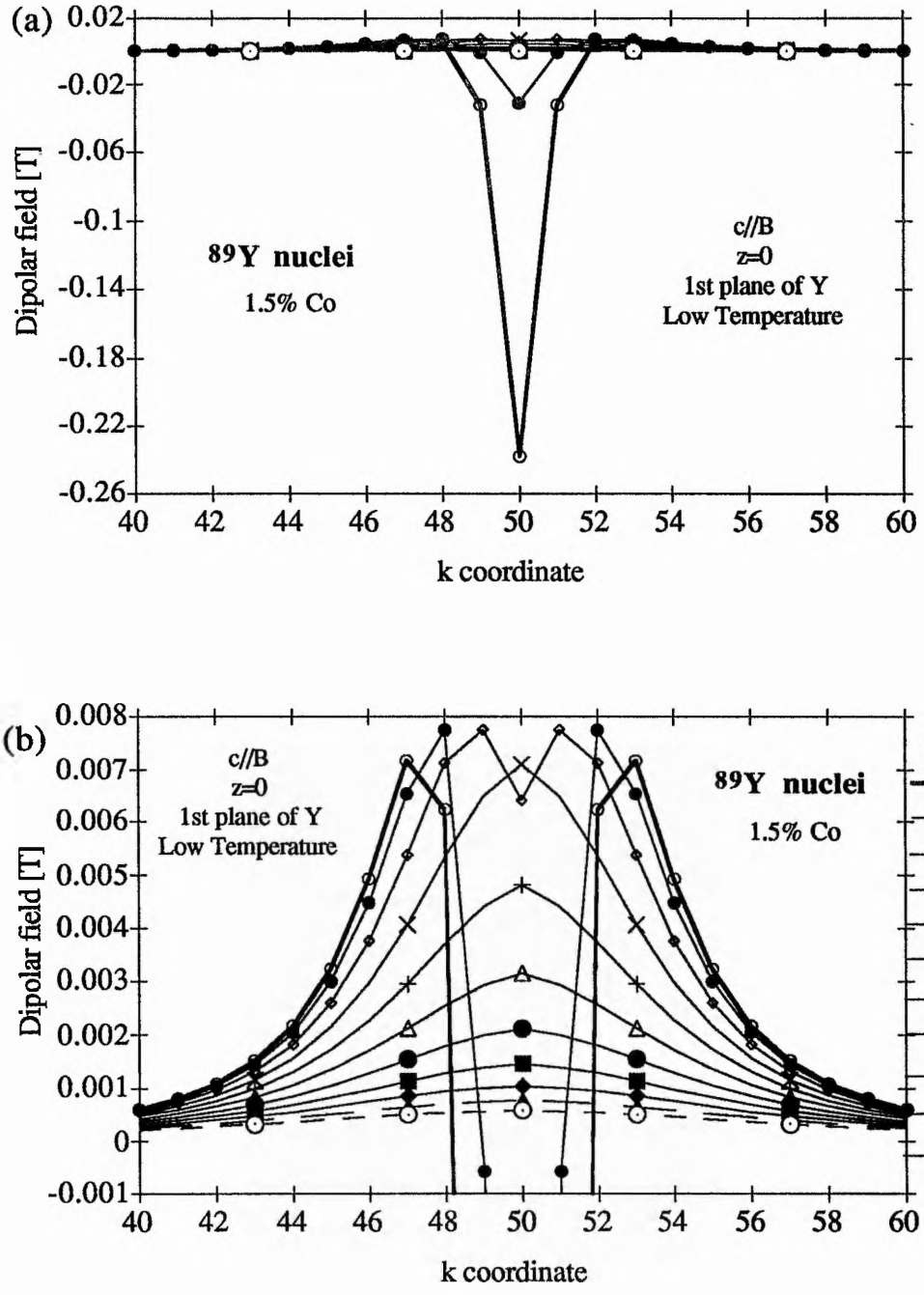

Figure 7.4

The low temperature (T<10K) dipolar field effects that a single Co moment placed at the point (50,50) has on the first (z=0) layer of Y ions immediately above it. The orientation of the crystal is c//B & the coordinates of the Y ions in the two dimensional plane are labelled (k, l). Figure (a) represents the full range of dipolar fields including those experienced by the Y ions in close proximity to the Co moment & figure (b) expands on that field interval which is experienced by many Y ions further away from the Co.

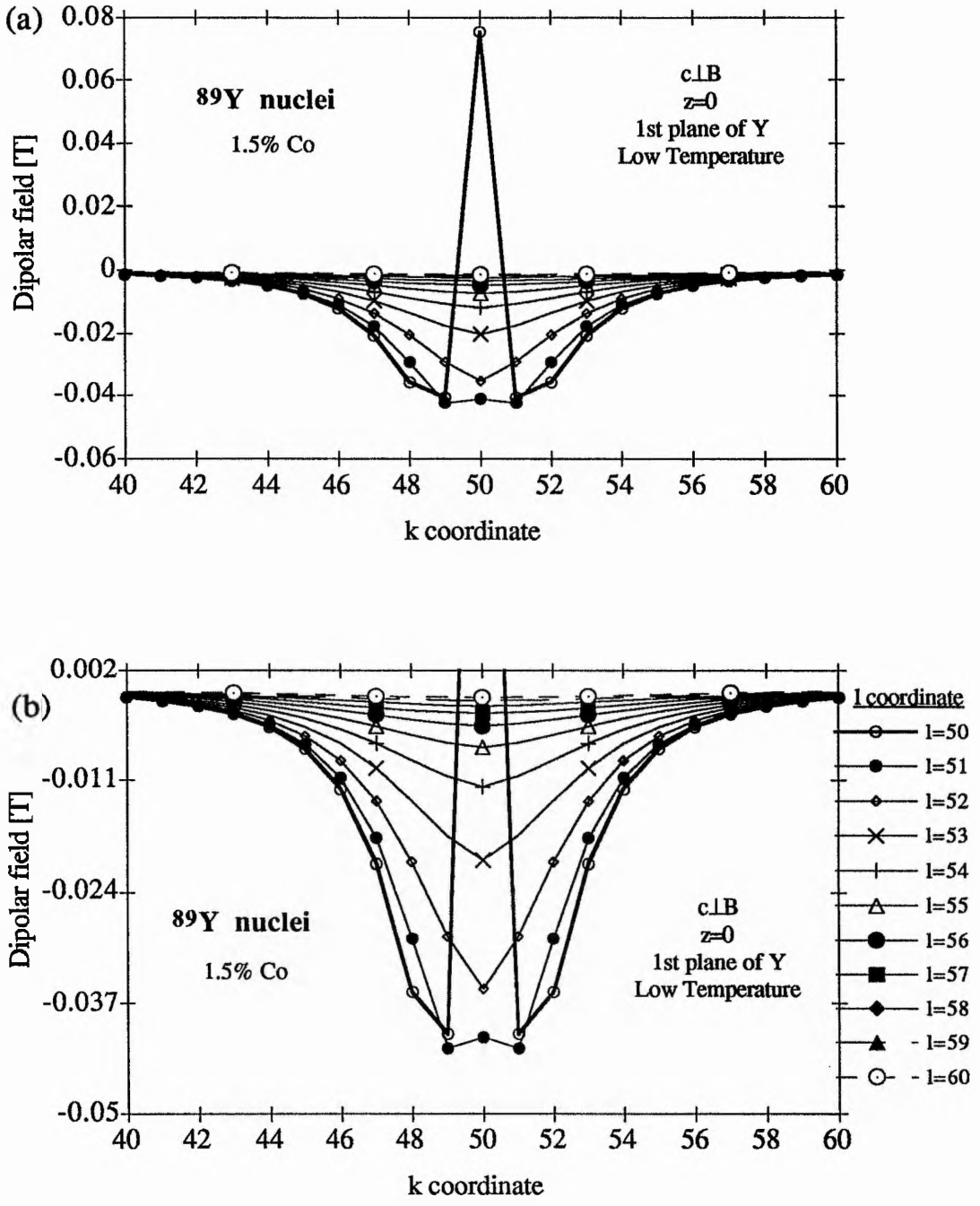

Figure 7.5

As for figures 7.4 (a) & (b) but with the crystal in the c⊥B orientation.

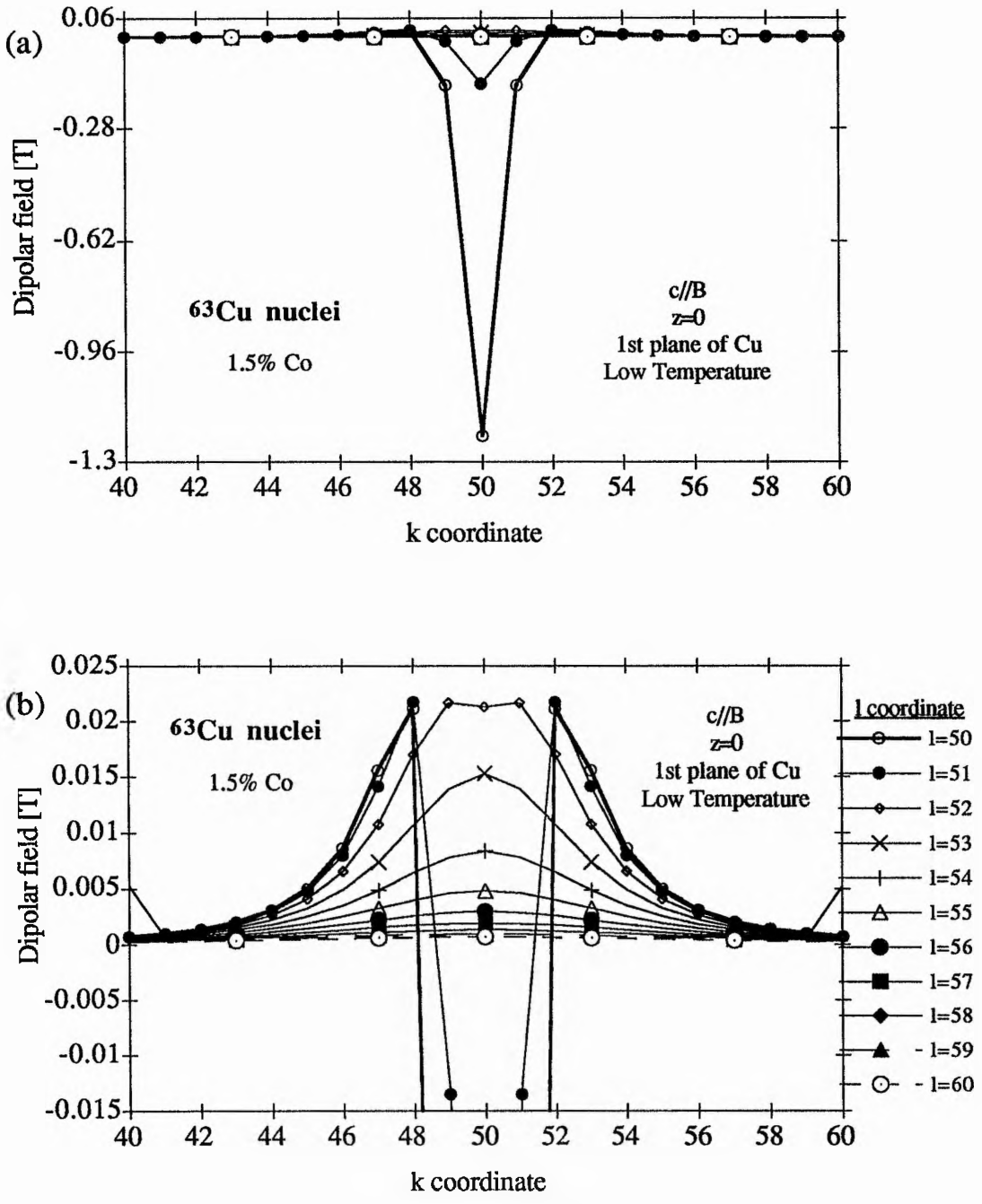

Figure 7.6

The low temperature (T<10K) dipolar field effects that a single Co moment placed at the point (50,50) has on the first (z=0) layer of Cu(2) ions immediately above it. The orientation of the crystal is c//B & the coordinates of the Cu(2) ions in the two dimensional plane are labelled (k, l). Figure (a) represents the full range of dipolar fields including those experienced by the Cu(2) ions in close proximity to the Co moment & figure (b) expands on that field interval which is experienced by many Cu(2) ions further away from the Co.

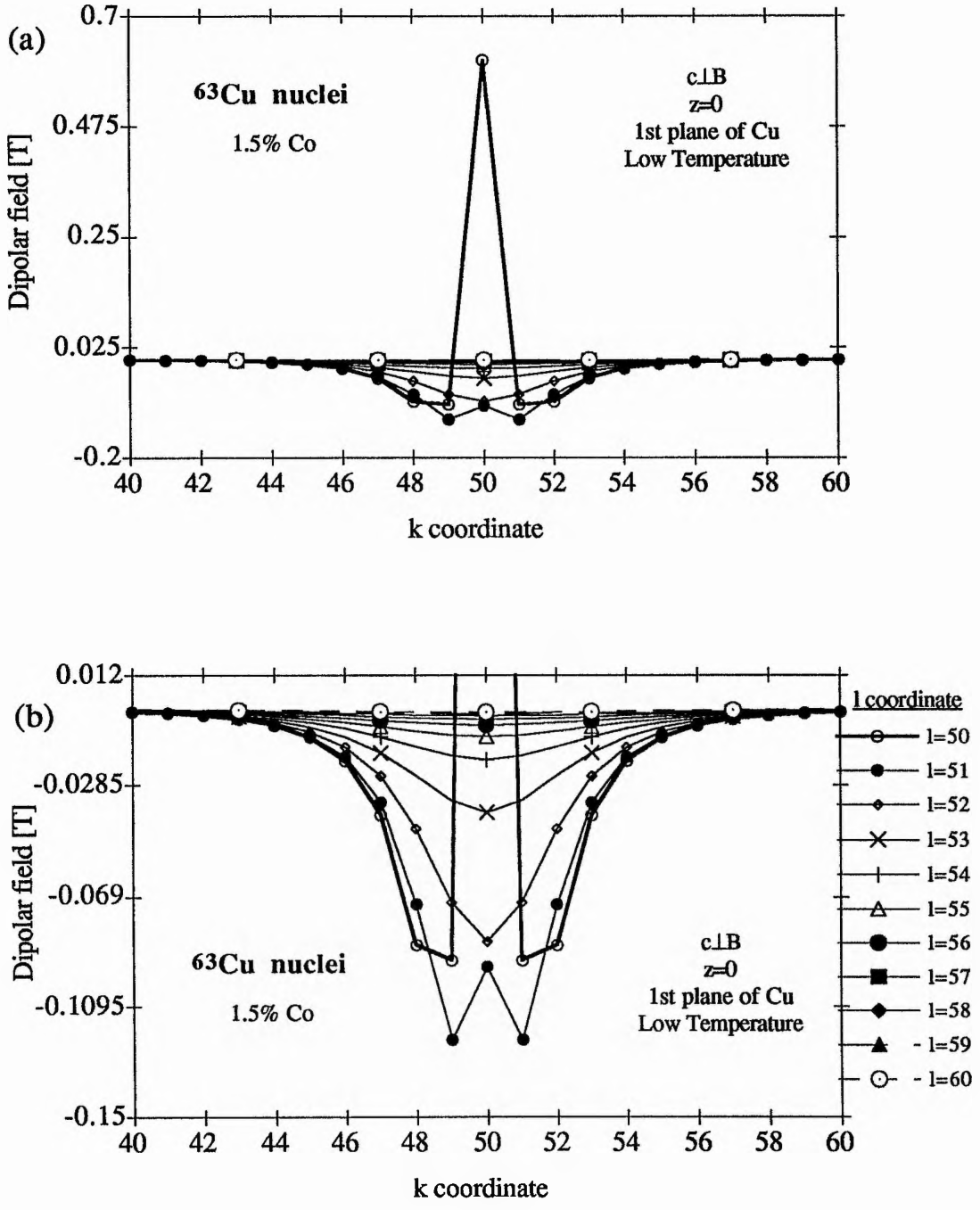

Figure 7.7

As for figures 7.6 (a) & (b) but with the crystal in the c⊥B orientation.

In all cases, the full range of dipolar fields experienced by Y or Cu* ions extending from k=40 to 60 and l=50 to 60 have been plotted in figure (a), so that the larger fields seen by those ions in closer proximity to the Co moment are realised. The second figure (b) expands that range of the dipolar field which is seen by the majority of ions, as we move away from the immediate vicinity of the Co moment. Note that the coordinates of k span from point 40 to point 60 so that the symmetry of the dipolar field distribution around the point k=50 can be seen.

As expected, when the crystal is in the c//B orientation, the Y and Cu ions which are nearest-neighbours to the Co moment experience a large negative field which rapidly becomes positive as we move to Y (Cu) ions which are further away. With the c⊥B orientation, the nearest-neighbour Y and Cu ions are influenced by a large positive dipolar field, while the slightly more distant ions sense a small negative field. The magnitude of the dipolar field also varies from Y to Cu site and for different orientations, as observed in each figure. Generally, for c//B, the magnitude of the dipolar fields experienced by the majority of Cu(2) ions is slightly larger than those experienced by the majority of the Y ions. The reverse is true for the c⊥B orientation. Note that equation (7.6) dictates that, at room temperature, the magnitude of the dipolar fields experienced by the same Y or Cu(2) ions will be around 30 times smaller than those seen at low temperatures.

It is interesting to see how the distribution of dipolar fields changes for the 2nd (z=1) and 3rd (z=2) layers of ions. As an example, we have plotted the dipolar fields experienced by the 2nd and 3rd layers of Y ions for a crystal in the c//B orientation in figures 7.8 (a) and (b), respectively. As we move up to the 2nd layer (figure 7.8 (a)), it is clear that more Y ions, over a larger span of k, experience a negative field than in the 1st layer. This is emphasized to a much greater extent for the 3rd layer (figure 7.8 (b)) and gives the impression that the dipolar field distribution fans out, both in terms of the k coordinate and in terms of shifting most of the Y nuclei to negative fields. It is also evident that the range of dipolar fields experienced is spread more evenly throughout the 3rd layer and there are no extremes in field, as seen for the first layer. In quantitative terms, for z=0, the majority of Y ions see a small positive field ($[B_{dip}]_z \leq 0.008$T) and only a relatively small number of ions see negative fields up to -0.22T. For z=1, it seems that approximately half the Y ions sampled experience even smaller positive fields ($[B_{dip}]_z \leq 0.00029$T) while the remainder see negative fields of up to -0.015T. Finally, for the 3rd layer, the majority of Y ions sample a negative field which extends to -0.0035T and a very small fraction of ions are exposed to a minute positive field of ≤0.00006T.

---

* For the 1.5% sample, the Cu(1)/Co(1)–Cu(2) distance for this calculation is 4.15 Å (see appendix A.8.2). The other lattice parameters used were a=3.8375Å, b=3.8775Å & c=11.6875Å (see chapter 6, section 6.1.4).

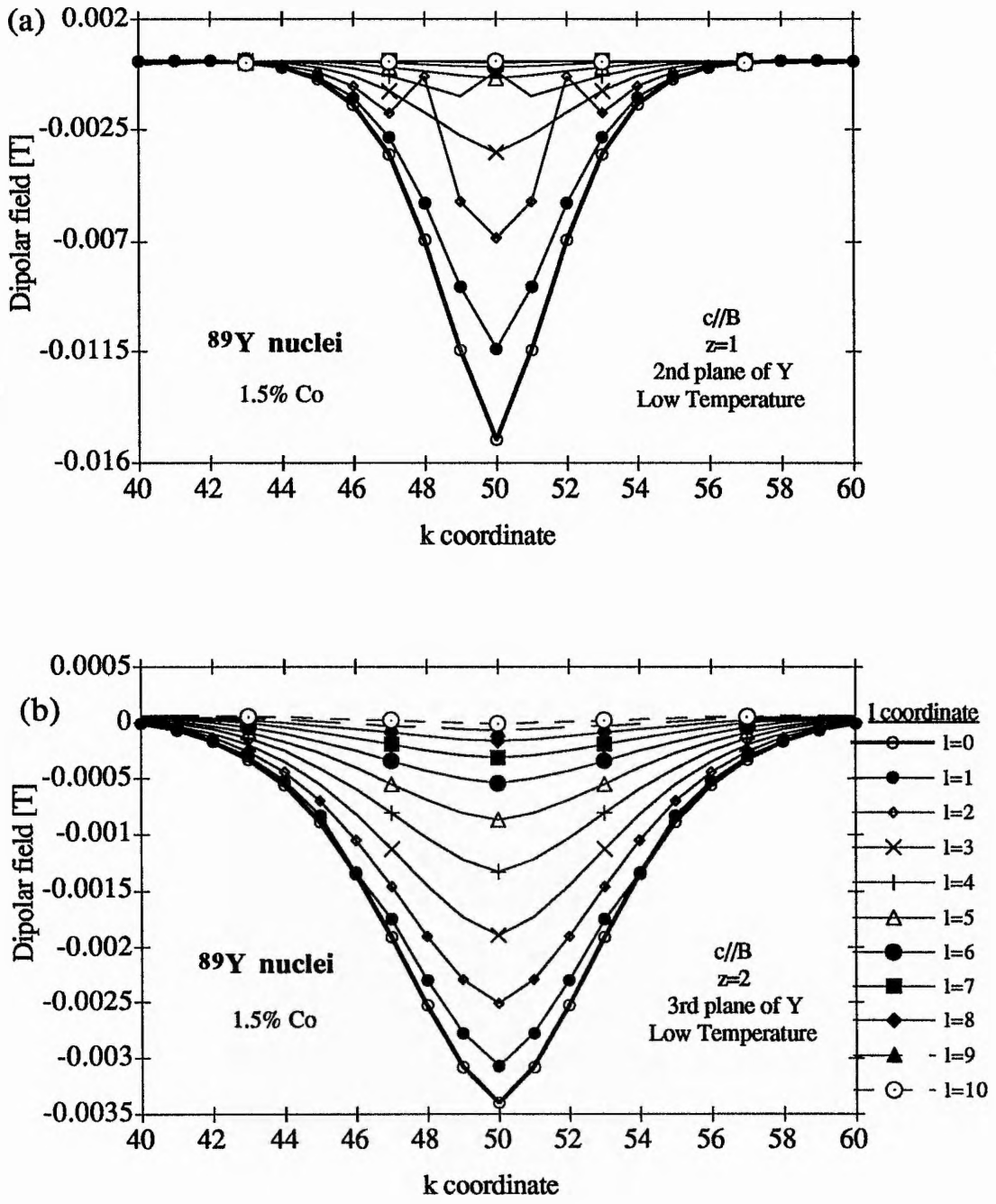

Figure 7.8

The low temperature (T<10K) dipolar field effects that a single Co moment placed at the point (50,50) has on the Y ions in (a) the 2nd (z=1) & (b) the 3rd (z=2) layers of the YBCO structure. The crystallographic orientation is c//B.

The trends in the dipolar field distributions in going from z=0 to z=2 are qualitatively similar for each of the Y(c⊥B), Cu(c//B) and Cu(c⊥B) plots (not shown), but these are slightly different to those found for Y ions at the c//B orientation. Where the majority of ions see a negative field for z=0 (Y(c⊥B) and Cu(c⊥B)), only the ions in close proximity to the Co moment (i.e up to a maximim of 4a lattice constants away from k=50, l=50) begin to see a positive field as we move up to the z=1 and z=2 layers. A large proportion of ions therefore still see a negative field. Similarly, for Cu(c//B) where the majority of the ions experience a positive field at the z=0 layer, only those ions within 5a lattice units away from the Co moment begin to see a negative field at the z=1 and z=2 layers. In all cases, the individual trends identified for the z=1 and z=2 layers continue to the z=3 layer, and beyond, in the case of Cu(2).

Having given some idea of the dipolar field distributions from a single Co moment in a selected section of the Y and Cu(2) sublattices, we can now move on to find out the combined effects of three such Co moments dispersed throughout the YBCO lattice with a Poission distribution. Due to the immense size of the intermediate arrays which store the resultant dipolar fields created by such a distribution of three Co moments, it is not possible to present a plot of dipolar field vs Y or Cu(2) ion coordinate, as previously (and even if it were possible, it would be a large and rather fruitless task). Instead, we move directly on to the final spectra of 'number of Y (Cu(2)) ions experiencing a given dipolar field vs dipolar field'.

Figures 7.9 (a) - (f) show the required spectra for the ^{89}Y nucleus with the crystal in the c//B orientation. The computer program was written in such a way that the binning process could be performed after each successive z layer was added. Thus, figure 7.9 (a) shows the spectrum for the z=0 layer, figure 7.9 (b) shows the spectrum for the z=0 and z=1 layer, and so on - up to z=3, which of course includes all of the Y layers specified for inclusion in the model. For clarity, figures 7.9 (d) and (f) present expanded scale versions of figures 7.9 (c) and (e), respectively.

For completeness, we have also included a series of spectra covering the $^{63}Cu(2)$ nucleus with the crystal oriented c⊥B. These spectra are shown in figures 7.10 (a) - (h), with figure 7.10 (a) representing the z=0 layer, figure 7.10 (b) representing the z=0 and z=1 layers, and so on, up to z=7.

(a)

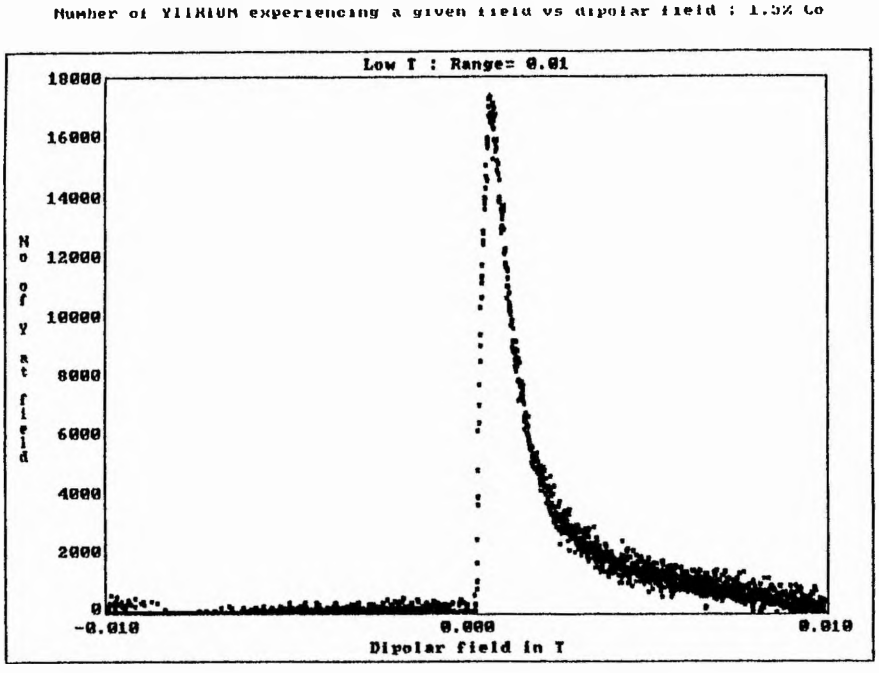

(b)

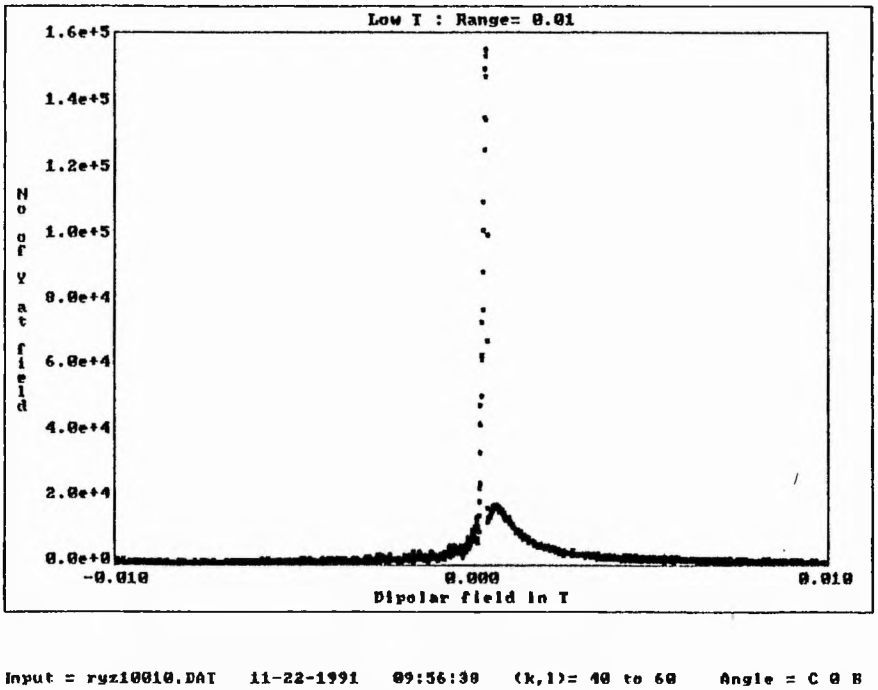

Figure 7.9 (a) & (b)

Spectra showing 'Number of Yttrium nuclei experiencing a given dipolar field vs dipolar field', for a 1.5% Co doped YBCO crystal in the c//B orientation and for the (a) z=0 & (b) up to the z=1 layers.

(c)

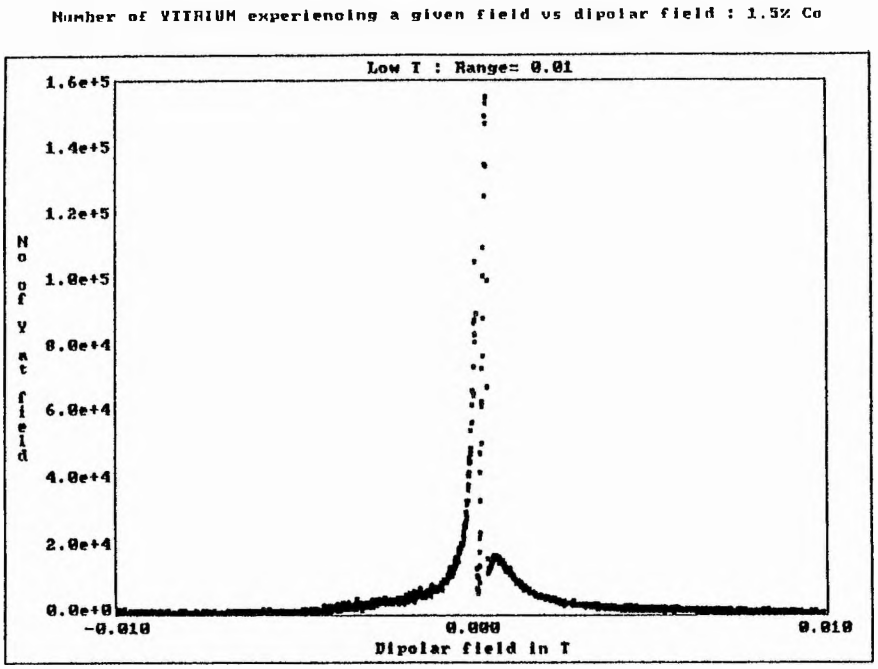

(d)

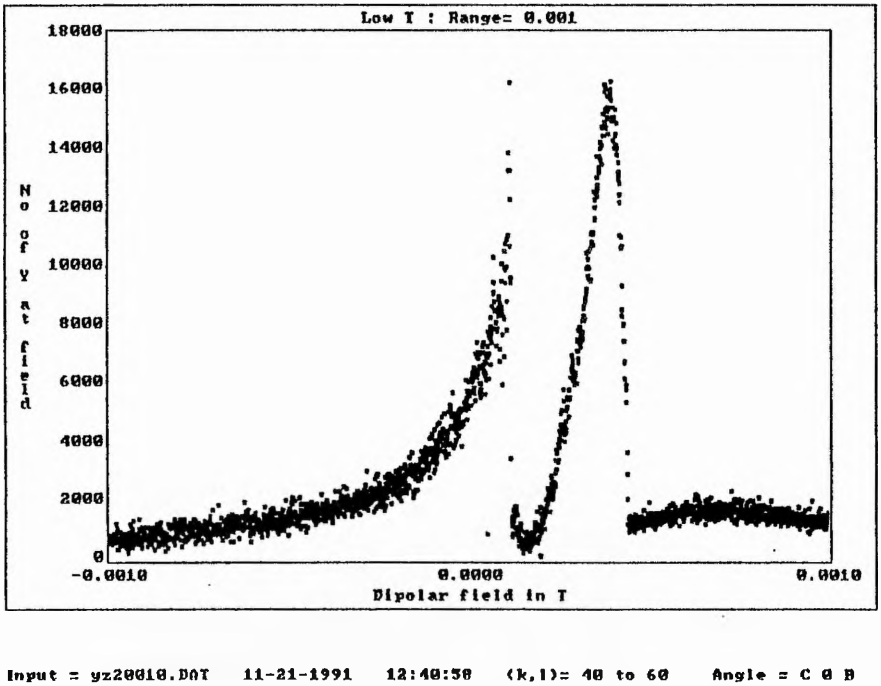

Figure 7.9 (c) & (d)

Spectra showing 'Number of Yttrium nuclei experiencing a given dipolar field vs dipolar field', for a 1.5% Co doped YBCO crystal in the c//B orientation.

(c) represents up to the z=2 layer & (d) is an expanded scale version of (c).

(e)

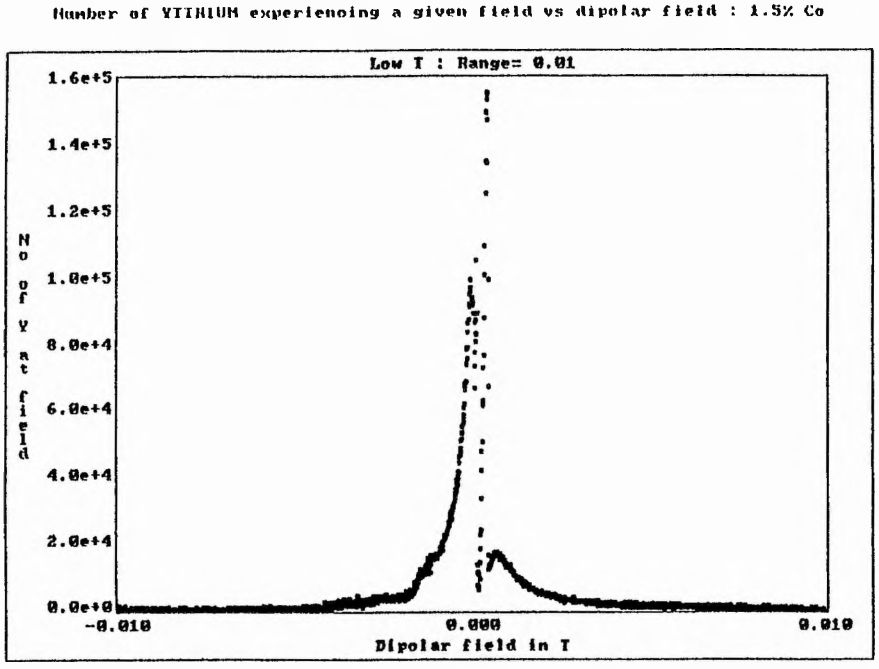

(f)

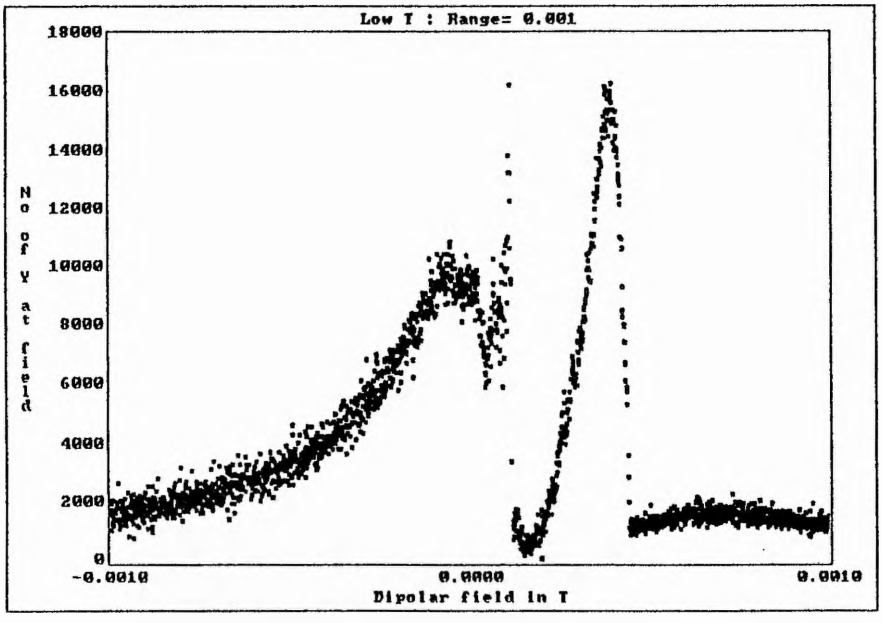

Figure 7.9 (e) & (f)

Spectra showing 'Number of Yttrium nuclei experiencing a given dipolar field vs dipolar field', for a 1.5% Co doped YBCO crystal in the c//B orientation.

(e) represents up to the z=3 layer & (f) is an expanded scale version of (e).

(a)

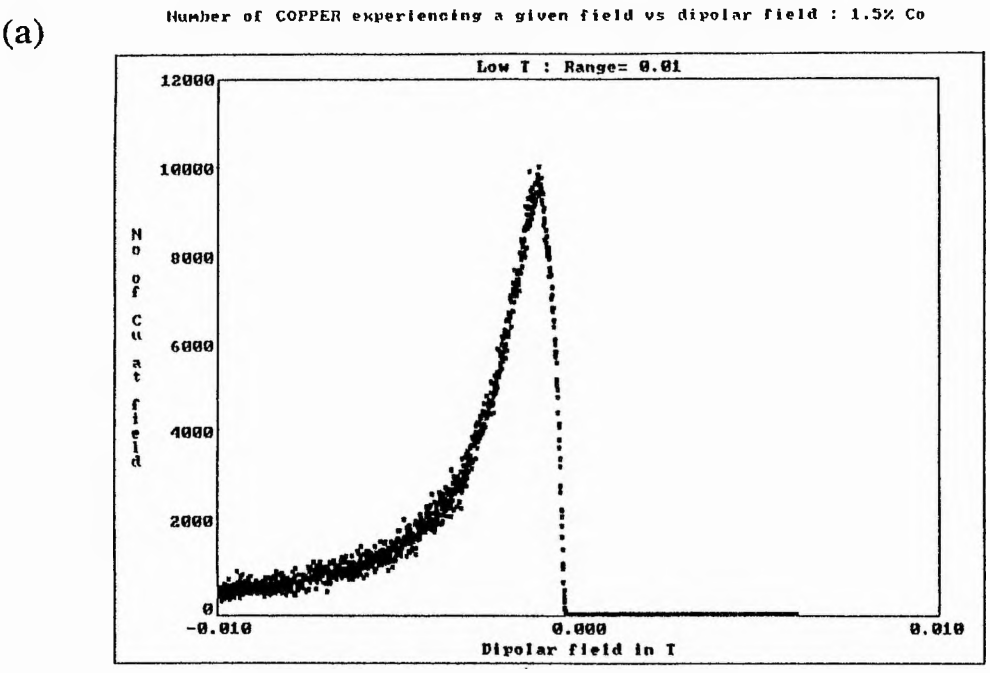

(b)

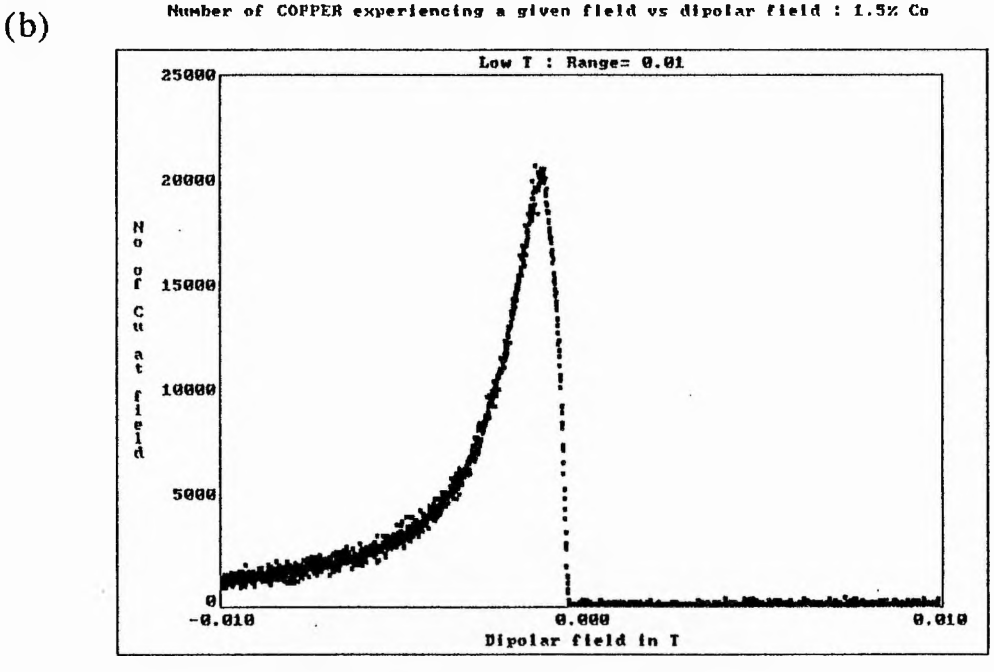

Figure 7.10 (a) & (b)

Spectra showing 'Number of Copper nuclei experiencing a given dipolar field vs dipolar field', for a 1.5% Co doped YBCO crystal in the c⊥B orientation and for the (a) z=0 & (b) up to the z=1 layers.

(c)

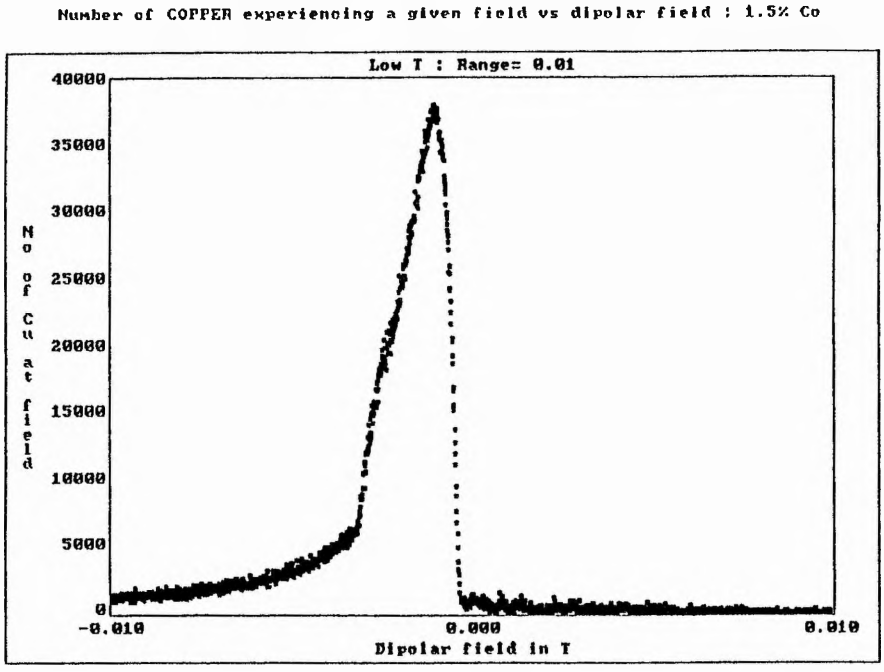

(d)

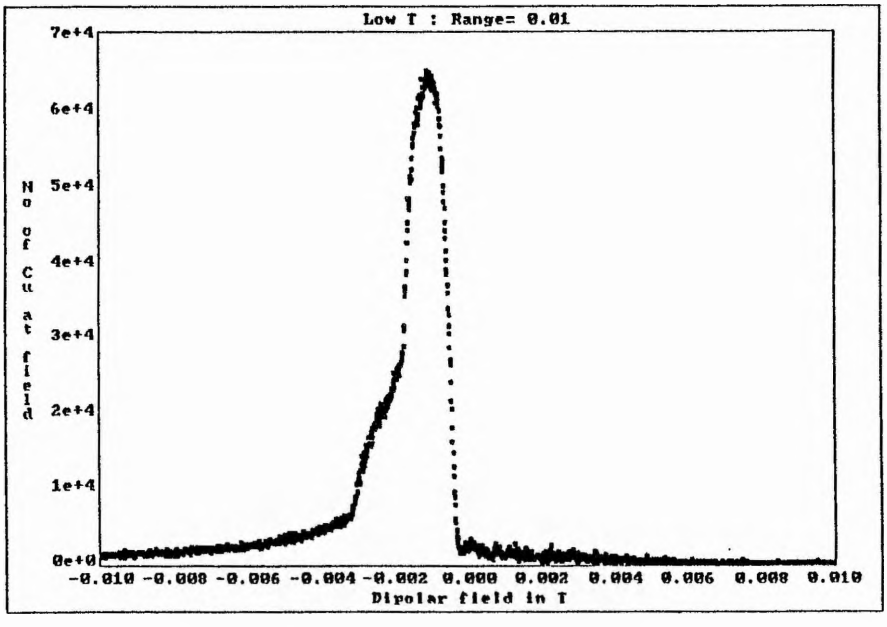

Figure 7.10 (c) & (d)

Spectra showing 'Number of Copper nuclei experiencing a given dipolar field vs dipolar field', for a 1.5% Co doped YBCO crystal in the c⊥B orientation and for the (c) up to the z=2 & (d) up to the z=3 layers.

(e)

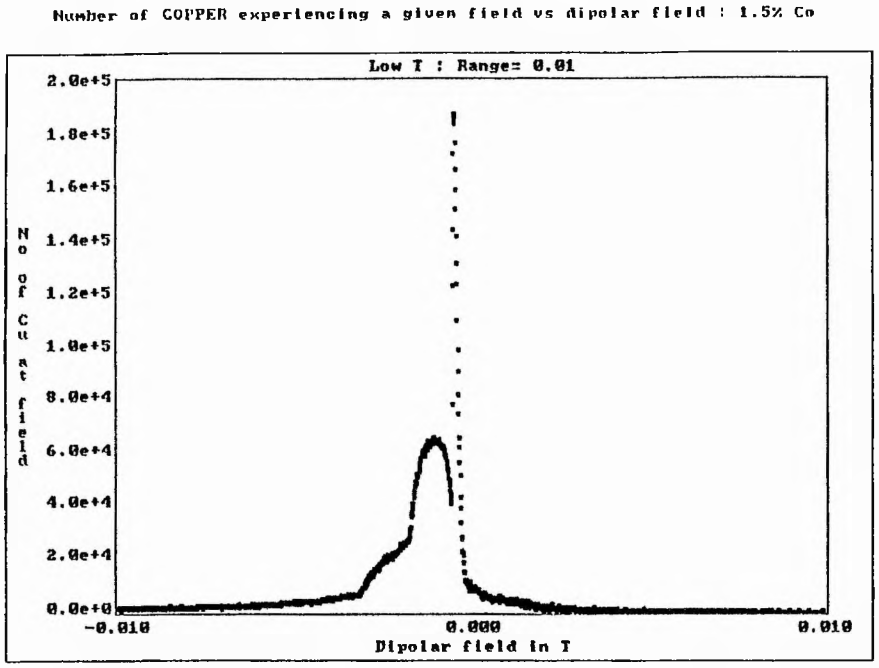

(f)

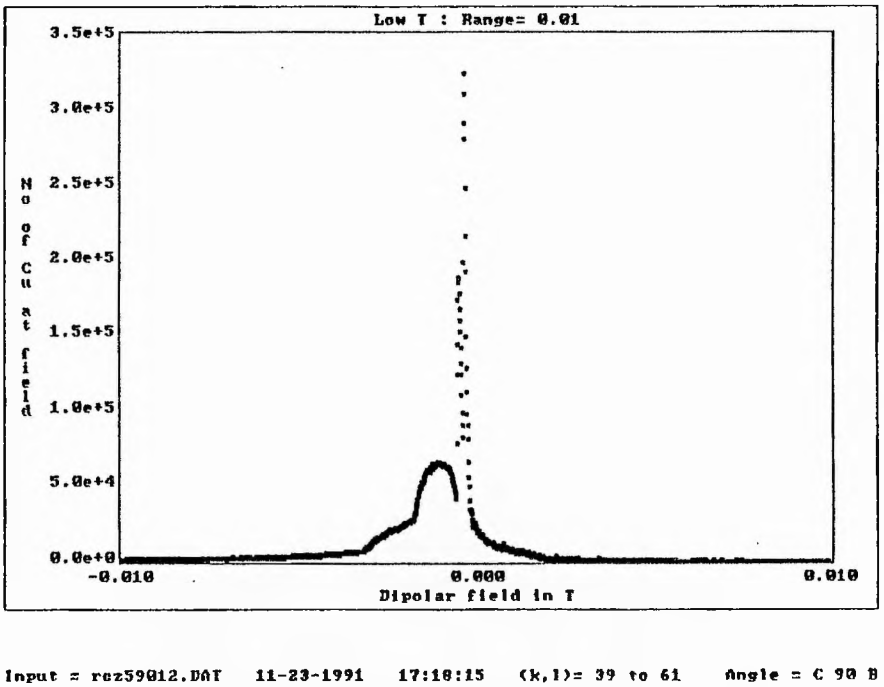

Figure 7.10 (e) & (f)

Spectra showing 'Number of Copper nuclei experiencing a given dipolar field vs dipolar field', for a 1.5% Co doped YBCO crystal in the c⊥B orientation and for the (e) up to the z=4 & (f) up to the z=5 layers.

(g)

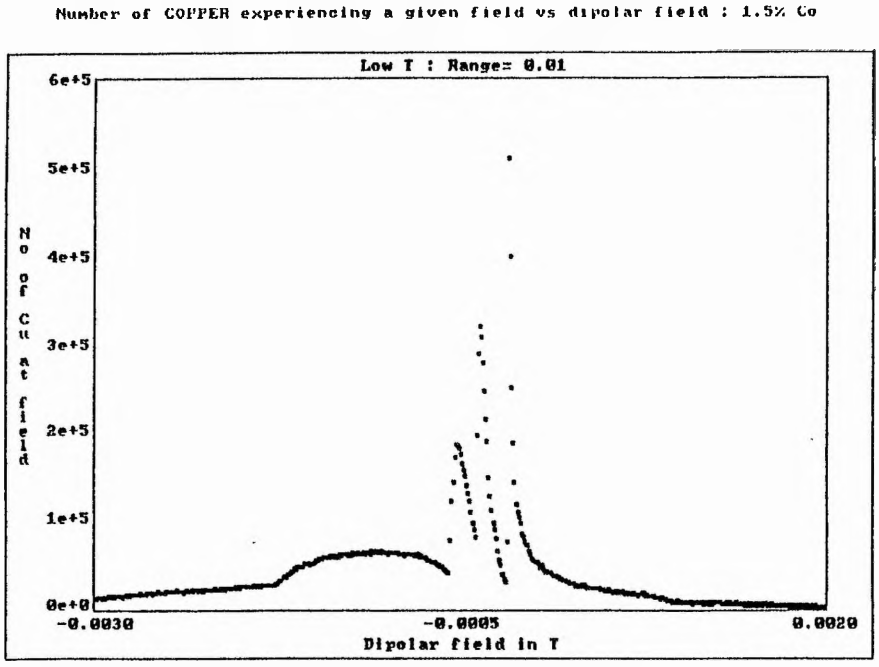

(h)

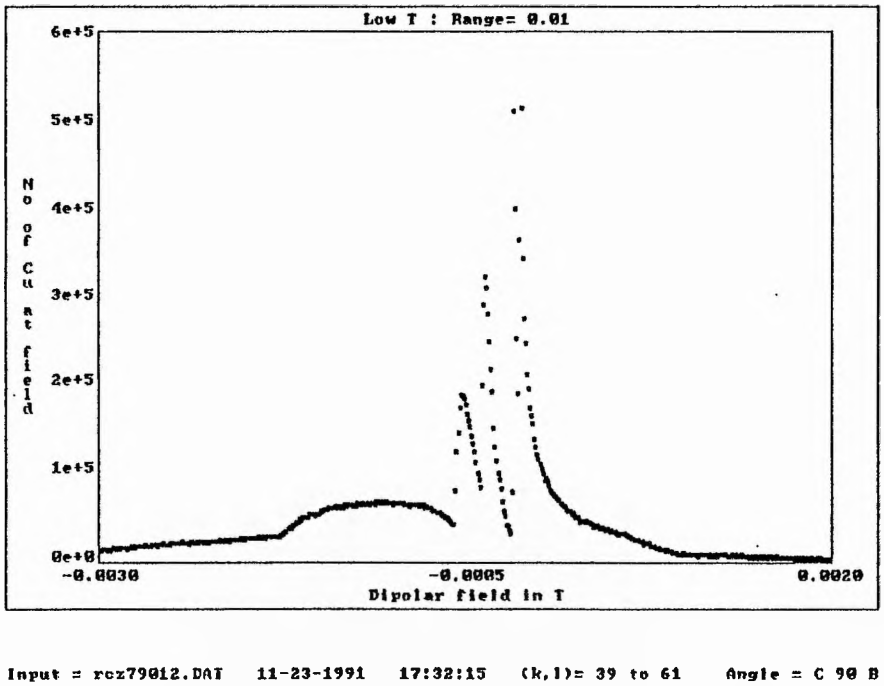

Figure 7.10 (g) & (h)

Spectra showing 'Number of Copper nuclei experiencing a given dipolar field vs dipolar field', for a 1.5% Co doped YBCO crystal in the c⊥B orientation and for the (g) up to the z=6 & (h) up to the z=7 layers.

Before moving on to describe the shifts and linewidths predicted by the model, we would first like to make a note about the peak intensities seen in these spectra. It is noticeable that, in the case of ^{89}Y(c//B), the major contribution to the line intensity comes with the addition of the second layer of Y (z=1) - as evidenced by the nine-fold increase in the number of Y nuclei seeing the most common dipolar field between layers one and two (z=0 and 1, see figures 7.9 (a) and (b)). Beyond the z=1 layer, the intensity of the principal line plateaus, while much smaller peaks, representing the contributions from larger dipolar fields, grow. For the Cu(2) nucleus at c⊥B(c//B), there is a two- or three-fold increase in the line intensity with the addition of each layer up to z=6(z=3), whereas for Y(c⊥B) (not shown), three- and six-fold increases in line intensity occur with the inclusion of the z=2 and z=3 layers, respectively.

A glance at figures 7.9 and 7.10 shows that there are indeed systematic shifts induced at both the ^{89}Y and ^{63}Cu(2) sites by the dipolar fields associated with the Co moments on the chain sites - but they are very small. As one would predict for the c//B orientation, the ^{89}Y (^{63}Cu(2)) resonance is pushed upfield, whereas for c perpendicular to B both the ^{89}Y and ^{63}Cu(2) resonances move downfield.

Considering the ^{89}Y nucleus (c//B) first, we find that if we only take into account the larger dipolar fields experienced by the first layer of Y (figure 7.9 (a)), the low temperature ^{89}Y resonance shifts by a sizeable +71ppm (1.7 kHz or 8.3 Gauss)† with the addition of 1.5% Co. However, as we include the smaller fields experienced by the second layer of Y nuclei (figure 7.9 (b)), the shift due the dipolar field halves to +34ppm (0.83 kHz or 4 Gauss) and remains at this position, even with the inclusion of the third and fourth Y layers (figures 7.9 (c) and (e), respectively). Here we must remember that the calculations have been performed for a low temperature, fully saturated Co moment, and that the shifts will be scaled down by a factor of $3k_BT/P_{eff}\mu_BB_0$ (see equation 7.5) for higher temperatures, T. At 295K, this is a factor of 30, while at 160K it represents a factor of 15. Thus, we can predict from our model that a magnetic moment consistent with 1.5% Co would produce ^{89}Y dipolar shifts of the order of +1ppm at room temperature and +2ppm at T=160K, provided the YBCO crystal is oriented c//B. The shifts predicted for the ^{89}Y resonance with the crystal in the c⊥B orientation are -0.5ppm at 295K and -1ppm at 160K.

The predicted effects of the dipolar fields on the ^{89}Y linewidth (FWHM) at low temperatures work out to about 1.25 kHz (51ppm) for c//B and 0.69kHz (28ppm) for c⊥B. This scales down to 42 Hz (84 Hz) for c//B and 23 Hz (46 Hz) for c⊥B at room temperature (160K).

---

† where 1kHz ≡ 41ppm ≡ 0.48mT or 4.8 Gauss for ^{89}Y.

Moving on to discuss the $^{63}Cu(2)$ nucleus, we find that our 8 layer model predicts a low temperature dipolar shift in the ^{63}Cu resonance of around +3.5 kHz for the c//B orientation and -0.71 kHz for c perpendicular to B. These low temperature results represent dipolar shifts of 0.12 kHz (c//B) and 0.02 kHz (c⊥B) at room temperature. Linewidth effects at the Cu(2) sites from the Co dipolar fields are estimated at around 5.7 kHz and 3.2 kHz for c//B and c⊥B, respectively, at low T. Thus, we predict $^{63}Cu(2)$ linewidth effects of 0.19 kHz (c//B) and 0.11 kHz (c⊥B) at T=295K.

In comparing these theoretically derived results with the experimental data presented in chapter 6 (figures 6.15 - 6.18 for ^{89}Y NMR and figures 6.22 - 6.23 for ^{63}Cu NMR), we see that both the temperature variation and magnitude of the ^{89}Y and $^{63}Cu(2)$ shifts and linewidths are not consistent with a dipolar mechanism. As an example of the mis-match between the theoretical and experimental data, we will cite the results for ^{89}Y and $^{63}Cu(2)$ NMR at c//B. Over a temperature range spanning 160K to 295K, there is a change in the experimental ^{89}Y magnetic shift of +25ppm for 1.5% Co. This shift is some 25 times larger than the temperature variation predicted from the dipolar field model. At room temperature, the change in ^{89}Y magnetic shift with the addition of 1.5% Co is +15ppm. This represents a shift which is 15 times larger than the model predicts. In addition, the discrepancy is 70 times greater at 160K. For consistency with a dipolar mechanism alone, the change in ^{89}Y NMR linewidth in going from 295K to 160K should be around +0.042 kHz. In actual fact, the experimental data suggests that this change with temperature is nearer +2 kHz. A similar mismatch of results can be found for $^{63}Cu(2)$, where, for example, we see that the addition of 1.5% Co at room temperature (c//B) causes a shift of 30 kHz in the resonance experimentally, while a dipolar mechanism suggests a shift of only 0.12 kHz. Likewise, there is a discrepancy of three orders of magnitude between the experimental and theoretically-predicted room temperature ^{63}Cu linewidths (c//B) with the addition of 1.5% Co.

Evidently, even when we take into consideration the approximations inherent in our calculations, we find that the variation and magnitude of shifts and linewidths suggested by the experimental ^{89}Y and $^{63}Cu(2)$ NMR data are wholly inconsistent with a dipolar mechanism. It is possible that our dipolar field model is not representative of the situation in the real YBCO crystal, although we must point out here that great care was taken to build a realistic model and to ensure that all the approximations used could be justified. We note that probably the most significant approximation made in our calculation was having the three Co moments in the same x-y plane, but it was felt that adding movement of Co ions in the z-direction would complicate the computer program considerably. In the event that the model is appropriate, we must look for additional mechanisms which may be operating in the real system that we have not taken into consideration in our dipolar

field model. For example, in our model we did not take account of any impurity clustering or dopant-oxygen interstitial defect clusters in the basal plane. Models incorporating defect clustering have recently been developed for the Al and Fe doped YBCO system by Islam et al[24].

We also note that in many metallic/non-metallic systems[14], the static field distributions caused by randomly placed magnetic impurities in a host lattice are evaluated using a combination of dipolar and **R**uderman-**K**ittel-**K**asuya-**Y**osida (RKKY)[25,26,27] interactions. In dilute alloy systems, such as CuMn, where a magnetic ion (Mn) is imbedded in a non-magnetic metal crystal (Cu), there is an exchange coupling between the localised moments of the impurity ion and the conduction electrons. When a magnetic ion is present, the conduction electron gas is magnetised or polarised in the vicinity of the magnetic ion. This magnetisation causes an indirect exchange interaction between two magnetic ions, because the second ion perceives the magnetisation induced by the first ion. In the CuMn system, the Cu nuclei couple to the magnetic Mn ion via the following path: first, there is a hyperfine coupling between the Cu nuclei and the conduction electrons. Then, there is a so-called s-d exchange coupling between the conduction electrons and the spin of the magnetic ion. The resulant ion-spin nuclear spin coupling is known as the RKKY coupling. In adapting these ideas to the YBCO system, the hole conduction band on the oxygens plays the role of the conduction electrons, while the Cu(2) ions are analogous to the magnetic ions. If, as suggested by this (see section 6.4.5) and other studies[28,29], the presence of a magnetic Co ion at the Cu(1) site changes the magnetic nature of the Cu(2) ion slightly, this will be sensed at the ^{89}Y nuclei through an interplay between the RKKY coupling of the Cu(2) spin with the oxygen holes and the transferred hyperfine coupling of the oxygens to the Y nuclei. An alternative scenario could be that the Co(1) moments themselves play the role of the magnetic ions and cause local fields at both the Y and Cu(2) sites via the RKKY interaction - that is the nuclear magnetic moments of the Y and Cu(2) couple indirectly to the electronic moments of Co via a conduction-electron spin polarisation in the CuO_2 plane.

Further evidence that other interactions, in addition to dipolar ones, may be relevant in this system can be found in the ^{89}Y NMR experimental data presented in section 6.2.3, figure 6.13. Here, our room temperature ^{89}Y isotropic magnetic shifts are plotted as a

---

24 M. S. Islam & C. Ananthamohan, *Phys. Rev. B* **44** 9492 (1991)

25 M. A. Ruderman & C. Kittel, *Phys. Rev.* **96** 99 (1954)

26 T. Kasuya, *Prog. Theor. Phys. Jpn.* **16** 45 (1956)

27 K. Yosida, *Phys. Rev.* **106** 893 (1957)

28 D. Hechel, I. Nowik, E. R. Bauminger & I. Felner, *Phys. Rev. B* **42** 2166 (1990)

29 T. Takatsuka, Y. Nakamichi & K. Kumagai, *J. Phys. Soc. Jpn.* **59** 3471 (1990)

function of Co concentration along with the corresponding MAS results of Dupree[30]. The MAS technique employed by Dupree averages out the dipolar field contributions from the Co moment and yet the magnitude and trends in the shifts are very similar in both studies. We must however note that the MAS linewidths are considerably narrower than the static linewidths due, presumably, to the averaging of the dipolar contributions to $\Delta\upsilon_{1/2}$.

From the analysis of the normal state magnetic susceptibility data presented in chapter 6 (sections 6.1.2 and 6.4.8), we find some evidence to suggest that the Curie terms induced arise from a local Co^{3+} moment with an intermediate spin state. The question we would briefly like to discuss in the final section of this chapter is 'Do the Co moments and the dipolar fields induced by these moments persist into the superconducting state ?'

In calculating the orbital component of the $^{63}Cu(2)$ Knight shift (section 6.4.5) in the Co doped YBCO system, we have already assumed that there is no spin or dipolar contribution to the shift as T tends to zero, but were we justified in our assumption ? In the pure $YBCO_7$ system, the spin lattice relaxation rate[31] ($1/T_1$) for both Cu(1) and Cu(2) nuclei drop rapidly below T_c, while the spin contribution to the total Knight shift[32,33] likewise decreases and vanishes at low temperatures. One explanation for the decreasing spin lattice relaxation time in the superconducting state is that, as the system goes superconducting, the Cu^{2+} local moments are less effectively scattered by the hole excitations, so that by the time one reaches the ground state at T=0, all spins are paired off and local moments no longer persist. In the absence of relaxation data in the superconducting state of Co-doped YBCO, one of the few indications we have of the disappearance of Co moments in the superconducting state is the absence of a Curie tail in the a.c. susceptibility data (see appendix B.1). These results, however, only extend to the 1.0% Co sample. Recent NQR studies[29] on the Co-doped A.F. $YBCO_6$ material find no evidence of the existence of a magnetic moment (up to x%=10) at the Cu(1) site at 1.4K, but there may be little comparison with the O_7 material.

---

30 R. Dupree, A. Gencten & D. McK. Paul, *Physica C* **193** 81 (1992)

31 W. W. Warren, Jr., R. E. Walstedt, G. F. Brennert, G. P. Espinosa & J. D. Remeika, *Phys. Rev. Lett.* **59** 1860 (1987); R. E. Walstedt, W. W. Warren, Jr., R. F. Bell, G. F. Brennert, G. P. Espinosa, J. P. Remeika, R. J. Cava & R. A. Reitman, *Phys. Rev. B* **36** 5727 (1987).

32 M. Takigawa, P. C. Hammel, R. H. Heffner & Z. Fisk, *Phys. Rev. B* **39** 7371 (1989)

33 S. E. Barrett, D. J. Durand, C. H. Pennington, C. P. Slichter, T. A. Friedmann, J. P. Rice & D. M. Ginsberg, *Phys. Rev. B* **41** 6283 (1990)

In the event that Co moments do persist into the superconducting state, the dipolar fields calculated theoretically here at low temperatures may just be large enough at c//B to cause the inhomogeneity in the Cu(2) planes (for x%>1.0), as seen via ^{63}Cu NMR at 1.5K. Such a phenomenon would at least explain why no such inhomogeneity is seen in the room temperature ^{63}Cu(2) c//B results, since the dipolar fields are much smaller at this higher temperature. From our model, we also note that the magnitudes of the low temperature dipolar fields for ^{63}Cu nuclei in the c⊥B orientation are always considerably smaller than those for nuclei in the c//B orientation - leading to much smaller predicted shifts and linewidths. This is consistent with the minimal broadening and lack of shift observed in the low temperature c⊥B ^{63}Cu spectra. Having proposed that the presence of a Co moment at low temperatures may explain the ^{63}Cu resonance at 1.5K, we point out that the dipolar c//B linewidth of 5.7 kHz calculated from the model, is wholly inconsistent with the huge broadening of around 11000 kHz observed experimentally.

We must finally conclude that we have insufficient evidence to decide whether the Co moment persists into the superconducting state or not. We thus assume that our derivation of the orbital and spin components of the ^{63}Cu(2) Knight shift in section 6.4.5 is valid - at least for the components in the a,b direction over all concentrations and up to 0.3% Co for components in the c direction.

Chapter 8

Concluding Remarks

8.1 Summary & Conclusions

In this thesis, we report static ^{63}Cu and ^{89}Y nuclear magnetic resonance (NMR) measurements in the superconducting (T=1.5K) and normal (T=160K-300K) states of the pure (chapter 5) and cobalt doped (chapter 6) Y-Ba-Cu-O systems. These magnetic measurements, performed on uniaxially aligned powders, are also supported by a wide range of physical characterisation measurements. In addition to studying the hyperfine interactions of the YBCO system, one of the initial experimental tasks of this work was to develop a reliable method of NMR sample preparation (chapters 4 and 5).

It has been known for some time that the magnetic and structural anisotropy of powdered cuprates leads to a nuclear magnetic resonance with a broad frequency spread, which is often difficult to interpret. In order to elucidate the anisotropic properties of the cuprates, it is therefore advantageous to work with single crystals. However, uni-phase single crystals have proved notoriously difficult to grow and any resulting pure crystals have invariably been too small to use with NMR techniques. By exploiting the anisotropy of the normal state magnetic susceptibility, a reliable method of preparing pseudo-single crystal specimens has been developed, which involves uniaxially aligning (c//B) the powdered sample at high magnetic fields (8T) in a non-magnetic (Stycast) epoxy matrix (epoxy to sample ratio = 10:1 by volume). During this investigation, satisfactory preparatory techniques were established prior to magnetic alignment by monitoring the morphology of the unaligned powder with a scanning electron microscope (SEM). Dispersion of the powder in the epoxy resin was then achieved with the use of an ultrasonic drill. The degree of crystallographic alignment in the epoxy set samples was later estimated, via X-ray diffraction techniques, at around 98% and the distribution of the powder in the epoxy resin, as observed under the high-resolution SEM, was found to be good. The general error in the c-axis alignment using this method was therefore judged to be $\pm 3°$.

In chapter 5, we report ^{63}Cu NMR spin echo experiments (at a temperature of 1.5K and at a frequency of 141MHz (i.e. fields of around 12.4T)) on a uniaxially aligned (Aberdeen) sample of pure, undoped $YBa_2Cu_3O_{7-\delta}$ which, after charaterisation using X-

ray powder diffraction, was calculated to have an oxygen content close to seven atoms per formula unit (δ=0). An initial investigation of the aligned sample using SEM techniques indicated that the true c axis was misaligned by some +30° to the expected position. Confirmation of this misalignment was sought via NMR techniques. A method was devised whereby field-swept ^{63}Cu NMR spin echo spectra were acquired for a number of orientations θ of the *expected* c-axis with respect to the applied field. A rotation pattern of the dominant ^{63}Cu(2) peak position as a function of θ was then constructed. Comparison with a theoretically derived curve confirmed that the misalignment of the c-axis was indeed of the order of +30° and a subsequent MINITAB regression analysis calculated the exact misalignment as +29°. The use of the known second order quadrupole plus anisotropic Knight shift pattern as the angular form in the MINITAB fitting procedure also allowed us to deduce that the NMR parameters υ_{NQR}=31.5 MHz, $K_{//}$=1.24%, $K_{\perp}$=0.32% and η=0 (see section 3.6) were appropriate for the Cu(2) site in the pure $YBa_2Cu_3O_7$ compound at 1.5K. These values compare well with those obtained from other studies. From a combination of NMR and X-ray diffraction results, the Aberdeen sample was found to have an actual degree of alignment of 82%. It was therefore concluded that the misalignment error lay not in the alignment procedure but in the marking of the c-axis alignment on the epoxy set sample. With the true orientation of the c-axis identified for this sample, a more complete evaluation of the NMR Knight shift tensors could be undertaken using only the θ=0° and θ=90° spin echo spectra.

At temperatures as low as 1.5K, the YBCO compound is well into the superconducting (mixed) state and so demagnetisation effects due to surface screening currents must be taken into account. In the absence of facilities with which to make our own evaluation of the demagnetisation correction, we have relied upon the work of the only two groups known to have performed such measurements - the Takigawa group[1,2] and the Barrett group[3]. Since these studies obtain dissimilar demagnetisation results using independent experimental methods, we have performed two separate analyses of our data. To start our analysis of the Cu(1) and Cu(2) shifts in $YBCO_7$, we first correct the experimental fields of resonance by the individual sets of demagnetisation values. Thereafter, the Knight shift tensor K^{α} (α=a,b,c) is determined numerically, using the exact Hamiltonian for the Zeeman and quadrupole energy (see appendix C.4). The two

---

1 M. Takigawa, P. C. Hammel, R. H. Heffner & Z. Fisk, *Phys. Rev. B* **39** 7371 (1989)

2 M. Takigawa, P. C. Hammel, R. H. Heffner, Z. Fisk, J. L. Smith & R. B. Schwartz, *Phys. Rev. B* **39** 300 (1989)

3 S. E. Barrett, D. J. Durand, C. H. Pennington, C. P. Slichter, T. A. Friedmann, J. P. Rice & D. M. Ginsberg, *Phys. Rev. B* **41** 6283 (1990)

orientations c//B and c⊥B are sufficient to evaluate the complete Knight shift tensor $K^{\alpha}(1,2)$, such that $K^{c}(1,2)$ is deduced from the c//B spectrum, while $K^{a,b}(1,2)$ is obtained from c⊥B.

The extremes at which our NMR data is acquired - low temperature and high magnetic field - have allowed us to considerably reduce some of the uncertainies incurred in previous studies. Since the Takigawa[1,2] and Barrett[3] groups perform their experiments at higher temperatures, they can only assume that the spin contribution to the Knight shift vanishes at T=0 and must extrapolate their data to absolute zero in order to decompose the total Knight shift into its orbital and spin contributions. If the spin shift is approximately zero at the temperature of 1.5K at which our data is taken, our results will be a direct measure of the temperature-independent orbital shift and should compare favourably with previous results. In addition, our data is acquired at high field, where demagnetisation effects, although still imperfectly known, are very much smaller than those found in the Takigawa and Barrett studies. This study therefore helps to dispel some of the doubt engendered by the discussion of demagnetisation factors in previous studies.

In conclusion, we find that generally the raw data (prior to demagnetisation corrections) obtained from this research scales very well with the data obtained from the Barrett and Takigawa studies. Although inconsistencies do arise in the values of the $K^{a,b}(1,2)$ orbital components, it is evident that the discrepancy lies in the difficulty in deducing the relevant peak positions from the c⊥B restricted powder pattern. Clearly, at our high fields, the size of c⊥B diamagnetic corrections obtained from previous studies is not an issue. In the case of orbital components deduced from the c//B spectrum, the reverse appears to be true. Peak positions can be accurately obtained from this well - defined spectrum and so the disparity in results between the Takigawa and Barrett studies can be traced directly to the demagnetisation corrections.

One of the most significant findings of the ^{63}Cu NMR study on pure $YBCO_7$ is the confirmation that all Cu(1) and Cu(2) spin components vanish at absolute zero, leaving the orbital shift as the residual shift. This is a clear indication of singlet spin pairing in the superconducting state. In addition, the size and anisotropy of the residual ^{63}Cu orbital shifts are consistent with a localised moment model in which there is a single hole of d_{x2-y2} symmetry in the d-shell of the Cu(2) ion with a crystal field splitting of 2-3eV, and in which there is single hole sitting in the d_{y2-z2} orbital of the d-shell of the Cu(1) ion.

The effects induced by the atomic substitution of cobalt into the Y-Ba-Cu-O system have been investigated in chapter 6 of this work. Detailed sample characterisations using T_c, magnetic susceptibility data, Hall effect measurements and X-ray diffraction were followed up by ^{63}Cu and ^{89}Y NMR investigations on a series of nine $YBa_2(Cu_{1-x}Co_x)_3O_{7-\delta}$ specimens in the concentration range, $0 \leq x \leq 0.04$. A combination of magnetic susceptibility, X-ray diffraction and nuclear magnetic resonance techniques,

all sensitive probes of sample purity, provide corroborative evidence to suggest that cobalt is readily soluble in the YBCO structure, producing a single phase, impurity free material at all concentrations used in this study. While the almost temperature independent macroscopic susceptibility of the pure YBCO sample is a clear indication that the oxygen stoichiometry of this sample is fairly near to O_7, the lack of variation in the structural c lattice parameter with Co concentration suggests that the oxygen content does not change significantly with x. From the X-ray diffraction analysis, we obtain an oxygen content of 6.9 (δ=0.1) for each sample in the Co-doped series and show that, in the epoxy set samples, the degree of alignment is good - varying from 77% to 98%. Double resonance peaks obtained in the ^{89}Y NMR spectra at low Co concentrations indicate a random powder element to the aligned samples, but these findings are not substantiated by the X-ray data.

From our magnetic measurements (susceptibility and NMR), we find that the cobalt ion enters the YBCO system at the Cu(1) site and bears an effective magnetic moment of around 3.7μ_B. While independent studies (see chapter 2) provide strong evidence to suggest that the cobalt ion is in a +3 state, we note that a magnetic moment of 3.7μ_B, corresponds more to the Co^{2+} state than either the high or low spin of the Co^{3+} state. There are several possibilities which could account for the reduced Co magnetic moment, including an itinerant electron contribution, a partially ordered magnetic moment or an intermediate spin configuration. The appearance of extra susceptibility due to Co-doping, evident from the macroscopic magnetic susceptibility analysis, has been interpreted with the help of ^{63}Cu and ^{89}Y NMR experiments performed in the normal state and ^{63}Cu NMR experiments performed in the superconducting state. The strong similarity in the variation of the ^{89}Y NMR shift, both as a function of increasing Co concentration in $YBa_2(Cu_{1-x}Co_x)_3O_{7-\delta}$ and decreasing oxygen concentration (δ) in the pure system, suggests that the extra susceptibility sits on the chain sites. However, the marked contrast observed in the linewidths of the two systems indicates that there must be substantial inhomogeniety induced in the planes susceptibility by Co which is not produced by oxygen vacancies. Our combined magnetic measurements therefore suggest that (i) we are dealing with a Co^{3+} localised magnetic moment of intermediate spin state (with s=1) and (ii) that the presence of Co at the Cu(1) site may result in a slight change in the magnetic moment at the Cu(2) site.

Having concluded that the cobalt ion behaves like a local moment on the Cu(1) site, we proceed in chapter 7, to address whether the dipolar fields associated with such a moment would induce the systematic shifts seen in the ^{89}Y and ^{63}Cu NMR. From our dipolar field model, we find that the magnitude and changes in experimental shift and linewidth, which occur as a function of temperature and Co concentration, cannot be explained in terms of a dipolar mechanism alone. We conclude that, either the model does

not accurately represent the situation in the real YBCO crystal, or that we need to take into account other interactions, such as RKKY interactions, that would be induced by the presence of the Co moment.

From our characterisation measurements, we observe that the T_c of $YBa_2(Cu_{1-x}Co_x)_3O_{7-\delta}$ remains fairly constant and equal to around 92K at low Co concentrations and then decreases rapidly, but linearly, for x%≥2.8%. The X-ray diffraction data on the powdered samples indicates that this characteristic change in T_c coincides with a macroscopic orthorhombic to tetragonal structural transition, which also occurs at x%=2.8%. There has, however, been some debate as to whether the impurity-induced tetragonal phase actually exists for the Co doped system, since some researchers claim that it is a pseudotetragonal phase consisting of randomly oriented orthorhombic microdomains. Fortunately, the ^{89}Y NMR chemical shift is an indirect probe of changes in crystallographic structure. From our study, we are able to show that the ^{89}Y chemical shift changes in a similar fashion to the variation of a and b lattice parameters for x%≤2.8%. At concentrations beyond 2.8%, where these lattice parameter are expected to vary only slightly, the chemical shift remains static at +220±5ppm, providing strong evidence to support the existence of a true orthorhombic to tetragonal transition. A correlation of the ^{89}Y magnetic shift (ΔK) with the T_c shows that the shift varies considerably over the concentration range 0≤x%≤1.5%, while the T_c is approximately constant. While the rapid change in ΔK can be attributed to the changing chemical shift contribution with increasing Co and also to the change in hole concentration, the reason for the constant T_c still remains uncertain. Further, a qualitative analysis of the Hall number indicates that the hole concentration in the planes falls with increasing Co concentration. From this, we must conclude that there is no correlation between T_c and hole concentration in the planes, and that T_c is not determined by hole concentration alone. Note that while the T_c is unaffected by Co substitution for x%<2.8%, a Co ion induces an effective magnetic moment of about 3.7 Bohr magnetons.

A comparison of the ^{89}Y Knight shift and T_c as a function of Co concentration suggests that the decrease of T_c in the concentration range x%≥2.8% is due to a reduction of the density of states at the Fermi level. Similar conclusions have been drawn from ^{89}Y NMR studies in the undoped system as a function of decreasing oxygen content. In this research, we seek to make further comparisons with the oxygen depleted system by plotting the isotropic ^{89}Y magnetic shifts for the 2.8% and 4% Co doped samples against the corresponding shifts of oxygen depleted samples with the same T_c (with temperature as the implicit variable). A linear correlation is found to hold for both samples, providing a strong indication that the mechanism responsible for temperature dependent behaviour in both the Co-doped and oxygen-depleted systems may be the same and may be directly related to T_c.

In the final paragraphs of this section, we would like to summarise individual conclusions which can be drawn from the NMR data, alone. With the knowledge that the integrated area under a spin echo curve provides a measure of the number of specific nuclei which contribute to the NMR line, we set about finding the integrated area under the room temperature ^{63}Cu spin echo curves, in the hope that it would provide a useful indication of the effect that Co substitution has on the number of ^{63}Cu nuclei which contribute to the resonance. Two major conclusions can be drawn from the data obtained. With the addition of small amounts of Co, the number of ^{63}Cu nuclei seen drops dramatically, while for concentrations greater than x%=0.5 the decrease is much more shallow and almost linear. This observation is qualitatively similar to the phenomenon of 'wipe-out' seen in the NMR of a number of dilute alloy systems, such as copper-manganese, and is generally explained in terms of second order quadrupole perturbations which are induced by the inclusion of magnetic impurities. The rapid drop in integrated area observed at low Co concentrations can be explained by wipe-out from single Co moments, while at higher concentrations, Co-Co interactions come into play. The second point to be made about this data concerns the relation between the numbers of Cu nuclei seen at each orientation. The total number of ^{63}Cu nuclei seen for the c//B orientation is always approximately twice that seen at c⊥B. The considerable difference in the number of nuclei seen at each orientation stems from the fact that the conductivity in the a-b plane is almost 50 times greater than along the c-axis and so the NMR signal at c//B is strong due to good rf penetration around the planes. From our results, we can predict that the ratio of σ_{ab}:σ_c remains constant over the entire range of Co concentration and that the rf penetration depth along the a-b plane is twice that along the c-axis.

An important part of this research concerns the derivation of the orbital and spin components of the ^{63}Cu(2) Knight shift from the room and low temperature Cu NMR data, as function of Co content. While the peaks in the room temperature Cu spectra at both orientations and the low temperature Cu spectra at c⊥B are well-defined, the low T spectra at c//B are completely devastated for Co concentrations greater than 0.5%. The a,b components of the orbital shift remain constant for all values of x, indicating that doping on the chain site produces little change in the quadrupole interaction on the planes. By a Co concentration of 4%, the Knight shift is dominated by the orbital shift in the a-b plane and the Cu(2) 3d spin does not appear to contribute to the Knight shift at all at the c⊥B orientation. The c//B data is consistent with the proposition that Co-doping causes strong inhomogeniety in the Van Vleck component of the planes susceptibility. However, the dipolar field model does not really confirm or dispel the idea that the observed behaviour for c//B may be due to dipolar fields induced by the Co moment.

The crystal field splittings, Δ_0 and Δ_1, are derived for the 0% and 4% Co samples from the K^{α}_{orb} components. The value for Δ_1 (3.59eV) is found to remain constant over all Co concentrations while a 3-fold increase occurs in Δ_0 from 1.98eV in the 0% sample to 5.27eV in the 4% sample. These values suggest that the energy levels of the d_{x2-y2} and $d_{yz,zx}$ orbitals change by the same amount, while the energy difference between the d_{xy} and d_{x2-y2} orbitals increases with the addition of Co. Alternatively, the observed trends in the orbital shift components are also consistent with an unknown admixture of the $3d_{z2}$ orbital into the Cu(2) $3d_{x2-y2}$ ground state.

Finally, we note that there is a linear correlation between both the c-components and the a,b components of the ^{63}Cu(2) Knight shift and the ^{89}Y Knight shift. Clearly as we add Co to the YBCO system, we still maintain a direct correlation between the ^{63}Cu and ^{89}Y nuclei. This provides strong evidence in favour of a single quantum spin fluid (one component model) with unique spin dynamics.

8.2 Suggestions For Further Work

In this research, we have concentrated heavily on the NMR shifts in the YBCO and Co-doped YBCO systems at the expense of investigating the spin dynamics of these systems. To complement the present study, it would be useful to obtain dynamic NMR measurements (i.e. relaxation measurements) on the Co doped YBCO system, since such measurements are generally lacking, especially for ^{63}Cu in the superconducting state.

Since the orthorhombic to tetragonal structural transition does not seem to hinder the superconductivity of the Co-doped system, it would be interesting to study this system, using NMR, at much higher Co concentrations where the system tends to the antiferromagnetic (insulator) state.

On a more specific level, we suggest that accurate a.c. susceptibility measurements performed over a wide temperature range would help to define the superconducting fraction as a function of Co doping and would indicate whether the Co magnetic moment persists into the superconducting state. In addition, orientation dependent magnetic susceptibility measurements in aligned samples would permit a more detailed study of the hyperfine interactions in this system.

As far as alignment techniques are concerned, much error in misorientation of samples could be avoided, if the epoxy set sample was aligned directly in the NMR probe and the NMR experiment performed without removing the sample from the probe.

Appendices

Appendix A

A Survey of Fundamental Properties of the Pure & Doped Y-Ba-Cu-O Systems

This appendix is a collection of lists and tables of established data, intended for reference. It is the result of a comprehensive survey of the most up-to-date work in this field, but it is by no means an exhaustive account.

A.1 Normal & Superconducting Properties of $YBa_2Cu_3O_7$

A.1.1 Normal State Properties[1]

General : Colour : Black — Structure: Orthorhombic
Density: 6.38 g/cm^3 — Space Group : Pmmm
Melting pt: 1040.9±0.5°C

Resistivity Data (295K) : (where ρ_a means ρ in the direction parallel to a, etc.)

(1) Single (twin-free) crystal

$\rho_a = 0.17$ mΩcm	$\alpha_a = 0.691$ μΩcm/K*
$\rho_b = 0.07$ mΩcm	$\alpha_b = 0.269$ μΩcm/K
$\rho_c = 5.30$ mΩcm	$\alpha_c = 12.5$ μΩcm/K
$\rho_a/\rho_b = 2.2 \pm 0.2$ (150-275K)	$\rho_{ab} \sim (\rho_a \cdot \rho_b)^{1/2} = 0.11$ mΩcm
$\rho_c/\rho_a \sim 35$	
$\rho_c/\rho_b \sim 75$	ρ_a & $\rho_b \rightarrow 0$ as $T \rightarrow 0$

(2) Single (twinned) crystal

$\rho_{ab} \sim 0.150$ - 0.250 mΩcm	$\alpha_{ab} = 0.2$ - 0.5 μΩcm/K
$\rho_c \sim 8$ - 20 mΩcm	$\alpha_c = 12.5$ μΩcm/K
$\rho_c/\rho_{ab} \sim 30$ - 100	

---

1 Adapted from 'Structure & Superconductivity in the Y123 & Related Compounds' by G. V. Subba Rao & U. V. Varadaraju in *Chemistry of High Temperature Superconductors*, ed. C. N. R. Rao, World Scientific Publishers, Singapore (1991)

* where α is equivalent to $d\rho/dT$

(3) Polycrystalline material

$\rho = 1 - 2$ mΩcm $\alpha = 1.7 - 2.1$ μΩcm/K

(4) Single crystal or Oriented Thin Films

$\rho = 0.5 - 2.0$ mΩcm $\alpha = 0.6 - 0.7$ μΩcm/K

Other Normal State Parameters:

Seebeck coefficient (300K)	S	= +3 - 6 μV/K
Hall coefficient (300K)	R_H	= 2 - 3 x 10^{-9} m^3/coul.
Hall mobility (100K)	μ_H	~ 34 cm^2/Vsec
Hole carrier density (300K)†	n_h	~ 3 - 9 x 10^{21} /cm^3
Magnetic Susceptibility (300K)*	χ	~ 4 x 10^{-7} cm^3/g
		~ (3 x 10^{-4} emu/mole)
Heat capacity (300K)	C_p	~ 300 J/mol-K
Heat capacity coefficient††	γ	= 14 - 25 mJ/mol-K^2
Debye temperature	θ_D	~ 400 - 450K
Thermal Conductivity (300K)**	κ	~ 5W/metre-K

Density of electronic states DOS at E_F ($N(E_F)$):

$N(E_F)$ (band structure calculation)	= 3.5 - 6.5 states/eV- f.u.
$N(E_F)$ (Experimental) (γ & C_p data)	= 8.5 - 9.5 states/eV- f.u.

Electron (Hole) effective mass (m*/m)

de Haas-van Alphen effect	= 2.8 - 4.4
Other methods	= 3 - 5

A.1.2 Superconducting State Properties[1]

Transition Temperature	$T_{c, zero}$	= 90 ± 1 K
	$T_{c, onset}$	= 92 - 94 K

---

† where there are 0.10 - 0.15 mobile holes per Cu(2) atom

* In the range, T_c to 300K, χ is the T-independent Pauli paramagnetic susceptibility. Below T_c, χ is diamagnetic.

†† where $C_p = \gamma T + \beta T^3$

** κ is T-independent in the range T_c to 300K. Below T_c, κ is proportional to T^2.

Ratio $2\Delta/k_BT_c$		
BCS theoretical prediction		= 3.5
Band structure calculation		= 3 - 6
Experiment (tunnelling, IR etc.)		= 5 - 8
Electron-phonon coupling const.	(λ_{ph})	= 0.5 - 1.5
Heat capacity anomaly†	($\Delta C_p/T_c$)	= 57 mJ/mol-K^2
Coherence length	ξ_a	= 14 ± 2 Å
	ξ_c	= 1.5 - 3.0 Å
Fermi velocity (a-b plane)	v_F	= 1.7 - 2.2 x 10^7 cm/sec
Penetration depth (T→0)	λ_{ab}	= 1400Å (20-40% anisotropy)
	λ_c	= 7000Å
Effective mass anisotropy	(m_a/m_b)	= 1.2 - 1.4
	(m_c/m_{ab})	= 5 - 6

Critical magnetic fields (type II superconductors)

$H_{c1,\,ab}$ (T→0)	= 180 - 250 Oe
$H_{c1,\,\perp ab}$ (T→0)	= 1 - 2 Oe
H_{c2} (extrapolated)	= 150 - 200 Tesla
$dH_{c2,\,ab}/dT$	= -10 Tesla/K
$dH_{c2,\,\perp ab}/dT$	= -1.8 Tesla/K

Critical current (J_c)

Thin film (epitaxial)	= 5 x 10^6 A/cm^2
Polycrystalline bulk or wire	~ 10^2 -10^3 A/cm^2
Melt textured polycrystalline	~ 5 x 10^4 A/cm^2
Melt textured polycrystalline with defects (irradiated sample)	~ 5 x 10^4 A/cm^2

† Sample dependent linear term (γT) at $T \ll T_c$ and an upturn in the C_p/T for T→0.

A.2 Variation of YBCO Cell Parameters with Oxygen

A.2.1 Lattice Parameters

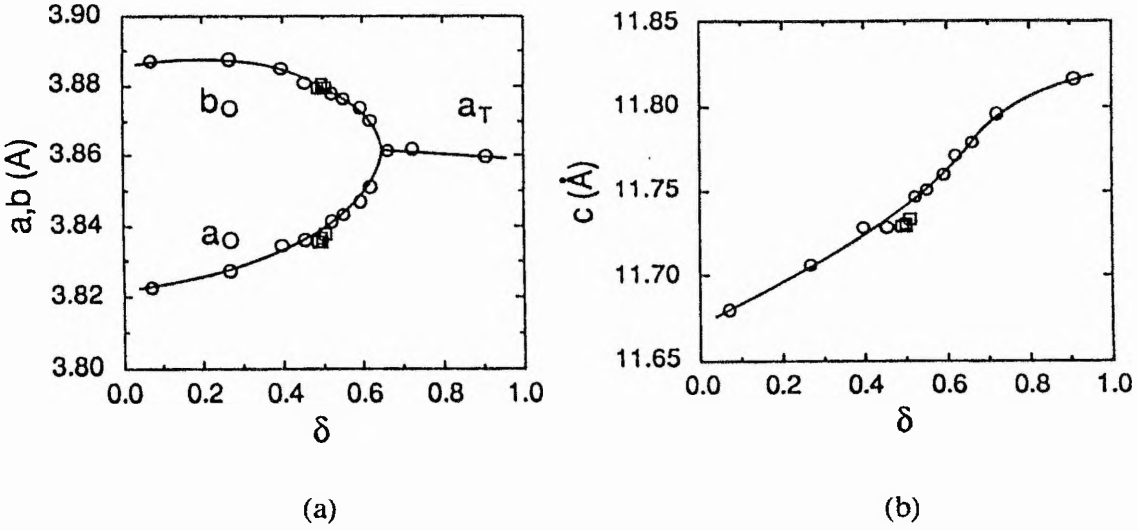

(a) (b)

Figure A.1

(a) Lattice parameters, a_O and b_O in the orthorhombic phase and a_T in the tetragonal phase of $YBa_2Cu_3O_{7-\delta}$ vs. δ. (b) c-lattice parameter of $YBa_2Cu_3O_{7-\delta}$ vs. δ. In both cases, open circles & squares represent two different sets of samples which were quenched from 520°C into liquid nitrogen[2].

A.2.2 Cell Volume

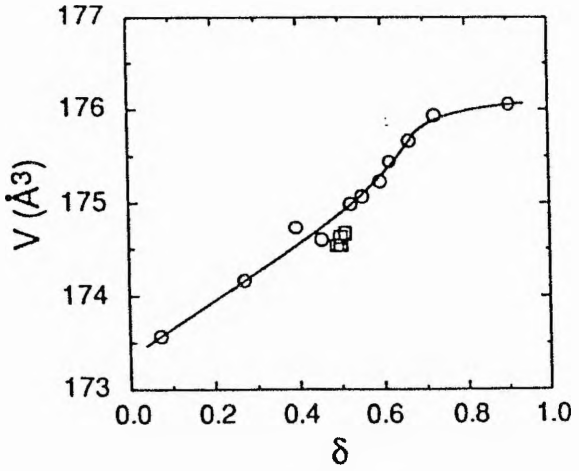

Figure A.2

Unit cell volume, V vs. δ for $YBa_2Cu_3O_{7-\delta}$. Samples, symbols & reference as in figure A.1.

---

2 J. D. Jorgensen, B. W. Veal, A. P. Paulikas, L. J. Nowicki, G. W. Crabtree, H. Claus & W. K. Kowk, *Phys. Rev. B* **41** 1863 (1990): Results obtained for non-quenched samples are very similar.

A.3 Orthorhombic Crystal Structure

The following tables give the parameters typical of an O_7 or near O_7 orthorhombic crystal structure at 297K.

A.3.1 Atomic Positions & Occupancies[3]

Oxygen Content : $O_{6.91}$ Space Group : Pmmm

a = 3.82030(8) Å b = 3.88458(10) Å c = 11.68349(23) Å

Atom	x	y	z	Occupancy
Y	$\frac{1}{2}$	$\frac{1}{2}$	$\frac{1}{2}$	1
Ba	$\frac{1}{2}$	$\frac{1}{2}$	0.18393(6)	1
Cu(1)	0	0	0	1
Cu(2)	0	0	0.35501(8)	1
O(1)	0	$\frac{1}{2}$	0	0.910(8)
O(2)	$\frac{1}{2}$	0	0.37819(15)	1
O(3)	0	$\frac{1}{2}$	0.37693(16)	1
O(4)	0	0	0.15840(13)	1

Table A.1

A.3.2 Selected Bond Lengths & Angles[4]

Oxygen Content : O_7 Bond lengths in Å

Y-O(2)	2.418(15)	Cu(1)-O(1)	1.947(5)
Y-O(3)	2.399(15)	Cu(1)-O(4)	1.834(27)
Ba-O(1)	2.891(2)	Cu(2)-O(2)	1.929(3)
Ba-O(2)	2.980(19)	Cu(2)-O(3)	1.961(3)
Ba-O(3)	2.948(19)	Cu(2)-O(4)	2.341(28)
Ba-O(4)	2.750(3)		

Table A.2

---

3 Adapted from A. Williams, G. H. Kwei, R. B. Von Dreele, A. C. Larson, I. D. Raistrick & D. L. Bish, *Phys Rev B* **37** 7960 (1988) : Positions determined from a combination of X-ray and neutron powder diffraction.

4 G. Calestani & C. Rizzoli, *Nature* **328** 606 (1987)

Bond Angles in degrees (°)

O(1)-Cu(1)-O(4)	90.0(5)
O(4)-Cu(1)-O(4)	180.0(7)
O(1)-Cu(1)-O(1)	180.0(0)
O(3)-Cu(2)-O(3)	166.3(1)
O(2)-Cu(2)-O(2)	165.3(7)
O(2)-Cu(2)-O(3)	89.1(0)
O(4)-Cu(2)-O(3)	96.9(6)
O(4)-Cu(2)-O(2)	97.4(6)

Table A.3

A.4 Tetragonal Crystal Structure

A.4.1 Atomic Positions & Occupancies[5]

Oxygen Content : $O_{6.06}$ Space Group : P4/mmm

a = b = 3.8570(1) Å c = 11.8194(3) Å

Atom	x	y	z	Occupancy
Y	$\frac{1}{2}$	$\frac{1}{2}$	$\frac{1}{2}$	1
Ba	$\frac{1}{2}$	$\frac{1}{2}$	0.1952(2)	1
Cu(1)	0	0	0	1
Cu(2)	0	0	0.3607(1)	1
O(1)	0	$\frac{1}{2}$	0	0.028(4)
O(2)	0	$\frac{1}{2}$	0.379(1)	1
O(4)	0	0	0.1518(2)	0.990(6)

Table A.4

5 A. Santoro, S. Miraglia, F. Beech, S. A. Sunshine, D. W. Murphy, L. F. Schneemeyer & J. V. Waszczak, *Mat. Res. Bull.* **22** 1007 (1987)

A.4.2 Selected Bond Lengths[4]

Oxygen Content : $O_{6.06}$ Bond Lengths in Å

Y-O(2)	2.4004(8)
Ba-O(2)	2.905(1)
Ba-O(4)	2.7751(5)
Cu(1)-O(4)	1.795(2)
Cu(2)-O(2)	1.9406(3)
Cu(2)-O(4)	2.469(2)

Table A.5

A.5 Substitutions For Yttrium

The general effects of replacing Y with other rare-earth metal (Lanthanide) ions have already been discussed in section 2.2.2. Table A.6 gives the slightly varying lattice parameters of $(RE)Ba_2Cu_3O_{7-\delta}$, along with the oxygen content and mid-point transition temperature for various dopants which replace Y. The data is taken at 295K. Observe that the degree of orthorhombicity increases and unit cell volume decreases with decreasing size of dopant ion. A brief discussion of the Pr doped system is given in section A.5.2

A.5.1. Common Dopants[1,6]

RE	Ionic (+3) Rad. (Å)	a(Å)	b(Å)	c(Å)	(b-a)/a x10^{-2}	Cell vol. (Å^3)	Oxygen value	T_c (K)
La	1.15	3.894	3.937	11.815	1.10	181.13	6.82	76
Pr	1.09	3.882	3.930	11.790	1.24	179.87	7.00	--
Nd	1.08	3.859	3.911	11.741	1.34	177.20	7.00	92
Sm	1.04	3.846	3.903	11.727	1.48	176.03	7.00	92
Eu	1.12 (+2)	3.838	3.897	11.707	1.54	175.10	7.00	92
Gd	1.02	3.835	3.895	11.699	1.56	174.75	7.00	92
Dy	0.99	3.825	3.886	11.686	1.59	173.75	7.00	92
Ho	0.97	3.821	3.885	11.682	1.67	173.41	6.96	91.5
Er	0.96	3.813	3.878	11.666	1.70	172.50	6.86	91
Tm	0.95	3.808	3.875	11.665	1.75	172.13	7.00	91
Yb	0.94	3.802	3.871	11.658	1.81	171.58	7.00	92

Table A.6

---

6 Also see R. M. Hazen in *Properties of High Temperature Superconductivity*, Vol II, ed. D. M. Ginsberg, World Scientific, Singapore (1990)

A.5.2 The Effect of Praesodymium

The $Y_{1-z}Pr_zBa_2Cu_3O_{7-\delta}$ system is orthorhombic over the entire range of z. As Y is increasingly replaced by Pr there is a monotonic decrease in the T_c of the material (see figure A.3) and a small reduction of the orthorhombic distortion, (b-a)/(b+a). For z>0.55, the compounds are not superconducting and the resistivity is characteristic of a semiconductor material. The oxygen content is essentially constant with increasing z, suggesting that the ordering in the Cu-O chains remains unchanged[7].

The valency of Pr in the system is controversial, as Pr has a tendency to form +4 ions (ionic radius=0.92Å). This is supported by magnetic susceptibility measurements[8], which reveal that the average valence of Pr over the entire z range is 3.87. However, experimental observations of the lattice parameters and bond lengths suggest that Pr is predominantly in the +3 state. With such contrary imformation, an explanation of the T_c behaviour based on the non-trivalency of the Pr ion has not been ruled out. A second explanation of its anomolous behaviour stems from the hybridisation effects between the Pr 4f electrons and the valence band. The hybridisation is expected to be strong for the large Pr ions and there is known to be a pressure induced electronic phase transition which is dependent on z. A weakening of the superconducting electron pairs, through a strong Coulomb repulsion within the Pr 4f state, could be responsible for a reduction in T_c.

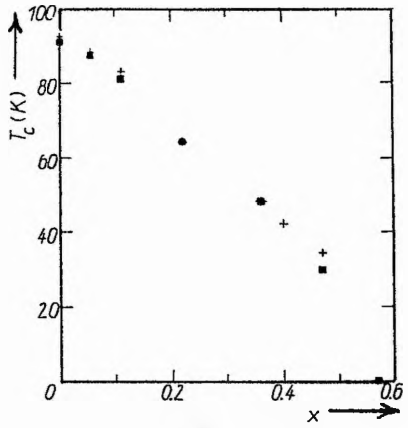

Figure A.3

Variation of T_c in $Y_{1-z}Pr_zBa_2Cu_3O_{7-\delta}$ (z=x). (•)=resistivity & (+)=magnetic measurements[9].

---

7 A. Matsuda, K. Kinoshita, T. Ishii, H. Shibata, T. Watanabe & T. Yamada, *Phys. Rev. B* **38** 2910 (1988)

8 See R. Beyers & T. M. Shaw, 'The Structure of $Y_1Ba_2Cu_3O_{7-\delta}$ and its Derivatives' in *Solid State Physics*, Vol. 42 : eds. H. Ehrenreich & D. Turnbull, Academic Press (1989)

9 U. C. Boehnke, H. Borner, J. Herrmann, B. Lippold, Ch. Semmelhack, L. Waldostl & M. Wurlitzer, *Phys. Stat. Sol. (a)* **120** 557 (1990)

A.6 Substitutions for Barium

The following gives a summary of the effects of various dopants, when substituted for barium. There appears no obvious trend.

Dopant Ion	y%	Structure of Y(BA)CO	Effect On T_c	Notes
Mg^{2+}	y≤2*	Orthorhombic	Rapid decrease to 82K	* Mg occupies oxygen vacancies in basal plane
	2<y%≤50†	Orthorhombic	Constant at 82K	†Mg occupies the Ba sites
Ca^{2+}	y≤12.5	Orthorhombic	Linear decrease	additional vacancies may appear in chains causing a decrease in T_c.
	y>12.5	Mixed phase	---	--
Sr^{2+}	y<50*	Orthorhombic	Monotonic decrease	*additional vacancies may appear in chains causing a decrease in T_c.
	y=50†	Orthorhombic	Almost plateau-like behaviour.	† possibility of ordering of Sr & Ba atoms
	y>50	Mixed phase	Linear decrease	-
	y=100	Mixed phase	Insulator	No orthorhombicity found
Cd^{2+}	y≤75	Orthorhombic	No effect	Cd does not substitute for Ba and does not enter the matrix of 123 structure.
Pb^{2+}	y≤15	Orthorhombic	No effect	Similar to Cd. Pb doping improves intergranular properties of sintered samples
K^{+}	y≤50	Orthorhombic	No effect	small changes in lattice parameters in observed
	y>50	Amorphous	Non-superconducting	oxygen loss & disordering of oxygen vacancies
La^{3+}	y≤20	Orthorhombic	Decreases moderately	Extra oxygen occupies the O(5) sites. Occurs a gradual depopulation of the O(1) sites into the O(5) sites until at the transition the occupancies are equal.
	20≤y≤30	Tetragonal	Decreases rapidly	
	y>20	Different Orthorhombic phase	Semiconducting	A possible change in the Ba ion position

Table A.7

Dopants which substitute for Barium in YBCO.

(Summary of results surveyed by Felner[10])

[10] I. Felner, *Thermochimica Acta* **174** 41 (1991)

A.7 Common Substitutions for Copper

Dopant M	Outer Electrons	Expected Valency	State of M	Structural Transition, x_c	Cu site	Ref.
Mn	$3d^5\ 4s^2$	+4	Magnetic	orthorhombic	Cu(2)	11
Fe	$3d^6\ 4s^2$	+3	Magnetic	3 - 5%	Cu(1)	12
Co	$3d^7\ 4s^2$	+3	Magnetic	~3%	Cu(1)	13
Ni	$3d^8\ 4s^2$	+2	Magnetic	orthorhombic	Cu(1)/(2)	14
Cu	$3d^{10}\ 4s^1$	+1/+2/+3	valency dependent	--	--	--
Zn	$3d^{10}\ 4s^2$	+2	Non-magnetic	orthorhombic	Cu(2)	15
Ga	$3d^{10}4s^2\ 4p^1$	+3	Non-magnetic	4 - 6%	Cu(1)	15
Al	$3s^2\ 3p^1$	+3	Non-magnetic	~4%	Cu(1)	16
Ag	$4d^{10}\ 5s^1$	+1	Non-magnetic	ortho ?	Cu(1)	17
Au	$4f^{14}5d^{10}6s^1$	+3	Non-magnetic	orthorhombic	Cu(1)	18

Table A.8

Basic properties of the common dopants which substitute on the Cu sites of YBCO.

Notes on Table A.8

1. The structural transition column gives the critical dopant concentration, x_C, at which the orthorhombic to tetragonal (II) transition in $YBa_2(Cu_{1-x}M_x)_3O_{7-\delta}$ occurs. In many

---

11 G. Kallias & D. Niarchos, *Physica C* **185-189** 555 (1991)

12 L. Nuñez, R. D. Rogers, G. W. Crabtree, U. Welp, K. Vandervoort, A. Umezawa & Y. Fang, *Phys. Rev. B* **44** 4526 (1991)

13 J. M. Tarascon, P. Barboux, P. F. Miceli, L. H. Greene, G. W. Hull, M. Eibschutz & S. A. Sunshine, *Phys. Rev. B* **37** 7458 (1988)

14 F. Bridges, J. B. Boyce, T. Claeson, T. H. Geballe & J. M. Tarascon, *Phys. Rev. B* **42** 2137 (1990)

15 G. Xiao, M. Z. Cieplak, D. Musser, A. Gavrin, F. H. Strietz, C. L. Chien, J. J. Rhyne & J. A. Gotaas, *Nature* **332** 238 (1988)

16 T. Takabatake & M. Ishikawa, *Solid State Comm.* **66** 413 (1988)

17 J. J. Lin, T. M Chen & Y. F. Chen, *Solid State Comm.* **76** 1285 (1990)

18 H. Renevier, J. Hodeau, T. Fournier, P. Bordet & M. Marezio, *Physica C* **172** 183 (1990)

cases the transition occurs over a range of x% and so the upper limits given are concentrations at which the structure in purely tetragonal.

2. The substituted systems that remain orthorhombic, do so up to x>10%, generally. Often at higher x values multi-impurity phases appear. The single phase orthorhombic structure is preserved for up to x%=20 in Mn doped YBCO. Systematic studies of Ag doping are complicated by the fact that samples tend to be multi-phase. The overall multi-phase samples tend to be orthorhombic in structure but the substitutional effects of Ag seem to be unclear.
3. The Cu sites given are those which the dopant predominantly occupies. For higher Fe content (x%>10), multiple-site substitution has been found.
4. At low concentration, Ni substitutes linearly onto both Cu sites, with a slight preference for the Cu(2) site[14]. At higher concentrations of Ni mixed impurity phases appear. The depression of T_c with Ni concentration is usually explained by two different mechanisms: since Ni^{2+} has one 3d electron less than Cu^{2+} there is a variation in the density of states near the Fermi level; Ni has a localised moment and so could cause a conventional pair-breaking effect.
5. In the case of Mn, which tends to have a +4 valency, but also substitutes on the Cu(2) site and remains orthorhombic, the T_c appears to be suppressed by classical spin exchange between the local magnetic moment and Cooper pair electrons.
6. The trivalent Au ion seems to be somewhat of an exceptional dopant. Relevant studies have shown that it substitutes on the Cu(1) site, yet neither T_c (T_c=89K at x%=10) nor crystal structure appear to change.
7. These figures are taken from a large number of modern papers and form the general concensus at present. Some papers, especially earlier ones, give contrary views, particularly for the site preference. Inconstistencies which appear from investigation to investigation can often be attributed to different preparative methods. The superconducting properties of the substituted system are sensitive to synthesis conditions and extra phases or varied oxygen stoichiometry can result.

A.8 Cobalt Doping

In order to be consistent, the graphs in sections A.8.1 and A.8.3 represent data collected on the same series of Co-doped samples[19].

A.8.1 Lattice Parameters & Cell Volume

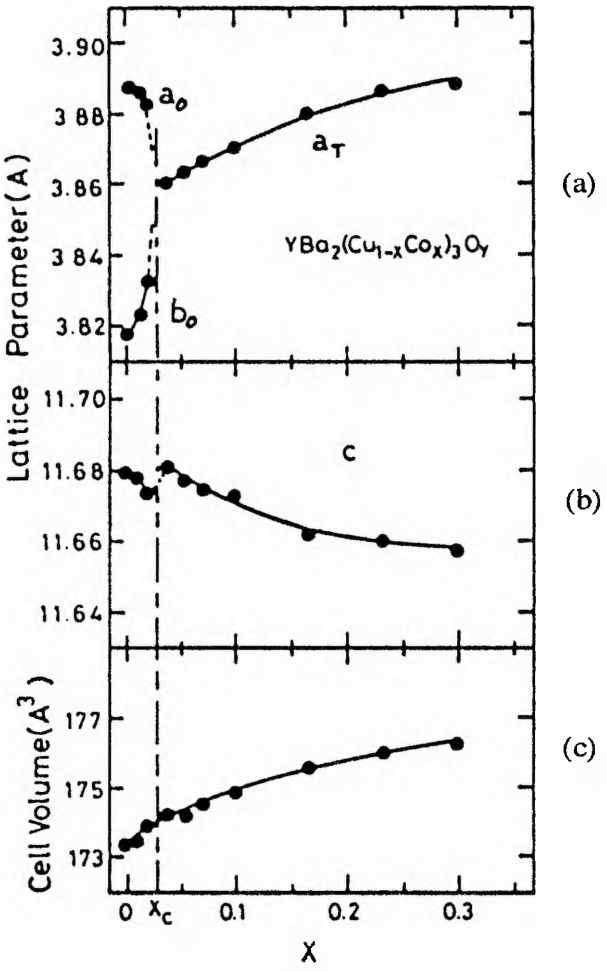

Figure A.4

Unit cell parameters of $YBa_2(Cu_{1-x}Co_x)_3O_{7-\delta}$ as a function of Co concentration[19]: (a) lattice parameters a_O and b_O for the orthorhombic structure and a_T for the tetragonal (II) structure, (b) the c-lattice parameter and (c) the unit cell volume. Note the x_c line.

---

[19] R. Aoki, S. Takahashi, H. Murakami, T. Nakamura, T. Nakamura, Y. Takagi & R. Liang, *Physica C* **156** 405 (1988)

A.8.2 Variation of Selected Bond Lengths

Although a number of papers[20,21,22,23,24,25,26,27] present structural data on Co-doped YBCO, in many cases the data is incomplete, random and strongly sample dependent. At the present time, it is difficult to get an idea of the absolute variation in bond length, etc. as a continuous function of Co concentration, since no single study has attempted to structurally characterise a complete series of Co-doped samples.

In order to observe the general trend in selected bond lengths, Miceli et al[28] have brought together data which shows the variation of T_c as a function of bond length for a number of Co-doped, Al-doped and pure YBCO samples. The data, which is represented in figure A.5 (overpage), incorporates the Co, Al and oxygen concentration as an implicit variable, only.

---

20 P. F. Miceli, J. M. Tarascon, L. H. Greene, P. Barboux, F. J. Rotella & J. D. Jorgensen, *Phys. Rev. B* **37** 7458 (1988)

21 D. C. Johnson, A. J. Jacobsen, J. M. Newsam, J. T. Lewandowski, D. P. Goshorn, D. Xie & W. B. Yelon, *Chemistry of High Temperature Superconductors*, p 136, ed. D. L. Nelson, M. S. Wittingham & T. F. George, American Chemical Soc., Washington (1987).

22 T. Kajitani, K. Kusaba, M. Kikuchi, Y. Syono & M. Hirabayashi, *Jpn. J. Appl. Phys.* **26** L1727 (1987)

23 P. F. Miceli, J. M. Tarascon, L. H. Greene, P. Barboux, F. J. Rotella & J. D. Jorgensen, *Phys. Rev. B* **37** 5932 (1988)

24 Yang Ying-Chang, Zha Yuan-Bo, Yuan Wei-Chun, Yang Ji-Lian, Zhang Bai-sheng, Zhou Hui-ming, Ding Yong-Fan, Jin Lan & Ye Chun-Tang, *Chinese Physics* **10** 681 (1990)

25 F. Bridges, J. B. Boyce, T. Claeson, T. H. Geballe & J. M. Tarascon, *Phys. Rev. B* **39** 11603 (1989)

26 P. Zolliker, D. E. Cox, J. M. Tranquada & G. Shirane, *Phys. Rev. B* **38** 6575 (1988)

27 S. Eriksson, L. G. Johansson, L. Börjesson & M. Kakihana, *Physica C* **162-164** 73 (1989)

28 P. F. Miceli, J. M. Tarascon, L. H. Greene, P. Barboux, J. D. Jorgenson, J. J. Rhyne & D. A. Neumann, *Mat. Res. Soc. Symp. Proc.* **156** 119 (1989)

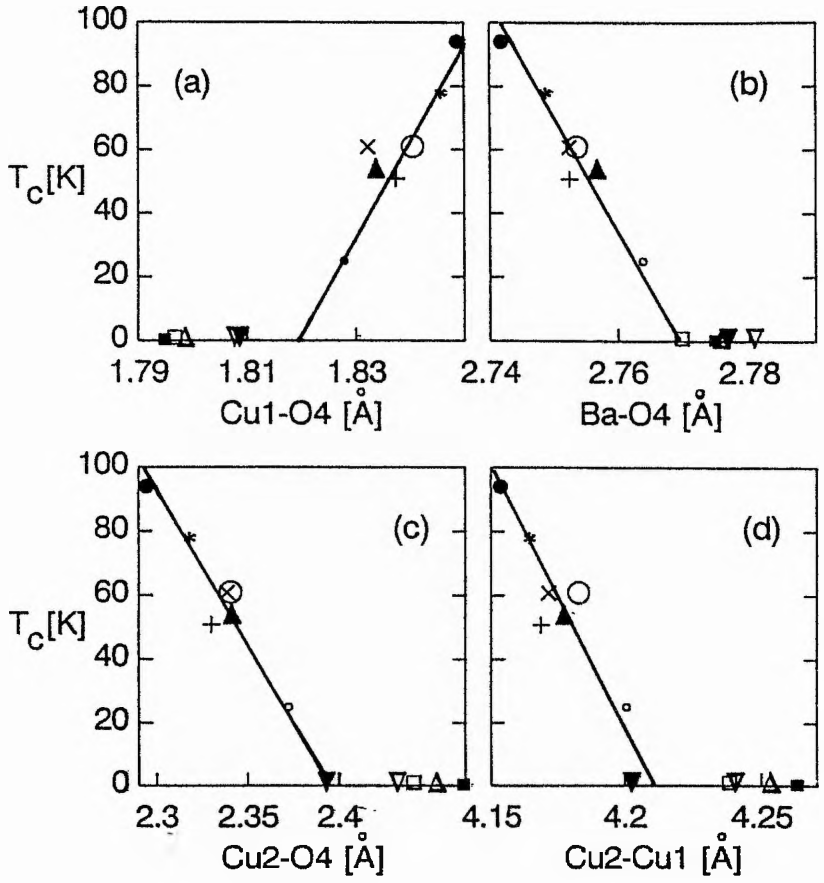

Figure A.5

T_c vs selected bond lengths for the various Co-doped, Al doped and pure YBCO samples listed in the key below[28].

Ref 20	$YBa_2Cu_{2.8}Co_{0.2}O_7$	▲	Ref 29	$YBa_2Cu_{2.9}Al_{0.1}O_7$	*
Ref 20	$YBa_2Cu_{2.8}Co_{0.2}O_{6.4}$	△	Ref 29	$YBa_2Cu_{2.8}Al_{0.2}O_7$	x
Ref 20	$YBa_2Cu_{2.2}Co_{0.8}O_{7.3}$	▼	Ref 29	$YBa_2Cu_{2.7}Al_{0.3}O_7$	+
Ref 20	$YBa_2Cu_{2.2}Co_{0.8}O_{6.9}$	▽	Ref 21	$YBa_2Cu_3O_{6.9}$	●
Ref 22	$YBa_2Cu_{2.7}Co_{0.3}O_{6.9}$	°	Ref 21	$YBa_2Cu_3O_{6.7}$	o
			Ref 21	$YBa_2Cu_3O_{6.4}$	□
			Ref 21	$YBa_2Cu_3O_{6.1}$	■

[29] P. F. Miceli, unpublished.

A.8.3 Variation of C, θ, P_{eff} & χ_0 with Co Content

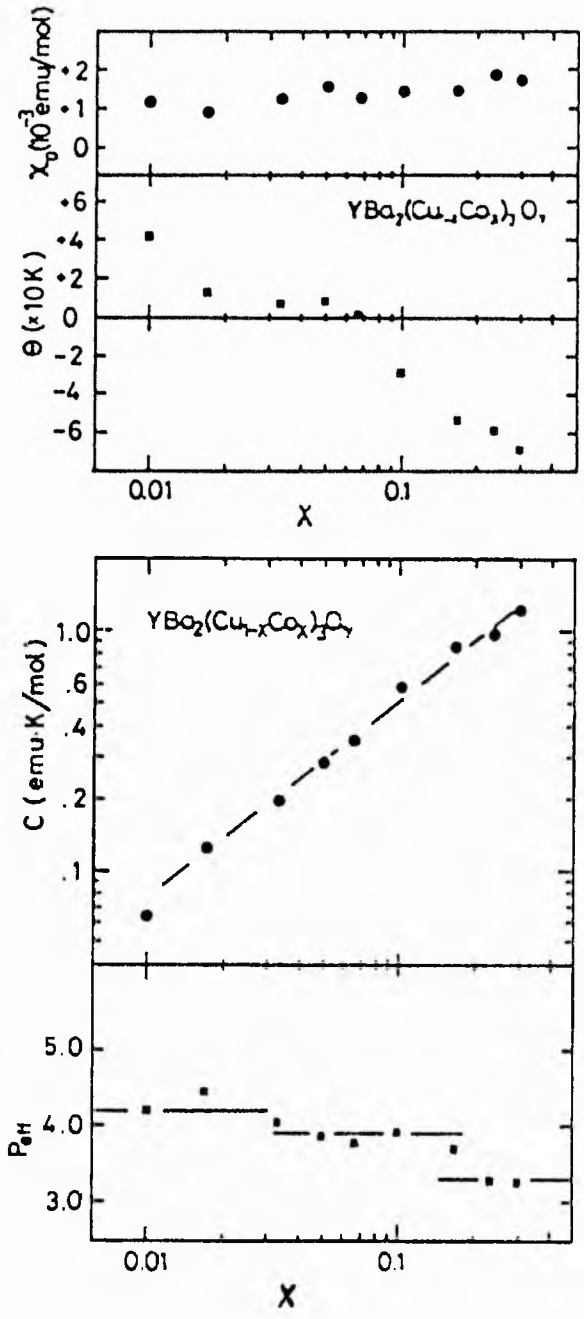

Figure A.6

(a) Constant paramagnetic term χ_0, (b) the characteristic Curie temperature θ, (c) the Curie constant C and (d) the effective Bohr magneton/Co atom P_{eff}, vs Co concenbtration x[19].

Appendix B

IRC Data on Cobalt-Doped YBCO

This appendix contains some of the raw a.c susceptibility and X-ray data obtained on the low percentage Co-doped samples by the IRC, University of Cambridge. It is intended for reference only and is supplied here without accompanying notes:

B.1 A.C. Susceptibility Data

333·3 Hz/g RMS.

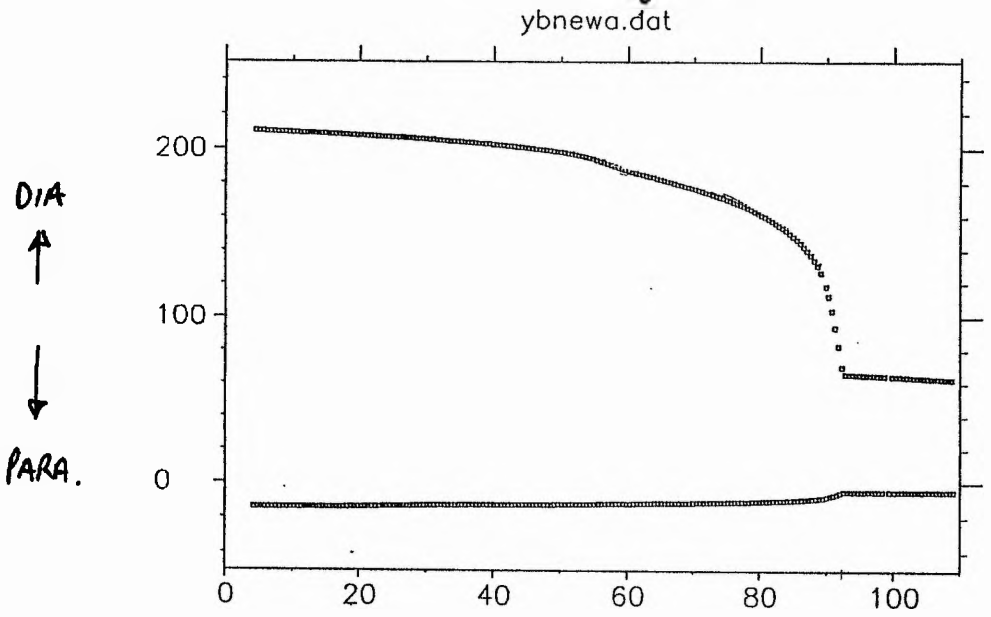

0.00% Cobalt

T_c = 92.363K.

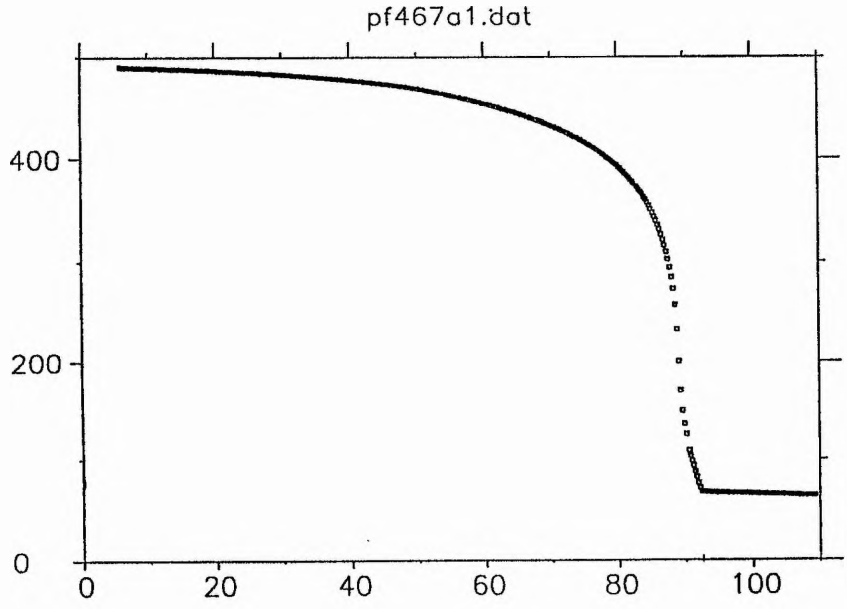

0.05% Cobalt.

T_c = 92.399K.

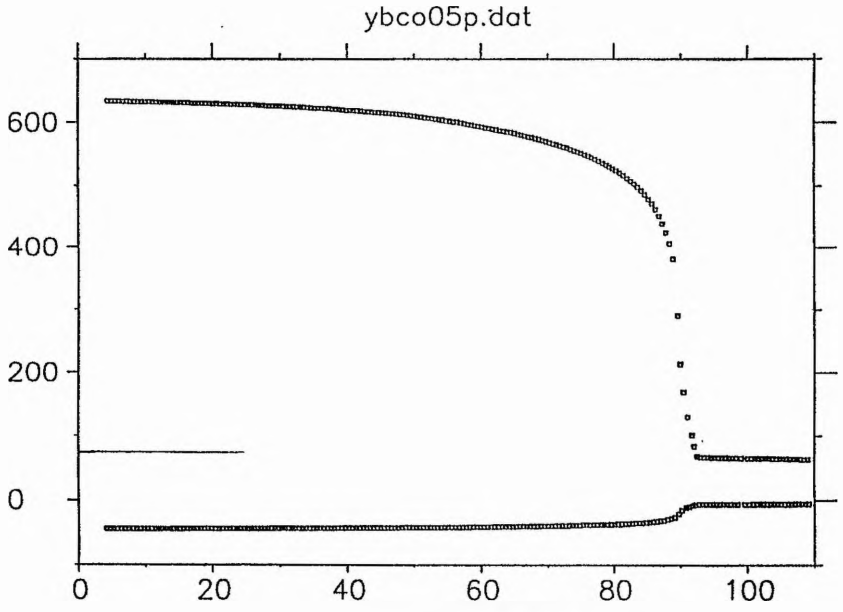

0.15% Cobalt.

T_c = 92.466K.

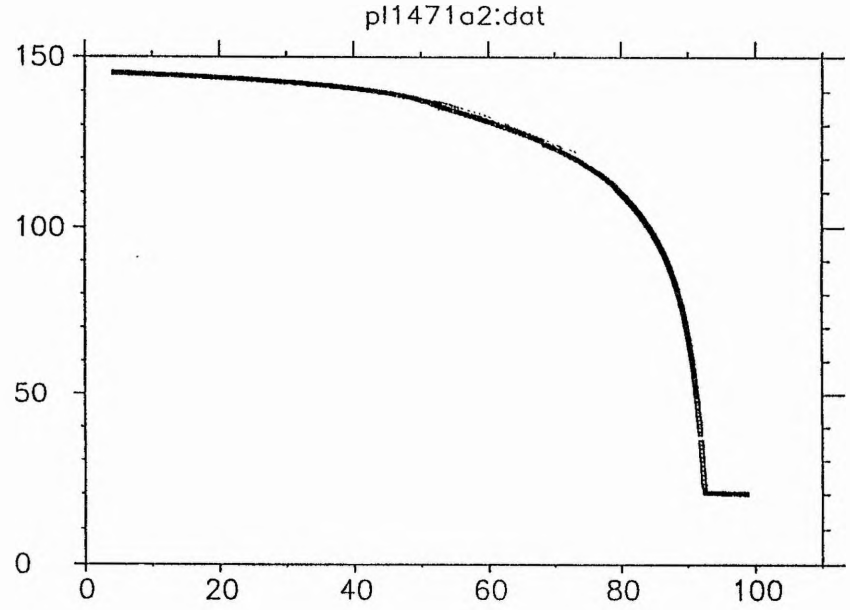

0.30% Cobalt.

T_c = 92.533K.

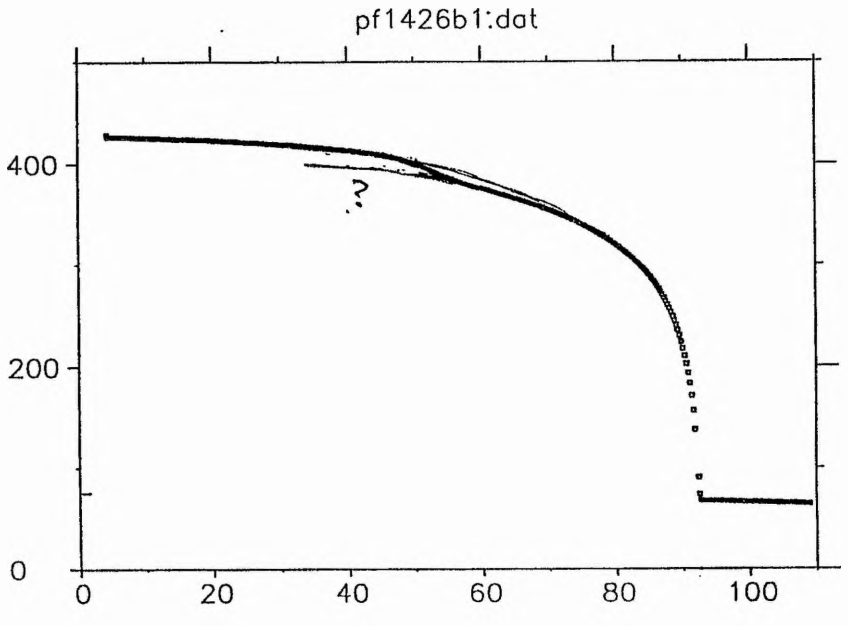

0.50% Cobalt

T_c = 92.599K.

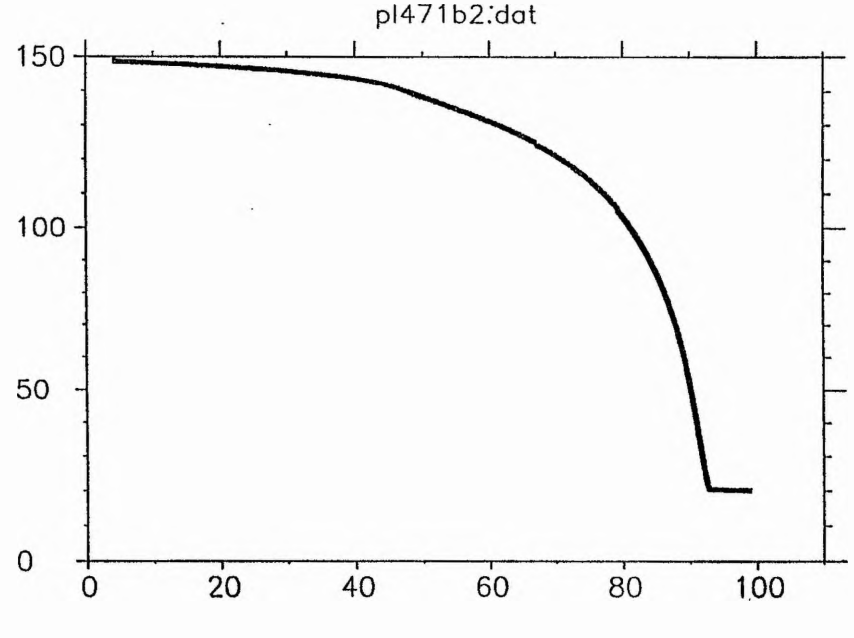

1.0% Cobalt

T_c = 92.733K.

B.2 X-Ray Data

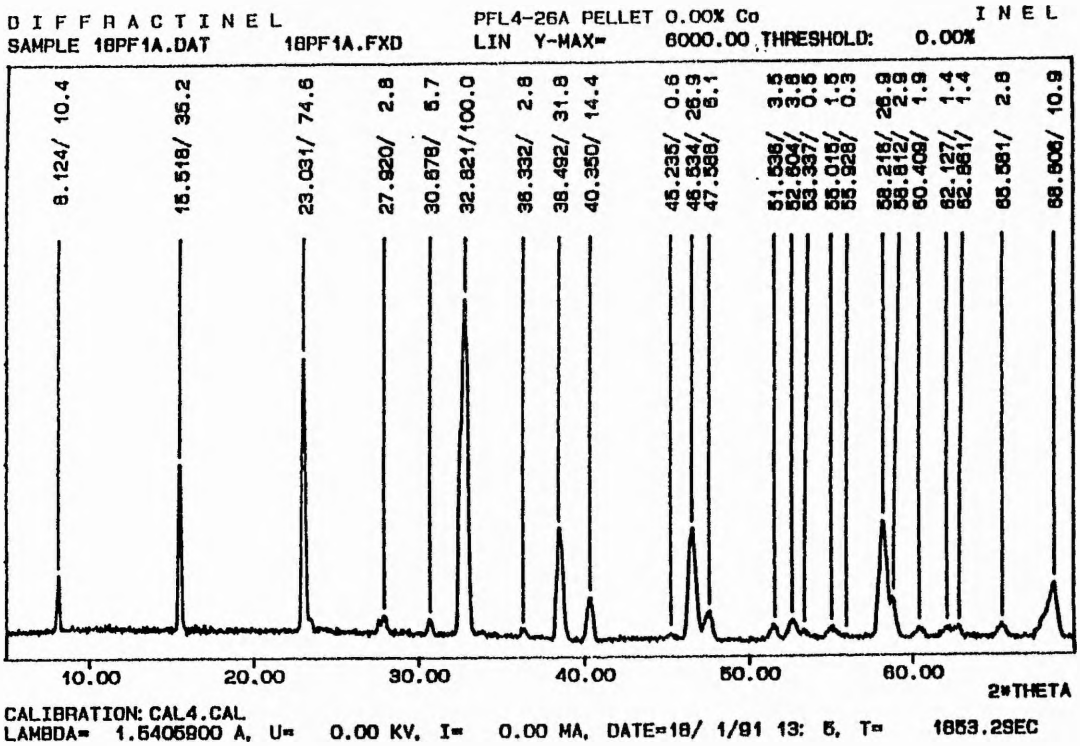
DIFFRACTINEL
PFL4-26A PELLET 0.00% Co
INEL
SAMPLE 18PF1A.DAT
18PF1A.FXD
LIN Y-MAX= 6000.00 THRESHOLD: 0.00%
8.124/ 10.4
15.518/ 35.2
23.031/ 74.6
27.920/ 2.8
30.878/ 5.7
32.821/100.0
36.332/ 2.8
38.492/ 31.8
40.350/ 14.4
45.235/ 0.6
46.534/ 26.9
47.588/ 8.1
51.536/ 3.5
52.804/ 3.6
53.337/ 0.5
55.015/ 1.5
55.928/ 0.3
58.218/ 26.9
58.812/ 2.9
60.409/ 1.9
62.127/ 1.4
62.881/ 1.4
65.581/ 2.8
68.606/ 10.9
10.00
20.00
30.00
40.00
50.00
60.00
2*THETA
CALIBRATION: CAL4.CAL
LAMBDA= 1.5406900 A, U= 0.00 KV, I= 0.00 MA, DATE=18/ 1/91 13: 5, T= 1853.2SEC

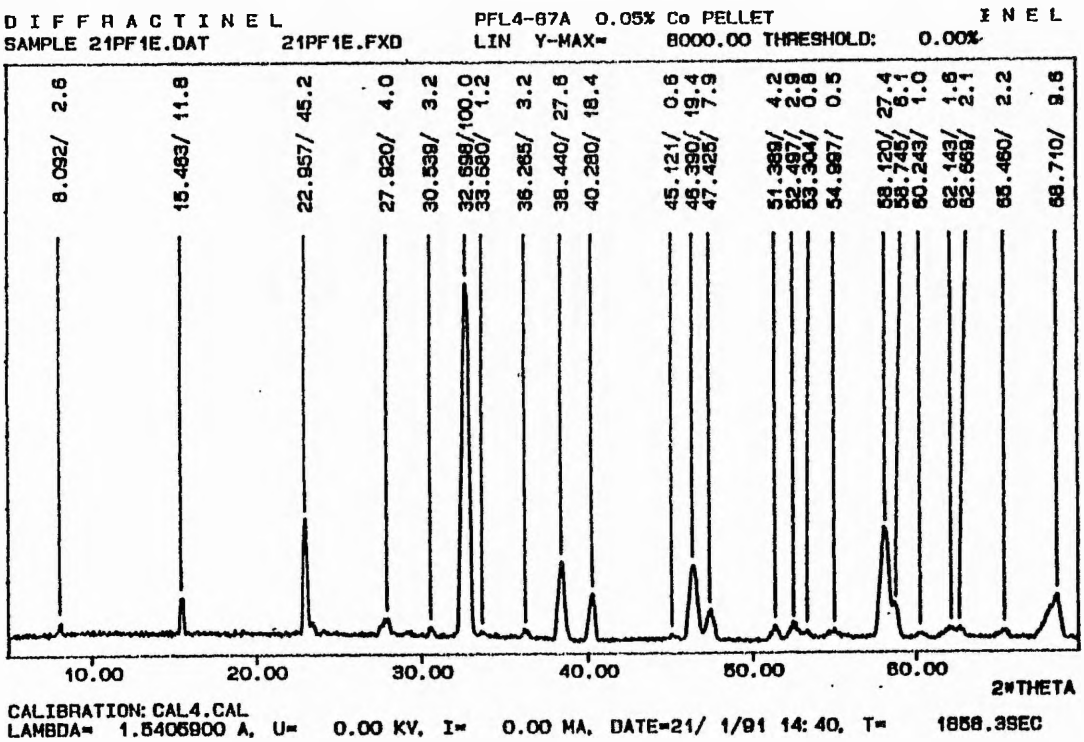
DIFFRACTINEL
PFL4-67A 0.05% Co PELLET
INEL
SAMPLE 21PF1E.DAT
21PF1E.FXD
LIN Y-MAX= 6000.00 THRESHOLD: 0.00%
8.092/ 2.6
15.483/ 11.8
22.957/ 45.2
27.920/ 4.0
30.539/ 3.2
32.698/100.0
33.680/ 1.2
36.265/ 3.2
38.440/ 27.6
40.280/ 18.4
45.121/ 0.6
46.390/ 19.4
47.425/ 7.9
51.389/ 4.2
52.497/ 2.8
53.304/ 0.8
54.997/ 0.5
58.120/ 27.4
58.745/ 6.1
60.243/ 1.0
62.143/ 1.6
62.869/ 2.1
65.460/ 2.2
68.710/ 9.6
10.00
20.00
30.00
40.00
50.00
60.00
2*THETA
CALIBRATION: CAL4.CAL
LAMBDA= 1.5406900 A, U= 0.00 KV, I= 0.00 MA, DATE=21/ 1/91 14: 40, T= 1858.3SEC

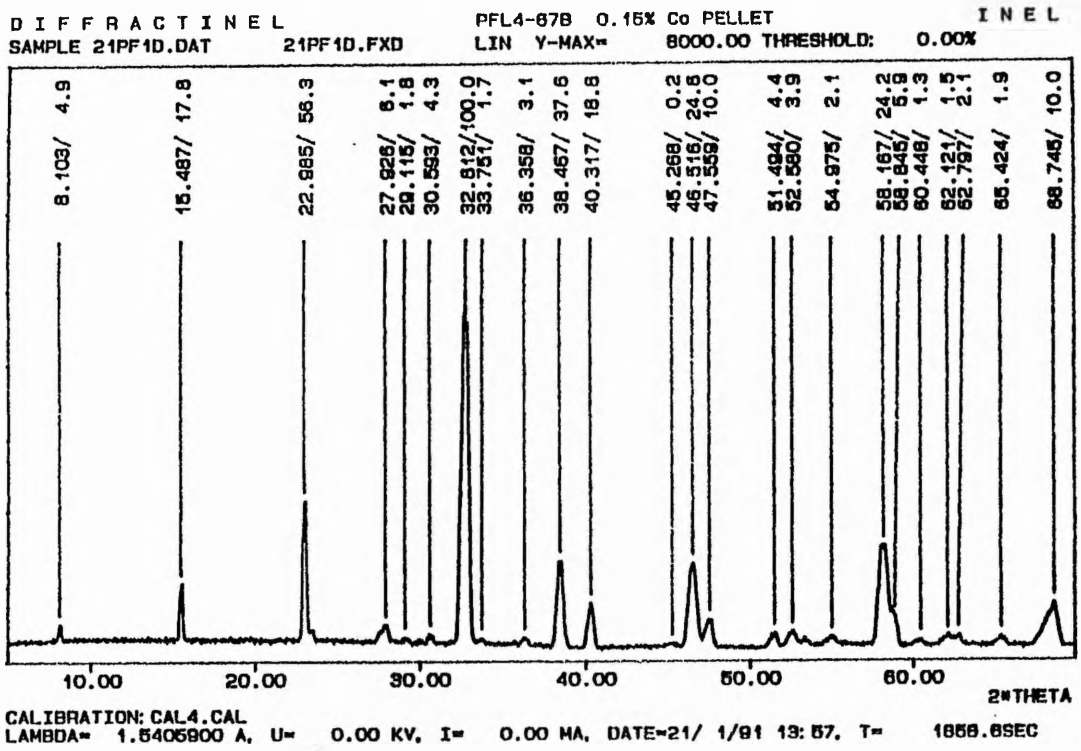
DIFFRACTINEL
PFL4-67B 0.15% Co PELLET
INEL
SAMPLE 21PF1D.DAT
21PF1D.FXD
LIN Y-MAX=
8000.00 THRESHOLD:
0.00%
8.103/ 4.9
15.487/ 17.8
22.985/ 56.3
27.926/ 8.1
29.115/ 1.8
30.593/ 4.3
32.812/100.0
33.751/ 1.7
36.358/ 3.1
38.467/ 37.6
40.317/ 18.8
45.268/ 0.2
46.516/ 24.8
47.559/ 10.0
51.494/ 4.4
52.580/ 3.9
54.975/ 2.1
58.167/ 24.2
58.845/ 5.9
60.448/ 1.3
62.121/ 1.5
62.797/ 2.1
65.424/ 1.9
68.745/ 10.0
10.00
20.00
30.00
40.00
50.00
60.00
2*THETA
CALIBRATION: CAL4.CAL
LAMBDA= 1.5405900 A, U= 0.00 KV, I= 0.00 MA, DATE=21/ 1/91 13:57, T= 1858.6SEC

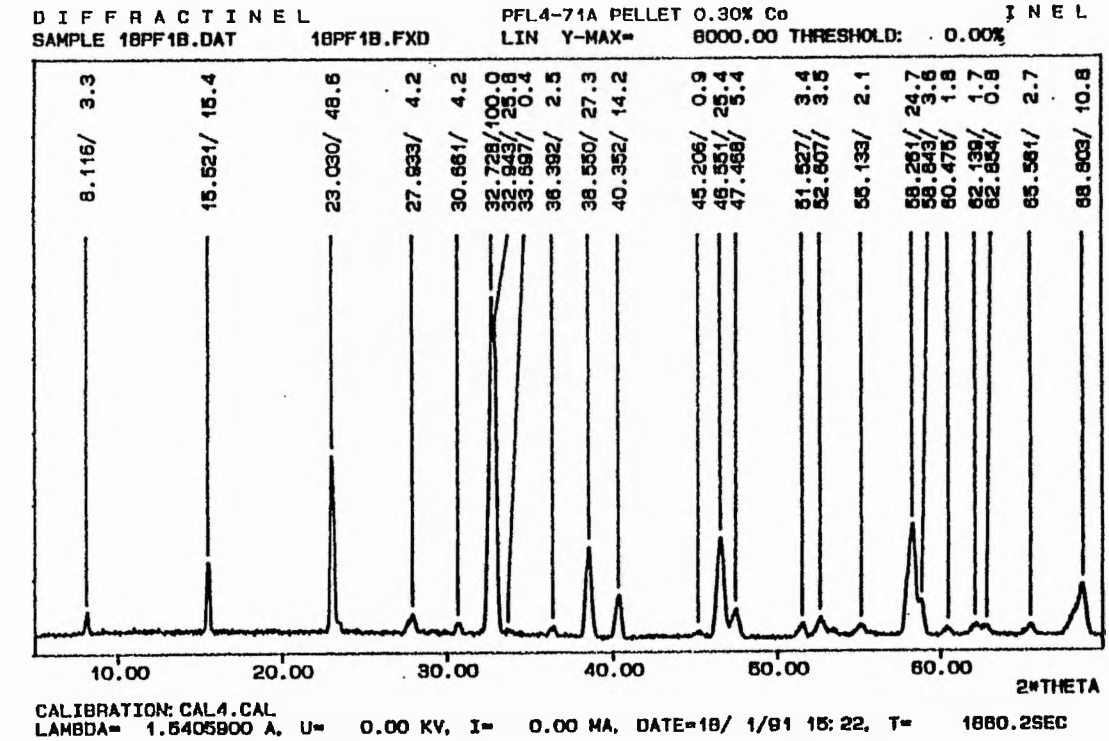
DIFFRACTINEL
PFL4-71A PELLET 0.30% Co
INEL
SAMPLE 18PF1B.DAT
18PF1B.FXD
LIN Y-MAX=
8000.00 THRESHOLD:
0.00%
8.116/ 3.3
15.521/ 15.4
23.030/ 48.6
27.933/ 4.2
30.681/ 4.2
32.728/100.0
32.943/ 25.8
33.897/ 0.4
36.392/ 2.5
38.550/ 27.3
40.352/ 14.2
45.206/ 0.9
46.551/ 25.4
47.468/ 5.4
51.527/ 3.4
52.607/ 3.5
55.133/ 2.1
58.251/ 24.7
58.843/ 3.8
60.475/ 1.8
62.139/ 1.7
62.854/ 0.8
65.561/ 2.7
68.903/ 10.8
10.00
20.00
30.00
40.00
50.00
60.00
2*THETA
CALIBRATION: CAL4.CAL
LAMBDA= 1.5405900 A, U= 0.00 KV, I= 0.00 MA, DATE=18/ 1/91 15:22, T= 1860.2SEC

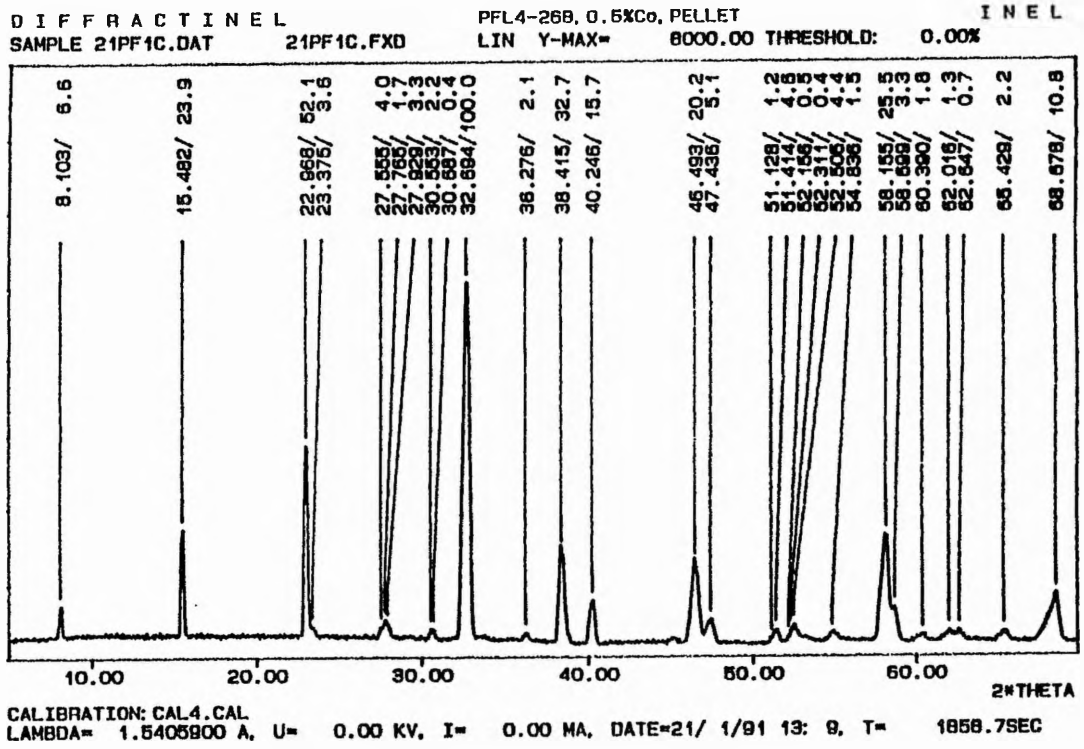
DIFFRACTINEL
PFL4-26B, 0.5%Co, PELLET
INEL
SAMPLE 21PF1C.DAT
21PF1C.FXD
LIN Y-MAX= 8000.00 THRESHOLD: 0.00%
8.103/ 6.6
15.482/ 23.9
22.968/ 52.1
23.375/ 3.8
27.555/ 4.0
27.765/ 1.7
27.929/ 3.2
30.553/ 2.4
30.887/ 0.4
32.694/100.0
36.276/ 2.1
38.415/ 32.7
40.246/ 15.7
46.493/ 20.2
47.436/ 5.1
51.128/ 1.2
51.414/ 4.6
52.156/ 0.4
52.311/ 4.4
52.505/ 4.5
54.836/ 1.5
58.155/ 25.5
58.599/ 3.3
60.390/ 1.8
62.016/ 1.3
62.647/ 0.7
65.429/ 2.2
68.678/ 10.8
10.00
20.00
30.00
40.00
50.00
60.00
2*THETA
CALIBRATION: CAL4.CAL
LAMBDA= 1.5405900 A, U= 0.00 KV, I= 0.00 MA, DATE=21/ 1/91 13: 9, T= 1858.7SEC

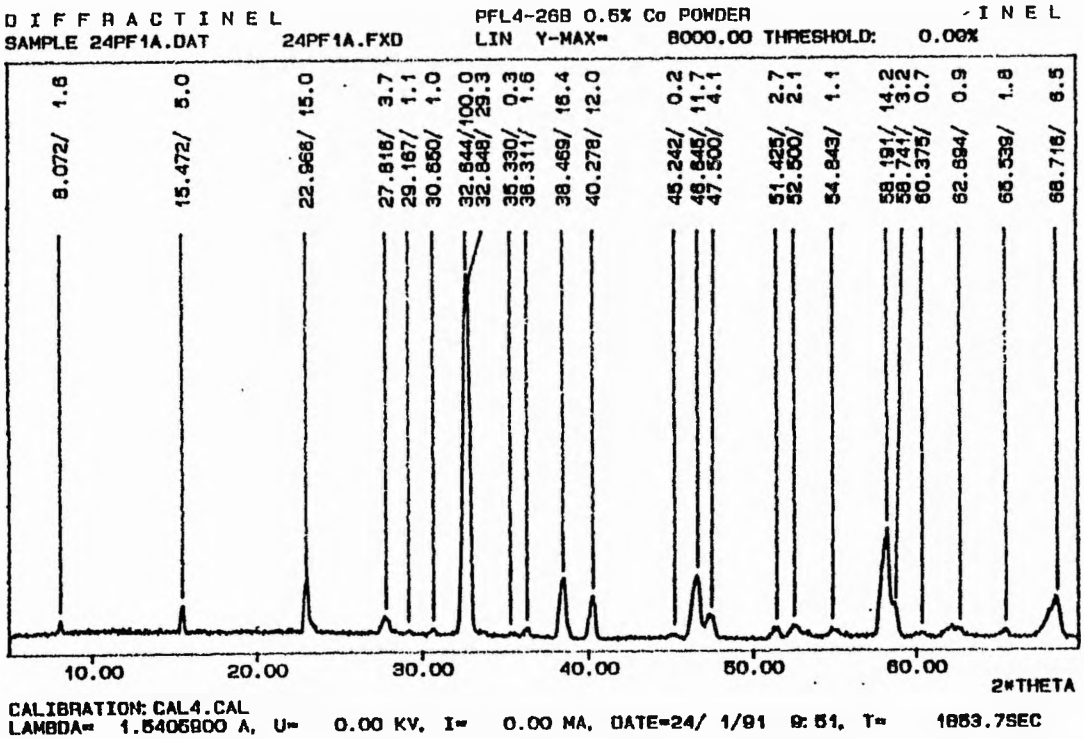
DIFFRACTINEL
PFL4-26B 0.5% Co POWDER
INEL
SAMPLE 24PF1A.DAT
24PF1A.FXD
LIN Y-MAX= 8000.00 THRESHOLD: 0.00%
8.072/ 1.8
15.472/ 5.0
22.968/ 15.0
27.818/ 3.7
29.167/ 1.1
30.850/ 1.0
32.844/100.0
32.848/ 29.3
35.330/ 0.3
36.311/ 1.6
38.469/ 16.4
40.278/ 12.0
45.242/ 0.2
46.845/ 11.7
47.500/ 4.1
51.425/ 2.7
52.500/ 2.1
54.843/ 1.1
58.191/ 14.2
58.741/ 3.2
60.375/ 0.7
62.894/ 0.9
65.539/ 1.8
68.716/ 6.5
10.00
20.00
30.00
40.00
50.00
60.00
2*THETA
CALIBRATION: CAL4.CAL
LAMBDA= 1.5405900 A, U= 0.00 KV, I= 0.00 MA, DATE=24/ 1/91 9:51, T= 1853.7SEC

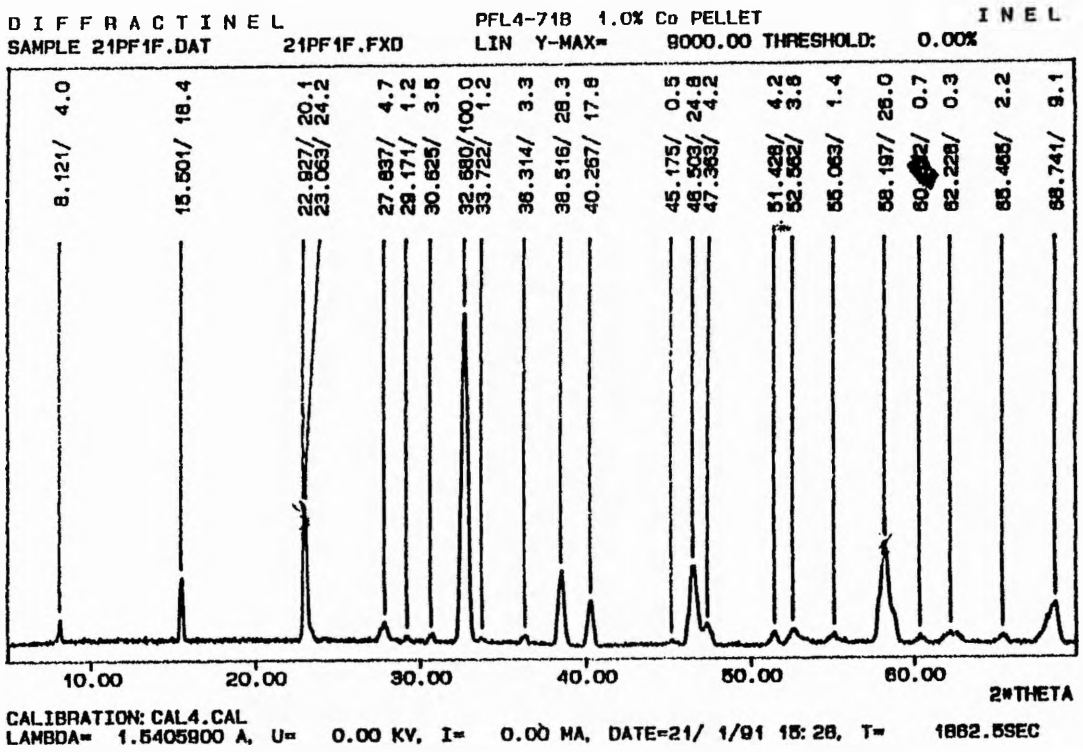

Good sample of YBCO → Resistivity through origin AC S results good.

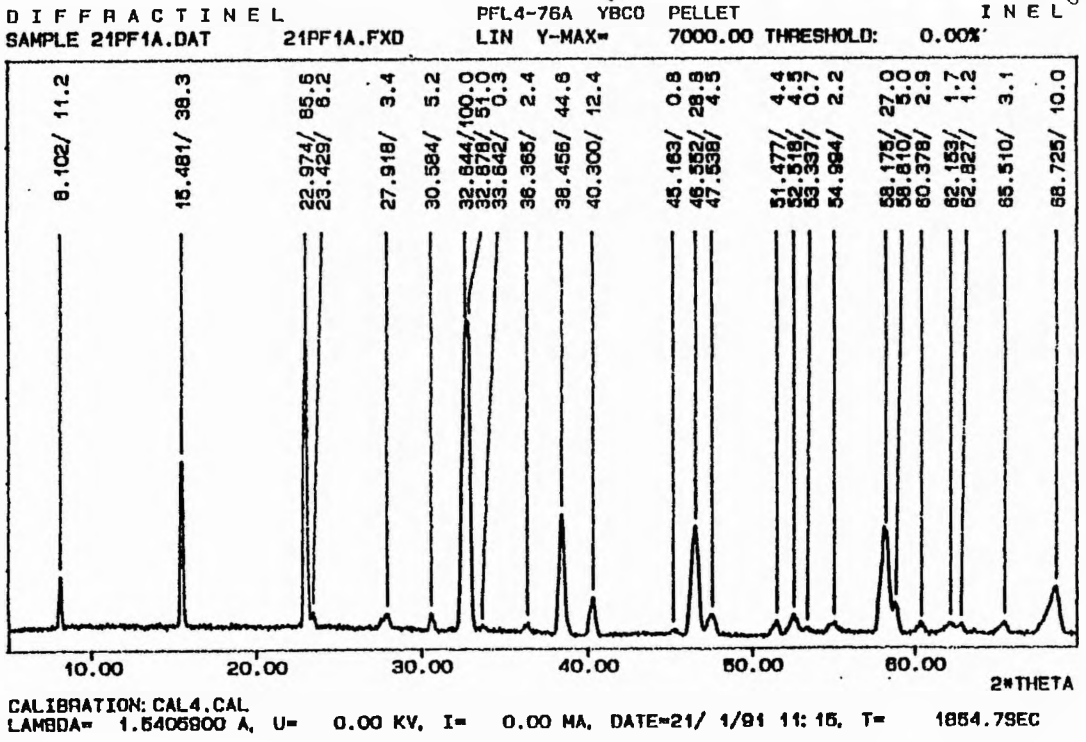

Appendix C

Computer Programs & Calculations

This appendix contains:

C.1 X-Ray (2θ) Program

This Microsoft™ QuickBasic program was compiled on a Compaq DeskPro 286e IBM clone with a Maths 80287 SX coprocessor. The program is designed to calculate the 'theoretical' 2θ values for a series of (hkl) X-ray powder peaks (using equation 4.2, then 4.1), provided that the estimated orthorhombic cell parameters a, b and c are input. The value of the X-ray wavelength built into the program was set at either $\lambda_{CuK\alpha}$=1.5405Å or $\lambda_{CuK\alpha}$=1.7902Å, depending on the X-ray source available.

```
OPEN "XRAY.DAT" FOR OUTPUT AS #1
INPUT ; "Enter A  ", a#
INPUT ; "Enter B  ", b#
INPUT ; "Enter C  ", c#
PRINT #1, " A = "; a#
PRINT #1, " B = "; b#
PRINT #1, " C = "; c#
a2# = a# * a#
b2# = b# * b#
c2# = c# * c#
lambda# = 1.5405
b$ = " "

h% = 0
WHILE h% <= 3
        PRINT #1, b$
        PRINT #1, " H = "; h%
        PRINT #1, b$
        PRINT #1, "K=   L=0      1      2      3      4      5      6      7
  8      9     10"

        k% = 0
        WHILE k% <= 3
                PRINT #1, USING "#"; k%;

                l% = 0
                WHILE l% <= 10
                        sum# = h% * h% / a2# + k% * k% / b2# + l% * l% / c2#
                        IF sum# > 0! THEN
                                dhkl# = 1! / SQR(sum#)
                                sint# = lambda# / (2! * dhkl#)
                                IF sint# < 1! THEN
                                        cost# = SQR(1! - sint# * sint#)
                                        tant# = sint# / cost#
                                        y# = 2! * ATN(tant#) * 57.29578
                                ELSE
                                        y# = 180!
                                END IF
```

Continued...

```
                        ELSE
                                y# = 0!
                        END IF
                        PRINT #1, USING "####.##"; y#;
                        l% = l% + 1
                WEND
                PRINT #1, b$
                k% = k% + 1
        WEND
        h% = h% + 1
WEND
CLOSE #1
END
```

C.2 MINITAB Statistical Regression Analysis

C.2.1 Theoretical Background & Procedure

In chapter 3, it was shown that the resonance frequency obtained from the known second order quadrupole plus anisotropic Knight shift pattern[1] is of the form,

$$\upsilon\,(m \leftrightarrow m\text{-}1) = \upsilon_L + \frac{6\upsilon_{NQR}^{\,2}}{32\upsilon_L}(9\cos^2\theta - 1)(1 - \cos^2\theta) - \left[\tfrac{1}{3}(K_{//} + 2K_{\perp}) + \tfrac{1}{3}(K_{//} - K_{\perp})(3\cos^2\theta - 1)\ x\ \frac{\upsilon_L}{100}\right] \qquad (C.1)$$

where θ is the angle between the c-axis alignment and the $\mathbf{B_0}$ field, υ_{NQR} is the quadrupole frequency for the Cu(2) site (31.5MHz), υ_L is the spectrometer frequency (141MHz) and where $K_{//}$ and $K_{\perp}$ are essentially the Knight shifts long the c-axis and randomly in the a-b plane, respectively. Equation C.1 can be generalised to a linear equation of the form,

$$\upsilon = A + B\,f(\theta_1) + C\,f(\theta_2) \qquad (C.2)$$

where $f(\theta_1) = (9\cos^2\theta\text{-}1)(1\text{-}\cos^2\theta)$ and $f(\theta_2) = (3\cos^2\theta\text{-}1)$.

From the high resolution micrographs of the aligned Aberdeen sample and the initial NMR rotation pattern, it was estimated that the degree of misalignment of the

---

1 G. C. Carter, L. H. Bennett & D. J. Kahan, *Metallic Shifts in NMR*, part 1, Progress in Materials Science 20 (1977)

marked c-axis to the true c-axis was approximately +30°. Thus, by subtracting 30° from the experimental θ (where -70°≤θ≤+75°) values, one obtains an approximate set of values for the true orientation, θ' (where -100°≤θ'≤+45°).

Using a VAX MINITAB statistical analysis routine (see section C.2.2), the corrected data can then fitted to a linear curve of the form shown in equation C.2. The routine applies standard linear regression techniques to the two input variables, υ (or B-field†) and θ', in order to calculate the numerical values of the constants A, B and C. By incrementing the input values of θ' by a given amount (i.e. θ'±0.5°, θ'±1.0°), one obtains an increasingly better fit to the experimental data, thus allowing (i) the degree of misalignment to be predicted with better accuracy and (ii) precise numerical values of $K_{//}$ and $K_{\perp}$ to be deduced by the comparison of equation C.2 with equation C.1.

C.2.2 Program & Analysis

The following program was written and compiled using a MINITAB Statistical Analysis package (Release 7.1) running on a VAX main-frame computer. Due to the format of MINITAB, any in-program calculations are performed and displayed during the MINITAB procedure.

The specific linear regression analysis shown below provides the 'best fit' to the experimental data and was performed on a 14 point data set with θ' equal to θ'+1°. The data file consists of two columns labelled C1 (angle θ) and C2 (Cu(2) peak field position).

```
MTB > EXEC 'Rotation.mtb;1'                    :Program name
MTB > let C3 = C1*2*k1000/360                  :θ in radians
MTB > let C4 = cos(C3)                         :Cos θ
MTB > let C4 = C4*C4                           :Cos²θ
MTB > let C5 = 0.116925*(9*C4-1)*(1-C4)        :calculates f1(θ)
MTB > let C6 = C2 + C5                         :adds f1(θ) to C2
MTB > let C7 = (3*C4-1)                        :calculates f2(θ)
MTB > REGRESS C6 1 C7 C10 C8                   :regression analysis on
                                                f1(θ) & f2(θ)
```

continued...

† Note that, in this analysis, no attempt was made to take account of the demagnetisation correction factors.

RESULTS

```
The regression equation is
C6 = 12.4 - 0.0384 C7

Predictor       Coeff         Stdev      T-ratio          p
Constant      12.4161        0.0039      3206.80      0.000
C7          -0.038411      0.002993       -12.83      0.000

s = 0.01206            R-Sq = 93.2%        R-Sq (adj)=92.6%
```

Analysis of Variance

SOURCE	DF	SS	MS	F	P
Regression	1	0.023932	0.023932	164.67	0.000
Error	12	0.001744	0.000145	-	-
Total	13	0.025676	-	-	-

```
MTB > let C9 = C8 - C5          :Field from analysis
MTB > let C10 = C9 - C2         :ΔH = analysis-exptal fld
MTB > Print C1 C2 C9 C10
```

Row	C1	C2	C9	C10
1	-99	12.3585	12.3627	0.0042
2	-89	12.3470	12.3379	-0.0091
3	-74	12.4139	12.4116	-0.0023
4	-64	12.5149	12.5013	-0.0136
5	-49	12.5733	12.5963	0.0230
6	-39	12.5972	12.5903	-0.0069
7	-29	12.5291	12.5281	-0.0010
8	-19	12.4524	12.4388	-0.0136
9	-9	12.3637	12.3643	0.0006
10	1	12.3488	12.3396	-0.0092
11	11	12.3813	12.3761	-0.0052
12	21	12.4524	12.4568	0.0044
13	31	12.5210	12.5439	0.0229
14	46	12.5954	12.6012	0.0058

```
MTB > NOOUTFILE
MTB > END
```

C.3 MSL Pulse Programs

C.3.1 Single Pulse Program for ^{89}Y

```
------ FILE: QUADCYCL.PC


; QUADCYCL.PC
; ONEPULSE ACQUISITION WITH QUADRATURE PHASE CYCLE
; F1 CHANNEL
DE=DW*3/4
PROT NONE
START,   D1 [XT +X]
         D1 [F1 @PLS1 XT +X RGATE]   ; PULSE WITH PHASE LIST 1
         D3 [STA RGATE]              ; RING DOWN DELAY AND TRIGGER
         DO [++ PLS1]                ; ACQUISITION
GOTO START

BEGIN LISTS
PLS1,    +X +X -X -X +Y +Y -Y -Y
RLS,     +X +X -X -X +Y +Y -Y -Y
END LISTS

; RECEIVER MODE : RPN
; TRIGGER MODE  : NT
```

C.3.2 Spin Echo Pulse Program for ^{63}Cu

```
------ FILE: SAM1ECHO.PC

 ; HAHNECHO.PC

 ; TWO PULSE SPIN-ECHO TECHNIQUE FOR REMOVING
 ; BASELINE DISTORTONS DUE TO RINGING OF PROBE WITH
 ; 16 PHASE CYCLING.  REF: A.C. KUNWAR ET AL.,
 ; JMR 69, 124-127 (1986).
PROT NONE
START,
         2U   [XT +X]
         D1   [F1 @PLS1 XT +X RGATE] ; 45 OR 90 DEG. PULSE
         D6   [XT +X RGATE]          ; TAU DELAY
         D2   [F1 @PLS2 XT +X RGATE] ; 2 TIMES D1
         D3   [XT +X RGATE]          ; SECOND TAU DELAY
         D8   [STA RGATE]            ; ACQUIRE WITH NT
         DO
         ++PLS1
         ++PLS2
GOTO START

BEGIN LISTS
PLS1,    +X +X +X +X
PLS2,    +X +Y -X -Y
RLS,     -Y +Y -Y +Y
END LISTS
```

C.4 Knight Shift Evaluation via the Exact Hamiltonian[2]

In this appendix, we present a brief description of the theory used to deduce the ^{63}Cu Knight shifts for the Aberdeen sample (see chapter 5).

Throughout this work it has been stressed that the Cu ions in $YBa_2Cu_3O_7$ occupy two sites, the Cu(1) chain site, which is four-fold oxygen coordinated and the Cu(2) plane site, which is five-fold oxygen coordinated. Since both sites have lower than cubic symmetry, the large quadrupole moments of both ^{65}Cu and ^{63}Cu cause a complete splitting of the Zeeman lines, in fields of only a few tesla. This gives rise to an intense central ($1/2 \leftrightarrow -1/2$) transition and to two weaker satellite ($\pm 3/2 \leftrightarrow \pm 1/2$) transitions for each of the isotopes at each of the sites.

The total interaction energy of a nuclear spin **I** in a magnetic field B_0 in the presence of nuclear quadrupole interactions and Knight shift (including any chemical shift present in the metal) is given by[3,4]

$$\mathcal{H} = \mathcal{H}_Z + \mathcal{H}_Q + \mathcal{H}_K \tag{C.3}$$

where

the Zeeman term is $$\mathcal{H}_Z = -\gamma\hbar B_0 I_Z \tag{C.4}$$

the quadrupole term[5] is $$\mathcal{H}_Q = \frac{1}{6}\sum_{\alpha,\beta} Q_{\alpha\beta} V_{\alpha\beta} \tag{C.5}$$

& the Knight shift term is $$\mathcal{H}_K = -\gamma\hbar B_0 I_Z K \tag{C.6}$$

and where $Q_{\alpha\beta}$ is the electric quadrupole moment tensor, $V_{\alpha\beta}$ is the electric field gradient (EFG) tensor and K is the Knight shift tensor. The resonance frequencies υ_m belonging to the transitions $m \leftrightarrow m-1$ are determined by the energy differences between two adjacent energy levels, i.e. by the eigenvalues E_m of $\mathcal{H}$. Note that the equations which follow refer to the system of principal axes x, y, and z of the EFG, where $|V_{zz}| \geq |V_{yy}| \geq |V_{xx}|$. In addition, the principal axes of K are also assumed to coincide with those of the EFG (i.e they are also x, y and z).

We begin by considering the complete expression for the resonance frequency υ, using only first order expressions for the Knight shift. In cases where the symmetry of a

---

2 Many of the Cu Knight shift calculations are courtesy of M. Solanki-Moser, *private communication.*

3 M. H. Cohen & F. Reif in *Solid State Physics*, Vol. 5: eds. H. Ehrenrich, F. Seitz & D. Turnbull, Academic Press (1957)

4 J. F. Baugher, P. C. Taylor, T. Oja & P. J. Bray, *J. Chem Phys.* **50** 4914 (1969)

5 See ref. 3, page 329.

nucleus is lower than cubic, anisotropic effects appear in the Knight shift† and, in the absence of any quadrupole contributions, the total Knight shift can be written as[6]

$$K = K_{iso} + \frac{K_1}{2}(3\mathrm{Cos}^2\theta - 1) + \frac{K_2}{2}\sin^2\theta\cos 2\phi \qquad (C.7)$$

where the first term K_{iso} is the isotropic shift ($K_{iso}=\frac{1}{3}(K_X+K_Y+K_Z)$), the second term respresents the axial shift and the third term respresents the variation due to X-Y (or a-b) asymmetry. The second and third terms together constitute the total anisotropic Knight shift, K_{an}, where K_1 and K_2 are the anisotropy parameters defined by Carter, Bennett and Kahan[6] as

$$K_1 \equiv K_{an}(Z) \qquad (C.8a)$$

$$K_2 = K_Y - K_X \equiv \varepsilon K_1 \qquad (C.8b)$$

where ε is the Knight shift asymmetry parameter and

$$K_X = K_{iso} + K_{an}(X) = K_{iso} - \frac{K_1}{2}(1+\varepsilon) \qquad (C.8c)$$

$$K_Y = K_{iso} + K_{an}(Y) = K_{iso} - \frac{K_1}{2}(1-\varepsilon) \qquad (C.8d)$$

and

$$K_Z = K_{iso} + K_{an}(Z) = K_{iso} + K_1 \qquad (C.8e)$$

Thus, if we use only first order expressions for the Knight shift, the complete expression for resonance frequency υ is given by

$$\upsilon = \upsilon_{ZQ} + \frac{\gamma}{2\pi}B_0\left[K_{iso} + \frac{K_1}{2}(3\mathrm{Cos}^2\theta - 1) + \frac{K_2}{2}\sin^2\theta\cos 2\phi\right] \qquad (C.9)$$

where υ_{ZQ} is the resonance frequency from $\mathcal{H}_{ZQ}$ ($= \mathcal{H}_Z + \mathcal{H}_Q$) and θ and ϕ are the (polar) angle between z and B_0 and the (azimuthal) angle between x and B_{xy}, the projection of B_0 to the x-y plane, respectively. For clarity, the (θ, ϕ) axis system used is defined for the two Cu sites in $YBCO_7$ in figures C.1 and C.2, later on in this section.

Since, in our high field spin-echo experiments, the Knight shifts are generally *much* smaller than the quadrupole shifts, we can continue our analysis by first neglecting the Knight shifts and dealing with the major contribution to the Hamiltonian, $\mathcal{H}_{ZQ}$. The

---

† Note that this also applies to some extent for cubic sites if the spin orbit interaction to first order is included.

6 See ref. 1, chapter 6.

differences between the experimentally measured and calculated peak positions will then provide an estimate for the Knight shift.

In order to evaluate the υ_{ZQ} term of equation (C.9), we turn to the work of Brown & Parker[7]. Using their procedures, we find that the characteristic polynomial of $\mathcal{H}_{ZQ}$ (i.e. neglecting the Knight shift) for an I=3/2 nucleus is given by

$$p(E) = E^4 - \frac{E^2\upsilon_L^2}{2}\left[5 + \frac{\upsilon_Q^2}{\upsilon_L^2}\left(\frac{\eta^2}{3} + 1\right)\right] + E\upsilon_L^2\upsilon_Q^2\left[1 - 3\mu^2 - \eta(1-\mu^2)\cos 2\phi\right] + \frac{9}{16}\upsilon_L^4$$

$$+ \frac{\upsilon_L^2\upsilon_Q^2}{8}\left[1 - 6\mu^2 + 4\eta\cos 2\phi\,(1-\mu^2) + \eta^2(2\mu^2-1)\right] + \frac{\upsilon_L^4}{144}(\eta+3)^2 \qquad \text{(C.10)}$$

where the various parameters are defined, in the fashion of chapter 3, by

asymmetry parameter $$\eta = \frac{V_{xx} - V_{yy}}{V_{zz}} \qquad \text{(C.11)}$$

pure quadrupole frequency $$\upsilon_Q = \frac{3eV_{zz}Q}{2I(2I-1)h} \qquad \text{(C.12)}$$

Larmor frequency $$\upsilon_L\,(\equiv \upsilon_0) = \frac{\gamma B_0}{2\pi} \qquad \text{(C.13)}$$

$$\mu = \cos\theta \qquad \text{(C.14)}$$

and where Q is the nuclear electric quadrupole moment. For the eigenvalues E_m of $\mathcal{H}_{ZQ}$, $p(E_i) = 0$. In general, no explicit expression exists for the eigenvalues of $\mathcal{H}_{ZQ}$ and so the resonance frequencies υ_{ZQ} must to be calculated either via perturbation expressions or numerically using the full exact Hamiltonian $\mathcal{H}_{ZQ}$, where

$$\mathcal{H}_{ZQ} = \begin{bmatrix} -\frac{3}{2}\upsilon_L\cos\theta + \frac{\upsilon_Q}{2} & -\frac{\sqrt{3}}{2}\upsilon_L\sin\theta\, e^{-i\phi} & \frac{\sqrt{3}}{6}\eta\,\upsilon_Q & 0 \\ -\frac{\sqrt{3}}{2}\sin\theta\, e^{+i\phi}\,\upsilon_L & -\frac{\upsilon_L}{2}\cos\theta - \frac{\upsilon_Q}{2} & -\upsilon_L\sin\theta\, e^{-i\phi} & \frac{\sqrt{3}}{6}\eta\,\upsilon_Q \\ \frac{\sqrt{3}}{6}\eta\,\upsilon_Q & -\upsilon_L\sin\theta\, e^{+i\phi} & \frac{1}{2}\upsilon_L\cos\theta - \frac{\upsilon_Q}{2} & -\frac{\sqrt{3}}{2}\upsilon_L\sin\theta e^{-i\phi} \\ 0 & \frac{\sqrt{3}}{6}\eta\,\upsilon_Q & -\frac{\sqrt{3}}{2}\upsilon_L\sin\theta e^{+i\phi} & \frac{3}{2}\upsilon_L\cos\theta + \frac{\upsilon_Q}{2} \end{bmatrix} \qquad \text{(C.15)}$$

---

7 L. C. Brown & P. M. Parker, *Phys. Rev.* **100** 1764 (1955)

Here, we determine the solution (υ_{exact}) numerically using equation (C.15). For experiments which are field swept at a constant frequency υ_L, an iterative procedure can be used to calculate the field values B_L (low field satellite (-1/2↔-3/2)) B_C (central line (1/2↔-1/2)) and B_H (high field satellite (3/2↔1/2)) at which the resonance with $\upsilon_{ZQ}=\upsilon_L$ occurs. In this way the exact resonance fields can be obtained numerically with any desired precision, provided the angles of θ and ϕ are known.

For a single crystal, only one pair of (θ, ϕ) are present and so the frequency υ_{exact} can be calculated fairly easily from the exact Hamiltonian. However, in a random powder or (partially) oriented powder sample, crystallites with a range of different orientations (θ_i, ϕ_i) are present and the intentsity maxima now depend on the angular distribution. In this case, the exact Hamiltonian $\mathcal{H}_{ZQ}$ cannot be diagonalised easily and so perturbation expressions are used to determine the pairs of (θ_m, ϕ_n), which are solutions (or 'saddle points') for the maximum intensities in the spectrum. The total second order perturbation expression $\upsilon(\theta,\phi)$ (including Knight shift) is given by Carter, Bennett and Kahan[6] as

$$\upsilon^{m}_{(\theta,\phi)} = \gamma' B_0(1 + K_{iso}) + \frac{\upsilon_Q}{2}(m - \tfrac{1}{2})\left[3\mu^2 - 1 + \eta(1 - \mu^2)\cos 2\phi\right] + \frac{K_1}{2}(3\mu^2 - 1) +$$

$$\frac{K_2}{2}(1 - \mu^2)\cos 2\phi + \frac{\upsilon_Q^2}{32\gamma' B_0}(1 - \mu^2)\left[\{102m(m-1) - 18I(I+1) + 39\}\mu^2\left(1 - \tfrac{2}{3}\eta\cos 2\phi\right)\right.$$

$$\left. - \{6m(m-1) - 2I(I+1) + 3\}\{1 + \tfrac{2}{3}\eta\cos 2\phi\}\right] + \frac{\eta^2\upsilon_Q^2}{72\gamma' B_0}\left[24m(m-1) - 4I(I+1) + 9\right.$$

$$\left. - \{30m(m-1) - 6I(I+1) + 12\}\mu^2 - \{\tfrac{51}{2}m(m-1) - \tfrac{9}{2}I(I+1) + \tfrac{39}{4}\}\cos^2 2\phi\,(\mu^2 - 1)^2\right] \qquad (C.16)$$

where the abbreviation $\gamma'=\gamma/2\pi$ has been incorporated, for simplification. Since we are presently considering the Zeeman and quadrupole contributions, the Knight shift terms in equation (C.16) are neglected in the determination of the solutions (θ_m, ϕ_n). With the saddle points (θ_m, ϕ_n) known, the resonance fields are calculated in the same manner as above, using the full Hamiltonian (C.15).

As an example, we will now introduce the conditions required in order to determine the saddle or critical points of the two Cu sites in the specfic case of a partially aligned powder sample of $YBCO_7$ with c⊥B:

(a) Cu(1) site

We first need to examine the coordinates which specify the direction of the magnetic field with respect to the EFG principal axis system. A combination of NQR and

crystal structure studies indicate that we can generally assign the x, y, z axes of the EFG to their respective a, b, c crystallographic axes as shown in figure C.1(a) (i.e x≡c, y≡a and z≡b). Note that figure C.1(a) also defines the polar and azimuuthal angles, θ and ϕ, introduced earlier. In the specific case considered here, c⊥B for Cu(1) implies that x⊥B and therefore that ϕ=90° and that θ varies statistically. This situation is shown in figure C.1(b). With the B-field oriented perpendicular to the crystallographic c axis, the intensity maxima in the NMR spectrum occurs at θ_0, given by

$$\left.\frac{\partial \upsilon}{\partial \theta}\right|_{\phi=90°,\,\theta_0} = 0 \qquad \text{(C.17)}$$

Since no simple, exact function $\upsilon(\theta,\phi)$ exists, θ_0 is determined from the perturbation expression (up to second order for the central lines (m=±1/2) and first order for the satellites (m=3/2,-1/2)) given by equation (C.16). The solutions to equation (C.17) with the use of equation (C.16) are shown in table C.1, along with the full perturbation terms.

	Critical Point	υ_{pert}
Central line	$\cos 2\phi=-1;\ \cos^2\theta=0$	$\gamma' B_0(1+K_{iso}-\frac{K_1}{2}-\frac{K_2}{2})+\frac{\upsilon_Q^2}{48\upsilon_L}(3-\eta)^2$
"	$\cos 2\phi=-1;\ \cos^2\theta=1$	$\gamma' B_0(1+K_{iso}+K_1)+\frac{\upsilon_Q^2}{12\upsilon_L}\eta^2$
"	$\cos 2\phi=-1;$ $\cos^2\theta=\frac{5+\eta}{3(3+\eta)}$	$\gamma' B_0(1+K_{iso}+\frac{K_1}{3+\eta}-\frac{K_2(2+\eta)}{(3+\eta)})$ $-\frac{\upsilon_Q^2}{3\upsilon_L}(1+\eta)$
Satellites m=3/2 (High field)	$\cos 2\phi=-1;\ \cos^2\theta=0$	$\gamma' B_0(1+K_{iso}-\frac{K_1}{2}-\frac{K_2}{2})-\frac{\upsilon_Q}{2}(1+\eta)$
	$\cos 2\phi=-1;\ \cos^2\theta=1$	$\gamma' B_0(1+K_{iso}+K_1)+\upsilon_Q$
m=−1/2	$\cos 2\phi=-1;\ \cos^2\theta=0$	$\gamma' B_0(1+K_{iso}-\frac{K_1}{2}-\frac{K_2}{2})+\frac{\upsilon_Q}{2}(1+\eta)$
(low field)	$\cos 2\phi=-1;\ \cos^2\theta=1$	$\gamma' B_0(1+K_{iso}+K_1)-\upsilon_Q$

Table C.1

Critical points & perturbation expressions for the resonance frequencies of Cu(1), c⊥B. The perturbation expressions for the frequencies are given for the satellites (first order) and the central lines (second order).

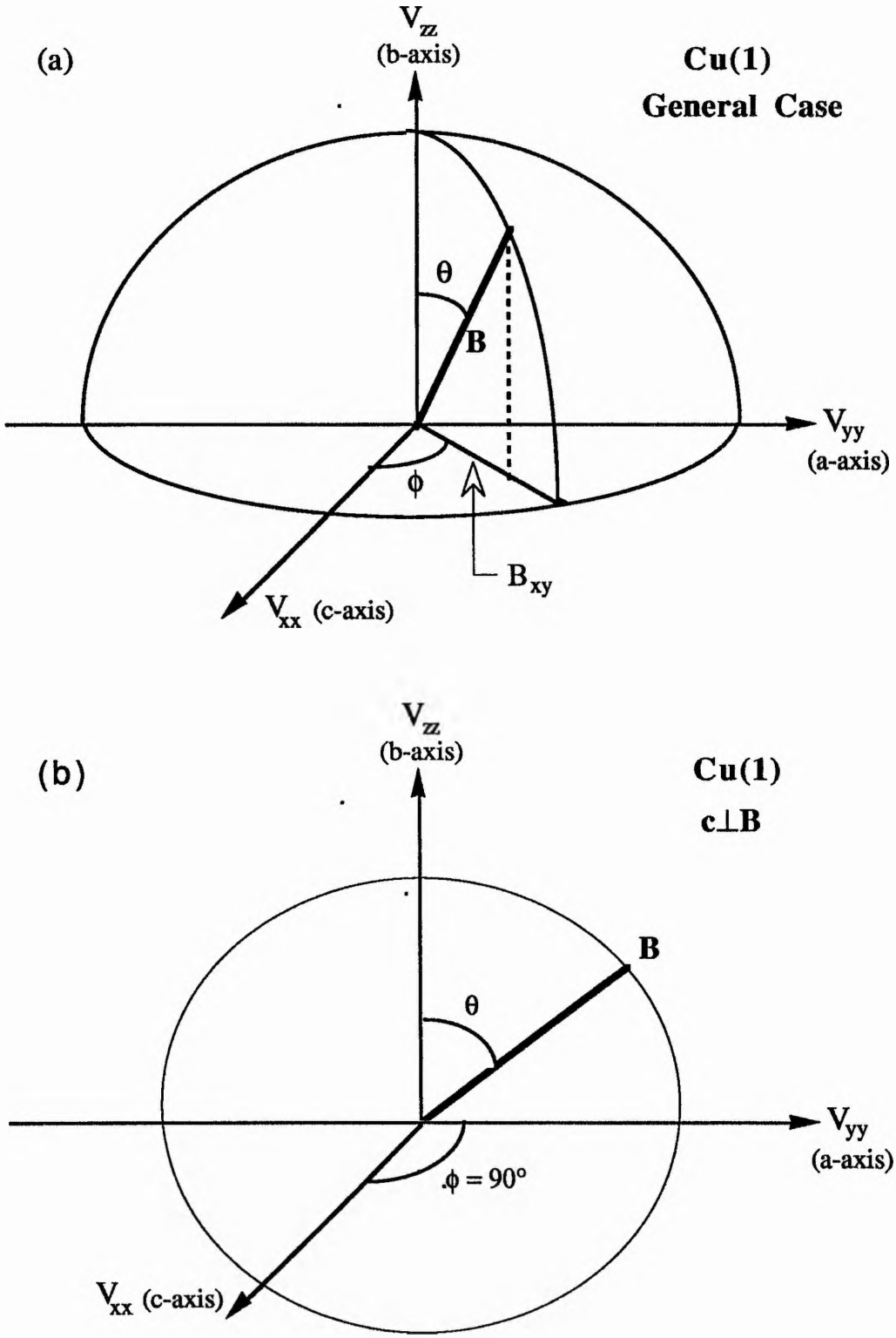

Figure C.1

Coordinates used to specify the direction of the magnetic B-field with respect to the Cu(1) EFG (x, y, z) principal axis system and the crystallographic (a, b, c) axes, for (a) the general case and (b) the specific case where c⊥B (ϕ=90° & θ varies statistically).

Note that for Cu(1), c//B corresponds to a single crystal experiment with $\cos^2\theta=0$ and $\cos 2\phi=+1$.

(b) Cu(2) site

For the Cu(2) site, we can assign the x, y, z axes of the EFG to their respective a, b, c crystallographic axes as shown in figure C.2(a) (i.e x≡a, y≡b and z≡c). In the case where c⊥B, $\theta=90°$ and ϕ is random (see figure C.2(b)) and the intensity maxima are given by the angles ϕ_0 with

$$\left.\frac{\partial \upsilon}{\partial \phi}\right|_{\theta=90°,\,\phi_0} = 0 \qquad \text{(C.18)}$$

Using equation (C.16), equation (C.18) leads to the angles shown in table C.2. Again the perturbation expressions for the frequencies are given for the satellites (first order) and the central lines (second order).

	Critical Point	υ_{pert}
Central line	$\cos^2\theta=0$; $\cos 2\phi=\pm 1$	$\gamma' B_0(1+K_{iso}-\frac{K_1}{2}+\frac{K_2}{2})+\frac{\upsilon_Q^2}{48\upsilon_L}(3\pm\eta)^2$
"	$\cos^2\theta=0$; $\cos 2\phi=-\frac{1}{3\eta}$	$1+\frac{4K_2\gamma' B_0\upsilon_L}{\eta\upsilon_Q^2}-\frac{K_2\upsilon_L}{3\eta}(\frac{K_2\upsilon_L^2}{\eta\upsilon_Q^2}+\frac{1}{2})$
Satellites m=3/2 (High field)	$\cos^2\theta=0$; $\cos 2\phi=\pm 1$	$\gamma' B_0(1+K_{iso}-\frac{K_1}{2}\pm\frac{K_2}{2})-\frac{\upsilon_Q}{2}(1-\eta)$
	$\cos 2\phi=-1$; $\cos^2\theta=1$	$\gamma' B_0(1+K_{iso}+\frac{K_1}{2}-\frac{K_2}{2})+\upsilon_Q$
m=-1/2	$\cos^2\theta=0$;$\cos 2\phi=\pm 1$	$\gamma' B_0(1+K_{iso}-\frac{K_1}{2}\pm\frac{K_2}{2})+\frac{\upsilon_Q}{2}(1-\eta)$
(low field)		

Table C.2

Critical points & perturbation expressions for the resonance frequencies of Cu(2), c⊥B. The first & second order perturbation expressions are included for the satellites & central lines, respectively.

Note that for Cu(2), c//B corresponds to a single crystal experiment with $\cos^2\theta=+1$.

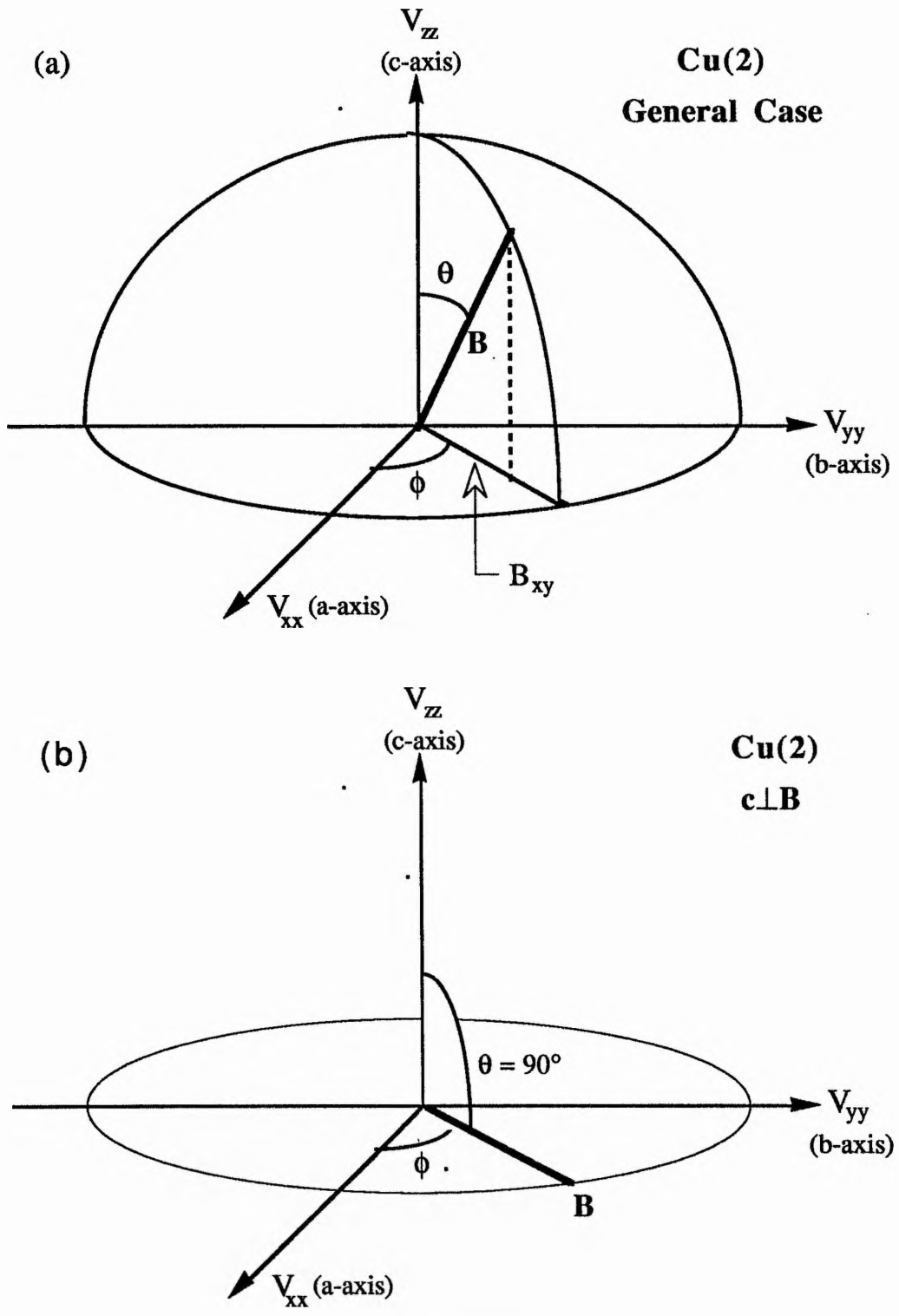

Figure C.2

Coordinates used to specify the direction of the magnetic B-field with respect to the Cu(2) EFG (x, y, z) principal axis system and the crystallographic (a, b, c) axes, for (a) the general case and (b) the specific case where c⊥B (θ=90° & ϕ is random).

The angles listed in tables C.1 and C.2 are used in the first step of the analysis. They can be introduced into equations (C.10) and (C.15) in order to provide the basis for the Knight shift evaluation. Once the resonance frequency υ_{ZQ} has been deduced, the calculated frequency can be compared to that measured experimentally, and values for the Knight shift tensors can be found with the help of equations (C.8) and (C.9). Diamagnetic field effects must also be accounted for if the experiment has been performed in the superconducting state.

In this study, we chose to evaluate the Knight shift tensors for the Aberdeen sample (see table 5.3) as described above, by first analysing the Zeeman and quadrupole contributions. However, the whole calculation can be approached from a slightly different perspective. Provided the solutions (θ_m,ϕ_n) are known, equation (C.10)/(C.15) can be substituted into equation (C.9), along with numerical values for η, υ_Q, γB_0 and an initial guess for K_i/K_{iso}. With the use of a computer program, the exact Hamiltonian can be diagonalised from within this equation and in one step, a theoretical prediction for the resonance frequency υ - corresponding to the particular K_i/K_{iso} input values - can be found. This calculated frequency is then compared to the measured resonance frequency, again accounting for demagnetisation corrections. The procedure is repeated, adjusting the K_i/K_{iso} values at each interation until the calculated and measured frequencies agree. Once the exact K_i/K_{iso} values are obtained, the Knight shift tensor can be found using equations (C.8), as before.

Such a computer program has been used to acquire the relevant ^{63}Cu satellite positions, which were not obtained experimentally. For reference, and to get an idea of the high (B_H) and low (B_L) field satellite positions in $YBa_2Cu_3O_7$ at υ_L=141MHz, table C.3 (overpage) gives the results from a calculation in which values of K_1=−0.0021, K_2= −0.0082 and K_{iso}=0.0066 were input, along with the following parameters for ^{65}Cu ($\gamma/2\pi$=12.089MHz/T) and ^{63}Cu ($\gamma/2\pi$=11.285MHz/T): $^{65}Cu(1) \rightarrow \eta=1$, υ_Q=17.67MHz: $^{63}Cu(1) \rightarrow \eta=1$, υ_Q=19.14MHz: $^{65}Cu(2) \rightarrow \eta=0$, υ_Q=29.5MHz: $^{63}Cu(2) \rightarrow \eta=1$, υ_Q=31.5MHz.

Finally, it should be noted that if the exact Hamiltonian in equation (C.15) is replaced by a perturbation expression, significant errors start to appear. The errors produced by the use of perturbation theory increase with increasing η. They are significantly larger for satellites than for central lines due to the considerable first order shifts that the former experience. For the central line, differences of up to 0.35% can occur, while 4.5% differences for the satellites are possible. θ=0, 90° are connected with smaller errors: 0.15% (η=1) and 0.01% (η=0) are upper limits for the central line, while 2.5% (η=1) and 0.2% (η=0) are the limits for the satellites.

	^{63}Cu (T)			^{65}Cu (T)		
Site	B_L	B_C	B_H	B_L	B_C	B_H
Cu(2) c//B	11.107	12.355	13.885	10.450	11.567	12.880
Cu(1) c//B	11.607	12.407	13.294	10.895	11.588	12.350
Cu(1) c⊥B, a//B	11.513	12.306	13.186	10.807	11.494	12.249
Cu(2) c⊥B	11.080	12.346	13.851	10.424	11.538	12.848
Cu(1) c⊥B, b//B	10.750	12.438	14.127	10.156	11.611	13.066
Cu(1) c⊥B, θ=45°	11.887	12.469	12.728	11.138	11.629	11.863

Table C.3

The central (B_C) lines at υ_L=141MHz for the $^{63/65}$Cu(1/2) sites in $YBa_2Cu_3O_7$, calculated using K_{iso}=0.0066, K_1=−0.0021 & K_2=−0.0082. The low (B_L) & high (B_H) field satellite lines have also been included for reference.

C.5 Dipolar Field Computation

C.5.1 Outline of the QuickBasic Programs

In this brief section, the basic outline and structure of the QuickBasic programs (see section C.5.2), which calculate the dipolar field effects of Co impurities in the YBCO lattice (see chapter 7), are provided for reference. The main program (y3Co4l.bas) contains a number of subroutines which perform all the various component calculations that contribute to the dipolar field model, such as the dipolar fields from a single Co ion and the Poisson distribution statistics. The central section of this program then combines all of these tertiary calculations to produce the resultant dipolar field arrays. A separate program (ybin.bas) performs the binning operation and plots the final spectrum. For clarity, we will outline the role of each subroutine in the main program first and then we will describe the function of the central stem of the main program. Finally, the mechanism for the binning process will be presented. Again, the programs for the calculation of the Y dipolar fields will be used here as an example.

Subroutine DIPY

This subroutine allows for the input of the fundamental parameters, such as the Co concentration, the lattice parameters, the effective magnetic moment and the orientation of the crystal with respect to the magnetic field. Using equation (7.7) and then equation (7.3), the subroutine proceeds to calculate the dipolar fields, from a single Co moment placed at the lattice point (0, 0), at all Y sites in the first quadrant of the first (z=0) layer. It does so by successively interating x and y from 0 to 49. DIPY then stores the dipolar fields at the first (49 x 49) Y sites in the initial layer (from the single fixed Co) in an array labelled a#(x, y).

Subroutine FULLAY

Clearly, to obtain a (99 x 99) Y site grid (see section 7.2.1) which is symmetrical about the point (50, 50) in both the ±x and ±y directions, we have to repeat the (49 x 49) Y matrix calculated for the first quadrant in a further three quadrants. FULLAY calculates the full (99 x 99) grid and puts the elements in a new array b#(x,y), where x and y are now both redefined to span from 0 to 99. FULLAY builds up the new array by cycling through each quadrant (q=1 to 4) and translating the (49 x 49) elemental grid found by DIPY, using the following equations,

$$
\begin{aligned}
&q=1 && b\#(x+50,\ y+50) = a\#(x,y) \\
&q=2 && b\#(x+50,\ y+49) = a\#(x,y) \\
&q=3 && b\#(x+49,\ y+49) = a\#(x,y) \\
&q=4 && b\#(x+49,\ y+50) = a\#(x,y)
\end{aligned}
\qquad \text{(C.19)}
$$

Hence the resultant array b#(x,y) now represents a (99 x 99) element grid of dipolar fields at Y from one Co placed at the grid point (50, 50).

The functions of the DIPY and FULLAY subroutines are represented pictorially by figure C.3.

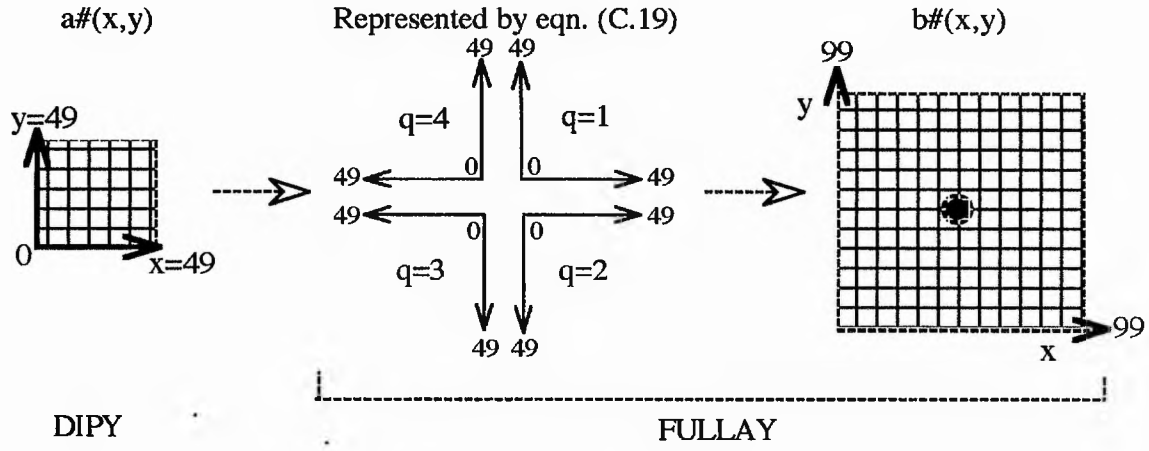

Figure C.3

A pictoral representation of the functions of the subroutines DIPY & FULLAY. DIPY (left) calculates the dipolar fields from a Co moment placed at (0,0) for a grid of (49 x 49) Y atoms in the first quadrant (q=1). FULLAY cycles through quadrants q=1 to 4 (centre) and translates the DIPY a#(x,y) array into the b#(x,y) using equations (C.19). The b#(x,y) array then renumbers the elements so that they run from x=0 to 99 and y=0 to 99 with the Co moment at the point (50, 50) (right).

Subroutines FIELDPT & ONECO

These two subroutines simply output the full dipolar field array at the Y sites in the YBCO lattice from one Co (b#(x,y)) in the form of a numerical table (FIELDPT) and a graphical plot (ONECO), so that the field values can be checked and the cut-off points for the extended calculation deduced.

Subroutine PD

Using equations (7.8) and (7.9), subroutine PD computes the Poisson distribution for Co ions in the YBCO lattice. That is, for a given Co concentration, the program calculates the probabilities of finding r (=0,1,2,3....r_{max}) Co atoms in n Cu(1) atoms, provided that a suitable value of the sample size n is input. The probabilities are simply stored as Pr(0), Pr(1), etc. for use in the central stem of the main program, at some later stage.

Central Block of the Main Program

The main body of the dipolar field program pulls together all of the subroutine calculations and computes the resultant dipolar field arrays which result from the random presence of three Co moments in an extended YBCO lattice. To perform this task, we somehow have to translate the physical model of three dipolar field grids sliding over each other into some mathematical form which the computer can recognise.

To re-iterate: the coordinate labels for the Co moments and the Y lattice points are as follows,

1st Co moment is fixed at the point (50,50)

2nd Co moment movements are labelled by (m,n)

3rd Co moment movements are labelled by (s,t)

Any given Y lattice point is labelled by (k,l).

At this point, we must introduce two new sets of coordinates: (i,j) which index the dipolar fields from the second Co moment to be added the fields from the fixed moment, and (e,f), which similarly index the dipolar fields from the third Co moment. A simple analysis shows that the equations linking the coordinates of the Y lattice point to the coordinates of the roving 2nd or 3rd Co moment and finally to the corresponding the dipolar field index, are

For the 2nd Co

$$j = l + 50 - n$$
$$i = k + 50 - m \qquad \text{(C.20a)}$$

For the 3nd Co

$$e = l + 50 - s$$
$$f = k + 50 - t \qquad \text{(C.20b)}$$

We have already specified in chapter 7 that the 2nd and 3rd Co moments are allowed to move on an (8a x 8a) unit surface, with the restriction that they can never be at the point (50,50) nor at the same point at the same time. With this in mind, we can now simulate the movements of the 2nd and 3rd Co (making sure that we get all possible configurations of the 3 Co moments on the defined surface) and calculate the resultant dipolar fields at all the Y lattice points by using 6 nested WHILE (-WEND) loops. That is, while m, n, s, t and l are fixed, we cycle through all the possible values of k and calculate (i,j) and (e,f) for each set of parameters. Then, we add together the dipolar fields from the 1, 2 and 3 Co, in the ratios specified by the Poisson probabilities. The resultant fields are stored in the relevant qed# array. The l parameter is then incremented by one and the process of cycling through all values of k and calculating the resultant dipolar fields begins again. We continue incrementing l by one and cycling through all the required k values until we reach l_{max}. Then we increment t by one and cycle through all the l values, then all the k values and so on. This process continues through all the incrementations of t, then s, then n and finally m, until we have calculated the resultant dipolar fields at all the Y sites from all possible configurations of the 3 Co ions.

The final part of the main program sets the range for the model, then scans through all the resultant field arrays checking that each point is within this range. All resultant dipolar fields which lie within this range are then placed in a new array labelled bin#(ibin), where ibin specifies the position of the each point in the array.

Finally the ybin.bas program creates 10,000 bins intervals between the specified ±range limits and bins the resultant dipolar fields from the bin#(ibin) array into the relevent field interval. This program also provides the final graphical output of 'number of Y experiencing a given dipolar field' vs 'dipolar field in T'.

C.5.2 The QuickBasic Programs

(a) The Main Dipolar Field Program (y3co4l.bas)

```
REM $INCLUDE: 'C:\LW\INCLUDE\LWSYSTEM.INC'
REM $INCLUDE: 'C:\LW\INCLUDE\GRAPHICS.INC'
REM $INCLUDE: 'C:\LW\INCLUDE\ANALYSIS.INC'
DECLARE SUB dipy()
DECLARE SUB fullay()
DECLARE SUB fieldpt()
DECLARE SUB pd()
DECLARE SUB oneco()
```

```
CALL GETMEM(64000)

DIM SHARED na%, nb%
na%=50
nb%=2*na%

REM Calculates 4 planes of Y dipolar fields from 3 Co & bins
them, creating a data file

DIM SHARED a#(na%,na%)
DIM SHARED b#(nb%,nb%)
DIM SHARED g#
DIM SHARED z%
DIM SHARED pr0#,pr1#,pr2#,pr3#,pr4#,pr5#
DIM SHARED angle AS STRING
DIM SHARED cr AS STRING
DIM sum#(nb%,nb%), ans#(nb%,nb%), bin&(10000)

angle$ = ""

z% = 0
WHILE z% <= 3

    CALL DIPY
    CALL FULLAY
    CALL FIELDPT
    CALL PD
    REM CALL ONECO

range#= 0.001
n% = 46
WHILE n% <= 54
    m% = 46
    WHILE m% <= 54
            t% = 46
            WHILE t% <= 54
                    s% = 46
                    WHILE s% <= 54
                        CALL SetPlotMode (0)
```

```
                    zcou$ = "z =  " + STR$(z%)
                    mcou$ = "m =  " + STR$(m%)
                    ncou$ = "n =  " + STR$(n%)
                    scou$ = "s =  " + STR$(s%)
                    tcou$ = "t =  " + STR$(t%)
                    count$ = "     " + zcou$ + "     "
+ mcou$ + "     " + ncou$ + "     " + scou$ + "     " +
tcou$
                    CALL GrfMsg (count$,15)
                    l% = 39
                WHILE l% < = 60
                  j% = l% + na% - n%
                  IF j% < 0 OR j% > nb%-1 THEN GOTO label250
                  f% = l% + na% - t%
                  IF f% < 0 OR f% > nb%-1 THEN GOTO label250
                  k% = 39
             WHILE k% <= 60
                 i% = k% + na% - m%
                 IF i% < 0 OR i% > nb%-1 THEN GOTO label251
                 e% = k% + na% - s%
                 IF e% < 0 OR e% > nb%-1 THEN GOTO label251
                 IF n% = na% AND m% = na% THEN GOTO label103
                 IF t% = na% AND s% = na% THEN GOTO label102
                 IF t% = n%  AND s% = m%  THEN GOTO label102
                 sum#(k%,l%) = b#(k%,l%) + b#(i%,j%)
                 ans#(k%,l%) = b#(k%,l%)+b#(i%,j%)+ b#(e%,f%)
                 qed# = pr0#*0.000479474 + pr1#*b#(k%,l%)
                          + pr2#*sum#(k%,l%) + pr3#*ans#(k%,l%)
                     IF ABS(qed#) <= range# THEN
                     ibin% = CINT((qed#+range#)*5000/range#)
                     bin&(ibin%) = bin&(ibin%) + 1
                     END IF
                 label251:
                 k% = k%+1
             WEND
             label250:
             l% = l%+1
                  WEND
```

```
                label102:
                s% = s%+1
                WEND
                t% = t%+1
            WEND
            label103:
            m% = m%+1
    WEND
    n% = n%+1
WEND

namef2$ = "YZ" + RTRIM$(LTRIM$(STR$(z%))) + angle$ + ".DAT"
OPEN namef2$ FOR OUTPUT AS #2

ibin%=0
WHILE ibin% <=10000

    IF bin&(ibin%) > 0 THEN PRINT #2, ibin%, bin&(ibin%)
    ibin%=ibin%+1
WEND
CLOSE #2
z% = z%+1
WEND

label100:
SLEEP
SLEEP
SLEEP
CALL SetDisplayMode (0)
END

SUB dipy

k#=11.654
g#=1.5
p#=4.15
a#=3.864
b#=3.864
c#=11.7
t90% = 90
```

```
IF t90% = 0 THEN angle$ = "00"
IF t90% = 90 THEN angle$ = "90"
xmax% = na%
cr$=CHR$(13)+CHR$(10)

ymax%= na%
x%=0
     WHILE x% <= xmax%
               y%=0
               WHILE y% <= ymax%
                    r2#=a#*a#*(x%+0.5)*(x%+0.5)
                              +b#*b#*(y%+0.5)*(y%+0.5)
                              +c#*c#*(z%+0.5)*(z%+0.5)
                    r#=SQR(r2#)
                    cost#=c#*(z%+0.5)/r#
                    sint#=SQR(1.0-cost#*cost#)
                    theta#=ATN(sint#/cost#)+t90%*3.1415927/180.0
                    df#=k#*p#*(13*COS(theta#)*COS(theta#))/(r2#*r#)
                    a#(x%,y%) = df#
                    y%=y%+1
               WEND
               x%=x%+1
     WEND

END  SUB

SUB  FULLAY

q% = 1
WHILE q% <= 4
     y% = 0
     WHILE y% <= na% - 1
            x% = 0
            WHILE x% <= na%-1
                 IF q% = 1 THEN b#(x%+na%, y%+na%) = a#(x%,y%)
                 IF q% = 2 THEN b#(x%+na%, na%-1-y%) = a#(x%,y%)
                 IF q% = 3 THEN b#(na%-1-x%, na%-1-y%) = a#(x%,y%)
                 IF q% = 4 THEN b#(na%-1-x%, y%+na%) = a#(x%,y%)
                 x% = x%+1
```

```
            WEND
            y% = y%+1
    WEND
    q% = q%+1
WEND
END SUB
```

SUB FIELDPT

```
namef1$= "AYZ" + RTRIM$(LTRIM$(STR$(z%))) + angle$ + ".DAT"
OPEN namef1$ FOR OUTPUT AS #1

x% = nb%-1
PRINT #1, "These are the results from Subroutine Fullay,
calculating the full dipolar field array"
PRINT #1, "This is the b#(x,y) array for the dipolar fields at
YTTRIUM sites"
PRINT #1, "The orientation is  ";angle$;"  and the %Co is  ";g#
PRINT #1,  " y =    00              01       02       03       04
05      06      07      08"
WHILE x% >= 0
    y% = 0
    PRINT #1,  "x=";
    PRINT #1,  USING "##";x%;

            WHILE y% <= 8
                    PRINT #1,  USING "##.#####"; b#(x%,y%) ;
                    y% = y%+1
            WEND

     PRINT #1,  " "
     x% = x%-1
WEND
PRINT #1, cr$,cr$

x% = nb%-1
PRINT #1,  " y =    09              10       11       12       13
14      15      16      17"
```

```
WHILE x% >= 0
     y% = 9
     PRINT #1,  "x=";
     PRINT #1,  USING "##";x%;

              WHILE y% <= 17
                       PRINT #1,  USING "##.#####"; b#(x%,y%) ;
                       y% = y%+1 WEND

      PRINT #1,  " "
      x% = x%-1
WEND
END SUB
```

SUB pd

```
n#=64
rmax%=10
u#=g#*n#*3/100

PRINT #1, cr$,cr$
PRINT #1, "These are the results from subroutine PD, calculating
the Poisson Distribution"
PRINT #1, "This program calculates the probability of finding r
Co atoms in n Cu atoms"
PRINT #1, "  The Co Percentage of this sample  = ";g#
PRINT #1, "The sample size (no of Cu atoms), n = ";n#
PRINT #1, "    The max no of Co required, r = ";rmax%
PRINT #1, "   The mean for this calculation = ";u#

PRINT #1, cr$,cr$

     PRINT #1, "                          Pr"
     r%=0
     fact&=1
     pr0#=u#^r%*2.718281828^(-u#)/fact&
     PRINT #1, "r=     ";r%;"          ";
     PRINT #1, USING "##.#######";pr0#
```

```
IF rmax% > 0 THEN
     r%=1
     WHILE r% <= rmax%
            fact& = fact&*r%
            pr# = u#^r%*2.718281828^(-u#)/fact&
            PRINT #1, "r=    ";r%;"          ";
            PRINT #1, USING "##.#######";pr#
            IF r% = 1 THEN pr1# = pr#
            IF r% = 2 THEN pr2# = pr#
            IF r% = 3 THEN pr3# = pr#
            IF r% = 4 THEN pr4# = pr#
            IF r% = 5 THEN pr5# = pr#
            r%=r%+1
     WEND
END IF
CLOSE #1
END SUB
```

SUB ONECO

```
DIM res#(nb%)
title1$ = "Dipolar field at YTTRIUM sites in the YBCO lattice
from ONE Co atom"

              CALL GrfReset (12)
              CALL SetAxGridVis (-1, 0)
              port% = CreatePort (0, 5, 100, 85)
              CALL SetPlotMode (0)
              CALL GrfPrint (6, 95, title1$)
              CALL SetAxAuto (0,2)
              CALL SetAxRange (0, 15, 25, 10)
              CALL SetAxName (0, "Y position, x-coordinate")
              CALL SetAxAuto (1,2)
              CALL SetAxRange (1, -0.03, 0.03, 10)
              CALL SetAxName (1, "Dipolar field in T")
              CALL SetCurv2D (1)
              CALL SetTitle ("Yttrium dipolar field 1")
              CALL SetFrmColor (15)
              CALL SetGrdColor (15)
```

```
            CALL SetLblColor (15)

y%=0
WHILE y% <= nb%-1
   x% = 0
   d% = 0
   WHILE x% <= nb%-1
         res#(d%) = b#(x%,y%)
         x% = x%+1
         d% = d%+1
   WEND
   d%=d%-1
   CALL SetPointStyle (2)
   CALL GrfYCurv2D (res#(), d%)
   xCol$ = "m =  " + STR$(na%)
   yCol$ = "n =  " + STR$(na%)
   y$ = "y =  " + STR$(y%)
   count1$ = "                    " + angle$ + "         " + xCol$ + "
   "       " + y$
   CALL GrfMsg (count1$,15)
   y% = y%+1
WEND
reply$=INPUT$(1)
IF LCASE$(reply$)="p" THEN CALL PRINTSCREEN
SLEEP
INPUT e$
END SUB
```

(b) The Binning & Graphing Program (ybin.bas)

```
REM $INCLUDE: 'C:\LW\INCLUDE\LWSYSTEM.INC'
REM $INCLUDE: 'C:\LW\INCLUDE\GRAPHICS.INC'
REM $INCLUDE: 'C:\LW\INCLUDE\ANALYSIS.INC'
CALL GETMEM(64000)
n% = 10000
DIM bin&(n%), y#(n%), xx#(n%)
INPUT "Enter sample Orientation (0 or 90)  ";ang%
INPUT "Enter lower limit  ";ll#
```

```
INPUT "Enter upper limit  ";ul#
INPUT "Enter a filename (without extension!!) for input";namef2$
namef2$=namef2$+".DAT"
OPEN namef2$ FOR INPUT AS #2

range# = 0.001
WHILE NOT EOF(2)
     INPUT #2, ibin%
     INPUT #2, bin&(ibin%)
WEND
nbin%=ibin%

co% =5
ibin%=0
j%=0
y#(0)=0
WHILE ibin% <= nbin%
     x# = ibin%*range#/5000-range#
     IF (j%+1)*co% = ibin% THEN j%=j%+1 : y#(j%)=0 : xx#(j%)=0
     y#(j%) = y#(j%)+bin&(ibin%)
     xx#(j%)= xx#(j%) + x#/co%
     ibin%=ibin%+1
WEND
npts%=j%+1

CLOSE #2
              CALL GrfReset (12)
              CALL SetAxGridVis (-1, 0)
              port% = CreatePort (0, 5, 100, 85)
              CALL SetPlotMode (0)
              title3$ = "Number of YTTRIUM experiencing a given
              field vs dipolar field : 1.5% Co"
              CALL GrfPrint (6, 95, title3$)
              CALL SetAxAuto (0,0)
              CALL SetAxRange (0, ll#, ul#, 10)
              CALL SetAxName (0, "Dipolar field in T")
              CALL SetAxAuto (1,2)
              CALL SetAxRange (1, -0.03, 0.03, 10)
              CALL SetAxName (1, "No of Y at field")
```

```
            CALL SetCurv2D (1)
            CALL SetTitle ("Low T : Range= 0.001")
            CALL SetFrmColor (15)
            CALL SetGrdColor (15)
            CALL SetLblColor (15)
            angle$ = "Angle = C"+ STR$(ang%) + " B"
            kl$ = "(k,l)= 40 to 60 "
            file$ = "Input = " + namef2$ + "    " + date$ + "
            " + time$+"    " + kl$ + "    " + angle$
            CALL GrfMsg (file$,15)
            CALL SetPointStyle (9)
            CALL SetPlotMode (0)
            CALL SetCurv2D (2)
            CALL SetXDataType (4)
            CALL SetYDataType (4)
            CALL GrfCurv2D (xx#(), y#(), npts%)

SLEEP
SLEEP
SLEEP
CALL SetDisplayMode(0)
label100:
CLOSE #1
END
```

Appendix D

Miscellaneous Details

This appendix contains:

D.1 Block Diagram of the 141MHz Spectrometer.

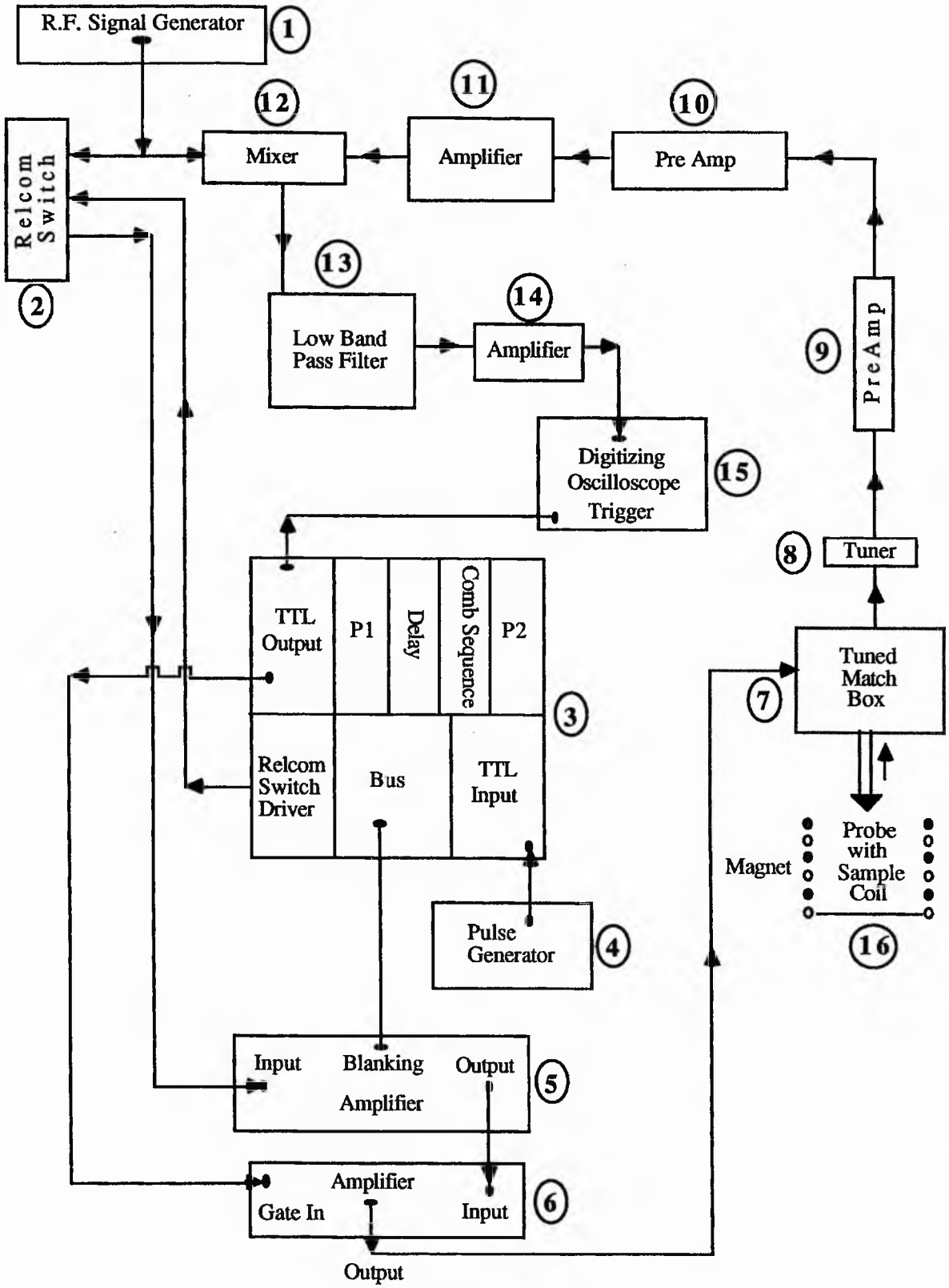

Figure D.1

A schematic diagram of the 141MHz Spectrometer. For key to components, see overpage.

Key to Figure D.1

1. FARNELL SSG 520 Signal generator
   Frequency range: 10-520 MHz with a resolution of 100Hz. Frequency stability ±2 in 10^6. Output level: 0dBm into 50Ω gives 224mV rms pd)
2. WATKINS JOHNSON (wj) S1 Relcom switch
   Frequency range: 0.5-500 MHz. Switching speed: 10 nsec (max): On-off ratio: 70 dB in the range 100-200 MHz.
3. 24 CHANNEL MODULAR SYSTEM Pulse generator
   Made to specification by J. M. Wade, Department of Physics, University of St. Andrews (1986). Developed to allow complex timing sequences involving fast and slow timing delays to be user defined. The rack system contains a number of monostable cards (pulse width generator) capable of producing pulses from 0.5 μsecs to 100 secs in eight one decade ranges. The TTL input allows the pulse sequences chosen to be 'triggered' by an external pulse generator, while the TTL output triggers the oscilloscope and the gate of amplifier 6. The system has a dedicated Relcom switch driver.
4. SIMPLE PULSE GENERATOR
   A home-made pulse generator which triggers the pulse sequences produced from (3) with a trigger frequency range of 0.1 to 50 Hz equivalent to an automatic pulse every 20 ms to 10 secs.
5. AMPLIFIER RESEARCH (AR) 150LA 60 to 150 Watt Pulse Amplifier
   Frequency range: 1-150MHz. Output level: 51dB (minimum)
6. KALMUS 500 WATT Linear Pulse Amplifier
   Frequency range (bandwidth): 80-200 MHz. Output level: typically 5dB
7. TUNED MATCHBOX
   Home-made tuned circuit for coupling the probe to the transmitter, incorporates a variable high voltage capacitor, an inductor and resistor. Crossed diodes protect the receiver from the transmitter pulse.
8. TUNER
   Home-made tuner circuit with a resistor, coil and variable capacitor.
9. MICROWAVE MODULES MMG144V 100 Watt Low Noise rf switched Preamplifier
   Frequency bandwidth: 144-148 MHz at ±1dB. Power gain: typically 12dB. Power requirement: 10-14V dc at 75mA, supplied by a COUTANT ELECTRONICS OA2 Operational Amplifier power supply.
10. PREAMPLIFIER
    Home-made preamp. with a power gain of 45dB and bandwidth of 5-400 MHz. Runs from a 15V COUTANT supply, as above.

11. VARIABLE GAIN AMPLIFIER
    Home-made variable gain amplifier. Requires two independent power supplies running at 24V (ROBARD VAREX 60-1) and 12V (COUTANT).
12. MINI CIRCUITS 15542 ZFM-2 DOUBLE BALANCED +7 dBm MIXER
    Frequency range 1-1000MHz. Impedence: 50 Ω.
13. LOW BANDPASS FILTER
    Home-made double filter system to control signal noise and deadtime.
14. STANDARD AMPLIFIER
    Home-made 1MHz amplifier with power gain of 20-25 dB.
15. HEWLETT PACKARD 54502A DIGITIZING OSCILLOSCOPE.
    A 400 MHz, 400 Msample/sec digizing scope with a signal averaging facility.
16. OXFORD INSTRUMENTS 12.7T CRYOMAGNET
    Variable field up to 12.7 T max. Field homogeneity: 1 in 10^5. Bore diameter: 40mm. Three coil magnet, in which the outer coil is Niobium tin wound and the inner is niobium titanium wound. Runs from an OXFORD INSTRUMENTS high current water cooled magnet power supply.

Notes

Figure D.1 contains the final spectrometer arrangement used in the NMR on all the Co-doped YBCO samples. An earlier version, used to obtain data on the pure YBCO compounds, produced significantly smaller signals and contained the following components in place of 6 and 15.

6' HEATHERLITE 2M EXPLORER 500 WATT LINEAR AMPLIFIER
Frequency range: 144-146 MHz

15' PHILIPS PM 3262 ANALOGUE OSCILLOSCOPE
Replaced by the trace function of 15.
THURLBY DSA 524 DIGITAL STORAGE ADAPTER
Replaced by the digizing, averaging and storage facility of 15.
PAR CW-1 BOXCAR INTEGRATOR
Gives the integrated area of a spin echo signal.

D.2 Simple Magneto-Resistance Probe

The following key refers to figure D.2, below.

1. SCHLUMBERGER SOLATRON 7150 Digital Multimeter
2. CAMBRIDGE INSTRUMENTS Co.Ltd. 1.0Ω Resistance Standard No. L-418015
3. OXFORD INSTRUMENTS 12.7 T superconducting magnet.
4. Non-inductively wound fine copper wire coil

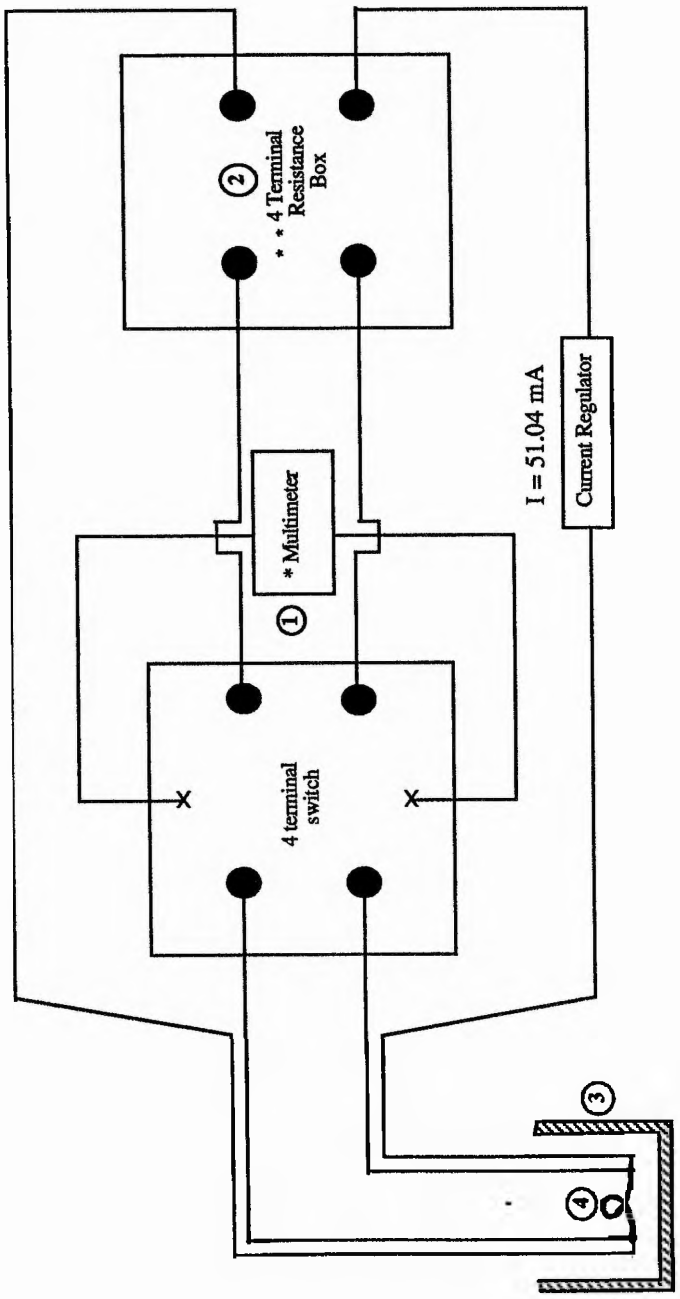

Figure D.2

Simple magneto-resistance probe circuit used to obtain magnetic field calibration (not drawn to scale).

D.3 Sample Channel Silver Coax

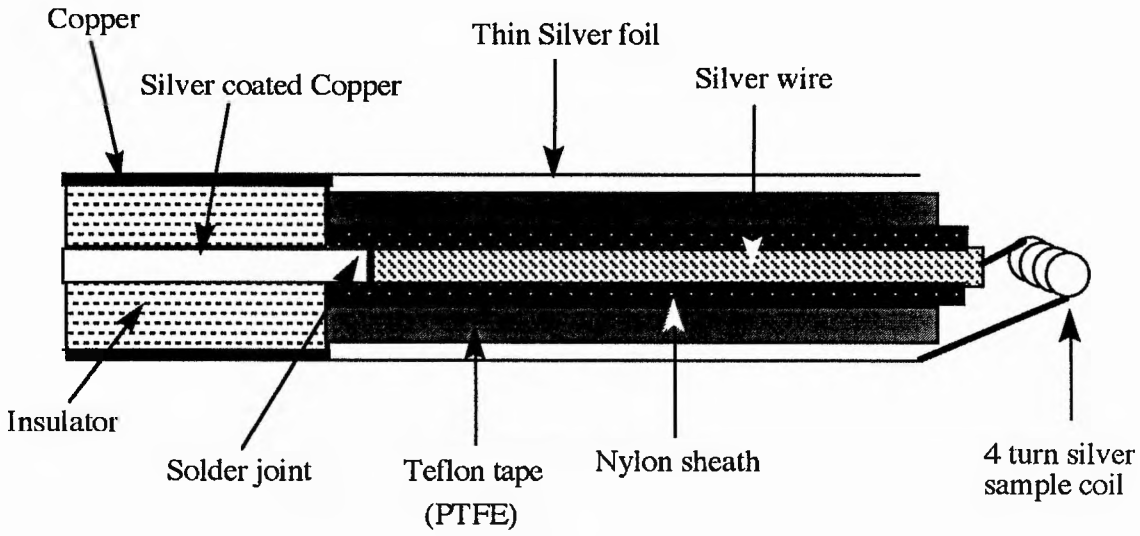

Figure D.3

Home-made sample channel silver coax, connected to a commercial Farnell copper coax.

Notes:

(i) A silver coax is necessary because the sample channel must be free from copper around the area of the sample.

(ii) The silver coax stretches approximately 15 cm from the sample and is then soldered to a standard Farnell copper coax. It is crucial that this solder joint is strong and clean as much signal could be lost in a weak joint.

(iii) Nylon protective winding was strapped around the silver coax to strenghten it. For clarity this has been omitted from the diagram.

D.4 Stycast Specifications

Emerson & Cuming, Inc.

DIELECTRIC MATERIALS DIVISION
CANTON, MASSACHUSETTS

TECHNICAL BULLETIN 7-2-26C

STYCAST 1266

Transparent High Impact Room Temperature Cure
Epoxy Casting Resin

Stycast 1266 is a clear, low viscosity casting resin which when fully cured has outstanding toughness and impact strength. Stycast 1266 can be cured at room temperature.

Stycast 1266 has been used for display embedments. It has been used to bond lenses and sheets of glass for good visibility. Stycast 1266 has good moisture resistance, electrical properties and adhesion to metal, glass and plastics. After catalyst addition, viscosity at room temperature is extremely low, making it easy to pour. Vacuum processing is not always needed. It will readily impregnate windings.

Long exposure of the cured resin to temperatures above 250°F will cause some discoloration. Physical and electrical properties are not appreciably affected.

Typical Properties:

Specific Gravity	1.18
Hardness, Shore D	75
Izod Impact, ft. lbs. /in. of notch	2
Compressive Strength, psi	10,000
Tensile Strength, psi	6,000
Volume Resistivity, ohm-cm	6×10^{14}
Dielectric Strength, volts/mil	400
Dielectric Constant, at 10^6 cps	3.5
Dissipation Factor, at 10^6 cps	0.02
Flexural Strength, psi	20,000

Instructions for Use:

1. Prepare materials and mold for use.
2. Add 28 parts of Part B to 100 parts by weight of Part A. Mix thoroughly. Pot life will be about 1/2 hour. Use small batches. Use multiple pouring for castings over 100 grams.
3. Pour. Use vacuum evacuation if necessary.
4. Allow to stand at room temperature for 8 hours. The casting can be removed from mold when hard. A post cure at 200°F for 2 hours will increase the hardness of the cured resin and its dielectric constant.
5. Curing at temperatures of 125°F - 150°F to speed production is possible, and depends both on resin mass, and the geometry of the unit to be potted. To determine optimum conditions, user should run a few experiments on his particular unit.

Appendix E

List of Publications & Contributions to Scientific Meetings

E.1 Publications in Scientific Journals

[1] M. Solanki-Moser, D. P. Tunstall & W. J. Webster, High-Field Nuclear Magnetic Resonance in Aligned Powders of $YBa_2Cu_3O_7$, *Supercond. Sci. Technol.* **3** 464 (1990).

[2] D. P. Tunstall & W. J. Webster, Nuclear Magnetic Resonance in Cobalt-Doped $YBa_2Cu_3O_{7-\delta}$, *Supercond. Sci. Technol.* **4** S406 (1991).

[3] W. J. Webster, D. P. Tunstall, P. F. Freeman & J. R. Cooper, Microscopic Aspects of Cobalt Doping in $YBa_2Cu_3O_{7-\delta}$: An Y-NMR Study, *Physica C* **185-189** 1079 (1991).

[4] D. P. Tunstall, G. P. Dai, W. J. Webster, H. F. Booth, S. Arumagam, R. S. Liu & P. P. Edwards, A Thallium, Yttrium & Copper NMR Study of the $(Tl_{0.5}Pb_{0.5})Sr_2(Ca_{1-y}Y_y)Cu_2O_{7-\delta}$ System, *Supercond. Sci. Technol.* **6** 33 (1993).

[5] G. P. Dai, D. P. Tunstall, W. J. Webster, H. F. Booth, S. Arumagam, R. S. Liu & P. P. Edwards, Yttrium NMR Study of the $(Tl_{0.5}Pb_{0.5})Sr_2(Ca_{1-y}Y_y)Cu_2O_{7-\delta}$ System, BHTSC '92 Conference Proceedings, special issue of World Scientific Publishing (in press, 1993).

[6] D. P. Tunstall, G. P. Dai & W. J. Webster, ^{63}Cu Nuclear Quadrupole Resonance in Co-doped $YBa_2Cu_3O_{7-\delta}$ (to be published).

E.2 Contributions to Scientific Meetings

[1] M. Solanki-Moser, D. P. Tunstall & W. J. Webster, NMR Experiments in Aligned Powders of $YBa_2Cu_3O_7$, Annual I.O.P Solid State Physics Conference, University of Warwick, U. K., 19th-21st December, 1989.

[2] W. J. Webster & D. P. Tunstall, Nuclear Magnetic Resonance Studies of Cobalt-Doped $YBa_2Cu_3O_{7-\delta}$, LT-19 Satellite Conference on High Temperature Superconductivity, University of Cambridge, U. K., 13th-15th August, 1990.

[3] W. J. Webster & D. P. Tunstall, Nuclear Magnetic Resonance Studies on the Cobalt-Doped Y-Ba-Cu-O System, Solid State NMR New Materials & New Techniques, British Radiofrequency Spectroscopy Group & Royal Society of Chemistry NMR Discussion Group Meeting, University of Warwick, U. K., 5th-7th September, 1990. (Oral Presentation)

[4] W. J. Webster & D. P. Tunstall, NMR Studies of Co-Doped YBCO, 39th Scottish Universities (NATO) Summer School on High Temperature Superconductivity - Materials, Mechanisms & Devices, University of St. Andrews, U. K., 16th-29th June, 1991.

[5] W. J. Webster, D. P. Tunstall, P. F. Freeman & J. R. Cooper, Microscopic Aspects of Cobalt Doping in $YBa_2Cu_3O_{7-\delta}$: An ^{89}Y NMR Study, Materials & Mechanisms of Superconductivity - High Temperature Superconductors III (M^2S-HTSC III) Internanational Conference, Kanazawa, Japan, 22nd-26th July 1991.

[6] D. P. Tunstall, W. J. Webster & S. Arumagam, Magnetic Effects of Co-Doping in $YBa_2Cu_3O_{7-\delta}$: A Microscopic Scale Experiment, Special Colloquia Ampére on Nuclear Magnetic Resonance, Zürich, Switzerland, August 1991.

[7] D. P. Tunstall, S. Arumagam & W. J. Webster, Cobalt doped YBCO - The Effect of Dipolar Fields, Condensed Matter & Materials Physics 1991 Conference (CMMP-91), University of Birmingham, U. K., 17th-20th December, 1991.

[8] G. P. Dai, D. P. Tunstall, W. J. Webster, H. F. Booth, S. Arumagam, R. S. Liu & P. P. Edwards, Yttrium NMR Study of the $(Tl_{0.5}Pb_{0.5})Sr_2(Ca_{1-y}Y_y)Cu_2O_{7-\delta}$ System, Beijing International Conference on High T_c Superconductivity (BHTSC '92), Beijing, China, 25th-29th May 1992. (Oral Presentation by G. P. Dai)

It is anticipated that other parts of this thesis will be submitted for publication in the future.